



**UNIVERSITÀ DEGLI STUDI DELL'AQUILA
DIPARTIMENTO DI INGEGNERIA INDUSTRIALE E DELL'INFORMAZIONE E DI
ECONOMIA**

Dottorato di Ricerca in
INGEGNERIA INDUSTRIALE E DELL'INFORMAZIONE E DI ECONOMIA
XXXIII ciclo

Titolo della tesi

*Innovative and sustainable processes for the synthesis of metal hydroxides/oxides
nanoparticles. Application developments*

SSD ING-IND/22

Dottorando
Ludovico Macera

Coordinatore del corso
Prof. Giuseppe Ferri

Tutor
Prof.ssa Giuliana Taglieri

A.A. 2019/2020

ABSTRACT

In the last decade, nanotechnologies have greatly developed in many research fields, such as engineering, biomedical, electronic and many others. They can offer several possibilities to design tools, to create new techniques or to improve the already existing ones, as well as to discover innovative applications. In fact, because of their small size, the characteristics and behaviours of nanomaterials can be very different compared to bulk materials having the same composition and can exhibit peculiar and new properties.

Nanomaterials are typically obtained through two main ways: one refers to the so-called "top-down" approach, the other is called "bottom-up". However, several of these synthesis methods are characterized by multistep or complex procedures, working at high temperature and non-ambient pressure, and requiring organic synthesis media or sophisticated apparatus. Such features lead to an unavoidable low production yield and to an increase of times and costs to obtain pure products. For these reasons there is a lack of an economic method able to realize productions on large scale, which is of paramount importance for industrial applications, assuring a good control of the particles size and, at the same time, a desired not detrimental impact on the environment.

In order to design and to engineer the nanoparticles as well as to tailor their characteristics to the final application, this thesis is aimed to define new scalable methods to produce a wide range of metal oxide/hydroxide nanoparticles with high production yields and low costs. These methods are characterized also by a special attention towards the environmental impact, limiting the production of wastes and the energetic costs of the process itself. The innovative synthesis techniques reported in this thesis and developed at the Laboratory of Technology of Materials and Applied Chemistry of the DIIE Department of University of L'Aquila, are also object of a European patent (EP2880101) and of two Italian patents.

By starting from the innovative procedure routes, both the synthesis, the characterization (by means of several consolidated laboratory techniques and of cutting edge techniques), and the application of the different kinds of

nanoparticles were performed, from alkaline earth metal hydroxides/oxides to several type of iron oxides. Concerning the applications, different kinds of applicative interests were considered. Specifically, in Cultural Heritage, calcium hydroxide nanoparticles and calcium/iron oxide nanoparticles were successfully applied in the conservation of natural stones from architectonic monuments (biocalcarenes of Agrigento), and, thanks to the development of a prototype for large-scale production, in this thesis an extensive nanolime consolidation was realized, for the first time, on the facade of a historic building in L'Aquila. In addition, magnesium hydroxide nanoparticles were applied in the deacidification of ancient wood samples of a historic vessel. Moreover, in biomedical sector, magnesium oxide nanoparticles were preliminary investigated as anticancer agents on melanoma cells, while superparamagnetic iron oxide nanoparticles (SPIONs) were tested as contrast agents for magnetic resonance imaging (MRI). Finally, this PhD work involved several relationships with different National and international research groups, including the Departments of Physics and Industrial Engineering of the University of L'Aquila, the Department of Life Health and Environmental Sciences (MESVA) of the University of L'Aquila and the CNR-IOM-OGG group in the European Photon and Neutron Science Campus (EPN) of Grenoble.

THESIS OBJECTIVES

The work presented in this thesis is focused on the design and the optimization of innovative and scalable methods to produce a wide range of metal oxide and hydroxide nanoparticles, with low environmental impacts, high production yields and low synthesis times. After the synthesis, a deep characterization study of the nanoparticles both by means of ordinary as well as by cutting edge-methods is carried out. In addition, a special attention to some applications of the produced nanoparticles were considered. In particular, this research has been aimed to:

- Realization and optimization of a scale-up procedure for the production of calcium hydroxide nanoparticles, in order to analyze the potentiality of the procedures towards the design of a pilot plant, and making possible the great potential of such innovative product to satisfy the wide demand and extensive applications in Cultural Heritage;
- Development of innovative scalable methods for the synthesis of other alkaline earth metal nanoparticles, overcoming the disadvantages of the existing methods, in order to extend their use in the field of Cultural Heritage;
- Development of a procedure to obtain innovative nanoparticles of calcium/iron oxides, which may be a new material for applications both in the field of Cultural Heritage and in the environmental remediation field;
- Preliminary application of magnesium oxide nanoparticles as anticancer agents;
- Development of an original and scalable procedure to synthesize iron oxide nanoparticles, overcoming the disadvantages of the methods reported in literature concerning production yields and environmental impact;
- Application as contrast agents in magnetic resonance imaging (MRI) of superparamagnetic iron nanoparticles synthesized by means of the innovative procedure.

ACHIEVED RESULTS

The main achievements earned during this PhD program have been:

- Design of a controllable and cyclic scale-up procedure to obtain calcium hydroxide nanoparticles, concerning the increase of the volume reaction by two orders of magnitude guaranteeing high quality, in terms of purity, crystallinity, nanosized dimension and reactivity;
- First extensive application of calcium hydroxide nanoparticles, in relation to the consolidation of the original mortar of a historic building of L'Aquila (Palazzo Pica Alfieri, 14th-16th century). The effectiveness of the treatment is analysed in terms of depth of penetration, surface cohesion and resistance to perforation;
- Complete study of the carbonation process for calcium hydroxide nanoparticles, using synchrotron light at the Elettra laboratories (Trieste) inside capillaries, on laboratory slides and on carbonate matrix surfaces, which show a complete transformation into pure calcite depending on the presence of water and CO₂, but also on the exposure surface;
- Production of innovative calcium/iron oxide hydrate nanoparticles and complete characterization using several instrumental techniques, such as XRD, FTIR, TEM, SEM, BET and XAS with synchrotron light, carried out at the European Synchrotron Radiation Facility of Grenoble. These nanoparticles are able to completely convert into coloured calcite as the only crystalline phase, with iron remaining in amorphous form to cover homogeneously the calcite crystals;
- Application of the synthesized calcium hydroxide nanoparticles and calcium/iron oxide nanoparticles in Cultural Heritage for consolidation treatments on the biocalcarenes of Agrigento, by using formulations aimed at guaranteeing the compatibility with the original substrate also in terms of chemical compatibility with the stone, together with a reinforcement of the substrate, proved by a considerable improvement of the superficial cohesion and of the average resistance to drilling;
- Production of alkaline earth metal nanoparticles with an innovative method, in particular magnesium, strontium and barium, and characterization using several

instrumental techniques, such as XRD, FTIR, TEM, AFM and BET, obtaining pure and crystalline particles with sizes lower than 50 nm;

- Application of magnesium hydroxide nanoparticles in restorative treatments on ancient wood samples of an historical vessel (Gallo-Roman wreck, 2nd century b.C.), obtaining always neutral pH values with treatments durable over time by penetrating inside the wood fibers;
- Preliminary cytotoxicological tests on cancer cells using magnesium oxide nanoparticles, in collaboration with the research group of Pharmacology (MESVA Department of University of L'Aquila), resulting in a toxicity towards cancer cells attributed to the generation of reactive oxygen species (ROS);
- Production of iron oxides nanoparticles by means of an innovative method and characterization by several instrumental techniques, such as XRD, XPS, FTIR, TEM, SEM, AFM, TG-DTA, BET and magnetic measurements. Several nanometric compounds were obtained, such as ferrihydrite, hematite, magnetite and maghemite, characterized by sizes ranging from 2 to 40 nm and specific surface areas ranging from 20 to 420 m²/g;
- Magnetic resonance imaging (MRI) tests using superparamagnetic iron nanoparticles as contrast agents, in collaboration with the high-field MRI Laboratory (MESVA Department of University of L'Aquila), resulting in good relaxivity values using magnetite nanoparticles coated with different polymers, in order to improve the suspension stability and biocompatibility.

PREFACE

During the PhD Program several papers were published as follows:

Scientific publications, indexed by SCOPUS:

- 1) Taglieri G, Daniele V, Macera L, Mondelli C. “Nano Ca(OH)₂ synthesis using a cost-effective and innovative method: reactivity study.” *Journal of American Ceramic Society* 2017; 100(12):5766-5778
- 2) Taglieri G, Otero J, Daniele V, Gioia G, Macera L, Starinieri V, Charola AE. “The biocalcarene stone of Agrigento (Italy): Preliminary investigations of compatible nanolime treatments.” *Journal of Cultural Heritage* 2018; 30:92–99
- 3) Daniele V, Taglieri G, Macera L, Rosatelli G, Otero J, Charola AE. “Green approach for an eco-compatible consolidation of the Agrigento biocalcarenes surface.” *Construction and Building Materials* 2018; 186:1188–1199
- 4) Taglieri G, Daniele V, Macera L. “Synthesizing alkaline earth metal hydroxides nanoparticles through an innovative, single-step and eco-friendly method.” *Solid State Phenomena* 2019; 286:3-14
- 5) Iacoboni I, Perrozzi F, Macera L, Taglieri G, Ottaviano L, Fioravanti G. “In situ syntheses of hydroxyapatite-grafted graphene oxide composites.” *Journal of Biomedical Materials Research Part A* 2019; 107(9):2026-2039
- 6) Taglieri G, Daniele V, Macera L, Mignemi A. “Innovative and green nanolime treatment tailored to consolidate the original mortar of the façade of a medieval building in L'Aquila (Italy).” *Construction and Building Materials* 2019; 221:643-650
- 7) Taglieri G, Rigaglia D, Arrizza L, Daniele V, Macera L, Rosatelli G, Romè V, Musolino G. “Microanalytical investigations on a Byzantine fresco of the Dormitio Virginis from Sicily.” *Journal of Cultural Heritage* 2019; 40:155-162
- 8) Macera L, Taglieri G, Daniele V, Passacantando M, D’Orazio F. “Nano-sized Fe(III) oxide particles starting from an innovative and eco-friendly synthesis method.” *Nanomaterials* 2020; 10(2):323
- 9) Daniele V, Macera L, Taglieri G, Di Giambattista A, Spagnoli G, Massaria A, Messori M, Quagliarini E, Chiappini G, Campanella V, Mummolo S, Marchetti E,

Marzo G, Quinzi V. "Thermoplastic disks used for commercial orthodontic aligners: complete physico-chemical and mechanical characterization." *Materials* 2020; 13:2386

10) Taglieri G, Daniele V, Macera L, Schweins R, Zorzi S, Capron M, Chaumat G, Mondelli C. "Sustainable Nanotechnologies for Curative and Preventive Wood Deacidification Treatments: An Eco-Friendly and Innovative Approach". *Nanomaterials* 2020; 10(9):1744

11) Macera L, Gigli L, Daniele V, Plaisier JR, Arrizza L, Taglieri G. "Synchrotron investigations of the nanolime reactivity on Biocalcarenite stone surfaces". *Construction and Building Materials* 2020; 262:120066

12) Macera L, Daniele V, Mondelli C, Capron M, Taglieri G, "New sustainable, scalable and one-step synthesis of iron oxide nanoparticles by ion exchange process". *Nanomaterials* 2021; 11(3):1–19, 798

13) Daniele V, Macera L, Taglieri G, Di Giambattista A, Spera L, Marzo G, Quinzi V "A first complete comparative analysis of the chemico-physical features of PETG and PU based orthodontic aligners for Clear Aligner Therapy", submitted to *BMC Oral Health* 11/04/2021

Other scientific publications:

1) Falvello L, Lotti P, Massera C, Tarantino S, ... Macera L, ... Tusha G. "Poly[(μ 4-phenyl-phospho-nato)zinc(II)]." *IUCr DATA* 2019; 4(9):191222

Patents:

1) "Procedimento per la sintesi di nanoparticelle di ferridrite o di magnetite mediante resine a scambio ionico". Inventors: Taglieri G, Daniele V, Macera L. Italian patent approved on: 01/07/2020

2) "Procedimento per la sintesi di nanoparticelle di ossido di calcio e ferro idrato, $\text{Ca}_4\text{Fe}_2\text{O}_7 \cdot 13\text{H}_2\text{O}$ ". Inventors: Taglieri G, Macera L, Daniele V. Italian Patent Application filed on: 09/12/2020

Attendance at PhD Schools:

- 1) Frontiers in Hybrid Materials, 6th ISGS Summer School, 16/09/2018 – 19/09/2018, Alghero
- 2) AIC International Crystallography School, Crystallographic Information Fiesta 2019, 28/08/2019 - 03/09/2019, Napoli
- 3) Durability and corrosion, diagnostics and restoration techniques of reinforced concrete structures, postgraduate and specialization school “Luca Bertolini”, 9/09/2019 – 13/09/2019, Milano

ACKNOWLEDGMENTS

Ho sempre pensato che il Dottorato di Ricerca fosse l'opportunità per proseguire l'attività di ricerca che mi è sempre piaciuta ed era iniziata con la tesi di laurea, e se tornassi indietro lo rifarei allo stesso modo.

Giunto alla conclusione del presente lavoro di tesi, dedico un ringraziamento speciale al mio relatore, la Prof.ssa Giuliana Taglieri, per avermi concesso questa opportunità, offrendomi la possibilità di conoscere il mondo vasto e affascinante della ricerca, sia dietro il bancone che in giro per l'Europa. Grazie ai suoi insegnamenti continui ed alla grande fiducia, devo a lei sia la mia crescita professionale che quella umana in questi 3 anni.

Un ringraziamento speciale va anche all'ing. Valeria Daniele, che mi ha insegnato molte cose e mi ha dato l'opportunità di migliorare ulteriormente le mie competenze scientifiche, dunque rimarrà sempre un punto di riferimento, un'insegnante e anche un'amica, sempre pronta a spiegare ed interpretare insieme ogni risultato e ogni idea.

Ringrazio anche il Prof. Angelo Galante del Dipartimento MESVA per i suoi preziosi insegnamenti, la sua professionalità e la sua disponibilità nell'ambito dell'imaging di risonanza magnetica.

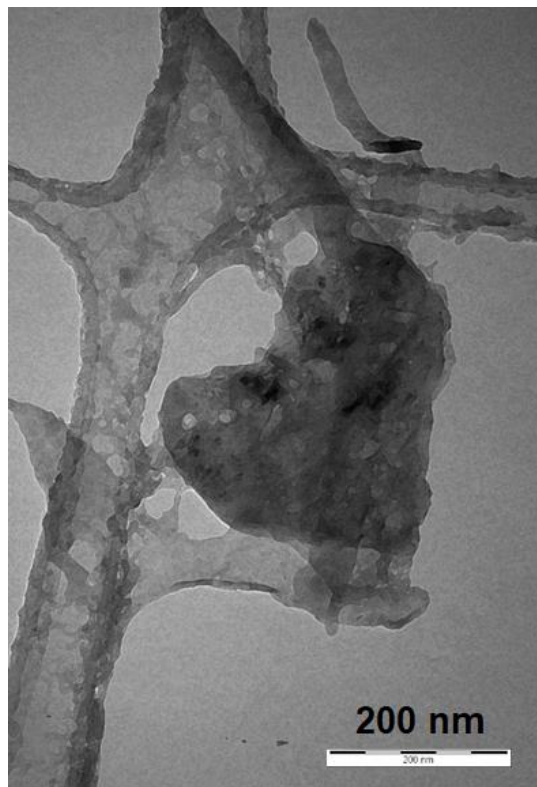
Un sentito ringraziamento va anche a tutte le persone che hanno collaborato con me e mi hanno guidato in questo percorso, in particolare Fabiola, Katia, Marcello e Giosy, sempre disponibili ad aiutare e a discutere insieme ogni risultato.

Durante questo dottorato ho avuto anche l'opportunità di viaggiare e di conoscere nuove realtà, in particolare a Grenoble (Francia) ho incontrato persone che mi hanno insegnato tanto, e da ogni viaggio sono tornato con nuove esperienze e conoscenze. Grazie al Prof. Francesco D'Acapito per avermi accolto presso l'European Synchrotron Radiation Facility (ESRF) di Grenoble e aver migliorato le mie conoscenze e le mie capacità. Ma soprattutto grazie alla Dr.ssa Claudia Mondelli che mi ha mostrato come si lavora negli esperimenti di ricerca internazionali, migliorando il mio modo di fare ricerca.

Per ultimo, ma non meno importante, poiché punto di riferimento per quanto riguarda tutta la microscopia elettronica, un ringraziamento a parte va al Dr. Lorenzo Arrizza, sempre disponibile ad eseguire le misure e fonte di idee per la sua vasta conoscenza nel settore scientifico.

Infine mi sembra doveroso ringraziare anche la mia famiglia, che mi ha sempre sostenuto e mi ha permesso di arrivare fino a questo punto. Inoltre, ringrazio tutte le persone che mi sono state vicine in questo periodo e hanno sempre creduto in me, trasmettendomi coraggio, amore e felicità nei momenti in cui ne avevo più bisogno.

Alla fine della storia un pensiero speciale va alle persone a me care che purtroppo non ci sono più, ma saranno sicuramente nel mio cuore.



INDEX

ABSTRACT	3
THESIS OBJECTIVES	5
ACHIEVED RESULTS	6
PREFACE	8
ACKNOWLEDGMENTS	11
INDEX	13
INTRODUCTION	16
PART I: PRELIMINARIES	19
CHAPTER 1: NANOPARTICLES SYNTHESIS AND APPLICATIONS	20
1.1 Nanotechnology and nanoscience	20
1.2 Nanomaterials classification	22
1.3 Nanomaterials synthesis	27
1.4 Properties, characteristics and applications of nanoparticles	30
1.4 Nanoparticles for medical applications	33
1.5 Nanoparticles effects on the health	37
CHAPTER 2: ALKALINE-EARTH METALS NANOPARTICLES.....	39
2.1 Calcium hydroxide nanoparticles (nanolime)	39
2.1.1 Synthesis methods of nanolime.....	41
2.1.2 Nanolime applications in Cultural Heritage	45
2.1.3 Other applications of nanolime	51
2.1.4 Commercial nanolime products: CaLoSiL and Nanorestore	52
2.2 Magnesium hydroxide and oxide nanoparticles	54
2.2.1 Synthesis and applications of magnesium oxide nanoparticles	54
2.2.2 Magnesium hydroxide nanoparticles in Cultural Heritage	57
2.3 Strontium hydroxide and carbonate nanoparticles	58
2.3.1 Synthesis and applications of strontium hydroxide nanoparticles	58
2.3.2 Strontium hydroxide nanoparticles in Cultural Heritage	59
2.4 Barium hydroxide and carbonate nanoparticles	60
2.4.1 Synthesis and applications of barium nanoparticles	61
2.4.2 Barium hydroxide nanoparticles in Cultural Heritage	62
CHAPTER 3: IRON OXIDE NANOPARTICLES.....	64
3.1 Magnetic properties of iron oxides.....	65
3.2 Superparamagnetic iron oxide nanoparticles (SPIONs).....	67
3.3 Synthesis of SPIONs and other iron oxide nanoparticles	70
3.4 Iron oxide nanoparticles in biomedical applications	76
3.5 Existing products containing iron oxide nanoparticles.....	80
PART II: EXPERIMENTAL SECTION	83

CHAPTER 4: NANOMATERIALS CHARACTERIZATION	84
4.1 X-ray diffraction (XRD)	84
4.2 X-ray fluorescence (XRF)	89
4.3 X-ray photoelectron spectroscopy (XPS)	90
4.4 X-ray absorption spectroscopy (XAS) with Synchrotron light.....	92
4.5 Fourier transform infrared spectroscopy (FTIR)	99
4.6 Thermogravimetric and differential thermal analysis (TG-DTA).....	100
4.7 Alternating gradient magnetometry (AGM).....	101
4.8 Transmission electron microscopy (TEM)	103
4.9 Scanning electron microscopy (SEM)	105
4.10 Atomic-force microscopy (AFM)	107
4.11 Surface area analysis (BET).....	109
4.12 Magnetic resonance imaging (MRI)	112
CHAPTER 5: SCALE UP SYNHTESIS OF NANOLIME	118
5.1 Nanolime synthesis with an innovative method.....	118
5.2 Scale-up procedure of the innovative method	121
5.3 Optimization of resin regeneration.....	129
5.4 Initial tests for a continuous nanolime production	134
5.5 Analysis of the nanolime reactivity	135
5.6 Aging tests for the storage of the produced nanolime.....	138
CHAPTER 6: SYNTHESIZED NANOLIME APPLICATIONS	142
6.1 The biocalcarenites of Agrigento	142
6.2 Nanolime treatments on biocalcarenites samples of Agrigrnto	147
6.3 Comparative treatments of nanolime on biocalcarenites with commercial products ..	157
6.4 Synchrotron investigations of nanolime carbonation process	164
6.5 Synchrotron investigations of nanolime reactivity on biocalcarenites	167
6.6 Nanolime treatments of the original mortar of a medieval building in L'Aquila	175
CHAPTER 7: SYNTHESIS AND APPLICATION OF TETRACALCIUM FERRITE HYDRATE NANOPARTICLES	185
7.1 Synthesis of tetracalcium ferrite hydrate in nanometric form	185
7.2 Design of a nanolime with iron tailored for Cultural Heritage	191
7.3 EXAFS measurements on tetracalcium ferrite hydrate NPs and tailored nanolime....	197
7.4 Possible applications of tetracalcium ferrite hydrate NPs	211
7.5 Application of tailored nanolime in Cultural Heritage.....	214
CHAPTER 8: SYNTHESIS AND APPLICATIONS OF OTHER EARTH-ALKALINE NANOPARTICLES	224
8.1 Synthesis of nanoparticles based on magnesium, strontium, and barium	224
8.2 Magnesium hydroxide nanoparticles for deacidification of waterlogged wood	235
8.3 Synthesis of magnesium oxide nanoparticles	243
8.4 Magnesium oxide nanoparticles for anticancer applications	253
8.5 Results of anticancer tests compared with the literature.....	263

CHAPTER 9: SYNTHESIS OF NANO-SIZED IRON OXIDES	266
9.1 Synthesis and characterization of various iron oxides NPs	266
9.2 Calcination of iron oxides NPs as precursors to obtain hematite and maghemite NPs	279
9.3 Tunable transformation of ferrihydrite NPs into of Hematite NPs	287
CHAPTER 10: COATED MAGNETITE NANOPARTICLES FOR MRI	298
10.1 Coating of the synthesized magnetite nanoparticles	298
10.2 Direct synthesis of coated superparamagnetic NPs (SPIONs)	301
10.3 MRI measurements using optimal samples of SPIONs	305
CONCLUSIONS	316
APPENDIX A –MATLAB PROGRAM	321
BIBLIOGRAPHY	328

INTRODUCTION

Nanotechnologies represent today an innovative approach based on the understanding and in-depth knowledge of the properties of matter at the nanoscale. Norio Taniguchi of Tokyo Science University coined the term in 1974 to describe the manufacture of materials and artefacts with nanometric tolerances. Currently, the term nanotechnology refers to a branch of science that deals with the design, characterization, production and application of structures, devices and systems that provide for the control of shape and size at the nanometric scale, known also as nanomaterials.

Nanomaterials have much larger and more active surface areas than bulk materials. This peculiarity is at the basis of the significant properties that make nanomaterials attractive both for their fundamental scientific interest and for their wide usage possibilities in many technological applications. According to the ISO (International Standards Organization), nanomaterials are defined as materials whose structural elements - clusters, crystals or molecules - have at least one external dimension in the range 1-100 nm. If all three external dimensions are in the range 1-100 nm, we talk about nanoparticles, having therefore characteristics not evident in the bulk materials.

Europe made investments in many nanoscience programs since 1990 and the current aim is to ensure that industry can take advantage of innovative products and processes derived from nanomaterials. In recent years, many research efforts have focused on the development of novel synthetic methods of nanomaterials, in order to make their production appealing for industrial applications.

Nanomaterials are typically obtained through two main ways: one refers to the so-called "top-down" approach, the other is called "bottom-up". The first one consists in reducing the dimensions of the structures to nanometric levels with physical methods, while the second has as its starting molecules or molecular aggregates that have the ability to self-assembly or self-organize into higher order structures. However, several of these synthesis methods are characterized by multistep or complex procedures, working at high temperature and non-ambient pressure, and requiring organic synthesis media or sophisticated apparatus.

Such features lead to an unavoidable decrease of production yields and increase of times and costs to obtain the final pure product. Despite the fact that production processes can be characterized by considerable costs, the production of nanomaterials is currently a booming sector, and so the real challenge is today represented from the possibility to increase the production to an industrial scale at affordable costs.

This thesis is aimed to define new scalable methods to produce a wide range of metal oxide and hydroxide nanoparticles with high yields and low costs. These methods are characterized also by a special attention towards the environmental impact, limiting the production of wastes and the energetic costs of the process itself. These bottom-up production methods are based on a single-step ion exchange process, which allows to obtain pure nanoparticles in extremely short times, working in water, at room temperature, atmospheric pressure and starting from cheap or renewable reagents, according to a cyclic procedure potentially scalable to an industrial level. The innovative synthesis techniques reported in this thesis, and developed at the Laboratory of Technology of Materials and Applied Chemistry of the DIIE Department, are also object of a European patent (EP2880101) and of two Italian patents.

Using this innovative method, the synthesis and the application of different kinds of nanoparticles were performed, from alkaline earth metal hydroxides/oxides to iron hydroxides/oxides. The structural and morphological features of the produced nanoparticles were investigated by several techniques, such as X-ray diffraction (XRD), X-ray absorption spectroscopy (XAS), X-ray photoelectron spectroscopy (XPS), Fourier transform infrared spectroscopy (FTIR), thermal analysis (TG-DTA), alternating gradient magnetometry (AGM), atomic-force microscopy (AFM), transmission and scanning electron microscopy (TEM, SEM), surface area analysis (BET). Then these nanoparticles were applied in different fields. In particular calcium hydroxide nanoparticles and calcium/iron oxide nanoparticles were successfully applied in the conservation of Cultural Heritage, and for the first time a large scale consolidation using nanomaterials was realized on the facade of a historic building. Magnesium hydroxide nanoparticles were applied both in the deacidification of ancient wood samples of a historic vessel

and in a preliminary study as anticancer agents. Finally, superparamagnetic iron oxide nanoparticles (SPIONs) were tested as contrast agents for magnetic resonance imaging (MRI).

PART I: PRELIMINARIES

CHAPTER 1: NANOPARTICLES SYNTHESIS AND APPLICATIONS

Starting a new project is always a challenge and one of the first difficulty is to understand the state of art of the topic, using literature to know how to handle research in the optimum conditions. This is the way to save money and time, to avoid useless experiments and to focus on variations and developments of tests already done and reported in the scientific literature.

To understand what are the properties characterizing nanoparticles (NPs), we need to know their purpose and usage. So, it is important to study the opportunities offered by the field of nanotechnology and its applications in several fields, from diagnosis and therapy for medicine to Cultural Heritage, in particular those obtainable with nanoparticles.

1.1 Nanotechnology and nanoscience

In the beginning, the terms “nanotechnology” and “nanoscience” had quite similar meaning. Actually, nanotechnology refers to production, characterization, design and application of devices and structures to control size and form of nanoscale components. On the other hand, nanoscience is the study of phenomena and the manipulation of materials at molecular or atomic scales, where properties are significantly different from major scales.

A nanometer (nm) is equal to one billionth of a meter (10^{-9}m). A human hair is wide about 80000 nm, while a red globule is about 3000 nm (Figure 1.1). Atoms are smaller than a nanometer, while some molecules, such as antibodies or proteins, are in the size range 1-100 nm.

The principal effects that mark the properties of nanomaterials, compared to the same materials at a greater scale, are the increase of the ratio between surface and volume and the quantum effects. Nanosciences study how they influence the properties of materials, while nanotechnologies try to use these effects to build systems and structures with new properties and functions.

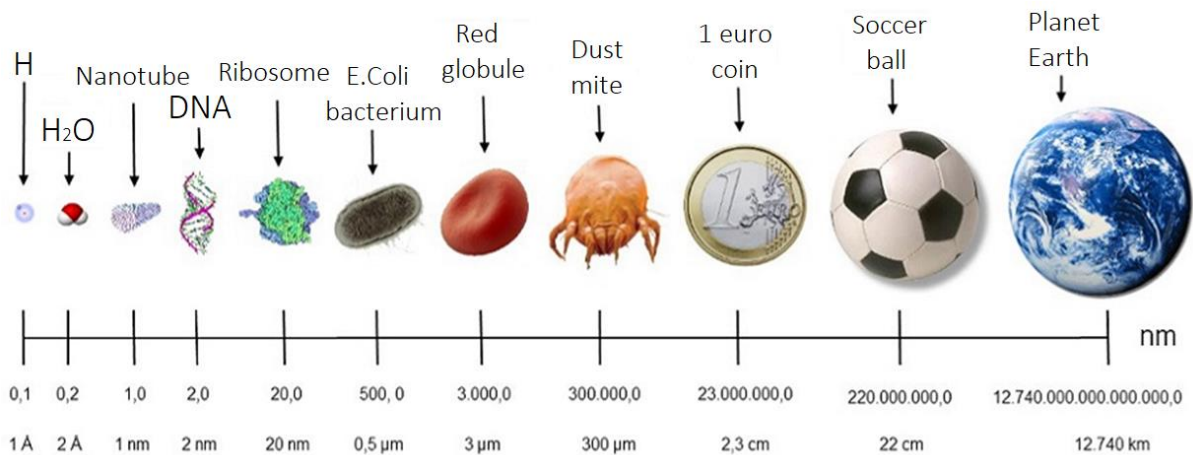


Figure 1.1: Nanoscale dimensions referred to the diameter of different forms of matter: from a hydrogen atom to planet Earth. [1]

The use of nanocomposites is very ancient; for example, in the tenth century, nanometric pigments were used as dyes in glass and ceramics. But only in recent years, the need to investigate and manipulate nanoscale systems has improved the interest in these materials and the design of instruments that can exploit these opportunities.

Nanosciences and nanotechnologies comprehend a great number of fields: physical, chemical, medical, biological, electronics and engineering. The main subdivisions of nanosciences are: nanomaterials, nanometrology, bio-nanotechnology and optoelectronics. The production of nanomaterials, with dimensions less than 100 nm, is advantageous for the fabrication of components in industrial fields, such as automotive sector, information technology and aerospace industry. Probably in future years, nanomaterials will increase performance in a multiplicity of products, such as displays, paints, silicon electronics, sensors and catalysts.

Actually nanomaterials are used to create thin coating films, for example, in electronics and in active surfaces, such as self-cleaning windows. In most cases nanomaterials are sited on some supports, but some types of nanoparticles are used free, as in sunscreens: the particles of these creams have a structure capable to absorb the UV rays of the sun and to protect the skin. Among nano compounds, carbon nanotubes result also very promising, consisting in hollow tubes with carbon molecules which have a great electrical conductivity, a great resistance and a good flexibility; they can change the field of electronics. New products that are likely to be popular are: lubricants

based on inorganic nano-spheres; medical nano-ceramics with better durability and better prosthetics applications; nano-membranes for a better water purification; magnetic nanomaterials for the storage of data. Quantum dots are semiconductor nanoparticles developed in recent years; they can be tuned to emit or absorb light of a specific colour to be used in solar cells or in the fluorescence labelling in biological experiments. Applications of nanotechnology in medicine are very promising, with different areas of interest, as the diagnosis of diseases, the molecular imaging and the drug delivery in specific parts of the body. In medical field, the goal would be to produce new materials and tools, such as scaffolds for cell engineering and sensors for direct monitoring of human parameters. Maybe in the coming years nanotechnology will help also to produce complex structures, as the cochlea and retina, and to understand how complex biological structures are composed. [2]

1.2 Nanomaterials classification

Materials, having well defined physical properties in the macroscopic scale, can express quite different properties in the nanometer scale. An example is the copper, usually malleable and ductile, which, if produced in size below 50 nm, loses its malleability and ductility becoming a very hard material.

Fundamental characteristics of a material, as resistance, surface reactivity and electrical properties are size-dependent, in particular related to the number of atoms on the surface respect to total amount of atoms. For a microstructure this ratio between surface atoms and total atoms is very low, while for example a particle with size of 30 nm has about 5% of atoms on its surface, a particle with size of 10 nm has about 20% on its surface. Therefore, a material will be more reactive in its nanometric form compared to the microscopic one.

Quantum effects modify electrical, optical and magnetic properties, depending on the size of the object. In some metals very small sizes can also affect the mechanical properties, because the grain boundaries slow or completely stop the propagation of defects when the material is stressed, so if the grains become nanometric, the number

of interaction between boundaries increases exponentially. For instance, in some experimental tests nanocrystals of nickel resulted much more resistant than steel. [3] Nanomaterials are defined as those structures that have at least one dimension in the nanometric range (1-100 nm). Films or coatings are nano-sized only in one dimension, nanotubes or nanowires have two nano-sized dimensions, nanoparticles and quantum dots have all three nano-sized dimensions. In this definition it is possible to find also materials with macroscopic scale or materials made of nanometer-sized grains. A typical classification of nanomaterials is to indicate the number of macroscopic dimensions (Figure 1.2):

- 3D nanomaterials: without dimensions at the nanoscale, because they are composed from the aggregation of clusters having nanometric dimensions (nano-porous materials);
- 2D nanomaterials: having one dimension at the nanoscale and two dimensions at the macroscale (thin films and layered surfaces);
- 1D nanomaterials: having two dimensions at the nanoscale and one dimension at the macroscale (nanotubes, nanofibers and nanowires);
- 0D nanomaterials: having all dimensions at the nanoscale (quantum dots, fullerenes, dendrimers and nanoparticles).

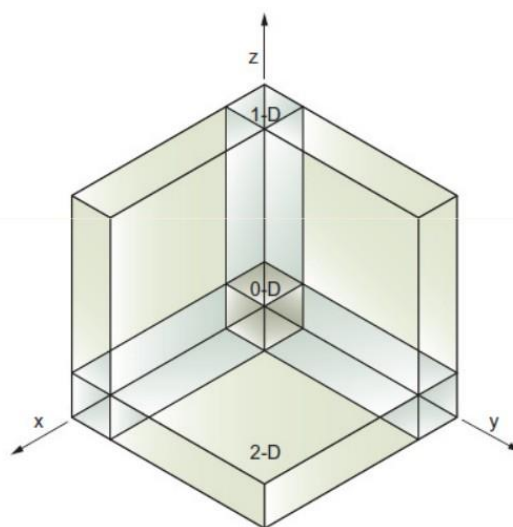


Figure 1.2. Classification of nanomaterials

3D nanomaterials have recently gained research interests because these kind of nanostructures have high surface areas and supply many absorption sites in small spaces. Such materials with high porosity in three dimensions can also lead to a better

transport of molecules. For these reasons, 3D nanostructures find applications in the area of catalysis, magnetic material and electrode material for batteries. In Figure 1.3 a typical 3D nanomaterial is reported. The behaviour of these materials depends on the sizes, shapes and morphologies of their sites, which are the key factors for their performances and applications. [3]

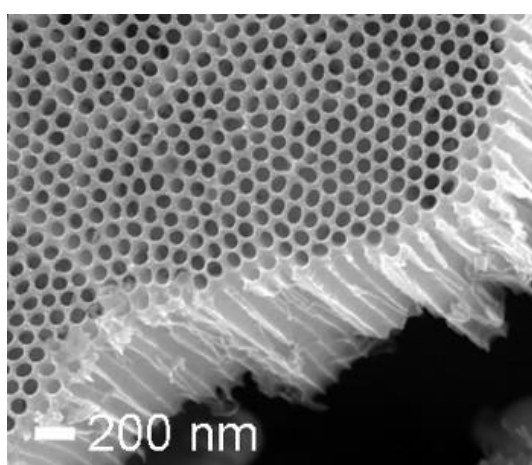


Figure 1.3. SEM image of a typical 3D nanomaterial: nanostructure is related to pore dimension

Materials having one nanometric dimension, or 2D nanomaterials, such as active surfaces and thin films, have been used for decades in chemistry, electronics and engineering; probably the greatest use occurred in the production of silicon integrated circuits. The use of monolayer thickness of a molecule is widespread in chemistry, lubricants and hydrophobic coatings. The large surface area can be employed in many applications, mainly in chemical and energetic sectors, as catalysts or cells with fuel, where great selectivity and reactivity are exploited to reduce the use of resources.

The investigation of nanostructures having two nanoscale dimensions, or 1D nanomaterials, covers about the last 20 years. The interest in this kind of structure is to have enhanced mechanical and electrical properties. The most common of these materials are carbon nanotubes, which are rolled graphene sheets single wall or multi-wall, as reported in Figure 1.5. Typically, the diameter is of few nanometres and the length can be from some micrometres to few centimetres. Carbon nanotubes are mechanically strong, the Young's modulus value is greater than 1 terapascal, which is similar to diamond; but they are also flexible and good electrical conductors. Their applications concern the reinforcement of composite materials, sensors, nano-

electronics and displays. There are also nanotubes of inorganic compounds, such as molybdenum disulphide or titanium dioxide, having very good properties as lubricants, catalysts and energy storage (high capability to stock oxygen and lithium).

The main structures having all three nanometric dimensions, or 0D nanomaterials, are quantum dots, fullerenes, dendrimers and nanoparticles especially.

Quantum dots are semiconductor particles lower than 100 nm, which were created in the 80's. When the particles of semiconductors are in the nanometric range quantum effects become relevant, because the semiconductors surface becomes no more homogeneous and presents electrons or no charge zones. The energy of these particles mainly depends on the wavelength of the quantum state characterizing the surface and the colour gives information on their size. In fact, semiconducting materials are able to absorb light and when they release that energy they transform it into different colour of light; the specific colour that is produced depends on the size of the material, as shown in Figure 1.4. So, the quantum dots can be created to absorb and emit a required wavelength, just changing the size. Semiconductor particles have established applications in the field of solar cells, composites and tools for fluorescence analysis of biological molecules. In these fields quantum dots can be used to emit at different energy levels. These applications led to the production of high quality particles, monodisperse, crystalline and coated, which can have dimensions lower than 2 nm in diameter, and can also be used as markers in processes or in treatments of reagents. [4]



Figure 1.4. Quantum dots effects on light emission depending on the size of the material [4]

In the last decades of the XX century was discovered also a new class of materials based on carbon named fullerenes: C60 is the most famous, which is a spherical

molecule (1 nm in diameter) composed by 60 carbon atoms forming 20 hexagons and 12 pentagons (Figure 1.5). A method to produce huge quantities of fullerene involves heating treatments of small bars of graphite in inert atmosphere (helium). The principal applications employing fullerene are: carrier for drug delivery, electronic circuits and lubricant for surfaces. [5]

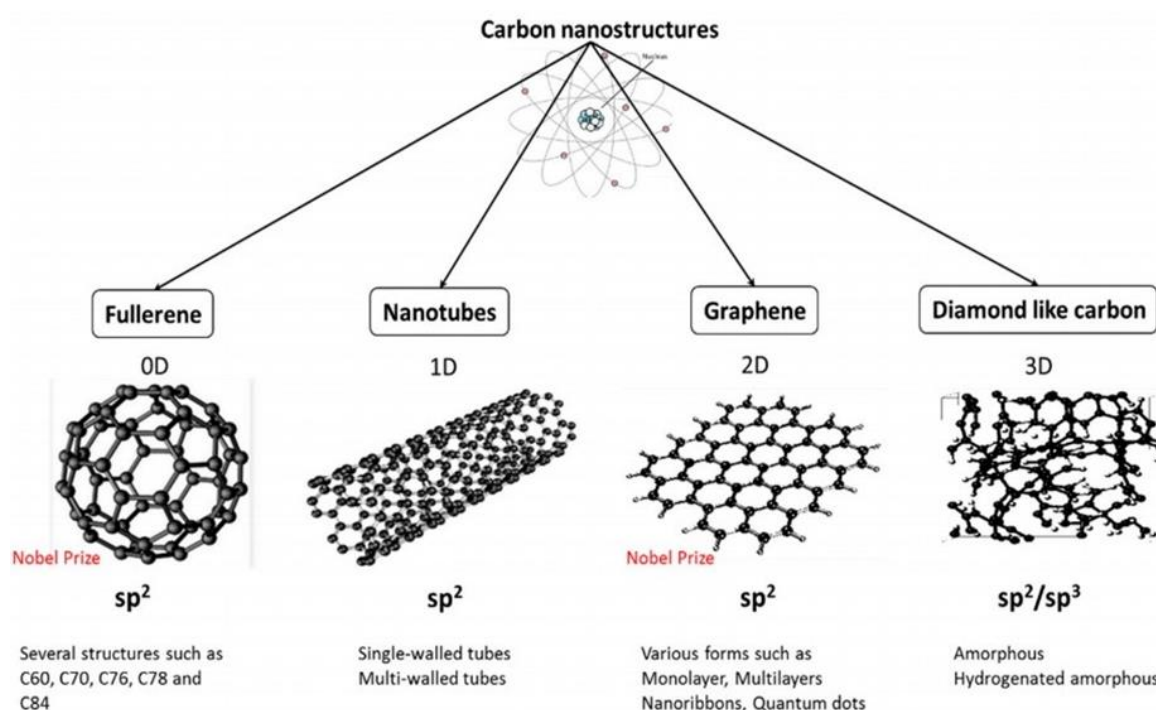


Figure 1.5. Several forms of carbon nanostructures, from 0D fullerene, to 1D nanotubes, 2D graphene layers and 3D diamond like amorphous materials [5]

Others compounds having all dimensions in the nanometric range are the dendrimers. Dendrimers consist in extremely branched molecules, characterized by perfectly symmetrical structures, which are divided into two categories, low and high, based on the molecular weight. Dendrimers can be formed through processes of hierarchical self-assembly operating at the nanoscale. Small dendrimers, having dimensions of several nanometres, are used in various applications, like inks and coatings, but they can also be used as filters to remove metal ions for water decontamination or as carriers for drug delivery. [4]

Finally, nanoparticles are metallic (or metal oxides) particles having all dimensions < 100 nm, which are the most synthesized 0D structures, but sometimes they are also present in the natural world, for instance produced by algae or plants in photochemical reactions or as a result of volcanic activity. They are also created accidentally by

human activity, for example as residues of combustion. In comparison to the amount of nanoparticles produced naturally or accidentally, the quantity of nanoparticles synthesized for research or industrial purposes represents still a small portion. This portion is continuously growing in recent years and will increase even more in the next years, thanks to discoveries of special size-dependent properties useful in various fields. For example, zinc oxide or titanium dioxide become transparent in form of nano-sized structures and reflect UV rays. In fact, nanoparticles possess a large range of applications: from cosmetics industry to textile, from medical diagnosis and drug delivery to paint industries, from lithium batteries to Cultural Heritage.

1.3 Nanomaterials synthesis

Nanomaterials can be obtained with top down or bottom up approaches, as shown in Figure 1.6. In the top down approach, nanoscale structures are produced starting from macro-materials, usually through mechanical processes of mass removal, such as grinding or exfoliation. On the contrary, in the bottom up approach, nanoscale materials are produced starting from atoms or molecules with smaller dimensions, usually through self-assembling techniques, in which the atoms or molecules are able to form structures based on their natural properties. Another way of the bottom up approach is the use of apparatuses that can move individual atoms or molecules. [1]

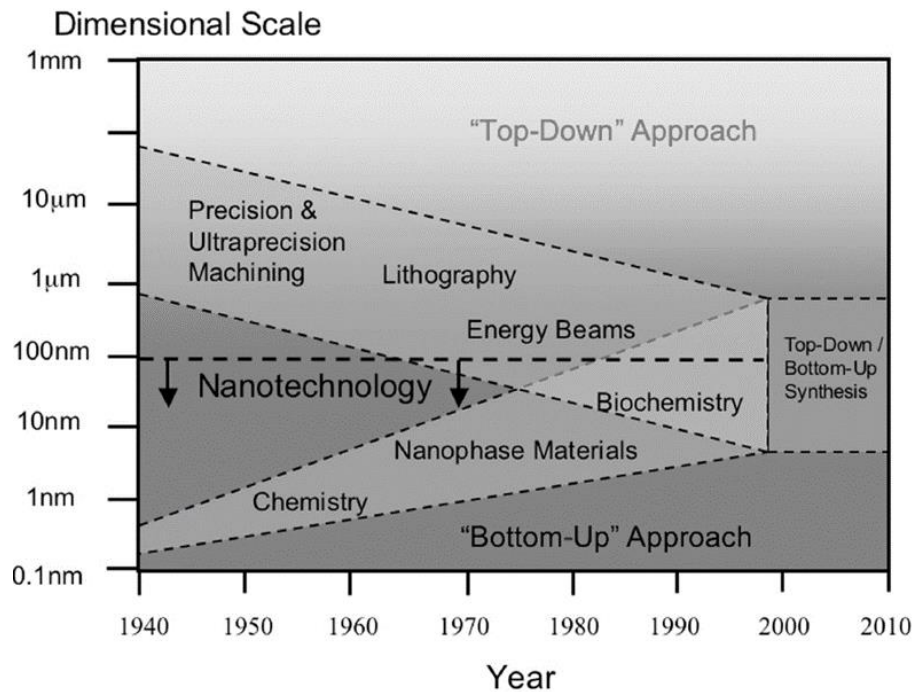


Figure 1.6. Production techniques “top-down” and “bottom-up” [1]

The main challenge of top-down techniques is the creation of nano structures with good precision, while for bottom-up techniques is the construction of large structures with quality and good resistance. These two approaches have developed separately to create nanoscale structures. The principal bottom-up methods are: aerosol-based processes, atomic or molecular condensation, arc discharge ionization, laser ablation processes, plasma processes, chemical vapour deposition, sol-gel methods, solvothermal methods and ultrasonic methods. Typical top-down methods are: mechanical friction processes (precision machining), nano-lithography and laser ablation. Actually top-down techniques are the most consolidated ones for larger productions, despite their limitations such as considerable costs, multiple steps and low specific production yields [6].

In addition to the top-down / bottom-up classification, the synthesis methods can also be classified according to the type of synthesis, chemical, physical or biological, as reported in Table 1.1.

Table 1.1. Main synthesis methods of nanoparticles classified into physical, chemical and biological

Physical methods	Chemical methods	Biological methods
<ul style="list-style-type: none"> • Mechanical methods • Physical vapor deposition (PVD) • Molecular beam epitaxy (MBE) • Laser ablation 	<ul style="list-style-type: none"> • Co-precipitation • Sol-gel • Microemulsion • Sonochemical synthesis • Hydrothermal / solvothermal synthesis 	<ul style="list-style-type: none"> • Synthesis by enzymes • Synthesis from plants • Synthesis from biomembranes • Synthesis from microorganisms

Different methods can be used to produce 3D, 2D, 1D and 0D nanomaterials. In particular, the most known processes to obtain thin films can be separated into two categories as well: physical methods and chemical methods. In the physical methods a material is physically transferred from a medium to a substrate to form the film, while in the chemical methods suitable chemical precursors are carried on a substrate to form the film through a chemical reaction [7]. Figure 1.7 reports the main preparation routes of 2D nanomaterials.

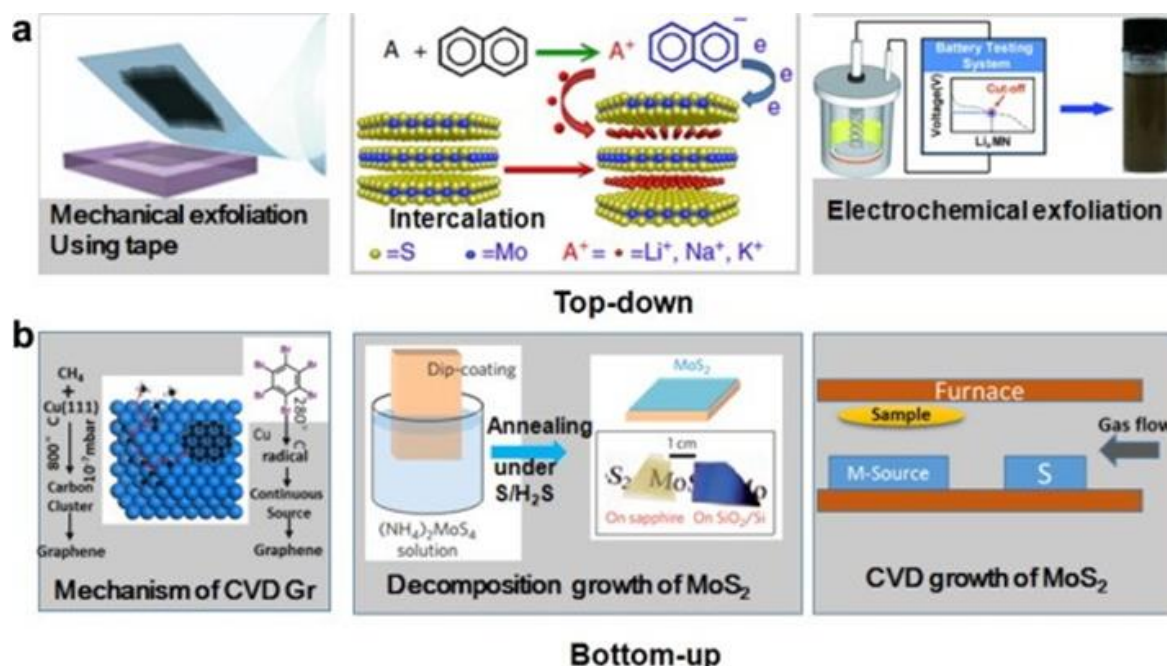


Figure 1.7. Typical 2D nanomaterials preparation processes [7]

In the synthesis of 1D nanostructures, the composition, the size and the crystallinity are the most important factors to control. The formation of a solid phase involves two main steps: nucleation and growth, in particular when the concentration of the

constitutive elements becomes sufficiently high, they aggregate into small clusters (or nuclei). Then, bonding to the other constitutive elements, these nuclei become the centres of growth in order to form larger structures. Typical strategies to obtain 1D nanomaterials involve different levels of control of the growth parameters, including: the use of anisotropic crystals to facilitate the growth of single-dimensional structures; the use of different 1D morphologies to orient the formation of single-dimensional structures; the use of appropriate reagents to kinetically control the growth rate of the various precursors; the self-assembly of 0D nano materials; or the size reduction 1D microstructures [8, 9].

For the production of nanoparticles both top-down or bottom up techniques can be used, in particular sol-gel method is a bottom up technique widely used for synthesizing metal oxides or ceramic materials. Sol-gel methods typically start from metal alkoxides or organometallic inorganic salts, then the precursors go through a series of hydrolysis and polycondensation reactions in order to form a colloidal suspension (called sol). This suspension undergoes a transition into a solid “gel” phase, then the drying of this gel through calcination treatments lead to a nano-powder. Another common bottom up technique to produce nanoparticles is the hydrothermal method, which is carried out in pressurized vessels (autoclave) with a reaction in aqueous solution, in this way the temperature in the autoclave can be raised above the typical boiling point of water, reaching the pressure of vapour saturation. Hydrothermal synthesis is generally used to synthesize metal oxide nanoparticles. This method can be useful to control grain size, morphology, phase and surface chemistry regulating different parameters: solvent properties, solution composition, temperature, pressure, additives and aging time. Other synthesis methods of nanoparticles will be described in the following chapters.

1.4 Properties, characteristics and applications of nanoparticles

Nanoparticles have acquired great scientific interest because of their particular behaviours, which sometimes are intermediate between the macroscopic scale and the atomic or molecular scale. Their mechanisms of interaction with other materials are also different, for example nanoparticles can remain in form of stable suspensions

because of the interactions that form between their surface and the solvent, which can be strong enough to overcome the density difference, avoiding the precipitation of the particles. In particular, nanoparticles coated with hydrophobic molecules can be suspended in non-polar solvents, while nanoparticles having specific surface charge can be suspended in solvents with specific amounts of ions.

The effect of dimensions represents a fascinating and decisive aspect to describe the behaviour of nanomaterials: reducing the dimensions of the materials, variations in the structural, thermodynamic, electronic, spectroscopic, chemical and electromagnetic characteristics can be appreciated (Figure 1.8).

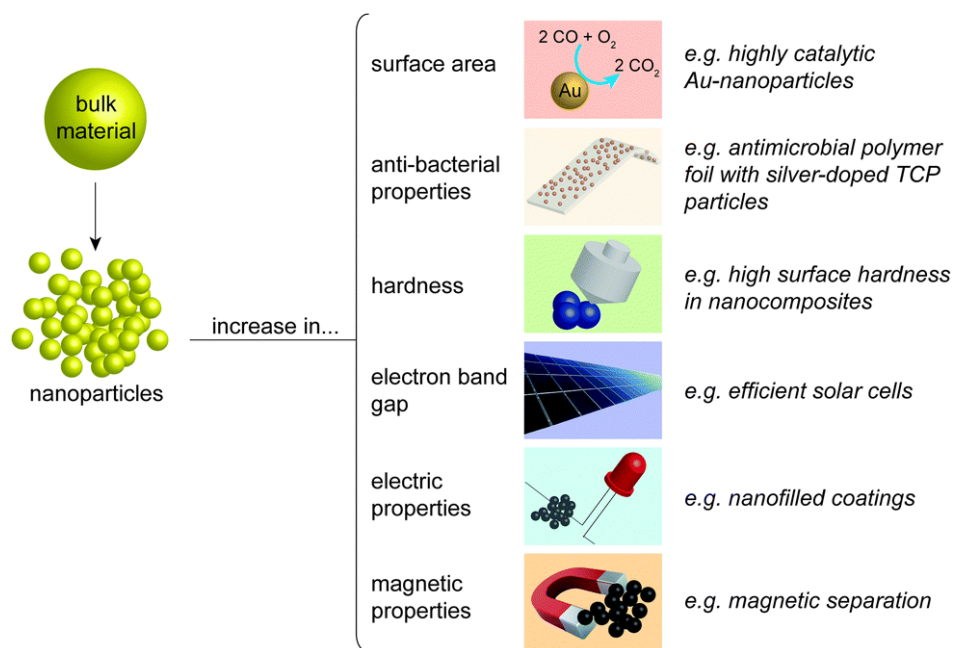


Figure 1.8. Principal effects of the nanoscale on material properties [4]

In particular, the main properties that can change on nanoscale respect to massive materials are [10]:

- **Electronic properties:** the electronic structure of nanocrystals depends on their size. For small particles, the energy of the electronic levels is not continuous as for bulk materials, but discrete, in fact the physical dimensions of the particles involve a confinement of the electronic wave functions.
- **Mechanical properties:** compared to massive materials, nanomaterials have higher Young's modulus and tensile strength, less plastic deformation and more brittle behaviour. Decreasing the size of the grains therefore causes an increase in strength

and ductility, and is therefore one of the most effective mechanisms for strengthening materials.

- **Electrical properties:** in magnetic and ceramic nanocomposites there is an increase in electrical conductivity, while in metallic nanomaterials there is an increase in electrical resistance.
- **Magnetic properties:** the large surface/volume ratio results in a substantial portion of atoms having different magnetic couplings with neighbouring atoms, leading to different magnetic properties. Non-ferromagnetic bulk materials can exhibit similar behaviour to ferromagnetic materials when prepared in the nano range. Ferromagnetic bulk materials can exhibit a different type magnetism, called supermagnetism in the nano range.
- **Thermal properties:** properties such as thermal conductivity, thermal expansion and heat capacity provide valuable information on the important physical characteristics of nanomaterials. Nanomaterials can have a much lower melting temperature than that of the corresponding bulk materials: through the fusion, the total surface energy of materials decreases, and how observed, the decrease in size anticipates the melting process, because the contribution of surface energy increases.
- **Optical properties:** visible light has wavelengths of the order of hundreds of nanometres and interacts in a different way with structures of similar size. In particular, with the nanometric dimensions there is a spectral shift in the properties of optical absorption and fluorescence and an increase in the quantum efficiency of semiconductor crystals.
- **Chemical reactivity:** is greatly amplified with decreasing size, in fact a 1 nm crystal has about 100% of the atoms on the surface, while a 10 nm crystal has about 15% of the atoms on the surface, and these atoms are the ones from which reactions are triggered.

So, the main properties of nanoparticles respect to bulk materials are: higher specific surface area, improved reactivity, increased mechanical strength, better conductivity, faster electrical and magnetic responses. Nanoparticles can have also properties in the visible field, because their dimensions are small enough to restrain their electrons, resulting in the production of quantum effects. Many other properties of nanoparticles depend on their composition and also on their production process, for example some

iron oxides become superparamagnetic under certain dimensions [11], gold nanoparticles possess optical and electronic properties that are tunable by changing the size, excellent biocompatibility and low toxicity [12], copper oxide nanoparticles possess antiviral and antibacterial properties [13].

The fields of research and applications of nanoparticles are numerous, ranging from biology to informatics, from engineering to quantum physics of materials, from medical purpose to commercial use for ordinary objects (cosmetics, sunscreens, textiles, paints, coatings, batteries, composites, fuel cells and optoelectronics). [4] Nanoparticles can be organised in layers placed on top of other structures, to increase the surface area and to improve the reactivity, and this way is suitable for applications in the field of catalysis or coatings. Generally, nanoparticles are not synthesized for direct uses, but they are employed as additives in other products, in order to improve or develop some properties. The diffusion of nanoparticles is still very low compared to other materials, both because there is a lack of an economic method able to realize productions on large scale, and more studies are needed to get in-depth information of their toxicity. Their potential toxicity, derived from the very small dimensions, can be reduced attaching them on the surface of other materials or binding them inside composite materials. [14-16]

1.4 Nanoparticles for medical applications

One of the most interesting field for nanoparticles application is the medical sector, where the research is greatly focused, especially in the last 10 years.

Living organisms are composed by cells, having dimensions of about 10 μm , which are constitute of other organic structures reaching sub-micrometre sizes. For dimensional reasons, nanoparticles could be used as probes to analyse the mechanisms and the interactions that happen inside the cell, perhaps without causing damage. The precise knowledge of biological processes from a nanometric level is one of the goals of biotechnology. Nanoparticles properties of interest in medical uses are strongly related to the size, such as magnetic and optical effects.

Their principal applications investigated for medicine are: MRI contrast agents [21-23], gene therapy [24], controlled drug release [25], fluorescence bio-markers [26, 27],

photogenic bio-sensors [28, 29], tissue engineering and probes for genetic structure [30, 31], magnetic hyperthermia [15], and cells purification [32]. Medical sector has different possibilities for nanomaterials, including building blocks of nucleic acids as nanoparticles binding agents comparable to antibodies, rather than characteristic genetic maps, or implantable patient monitoring using nanostructured biosensors, but also improved imaging contrast using nanoparticles as agents. Nanoparticles and proteins have similar dimensions, which means that nanomaterials may be used as markers for biomolecules. For example, labelling different cells it is possible to bind nanoparticles on their surface, which interact with them modifying the structure, so that they can be viewed with fluorescence or ultraviolet probes.

The approach used to design a nano-biomaterial is represented in Figure 1.9. The dimensions and the size distribution especially are extremely important when the particles are realized to penetrate inside the cell membrane, because an incompatible size of NP can cause a complete lack of penetration inside the cell. These two parameters are fundamental also when quantum effects (size dependent) are used to control some properties. Very precise average dimensions and narrow size distributions are fundamental also to make efficient fluorescence probes.

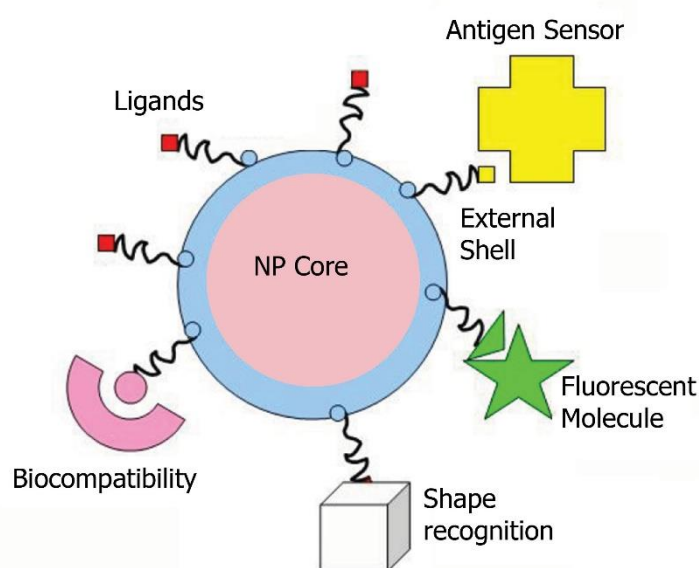


Figure 1.9. Configuration scheme for medical or biological problems in biomaterials approach [33]

Nanoparticles can also be functionalized in the external layer, using polymers, small molecules or proteins, to make them more bio-compatible. It is possible to realize one or more layers, but the nanoparticles core provides the main properties, such as superparamagnetic behaviours for iron oxides. This core can be protected by some monolayers of inert materials, in particular silicon, then organic molecules can be absorbed or chemisorbed on the surface, and the same layer act also as a biocompatible material. Often an extra layer of ligands is needed to proceed with additional functionalization. Ligands are molecules having reactive groups on both ends: one to bind with the nanoparticles, the other for binding to some biocompatible molecules, usually poly-ethylene glycol (PEG) or dextran, other molecules depend on the function needed for the application. [33]

One of principal applications of nanoparticles in the medical field is diagnosis, to improve the diagnostic of some diseases in time and precision. Using nanotechnology tools or probes can be a way to perform more accurate diagnosis. Existing diagnostic techniques include medical imaging, immune-assays, cell-based assays, genetic-based tests, tissue and histological tests. Nanotechnology is improving diagnostic methods, such as magnetic, electrical, optical and electrochemical techniques. Particular nanostructures, such as nanotubes, dendrimers and nanoparticles, can be designed for diagnosis and therapy. [34-40]

Medical imaging for diagnostics include magnetic resonance imaging (MRI), X-ray imaging, positron emission tomography (PET) scans, computed tomography (CT) scans, ultrasounds and other optical techniques, such as optical coherence tomography (OCT). The advantage of imaging, respect to assays and biosensors, for diagnosis is the possibility to carry out the analysis without samples of blood or tissues taken from the patient. Therefore, they are not invasive and sometimes they require the injection of contrast agents. However, most medical imaging instruments are expensive and the resolution has limits, which depend both on the sensitivity of the instrument and on the contrast agent used. Nanoparticles as contrast agents can be useful to increase the resolution, which may allow better diagnosis of diseases or may guarantee the same sensitivity also reducing dimensions and costs of diagnostic instruments. [41] Furthermore, functionalized magnetic nanoparticles can be targeted

to chosen analytes and then detected with small magnetic sensors, building portable diagnostic tools.

Fluorescent tags, such as rhodamine and fluorescein isothiocyanate (FITC), have been used as optical markers for a large range of biological assays. Traditional fluorophores are available in various forms, such as membrane-specific chemistries, voltage-sensitivity dyes and pH-sensitive structures. But traditional fluorophores have some disadvantages, in particular broad emission spectra, photo-bleaching and short emission lifetimes. Nanomaterials can improve the use of fluorophores and develop new markers to convert optical detection methods with higher sensitivity, single-molecule detection, multiplexed assays and in vivo diagnostics. Fluorescence emission can be controlled by adjusting the size of nanoparticles, so various dimensions of nanoparticles can be employed together for multiplexed assays, having each size emitting a different colour. [33, 42] However not all materials have fluorescence properties even in nanometric dimensions, so it is possible to bind fluorescent molecules on their surface to realize a fluorescent probe. This is a possibility for iron oxide nanoparticles, using specific molecules.

Also in ultrasound analysis, the use of fluorine-carbon nanoparticles and liposomes as contrast agents contrast agents can affect the propagation of sound waves, by altering the acoustic properties. An advantage of particles in the nanometric size is that they can survive more time inside the body, because their dimensions delay the activation of inflammatory responses causing their elimination.

Gold nanoparticles are very promising, because they can be used in optoacoustic imaging as contrast agents, in fact by controlling size and shape they can be realized to optimally absorb at specific wavelengths. They can produce luminescence at lower excitation intensities and are also more stable respect to typical fluorophores. Gold nanoparticles can be readily adjusted for biological specificity and possess very low toxicity respect to quantum dots. These characteristics represent a potential for gold nanoparticles as the technology to reach in vivo imaging of single-molecules for diagnostics [43, 44].

Iron oxide nanoparticles have been largely synthesized during the last years because of their potential applications in medical field. One of the most investigated application is magnetic separation: magnetic nanoparticles functionalized with ligands, which can

bind particular molecules, can be used to separate these molecules in solution using a magnet. Magnetic nanoparticles conjugated with antibodies can be employed to tag proteins in magnetic immunoassays. Functionalized magnetic nanoparticles can also be moved inside cells through external magnetic forces. Also sensors may use magnetic nanoparticles for portable diagnostics, comparable to chip-based electrical methods used in biological analysis, for example in tests concerning DNA. Medical imaging diagnostic is one of the most interesting field for magnetic nanoparticles application: as contrast agents they can enhance the sensitivity of these imaging techniques, in particular of MRI using superparamagnetic iron oxide nanoparticles (SPIONs), where typical contrast agents include gadolinium. Non-invasive detection methods at a cellular level can be realized using nano-carriers functionalized with specific biological receptors and loaded with contrast agents. For instance, magnetic nanoparticles for MRI can be altered to target a precise cell type and they can be also monitored optically functionalizing them with optical tags. [45, 46]

A future perspective for magnetic nanoparticles is the drug delivery, moving them to a cancer, in order to release the drug only after reaching the diseased area. Another perspective is magnetic hyperthermia, in order to locally heat and destroy only diseased tissues.

1.5 Nanoparticles effects on the health

The dimensions of nanostructures make them suitable to evade the natural defences of the body and reach the inside of the cells, resulting cytotoxic. But all living animals have to deal with particles having nanometre dimensions, such as those resulting by air pollution, by forest fires or by pollen.

The common approach in the estimation and control of risks derives from hazards identification, so is also important to evaluate a probability of exposure to the hazard with the related consequences. In this way the risk is typically controlled by decreasing this probability of exposure. Regarding nanoparticles, the main characteristics determining their risks are their chemical composition, their dimensions, which can

allow them to penetrate inside organs or cells, their specific surface area and their reactivity, in particular their ability to generate free radicals or to cause toxic reactions. Then the two main ways in which nanoparticles can enter the human body are contact with the skin and inhalation. The size of the nanoparticles affects both the penetration into cells and the penetration into the lungs by inhalation. In the lungs, there are specific phagocytes, such as leukocytes or macrophages, which can destroy large particles, such as unicellular organisms or bacteria. However, for a possible toxicity, also the total of surface and the inhaled amount have great importance. For the inhalation of small amounts of nanoparticles, the risks for health can be considered minimal; instead with high amounts the risks become high, such as breathing problems, depending on the size, type and reactivity of the particles. Supposedly only people working with their production processes risk to inhale so large quantities of nanomaterials, but they can be protected using appropriate protection devices, or storing the nanoparticles in liquid suspensions instead of powder form, and also by monitoring with specific sensors the concentration of particles in air. [4, 33]

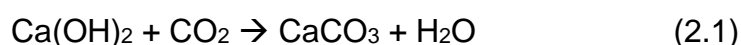
CHAPTER 2: ALKALINE-EARTH METALS NANOPARTICLES

The Group 2 alkaline-earth metals include beryllium (Be), magnesium (Mg), calcium (Ca), strontium (Sr), barium (Ba) and radium (Ra). All the elements in Group 2 have two electrons in their valence shells, giving them an oxidation state of +2. They are all fairly reactive metals, which easily lose the two electrons in the external electronic level forming M^{2+} cations.

Using the innovative synthesis techniques reported in this thesis, it is possible to produce nanometric compounds based on these elements; in particular magnesium, calcium, strontium and barium nanoparticles have been produced. Therefore, characteristics, synthesis routes and applications of these nanoparticles reported in the literature will be here described.

2.1 Calcium hydroxide nanoparticles (nanolime)

In the field of nanoparticles, calcium hydroxide nanoparticles will be here introduced, as they represent the starting point of this work. Calcium hydroxide, having chemical formula $Ca(OH)_2$, is also called hydrated lime or slaked lime. Calcium hydroxide, known by the mineral name of Portlandite, is a member of the "layered" family of hydroxides, characterized, from a crystallographic point of view, by a Trigonal - Hexagonal crystalline system [1]. It is typically produced in form of powder by dry hydration of calcium oxide, CaO (also called quicklime). Due to its strong base property, calcium hydroxide has many uses, including: construction, painting, water treatment, chemical industry, acid neutralization, food industry, refinery, metallurgy, pesticides, fertilizers, dentistry. In particular, calcium hydroxide was one of the oldest building materials used by man, thanks to its ability to transform into calcium carbonate in the presence of carbon dioxide, according to the well-known carbonation process:



In relation to this process, lime has been considered a very promising material in the field of Cultural Heritage, suitable for conservative and protective treatments on all carbonatic substrates (frescoes, stuccos, plasters, stone materials as well as historical

mortars), as it fully satisfies the compatibility requirements on such materials. However, the use of commercial lime may have some limitations, linked to the micrometric size of the particles: reduced penetration capacity, whitening effect on the surface, low specific surface area, low reactivity and incomplete carbonation process. To overcome the limits of traditional lime-based treatments, alcoholic or hydro-alcoholic dispersions of calcium hydroxide nanoparticles (also called nanolime) have been introduced (figure 2.1a). In fact, these nanoparticles possess a greater ability to penetrate into carbonatic surfaces, thanks to their smaller size, ensuring a greater reactivity and a lower whitening effect after their application. Calcium hydroxide nanoparticles are crystalline particles, having the form of hexagonal lamellae with dimensions less than 200 nm (figure 2.1b).

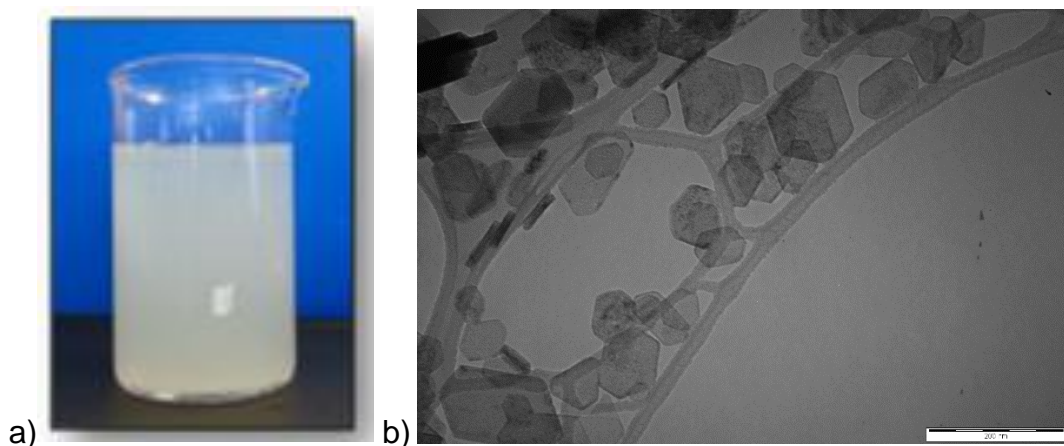


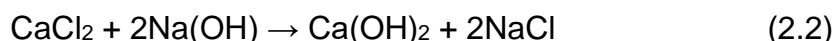
Figure 2.1. a) Alcoholic dispersion of nanolime; b) Transmission electron microscopy (TEM) image of the nanolime hexagonal particles with marker 200 nm

Therefore, thanks to its properties, nanolime is able to restore the surface cohesion of deteriorated materials, as it ensures a complete carbonation process when exposed to air, recreating a thin web of new calcium carbonate, which adheres to the grains of the original substrate. [2] In this sense, nanolime represents the best consolidant, in terms of compatibility, to be used on frescoes and on substrates with a carbonatic matrix. [3]

2.1.1 Synthesis methods of nanolime

As already described in the first chapter, there are two main ways leading to the synthesis of nanomaterials: one refers to the top-down approach, the other is called bottom-up approach. Calcium hydroxide nanoparticles have been synthesized by different processes, generally belonging to the bottom-up category, such as chemical precipitation, synthesis in diols, synthesis in water-oil microemulsions or by solvothermal reactions.

Nanolime suspensions are typically obtained by precipitation, in supersaturation conditions, by mixing slowly (drop by drop) an aqueous solution of a strong base (NaOH) with an aqueous solution of calcium salt (CaCl₂), at a temperature of 90°C. The reaction that occurs is:



Thanks to the low solubility of Ca(OH)₂ in water (1.7 g/L at 25°C), which decreases with increasing temperature, supersaturation conditions can be easily established, generating a nucleation rate greater than the growth rate, thus leading to the formation of very small particles. Despite the simplicity of the reaction from a stoichiometric point of view, it is necessary to consider different parameters to obtain nanoparticles, such as the temperature, the molar ratio of the solutions and the speed of synthesis. Moreover, at the end of the synthesis it is necessary to carry out several washes to remove the sodium chloride (NaCl) formed. Hexagonal nanoparticles with a size of about 300 nm can be obtained with this method. [4]

To further reduce the size of the formed particles, it is possible to carry out the same synthesis by replacing the aqueous medium with diols. Diols are organic compounds, which have boiling points higher than water (for example for ethylene glycol $T_{\text{eb}} = 197.6^\circ\text{C}$), so it is possible to reach higher temperatures during the reaction, reducing the Ca(OH)₂ solubility and favouring the nucleation step. The synthesis is followed by several washes to remove the sodium chloride (NaCl) formed as well, and by peptization stages of the obtained suspension to remove the diols. Peptization occurs when the ionic concentration of the solution in contact with the precipitate reaches certain limit, called flocculation value, and is carried out with 2-propanol in an ultrasonic bath. From this method a low specific yield of Ca(OH)₂ nanoparticles is inevitably

obtained, characterized by a lamellar shape with hexagonal morphology and a final size of 150-200 nm. [5]

Another way is to introduce in the same synthesis a non-ionic surfactant (such as Triton X-100) and rapidly mixing the obtained solutions together. The formation of a white precipitate is instantly observed, however, as in the previous precipitation syntheses, it is necessary to work at relatively high temperatures (90°C) and carry out the several washes to remove both NaCl and surfactant from the final suspension. Following this procedure, the production of nanolime is achieved, which is morphologically and dimensionally comparable with the nanolime obtained through the synthesis in diols, but in reduced time. The surfactant is able both to limit the growth process of the particles and to avoid their agglomeration. Therefore, $\text{Ca}(\text{OH})_2$ nanoparticles in form of hexagonal lamellae and with sizes always lower than 200 nm are obtained, as can be seen in figure 2.2. [6]

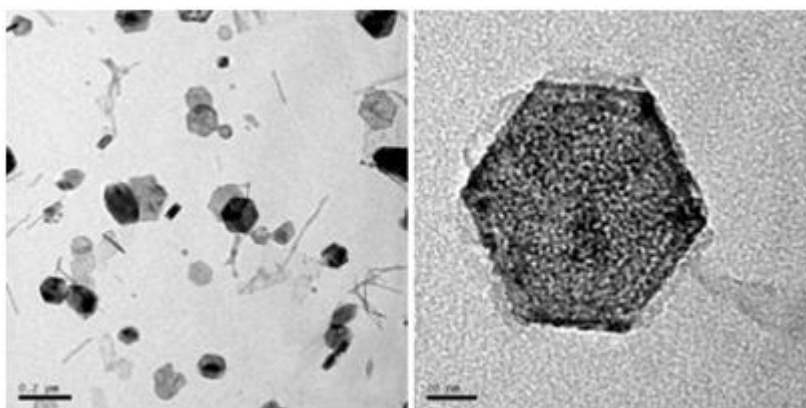


Figure 2.2. TEM images of calcium hydroxide particles obtained by surfactant synthesis: overview and detail of a single perfectly hexagonal particle [6]

Solvothermal reaction is also a way to obtain nanolime. Working at high pressure and high temperature, calcium alkoxide is formed from metallic calcium and short-chain alcohol (ethanol or n-propanol). With a subsequent hydrolysis of this compound, calcium hydroxide nanoparticles are obtained, already dispersed in a solvent suitable for their stability, the addition of water is carried out at 70°C for one hour. Before starting the reaction, vacuum-nitrogen cycles are carried out to ensure an inert atmosphere inside the container. The average size of the final particles is about 200 nm. [7]

The calcium hydroxide nanoparticles can be synthesized by the reaction of calcium acetate with sodium hydroxide using a sonochemical method as well. Sonochemistry is the research area where molecules are subjected to a chemical reaction due to the application of powerful ultrasonic radiation (20 KHz – 10 MHz). In recent years, many types of nanomaterials have been prepared using this method. Compared to other chemical methods, such as hydrothermal and solvothermal, this method does not require pressure and temperature controls. [8, 9] Experimentally to prepare the nanolime a NaOH solution was added to a solution of calcium acetate in ethanol. Then the suspension was irradiated with ultrasound using a high density ultrasonic probe, immersed directly into the solution. The ultrasonic wave generator (Sonicator_3000, Misonix) operates at 20kHz with a maximum power of 600W. The effects of ultrasound on chemical reactions derive from the development of elevated conditions of pressure and temperature locally, during the collapse of the bubbles due to acoustic cavitation. There are two regions: the inside of the collapsing bubble and the interface between the bubble and the liquid; the temperature of the inside can reach very high temperatures (based on the vapour pressure of the solvent), while at the interface it reaches lower temperatures. If the solute is ionic, as in this reaction, the quantity of the ionic species will be very small inside the bubbles, therefore calcium hydroxide nanoparticles are formed at the interface that, thanks to high cooling rates. The samples obtained with this method are characterized by primary nanometric structures, but the structures visible at TEM are aggregates reaching sizes of 500nm or more. [10] Calcium hydroxide nanoparticles can be obtained also with insolubilisation-precipitation method, thanks to the solubility of calcium hydroxide, which is soluble in water and insoluble in propanol and ethanol. Starting from a saturated solution of $\text{Ca}(\text{OH})_2$, kept at 90°C in nitrogen to avoid carbonation, and adding 2-propanol (20%, 50% or 90% in volume), the precipitation of nanolime is immediate. Hexagonal and monodispersed nanoparticles having sizes of about 200 nm are obtained with this method. [11]

Table 2.1 shows the features of the main synthesis methods of nanolime reported in literature, together with the characteristics of the obtained nanoparticles in terms of size.

Table 2.1. Features of the main synthesis methods of nanolime reported in literature. HPS = heterogeneous phase synthesis; CP = chemical precipitation; S = solvothermal method; I = insolubilisation/precipitation

Synthesis route	Precursors	Synthesis medium/ atmosphere	T (°C)	Brief processing conditions	Particle dimensions (nm)	Ref
HPS	Carbonate stones CaO pebbles	Air Deionized water	850 – 900 25	5 years aging time under controlled atmosphere prior to its use	30 - 400	12
HPS	Carbide lime	Oxygenated water		Addition of barium hydroxide; filtration; addition of lignosulfonates	30 - 200	13
HPS	Slaked lime			Thermomechanical treatment at high temperature and pressure	300	14
CP	CaCl ₂ ·H ₂ O and NaOH	Organic: 1,2-ethanediol, 1,2-propanediol and 2-propanol	195	Several washings, peptization; filtration at high temperature	60 - 150	15
CP	CaCl ₂ and NaOH	Deionized water; Triton X-100	90	Several washings to remove NaCl and surfactant	20 - 200	16
S	Metallic Ca	Water or Aliphatic alcohols	90	Release of H ₂ gas	30 - 300	17
S	Metallic Ca	Aliphatic alcohols, Vacuum/nitrogen	> 70	High pressure reactor (p=350bar), release of H ₂ gas	80 - 300	18
HPS/ CP	Waste clampshell	Air Organic: Ethylene glycol and Diethyl Ether	800 400	Calcination of raw materials. Used surfactants: N-Cetyl-N, N,N-trimethylammonium bromide	32 - 53	19
I/P	limewater	Under nitrogen	40 - 76	Reduced production, limited to the low Ca(OH) ₂ solubility	10 - 200	20

From this summary table, it is possible to notice that the existing methods to synthesize nanolime have some limitations, such as procedures with complex equipment or requiring organic compounds; high synthesis temperature or pressure; multistep processes with intermediate steps (filtration, washing, peptization of the suspension); long synthesis times and limited produced amounts. So, the development of a cost-effective and scalable method to synthesize nanolime is still essential to extend the use of this compound to widespread applications.

An innovative synthesis method of calcium hydroxide nanoparticles has been developed at the Laboratory of Materials Technology and Applied Chemistry of the

University of L'Aquila, and recently patented at European level (EP2880101). It is a bottom-up method based on a single-step ion exchange process, which allows to obtain pure nanoparticles in extremely short times, working in water, at room temperature, atmospheric pressure and starting from cheap or renewable reagents, according to a cyclic procedure potentially scalable to an industrial level. The nanolime produced can be dispersed in water-alcohol mixtures, varying the solid concentration if necessary, in order to improve the colloidal stability or the amount of consolidant. This patented method is the starting point of the experimental development of this Thesis, so it will be better discussed in the following chapters.

2.1.2 Nanolime applications in Cultural Heritage

In the field of conservative treatments in Cultural Heritage, commercial lime finds application as lime water or lime milk. Lime water is a saturated aqueous solution of $\text{Ca}(\text{OH})_2$, which is obtained by dissolving an excess of lime in water and taking the supernatant. In such solution there are Ca^{++} and OH^- ions, so the calcium cations react with the CO_2 in the air to form calcite crystals, CaCO_3 , directly on the treated surface. Calcite, which is poorly soluble in water (0,014 g/l at $T = 20^\circ\text{C}$), has a fixing and insulating effect against some aggressive compounds present in the atmosphere; moreover, by adhering to the grains of the substrate, it can increase the structural cohesion of the treated area. However, lime water has some limitations related to its low concentration (the solubility of $\text{Ca}(\text{OH})_2$ in water is 1,7 g/l at $T = 20^\circ\text{C}$), so too many treatments and too much water intake are needed to have visible results on the substrate. The lime milk is an aqueous suspension of $\text{Ca}(\text{OH})_2$ and it is used on the same principle as lime water, because, compared to the treatment with lime water, the lime milk involves a greater intake of $\text{Ca}(\text{OH})_2$ for the same volume of water. [21] But also the lime milk has limitations due to the micrometric size of the particles, which have a limited penetration on the substrate and a low reactivity, thus determining an incomplete carbonation and a whitening effect on the surface. To increase the efficacy of these kind of treatments, calcium hydroxide nanoparticles in hydro-alcoholic dispersions have been introduced, since thanks to the reduced size, a greater

penetration depth on the substrates together with a greater reactivity and a less whitening effect on the surfaces are obtained.

The nanolime suspensions can be applied by nebulization, by brush, by spray or by imbibition on different substrates. Furthermore, the suspension can be diluted or applied using Japanese paper for application on frescoes or mural paints, to completely avoid the formation of unwanted white veils on the surface. After application, the solvent evaporates in short times, depending on the environmental conditions (relative humidity), on the type of solvent and on the amount of product applied. However, the carbonation process can require from a few minutes to a few days to be completed, depending also on the suspension concentration, on the type of solvent and on the environmental conditions. [22]

Nanolime applications in the conservation of frescoes

All the artistic artefacts represent systems whose materials are subject to natural degradation. The typical degradation phenomena in plasters and paints involve the loss of cohesion of the various constituents, due to a loss of the binding function of calcium carbonate, with consequent detachments of pigment particles, chalking of the plasters and small mechanical collapses of the structure.

For stone materials the deterioration can be triggered by the action of water, acting through physical-mechanical phenomena (such as freezing/thawing), but also by chemical attacks from aggressive substances present in the atmosphere (carbon dioxide, nitrogen oxides and sulphur dioxide). This leads in time to manifestations of corrosion, detachment and exfoliation of the surfaces.

The restoration operation is developed in three main phases, which can be defined in chronological order as cleaning, consolidation and protection. [23]

Cleaning is the operation aimed at removing everything that is inadequate for the conservation of the material. In fact, the substances deposited on a work of art can have different origins: natural aging (dirt and dust), bacteria and fungi (biological patinas), black crusts, extraordinary events (mud and earth from floods or other catastrophic events) or also incorrect restoration interventions.

The consolidation operation aims to restore adhesion, cohesion and compactness, thus improving the mechanical strength of the structure. This operation is typically

carried out by impregnating the substrate with a product, which, penetrating deeply, improves the cohesion of the deteriorated areas and the adhesion between them and the intact substrate. So, in the case of stone materials, a good consolidating product must be absorbed uniformly, reach all the deteriorated areas, consolidating them and connecting them to the whole substrate, without producing discontinuities. It must also preserve the appearance and the chromatic values of the original material, without causing significant changes in thermal expansion, elastic modulus and vapour permeability, or the formation of harmful secondary by-products.

The last step to conclude a restoration intervention is the protection, usually carried out by spreading transparent and water-repellent chemicals or covering layers of plaster on the surfaces, to create a barrier surface against the aggression of chemical agents and atmospheric pollutants.

However, the concept of compatibility between the original material and the applied material has been ignored for several years in many restoration interventions, resulting often in dramatic effects on works of art. In the consolidation of wall paintings, for example, synthetic organic fixatives, polymers and vinyl or acrylic copolymers have been used for a long time, having a considerable chemical and structural diversity compared to the original substrates on which they are applied. These products, usually high molecular weight polymers, form molecules with dimensions equal to or greater to the pores present in the substrates, causing a closure of these pores and triggering corrosion phenomena in previously intact areas of the material.

The frescoes are wall paintings made on fresh plaster based on lime and sand; they are made by painting with pigments of mineral origin diluted in water: in this way, once the carbonation process is completed in the plaster, the colour remains completely incorporated, thus acquiring particular resistance to water and time. [24] The consolidating action of synthetic organic fixatives or polymers in these substrates is due to their strong adhesive power: penetrating through the macro-pores and micro-cracks, they more or less continuously cover the walls, binding together the mineral elements, reducing the vapour permeability of the treated surfaces and giving them a more or less strong water repellence. For example, when the surface of a painting on a wall is covered with a polymeric film, the crystallization of the salts takes place under the film, leading to a strong mechanical stress for the pictorial layer, bringing the work

of art to degradation in few years depending on the environmental conditions. In addition to the degradation of the support, the aging of the polymer can produce drastic changes in the physico-chemical properties of the inorganic constituents of the painting and of the polymer itself (colour changes over time, loss of permeability to water vapour, loss of mechanical properties), making it necessary to remove it immediately. Moreover, by presenting a basic incompatibility with the inorganic substrate of the art works, they can also trigger a series of degradation mechanisms that are extremely dangerous for the conservation of the original material, such as the loss of cohesion between the various layers of the painting, with consequent exfoliation or detachment of the pictorial layer, phenomena which cause a strong alteration both from a mechanical and aesthetic point of view.

In many cases of deteriorated pictorial pigments, the consolidation with nanolime restored a cohesion of the wall painting, thanks to the small size of the particles allowing them to pass through the pigment layer. In fact, these nanoparticles allow the re-adhesion of the original pigments to the wall support and, following the carbonation process, the consolidation of the pictorial pigment on the surface is also obtained, without introducing materials incompatible with the original work.

In this regard, one of the first examples of the use of nanolime for the consolidation of a work of art is for the frescoes in the crypt of San Zeno in Verona. The medieval wall paintings (13th and 14th centuries) in the crypt of the Basilica of San Zeno in Verona (Figure 2.3) showed a strong deterioration, in particular a loss of cohesion of the pigments and some whitish layers on the surface.



Figure 2.3. Paintings in the crypt of San Zeno, before and after the treatment with nanolime [24]

After the application of nanolime dispersions for the consolidation phase, the cohesion of the pictorial pigment on the surface is obtained, without any chromatic alteration of the surface, as shown in figure 2.3 after the treatment.

Nanolime applications in the consolidation of stones

In the case of stone materials, the nanoparticles of calcium hydroxide can be applied by immersion, spray or injection. A stone material exposed to the atmosphere degrades through a process that proceeds progressively from the outside to the inside. In most cases, deterioration is accompanied by the formation of hard and not porous superficial black crusts, below which the material is non-cohesive and more porous. The inland areas, on the other hand, are generally better preserved and present a limited porosity compared to the degraded layers above. Water can be of the factors that induce alterations within the material, penetrating inside the pores of the stone in the liquid state, by capillarity, but also in the gaseous state and condensing inside the pores. In general, the effects of water in the degradation process can be summarized as follows:

- mechanical action due to the tensions that are generated due to the freeze-thaw cycles of the water;
- erosive phenomena caused by rainfalls;
- chemical action in the porous structure of the material, connected to the transport and storage of pollutants (dispersed acids) in the surrounding environment.

There are also thermal factors that cause contractions and dilations of the material and therefore stress and decohesion of the same. [25]

Consolidation is an action that is necessary when the damage caused by degradation is high enough to require the restoration of the structural characteristics of the material, or to recreate a sufficient degree of adhesion between the grains. A consolidation treatment must meet three main requirements:

- effectiveness, or improvement of mechanical resistance;
- compatibility (with the treated support);
- durability (resistance in time to various degradation mechanisms).

Therefore, the products used to solve conservation problems on natural stones must be chemically, mechanically, physically and aesthetically compatible with the substrate on which they are applied. The term compatibility means the similarity between the chemical and physical characteristics of the product and those of the substrate, which is to avoid discontinuities in the properties of the consolidated stone. At a chemical level, the product must not trigger any type of reaction with the treated support and must not generate by-products, which can cause degradation phenomena in the substrate. Furthermore, the consolidant should penetrate as deeply as possible and be uniformly absorbed by the stone. Finally, the product should not completely occlude the pores of the stone, but rather restore the porosity of the material to the characteristic levels of intact substrates. These products, both organic and inorganic in nature, are generally liquid substances capable, once penetrated into the porosity of the stone (generally by impregnation), to pass to the solid state, generating reticulated structures adhering to the surface of the pores, having the ability to restore some mechanical properties of the substrate.

Nanolime applications in the deacidification of ancient woods

Finally, another application of calcium hydroxide nanoparticles in Cultural Heritage is in the deacidification of historical documents and ancient woods. In fact, the combination of sulphur and iron ions inside their fibers can lead, in favourable environmental conditions (low pH), to the formation of acidic compounds which quickly degrade the cellulose matrix. A controlled treatment of ancient woods under vacuum using nanolime suspensions can represent a solution to protect objects made of degraded wood, such as sculptures, works of art or archaeological finds. The efficiency of the deacidification treatment of some wood samples using nanoparticles was confirmed from the restoration of pH to neutral conditions (Figure 2.4). [26]

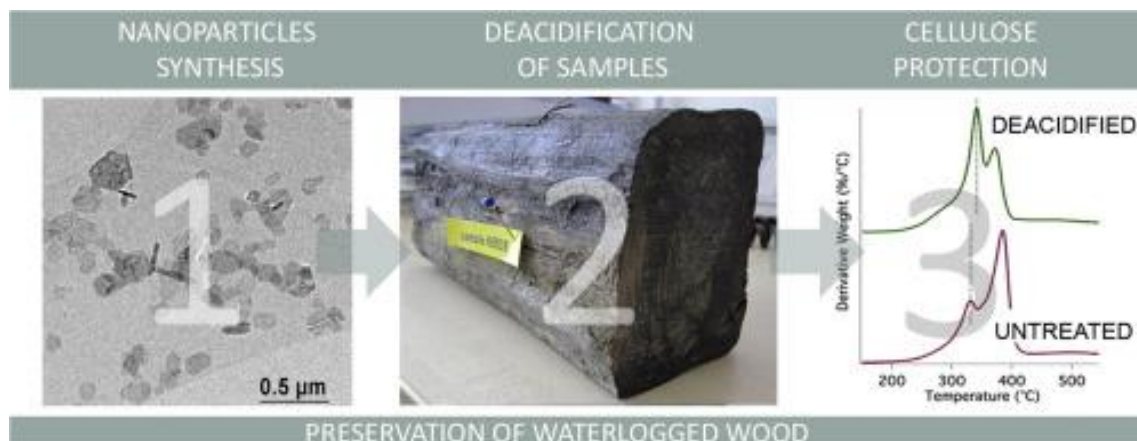


Figure 2.4. Nanoparticles for the deacidification of ancient wood [26]

2.1.3 Other applications of nanolime

In addition to the Cultural Heritage field, thanks to its binder properties combined with its non-toxicity and highly alkaline characteristics, nanometric calcium hydroxide is being studied in other fields of application, for example in dental treatments [27, 28]. In fact, some bacteria, such as the *Enterococcus faecalis*, which is a gram positive bacterium that habitually populates the stomach and intestines of humans, can invade the dental tubules causing acute or chronic infections and resist up to high pH levels. The traditional lime results not very effective on the *Enterococcus faecalis*, but the nano structured calcium hydroxide seems to guarantee a penetration into the deeper layers of the tooth and greater effectiveness on this bacterium. A study in this regard was conducted to compare the antimicrobial activity of nanolime compared to traditional lime, using independent tests. From the results, the nanolime showed a higher antimicrobial activity at a depth of 200 and 400 μm [27].

Another possible use of nanolime, found in recent literature, is in photocatalytic degradation. Samples of $\text{Ca}(\text{OH})_2$ nanoparticles were immobilized in Alginate beads and showed excellent photocatalytic degradation activity in the presence of UV radiation. The dependence of this activity from different experimental conditions was also studied, showing promising results for the use of nano $\text{Ca}(\text{OH})_2$ as photocatalysts. Studies on the recyclability of immobilized catalysts were also conducted and the results showed that they maintain a high efficiency for several cycles. [29]

Calcium hydroxide can also be used as a precursor to obtain nanometric calcium oxide (CaO), which has interesting applications from an industrial point of view: it can be used as a catalyst in the production of biodiesel by transesterification of waste oils [30, 31], in gasification [32] or in decarboxylation reactions [33]; it can also be used in the production of optical fibers [34] and of technologically advanced sensors [35]. In particular, the production of biodiesel was investigated through the transesterification method, using a combination of nano CaO and nano MgO. Indeed, nano magnesium oxide alone is not able to catalyse transesterification, because it has a much weaker base affinity, but when it is used together with nano CaO, due to its surface structure, the contact surface of the CaO and the base affinity increase, with consequent improvement of the transesterification reaction. [36]

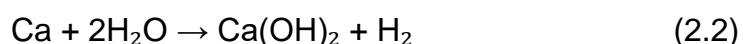
2.1.4 Commercial nanolime products: CaLoSiL and Nanorestore

The principal nanolime products on the market are actually CaLoSiL and Nanorestore. CaLoSiL products, developed by IBZ – Salzchemie GmbH & Co. Kg, are stable colloidal alcoholic suspensions of calcium hydroxide nanoparticles. There are different types of CaLoSiL products on the market:

- CaLoSiL® E-5, E-25 and E-50
- CaLoSiL® IP-5, IP-15 and IP-25
- CaLoSiL® NP-5, NP15 and NP-50

The letters indicate the type of solvent while the numbers give the total calcium hydroxide concentration in g/l.

These suspensions are obtained by solvothermal reaction of metallic calcium with water, in an alcoholic medium:



The solvothermal synthesis is a method used for a variety of materials, such as metals, semiconductors, ceramics, and polymers. This process involves the use of a solvent at moderate temperature (typically between 100°C and 1000°C) and high pressure, to facilitate the interaction of the precursors during the synthesis. Depending on the experimental conditions, the solvothermal reaction can be heterogeneous or homogeneous, taking place under subcritical or supercritical conditions. If water is

used as a solvent, the method is called "hydrothermal synthesis" and the synthesis is usually performed below the supercritical temperature of the water (374°C).

According to the product data sheet, the nanoparticles present in the suspension of CaLoSiL have a hexagonal shape with a size between 50-150nm. The suspensions are also characterized by great stability, resulting from the physical adsorption of alcohol above the surface of the particles. In fact, particle agglomeration is known to occur in water through a connection mechanism guided by the hydrogen bond. [37]

Nanorestore products, produced by CSGI, are stable hydro-alcoholic suspensions of calcium hydroxide nanoparticles. There are different types of CaLoSiL products on the market:

- Nanorestore® Propanol or Ethanol, 5 or 10 g/l
- Nanorestore Plus® Propanol or Ethanol, 5 or 10 g/l
- Nanorestore Paper® Propanol or Ethanol, 3 or 5 g/l

Nanorestore suspensions are sold in bottles of HPDE (high density polyethylene), which must be kept tightly closed in order to avoid carbonation in air and the possible formation of aggregates. The suspensions of the Nanorestore Plus line are formulated to prevent sedimentation for long storage periods. The Nanorestore products are obtained in small quantities from a precipitation method and formulated with lower concentrations respect to Calosil products. Moreover, Nanorestore suspensions have much higher market prices compared to Calosil suspensions. [38]

The consolidating effect of these nanolime products is obtained after some applications on the surface of the substrates, which can be done by brush, by spray or by immersion. The suspensions must be applied until the porous matrix is saturated; after the solvent evaporation, it is possible to proceed to further applications. Considering that various factors affect the consumption of the products (in particular the solvent evaporation and the application losses), it is difficult to predict the exact amount of suspensions required for a standard intervention. Approximately 1 litre of alcoholic nanolime at 5 g/l can be used to consolidate 10 m² of painted surface, corresponding to 0.5 g/m² of calcium hydroxide nanoparticles. Generally, it is recommended to repeat the application several times (up to 12 times) of less concentrated suspensions, rather than perform fewer applications with more concentrated dispersions, in order to allow the penetration of smaller particles and to reduce the probability of white glazes

formation. Following the various applications, the calcium hydroxide nanoparticles react with atmospheric carbon dioxide to form calcium carbonate (CaCO_3), to which the consolidating effect is attributed. However, it is usually recommended to wait at least one month before checking the effectiveness of the consolidating treatment, because the complete nanolime carbonation can take 4 weeks or more, depending on the environmental conditions. [38]

2.2 Magnesium hydroxide and oxide nanoparticles

Magnesium hydroxide, $\text{Mg}(\text{OH})_2$, is an inorganic compound existing in nature as a mineral called Brucite. Most magnesium hydroxide is produced from seawater or brines. $\text{Mg}(\text{OH})_2$ is poorly soluble in water, where it acts as a weak base, but it is often used in the form of an aqueous suspension, called milk of magnesia or magnesia. It is a compound of considerable industrial importance, in particular in the paper industry. Magnesium hydroxide can greatly increase the strength, stiffness, dimensional stability and high temperature deformation of some polymers. It is used as non-toxic, non-corrosive and thermally stable flame retardant in composite materials [39-42]. Moreover, it is also used as a desulfurizing and bleaching agent [43, 44], as an anti-acid excipient in drugs [45], as a neutralizing agent for acidic water pollutants [46, 47], as an additive in fertilizers and as main precursor in the production of magnesium oxide.

2.2.1 Synthesis and applications of magnesium oxide nanoparticles

The development of magnesium hydroxide on the nanometric level has received considerable interest, due to the potential peculiar properties related to the small size and high specific surface area. $\text{Mg}(\text{OH})_2$ nanoparticles were found to be effective in treatments of deacidification and protection of cellulose and as antibacterial agents [48, 49]. Magnesium hydroxide in the nanoscale used as flame retardant allows to reduce the load level, both increasing efficiency as a flame retardant and improving compatibility in polymer matrices. Furthermore, improvements in specific mechanical

and physical properties of the polymer can be achieved by using the filler particles in the form of lamellae or needles [50-54].

Magnesium hydroxide nanoparticles can be prepared by different methods: solvothermal method [55], hydrothermal method [56-58], laser ablation technique [59], sonochemical process [60], microwave irradiation [61] or precipitation of magnesium salts using precipitant agents or other additives, polymers and copolymers [62-69]. However, these methods are generally characterized by some drawbacks, such as the use of organic solvents, high synthesis temperatures, long times of synthesis or many steps of purification or washing. For this reason, there are ongoing studies to develop versatile, cost-effective and scalable methods to produce magnesium hydroxide nanoparticles, in order to successfully introduce these materials for widespread use. From nanometric magnesium hydroxide, the nanometric magnesium oxide can be directly obtained by thermal decomposition: this nanomaterial can be used in a wide range of applications thanks to its electrical and thermal properties. Table 2.2 shows the main methods in literature to obtain MgO nanoparticles, indicating the process conditions, the precursors and the solvents used. [70-78]

Table 2.2. main methods in literature to obtain MgO nanoparticles, indicating the process conditions, the precursors and the solvents used, together with the dimensions of the obtained NPs

Synthesis route	Reagents	Solvents	Surfactants or polymers	T(°C)	Time	Conditions	Size NPs (nm)
Sol-gel	Mg(NO ₃) ₂ , oxalic acid	Water	No	25	Some minutes + washings	Formation of gel, dehydration of MgO and decomposition of magnesium oxalate (500-1000°C)	6,5-73,5
Micro-emulsion	Mg ₅ (CO ₃) ₄ paraffine	PEG, water	CTAB	25	Some hours	Precursor precipitation from the paraffin system in water. Calcination at 823-1123 K.	25-70
Sono-chemical	NaOH, Mg(CH ₃ COO) ₂	Ethanol, water	No	25	Some hours	Ultrasonication suspension of precursors (20kHz, 600W); calcination at 400°C	72,4
Hydro-thermal	MgCl ₂ · 6H ₂ O, EDTA, KCl, NaOH	Water	No	160	3-72 hours	Sol in autoclave (160°C, 3-72h). Filtered, washed and dried precursors (100°C, 24h) Calcination (400°C, 60 min).	80-100
Spray pyrolysis	C ₄ H ₁₀ Mg O ₂	Methanol	No	320	Some minutes	Solution of the precursor on flame of CH ₄ /O ₂ , dispersed as a spray by O ₂	50
CVD	MgB ₂ , ZnO, graphite	-	No	850	30 minutes	Synthesis in a quartz horizontal tube. Protection with Ar gas	80-200
Flame metal combustion	Mg powder	O ₂ , H ₂	No	200-700	Some minutes	Transport of O ₂ and Ar powders on flame	60-120
Coprecipitation	Mg(NO ₃) ₂ , NaOH	Water	No	25-30	Alcunore +lavaggio	Coprecipitation followed by washing, centrifugation, drying (100°C) and calcination (400°C)	20
Surfactants method	Mg(NO ₃) ₂	Water	Brij 56, Triton X-100	80	Some hours	Solution of the precursor added to the surfactant with stirring. Calcination of the gel (4h at 550°C)	6-18

Magnesium oxide insulating properties make it a suitable additive material for the production of electrodes, insulated conduits and other electronic devices. Its refractory properties make it ideal for the production of various refractory materials, for use as a lining material and for the production of various high temperature optical and electrical devices. Several magnetic devices use magnesium oxide in their manufacture as a filler, insulator or component of material (widely used within the radio industry). Magnesium oxide is also a common additive in a lot of materials due to its unique anti-rust properties. In addition to uses in the manufacture of various advanced materials, it can be used as a dehydrating additive for some raw chemical materials. Moreover, magnesium oxide nano powder added to fuel is useful to inhibit static exhaust, to prevent corrosion and to keep the fuel system clean. [79]

2.2.2 Magnesium hydroxide nanoparticles in Cultural Heritage

The dolomitic stones are among the most used materials in the history of buildings in the world. These stone materials during time are damaged by different factors, causing losses in internal cohesion, which makes necessary the use of consolidant products. As mentioned, calcium hydroxide nanoparticles are, among nanomaterials, the most used product in stone consolidation. However, it is important to consider that dolomite crystals are composed by layers of magnesium and calcium ions alternate with layers of carbonate ions [80]. Therefore, the application of pure nanolime in dolomitic stones could form nano-calcite recrystallized, leading to the stone dissolution due to an enrichment in calcium ions [81]. The de-dolomitization is another problem of using nanolime for this kind of stone: in alkaline conditions, the dolomite can react with hydroxides generating an intergrowth of brucite, calcite and other alkali carbonates. When these reactions happen, the expansion and the cracking of dolomitic substrates occur [82-84]. In this kind of stone is suitable the development of new consolidant products based on magnesium hydroxide nanoparticles, with morphologies and crystalline structures appropriate for applications in the dolomitic stone used in buildings [85]. Also for this kind of nanoparticles, the consolidant effect is based on their carbonation process with atmospheric CO₂ in high humidity conditions, resulting is the precipitation of magnesium carbonate, MgCO₃. The consolidation of dolomitic

stones can be obtained using mixed suspensions of calcium and magnesium hydroxides nanoparticles. Therefore, to reach a durable consolidation, mixed $\text{Ca}(\text{OH})_2$ and $\text{Mg}(\text{OH})_2$ suspensions have been applied in a high porosity dolomitic stone [86]. Another application of magnesium hydroxide nanoparticles in Cultural Heritage is in the deacidification of historical documents and ancient woods. In fact, the combination of sulphur and iron ions inside their fibers can lead, in favourable environmental conditions (low pH), to the formation of acidic compounds which quickly degrade the cellulose matrix. Small alkaline particles, such as $\text{Mg}(\text{OH})_2$ in lamellar form, can penetrate inside the fibers of ancient woods to restore neutral pH values and can remain inside the substrate to protect it from further acid degradations. Therefore, the use of these nanoparticles can represent a solution to protect objects made of degraded wood, such as works of art, sculptures or archaeological finds.

2.3 Strontium hydroxide and carbonate nanoparticles

Strontium hydroxide, $\text{Sr}(\text{OH})_2$, is a caustic alkali compound, existing in anhydrous, monohydrate or octahydrate form. Since $\text{Sr}(\text{OH})_2$ is slightly soluble in cold water and it is usually obtained by adding a strong base (NaOH or KOH) drop by drop to a solution of a strontium salt, commonly strontium nitrate, $\text{Sr}(\text{NO}_3)_2$. Strontium hydroxide can react with CO_2 to form strontium carbonate, SrCO_3 , having properties similar to those of calcium carbonate: it is poorly soluble in water, but it dissolves in acids. Strontium carbonate is present in nature as the mineral strontianite, which is one of the main sources of strontium. Strontium is in fact named after the discovery of the mineral strontianite which, in turn, is named after the location of Strontian (Scotland), where the first strontium mineral was discovered.

2.3.1 Synthesis and applications of strontium hydroxide nanoparticles

Strontium hydroxide nanoparticles are obtained mainly by precipitation routes from strontium salts with organic additives [87, 88]. However, these synthesis methods have typically some drawbacks, such as long times, limited amounts of production, high

number of steps or organic additives, which do not make this product economically sustainable for large scale productions. Strontium carbonate nanoparticles can be obtained directly from the reaction between $\text{Sr}(\text{OH})_2$ nanoparticles and CO_2 (controlling the growth of the new phase), or by precipitation routes as well.

Strontium carbonate with high purity is widely used by the electronics industry, in the production of strontium titanates for MLCC and PTC devices. It is also widely used as a raw material for the production of strontium aluminates, of phosphorescent pigments and of transparent ceramic glazes. Its main application is in the production of glass for cathode ray tubes, LCD and plasma screens. For what concern the risks of such compounds, strontium hydroxide and strontium carbonate are non-flammable in the form of a nano-sized dust, even when mixed with air under an ignition source, so there is no possibility of dust explosion.

2.3.2 Strontium hydroxide nanoparticles in Cultural Heritage

Cultural Heritage is an incalculable patrimony and integral legacy to our future, for this reason we need to preserve it and provide access to it for the next generations. Nowadays, this rich and fragile heritage has reached a situation of strong degradation and conservation of stone heritage is always a complex challenge. Several variables have to be considered to identify the problems, define the conservation actions and to select the materials to be used. Compatibility, durability, depth of penetration, water permeability, biological resistance and also health matters are important factors to take into account.

Conservation of Cultural Heritage is mainly based on the traditional restoration treatments, such as the use of synthetic polymers. Only recently nanomaterials are being applied in the maintenance of the architectural heritage, in order to improve the consolidation and protection of damaged building materials. Moreover, atmospheric pollution is dramatically increasing the external degradation of numerous monuments, due to the deposition of contaminants and organic matter. In this context, one of the main advantages on the use of nanomaterials can be their photocatalytic capacity, which prevents the growth of microorganisms on the surfaces, allowing an easier removal of biofouling, biological stains and soiling from surfaces [89, 90]. In this way,

innovative applications use nanoparticles in building materials for self-cleaning, environmental pollution remediation and anti-microbial effects.

Among these innovative applications, strontium hydroxide nanoparticles were tested as consolidant products and also as de-sulphating agents for mortars, stones and wall paintings. These nanoparticles were tested in the consolidation of porous stone substrates, namely the stone of Lecce (Italy), and of some wall paintings, the frescoes of the "Grotta del Crocifisso" of Sicily (Italy). The strengthening effect of the nanoparticle-based treatments was compared with that shown by the well-known consolidant ethyl silicate (or tetraethoxysilane). All the results suggested that $\text{Sr}(\text{OH})_2$ nanoparticles, applied in 2-propanol dispersions, exhibit some good properties as consolidating agents, thanks to the carbonation reaction. In particular, the treatment with nanometric $\text{Sr}(\text{OH})_2$ was able to increase the resistance of stone to aging. Moreover, $\text{Sr}(\text{OH})_2$ in nanometric form is able to react with gypsum, forming a strontium sulphate, which can replace the more soluble gypsum, reducing the mechanical stress. [91]

2.4 Barium hydroxide and carbonate nanoparticles

Barium hydroxide, $\text{Ba}(\text{OH})_2$, is a caustic alkali compound, existing in anhydrous or octahydrate form. Due to its solubility in water (from 1.7 g/l at 0°C, up to 101.4 g/l at 100°C), it is a very strong base. Its 5% aqueous solution is known as "barite water", and it is used to search carbonates and sulphates in the analytical field. However, its main application is in the ceramic industry.

Barium hydroxide can be transformed in a compound of greater interest, namely barium carbonate, BaCO_3 , having properties similar to those of calcium carbonate, which can be found in nature as the mineral Whiterite (Figure, but it is a rather rare mineral (Figure 2.5).



Figure 2.5. Whiterite mineral (barium carbonate)

Whiterite crystallizes in the orthorhombic system similar to aragonite. The crystals are constantly linked in groups of three, giving rise to pseudo-hexagonal shapes resembling bipyramidal quartz crystals, with faces that are generally rough and horizontally streaked [92, 93].

2.4.1 Synthesis and applications of barium nanoparticles

Barium hydroxide nanoparticles are obtained mainly by precipitation routes from barium salts, using organic additives or microwave irradiation. [94] However, these methods are characterized by some drawbacks (long times, limited quantities, high number of steps, high temperatures, organic additives), which do not make this product economically sustainable for large productions. The development of barium hydroxide on the nanoscale has received interest due to its peculiar properties related to the small size and high specific surface area. In particular, thanks to the carbonation reaction, these nanoparticles can be applied for the conservation of cultural heritage.

Barium carbonate nanoparticles are obtained by precipitation routes as well or using sol-gel combustion methods. [95] Barium carbonate is an important material in industry to produce barium salts, pigments, optical glasses, ceramics and electric capacitors.

2.4.2 Barium hydroxide nanoparticles in Cultural Heritage

Barium hydroxide has already been used as a consolidant product for carbonatic stones, representing a potential alternative to the use of lime given its greater solubility in water. Moreover, when barium ions are in contact with calcite crystals, a relevant exchange of barium ions with calcium ions can be reached. In this way, the precipitated barium carbonate is bonded to the calcite crystals, increasing its adherence to the stone material [96, 97]. The consolidant action of $\text{Ba}(\text{OH})_2$ is based on its carbonation reaction as well, but a disadvantage in the use of this product in the consolidation of stones is its low penetration ability [98]. For this reason, numerous techniques have been proposed to introduce this hydroxide into the matrix of the stone, such as the addition of urea to the solution to obtain a slow and controlled precipitation of BaCO_3 , but to increase the penetration depth, the use of controlled nano-sized $\text{Ba}(\text{OH})_2$ particles is essential [99]. Moreover, $\text{Ba}(\text{OH})_2$ solutions have been applied to consolidate gypsum materials and wall-paintings using the Ferroni-Dini method [100]. As for the strontium, the gypsum can be converted into barium sulphate as well, then the application of $\text{Ba}(\text{OH})_2$ solutions allow the stone consolidation. Also mixed formulations of nanolime and barium hydroxide nanoparticle were tested for the pre-consolidation of surfaces particularly affected by sulphates.

$\text{Ba}(\text{OH})_2$ has also been used as an additive material in the conservation of mortars. Barium hydroxide made a homogeneous binding material, composed by Whiterite (BaCO_3), calcite (CaCO_3) and a mixed barium-calcium carbonate ($\text{BaCa}(\text{CO}_3)_2$), without generating any defect [97]. Moreover, $\text{Ba}(\text{OH})_2$ was found to have a positive impact for the sulphate-resistance of lime mortars, by avoiding calcium dissolution when used as an additive to the lime binder [101]. So, the presence of barium phases inside lime binders can increase the durability of conservation mortars. And the addition of barium hydroxide can lead to the development of alkali-activated mortars as well, having a greater strength due to the formation of hydrated calcium silicates and aluminates with higher molar ratios of Si/Al and Ca/Al.

A further application of barium hydroxide in Cultural Heritage is in the deacidification of historical documents and ancient woods. Barium hydroxide nanoparticles suspended in aqueous or alcoholic solvents were applied to various ancient paper samples to verify their effectiveness. The treatment effect was measured by the pH

value and the reserve alkalinity test. The results of the reserve alkalinity tests indicate an improvement in the alkaline index, with a significant reduction in the acidity of the paper and an improvement in the pH value. For this kind of application, ethanol was the best solvent based on pH value, nanoparticle dispersion and spray use. Moreover, these nanoparticles possess a reinforcing effect on paper, and the accelerated aging test revealed that this effect remains also during aging. All the obtained results converge in the identification of these nanometric particles as an innovative, fully compatible and effective material for the consolidation and deacidification of old or also new paper surfaces. [94]

CHAPTER 3: IRON OXIDE NANOPARTICLES

Iron oxide nanoparticles are the most popular magnetic nanoparticles in biomedical applications due to low cost, low toxicity and superparamagnetic properties. Oxides are chemical compounds containing iron and oxygen, overall there are 16 pure phases between oxides, hydroxides and oxy-hydroxides. Among these are 6 iron compounds exclusively with oxygen: wüstite (FeO), magnetite (Fe_3O_4), hematite ($\alpha\text{-Fe}_2\text{O}_3$), beta phase ($\beta\text{-Fe}_2\text{O}_3$), maghemite ($\gamma\text{-Fe}_2\text{O}_3$) and epsilon phase ($\epsilon\text{-Fe}_2\text{O}_3$). As shown in the figure, compounds of iron with oxygen find applications in various sectors: from catalysis to semiconductors, from magnetic resonance to waste water treatment, from pigments to gas sensing, as shown in Figure 3.1.

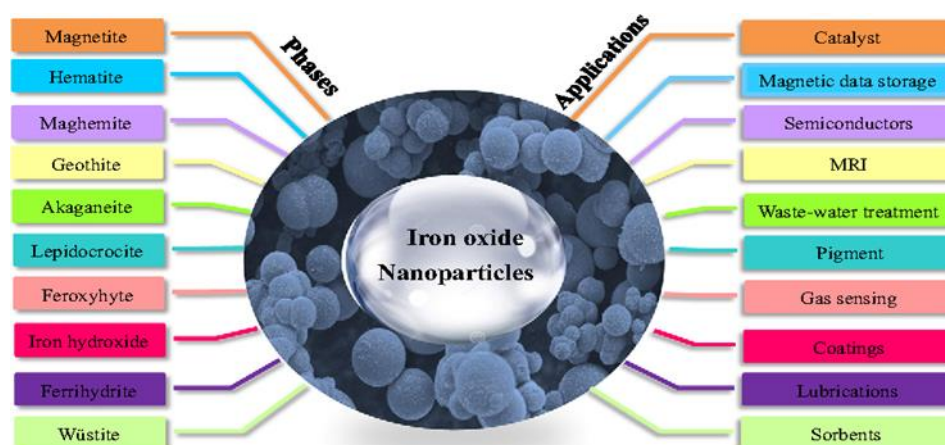


Figure 3.1. Example of iron oxides and hydroxides with possible applications [1]

Iron oxides nanoparticles are principally investigated as tools for medical imaging with a lot of applications, in particular in the diagnostic of a vast number of diseases (from atheromatous plaques to multiple sclerosis). It is possible to find applications of iron oxides nanoparticles also in the stem cell field, which has gained a lot of attention in both cardiologic and neurological research over recent years.

3.1 Magnetic properties of iron oxides

The magnetic properties of a material depend on how it behaves when subjected to an external magnetic field \vec{B}_0 [T]. To evaluate this behaviour, the following 3 vector quantities are used: the magnetic induction field \vec{B} [T], the magnetic field \vec{H} [A/m] and the magnetization vector \vec{M} [A/m], which represents the magnetic moment of the material for volume unit. There is a relationship between these 3 vectors:

$$\vec{B} = \mu(\vec{H} + \vec{M})$$

where $\mu = \mu_r \mu_0$ [H/m] is the absolute magnetic permeability of the material, given by the product between the relative magnetic permeability μ_r and the magnetic permeability of vacuum $\mu_0 = 4\pi \cdot 10^{-7}$ H/m.

Therefore, the magnetic induction field \vec{B} is the sum of a component $\mu\vec{M}$ that takes into account how the intrinsic magnetic moments of the electrons (spin) are oriented, and of a component $\mu\vec{H}$ which depends mainly on the presence of free charges in the medium.

For materials in massive form, 5 different types of magnetism are distinguished, and this classification can be expressed in terms of magnetic susceptibility ($\chi_m = \vec{M} / \vec{H}$), a dimensionless number. Materials can therefore be classified into:

- Diamagnetic ($-10^{-1} < \chi_m < -10^{-6}$): materials without a magnetic dipole moment. Under the action of an external magnetic field, the intrinsic magnetic moments are oriented in the opposite way respect to the applied field, and therefore a diamagnetic material is weakly rejected by it (e.g. water, gold, copper, silver).
- Paramagnetic ($10^{-6} < \chi_m < 10^{-1}$): materials having randomly oriented intrinsic magnetic moments that tend to align themselves in a not very rigid way in the direction of the external magnetic field when it is applied, therefore the paramagnetic substances are weakly attracted to it (e.g. hematite, ferrihydrite, aluminium).
- Ferromagnetic ($10^3 < \chi_m < 10^5$): materials show a long-range ordering at the atomic level in regions called Weiss domains, in which the magnetic moments are oriented in the same direction. In the presence of an external magnetic field, ferromagnetic substances are capable of magnetizing themselves in a

particularly intense way, thus becoming permanent magnets (e.g. iron, nickel, cobalt, gadolinium).

- Antiferromagnetic ($0 < \chi_m < 10^{-2}$): materials which in the presence of an external magnetic field tend to orient the intrinsic magnetic moments which are all parallel, but, unlike ferromagnetic materials, this occurs with two-by-two opposite directions, resulting in therefore the overall magnetization of the material is null (e.g. goethite, lepidocrocite, manganese).
- Ferrimagnetic: as for antiferromagnetic materials, the dipole moments are oriented with opposite directions, but in this case the magnetization is of different amplitude in the two orientations with consequent total magnetic moment non-zero, thus becoming permanent magnets (e.g. magnetite and maghemite).

Other than these types of magnetism, in ferromagnetic or ferrimagnetic nanomaterials it is possible to observe also superparamagnetism, which is a particular type of magnetism. To have this behaviour, materials must be composed of only one magnetic domain and this implicates particle dimensions generally less than 100 nm. This type of nanoparticles often has a magnetic anisotropy (the total magnetic moment tends to align itself along a preferential direction in the absence of an external magnetic field). If the thermal energy is high enough, they continuously change the direction of their magnetization and the average time that passes between two inversions of the direction is called Neel's relaxation time. For this reason, in the absence of an external magnetic field, it appears null on average. When a magnetic field is applied, these materials become magnetized in a similar way to a paramagnetic material, but with much higher magnetic susceptibility, which leads to higher magnetization values, similar to those of a ferromagnetic material. However, to observe the superparamagnetic behaviour, the temperature of the material must be below its Curie temperature as well. [2]

There is a critical radius, different for each ferromagnetic material and dependent on the crystalline structure, below which the material acquires a superparamagnetic behaviour. For instance, magnetite has a critical radius of 12.8 nm and maghemite has a critical radius of 16.6 nm, so under these dimensions they become superparamagnetic that makes them usable in different types of applications. [3]

3.2 Superparamagnetic iron oxide nanoparticles (SPIONs)

Superparamagnetic nanoparticles formed by iron oxides have great importance. Their main applications are: catalysts, biomaterials, fluids for heat transfer, transparent conductive coatings, nanocomposites, optical devices capacitors, materials for optical fibers and lasers, semiconductor transistor, additives for different types of material and dyes to glass.

One important research field is the realization of contrast agents for magnetic resonance imaging (MRI). For this application the most suitable iron oxides nanoparticles are magnetite (Fe_3O_4), maghemite ($\gamma\text{-Fe}_2\text{O}_3$) or other insoluble ferrites, such as hematite or ferrihydrite. These compounds have ferromagnetic properties when they are micrometric in size, but below certain dimensions of the magnetic domains, in the nanometric range, they acquire superparamagnetic properties. Superparamagnetic agents possess no magnetic properties outside an external magnetic field, but they are highly effective in MRI as enhancers of proton relaxation. In fact, the interaction between the magnetic moment of superparamagnetic particles and the protons of water molecules results in a decrease of relaxation time (T_1 and T_2). [4]

The maghemite ($\gamma\text{-Fe}_2\text{O}_3$) is an oxide of iron Fe^{3+} and it is possible to find it in nature from the oxidation of magnetite at low temperature; its name originates from the compounds MAGnetite and HEMatite, having the same magnetic properties as the first and the same composition as the second. Its typical appearance and molecular structure are reported in Figure 3.2a. The magnetite (Fe_3O_4) instead is the oxide with the higher content of iron (about 72.5%) and it is widely used in industries dealing with metals. It represents one of the minerals with the strongest magnetic properties existing in nature, in particular it can be found in igneous and metamorphic rocks. It is a combination of both oxidation of iron (Fe^{3+} and Fe^{2+}) in a 2:1 ratio and it can also be produced biologically by some organisms. Its typical appearance and molecular structure are reported in Figure 3.2b.

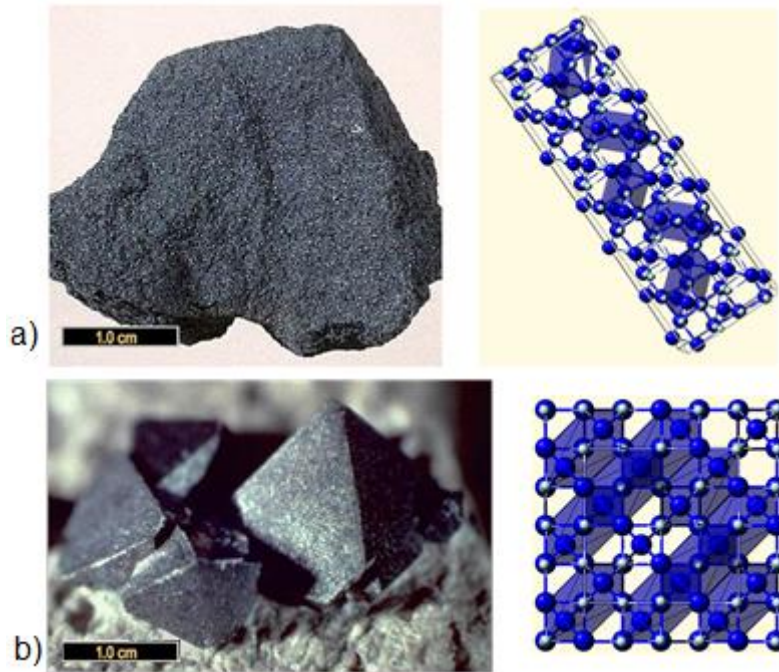


Figure 3.2. a) mineral morphology and molecular structure of maghemite; b) mineral morphology and molecular structure of magnetite [5, 6]

The maghemite nanoparticles are principally employed as: catalysts, gas sensors, anti-corrosion agents, nonlinear optics, semiconductors, pigments and biomedicine. While, the magnetite nanoparticles find applications especially in: magnetic contrast agents in MRI, detoxification of biological fluids, ferrofluids, absorption of electromagnetic waves, magnetic coatings, magnetic separation of cells, magneto-optical devices, magnetic detectors, semiconductors and biomedicine [5, 6]. A specific application of iron oxide nanoparticles is as ferrofluids, which are liquids that become intensely magnetized exposed to a magnetic field. Ferrofluids are colloidal liquids having nanostructured magnetic particles suspended in a carrier fluid, typically water or organic solvents. The particles are coated with surfactants or polymers to inhibit the aggregation. Large ferromagnetic particles can be separated from the homogeneous colloidal suspension, creating magnetic dust when exposed to high magnetic fields. Ferrofluids are usually composed of superparamagnetic nanoparticles, so they do not retain magnetization without an external magnetic field and their magnetic attraction is weak enough to prevent magnetic agglomeration, due to the presence of the Van der Waals force of the surfactant. Their main application is the reduction of friction in the surface of strong magnets. [7]

There are two main categories of superparamagnetic iron agents:

- superparamagnetic iron oxides nanoparticles (SPIONs), ≥ 50 nm in hydrodynamic size;
- ultra-small superparamagnetic iron oxides nanoparticles (USPIONs), < 50 nm in hydrodynamic size.

This difference has relevant effects on the relaxivity constants and in bio-distribution and plasma half-life as well.

The iron core size is generally between 4 and 10 nm. [4] The hydrodynamic size of SPIONs includes the whole size of the particle, comprising the magnetic crystal surrounded by coating molecules and coordinated water molecules as well (Figure 3.3). This size is typically measured by dynamic light scattering (DLS) and photon correlation spectroscopy (PCS), in which the intensity of the diffused light is modulated using the Brownian motion of particles in solution. [8]

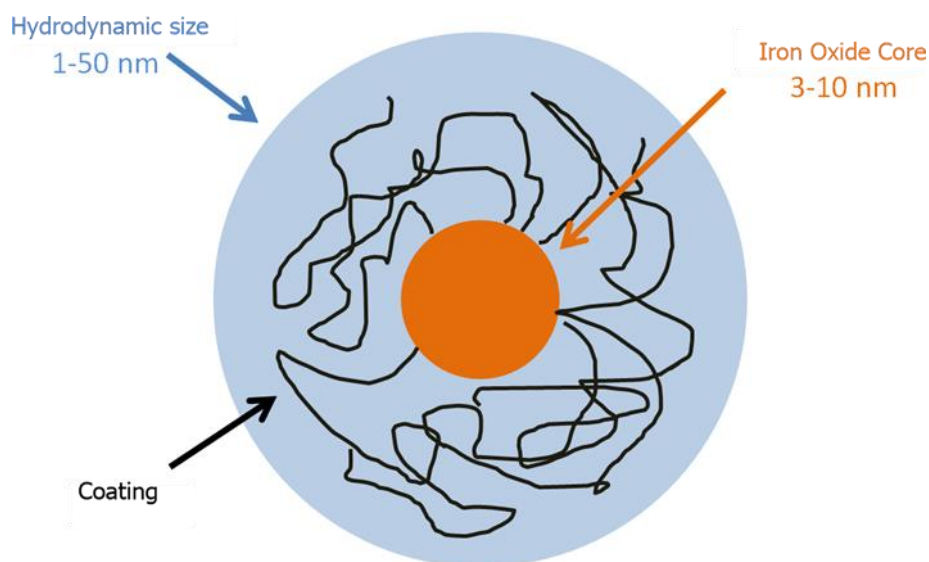


Figure 3.3. Typical structure of superparamagnetic iron oxide nanoparticles

3.3 Synthesis of SPIONs and other iron oxide nanoparticles

Iron oxide nanoparticles usually require surface modifications to achieve the biocompatibility and stability required for biological applications. In the absence of an external coating, they would tend to agglomerate under the action of the magnetic forces existing between them, causing various disadvantages such as the loss of superparamagnetic properties or the rapid removal from the human body by the reticulum endothelial system. To stabilize the particles in this sense, it is possible to modify the electrostatic repulsion force, which depends on the ionic strength and the pH of the solution in which the synthesis takes place, or on the steric hindrance which, in the case of polymeric coatings, is a function of the molecular weight of the polymer. For this reason, the techniques used in this context are numerous, and may include the addition during the synthesis of surfactants or different types of substances or the post-synthesis dispersion of nanoparticles. The surface coatings also protect the particles from oxidation and corrosion and allow the surface to be functionalized according to the application for which they are projected. They can be of different nature, as shown in Figure 3.4 and in Table 3.1.

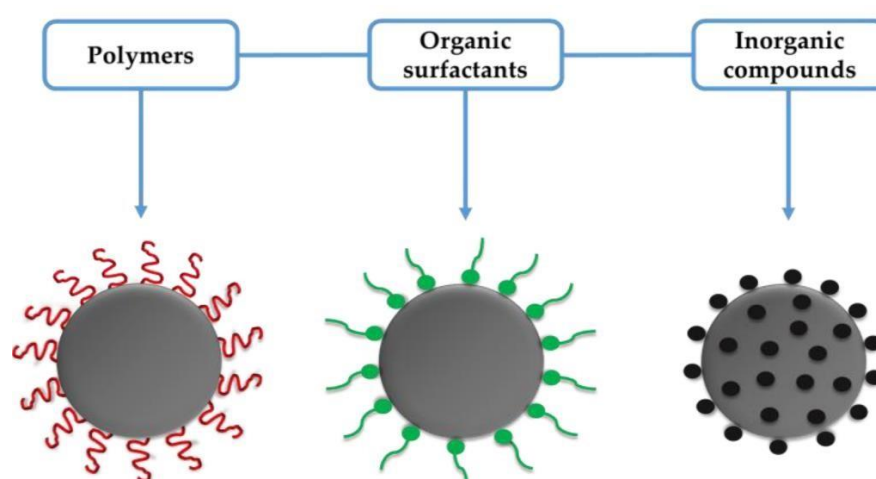


Figure 3.4. Different coatings for iron oxide NPs, the iron core is in grey [9]

Table 3.1. Coating agents typically used for iron oxides NPs, with principal features in terms of size, distribution, applications and advantages [9]

Materials used	Size and size distribution	Applications	Advantages
Amorphous silica	20–200 nm, broad	Isolation of biomolecules, for example, genomic and plasmid DNA, extraction of nucleic acids from soil, drug delivery, extraction of phenolic compounds from environmental water	Does not require any organic solvents and eliminates the need for the repeated centrifugation, vacuum filtration or column separation
Mesoporous silica	10–300 nm, broad	Controlled drug delivery, removal of mercury from industrial effluent, support for enzyme immobilization for bio-catalysis, fluorescence, isolation of genomic and plasmid DNA	Uniform pore size, large surface area, and high accessible pore volume
Polyethylene glycol (PEG)	10–50 nm, narrow	In vivo NMR imaging, in vivo contrasting	Improves the biocompatibility, blood circulation time, and internalization efficiency of the NPs, easy to functionalize
Polyvinyl alcohol (PVA)	10–50 nm, narrow	In vivo imaging and drug delivery	Prevents coagulation of particles, giving rise to monodisperse particles
Polyvinyl pyrrolidone (PVP)	10–20 nm, narrow	Contrasting and drug delivery	Enhances the blood circulation time and stabilizes the colloidal solution
Polyacrylic acid	~250 nm, narrow	Target thrombolysis with recombinant tissue plasminogen activator	Increases the stability and biocompatibility of the particles and also helps in bioadhesion
Polystyrene	10–20 nm, narrow	Cellular imaging and DNA hybridization	Stable and uniform size particles in suspension
Polymethyl methacrylate	10–50 nm, narrow	DNA separation and amplification	Novel, simple, and labor-saving; can be applied in automation system(s) to achieve high-throughput detection of single nucleotide polymorphisms
Polydipyrrole/dicarbazole	20–100 nm, broad	DNA hybridization	Molecular diversity for engineering functional polyDPyr-/polyDCbz-shell outer layers of magnetic nanocomposites
Ethyl cellulose	20–50 nm, broad	Extraction of pharmaceutical chemicals	Enhances the drug absorption into the surrounding tissues for a prolonged period of time
Chitosan	20–100 nm, broad	Tissue engineering, hyperthermia	A natural cationic linear polymer that is widely used as non-viral gene delivery system, biocompatible, hydrophilic, used in agriculture, food, medicine, biotechnology, textiles, polymers, and water treatment
Dextran	10–200 nm, narrow	Isolation of <i>Escherichia coli</i> , drug delivery, imaging	Enhances the blood circulation time, stabilizes the colloidal solution
Starch	10–20 nm, narrow	Contrasting and imaging	Natural polymers, biocompatible
Liposome	50–200 nm, broad	Imaging, drug delivery, hyperthermia, contrasting	Long-circulating time
Albumin	100–200 nm, broad	Cell separation	Magnetic tagging and separation, does not affect cell viability and proliferation
Erythrocytes	10–100 nm, broad	MRI imaging, drug delivery	Avoids the rapid clearance by the reticuloendothelial system (RES) and permits a long half-life in blood circulation
Gelatin	50–100 nm	Isolation of genomic DNA, drug delivery	Hydrophilic, biocompatible, natural polymer. Improves the efficiency of drug loading and is a rapid, simple, and a well-suited method for DNA extraction

One of the problems of the synthesis of superparamagnetic iron nanoparticles (SPIONs) is the aggregation of magnetic nanoparticles, so various methods are required to characterize their purity, their efficacy (in terms of magnetization and relaxivity) and the reproducibility of the synthesis. Moreover, both the biological and the physicochemical behaviour of the particles can be influenced by the size, the morphology and the composition of the particles and also by the nature and the charge of the coating. For this reason, synthesis methods are manifold and can be very complex. For all of them it is possible to outline advantages and disadvantages:

- 1) Bulk solution: allows to synthesize spherical nanoparticles, in the range size 10-50 nm with a very wide distribution, having a magnetization value in the range 20- 50 emu/g and a superparamagnetic behaviour. This method can be used to produce a large amount of nanoparticles in a single synthesis, but the oxidation that may occur to nanoparticles is uncontrolled, causing the presence of a diamagnetic contribution.
- 2) Pyrolysis/aerosols: allows to obtain spherical nanoparticles, in the range size 5-60 nm with a very wide distribution, having a magnetization value in the range 10-50 emu/g and good magnetic properties. This method can be used to produce a large amount of nanoparticles in a single experiment, but the produced particles agglomerates too easily.
- 3) Sol-gel: allows to synthesize spherical nanoparticles, with high porosity values, in the range size 20-200 nm with a very wide distribution, having a magnetization value in the range 10-40 emu/g and a paramagnetic behaviour. With this method it is possible to mix different components to obtain a type of nanoparticles, but the matrix can remain attached to the nanoparticles surface.
- 4) Gas deposition: allows to obtain spherical nanoparticles in the range size 5- 50 nm with a narrow distribution, having a magnetization value of about 20 emu/g and a superparamagnetic behaviour. This method is very effective for the production of thin films, but it requires high temperatures for the gas production.
- 5) Microemulsion: allows to synthesize cubic or spherical nanoparticles in the

range size 4-20 nm with a very narrow distribution, having a magnetization value of about 30 emu/g and a superparamagnetic behaviour. This method allow to produce nanoparticles having a great uniformity of the properties, but only a small amount of nanoparticles can be produced at the same time. [10-16]

Table 3.2 shows some of the principal syntheses of SPIONs, reporting the initial reagents together with the experimental procedure. For each synthesis, the main characteristics of the produced nanoparticles in terms of hydrodynamic size and efficiency as contrast agents are also reported, evaluated through the relaxivity, which represents the angular coefficient of the regression line obtained by reporting the values of the reciprocal of the T_2 times as a function of the concentration of iron. The greater the relaxation, the lower the T_2 with the same concentration, and this leads to a better contrast.

Table 3.2. Principal syntheses of SPIONs, with initial reagents, experimental procedure, hydrodynamic particle size and MRI results as r_2 of the obtained nanoparticles

Nanoparticles phase	Initial reagents	Experimental procedure	Particle size (nm)	MRI results as r_2 ($s^{-1}mM^{-1}$)	Ref
Magnetite	Polylactic acid (PLA), acetone, Pluronic F68, magnetite nanoparticles in water	PLA and acetone added drop by drop in to magnetite in water, mixed vigorously for several hours in order to allow the acetone to evaporate at RT	120-200	171-339 at 4.7 T	17
Magnetite	$Fe(SO_4)_2 \cdot 7H_2O$, $FeCl_3 \cdot 6H_2O$, NH_3 , deionized water, PAA, PAH, PVA	polymer added in the synthesis in N_2 atmosphere at $90^\circ C$ under vigorous mixing, then ultrafiltration and several washings	56-230	62-232 at 1T	18
Magnetite	$FeCl_2 \cdot 4H_2O$, $FeCl_3$, NaOH, HCl, deionized water, sodium citrate (TSC)	After coprecipitation of Fe_3O_4 and washings, dispersion in TSC for 6h at $80^\circ C$, washing the excess	30	102 at 1.5 T	19

Magnetite	FeCl ₂ •4H ₂ O, FeCl ₃ , NaOH, deionized water, dextran	After coprecipitation of Fe ₃ O ₄ , magnetic separation and washings, the pH is adjusted and the nanoparticles are dispersed in a dextran solution, mixing for 6 hours at 80°C, washing the excess	50	102 at 1.5 T	20
Magnetite	Fe(acac) ₃ , DEG, ethanol, ether, PEG600, deionized water	Synthesis in DEG at 140°C under N ₂ flow for 1h, then 200°C for 8h, then a ethanol/ether solution is added, several washings, finally PEG600 diacid is added, mixing for 24h and washing the excess	30	67 a 7 T on laboratory mice	21
Ferrihydrite	FeCl ₃ •6H ₂ O, NH ₄ OH, deionized water, HNO ₃ , carbossi-metil dextran (CMD), glucuronic acid	After coprecipitation at 90°C and washings, the ferrihydrite nanoparticles are dispersed for 2h at 80°C in a concentrated CMD solution (200 g/l), washing the excess	100	Tests on laboratory mice	22
Magnetite	C ₁₃ H ₂₆ O ₂ , Fe(CO) ₅ , C ₇ H ₅ O ₂ Cl, C ₆ H ₃₄ O, ethanol, toluene, poly(maleic anhydride alt-1-tetradecene), bis(6-aminohexyl) amine, chloroform	A solution of C ₁₃ H ₂₆ O ₂ in C ₆ H ₃₄ O is heated to 293°C under flow of Ar. Then a solution of Fe(CO) ₅ in ether and a solution of C ₇ H ₅ O ₂ Cl in ether are quickly added. The precipitated nanoparticles are washed and put in toluene, then poly(maleic anhydride alt-1-tetradecene) in chloroform and bis(6-aminohexyl) amine are added	9 a 44	15-120 at various T	23
Magnetite	FeCl ₃ •6H ₂ O, FeSO ₄ •7H ₂ O, bromoacetic acid, PEI-25, PEI-500, NH ₄ OH, deionized water	The coprecipitation reaction takes place in a solution of bromoacetic acid and PEI-25 or PEI-500, then the mixture is heated at 80°C for 1h, finally dialysis and ultrafiltration are executed	146-242	53 at 4.7 T	24

Iron oxide nanoparticles can be coated and dispersed in organic solvents also after the synthesis process, therefore in the following tables the main synthesis methods of the principal iron-based nanoparticles are reported, in particular ferrihydrite (Table 3.3), hematite (Table 3.4) and magnetite (Table 3.5). For each synthesis, the main features of the produced nanoparticles in terms of size and specific surface are also reported, which are relevant for their applications. [25-36]

Table 3.3. Principal syntheses of pure ferrihydrite nanoparticles, with initial reagents, synthesis environment, conditions and steps, particle size and specific surface of the obtained nanoparticles

Synthesis method	Initial reagents	Synthesis environment	Temperature and time	Further steps	Particle size	Specific surface
Chemical precipitation	Fe(NO ₃) ₃ ·9H ₂ O KOH	Deionized water Air	20°C 1h	Several washings	15-20 nm	347 m ² /g
Chemical precipitation	Fe(NO ₃) ₃ ·9H ₂ O NaOH	Deionized water Air	20°C 1h	Five washings	2-3 nm	277 m ² /g
Chemical precipitation	FeC ₆ H ₅ O NH ₃	A Deionized water Air	90°C 24h	Five washings	15-20 nm	176 m ² /g
Chemical precipitation	Fe(NO ₃) ₃ ·9H ₂ O NaOH	Deionized water Air	25°C 1h	Several washings	3-4 nm	133 m ² /g

Table 3.4. Principal syntheses of pure hematite nanoparticles, with initial reagents, synthesis environment, conditions and steps, and particle size of the obtained nanoparticles

Synthesis method	Initial reagents	Synthesis environment	Temperature and time	Further steps	Particle size
Chemical precipitation	FeCl ₂ ·4H ₂ O, NaOH	Deionized water Air	80°C 1h, 700°C 3h	Several filtrations and washings; drying and calcination	200 nm
Hydrothermal with microwave	FeCl ₃ ·6H ₂ O, NaOH	Deionized water Air	180°C 3h	Several centrifugations and washings; drying and calcination	600 nm

Micro-emulsions	Fe(NO ₃) ₃ ·9H ₂ O, NH ₃ , n-heptane, DDAB, TBAH	Deionized water Air	100°C 24h, 800°C 2h	Several centrifugations and washings; drying and calcination	50 nm
Hydrothermal	Fe(NO ₃) ₃ ·9H ₂ O, HMTA	Water/Ethanol, Air	100°C 2h, 500°C 3h	Several filtrations and washings; drying and calcination	70 nm

Table 3.5. Principal syntheses of pure magnetite nanoparticles, with initial reagents, synthesis environment, conditions and steps, particle size and specific surface of the obtained nanoparticles

Synthesis method	Initial reagents	Synthesis environment	Temperature and time	Further steps	Particle size	Specific Surface
Chemical precipitation	FeCl ₂ ·4H ₂ O FeCl ₃ ·6H ₂ O NaOH, HCl	Deionized water Argon	20°C 1h	Several washings	12-14 nm	100 m ² /g
Chemical precipitation	FeCl ₂ ·4H ₂ O FeCl ₃ ·6H ₂ O NH ₃ , C ₃ H ₆ O, HCl	Deionized water Air	40°C 0.5h	Several washings with various solvents	10-15 nm	87 m ² /g
Chemical precipitation	FeCl ₃ ·6H ₂ O FeSO ₄ ·7H ₂ O NH ₃ ·H ₂ O	Deionized water Air	30°C 0.5h	Six washings	23 nm	56 m ² /g
Chemical precipitation	FeSO ₄ ·7H ₂ O KOH, KNO ₃	Deionized water Nitrogen	80°C 18h	Dialysis	29-41 nm	12-14 m ² /g

3.4 Iron oxide nanoparticles in biomedical applications

Biomedical applications have certainly attracted the most interest for iron nanoparticles, in particular: contrast agents for MRI, hyperthermia and drug delivery. In particular, as contrast agents, superparamagnetic nanoparticles decrease the relaxation times of the magnetization vector in the tissues containing them, in this way these tissues can be mapped better on the magnetic resonance images. Therefore, if

the nanoparticles could selectively bind cancer cells, tumour regions would be more visible than other anatomical zones, facilitating both their identification and their therapeutic practice, such as radiation therapy or surgical excision.

The drug delivery is a process to administer pharmaceutical components for therapeutic effects, in this way the administered drugs can be conveyed together with other molecules. These molecules can locate the tissues or areas requiring the cure or can enable the absorption of the drug by these areas. Nanoparticles alone are not the cure for cancer or other diseases, but possess some advantages: their large surface reactivity gives the possibility to form bonds with different types of molecules. These molecules can be specialized drug for a type of cancer, different biocompatible coatings, various types of ligands, antibodies and some other structures. [4] So for each type of application are possible a lot of combinations between core materials, coatings, drugs and activators. The ligands, which are bound to the external coat, have the role of intermediaries between the drug carrier and tissue cells, leading to three main benefits. The first one is the regulation of immune response: interacting with the immune cells, ligands must make sure that the immune response does not interfere with the nanoparticles, limiting their strength and action range. The second one is the direct interaction with the cell membrane in order to modify membrane permeability. In this way nanoparticles are able to leave the bloodstream and penetrate into tissues, so that the released drug can reach easier the cytoplasm of cells. And the third one is the cancer targeting: through oncology analysis it is possible to determine the proteins on the surface of cancer cells. So producing a type of nanoparticle having this specific ligand, it will accumulate mostly on cancer cells, limiting the dose to healthy cells, also reducing the required quantity of a drug. Independently from the specific nanoparticle and coating, the solution will be injected intravenously to the patient: the first interaction will be with the blood and then with the immune system. Thanks to the coatings, it is possible to increase the half-lives and the stability of the carriers inside the bloodstream and the duration of entrapment of the drug. The scheme in Figure 3.5 describes the nanoparticles pathway from injection in bloodstream to drug release inside the cancer cells. The surface reactivity and the size of the nanoparticles have a great influence for both the drug delivery and the magnetic resonance imaging or hyperthermia. [37]

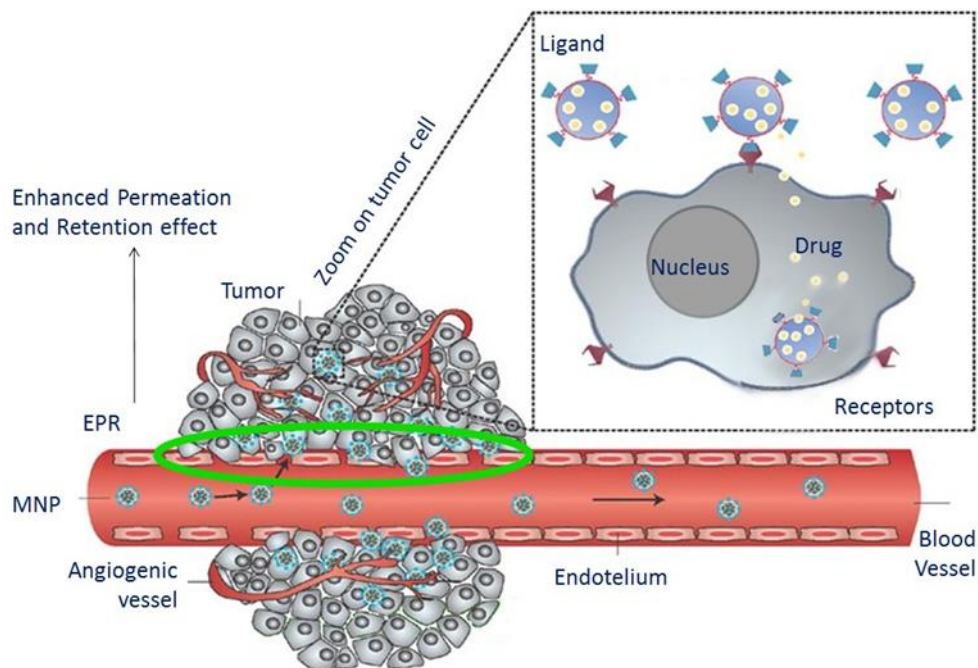


Figure 3.5. Scheme of the magnetic nanoparticles (MNPs) pathway from injection to drug release [38]

Human body has two organs acting as filters: the liver removes large particles from the bloodstream and the venous sinuses of the spleen remove particles larger than 200 nm. Therefore, since the half-life of coated particles decreases with increasing their size, the choice of the size depends on several parameters. Increasing the complexity of the coatings, the longevity of the nanoparticles with the immune system can be in contrast with the presence of functionalities for targeted action on the surface. A possible solution is based on the EPR effect (Enhanced Permeation and Retention), which is an effect caused by cancer cells altering the porosity of the capillaries and destroying their filtering mechanisms. Therefore, the number of selected ligands must be limited to enable nanoparticles to exit the bloodstream and penetrate cancer tissues. Another possible solution can be the synthesis of biological membranes containing nanoparticles. Some examples of these biological cages are the liposomes, the polymeric micelles, the cages protein and the cages of hydrogel.

The hyperthermia is a therapy performed using heat, which is based on some studies reporting that cancer cells mortality is greater than normal cells with increasing the temperature. Moreover, drugs and radiation, at the base of chemotherapy and radiotherapy, have demonstrated to be more effective increasing the temperature. So

the effects of hyperthermia are both the destruction of cancer cells and facilitation of the action of drugs and radiation, and collateral effects are limited and with low intensity. The magnetic hyperthermia uses fluids containing magnetic nanoparticles dispersed in an organic matrix, because of their superparamagnetic behaviour. In this way it is possible to heat the cancer tissue in an effective, uniform and targeted manner applying external magnetic fields (100-500 kHz) with an amplitude in the order of kA/m. The heating of these particles is related to relaxation processes: Brown and Neel. The relaxation of Brown is due to the rotation of a particle in the immersion fluid and the heat is produced by friction. The relaxation of Neel is due to a rotation of the magnetic moment, generating eddy currents heating the tissue. The effectiveness of the treatment can be evaluated in terms of heat transferred to the cancer tissue, which is related to the size and concentration of nanoparticles. [39]

In general, superparamagnetic nanoparticles have a higher absorption rate than ferromagnetic/ferrimagnetic nanoparticles, and the maximum value is obtained for a dimension close to that of the critical diameter, as reported in Figure 3.6 [40].

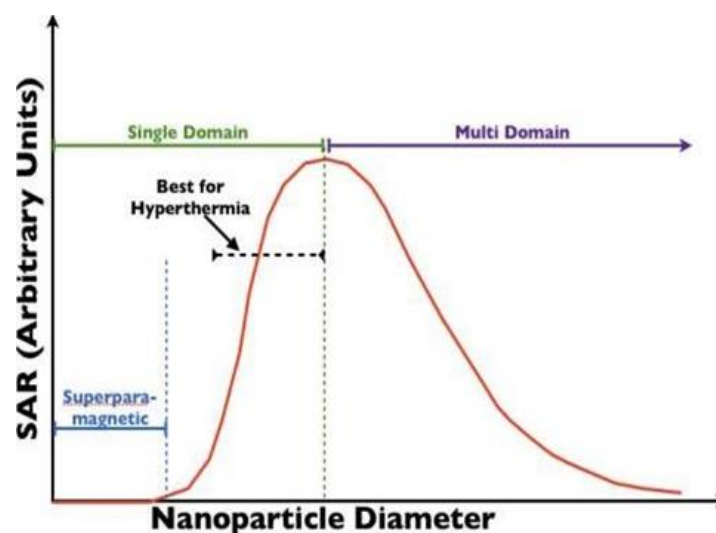


Figure 3.6. Ideal dimensions of the nanoparticles for magneto-fluid hyperthermia [40]

Furthermore, the effectiveness of the treatment also depends on the viscosity of the fluid in which the nanoparticles are dispersed and increases as the frequency of the alternating magnetic field increases. In addition, iron nano-oxides have a higher heating rate than other compounds used in fluid magneto hyperthermia obtained from the combination of iron with elements such as Barium, Nickel and Cobalt [41].

3.5 Existing products containing iron oxide nanoparticles

Some patented products based on iron oxide nanoparticles are already on the market, the most interesting nanoparticles among them are:

- Feridex: known also as Ferumoxide and Endorem, is an aqueous colloidal suspension of superparamagnetic iron oxide coated with dextran. It is used for intravenous administrations as contrast agent for MRI, for the diagnosis of liver lesions, typically associated with an alteration in the reticuloendothelial system (RES). Feridex is absorbed by macrophages only in healthy liver cells and not in cancers cells, increasing in this way the contrast between normal and abnormal tissue.
- Sinerem: known also as Combidex, contains ultrasmall superparamagnetic iron oxide nanoparticles for the diagnosis of metastatic disease in lymph nodes in MRI. As for Feridex, metastatic nodes have less uptake of this contrast agent, allows the differentiation of normal lymph nodes from metastatic nodes. Lymph node imaging with Sinerem is performed after 24 hours of slow infusion.
 - Resovist: is another MRI contrast agent containing organic coatings, used to detect small focal liver lesions. It contains superparamagnetic iron oxide nanoparticles coated with carboxydextran, which are accumulated by the phagocytosis in reticuloendothelial system (RES) cells of the liver. The uptake of Resovist from injection in the RES cells results in a decrease of both T2 and T1 weighted images. Most liver cancers do not contain RES cells, so they do not absorb the nanoparticles, resulting in an improved contrast of the cancer areas. Resovist can be injected also as intravenous bolus, allowing immediate imaging of the liver.
 - Lumirem: is a negative oral contrast agent, used to discriminate the intestinal loops from other abdominal structures. After the ingestion, Lumirem flows through the stomach and the intestine in 30 to 45 minutes. Lumirem improves also the visualization of adjacent abdominal tissues, like the pancreas.

- Clariscan: is another iron-based contrast agent, but with large molecular size to prevent diffusion into body tissues, developed only for MRI of the liver (uptake by macrophages), cancer microvasculature and micro-vessel permeability.
- VSOP-C184: contains ultra-small superparamagnetic iron oxide particles in aqueous solution, coated with a citrate and the overall particle size of 4-8 nm.

There are numerous methods to administrate iron nanoparticles: slow intravenous injection (Endorem/Feridex), subcutaneous injections (Sinerem) and injected as a bolus (Resovist). Advantages and disadvantages depends on the particles type and on the application. After the injection in the bloodstream, iron oxide nanoparticles are internalized into macrophages (Figure 3.7) or other phagocytic cells. Their interactions depend particularly on their size. Nanoparticles having a hydrodynamic size of 15-30 nm show a long residence time inside blood, allowing them to access macrophages deeply localized in pathologic tissues (such as lymph nodes, osteoarticular tissues, brain etc.). [42-44]

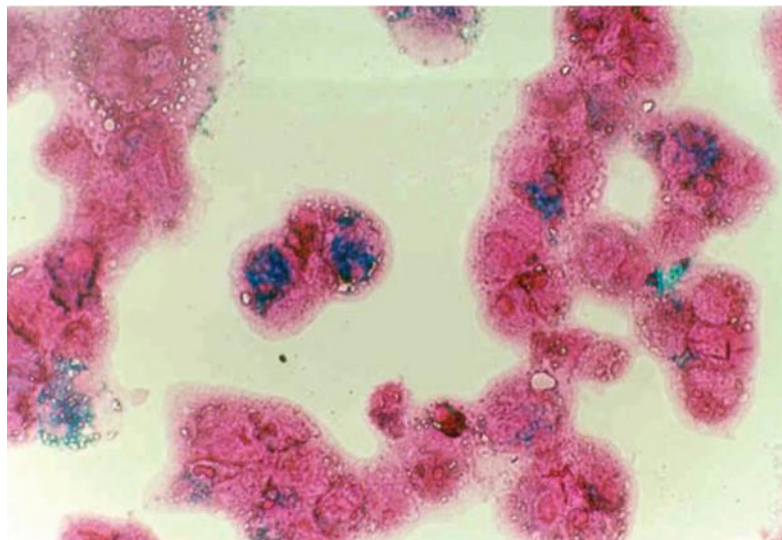


Figure 3.7. Iron nanoparticles intracellular localization after 24h incubation in human monocytes (iron staining with Prussian) [45]

Not only is the size important for tissue interaction, but also the chemistry of the surface. For example, superparamagnetic nanoparticles coated with an amino-functionalized PVA can interact with melanoma cells without any cytotoxicity. [46] The macrophages are specialized defensive cells with endocytic properties, which are involved in many diseases, so they are among the most used pharmaceutical target.

The value of charge of the coating gives to the particles specific properties: the negative coating results more biocompatible, while the positive one has an improved interaction with cell membranes. [47] To better produce tailored nanoparticles it is fundamental the knowledge of the typical velocity of their in vivo processes. Considering that the nanoparticles diffusion in tissues depends on blood residence time, animal imaging experiments are usually performed with high doses (200-1000 mmol/kg) and human experiments are performed with about 45 mmol/kg. The iron derived from the uptake of these nanoparticles is bioavailable, so it is incorporated into the body iron pools, in particular haemoglobin. This phenomenon is showed by the increment of ferritin levels, which is an intracellular protein that stores and releases iron. [48-50]

PART II: EXPERIMENTAL SECTION

CHAPTER 4: NANOMATERIALS CHARACTERIZATION

Dealing with nanomaterials synthesis means to characterize the obtained product from chemical, microstructural and practical points of view. It has been emphasized that nanoparticles possess special properties which make them useful for some different applications. In order to analyse these properties, it is necessary to use different kinds of techniques. This chapter is dedicated to the description of the main characterization techniques used during this thesis, with the related sample preparation procedure:

- ✓ X-ray diffraction (XRD),
- ✓ X-ray fluorescence (XRF),
- ✓ X-ray photoelectron spectroscopy (XPS),
- ✓ X-ray absorption spectroscopy (XAS) with Synchrotron light,
- ✓ Fourier transform infrared spectroscopy (FTIR),
- ✓ Thermogravimetric and differential thermal analysis (TG-DTA),
- ✓ Alternating gradient magnetometry (AGM),
- ✓ Transmission electron microscopy (TEM)
- ✓ Scanning electron microscopy (SEM),
- ✓ Atomic-force microscopy (AFM),
- ✓ Surface area analysis (BET),
- ✓ Magnetic resonance imaging (MRI).

4.1 X-ray diffraction (XRD)

Electromagnetic radiation is able to interact with matter through two main processes:

- Absorption: the radiation transfers all or part of its energy to the material system, increasing its temperature or causing its transition to an excited state. In the case of X-rays, the incident radiation has enough energy to cause electronic transitions, and to expel electrons from atoms (photoelectric effect).
- Scattering: during which the radiation is diffused by the matter and the electromagnetic waves associated with it change direction of propagation. This change can be accompanied by energy exchange between photons and matter (inelastic scattering; diffuse thermal scattering) or not (elastic scattering).

The X-ray diffraction technique is based on coherent elastic scattering: the macroscopic phenomenon of diffraction arises in fact from the coherent sum of all the electromagnetic waves diffused by the atoms that are located along the same family of lattice planes. To have this phenomenon, the presence of a lattice order is required, as is found in crystals, although this phenomenon can also be successfully observed in liquids using an energy dispersion X-ray diffraction (EDXD) instrument. However, X-ray diffraction is typically used measure substances in the solid state, depending on the nature of the sample, it is divided into single crystal X-ray diffraction (SC-XRD) and powder diffraction (XRPD, X-ray powder diffraction). The first technique is able to give three-dimensional information on the electronic density and on the thermal motions of each atom making up the crystal: however, the difficulty of obtaining single crystals and the complexity of data analysis make it a non-routine technique. Instead, the X-ray diffraction of powders is more used, which is much faster and cheaper, and allows to quantify the various components of a solid sample, and also to obtain information on the crystalline structure and on the size of the crystallites.

An XRD measurement is based on measuring the distances between lattice planes using a radiation source with a wavelength of about 1\AA , typically copper having $\lambda=1.54\text{\AA}$. Based on Bragg's law, the detector will collect, in the direction of the angle, a peak with a certain intensity depending on the radiation reflected by the sample (Figure 4.1).

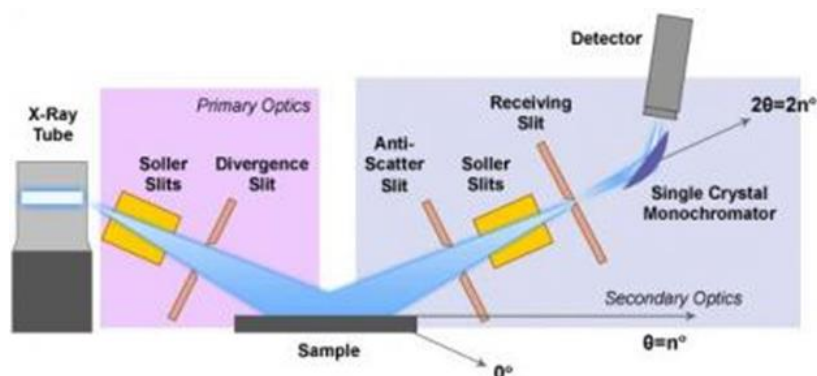


Figure 4.1. Schematic representation of the photoelectric effect in XRD

The Bragg's law it is a geometric law based on the optical path difference between two incident waves, as represented in Figure 4.2, where the points constitute the atomic rows and the blue lines the incident beams then diffracted at a certain angle θ . The mathematical expression of the Bragg's law is: $n \lambda = 2 d \text{sen}(\theta)$, where θ is

the angle that the diffracted beam forms with the crystalline plane, λ is the wavelength of the incident radiation, n is a positive integer and d is the distance between two adjacent parallel planes.

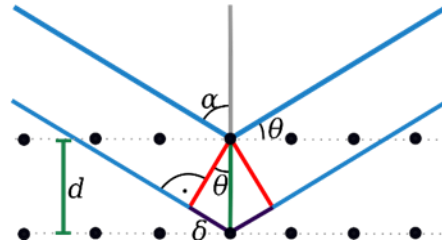


Figure 4.2. Bragg's law schematization

Parallel planes of atoms intersecting the unit cell, which is the basic repeating unit that defines a crystal, are used to define directions and distances in the crystal, these crystallographic planes are identified by Miller indices (hkl) , as reported in Figure 4.3.

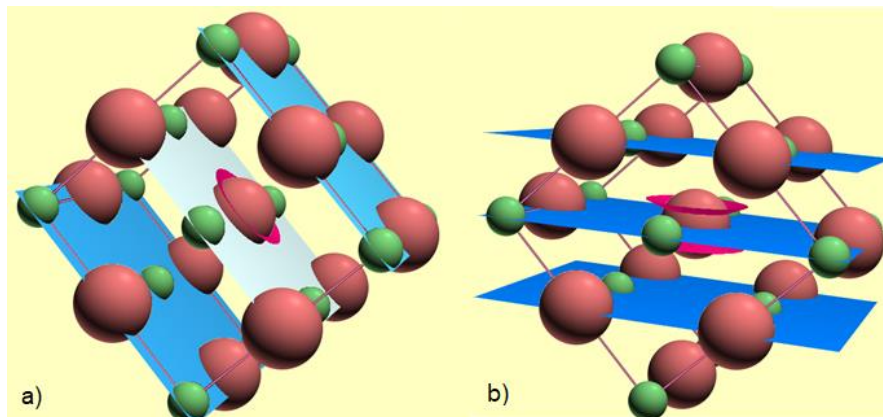


Figure 4.3. Miller indices of a) the (200) planes of atoms and b) the (220) planes of atoms in NaCl

In fact, atoms in a crystal form a periodic array of coherent scatterers and the wavelength of X-rays are similar to the distance between atoms. Diffraction from different planes of atoms produces a diffraction pattern, which contains information about the atomic arrangement within the crystal. A single crystal specimen in a diffraction pattern would produce only one family of peaks, therefore not all planes could be detected on a diffractometer. While a polycrystalline sample should contain thousands of crystallites, so all possible diffraction peaks should be observed. Basic assumptions of powder diffraction are that for every set of planes there is an equal

number of crystallites, which will diffract, and that there is a statistically relevant number of crystallites, as shown in Figure 4.4.

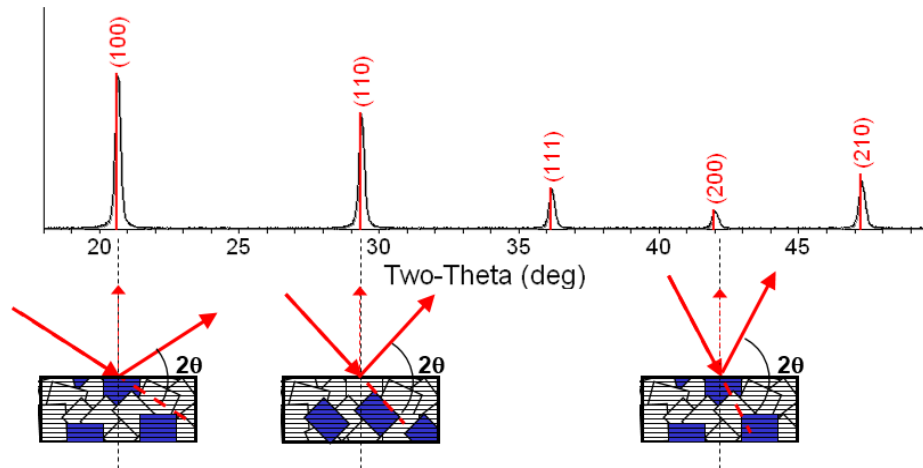


Figure 4.4. Crystallites of a polycrystalline sample that are properly oriented to diffract

Powder diffraction data consists of a record of photon intensity versus detector angle 2θ , so diffraction data can be reduced to a list of peak positions and intensities, where each d corresponds to a family of atomic planes (hkl). For instance, in figure 4.5 is reported the diffraction pattern of a polycrystalline TiO_2 sample: structural information is obtained from the position, intensity, width and shape of diffraction peaks.

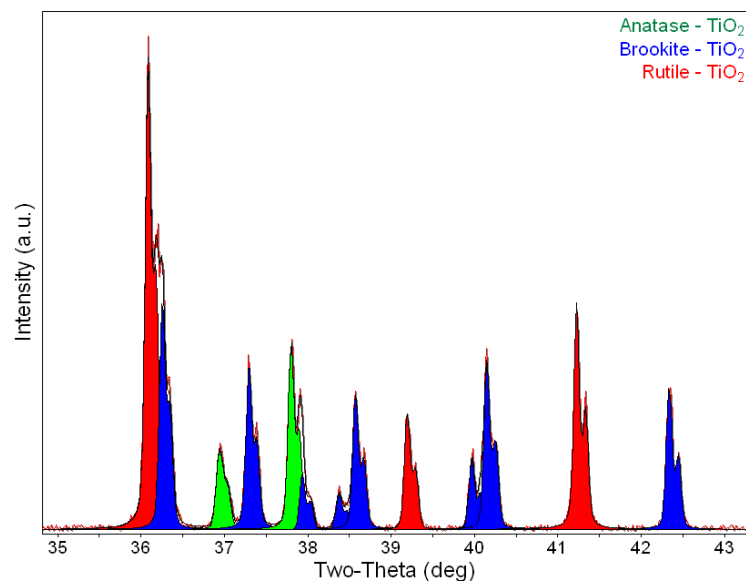


Figure 4.5. Diffraction pattern of a polycrystalline TiO_2 sample, with different colors for the different phases: Anatase, Brookite and Rutile

With powder XRD technique it is possible to determine:

- ✓ Phase composition and quantitative phase analysis of a sample, identifying the relative amounts of phases in a mixture by referencing the relative peak intensities;
- ✓ Unit cell lattice parameters and Bravais lattice symmetry through index peak positions, lattice parameters can vary as a function of alloying, doping, solid solutions, strains, etc.;
- ✓ Crystallite size and microstrain, indicated by peak broadening analysis;
- ✓ Crystal structure through Rietveld refinement of the entire diffraction pattern;
- ✓ Presence of preferred orientation of crystallites, indicated by a systematic variation in diffraction peak intensities;
- ✓ Residual stress and other defects (stacking faults, etc.), measured by analysis of peak shapes and peak width.

An ideal powder sample should have many crystallites in random orientations, because the distribution of orientations should be smooth and equally distributed amongst all orientations. If the crystallites in a sample are very large, there will not be a smooth distribution of crystal orientations, therefore the samples must first be ground and deposited randomly.

In this thesis, the data obtained from the XRD analysis were processed using the PANalytical Highscore Plus software. Then the search for the main peaks is carried out by the program using a method based on the second derivative. From the search for the peaks, all the information about the angular position of the peak, the interplanar distance, the relative intensity, the width and the crystalline size are derived. Then the identification of the phases is obtained by comparison with data sheets present on international databases, such as ICDD (International Centre for Diffraction Data) and ICSD (Inorganic Crystal Structure Database). The analysis can then be extended quantitatively to evaluate the relative % weight of the phases present in the spectrum, using the Rietveld refinement method. This procedure minimizes, by means of the least squares method, the difference between observed and calculated points using, as variables, the structural and instrumental parameters. The calculated spectrum contains two contributions, one for the background and one for each single Bragg reflection that are in a certain range around the step considered.

X'Pert Pro diffractometer PANalytical equipped by PIXcel1D detector, operating at 40 kV and 30 mA using CuK α 1 monochromatic radiation, is used during this thesis.

The XRD data were recorded generally with a step size of 0.026° , in a range $5-70^\circ$ 2θ . The structural as well as crystallite size and average lattice strain of the samples are estimated from the XRD line profile analysis using Rietveld analysis, by X'Pert High Score Plus software (PANalytical). ICSD and ICDD reference databases are used for the phase identification. X-ray data are fitted using the pseudo-Voigt profile function. Specimen displacement, polynomial coefficients for the background function, lattice parameters, profile parameters, and Gaussian and Lorentzian profile coefficients are refined. [1]

4.2 X-ray fluorescence (XRF)

XRF is an X-ray emission spectroscopy technique that allows the identification of the chemical composition of the sample examined, therefore it is often used as a complementary technique to XRD. This technique allows to establish the presence of elements with an atomic number greater than sodium, and by using an appropriate method of measurement and data analysis, this type of analysis can also be quantitative. The qualitative analysis is carried out by identifying the presence at least of the K_α and K_β emission of an element; the quantitative analysis is generally carried out by comparison with standards. The instrument employs an X radiation in order to create, due to the photoelectric effect, an electronic vacation in an inner shell of the atom of an element. This position is subsequently reoccupied by an electron that decays from one of the outermost shells, which in this way produces a photon that has an energy equal to the difference between the energies of the electron in the initial and final positions, as represented in Figure 4.6. In particular, from the vacation of an electron in the innermost shell (called K), photons of two different energies (lines K_α and K_β) are produced by decay from the successive orbitals. If the vacation occurs in the successive shell (the L one) the number of possible photons produced increases (L lines). The energy of the various decays $K_{\alpha 1}$, $L_{\alpha 1}$ and $M_{\alpha 1}$ increases as a function of the atomic number Z of the elements.

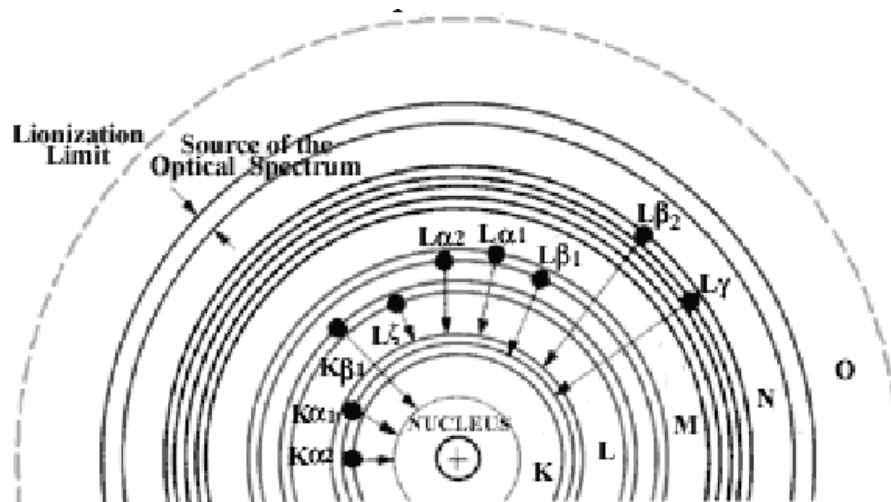


Figure 4.6. Main transitions in the internal atomic shells that produce the characteristic X-rays emission of the various elements in XRF

As a consequence of the penetration of an X-ray beam into a material, several photons are produced that form a pattern, which is made up of the peaks relating to the characteristic emissions of the elements making up the sample, but also by the elastic and non-elastic diffusion effects of the photons in the material itself. The number of photons present in a given peak is proportional to the weight fraction of the corresponding element in the volume of observed material. In practice, by measuring the area of the peak it is possible to identify the presence of the element to which it corresponds and its concentration, by preparing the sample according to a standard. The X-ray fluorescence method is extremely accurate; however, it is difficult to detect the presence of an element $< 10^{-8}$ g in the sample. The size of the particles and their shape are also important and determine the degree to which the incident beam is absorbed or scattered by the material, hence the samples are usually observed in tablet form. Elements with an atomic number lower than sodium are not detectable, as their emission energies are too low and are often reabsorbed by the atom itself or by other atoms.

4.3 X-ray photoelectron spectroscopy (XPS)

XPS is a qualitative spectroscopic technique to measure different parameters of solid materials, such as their elemental composition, together with the chemical state and the electronic state of the present elements. This technique is very useful

to analyse material surfaces. It is on the photoelectric effect: when a solid material is exposed to monochromatic R-X photons under vacuum conditions, the material emits electrons with a certain kinetic energy, as reported in Figure 4.7.

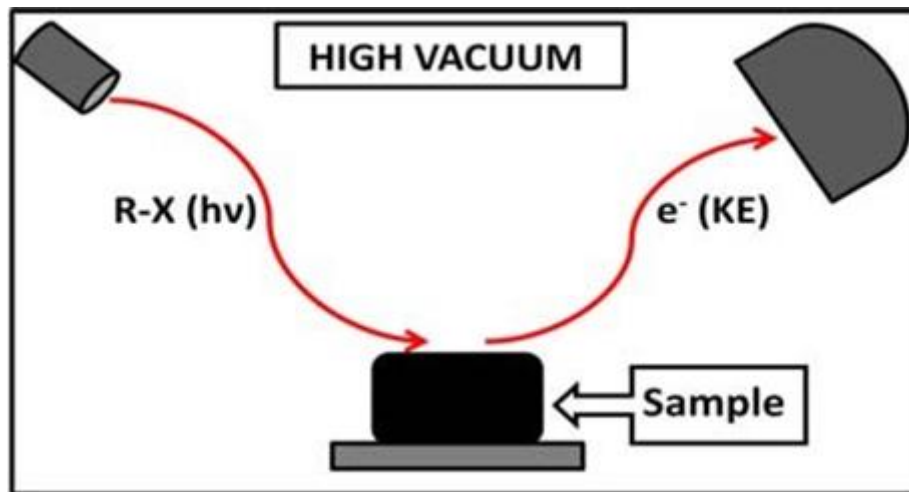


Figure 4.7. Schematic representation of the photoelectric effect in XPS

The resulting emitted electrons possess a kinetic energy given by the equation:

$$BE = hv - KE - \phi \quad (4.1)$$

Where KE is the kinetic energy of the emitted electrons, hv is the energy of the irradiated photons, BE is the binding energy of the initial atomic orbital of the emitted electrons and ϕ is a function of the spectrometer work. Since each element has an exclusive group of energies, this value can be isolated from the equation (KE is measured, ϕ and hv are fixed) in order to identify the different elements and also to know their chemical environment. There is also an AUGER emission, which is given by an X-Ray fluorescence process, in which an excited electron (L) occupies a vacancy in a less energetic orbital (K). The difference of energy is given to another electron in an L orbital, which is finally emitted out with 10-15 seconds of delay in comparison with the photoelectric emission. All the obtained spectra show the number of electrons for energy interval (CPS) respect to their corresponding binding energy. When there are different elements, the resulting signal is the sum of the different contributions, so, by analysing mathematically the obtained signal, it is possible to detect the different contributions, as reported in Figure 4.8.

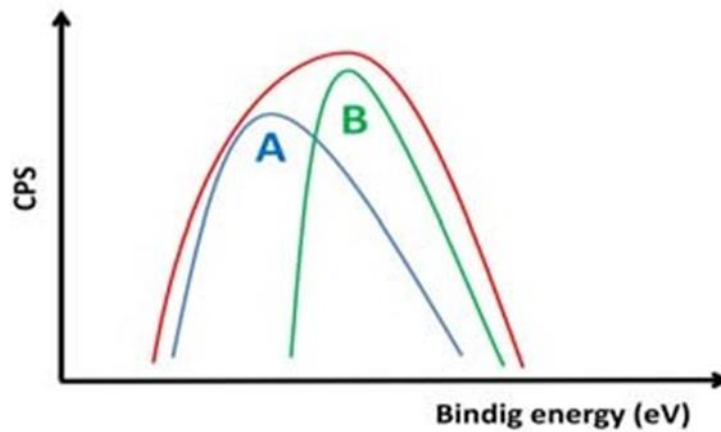


Figure 4.8. Representation of a typical XPS spectrum with mathematic operations to show two different contributions to obtain the original signal

From the analysis of XPS spectra, it is possible to obtain:

- ✓ quantitative data from the peaks height and width;
- ✓ chemical state from the peaks positions and space with neighbour peaks.

So this technique is useful to measure:

- ✓ elemental composition of a surface (top 1-10 nm of the material usually);
- ✓ elements that contaminate a surface;
- ✓ empirical formula of pure materials (except for H and He) with chemical or electronic state of each element;
- ✓ homogeneity of the surface elemental composition.

XPS measurements are here recorded at room temperature using a PHI 1257 system equipped with an Mg X-ray source ($h\nu = 1253.6$ eV) with a hemispherical analyzer. [2]

4.4 X-ray absorption spectroscopy (XAS) with Synchrotron light

XAS is a technique for measuring the linear absorption coefficient $\mu(E)$ of a material as a function of the incident photon energy (E) in the X-ray regime. This technique is element and orbital-specific because determines the local electronic and atomic structure of matter. Indeed, the XAS spectrum is conventionally divided into the XANES region (X-ray absorption near edge structure), from before the threshold to 60-100 eV after the threshold, and into the EXAFS (extended X-ray absorption fine structure) region, which extends until the end of the spectrum. In particular, XANES

is an element specific and local bond sensitive spectroscopic analysis that determines the partial density of the empty states of a molecule.

XAS has been extensively used since about 1950 to obtain information about molecular structure, bond type, coordination stoichiometry, ionic charges, etc. However, experimental X-ray absorption spectroscopic data from X-ray tube sources is affected by noise and systematic errors. So, since 1970 high brilliance synchrotron radiation started to be used to gain better absorption spectra. Experimental techniques have continued to develop and thanks to the exponential increase in brilliance over time, high quality XAS data is now routinely collected at a multiplicity of second and third generation synchrotron sources. These sources have a typical beamline set-up, made of a double crystal monochromator (DCM), which selects a particular energy from the incident synchrotron beam.

As discussed in the XRF section, an internal electronic vacation in an atom can be created when a core electron absorbs an X-ray photon and is ejected from its core shell. The successive process is the decay of an electron from another orbital, accompanied by an emission: Auger electron emission or X-ray fluorescence. For higher-energy excitation (K edges of elements with atomic numbers > 40), X-ray fluorescence is the primary relaxation process. Different core electrons have distinct binding energies, therefore, plotting the X-ray absorbance of a specific element as a function of energy, it is possible to obtain a spectrum similar to Figure 4.9. Obviously the energy will progressively decrease from the inner to the outer orbital, and the name of the absorption edges (K, L, M) are given, as for XRF technique, according to the principle quantum number n of the excited electrons (s, p, d).

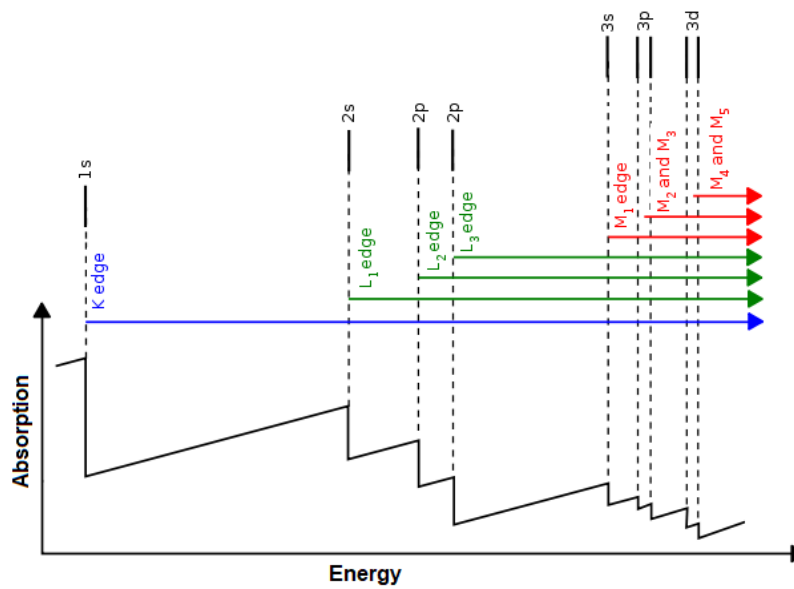


Figure 4.9. Main transitions in the internal atomic shells that produce the characteristic absorption edges of the various elements in XAS

Generally, as the energy of X-ray radiation is scanning through the binding energy regime of a central shell, a sudden increase in absorption appears, and this phenomenon corresponds to the absorption of the X-ray photon by a specific type of electrons of the nucleus (for example 1s electrons of Fe). This gives rise to a so-called absorption edge in the XAS spectrum due to its vertical aspect, as shown in a typical spectrum (Figure 4.10).

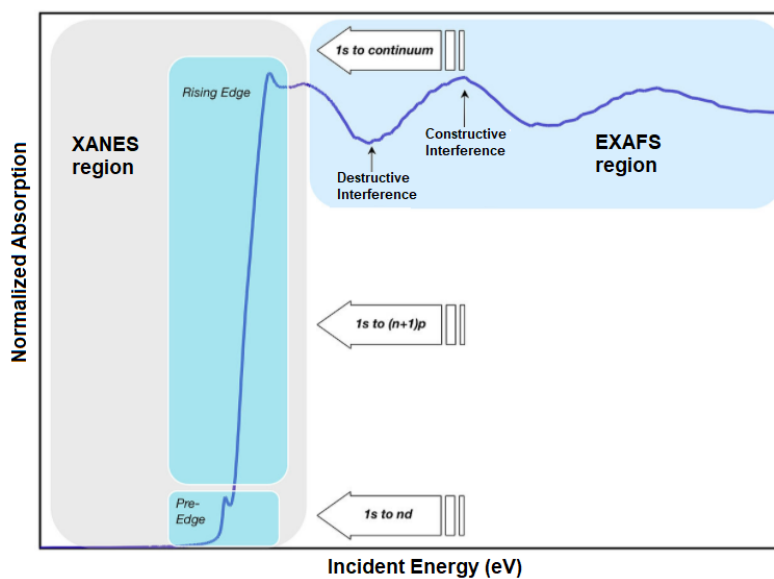


Figure 4.10. Typical X-ray absorption pattern, divided into XANES region (near edge) and EXAFS region (after the edge)

The absorption K edge is represented from the sharp rise in absorption, which occurs for each element at a characteristic incident energy expressed in eV. There are weak transitions below the absorption edge, called pre-edge structures, as well as significant absorption features in the immediate nearby area of the absorption edge and well above the edge. The structure that is located in the immediate nearby area of the absorption edge, conventionally within 50 eV of the absorption edge, is called XANES region. Beyond XANES, the oscillatory structure caused by interference between the outgoing and backscattered photoelectronic waves is referred to as EXAFS region, which can extend up to 1000 eV or more above the edge absorption. XANES directly probes the angular momentum of unoccupied electronic states: these states can be unbound (continuous) or bound (exitonic), broad or discrete, molecular or atomic states.

The commonly observed allowed transitions are indicated in the Figure 4.10. Weak pre-edge structures usually arise from constrained state transitions. The pre-edge structures before the K edges of the first row transition metals result from the 1s transition to the 3d transition. These pre-edge structures are observed for each transition metal of the first row until its 3d orbital is fully occupied. Although the transition from 1s to 3d is prohibited by the dipole selection rules, it is still observed due to the 3d to 4p orbital mixing and direct quadrupole coupling. As the mixing from 3d to 4f improves, the transition from 1s to 3d increases, which means that this trend can be used as a tool to probe the molecular geometric properties of the absorption sites. As the transition from 1s to 3d increases, the geometry of the absorption site distorts from a centrosymmetric geometry. The so-called L1 edge corresponds to the excitation of a 2s electron which requires more energy than a 2p electron. The 2p electron excitation is divided into two edges, i.e. L2 and L3, when a 2p electron is excited, an open-shell 2p⁵ electron configuration is formed, so spin-orbit coupling of such a system occurs.

Moreover, as the oxidation state of the absorption site increases, the energy of the absorption edge increases correspondingly. This observation is explained using an electrostatic model: atoms with a higher oxidation state require higher energetic X-rays to excite its central electron, because the nucleus is less shielded and has a higher effective charge.

Edge energies can be treated also as continuum resonances. A continuum resonance refers to a short-lived excitation process in which a central electron is

excited into a higher energy state that is usually above the continuum. An example is the potential well created by the absorbing and scattering between closest neighbouring atoms. When the distance between the absorber and the scatter is shortened, the energy of the continuous state increases as $1/R^2$. Since higher oxidation states imply shorter bond lengths in molecules, the edge energies increase as oxidation states increase. [3-5]

EXAFS region, typically starting at ~ 50 eV above the absorption edge, can be interpreted as due to the dispersion of the photoelectron expelled from the absorbing atom by the photoelectric effect. The photoelectron will disperse from the surrounding atoms and some of it will coherently return to the absorbing atom still in its excited state (before the hole in the electron level of the nucleus has been filled). The amplitude of the scattered photoelectron in the absorbing atom will change the probability of creating a photoelectron, and therefore the probability of X-ray absorption. EXAFS general equation is:

$$\chi(k) = \sum_j \frac{N_j S_0^2}{k R_j^2} F_j(k) e^{-2R_j/\lambda_j(k)} e^{-2k^2 \sigma_j^2} \sin \left[2k R_j + \Phi_j(k) \right] \quad (4.2)$$

with
$$k = \frac{2\pi}{\lambda} = \sqrt{\frac{2m_e(E-E_0)}{\hbar^2}}$$

where k is the wavenumber of the photoelectron, E is the energy of the X-rays, E_0 is the energy of the absorption edge and m_e is the electron mass. The normalized value of $\chi(k)$ is dimensionless, because the (standard) expression has F in units of $1/k$. Other definitions for a dimensionless F have $(kR)^2$ in the denominator to maintain consistency of units. The sum in the EXAFS equation is over shells of atoms of a particular type j and similar distances from the origin of the initial photoelectron. Therefore, R_j is the interatomic distance, N_j is the coordination number and σ_j^2 represents the mean-square disorder in the distance for the shell j . F_j is the photoelectron back scattering amplitude having $\Phi_j(k)$ as corresponding back scattering phase for the shell j . S_0^2 is an amplitude reduction factor for relaxation of the absorbing atom, because of the presence of the empty core level and multi-electron excitations. $\lambda_j(k)$ is the photoelectron inelastic mean free path, having a strong dependence upon k and a values range of 1-100 Å. For many systems works the approximation of $\Phi_j(k) \approx -2a_0k$ (a_0 is the Bohr radius), generating peaks shift ~ 0.5 Å below the actual interatomic distance for a particular shell in the Fourier transform of $\chi(k)$. Both $F_j(k)$ and $\Phi_j(k)$ depend upon the atomic number Z of the

scattering atom, having non-linear dependence on k . The $\exp(-2k^2\sigma_j^2)$ is typically called effective Debye–Waller factor, including thermal vibration and static disorder. The sum in the EXAFS equation can be considered over photo-electron scattering paths instead of atomic shells. In this way it is possible to include multiple scattering paths for the photo-electron, which can give important contributions in various systems. The interpretation of some components of the EXAFS equation becomes slightly modified: R_j is the half the path length, $F_j(k)$ and $\Phi_j(k)$ are the multiple scattering amplitude and phase-shift for the entire path. The EXAFS equation allows the numerical determination of the structural parameters N_j and R_j , then σ_j^2 knowing the amplitude $F_j(k)$ and $\Phi_j(k)$ for a small number (< 10) of paths (or shells). It does not work at low k , which is in the XANES region, because the $1/k$ term increases, $\lambda_j(k)$ increases, so the disorder terms do not strongly dampen the EXAFS, for this reason the EXAFS model of single particle scattering becomes no longer a good approximation. [6-9]

The data acquired from EXAFS beamline can be analysed using available computer software packages, such as Athena and Artemis. These programs contain AUTOBK for the background removal, FEFF6L for the generation of the theoretical EXAFS models and FEFFIT for the parameter optimization. Firstly, data has to be normalized in $\mu(E)$: a linear function is regressed to the pre-edge region and a quadratic function is regressed to the post-edge region. Normalized $\mu(E)$ spectra are obtained by subtracting the pre-edge line from the entire spectrum. At this point $\mu(E)$ data is converted to $\chi(k)$ data, which is then Fourier transformed in Artemis. The distances found in Fourier transform are shorter (0.2-0.5 Å) than real distances due to the energy dependence of the phase factors of the EXAFS equation, therefore the data has to be matched to theoretical models. This can be done using Artemis software, which an interface called “Atoms” that can convert crystal structure information into a cluster of atoms, providing in this way a list of atom positions in spatial coordinates to be used in FEFF computations. This generated structure is given as input to the FEFF code, which generates a theoretical EXAFS model (Figure 4.11).

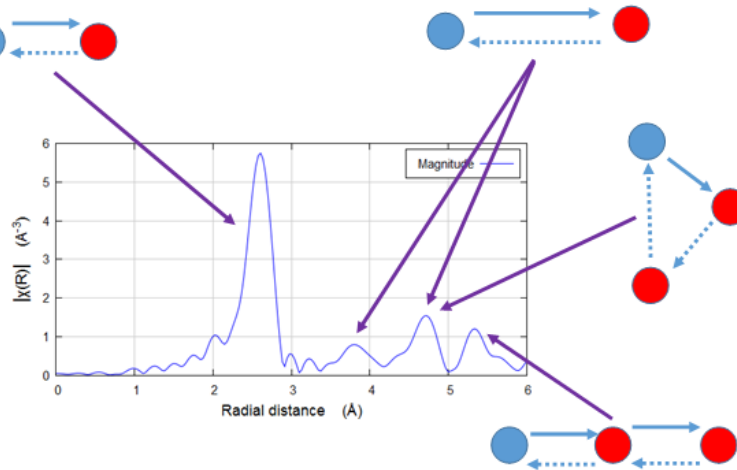


Figure 4.11. Example of the effect of the possible contributions of various scattering paths on a spectrum elaborated in radial distance (Å).

The theoretical model, according to the EXAFS equation, is written as a sum of paths of the contribution from all scattering paths of various photoelectrons, which originate from the absorbing atoms and are scattered from the neighbouring atoms, then finally return to the absorbing atoms. Each path owns several adjustable parameters optimized by the FEFFIT computer code to fit the data. These parameters include the electron reduction factor (S_0^2), the number of equal paths (N_i), the relative mean-square displacement of the atoms included in the path (σ_i^2), the energy shift for each path (ΔE_0) and a variation in the path length (ΔR_i). The theoretical model is modified as needed, for example including different atom types, until the best fit is obtained between experimental and theoretical spectra, as reported in Figure 4.12.

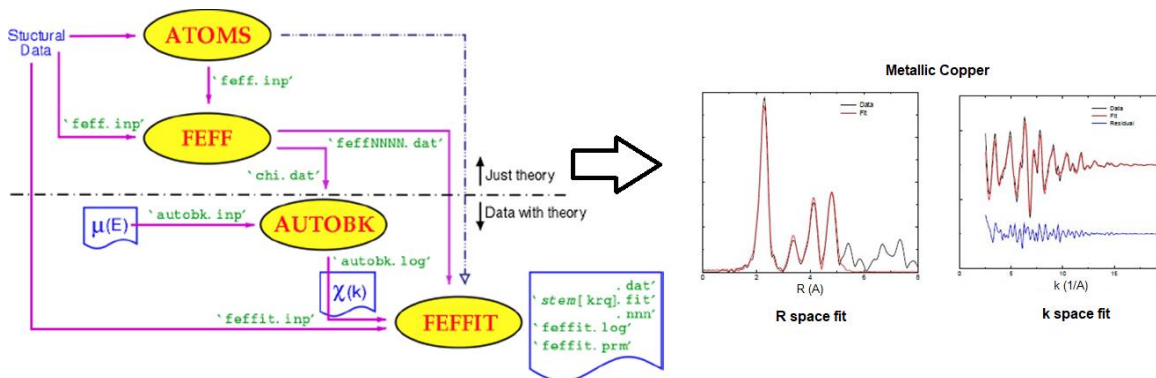


Figure 4.12. Computer software analysis scheme for EXAFS data

The parameters that are typically determined from this fit are the amplitude of the EXAFS oscillations (N , S_0^2 , σ^2) or the phase of the EXAFS oscillations (ΔE_0 and ΔR).

4.5 Fourier transform infrared spectroscopy (FTIR)

Infrared (IR) spectroscopy is an absorption spectroscopic technique normally used in the field of material characterization for the analysis of chemical bonds. The basic principle of this technique is the absorption of infrared photons by molecules, which pass from their fundamental vibrational state to an excited vibrational state. In a typical infrared spectrum, it is possible to find on the abscissa the wave number of the incident photons and on the ordinate the transmittance. The vibrations can be of two types: stretching of the chemical bond (stretching) and deformation of the bond angle (bending). Fourier transform IR spectroscopy or FTIR is performed using an interferometer, which allows the scanning of all the frequencies present in the IR radiation generated by the source. Scanning is possible thanks to a moving mirror which, by moving, introduces a difference in the optical path, causing constructive or destructive interference with the ray reflected from a fixed mirror. In this way an interferogram is obtained, with the representation of intensity in the time domain. By applying the Fourier transform, the infrared spectrum is obtained, consisting in the representation of intensity in the frequency domain. Among the main advantages of FTIR, which guarantees great reliability in the analysis of many organic and inorganic compounds, is the high availability of the used energy, resulting in a much better signal/noise ratio respect to traditional infrared spectroscopy. Furthermore, the analysis times are significantly reduced. [11]

FTIR measurements are performed by means of a spectrophotometer Thermo Nicolet Nexus; data are collected in the range $400\text{-}4000\text{ cm}^{-1}$, typically on samples in form of powder.

4.6 Thermogravimetric and differential thermal analysis (TG-DTA)

The analysis of the change in the mass of a sample during heating is known as Thermogravimetric analysis (TG). TG measures weight changes in a material as a function of temperature (or time) under a controlled atmosphere (generally nitrogen). Its principal uses include measurement of thermal stability or phase transitions of materials. TG is most useful for oxidation, dehydration, decomposition and desorption processes. The most used thermal method of analysis is the differential thermal analysis (DTA), in which the temperature of a sample is compared with the temperature of an inert material as reference during a programmed change of temperature (the temperature should be the same until thermal event occurs). If an endothermic event occurs inside the sample, its temperature will be lower than that of the reference material and a minimum will be observed on the curve. In contrast, if an exothermic event occurs, the temperature of the sample will exceed that of the reference material and a maximum will be observed on the curve. The area under the endothermic or exothermic event is related to the specific enthalpy, ΔH .

Thermogravimetric analysis is based on heating a mixture and some of the components can decompose into a gas during the whole process. An example of thermogram is reported in Figure 4.13, showing how the sample weight decreases with increasing temperature, in particular each slope corresponds to a weight loss produced by the evaporation of one or more components in the analysed mixture.

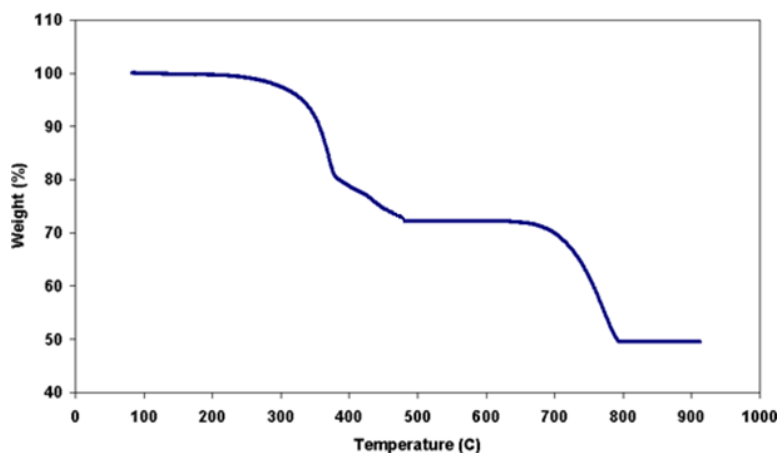


Figure 4.13. Example of thermogram of a mixture

Thermogravimetric analyses are useful also to determine the composition and purity of a sample, using stoichiometry ratios to determine the percent by mass of different

compounds (having different boiling points) in a mixture. Another technique usually combined with TG is the differential scanning calorimetry (DSC), based on comparing the difference between the amount of heat necessary to increase the temperature of the sample respect to the amount needed from a reference material to have the same temperature rise. Since the amounts of heat needed from the reference and the sample will be different to maintain both nearly at the same temperature, the resulting diagram will show the heat flow differences between them (Figure 4.14). [12]

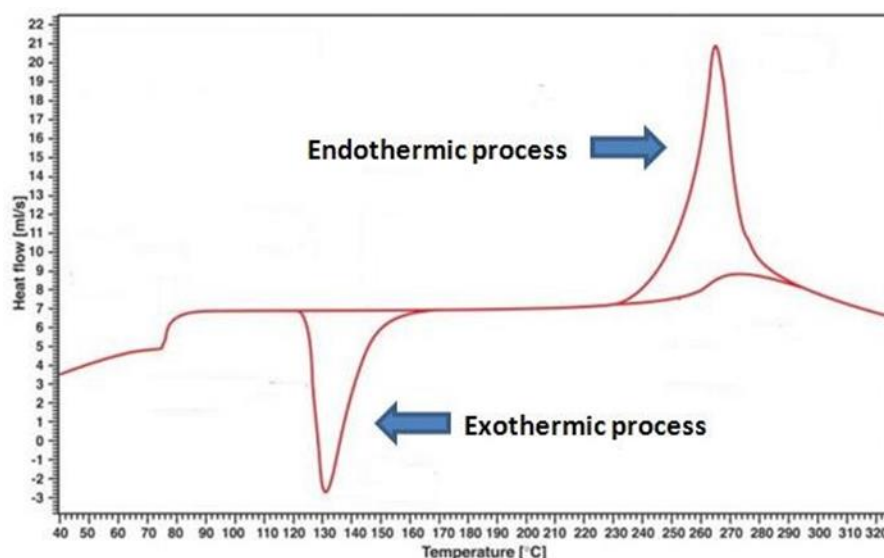


Figure 4.14. Example of DSC diagram of a hypothetical mixture

Thermal analyses are here carried out in air at a general heating rate of 10°C/min, using a LINSEIS L81 apparatus.

4.7 Alternating gradient magnetometry (AGM)

Magnetometers are used to characterize magnetic material properties. Magnetometry techniques can be typically classified into two categories: inductive and force-based. The inductive methods comprise extraction magnetometry, vibrating sample magnetometry, susceptometry and superconducting quantum interference device magnetometry. Alternating gradient magnetometry (AGM) is the most used force-based technique, which is commonly performed to characterize magnetic hysteresis loop. AGMs can achieve sensitivities up to 10^{-9} emu and the

measurements are very fast: a typical hysteresis loop requires seconds to minutes. Commercial AGM systems can be used for ambient temperature measurements using fields of 2-3 T fields achievable with electromagnets. Using AGM, through alternating cycles of magnetization in opposite directions, is possible to determine for a material the saturation magnetization M_s (its maximum magnetization), the residual magnetization M_R (magnetization at zero applied field after applying a saturating field) and the coercivity H_c (the magnetic field required to demagnetize the material). Magnetic hysteresis (Figure 4.15) is a phenomenon that characterizes ferromagnetic and ferrimagnetic substances, which can be detected by placing a bar of the material inside a solenoid connected to a generator.

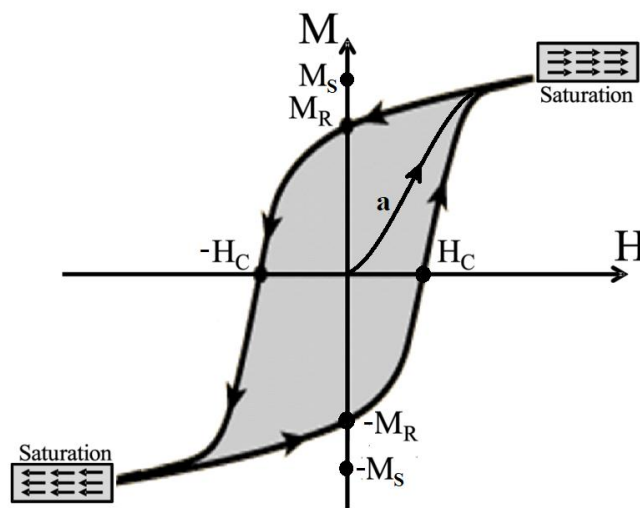


Figure 4.15. Example of magnetic hysteresis cycle: on the abscissa the magnetic field H , on the ordinate the magnetization of the material

The curves in the graph for a ferromagnetic medium are obtained by measuring the magnetic induction B in the material at different values of H , proportional to the current flowing in the device, and then calculating the magnetization. Starting from a non-magnetized material, by alternating cycles of magnetization, from the origin of the axes the curve "a" is obtained, called the first magnetization curve. The value of M increases until the saturation magnetization M_s is reached (the material reaches saturation). Then removing the magnetic field, the material has residual magnetization, so the descendent curve changes slope and intersects the ordinate axis for a magnetization value other than zero, called residual magnetization M_R . The material therefore remains magnetized even in the absence of current becoming a permanent magnet. To annul its magnetization, it is necessary to go in

the opposite direction of H, making the current flow in the opposite direction. The value of H to be applied to remove the residual magnetization is called coercive field H_c , which is dependent on the particle size. By continuing to increase the value of H, the material reaches the saturation magnetization with the opposite direction to the previous one, then removing the magnetic field the curve intersects again the ordinate axis for a value of M other than zero, which is again the residual magnetization M_R , but in the opposite direction. The magnetic permeability is not constant but is a function of H.

Magnetic characterizations are here performed using a PMC Micromag 2900 alternated gradient magnetometer (AGM) (Lake Shore Cryotronics)

4.8 Transmission electron microscopy (TEM)

The electron microscope is a type of microscope that does not use light as a source of radiation, but a beam of electrons. It was invented by the Germans Ernst Ruska and Max Knoll in 1931. The electron microscope uses a beam of electrons, rather than photons like an optical microscope, to have a lower wavelength. Since the resolving power of a microscope is inversely proportional to the wavelength of the radiation it uses, a resolution several orders of magnitude higher can be achieved using an electron beam. However, to use an electron beam it is necessary to operate in vacuum conditions, to avoid interference with the air molecules. In a "TEM" (Transmission Electron Microscope) the electrons of the beam cross completely the sample, then they hit a sensitive fluorescent screen, projecting on it a real and highly magnified image of the portion of the sample previously crossed. This technique can provide information about the structure, crystallization, morphology and strain of a sample. The schematic representation of a TEM is reported in figure 4.16: an electron gun produces a beam of electrons and accelerates them to high speeds using electromagnetic spirals with voltages of up to several volts. Then the electron beam is focused in a thin and small beam by an optical capacitor, which has a high aperture to eliminate high angle electrons. By reaching their highest brightness, the electrons zoom through the ultra-thin specimen and parts of the beam are transmitted according to how transparent the specimen is to the electrons.

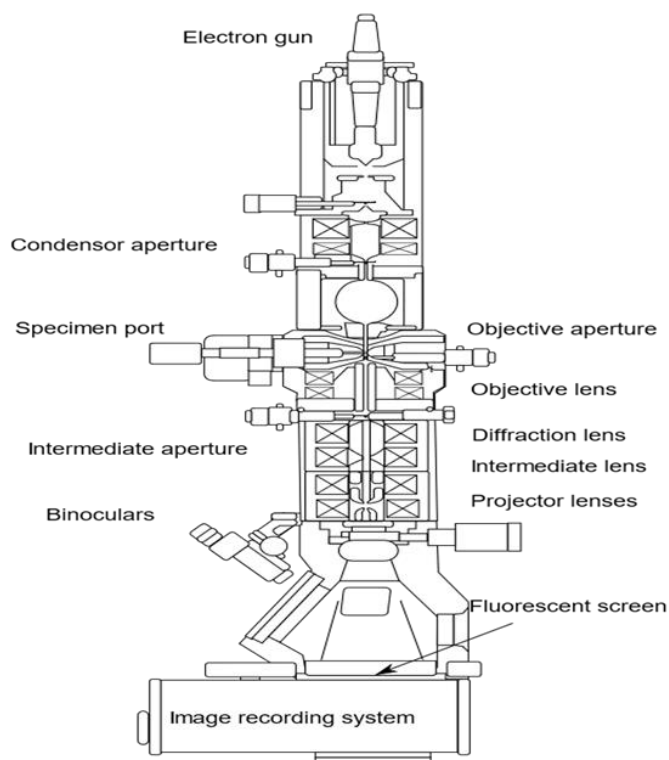
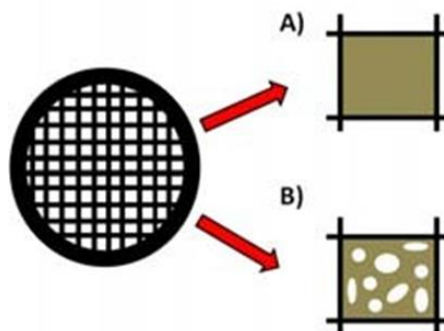


Figure 4.16. Schematic representation of a TEM

The lens focuses on the part of the beam that is emitted by the specimen in an image. Another component of the TEM is the vacuum system, which is essential to make sure that the electrons do not collide with the atoms of the air. A low vacuum is first achieved by using either a rotor pump or diaphragm pumps, which decrease enough pressure for a diffusion pump to operate, which then reaches a high vacuum level. The image produced by the TEM, called a micrograph, is seen through projection onto a fluorescent screen, which emits photons once irradiated by the electron beam. A camera positioned below this screen can be used to capture the image. This microscope provides black and white images, but many times images can be digitally processed to be improved. The limit of TEM resolution is 0.3 nm, because it depends on the electrons wavelength.

Depending on the kind of sample, some different preparatory techniques can be used for TEM. The optimal sample must be thin enough to allow electrons to get through it (a bulk material has to be reduced to a disc < 3 μm). However, all the samples prepared during this thesis are composed of nanoparticles, which can be dispersed in aqueous or alcoholic media. So, the samples have been prepared just by placing diluted nanoparticle dispersion drops on a suitable TEM grid and evaporating all the solvent. Typical grids are formed by copper covered by a thin

carbon monolayer, on which the nanoparticles remain fixed after evaporating the solvent. Grids are realized with a continuous carbon monolayer surface or with some hollows on the carbon monolayer (Figure 4.17). Grids with hollows are useful to study bigger particles, because they improve the contrast in the regions without carbon.



4.17. Representation of two different TEM grids: A) continuous carbon surface, B) carbon with hollows surface

Once the specimen has been properly prepared, it has to be inserted into its corresponding place inside the TEM column with its holder (a rod that keeps the sample attached, allowing also tilting or rotating the specimen). [13]

TEM microscope Philips CM100 is used in this thesis, the samples are prepared by immersion of the grids into diluted suspensions, working, if necessary, under a nitrogen atmosphere in order to avoid any reaction with the atmospheric O₂.

4.9 Scanning electron microscopy (SEM)

In a scanning electron microscope, the beam is generated by an electronic source as well, typically a Tungsten filament, which emits a flow of primary electrons concentrated by a series of electromagnetic lenses and deflected by an objective lens. The objective lens, in addition to further focusing the beam, imposes a controlled deflection on it, to allow the scanning of areas of the sample. SEM microscopes produce images bathing the sample with a focused electron beam which is scanned across an area of the specimen. Once the electrons hit the sample, some of them lose energy with various mechanisms. This energy lost turns into heat, light or X-ray emission, or other kinds of emissions. All the emissions have information about the properties of the sample surface, such as its composition and

form. The interaction between the electron and matter is revealed through detectors and converted into an electrical signal which, treated and amplified, is modulated into a television signal: one pixel of a monochrome monitor is associated with one point of the sample. The magnification is given by the ratio between the size of the image and the size of the scanned region. The result is a black and white image with high resolution and large depth of field, which has characteristics similar to those of a normal photographic image. For this reason, the SEM images are immediately intelligible and intuitive to understand. The scanning electron microscope can obtain nearly three-dimensional images of even relatively large objects (such as an insect). A Schematic representation of a SEM is reported in Figure 4.18, it must operate in high vacuum as TEM and the sample must be conductive and grounded, to be able to remove from the analysis area any possible accumulation of charge that would make observation impossible. Non-conductive samples can be observed by SEM operating metal coatings or performing the scansion quickly, to prevent the accumulation of charges from overheating the sample.

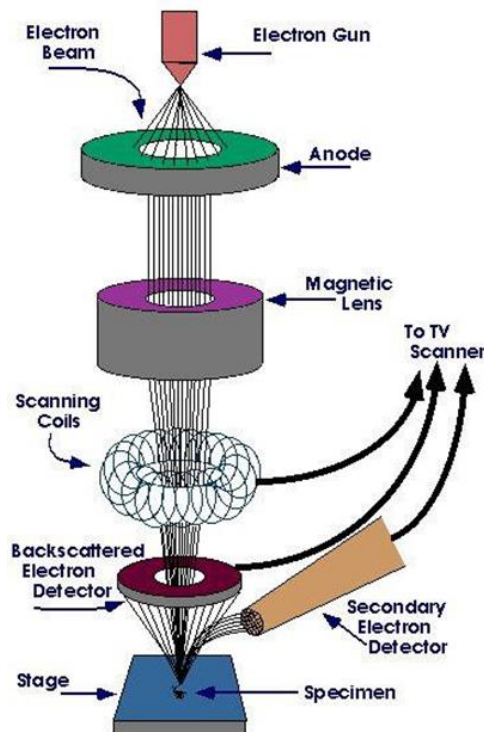


Figure 4.18. Schematic representation of a SEM

In conventional SEM, the observation of the sample can mainly take place in two ways: by detecting the secondary electrons or by detecting the backscatters. The limiting resolution of this instrument depends on the size of the incident beam focused on the sample, but generally it is of about 5 nm. [14]

SEM microscope Gemini 500 is used in this thesis, the samples are prepared on suitable stubs as solids or powders, working, if necessary, under a nitrogen atmosphere in order to avoid any reaction with the atmospheric CO₂.

4.10 Atomic-force microscopy (AFM)

The atomic-force microscope is a scanning probe microscope, consisting of a cantilever at the end of which a sharp tip (tip) is mounted, typically composed of silicon or silicon nitride, which has a radius of curvature of the order of nanometers. This investigator tip is placed in close proximity to the surface of the sample to be scanned. The van der Waals force acting between the tip and the sample causes a deflection of the microlift (whose elastic constant is known), in accordance with Hooke's law. Then the deflection of the lever is measured using a laser dot reflected from the top of the micro lever towards a photodiode array. However, a laser detection system can be expensive; an alternative method to determine the deflection of the microlift is to use piezoresistive AFM probes. These probes are manufactured with piezoresistive elements which act as resistance strain gauges. Deformations of the atomic force microscope probe due to deflection can be measured using a Wheatstone bridge, but this method is not as accurate as the laser deflection method.

If the tip were explored at a constant height, there would be a risk that it could collide with the surface, damaging it. As a result, a feedback mechanism is used in most cases to adjust the distance between the tip and the sample in order to keep the force acting between them constant. Generally, the sample is placed on a piezoelectric tube, which can move it in the perpendicular direction (z direction) to maintain a constant force and in the plane (x and y directions) to analyze its surface. The resulting map $s(x, y)$ represents the topography of the sample surface.

The atomic force microscope has three main modes of operation: force measurement, imaging, and manipulation. The force measurements allow to evaluate the forces present between the tip and the sample as a function of their distance. This method of operation can be applied during force spectroscopy measurements to measure certain properties of the sample, such as the modulus of elasticity (Young's modulus). In particular, force spectroscopy measures the

interaction and bonding forces between individual molecules, using mechanical stretching or torsional forces. Imaging is based on the fact that the force of interaction between tip and sample can be used to form a three-dimensional image (topography) of the sample surface at high resolution. The topographic image is constructed by recording the position of the sample relative to the tip and recording the height of the probe while maintaining constant interaction between the tip and the sample. Surface topography is commonly displayed using a false color chart. In manipulation methods, it is possible to change the properties of the sample in a controlled manner by exploiting the forces between the tip and the sample. Manipulation can take place at the atomic level and is used in applications such as probe scan lithography or for cell stimulation.

In addition to the acquisition of the sample topography, several local properties can be simultaneously measured at high resolution. Interesting examples are both mechanical properties such as sample stiffness or adhesion forces, and electrical properties, such as conductivity or surface potential.

The three main operating modes are distinguished according to the type of motion of the tip, that is the static mode, or contact mode, and two dynamic modes, the tapping mode and the non-contact mode. Tapping mode is defined as an intermittent contact (or AC) or AFM amplitude modulation method of acquisition by the acquisition mechanism. Similarly, non-contact mode is also referred to as frequency modulation AFM, by the image acquisition mechanism. The choice of tip is a fundamental element for all types of AFM scanning, whether it is scans in air or in liquid. In addition to the geometry of the tip and the type of sample, particular attention must be paid to the material the tip is made of, as well as to the coating, especially in the presence of liquid and in an acid environment.

AFM is very suited for characterizing nanomaterials, because it offers both qualitative and quantitative information on many physical properties including size, morphology, surface texture and roughness. A wide range of particle sizes can be characterized in the same scan, from 1 nm to 8 μm . AFM microscope Cypher Asylum Research available at the AFM platform of the PSCM in tapping mode is used for analysing some samples, which are prepared in by spin coating on suitable AFM grids from diluted suspensions.

4.11 Surface area analysis (BET)

In the characterization of nanomaterials, it is useful to measure the specific surface of the materials obtained as well, because this parameter has great interest for many applicative fields, such as catalysis, gas sensing, batteries, absorbents, pharmaceuticals, ceramic products or additives. The surface area is measured through gas porosimetry (generally nitrogen), which is an analytical technique that uses physical adsorption carried out at low temperatures (generally liquid nitrogen temperature), to obtain information about the pores and the specific surface area of a material, a characteristic dependent on the particle size. Following nitrogen absorption test, different types of isotherms are obtained, depending on the nature of the material. According to the IUPAC classification, it is possible to have six different types of adsorption isotherm, as shown in Figure 4.19a.

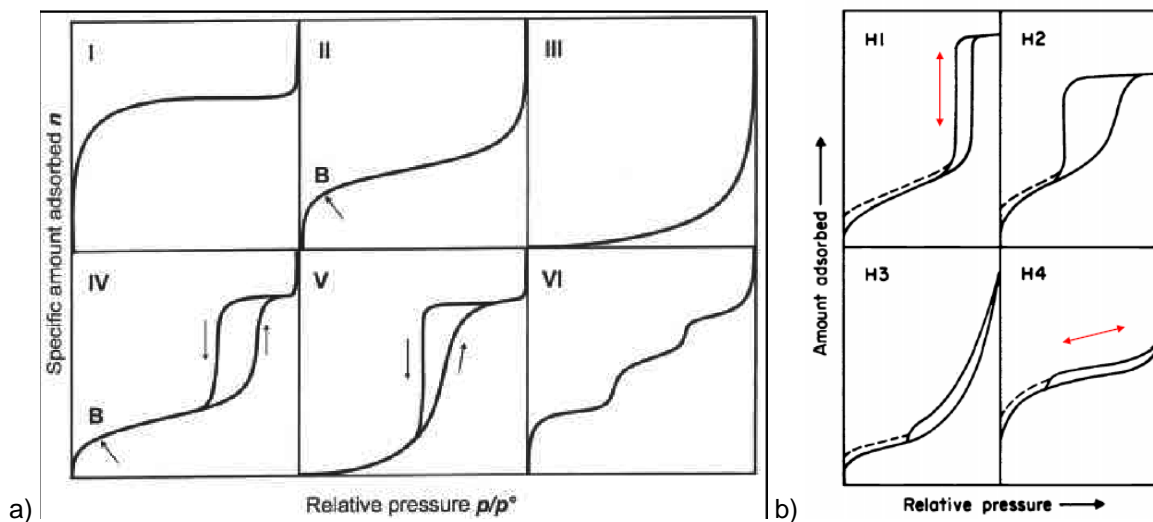


Figure 4.19. IUPAC classifications of a) adsorption isotherms and b) hysteresis loops [15]

Type I isotherms are given by microporous solids having relatively small external surfaces, this graph represents monolayer adsorption. Type II and III isotherms are given by non-porous or macroporous materials, representing unrestricted multilayer adsorption, in particular in type III adsorbent-adsorbate interactions are relatively weak. Adsorption on mesoporous solids proceeds through multilayer adsorption followed by capillary condensation, resulting in type IV and V isotherms; the distinction between these two types analogous to that between types II and III. Finally type VI isotherms represent stepwise multilayer adsorption on uniform non-

porous materials. Characteristic features of the Type IV and V isotherm are the hysteresis loops, reported in Figure 4.19b, which are associated with capillary condensation taking place in mesopores and can be divided in four kinds from H1 to H4. The hysteresis is usually attributed to thermodynamic or network effects or to the combination of both effects. H1 is associated to agglomerates or spherical particles arranged in a fairly uniform way, with a cylindrical pore geometry, indicating pore size uniformity. H2 is attributed to pores with narrow mouths (ink-bottle pores). H3 is associated to aggregates plate-like particles forming slit like pores. Finally, H4 is attributed to narrow slit-like pores, hollow spheres or particles with internal voids of irregular shape and broad size distribution. [15]

The analysis of the specific surface area is typically performed with the BET method, which allows to calculate the size distribution and volume of the pores of solids and powders. Surface area and porosity are physical properties that affect the quality and behaviour of porous materials, generally as the particle size decreases there will be an increase in the surface area and porosity. Materials with identical weight and volume may differ in terms of surface activity and adsorption volume based on their specific surface. Samples are commonly measured after a degassing process (heating in vacuum conditions) in order to remove impurities before the analysis, then they are analysed by measuring the volume of adsorbed gas at specific pressures and at low temperatures (77K for liquid nitrogen). The BET theory is the most used model to determine the area, the application concept is an extension of Langmuir's theory on single-layer molecular adsorption to multi-layer adsorption, with the following assumptions:

- the gas molecules are physically adsorbed on a solid in monolayers;
- the gas molecules interact only with adjacent molecules;
- Langmuir's theory can be applied at any level, because the adsorbed molecules become new adsorption surfaces and the process becomes continuous;
- the heat of absorption of all monolayers is equal to the heat of condensation, except for the first monolayer where it is higher.

From the BET theory we obtain the following equation, which allows to determine the volume of the monolayer:

$$\frac{p}{V(p_0-p)} = \frac{1}{V_m c} + \frac{c-1}{V_m c} \frac{p}{p_0} \quad (4.3)$$

where p is the pressure of the adsorbed gas at dynamic equilibrium; p_0 is the gas saturation pressure at the operating temperature; V is the volume of adsorbed

gas, proportional to the mass; V_m is the volume of the monolayer, proportional to the mass corresponding to the monolayer; c is the BET constant, linked to the adsorption enthalpy. Once V_m is known, it is possible to calculate the specific surface area, expressed in m^2/g , through the following equation:

$$S = \frac{a_m n_a V_m}{V_L m} \quad (4.4)$$

where n_a is the Avogadro constant ($6.02 \times 10^{23} \text{ mol}^{-1}$); a_m is the area covered by a nitrogen molecule (0.162 nm^2); V_L is the molar volume of nitrogen (22.414 dm^3).

To measure pore size by gas adsorption, the isotherms are recorded from low pressures to saturation pressure. The pressure range is determined by the range of pore sizes to be measured: microporous materials ($< 2 \text{ nm}$) are measured with isotherms in a pressure range of approximately 0.00001 torr to 0.1 torr , while mesoporous materials ($2\text{-}50 \text{ nm}$) are typically measured in a pressure range of 1 torr to about 760 torr . Generally, size of the pores that can be analysed with nitrogen adsorption measurements has a large range: from 0.2 nm up to about 400 nm . Available methods for measuring micropores distribution include: Density Functional Theory (DFT), MP-Method, Dubinin Plots (Dubinin-Radushkevich D-R, Dubinin-Astakov D-A) and Horvath-Kawazoe (H-K). Mesopore methods available include: Barrett, Joyner and Halenda method (BJH) and Density Functional Theory (DFT). In this thesis, the distribution and size of the pores, is determined by the numerical integration method BJH, which is an iterative mathematical procedure based on the hypothesis of open cylindrical pores and the absence of intercommunicating pores. It starts from the Kelvin equation, which relates the radius of pores r_k with the relative pressure p/p_0 , at which the capillary condensation of N_2 occurs within the pores having that specific size: [16, 17]

$$\ln \frac{p}{p_0} = - \frac{2\gamma V_L}{RT r_k} \quad (4.5)$$

The nitrogen adsorption measurements are here carried out at 77K , using a Micromeritics ASAP2000 system, utilizing Brunauer Emmett-Teller (BET) method for the surface area estimation. For each sample, about 0.2 g of dry powder are outgassed for about 15 h at 150°C ($5 \cdot 10^{-3} \text{ Torr}$) before performing the measure. The pore-size distribution is determined as well, generally considering the desorption branch of the isotherms with the BJH (Barrett–Joyner–Halenda) method.

4.12 Magnetic resonance imaging (MRI)

Nuclear magnetic resonance, or simply magnetic resonance (MRI), is a diagnostic imaging technique that exploits the magnetic properties of the nuclei of certain chemical elements present in the human body, mainly used for soft tissue investigations. An important advantage of this type of diagnostic test, unlike, for example, CT (computed axial tomography), is that it does not use ionizing radiation. At the base of the phenomenon of nuclear magnetic resonance there is the quantum property of spin. This phenomenon is in fact possible only for nuclei with non-zero spin, and this occurs for nuclei with an odd number of protons and neutrons [18]. For this reason, hydrogen having only one proton is used in the creation of biomedical images, due to its abundant presence in the human body. For the formation of the magnetic resonance signal, a static magnetic field B_0 with an intensity between 0.5 T and 1.5 T is generally applied, due to which a precession motion is generated, called Larmor's (Figure 4.20), of the particle axis, and therefore of the intrinsic magnetic moments, around the direction of B_0 , with a frequency called Larmor.

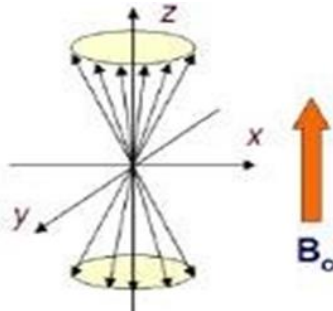


Figure 4.20. Larmor precession: precession motion of magnetic moments around the direction of the applied magnetic field

These moments can orientate parallel or antiparallel to the field. In the first case it is said that the protons assume a down state (minimum energy state), since they have a lower energy content than the second, indicated with up state (maximum energy state). Due to the Larmor precession, the magnetization vector M , that is the sum of all the intrinsic magnetic moments of each individual proton, forms a certain angle with respect to the z axis, and therefore has a longitudinal component M_z parallel to z , and therefore to B_0 , and a transversal component M_{xy} lying on the xy plane (Figure 4.21).

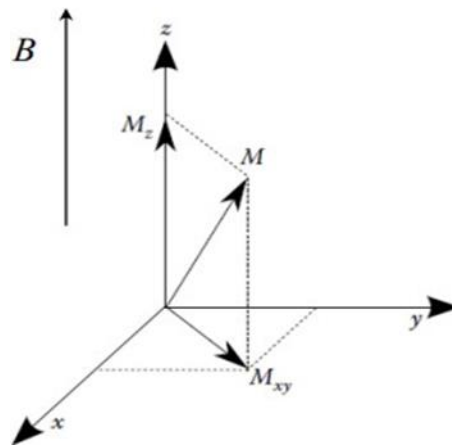


Figure 4.21. The two components of the magnetization vector M

In equilibrium conditions, the M_z component is different from zero since there is a greater number of protons in the down state, while the M_{xy} component is zero since the precession motion of the nuclei occurs with different phases and therefore the transverse contributions of the individual protons they cancel each other out. The component M_z in module is several orders of magnitude lower than B_0 and consequently is not measurable. Hence the need to overturn it on the xy plane by phasing the precession movements of the protons. This can be done by sending a polarized electromagnetic wave (called a 90° RF pulse) on the xy plane with a frequency equal to that of Larmor. The system thus enters into resonance and therefore there is a passage of energy from the electromagnetic wave to the proton system, which causes both the cancellation of the M_z component due to the fact that some protons receive the energy necessary to pass from the down state to the up state, both the synchronization of the precession of the nuclei.

With the passage of energy from the RF impulse to the proton system there is an increase in the potential energy of the latter which causes a situation of instability and therefore a tendency for the protons to return to the initial equilibrium conditions. Because of this, proton relaxation occurs, which consists of the recovery of the M_z component and the cancellation of the M_{xy} , two phenomena that begin simultaneously with the cessation of the RF pulse.

The relaxation process brings the system back to the equilibrium situation in which $M = M_z$ goes back to being parallel to the axis of the external magnetic field. In it two phenomena occur simultaneously and independently:

1. The longitudinal component of the magnetization, M_z , grows exponentially towards the initial equilibrium condition. The mechanism is associated with the loss

of energy of the spin system and occurs with a time constant T_1 . The lost energy is supplied to the sample (for example in the form of thermal energy) and for this we speak of longitudinal relaxation or spin-lattice;

2. The transverse component of the magnetization, M_{xy} , decreases exponentially towards the initial null condition. The mechanism is associated with the loss of phase coherence of spins and occurs with a time constant T_2 . This phenomenon is not associated with a loss of energy but with local fluctuations in the magnetic field that generate the loss of phase coherence of the precessing spins. It is called transverse relaxation or spin-spin.

After a 90° pulse the longitudinal relaxation of M_z is described by the function:

$$M_z = M_0 \left(1 - e^{-\frac{t}{T_1}} \right) \quad (4.6)$$

where M_0 is the value of the magnetization in the equilibrium condition. T_1 is the time needed to recover 63% of the longitudinal magnetization (Figure 4.22).

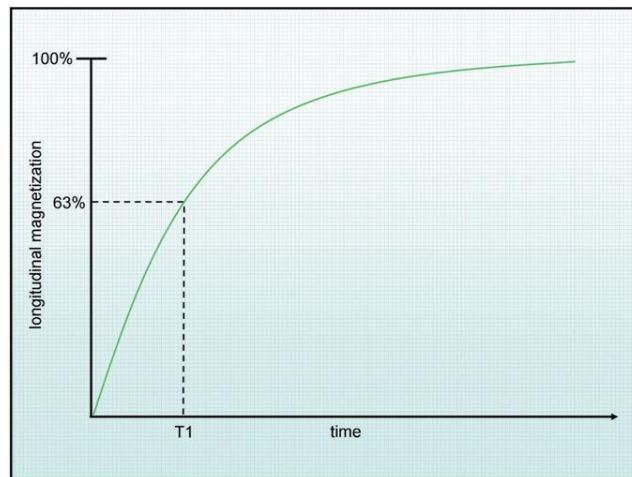


Figure 4.22. Longitudinal relaxation curve (T_1); the time is shown on the horizontal axis and the % of longitudinal magnetization on the vertical axis [19]

The relaxation time T_1 depends on the specific tissue. The lower T_1 , the higher the % of M_z recovered in a given time. This is important because in a magnetic resonance sequence the proton system is excited several times and to obtain an image of the tissue it is essential that between two RF pulses it recovers a good part of the M_z , so that with each RF stimulus the amount of magnetization to be overturned on the xy plane and therefore the intensity of the signal is greater.

The cancellation of the transverse magnetization M_{xy} occurs due to a loss of phase coherence between the various nuclei. This process is called spin-spin and, unlike

the spin-lattice, it is not accompanied by a release of energy. It is due to the fact that the spins are a source of small magnetic fields capable of influencing the local magnetic field. Consequently, each spin is subjected (in addition to B_0) to a local magnetic field which is a function of the molecular structure and relative movement and which will therefore be different for each spin. According to the Larmor equation, therefore, there is a non-uniform precession frequency that causes the loss of phase coherence. The decay of M_{xy} also occurs with an exponential law:

$$M_{xy} = M_0 e^{-\frac{t}{T_2}} \quad (4.7)$$

where the relaxation time T_2 is defined as the time needed to reduce the transverse magnetization by 37% (Figure 4.23). T_2 is always less than or equal to T_1 .

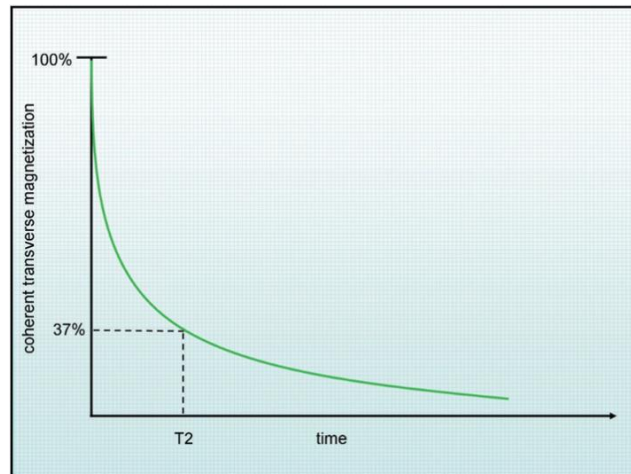


Figure 4.23. Transverse relaxation curve (T_2); the time is shown on the horizontal axis and the % of transverse magnetization on the vertical axis [19]

Tissues with a higher T_2 lose less transverse magnetization and therefore produce a higher signal. The overall signal of a tissue or organ can be obtained by arranging a radio frequency antenna, consisting of a closed circuit, perpendicular to B_0 (and therefore to M_z). According to Faraday's law, the variation of the magnetic field flux through the circuit, due to the precession of the nuclei, and therefore of the M_{xy} , generates an electromotive force induced in the circuit. The latter constitutes the magnetic resonance signal and has a sinusoidal trend due to the continuous moving away and approaching of the M_{xy} from the circuit. The maximum amplitude of the signal depends on the value of M_{xy} , in fact the higher it is, the greater the f.e.m. induced, while the exponential decay of intensity is due to the phenomenon of proton relaxation.

For the acquisition of images in MRI, sequences of RF pulses combined with free evolution intervals of the analyzed system are used (Fig. 1.9). The entire sequence is therefore made up of different time periods, determined through two parameters:

1. The repetition time (TR): is the time that elapses between the application of two RF excitation pulses, typically measured in milliseconds for biological samples. It determines the amount of longitudinal magnetization recovered between the excitation pulses;

2. The echo time (TE): is the time that elapses between the application of the RF pulse and the peak of the signal induced in the receiving coil, typically measured in milliseconds for biological samples. It determines the amount of transverse magnetization lost.

A typically used sequence is the Spin-Echo sequence, which uses a 90° RF pulse, followed by a 180° pulse to compensate for the spin phase shift due to external field inhomogeneities. In this sequence, after the 180° pulse, there is a time in which all the spins are back in phase and therefore the transverse magnetization and the signal on the receiving coil are maximum. This sequence of pulses is called spin-echo (Fig. 1.10). [19]

In the Spin-Echo sequence the TR indicates the time elapsed between two excitation pulses at 90° , τ indicates the time between the start of the 90° pulse and the beginning of the 180° pulse and $TE = 2\tau$ indicates the time elapsed between the 90° excitation pulse and the peak of the spin-echo signal (Figure 4.24).

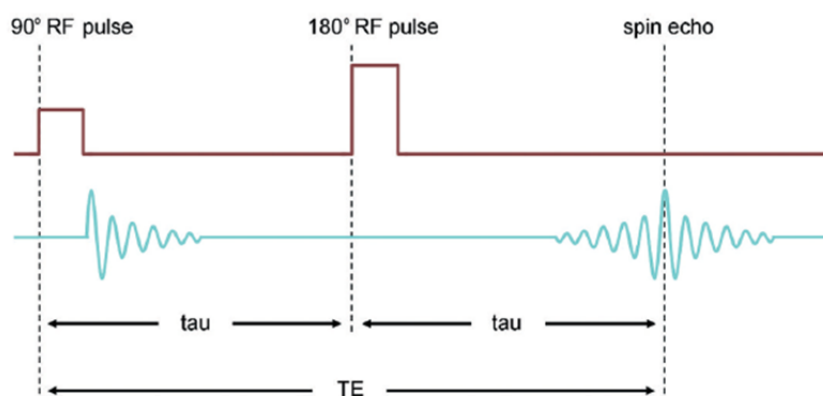


Figure 4.24. Spin-Echo sequence with associated parameters [19]

In obtaining the image in an MRI examination, it can be weighed in T_1 or T_2 . What varies is the type of tissue or substance (e.g. blood, water or CSF) that will appear hyperintense (white) or hypointense (black) depending on the T_1 or T_2 value.

Referring to formula of M_z , it is noted that in a T_1 -weighted image the tissues with a lower T_1 will appear hyper-intense, and this is due to the fact that there is a greater recovery of the longitudinal magnetization. Considering instead M_{xy} , for T_2 -weighted images, tissues with a higher T_2 will be hyperintense. To improve the contrast, appropriate contrast agents are used which vary according to how the image is weighed. In particular, it is possible to use:

- positive contrast media, which aim to reduce T_1 , such as gadolinium ion Gd^{3+} , which however has a certain toxicity and therefore coordination with chelating agents is required in order to produce a non-toxic complex;
- negative contrast agents, among which the most used are the SPIONs, whose presence is able to reduce T_2 . In fact, their high magnetic susceptibility leads to a greater local magnetic field and consequently there will be protons experiencing a greater local field with a slightly higher precession frequency and protons experiencing a smaller local field with a slightly lower frequency. This different precession speed therefore causes a loss of phase coherence between the protons, with consequent decay of the transverse magnetization and of the signal generated by it. The decay of the M_{xy} is much faster the greater the difference of the local magnetic field between spin and spin [18, 20].

CHAPTER 5: SCALE UP SYNTHESIS OF NANOLIME

An innovative synthesis method of nanolime was developed and patented (EP2880101) at the laboratory of materials science and technology of the University of L'Aquila (DIII department), where the present thesis work was carried out. Therefore, the experimental work of this thesis starts from the realization of a scale-up procedure for the production of calcium hydroxide nanoparticles through this innovative method, in order to realize extensive applications in the field of Cultural Heritage. Moreover, during this phase, some synthesis parameters have been optimized, such as concentration, time and regeneration of the resin.

5.1 Nanolime synthesis with an innovative method

This method, patented in the main European countries (EP2880101) in 2016, is based on an ion exchange process and overcomes the limitations of current production techniques, allowing to obtain pure $\text{Ca}(\text{OH})_2$ nanoparticles in aqueous suspension, in a single step, without the need for further purification or washing steps. The process operates at room temperature and ambient pressure, using cheap and regenerable reagents, and is characterized by a high yield of production in very short times. [1] The reagents used in the patent are calcium chloride (CaCl_2) and anion exchange resin in OH^- form (Dowex Monosphere 550A), using deionized water (specific conductivity $2 \mu\text{S}/\text{cm}$) as solvent. The production of $\text{Ca}(\text{OH})_2$ nanoparticles is represented by the following reaction:



This reaction is carried out, at room temperature, by pouring a 100 ml aqueous solution of calcium chloride (concentration 0.1 M) into an appropriate amount of wet resin (22 ml, considering a small excess of resin to have a complete exchange) and keeping the mixture under moderate stirring for 60 minutes. After this time, the resin is separated from the white precipitate phase of $\text{Ca}(\text{OH})_2$ that has formed in the synthesis through a simple sieving procedure. Following the separation, the resin could be regenerated to be reused in a new reaction, making the process sustainable. The scheme of the whole process is shown in the figure 5.1.

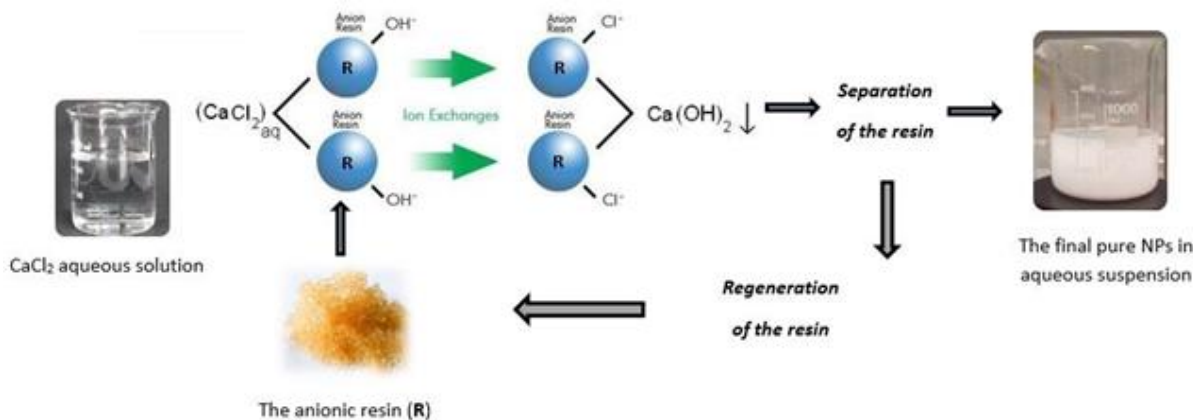
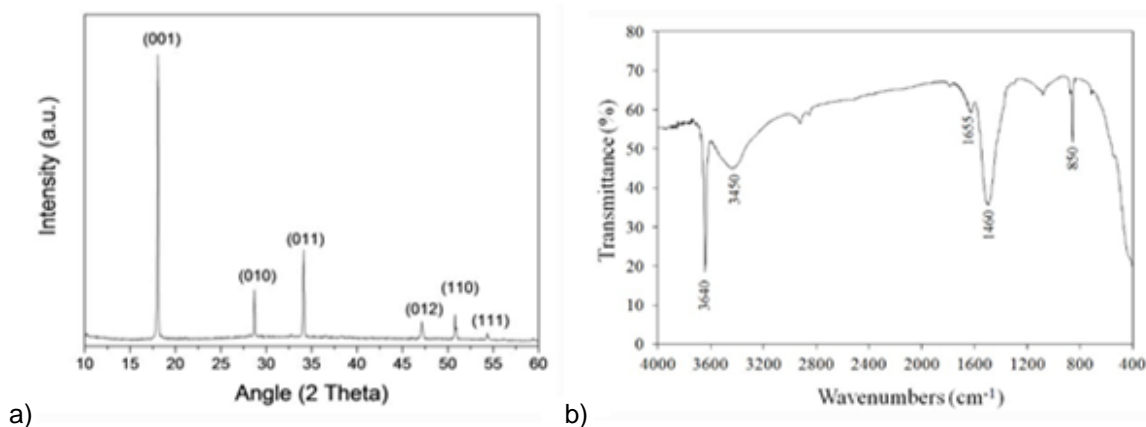


Figure 5.1. Scheme of the innovative synthesis method of $\text{Ca}(\text{OH})_2$ NPs

The nanoparticles produced in this way are pure, crystalline and with a hexagonal lamellar morphology, having thickness of about 10 nm and medium size $< 200\text{nm}$. In fact, the substitution of the $-\text{OH}$ groups on the resin substrate with Cl^- ions in solution leads, in supersaturation conditions, to the formation of crystalline nanolime, without any secondary phase. [1]

According to the reaction (5.1), about 0.7 g of $\text{Ca}(\text{OH})_2$ nanoparticles are obtained from this synthesis, because the stoichiometric moles of $\text{Ca}(\text{OH})_2$ are 0.01, having a molar weight of 74 g/mol. These obtained NPs are characterized by structural, spectroscopic and morphological techniques, such as XRD, FTIR and TEM, reported in Figure 5.2.



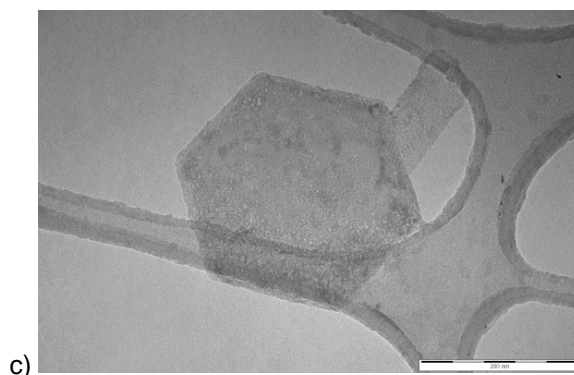


Figure 5.2. a) Characterization of the synthesized calcium hydroxide NPs using: a) XRD pattern (Bragg peaks indexed according to ICSD #98-020-2221), b) FTIR spectrum, c) TEM image with 200 nm marker [1]

The XRD pattern of Figure 5.2a revealed that the suspension consists of pure and crystalline $\text{Ca}(\text{OH})_2$ (portlandite, ICSD #98-020-2221). It is possible to observe that with the solvent evaporation, the particles of $\text{Ca}(\text{OH})_2$ tend to line up in a preferential direction along the basal plane (001).

FTIR investigation of Figure 5.2b showed a strong and sharp O-H absorption band at 3640cm^{-1} and an H-O-H bond vibration at 1655cm^{-1} due to the presence of $\text{Ca}(\text{OH})_2$. The wide band centred at 3450cm^{-1} is related to the O-H elongation modalities of free water molecules [2-4], but could also be attributed to the presence of structural water within an amorphous calcium carbonate [5]. The well-defined band at 850cm^{-1} (ν_2 asymmetric deformation of CO_3), together with the broad band at 1460cm^{-1} (ν_3 asymmetric elongation of CO_3), highlighted the presence of CaCO_3 [6], which probably formed in a superficial layer during oven drying procedure or during the analysis itself. Further sharp streaks were observed at 713cm^{-1} and 1082cm^{-1} related to the ν_4 and ν_1 modes of CO_3 in calcite [7]. The doublet at approximately 2800cm^{-1} corresponds to the elongation of the C-H for adsorbed alcohol (during dry procedure) [7].

Finally, the TEM image in Figure 5.2c show a hexagonal lamella, with lateral dimensions up to 200nm, probably composed of smaller primary nanoparticles (< 10 nm). [1]

The formation of solid $\text{Ca}(\text{OH})_2$ particles from this innovative method proceeds through different stages: after the reagents are mixed, the nucleation step rapidly occurs in supersaturation conditions, leading to the formation of nuclei, which grow through diffusion mechanisms up to nanometric size units (singlets). These singlets or primary nanoparticles, having a high surface energy, aggregate with self-

assembling mechanisms to form much larger secondary aggregates, through a process based on the irreversible capture of the nano-units, regulated by diffusion. [8] So the resulting particle growth is achieved by eliminating water molecules at the interface and forming iron-oxygen bonds. The self-assembly takes place on several sites leading to the obtainment of a polycrystalline material. Point defects (from surface impurities) and dislocations are formed as a consequence of this growth mechanism and can considerably influence the subsequent reactivity. [9] Therefore, the irreversible colloidal behaviour of calcium hydroxide suspensions can be the result of an oriented aggregation mechanism. The primary nano-crystals assemble themselves in an oriented way, both along the direction (100) and along the basal planes (001), forming secondary oriented structures separated from others structures with different orientations in space. In fact, hexagonal plate particles of 50-200 nm have been observed by TEM, inside which there appear to be smaller particles (< 10 nm) aggregated in an oriented way.

5.2 Scale-up procedure of the innovative method

To realize a scale-up procedure for the production of calcium hydroxide NPs through the presented innovative method, the influence of various factors on the characteristics of the final particles was first analysed. Firstly, the effect of the use of tap water rather than deionized was evaluated, to minimize solvent costs. Then, to increase the production of NPs, the concentration of the reagents is raised by an order of magnitude. After that, the procedure was also extended to large reaction volumes.

The patented procedure to synthesize nanolime at laboratory level consists of few steps. First of all, the reagents are prepared dissolving CaCl_2 in 100ml of deionized water with a concentration 0.1 M and taking a proportional amount of anion exchange resin (Dowex 550A), which must be wetted up to the free surface (total wet resin 22 ml). Then for the reaction step, the resin is placed in magnetic stirrer under and the chloride solution is poured into it, maintaining them in contact under moderate stirring for a chosen time (60 minutes). When the solution comes into contact with the resin, a white precipitate instantly forms (Figure 5.3a), corresponding to the calcium hydroxide NPs.

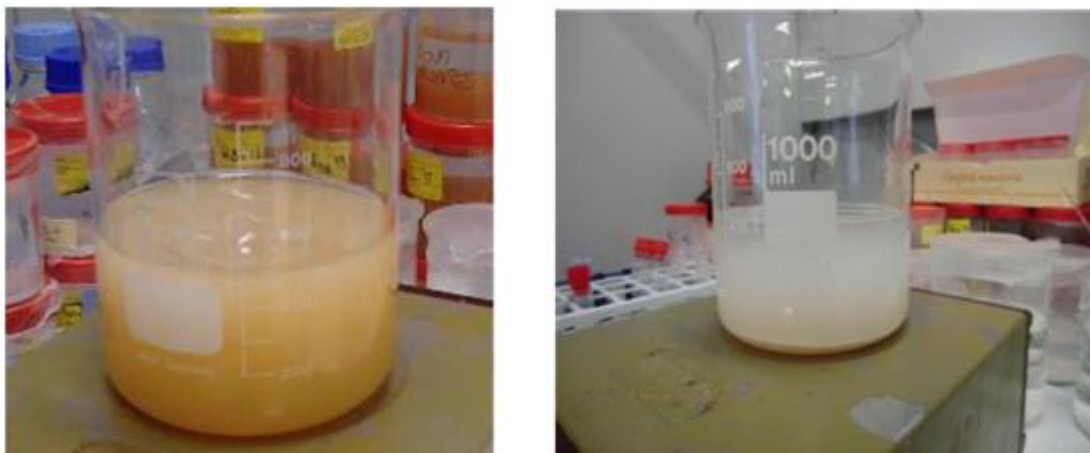


Figure 5.3. a) Resin under stirring with a white precipitate of $\text{Ca}(\text{OH})_2$ visible on the top. b) Suspension of pure $\text{Ca}(\text{OH})_2$ NPs with a precipitated layer in the bottom

Once the established reaction time has elapsed, a simple sieving step is carried out (mesh size $180\ \mu\text{m}$) to retain only the resin. In this way a suspension containing about 0.7g of $\text{Ca}(\text{OH})_2$ NPs is obtained, which precipitate over time (usually a few hours) and the formation a precipitated layer in the bottom of the suspension is observed, as shown in Figure 5.3b. This makes it possible to easily remove the solvent, but it is also possible for the nanoparticles to return in suspension by moderate stirring. However, is better to store the nanolime suspension in a sealed bottle, in order to limit the exposure to air, because in time CO_2 triggers the carbonation process.

This synthesis procedure is carried out in the parameter investigation. The influence of tap water rather than deionized was evaluated using the available tap water, having a specific conductivity of $250\ \text{mS/cm}$, with a composition reported in Table 5.1, measured using high performance liquid chromatography (HPLC - DionexDx120).

Table 5.1. Analysis of the tap water used for the production of nanolime

pH	Conductivity ($\mu\text{S/cm}$ at $20\ ^\circ\text{C}$)	NO_3^- (mg/L)	NH_4^+ (mg/L)	Ca^{2+} (mg/L)	Mg^{2+} (mg/L)	Na^+ (mg/L)	K^+ (mg/L)	Cl^- (mg/L)	SO_4^{2-} (mg/L)	HCO_3^- (mg/L)	Total hardness ($^\circ\text{F}$)
7.83	255	1.38	<0.05	40.80	1.52	0.86	0.42	1.04	2.72	127	10.84

The operating steps at laboratory level are the same, but with tap water. During the synthesis the kinetics of the ion exchange process, in terms of chloride concentration (CC) versus time, is monitored. Samples are homogeneously taken during the reaction at different times until 60 minutes, from the beginning to the end of the process, and the CC values are measured by ion-selective electrodes (Chloride Ion-Selective Electrode - Vernier). Through these tests it has been observed that the kinetics of the exchange between the OH⁻ groups on the resin and the Cl⁻ ions in solution is particularly fast, leading to a reduction > 93% of the initial reagent in 1 minute, corresponding to a very fast Ca(OH)₂ production. As can be seen in Table 5.2, the initial chlorides in solution are almost completely removed in the first 15 minutes and almost all hydroxide NPs are produced, but it is convenient to reach 60 minutes of synthesis time to have a better purity of the final nanolime.

Table 5.2. Measurements of the chloride concentration (CC) in time as % of the initial quantity, for the synthesis 0.1 M with tap water

Time (min)	Chloride concentration (CC)
0	100%
0.5	7.2%
1	6.1%
5	5.2%
15	3.5%
30	2.9%
45	2.2%
60	1.8%

The formation of the nanolime is almost instantaneous when the resin and the chloride solution come into contact. Then when the ion exchange is complete, the particles maintain the same characteristics even if they remain in contact with the resin for longer times. This occurs because, despite the ion exchange being a chemical equilibrium, the selectivity of the resin used towards chlorine ions compared to hydroxyls is much higher (22:1). The obtained particles are therefore nanometric due to the high nucleation rate caused by ion exchange and the low growth rate due to the poor solubility of calcium hydroxide in water (about 1.7 g/l at 293K). A slight excess in the amount of resin used in this system is used to make sure that the equilibrium is almost completely shifted towards the capture of chlorine ions. Moreover, at the end of the synthesis the production yield (Y) is also evaluated.

The yield is defined as % of the dry residue measured by the final suspension (CH_{meas}) with respect to the stoichiometric $Ca(OH)_2$ value (CH_{stoic}) evaluated by the reaction (5.1):

$$Y = \frac{CH_{meas}}{CH_{stoic}} * 100 \quad (5.2)$$

In particular, CH_{meas} is measured by taking 10 samples of 1 ml from the suspension, immersed in 2-propanol and dried in an oven at 100°C to avoid the carbonation process, then estimating the average value. From the synthesis 0.1 M with tap water 0.69 g of $Ca(OH)_2$ NPs are obtained, corresponding to a yield $Y = 93\%$.

These obtained NPs are characterized by structural and morphological techniques, such as XRD and TEM, reported in Figure 5.4. From these analysis, tap water does not seem to have a particular influence on the nanoparticles obtained. In fact, the XRD pattern of Figure 5.4a shows that the suspension consists of pure and crystalline $Ca(OH)_2$ (portlandite, ICSD #98-020-2221), always with a preferential orientation on the basal plane (001). TEM image shows the presence of a hexagonal lamella with lateral dimensions up to 200nm, as observed for the synthesis in deionized water of Figure 5.3b. So to minimize solvent costs, it is better to use tap water in the synthesis.

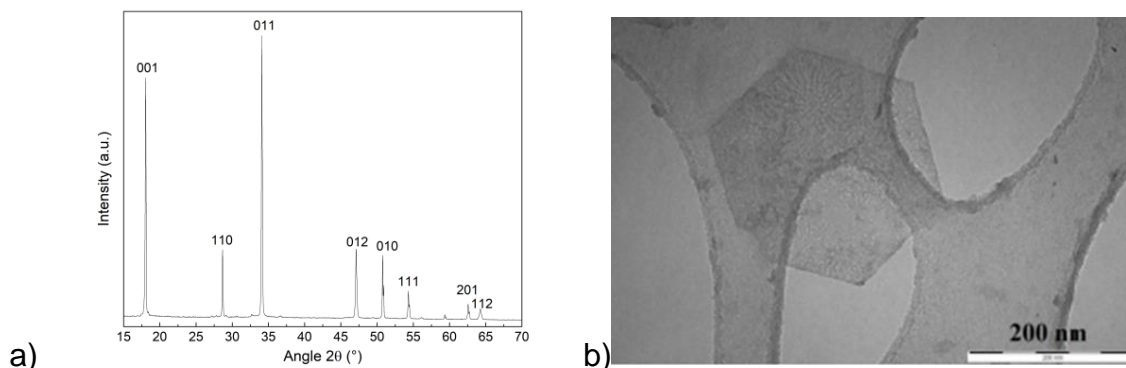


Figure 5.4. a) Characterization of the synthesized calcium hydroxide NPs with tap water using: a) XRD pattern (Bragg peaks indexed according to ICSD 98-020-2221), b) TEM image with 200 nm marker

Now, to increase the production of NPs, an increase of the $CaCl_2$ concentration from the initial value of 0.1 M (corresponding to 11 g/l) to 1 M (corresponding to 111 g/l) is performed, having a solubility of 740 g/l at 293 K. The operating steps at laboratory level are the same, but with the quantities of both the reagents increased by 10 times, increasing the production by 10 times for the same synthesis time. During the

synthesis the kinetics of the ion exchange process, in terms of chloride concentration (CC) versus time, is monitored as before. Through these tests it has been observed that the kinetics of the exchange between the OH⁻ groups on the resin and the Cl⁻ ions in solution is enhanced for higher chloride concentrations, leading to a reduction > 98% of the initial reagent in 1 minute, corresponding to an increased Ca(OH)₂ production. As can be seen in Table 5.3, the initial chlorides in solution are almost completely removed in the first 15 minutes and almost all hydroxide NPs are produced, but it is convenient to reach 60 minutes of synthesis time to have a better purity of the final nanolime.

Table 5.3. Measurements of the chloride concentration (CC) in time as % of the initial quantity, for the synthesis 1 M with tap water

Time (min)	Chloride concentration (CC)
0	100%
0.5	2.5%
1	1.6%
5	0.9%
15	0.6%
30	0.4%
45	0.2%
60	0.1%

The formation of the nanolime is almost instantaneous when the resin and the chloride solution come into contact and the kinetics is regulated from a chemical equilibrium of the resin, having a selectivity shifted towards chlorine ions compared to hydroxyls (22:1). Therefore, using an initial concentration of the reagents 10 times higher, the capture of chlorides by the resin is faster in order to restore the equilibrium, causing an enhanced nucleation rate with a low growth rate due to the poor solubility of calcium hydroxide in water (about 1.7 g/l a 293K). A slight excess in the amount of resin used in this system is always maintained to make sure that the equilibrium is almost completely shifted towards the capture of chlorine ions. Moreover, at the end of the synthesis the production yield (Y) is evaluated as well. From the synthesis 1 M with tap water 7.19 g of Ca(OH)₂ NPs are obtained, corresponding to a yield Y = 97%.

These obtained NPs are characterized by structural and morphological techniques, such as XRD and TEM, reported in Figure 5.5. These analyses confirm the kinetics

behaviour because increasing the reagent concentrations the particles seem to be smaller, and this can be attributed to higher supersaturation conditions, which accelerate the nucleation step, resulting in smaller primary nanoparticles. In fact, the XRD pattern of Figure 5.5a reveals that the suspension consists of pure and crystalline $\text{Ca}(\text{OH})_2$ (portlandite, ICSD #98-020-2221), always with a preferential orientation on the basal plane (001). TEM image shows the presence of a hexagonal lamella with lateral dimensions lower than 100nm, smaller than that observed for the synthesis 0.1 M of Figures 5.3b and 5.4b. So, taking into account both the size of the NPs and the synthesis time, it is better to carry out the synthesis at 1 M concentration.

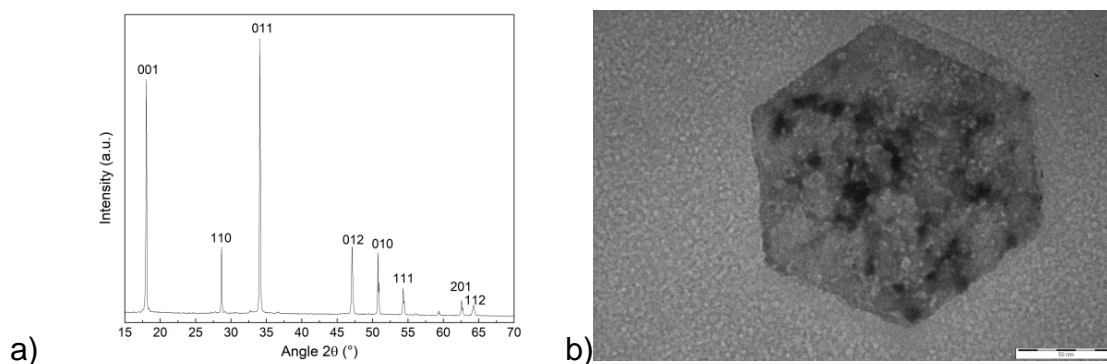


Figure 5.5. a) Characterization of the synthesized calcium hydroxide NPs with 1 M concentration using: a) XRD pattern (Bragg peaks indexed according to ICSD 98-020-2221), b) TEM image with 50 nm marker

However, with 100 ml of CaCl_2 solution 1 M as initial reagent, also the volume of the wet resin is greatly increased, changing from 22 ml to 220 ml. It would also be possible to reach a CaCl_2 concentration of 2 M or more, but higher concentrations are not easy from an operational point of view, since the amount of the solution would be too low compared to the amount of resin, with problems related to mixing that prevent having homogeneous reaction conditions. Therefore, a maximum concentration of 1 M for the CaCl_2 solution is chosen to study the influence of this parameter on the properties of the obtained NPs.

Actually, with the procedure carried out at the laboratory level, using a beaker, a stirrer and a sieve, it is not easy to obtain greater amounts of nanolime (7.19 g with 100 ml solution of calcium chloride 1 M) in a single step, because there are operational problems regarding the separation of the resin (220 ml). To solve these problems, an appropriate prototype system is designed by my tutor (Prof. Giuliana

Taglieri), allowing the production to be easily scaled up. Using this system, it is possible to obtain a total production volume increased by 2 orders of magnitude compared to the beginning, which allows to obtain daily productions up to 200 g of pure nanolime, that are considerably greater than the syntheses reported in literature (in the order of few grams for day). The system implemented could be scaled in the future by a further order of magnitude or more. For reasons of industrial secrecy, the prototype of this system is not described in this thesis work. However, the properties of the obtained nanoparticles are reported.

To definitely increase the amount of nanolime production, an increase of the volume reaction from the initial value of 0.12 l to 10 l is performed (considering the volume of solution plus wet resin), maintaining the concentration 1 M and the use of tap water as solvent. In this volume about 2/3 are occupied by the wet resin, having the density of water (dry density of 0.68 g/l, wet density of 1.01 g/l). The operating steps with this system are conceptually the same, but without using beakers or sieves. From TEM image of Figure 5.6, using this new system and increasing the volume by 2 orders of magnitude, the particles seems to be smaller than the initial synthesis, this can be attributed both to higher supersaturation conditions and to better mixing conditions, which accelerate the nucleation step, resulting in smaller primary nanoparticles. The XRD pattern of Figure 5.6a shows that the suspension consists of pure and crystalline Ca(OH)_2 (portlandite, ICSD #98-020-2221), always with a preferential orientation on the basal plane (001). TEM image shows the presence of hexagonal lamellae with lateral dimensions of about 70 nm, smaller than that observed for the synthesis 0.1 M of Figures 5.3b and 5.4b. The production of about 100 g of Ca(OH)_2 NPs is obtained ($Y = 95\%$), respect to about 0.7 g of the 0.1 M initial synthesis, without getting worse the final product, but improving it in terms of size. Therefore, it is better to carry out the synthesis of nanolime with this prototype system.

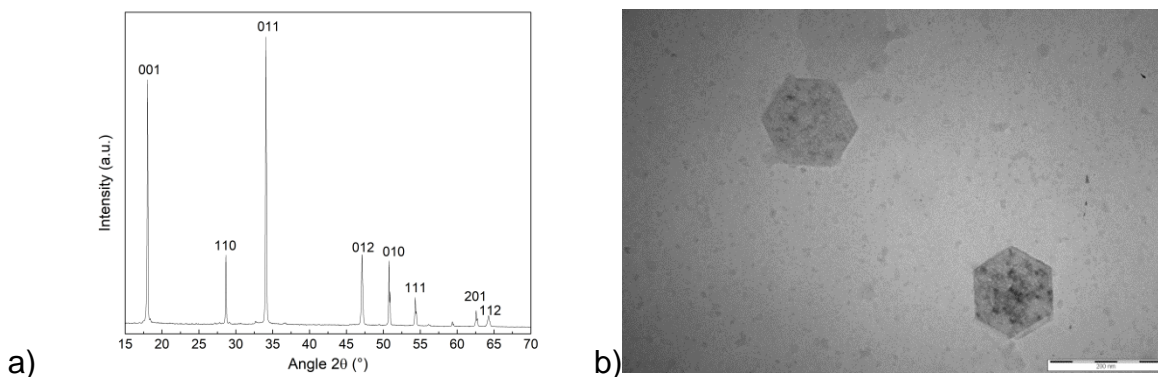


Figure 5.6. a) Characterization of the synthesized calcium hydroxide NPs in 10 litres volume: a) XRD pattern (Bragg peaks indexed according to ICSD 98-020-2221), b) TEM image with 200 nm marker

Finally, using the scaled system, also the optimization of synthesis time is evaluated, so the kinetics of the ion exchange process, in terms of chloride concentration (CC) versus time, is monitored as before. The kinetics of the exchange in the prototype system remains particularly fast, leading to a reduction of the initial reagent > 97% in 1 minute, corresponding to a very fast $\text{Ca}(\text{OH})_2$ production considering the total amount of initial CaCl_2 . These tests are in agreement with the type of reaction, which is very fast also in great volumes (10 litres), because it is based on an ion exchange, so the formation of the nanolime is almost instantaneous when the resin and the chloride solution come into contact.

Table 5.4. Measurements of the chloride concentration (CC) in time as % of the initial quantity, for the synthesis 1 M with tap water in the prototype system

Time (min)	Chloride concentration (CC)
0	100%
0.5	4.5%
1	2.9%
5	1.8%
15	1.2%
30	0.5%
45	0.3%
60	0.2%

As reported in Table 5.4, the chlorides in solution are almost completely removed in the first 15 minutes, but it is still necessary to reach at least 45 minutes of synthesis time to have a better purity of the final nanolime. Further studies and production

systems could be designed to reduce the synthesis time, for example by providing more than one step of contact with different resins. In this way a residual chloride value $< 0.2\%$ could be reached even in 10-15 minutes. However, for now the prototype system reported has proved to be an optimal solution taking into account other steps, since the subsequent regeneration of the resin is the kinetically controlling stage to obtain a continuous nanolime production.

5.3 Optimization of resin regeneration

The innovative method to produce calcium hydroxide NPs involves the contact of a calcium chloride solution with an anion exchange resin in OH^- form, to allow the replacement of the hydroxyl groups on the resin substrate with the chlorine ions in solution. At the end of the exchange phase, the solution obtained is separated and the resin can be regenerated. Resin regeneration in such a designed system is the critical point to make the process cyclical and scalable. In fact, the regeneration of the resin is the operation that makes the process sustainable both from an economic and environmental point of view, but usually the resins are regenerated in fixed bed columns. Again for reasons of secrecy, this section does not describe in detail how the system regeneration is carried out, but only the results of this operation are reported.

During the regeneration phase, a suitable solution of a strong base (such as NaOH) is sent into contact with the resin, in order to condition it by shifting the equilibrium towards the presence of OH^- ions. This operation is evaluated by measuring the quantity of chlorine released by the resin, which must be similar to that absorbed in the synthesis phase. There are several parameters to control in order to optimize this operation, in particular the size of the exchange bed, the stirring, the inlet and outlet flow rate, the amount and the concentration of the basic solution. Preliminary tests on the regeneration of small quantities of resin are carried out in a fixed glass column, which has a height of about 27 cm and a diameter of 2 cm, as shown in Figure 5.7. The basic solution is pumped inside the column by means of a peristaltic pump, in order to have a constant flow rate. The column is equipped with an outlet T valve, to regulate the outlet flow in order to have a stationary system.



Figure 5.7. Experimental regeneration apparatus for small amounts of resin

In order to have exactly repeatable values, tests are carried out on a resin almost fully conditioned in Cl^- form. In this way the scope of the work is extended to a more general situation. The conditions of the regeneration tests are:

$h = 27 \text{ cm}$ (height of the resin column)

$d = 2 \text{ cm}$ (column diameter)

$S = 3.1 \text{ cm}^2$ (section of the column)

$V_{\text{res}} = 83.2 \text{ ml}$ (resin volume)

$C_{\text{res}} = 1.1 \text{ eq/l}$ (resin exchange capacity)

$\rho_{\text{res}} = 0.68 \text{ g/l}$ (resin density)

$\text{Sel}_{\text{Cl}/\text{OH}} = 22$ (selectivity of the resin towards chlorine)

The considered height of the resin is referred to the Cl^- form, because in the transition from the Cl^- form to the OH^- form there is a swelling of about 20% in volume.

During the regeneration tests, samples are collected from the flow out of the column and a graph is obtained measuring the concentration of chlorides over time (Figure 5.8).

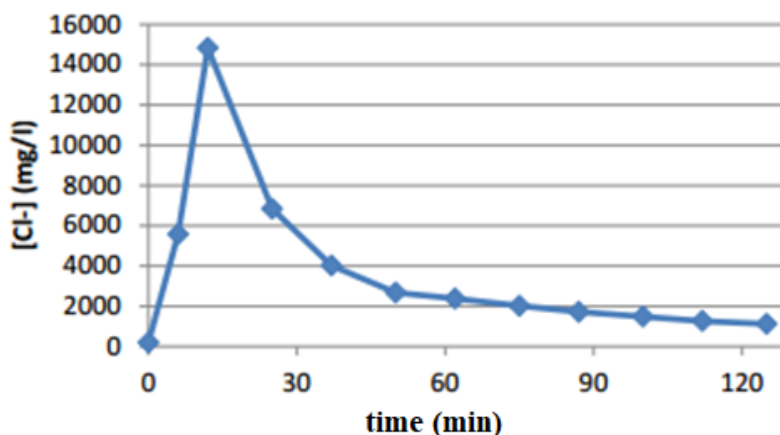


Figure 5.8. Typical trend in the resin regeneration phase

The growing trend observed in the first 10 minutes of the regeneration phase can be attributed to the initial dead time, during which the deionized water (in which the resin was suspended) is first expelled, as well as to gradual diffusion phenomena between substrate and solution. In fact, the chlorine ions leave the resin when the equilibrium is very shifted towards the OH⁻, since the selectivity value equal to 22 expresses a balance between the concentrations of the ions on the substrate and those in solution. Therefore, there is an initial transient that explains the climb.

In investigating the optimal regeneration conditions with this column, a factorial experimentation evaluates the significance of two main parameters: the inlet and outlet surface velocity (flow/section) and the concentration of the basic solution (considering the same volume of solution), compatibly with the technical data sheet of the resin (Dowex Monosphere 550A), reported in the Table 5.5.

Table 5.5. Data sheet for the regeneration of Dowex 550A resin

Maximum operating temperature	
OH ⁻ form	60°C (140°F)
Cl ⁻ form	100°C (212°F)
pH range	0–14
Bed depth, min.	450 mm (1.5 ft)
Flow rates:	
Service/fast rinse	5–60 m/h (2–24 gpm/ft ²)
Service/condensate polishing	40–150 m/h (16–60 gpm/ft ²)
Backwash	See figure 1
Co-current regeneration/displacement rinse	1–10 m/h (0.4–4 gpm/ft ²)
Total rinse requirement	2–5 BV*
Regenerant:	
Type	4–8% NaOH
Temperature	Ambient or up to 60°C (140°F) for silica removal

*1 BV (Bed Volume) = 1 m³ solution per m³ resin or 7.5 gals per ft³ resin

In particular, a 2-level factorial experimentation is performed: A is the inlet and outlet surface velocity, B is the mass concentration of NaOH in the basic solution, as shown in table 5.6.

Table 5.6. Plan of 2-level factorial experimentation with 2 factors

	-	+
A, m/h	1,5	3
B, % w/w	2	4

The response variable is the quantity of Cl⁻ equivalents exchanged during the resin regeneration phase. This is a 2ⁿ factorial experimentation, with n = 2 factors at two levels, for which the plan of 2² = 4 experimental tests are defined. Then, to evaluate the effect of the factors and their interactions and verify their significance, the analysis of variance (ANOVA) can be used. On an experimental level, the variance analysis is performed by implementing the Yates algorithm, consisting in designating each treatment with lowercase letters corresponding to the factors which in this test assume the highest level. The test plan is represented in Table 5.7 where the values of Cl⁻ equivalents exchanged at each of the investigated condition are reported as well.

Table 5.7. Factorial plan with Yates notation

Prove	A, m/h	B, % peso	y, meq Cl⁻
(1)	-	-	87,68
a	+	-	87,63
b	-	+	95,14
ab	+	+	95,84

Determining the effects, using the Yates algorithm, it is obtained that both increases in the surface velocity and in the concentration of the basic solution increase the value of Cl⁻ equivalents exchanged. In particular, this value is slightly influenced by the factor A, while it is significantly influenced by the factor B. The interaction AB is positive, it therefore appears that a simultaneous increase of factors A and B determines the higher increase in chloride exchange.

At this point even higher concentrations in the basic solution are evaluated (until 10%), in order to reduce regeneration times, but allowing to reach high levels of regeneration. From the various tests it is obtained that the shortest time to reach a regeneration higher than 95% is obtained with a concentration in the basic solution of 8% by weight, with a surface speed of 3 m/h.

However, in this way a huge amount of base is needed in order to reduce regeneration times, because there is a low effective % of base utilization (about 10%), and on a greater scale this corresponds to an increase in the cost of the regenerating solution, as well as a waste of solution. The effective % of base utilization is evaluated by calculating the amount of base that the resin takes by releasing chlorine (1.1 eq/l), compared to the total amount sent in the regeneration phase (this value is never greater than 20% with this procedure because it is influenced from the resin selectivity). So, the theoretical-speculative aspect linked to the quality of the regeneration is followed by one linked to the effective % of NaOH utilization: the aim is to increase this percentage without increasing the regeneration times. A solution to solve this problem can be the implementation of a multi-step regeneration recycling the soda already used. Several steps have been attempted to optimize this process, which are here omitted always for reasons of industrial secrecy. However, these steps allowed to reach an effective % of base utilization of about 40%.

The considerations obtained in the preliminary tests are useful for performing regeneration tests also on the prototype of the scaled system, with a capacity of 10 litres. These tests confirmed a low dependence on the surface velocity and a high dependence on the concentration of the basic solution. Therefore, it is convenient, from an industrial point of view, to work at the maximum effective concentration (8%) with the maximum permissible surface velocity, in order to have a high level of regeneration in the shortest possible time. Again there is an initial low effective % of base utilization, which is partially solved with a multi-step regeneration, but with prototypes of this size or more purification systems for the regenerating solution can be also considered, with plant costs that can be easily amortized over time.

However, given the size of a 10-liter prototypal system and the characteristics of the available instrumentation, such as peristaltic pumps, the regeneration phase remains the kinetically controlling stage (average regeneration time of 120 minutes) of a hypothetical continuous nanolime production.

5.4 Initial tests for a continuous nanolime production

The ion exchange process scaled on a volume of 10 litres can be divided into 2 main steps, which are the synthesis phase and the regeneration phase. As seen in the previous sections, an optimized synthesis phase lasts 60 minutes allowing to obtain 100 g of $\text{Ca}(\text{OH})_2$ NPs, while an optimized regeneration phase lasts 120 minutes. Now with the realized prototype it is possible to define a cyclic procedure for a continuous production of nanolime always using the same exchange resin, obviously adding dead times for other operations, such as preparation of the reagents and filling of the systems.

Using this prototype, 10 complete cycles of production and regeneration are performed, maintaining the same operating conditions to evaluate the trend of the production yield over time and the feasibility of a pilot production already with this system, including the evaluation of total cycling time. The results of the 10 production cycles with the relative production and regeneration yields are shown in the Table 5.8, where the yield of production refers to the amount of dry nanoparticles obtained respect to the theoretical amount estimated from the reaction (5.1), and the yield of regeneration refers to the amount of chlorides removed from the regeneration respect to the chlorides absorbed by the resin in the production phase.

Table 5.8. Production and regeneration yields with total cycling times of the first 10 production cycles with a 10 litres prototype system

N production cycles	Yield of production	Yield of regeneration	Total cycling time
1	92.2 %	95.7 %	4.5 h
2	93.8 %	92.4 %	4.3 h
3	91.8 %	91.7 %	4.2 h
4	91.3 %	93.8 %	4.4 h
5	90.8 %	96.5 %	4.1 h
6	94.8 %	96.9 %	4.3 h
7	95.8 %	91.6 %	4 h
8	90.3 %	96.7 %	3.9 h
9	95.0 %	96.2 %	4.1 h
10	95.4 %	96.4 %	4 h

These first 10 tests of continuous production with the 10 litres prototype system show that the production and regeneration yields remain approximately constant during 10 production cycles, with values always higher than 90%. Some steps need further optimization to further increase the yields, also the total cycling time (about 4 h) could be further reduced, but the important result is the effectiveness of the system, together with the fact that the resin works in the same way for at least 10 cycles. However, other cycles on the same resin are necessary to evaluate how many production cycles it can guarantee before being disposed of, as the greater the number of cycles allowed, the lower the production costs, since the resin is the most expensive reagent.

5.5 Analysis of the nanolime reactivity

The reactivity in relation to the carbonation process of the nanolime synthesized on large scale (10 l reaction volume) is evaluated, considering both aqueous and hydroalcoholic dispersions, as the nanolime is typically applied in alcohol. Through the carbonation process, calcium hydroxide turns into calcium carbonate plus water, in the presence of CO₂ and water. Suspensions at 5 g/l and 10 g/l (typical concentration of commercial nanolime) and different alcohol/water (A/W) ratios (25%, 50% and 90% respectively) are considered. The carbonation is monitored by exposing each suspension in air and evaporating it under different relative humidity (RH): 45 ± 5%, 75 ± 5% and 95 ± 5%, in environmental conditions (T = 20 ± 2°C; pCO₂ ≈ 10^{-3.5} atm, i.e. the standard concentration of CO₂ in the air). Three samples of 0.12 ml are taken from each suspension, placed on a zero background XRD sample holder and dried at the established conditions, as showed in Figure 5.9. Then XRD analysis are carried out on each sample, to evaluate the amount of CaCO₃ formed after the evaporation of the solvent.

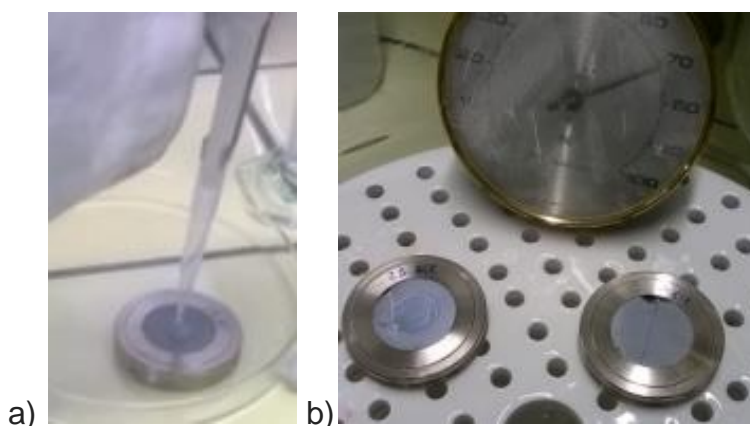


Figure 5.9. Preparation of different nanolime samples at different RH conditions: a) $45\pm 5\%$, b) $75\pm 5\%$

At least six different phases of CaCO_3 are possible in the carbonation process: three anhydrous crystalline polymorphs (calcite, aragonite and vaterite), two hydrated crystalline forms called mono hydro-calcite ($\text{CaCO}_3\cdot\text{H}_2\text{O}$, $\text{CaCO}_3\cdot 6\text{H}_2\text{O}$) and amorphous CaCO_3 (ACC). [1] Intermediate stages of CaCO_3 hydrates are also recognizable, such as calcium carbonate hydroxide hydrate ($\text{Ca}_3(\text{CO}_3)_2(\text{OH})_2\cdot 1.5\text{H}_2\text{O}$, called CCH). [10] The carbonation process of nanolime can be influenced by the physical properties of the Portlandite crystals (particle size and surface area) [11], as well as by the type of solvent and concentration [12, 13], or by the environmental conditions. [5] In this sense, the carbonation process can be considered an important means of investigation, not only to provide useful information for the nanolime application, but also because it can offer indirect indications both on the size of particles and aggregates, the whose presence could be related to the solvent and the concentration of the suspension.

Both aqueous and $A/W = 25\%$ samples at 5 g/l and 10 g/l are completely converted into CaCO_3 , in the form of pure calcite at every RH conditions. This result shows how the produced nanoparticles are extremely reactive in the presence of water. When the alcohol content increases, the carbonation process is slowed down, also due to a faster evaporation rate of the solvent, indicating the harmful role of alcohol in this respect. However, for application needs (some commercial products are sold in alcoholic solvents), tests are carried out at higher alcohol % and table 5.9 summarizes the results obtained from the samples $A/W = 50\%$ and $A/W = 90\%$, at different RH conditions, in concentrations of 5 g/l and 10 g/l.

Table 5.9. XRD results of the crystalline phases of CaCO₃ formed in the nanolime samples, in relation to A/W ratios, suspension concentrations and RH conditions, as an average of 3 measures, where C = calcite ICSD #98-002-0179, CCH = calcium carbonate hydroxide hydrate ICDD #00-023-0107

A/W ratio	A/W 50%		A/W 90%	
Concentration	5 g/l	10 g/l	5 g/l	10 g/l
RH 45 ± 5%	81 ± 2% C	40 ± 5% C	20 ± 10% C	10 ± 5% C
	17 ± 2% CCH	20 ± 5% CCH	20 ± 10% CCH	10 ± 5% CCH
RH 75 ± 5%	100% C	80 ± 5% C	50 ± 20% C	30 ± 10% C
		12 ± 3% CCH	10 ± 5% CCH	20 ± 10% CCH
RH 95 ± 5%	100% C	100% C	100% C	70 ± 10% C
				20 ± 10% CCH

The fundamental role of water is evident, both in the dispersion medium and in the content of moisture in the air. In particular, at RH = 45±5% the samples having A/W = 50% show higher conversions into calcium carbonate forms in comparison to the samples having A/W = 90%. Furthermore, samples with A/W = 90% presented the greatest variability of results (resulting in greater uncertainty) than all samples with A/W = 50%, probably related to the faster evaporation rate of the solvent. Increasing the RH to 75±5% the previous values of calcite and CCH becomes approximately double. Reaching RH = 95±5% almost all the sample reach a complete conversion into calcite. Therefore, the formation of carbonates is strictly connected to the presence of water, and it is preferable to have more water already in the suspension (A/W < 50%) to avoid applying the nanolime as a consolidant at too high RH values. When compared with the results of the literature [5, 14-16], all the investigated suspensions present a greater reactivity. In the considered works, at RH ≤ 54%, the nanolime remained substantially untransformed for 7 days [15] and the carbonation process was completed after 28 days. At higher RH conditions (75% and 90%), the carbonation process was completed after 7 days. [16] Furthermore, in these works, calcite was never the only final phase, but vaterite, aragonite and mono hydro-calcite were also observed, depending on the RH conditions. The transformation of calcium hydroxide into calcite in low time (few hours), as a single and pure phase, is of fundamental importance in the application fields, since calcite guarantees perfect compatibility with all substrates with a carbonate matrix, as well as better mechanical properties.

5.6 Aging tests for the storage of the produced nanolime

Considering the greater reactivity of the nanolime synthesized with the ion exchange method compared to the commercial nanolime supplied in alcohol, it is useful to carry out tests to evaluate the preservation of this product over time. In order to evaluate a possible "aging" of the nanolime suspensions, the following tests were considered:

- investigations by transmission electron microscopy (TEM), to evaluate any variation in the size or morphology of the nanoparticles;
- analysis of the carbonation process in environmental conditions ($T = 20 \pm 2^\circ\text{C}$, $\text{RH} = 45 \pm 5\%$), to estimate possible variations in the reactivity (related to the possible presence of aggregates within the suspension).

This aging was observed in various solvents, 100% water, 50% alcohol/water and 100% alcohol, three months after synthesis, these samples are named nCH_3mW, nCH_3mAW and nCH_3mA, respectively. Moreover, other two nanolime samples were compared with them, one just synthesized and one aged two years in water, called nCH_new and nCH_2yW respectively. Any sample is stored in PET bottles at ambient conditions to avoid carbonation over time. Firstly, the TEM investigations are shown in Figure 5.10. The nCH_new sample of Figure 5.10a consists of very thin hexagonal-shaped lamellae with lateral dimensions of about 70 nm, which in turn seem to be composed of primary nanoparticles $\leq 10\text{nm}$. In the nCH_2yW sample of Figure 5.10b, hexagonal-shaped lamellae are still observed and some seem even smaller than the original ones, but they tend to form a great quantity of aggregates.

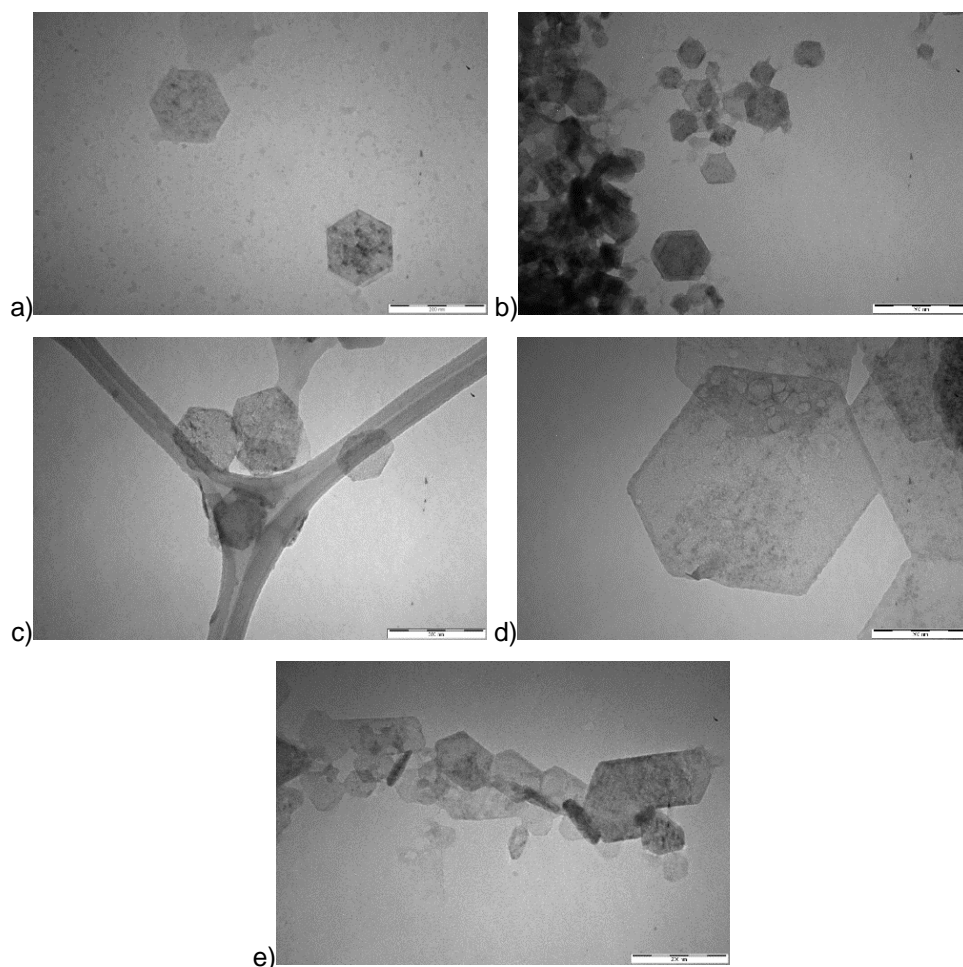


Figure 5.10. TEM images with 200 nm marker of various nanolime samples at different aging times: a) nCH_new just synthesized, b) nCH_2yW aged two years in water, c) nCH_3mW aged three months in water, d) nCH_3mA/W aged three months in alcohol/water, e) nCH_3mA aged three months in alcohol

The nCH_3mW sample of Figure 5.10c consists of thin hexagonal-shaped lamellae very similar to the just synthesized sample. While the nCH_3mA/W sample of Figure 5.10d is composed by very thin hexagonal-shaped lamellae but having lateral dimensions greater than the other samples, reaching dimensions of about 300 nm. Finally, the nCH_3mA sample of Figure 5.10e appears to have thin hexagons similar in size to those of the sample just synthesized, but with a more flattened shape, which are more agglomerated and in turn seem to be composed of primary nanoparticles $\leq 10\text{nm}$.

From TEM observations, it seems that all the particles keep their original features, remaining with the typical hexagonal shape of calcium hydroxides, but depending on the solvents there are influences on agglomerations or dimensions. In particular, pure water is more advantageous as a solvent for short aging (three months), while

over long periods (two years) it could favour the formation of aggregates, to be dispersed for example with ultrasounds. Alcohol tends to change the size of the particles, making them larger or more flattened in shape (50% alcohol/water). Therefore, the synthesized nanolime can be aged for at least 2 years and water is the most suitable solvent.

For what concerns the analysis of the carbonation process of the aged nanolime, it is evaluated considering suspension at 5 g/l (typical concentration of commercial nanolime). Then the carbonation is monitored by exposing each suspension in air and evaporating it under different relative humidity (RH): $45 \pm 5\%$, $75 \pm 5\%$ and $95 \pm 5\%$, in environmental conditions ($T = 20 \pm 2^\circ\text{C}$; $p\text{CO}_2 \approx 10^{-3.5}$ atm, i.e. the standard concentration of CO_2 in the air). Three samples of 0.12 ml are taken from each suspension, placed on a zero background XRD sample holder and dried at the established conditions. XRD analysis are carried out on each sample, to evaluate the amount of CaCO_3 formed after the evaporation of the solvent, and reported in Table 5.10.

Table 5.10. XRD results of the crystalline phases of CaCO_3 formed in the samples of aged nanolime: nCH_new, nCH_2yW, nCH_3mW, nCH_3mA/W and nCH_3mA, as an average of 3 measures, where C = calcite ICSD #98-002-0179, CCH = calcium carbonate hydroxide hydrate ICDD #00-023-0107

sample 5 g/l	nCH_new	nCH_2yW	nCH_3mW	nCH_3mA/W	nCH_3mA
RH $45 \pm 5\%$	100% C	100% C	100% C	$75 \pm 4\%$ C $18 \pm 4\%$ CCH	$3 \pm 2\%$ C $2 \pm 1\%$ CCH
RH $75 \pm 5\%$	100% C	100% C	100% C	100% C	$20 \pm 5\%$ C $4 \pm 2\%$ CCH
RH $95 \pm 5\%$	100% C	100% C	100% C	100% C	$40 \pm 10\%$ C $10 \pm 5\%$ CCH

The fundamental role of water is again evident, both in the dispersion medium and in the content of moisture in the air. The samples with water or A/W 50% have the expected reactivity towards the carbonation process, despite of the aging (until two years). Furthermore, the reactivity of the completely alcoholic sample (nCH_3mA) is strongly related to the presence of water, therefore it reaches about 50% only at $95 \pm 5\%$ RH conditions.

At this point, to have a better comparison on reactivity, only the sample aged two years in water is considered, dispersing it in alcohol as done for the reactivity tests

in table 5.9. Suspension at 5 g/l and 10 g/l (typical concentration of commercial nanolime) and different alcohol/water (A/W) ratios (25%, 50% and 90% respectively) are considered. The carbonation is monitored by exposing each suspension in air and evaporating it under different relative humidity (RH): $45 \pm 5\%$, $75 \pm 5\%$ and $95 \pm 5\%$, in environmental conditions. Three samples of 0.12 ml are taken from each suspension, placed on a zero background XRD sample holder and dried at the established conditions. XRD analysis are reported in Table 5.11.

Table 5.11. XRD results of the crystalline phases of CaCO_3 formed in the samples of two years aged nanolime, in relation to A/W ratios, suspension concentrations and RH conditions, as an average of 3 measures, where C = calcite ICSD #98-002-0179, CCH = calcium carbonate hydroxide hydrate ICDD #00-023-0107

A/W ratio	A/W 50%		A/W 90%	
Concentration	5 g/l	10 g/l	5 g/l	10 g/l
RH $45 \pm 5\%$	70 \pm 5% C 22 \pm 4% CCH	35 \pm 5% C 30 \pm 5% CCH	9 \pm 4% C 20 \pm 5% CCH	5 \pm 3% C 15 \pm 5% CCH
RH $75 \pm 5\%$	100% C	70 \pm 4% C 25 \pm 3% CCH	40 \pm 10% C 30 \pm 10% CCH	20 \pm 10% C 30 \pm 10% CCH
RH $95 \pm 5\%$	100% C	100% C	100% C	40 \pm 20% C 30 \pm 10% CCH

These tests show that if the two years aged nanolime is dispersed in a hydro-alcoholic mixture with 50% alcohol, the reactivity remains similar to that of the just synthesized nanolime (see Table 5.9). While if this aged nanolime is dispersed in a more alcoholic mixture (A/W = 90%), the formation of calcite results almost halved, with a slight increase in the formation of CCH. From this result it can be hypothesized that over time weak bonds are established between the sedimented particles, leading to the formation of agglomerates that are not well dispersed in alcohol by simple mixing procedures, as happens for just synthesized nanolime. Therefore, the nanolime aged for long periods (two years) requires more water or longer dispersion times (or ultrasounds), but still remains a nanomaterial that maintains its initial characteristics, remaining however useful for application purposes.

CHAPTER 6: SYNTHESIZED NANOLIME APPLICATIONS

The main applications of nanolime concern its use for the conservation and consolidation of cultural heritage. Therefore, in the present chapter conservative treatments on different kinds of carbonatic stones are considered, such as biocalcarenites and historical mortars. Thanks to the scalability of the process and the production of huge amounts of nanolime in water, the first extensive application using these nanoparticles is realized to consolidate the original mortar of a historic building of L'Aquila (Palazzo Pica Alfieri, 14th-16th century). The used non-commercial aqueous nanolime, suitable for compatible and eco-friendly extensive applications, can be considered a green product for the safety both of environment and human health (of the restorer). Moreover, the effectiveness of the treatments is analysed in terms of depth of penetration, surface cohesion and resistance to perforation. In particular, this new nanolime yielded very promising consolidation effectiveness for all the treated biocalcarenites and historical mortars, increasing the superficial cohesion and the drilling resistance without significantly altering the stone porosity and the esthetical features.

6.1 The biocalcarenites of Agrigento

Historical monuments in Mediterranean regions (from Sicily, Italy, to Malta, Cyprus, and Israel) are mainly composed of sedimentary soft porous rocks, commonly called calcarenites, which are characterized by a highly porous carbonate structure. Due to the high porosity, they are vulnerable to progressive deterioration phenomena, which are induced by the combined action of sea spray, sea-waves, and water infiltration. The damage processes are mainly relevant when these rocks were employed as building stones for historical monuments, since those stones underwent degradation phenomena due to environmental exposure for centuries. The main consequence of these deterioration processes is the progressive dissolution of the mineral matrix, that in the case of calcarenite stone, corresponds to the leaching of calcite. In particular, some publications underline that in the long-term, in continuously water-saturated environments, the calcite of calcarenites is continuously being dissolved and washed away thus weakening both bonds and grains [1-3]. The long-term chemical dissolution of calcite is the fundamental

mechanism affecting the mechanical behavior of these soft calcareous rocks. The degradation phenomena cause an increase in porosity over time, powdering, and a decrease of the mechanical features [3-5]. Many studies have focused on finding suitable treatments for the reinforcement of weathered calcareous stones. To date, the most common consolidation treatments reported in literature are based on synthetic polymers and other organic materials (i.e. alkoxysilanes, acrylic, epoxy or vinyl resins) which are mainly used as pore fillers [6-8]. Nevertheless, although often effective, these treatments are characterized by some drawbacks; the main disadvantages being related to their irreversible behaviour that can accelerate deterioration processes of the monument and health hazard to humans during application from the employed solvents. These polymer-based treatments often lack the physicochemical compatibility with the original substrate, so that in several cases their performance decreases significantly over time, and often alters, in a drastic way the colour of the treated stone [9].

Currently, the application of nanotechnology offers the possibility of designing inorganic consolidant products highly compatible with the original stone substrate. Due to their features, nanolime particles can be considered the best binder to be used in a fully compatible way for the consolidation of all carbonatic substrates in Cultural Heritage. This can be attributed to their total chemical compatibility with the carbonatic substrates related to their ability in reacting with atmospheric CO₂ to produce calcium carbonate, combined with the deep penetration of the nanoparticles into the treated substrates.

For this reason, a complete investigation on the effectiveness of the synthesized nanolime for conservation treatments on the Agrigento's biocalcarenes is carried out, according to standard procedures. For the first time, the nanolime particles are applied also fully dispersed in water. The use of water could be considered a direct improvement of the traditional limewater treatments, allowing working in safety both for the restorer as well as for the environment. The increased regulations on Health and Safety have established that volatile organic compounds emissions (VOCs) produced by alcohol are harmful to the environment, harmful to human health as well as posing a fire hazard in the early stages [10, 11]. In this context, the alcoholic nanolime dispersions could be an important drawback of nanolime treatments when required in extensive stone consolidation projects.

First, petrographic, mineralogical and chemico-physical investigations on the different kinds of biocalcarene stones are also performed. Then the nanolime efficacy is evaluated in terms of protection against water, of increase in superficial consolidation and in increase in drilling resistance on different kinds of Agrigento's biocalcarenes. This is studied by varying both the application procedures and the dispersion medium for the suspensions. For each kind of stone, several cubic standard samples are tested, in order to examine average results and to guarantee a reproducible application.

Taking into account the visual differences of the available samples in terms of porosity, composition and degree of powdering, five kinds of biocalcarene samples, named as A, B, C, D and E respectively, are considered. These samples were collected from the local quarry of Villaseta (Agrigento, Italy), which present similar characteristics to the ones used for the construction of the Temples [12]. All the samples are cut to obtain regular cubic specimens (about 3*3*3 cm). A general examination of the structure and texture of the biocalcarene samples was performed on thin-sections, using polarization-fluorescence microscopy (PFM, AXIO Scope A1-Zeiss). The porosity and the pore size distribution of these samples are measured by Mercury Intrusion Porosimetry (MIP) using a PASCAL 140/240 instrument. Additionally, to determine the stone density and its open porosity, a pycnometer (Micromeritics AccuPyc 1330 and GeoPyc 1360) is also used. The samples were characterized in terms of chemical and mineralogical composition by means of XRF and XRD.

Observation of thin sections, as shown in Figure 6.1, confirmed that the stone samples belong to the Agrigento Formation of Early Pleistocene age. The formation was composed of medium to coarse-grained bioclastic packstone and grainstone/rudstone, locally lumachella beds, interbedded with a heterogeneous sequence of clay, sandy clays and sands [13]. The calcarenites showed parallel or cross lamination internal structures; they were hybrid, having variable content of terrigenous clasts (1-50% in volume) mixed with bioclasts. The terrigenous elements were well-rounded quartz and quartzites of igneous and metamorphic origin. The bioclasts were mainly of pelecypods (*Ostrea*), bryozoan, red algae (Rhodophyta), fragments of echinoderms, as well as of gastropods. Benthic micro-foraminifera as Globigerinidae, were also frequent, whereas macro foraminifera, as nummulites, were rare. Generally, the clasts were cemented by sparry or drusy calcite.

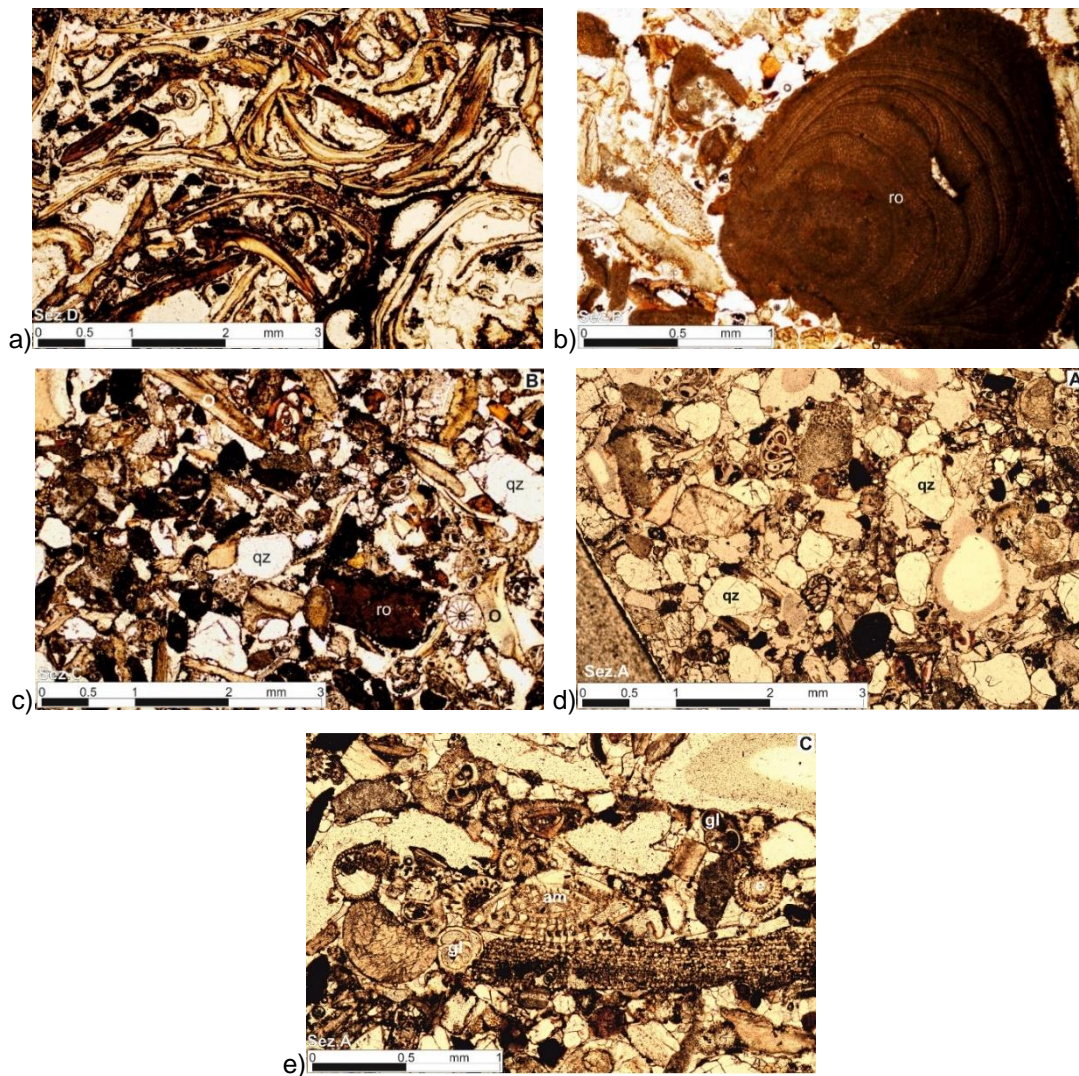


Figure 6.1. a) thin section image of A stone: calcite cemented rudstone with dominant bioclasts of oostrea; b) thin section image of B stone with red algae rodoficeae (ro); c) thin section image of C stone: hybrid calcarenite with a few rounded quartz clast (qz), bioclasts of *Rhodoficeae* (ro), *Globigerinidae* micro-foraminifers (gl), echinoderms (e) and *Ostrea* (o); d) thin section image of D stone: hybrid calcarenite with rounded quartz clasts (qz) mixed with bioclasts; e) thin section image of E stone: rounded quartz crystals (qz) fragments of echinoderms (e) and *Globigerinidae* micro-foraminifers (gl)

The A stone is a grainstone/rudstone composed of oostrea fragments (Figure 6.1a) and calcareous red algae as well as *Globigerinidae* foraminifera. The terrigenous grains represented by rounded quartz crystals were very rare.

The B stone is a packstone containing fragments of *Ostrea*, bryozoans, red algae and echinoderms (coquina, Figure 6.2b). Drusy calcite cements the larger cavities within and between the bioclasts. The matrix does contain little terrigenous fragments, mainly rounded quartz. Few fragments of *Globigerinidae* micro-foraminifera were observed.

The C stone is a hybrid calcarenite with medium to coarse clast size. The terrigenous clasts, mainly quartz of igneous origin, were rounded and their volume does not exceed the 10%, while the bioclasts were mainly of *Ostrea*, bryozoans, red algae, echinoderms, macro foraminifera and only rarely Globigerinidae (Figure 6.1c).

The D stone is a hybrid calcarenite with variable content of terrigenous clasts, mainly rounded quartz of igneous, and more rarely, metamorphic origin (Figure 6.1d). Few fragments of fine-grained polycrystalline quartzite, mixed with bioclastic fragments were observed.

The E stone is a hybrid calcarenite with variable content bioclastic fragments, composed of abundant bivalve *Ostrea*, frequent benthic micro-foraminifera Globigerinidae, rare macro foraminifera *Amphistegina*, fragments of bryozoans and of echinoderms (Figure 6.1e). The rock forming clasts were cemented by sparry or drusy calcite.

From the pore size distributions carried out by MIP, the stones are characterized by an average porosity, evaluated in the range 0.01-100 μ m, from 18% to 39%, as showed in Table 6.1, in agreement with literature results [12].

From the porosity measurements carried out with a pycnometer, also reported in Table 6.1, porosity average values from 30% to 41% are obtained. These values were higher than MIP results related to the presence of pores with dimensions > 100 μ m, not detected by the MIP technique. These results confirmed that the calcarenite rocks have an important fraction of open pores, which were easily accessible to water and so directly involved in the stone durability, as previously reported [14, 15].

Also the chemical compositions from XRF measurements of the different stones are reported in Table 6.1, while XRD results are reported in Table 6.2. In particular, these XRD analysis show that, in all biocalcarenite samples, the main phase is calcite (from 63% to 97%), with a low quartz content (from 1.6% to 8.3%) apart from E stone (32.7% of quartz), in agreement with XRF analysis. In addition, different amounts of aragonite are observed, ranging from 2.1% for the A sample to 31.4% for the C one, but it is not detectable in either the D or E samples. Traces of andradite, gypsum or enstatite can be also identified.

Table 6.1. Results of chemical analysis (XRF) and of porosity measurements (MIP and GeoPyc pycnometer) referred to the different kinds of biocalcarenite samples.

Stone	XRF							MIP (%)	GeoPyc (%)
	Ca (%)	Si (%)	Fe (%)	Mg (%)	K (%)	P (%)	S (%)		
A	38.96	4.76	2.28	0.68	-	0.18	-	26±3	38±2
B	41.97	1.53	2.85	0.90	-	0.14	0.43	19±1	36±1
C	39.11	2.30	3.81	1.98	0.18	0.25	0.19	38±1	40±1
D	43.04	2.06	2.45	0.73	-	0.16	-	25±5	34±2
E	35.49	15.5	1.38	0.59	0.27	0.19	-	18±1	30±1

Table 6.2. XRD quantitative analyses, by means of Rietveld refinement, carried out on the different kinds of biocalcarenite samples.

Stone	Calcite (CaCO ₃) (ICSD #98-004-0107)	Aragonite (CaCO ₃) (ICSD #98-016-9891)	Quartz (SiO ₂) (ICSD #98-004-2498)	Andradite (Ca ₃ Fe ₂ (SiO ₄) ₃) (ICSD #98-005-2393)	Gypsum Ca(SO ₄) (H ₂ O) ₂ (ICSD #98-000-2057)	Enstatite (Mg ₂ (Si ₂ O ₆)) (ICSD #98-008-1130)
A	89.3%	2.1%	8.3%	0.4%	--	--
B	88.6%	8.7%	1.6%	0.2%	0.8%	--
C	63.0%	31.4%	5.7%	--	--	--
D	97.0%	--	1.9%	1.1%	--	--
E	65.5%	--	32.7%	--	--	1.8%

6.2 Nanolime treatments on biocalcarenites samples of Agrigento

The nanolime particles, synthesized with the ion exchange method in the prototype system, as described in chapter 5, are dispersed in 3 different solvent mixtures, at a concentration of 5 g/l (typical of commercial nanolime):

- 1) an alcoholic dispersion in pure ethanol (CH_A sample),
- 2) a water/ethanol mixture W/A = 50% (CH₅₀ sample),
- 3) an aqueous dispersion in pure water, referred to as CH_w.

The carbonation process of the obtained dispersions is followed by means XRD at 20±2°C and RH 75±5%, until complete evaporation of the solvent, in order to maintain the same conditions to store the biocalcarenite stones after the treatments.

These analyses reveal that at RH 75±5%, all the nanolime dispersions show complete carbonation resulting in pure calcite, as reported in Figure 6.3. The complete conversion of Ca(OH)₂ into pure calcite in low time (solvent evaporation) is of fundamental importance because it guarantees perfect compatibility with the substrate from a structural and morphological point of view [16].

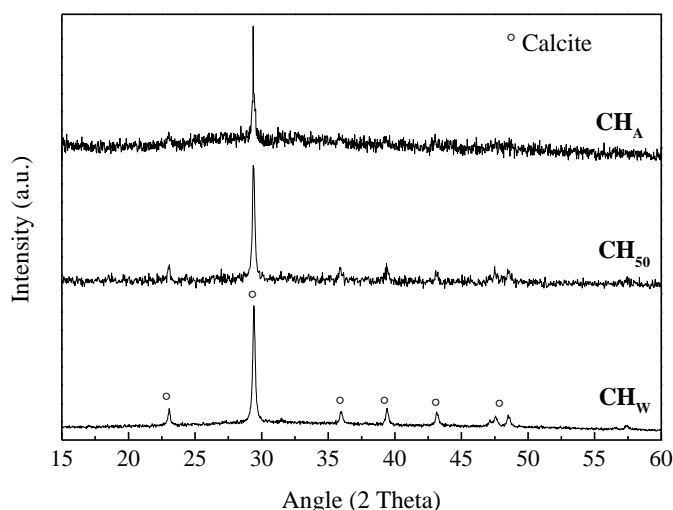


Figure 6.3. XRD spectra related to the analysis of the carbonation process at RH 75%±5% of the different nanolime dispersions used for the treatments (Calcite, ICSD #98-015-8258)

The kinetic stability of the obtained nanolime dispersions was determined by turbidity measurements, analysing their absorbance at $\lambda = 600$ nm by using UV/VIS Spectrophotometer (Lambda 2 Perkin-Elmer) for 20 minutes. Before the test, the nanolime formulations were put into an ultrasonic bath (*Ultra Sonik 300*) in order to reduce the nanoparticles agglomeration. The KS % is measured in function of time and it is calculated using the following formula:

$$\text{KS \%} = 1 - [(A_0 - A_t) / A_0] \times 100 \quad (6.1)$$

where A_0 is the starting absorbance and A_t the absorbance at time t . The relative kinetic stability (KS %) decreases as result of the nanoparticle settling; values range from 0 (unstable dispersion) to 100 (not settling of the nanoparticles). From these stability measurements (Figure 6.4), all the dispersions remain stable during the first 5 minutes, then CH_A continues to be stable for 20 minutes and both CH_W and CH₅₀ show a slow settling process, with a KS reduction up to 45% in 20 minutes, however there is enough time to guarantee an appropriate application of the treatments. The application of dispersions with lower stability is considered more effective on substrates with very fast moisture transport properties. In fact, the lower stability of

the dispersions can limit back-migration of the particles to the drying surface, thus favouring their precipitation in depth and improving the consolidation effect [17].

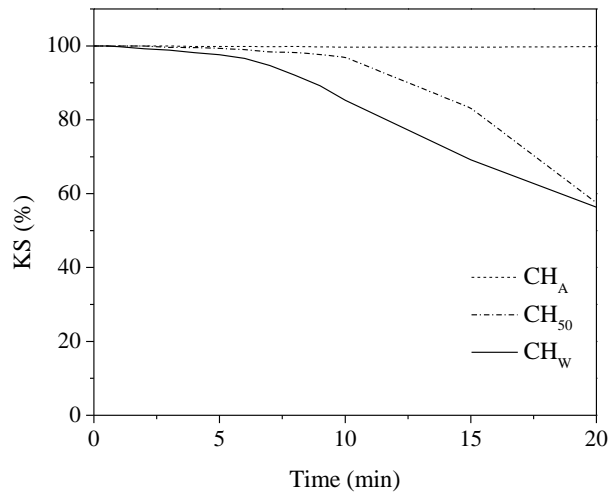


Figure 6.4. Kinetic stability measurements (KS) versus time, at $\lambda = 600$ nm, for the different nanolime dispersions

After these tests, the treatments on biocalcarene stones are carried out by varying the application procedure, using both spray and brushing, other than the solvent, in order to achieve an effective treatment in terms of consolidation, with the lower chromatic alteration. To investigate the application procedure, only the A stone is considered, because of the higher number of available samples. These treatments are performed by using the nanolime suspension dispersed in pure water (CH_W), since this can cause more problems in chromatic alteration of the treated surface, due to the higher agglomeration ability of water [18]. The CH_W suspension was applied until stone saturation, thus providing about 100 mg of calcium hydroxide to each stone. Moreover, during the treatment, the specimens were wiped with a wet cloth to remove the consolidant excess and to reduce surface whitening. Subsequently, the samples were stored for one day at RH 75±5%. As shown in Figure 6.5, from a visual inspection of stereomicroscope images (SM, Leica Stereozoom S8 APO), the treatment performed by spray gives no variation in the chromatic surface respect to the untreated material. On the contrary, the samples treated by brush give a whitening effect, which is visible also by naked eye, particularly inside the superficial porosity of the sample.

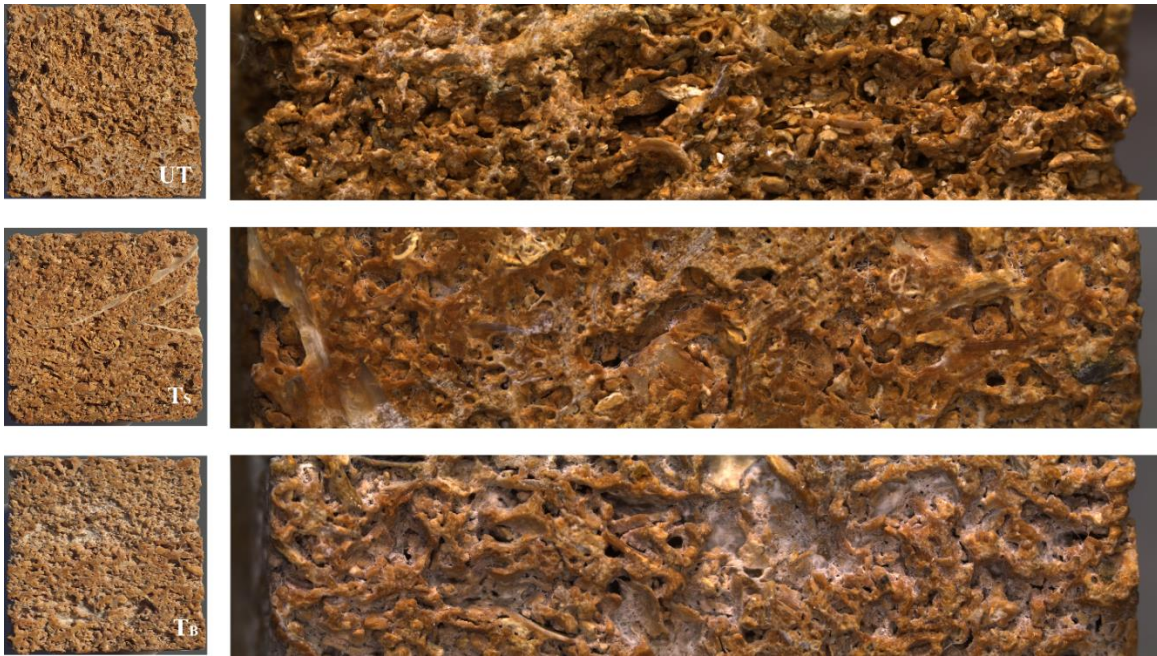


Figure 6.5. Photos and stereomicroscope images (magnification 10x) of the A stone sample untreated (UT) and the samples treated by the CH_w nanolime applied by spray (T_s) and by brush (T_B)

In addition, in Table 6.3 on these A samples are reported the standard water absorption by capillarity (WAC) measurements. For each sample, we measured the values of the average absorption coefficient at 30 minutes (CA), the amount of absorbed water at the end of the test (Q_f) and the variation of CA values related to untreated and treated stones (ΔCA). The effective protective efficacy (E_p), defined as the variation % of Q_f before and after treatment, was also evaluated. [19] The nanolime treatments by spray or brush do not particularly affect their behaviour towards water (the E_p values varied from about 9 to 15%), but the absorption kinetics are affected. There is a ΔCA variation up to 55%, between the treated samples (T_B and T_s) and the untreated ones (UT), suggesting a reduction of the pore sizes. Surface cohesion is also estimated and reported in Table 6.3, by the “Scotch Tape Test” (STT), according to ASTM D3359, and the mean of three tests for each sample was used to evaluate the different treatments. [20] From the STT results, it can be observed that the nanolime treatment carried out by spray yielded the highest increase in surface cohesion, with a reduction of the removed material (ΔM) of 82%.

Table 6.3. WAC and STT results performed on cubic samples of A, before and after the nanolime treatment with CH_w suspension. The treatment was performed by varying the application procedures, by spray (T_s) and by brush (T_B) respectively.

	WAC [*]			STT [*]	
	Q _f (mg cm ⁻²)	ΔCA (%)	E _p (%)	M (mg cm ⁻²)	ΔM (%)
UT	655	53±1	9±1	6.83	30±10
T _B	595			5.06	
UT	715	55±1	15±1	9.13	80±10
T _S	605			1.44	

* The results are taken as the average of three measurements for each application procedure

The consolidation improvement is evaluated using a Drilling Resistance Measurement System (DRMS) from SINT-Technology and considering the difference between the resistance of the untreated and treated samples. The DRMS measures the force required to drill a hole at constant rotation (600 rpm) and lateral feed rate (10 mm/min), using drill bits typically of 5 mm diameter (the mean value is calculated from 10 measurements). As reported in literature, DRMS is generally considered the most suitable methodology for quantifying consolidation effectiveness and penetration depth of the consolidant, particularly in soft stones [21]. The drilling resistance profiles of these A samples are reported in Figure 6.6: the untreated A sample has an average resistance value of about 7±2 N, the A sample treated by spray has a clear improvement of the resistance, with an average value of 13±5 N, while the A sample treated by brush reveals no significant changes of the average resistance.

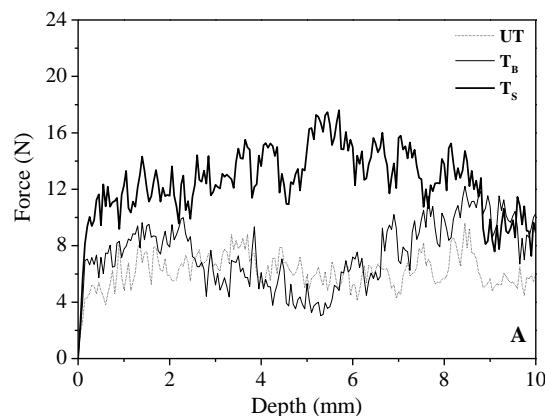


Figure 6.6. Drilling resistance profiles of biocalcarenite A samples: untreated (dot line), treated by brush (continuous lines), treated by spray (marked continuous line)

Considering all the obtained results, it is clear that a higher consolidation efficacy, both in terms of reduction of water absorbed by capillarity and of adhesion and

drilling resistance, is obtained by spray application of the nanolime. Probably the differences in the various observed results are due to the fact that the nanolime applied by brush remained more on the surface (as seen visually), without therefore internally reinforcing the material.

Therefore, the spray application procedure is established and other samples of A stone are treated in this way, by using the three nanolime dispersions (CH_w , CH_{50} , CH_A), to investigate the optimal solvent to be used for the considered stones. The stereomicroscope examinations of the untreated A sample compared to the treated samples reveal that all the spray treatments produce no relevant chromatic alterations, independently from the solvent (Figure 6.7). Only the CH_{50} dispersion gives a very slight whitening effect at magnification 10x.

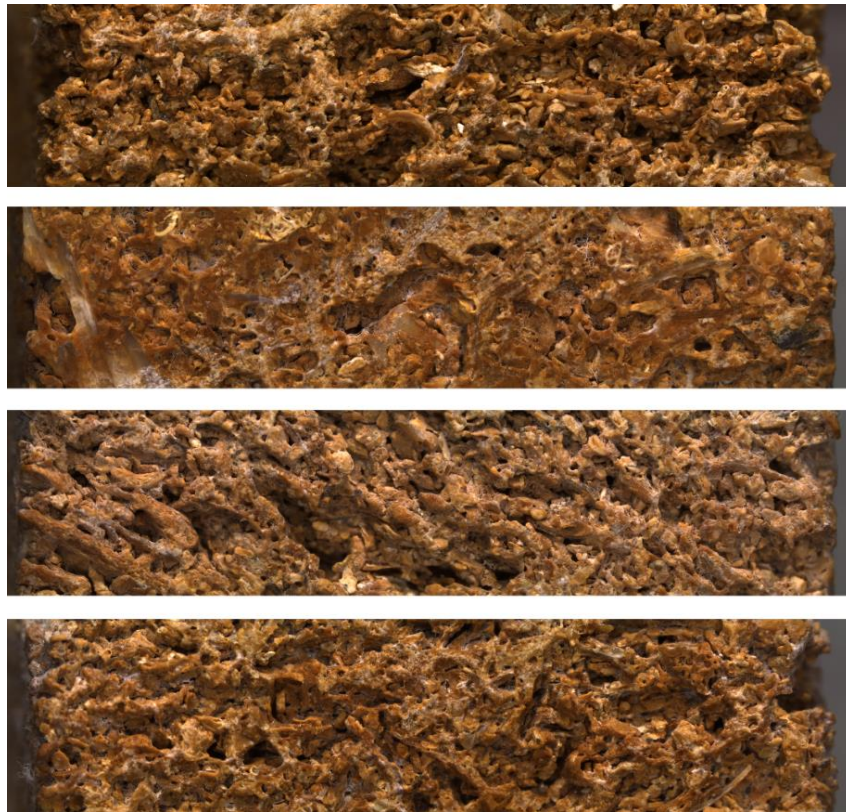


Figure 6.7. Stereomicroscope images (magnification 10x) of the A stone samples, from top to bottom: untreated UT; treated by CH_w dispersion; treated by CH_{50} dispersion; treated by CH_A dispersion

Subsequently, WAC and STT tests are performed and the obtained results, taken as the average of three measurements for each nanolime treatment, are summarized in Table 6.4. CH_w and CH_A have a similar behaviour toward water, with

a ΔCA of about 60%, except for a slight higher E_p ($17\pm 2\%$) value for the CH_w suspension. However, in terms of superficial cohesion only the aqueous dispersion CH_w revealed a drastic reduction in the material removed from the surface after the treatment, with a ΔM of 90 ± 10 .

Table 6.4. WAC and STT results referred to cubic samples of A stone, before (UT) and after the nanolime treatment by spray (T_s). The samples are treated by varying the dispersing medium of the nanolime dispersions

Nanolime dispersions		WAC*			STT*	
		Q_f ($mg\ cm^{-2}$)	ΔCA (%)	E_p (%)	M ($mg\ cm^{-2}$)	ΔM (%)
CH_w	UT	695	58 ± 4	17 ± 2	19.19	90 ± 10
	T_s	575			2.75	
CH_{50}	UT	725	20 ± 10	6 ± 2	19.19	50 ± 20
	T_s	685			10.18	
CH_A	UT	680	60 ± 3	13 ± 2	19.19	40 ± 10
	T_s	590			11.41	

*The results are taken as the average of three measurements for each nanolime treatment

The ability of the aqueous dispersion to consolidate the surface of the calcarenite stone was confirmed by the DRMS measures as well, reported in Figure 6.8. When compared to the alcoholic and to the hydro-alcoholic treatment, the aqueous treatment exhibited a good increase of the superficial resistance up to 10 mm, with a reinforcement particularly marked in the first 2 mm. This fact can be mainly ascribed to the crucial role of water to promote high efficiency in accelerating the carbonation process [16, 22, 23], so guaranteeing the formation of the new calcite network between the original grains of the stone. In addition, the presence of alcohol can play a detrimental role because of the formation of $CaCO_3$ polymorphs different from calcite, as discussed in several recent literature papers [24, 25], or because of the described back-migration phenomena [17].

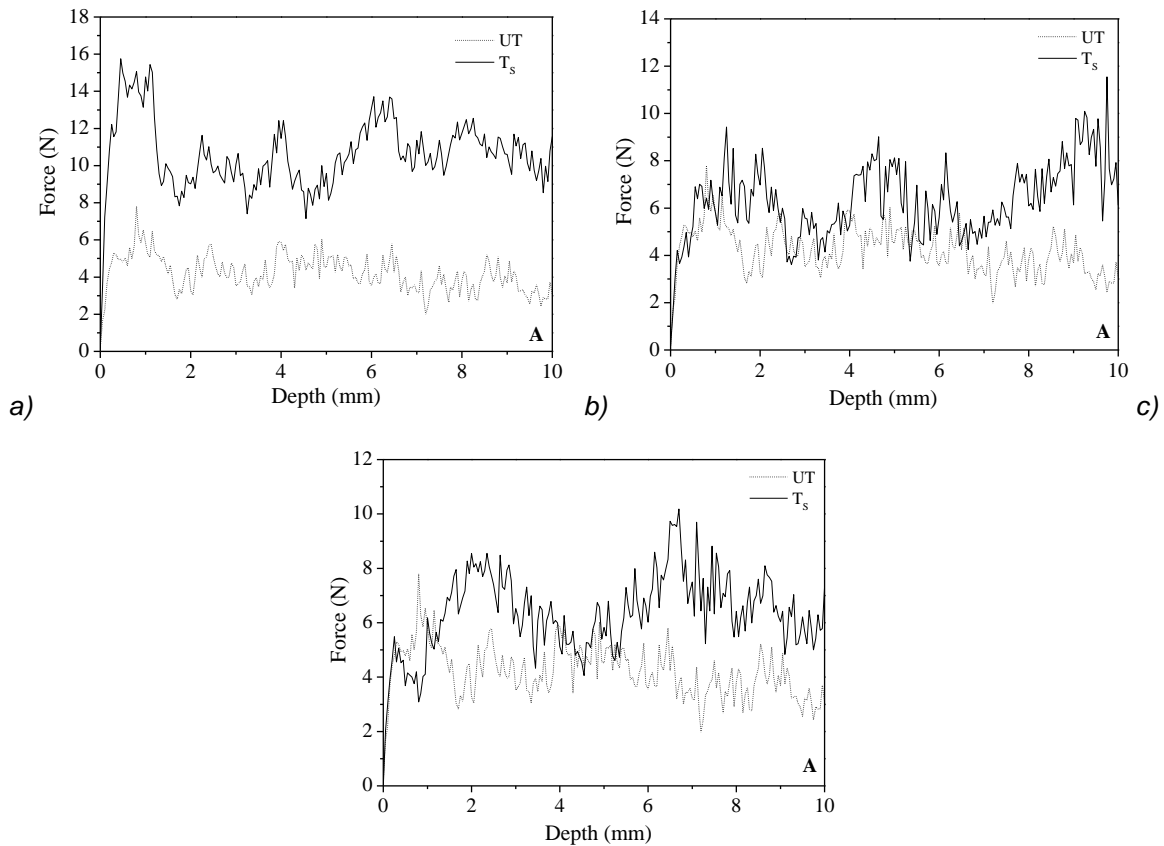


Figure 6.8. Drilling resistance profiles of untreated (dot line) and treated (continuous lines) A stones: a) treated by CH_w suspension; b) treated by CH₅₀ suspension; c) treated by CH_A suspension

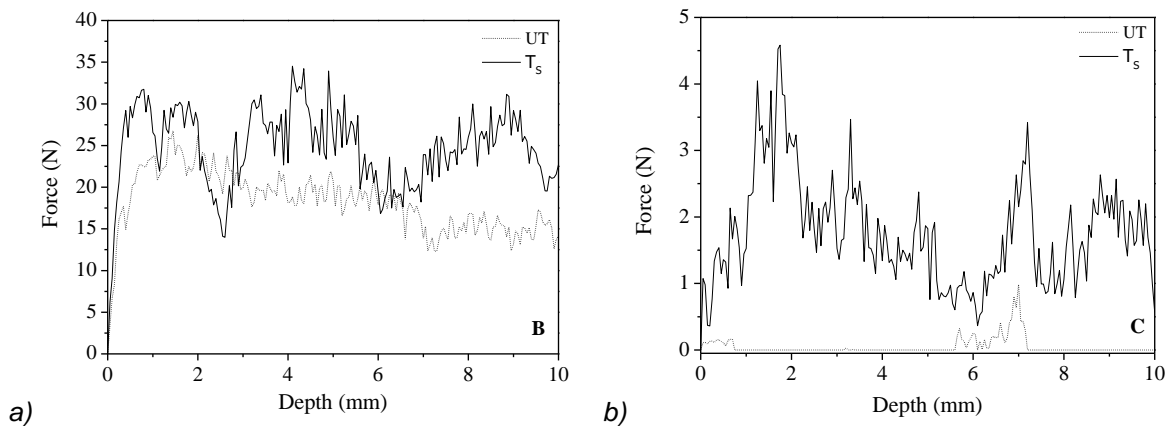
Taking into account these results, the other biocalcarenite stones (B, C, D and E), are treated directly with the CH_w nanolime suspension applied by spray, because it possesses the greatest effectiveness on this kind of stone for every considered test. The WAC and STT results, before and after the treatment, are reported in Table 6.5. Analysing WAC results, it is confirmed that for all stones, independently of their pore size distribution, the nanolime treatment does not significantly change the amount of water absorbed by capillarity (E_p average values ranging from 12 to 17%), but it affected the absorption rate (ΔCA values up to $70 \pm 10\%$). Regarding the STT, for all the stones, the results confirm the nanolime treatment efficacy in surface consolidation, restoring the cohesion between the superficial grains, with ΔM values up to $87 \pm 3\%$ on the sample E (the most degraded).

Table 6.5. WAC and STT results referred to cubic samples of B, C, D and E stones, before (UT) and after the nanolime treatment by spray (T_s) with the CH_w suspension

Type of biocalcarene stone		WAC*			STT*	
		Q_f (mg cm ⁻²)	ΔCA (%)	E_p (%)	M (mg cm ⁻²)	ΔM (%)
B	UT	286	50±10	13±5	13.87	60±10
	T_s	247			5.00	
C	UT	881	60±20	15±2	60.94	50±10
	T_s	743			30.21	
D	UT	418	70±10	12±5	9.27	40±20
	T_s	367			5.46	
E	UT	405	40±10	17±1	42.75	87±3
	T_s	335			5.41	

*The results are taken as the average of three measurements for each nanolime treatment

DRMS tests performed on these 4 types of stones, before treatment, reveal a very different behaviour in terms of mechanical resistance. While B and D samples present an average mechanical resistance from 10 to 20 N (Figures 6.9 a-c), a weak resistance is measured in C and E samples, so that most samples are broken during the drilling operation itself. In the sporadic cases where the C and E samples did not break, they presented a very low resistance values (Figures 6.9 b-d). After the nanolime treatments, if B and D appear only slightly reinforced, C and E samples do not break anymore during the drilling test, reaching average values of resistance from 2 N to 5 N, respectively. The obtained results show a general increment of resistance in depth, underlining the ability of the nanolime particles, dispersed in pure water, to penetrate at least until 10 mm from the surface.



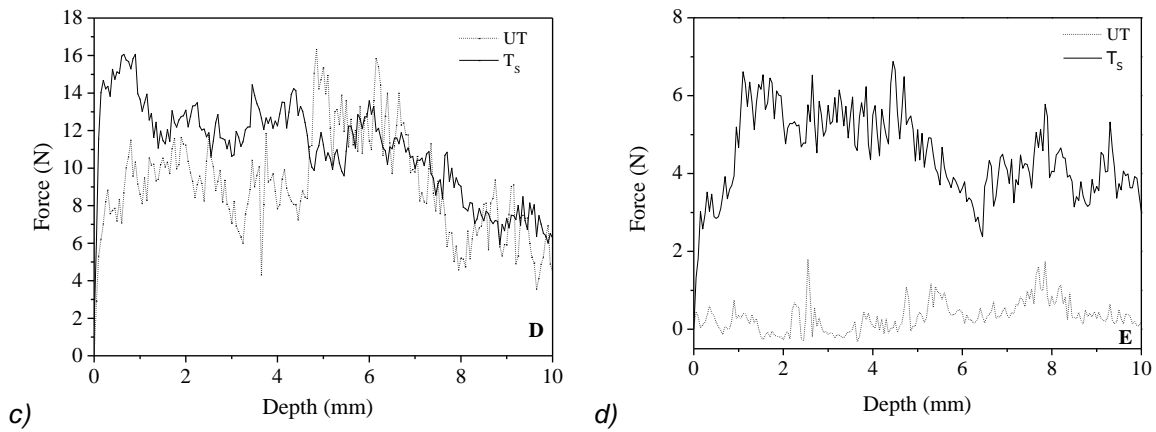


Figure 6.9. Drilling resistance profiles of untreated (UT, dot line) and treated by spray (T_s) with the CH_w suspension (continuous lines) biocalcarenite stones: B, C, D and E

Also the pore size distributions, previously showed in Table 6.1, are carried out by MIP before and after these nanolime treatments. In particular, except for B samples, the populations of pores are mainly found in the range 10-100 μm ; moreover, in the graphs relative to A, B, D and E samples the pore population tend to continue also for diameters $> 100\mu\text{m}$. However, after the CH_w treatment, all the stones show a general reduction of pores between 10 and 100 μm , together with the development of a pore population with sizes lower than 0.05 μm , as reported in Figure 6.10.

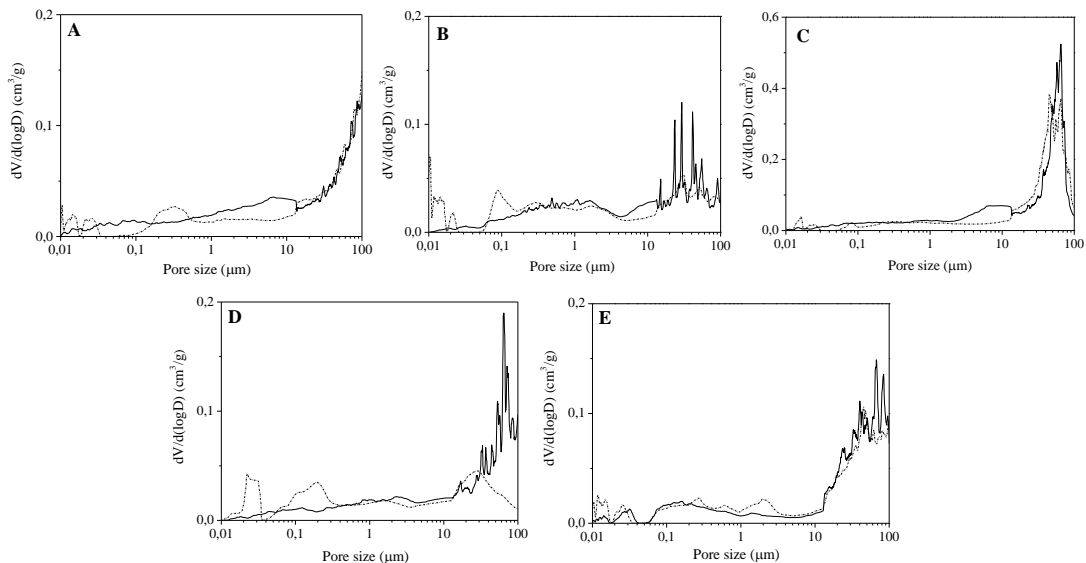


Figure 6.10. Differential volume of intruded mercury versus pore diameter of untreated (*continuous lines*) and treated (*dotted lines*) biocalcarenite stones: A, B, C, D and E

The aqueous nanolime suspension at 5 g/l can be considered a compatible and green consolidative treatment on biocalcarenite stones, because in all the samples

it produced only a slight decrease of the water adsorption by capillarity, with a kinetic rise variation up to 67%, in accordance to the observed reduction of the pores population between 10 and 100 μm . Moreover, this aqueous nanolime treatment increased both the superficial cohesion, with a reduction of material removed from the surface up to 90%, and the mechanical resistance up to 10 mm from the surface. The usage of nanolime dispersions in pure water, together with the versatile, cost effective and up-scalable production method, seem to be very promising for widespread use, such as in the protection and superficial consolidation of carbonatic architectural substrates. The use of water as solvent possess some advantages, such as: a reduced time required for a complete carbonation process; the transformation of $\text{Ca}(\text{OH})_2$ nanoparticles into pure calcite; the absence of back-migration phenomena towards the surface together with the solvent; the employment of a green product, avoiding the use of organic and volatile compounds, with all the problems connected to the transportation as well as the direct use. For this reason, this type of nanolime is used for the first time on the entire facade of a historic building in L'Aquila.

6.3 Comparative treatments of nanolime on biocalcarenites with commercial products

In this paragraph comparative treatments are realized using the two main commercial products of nanolime (Calosil and Nanorestore plus) and the nanolime synthesized with the ion exchange method, called Nano-LAQ. For the comparative tests, the nanolime synthesized by ion exchange is dispersed in water or isopropanol and the characterization of all the products is carried out using various techniques, such as XRD, TEM and UV spectrophotometry, also analyzing the carbonation process at different relative humidity (RH) conditions. In addition to nanolime-based products, it is considered a further consolidant widely used in the Cultural Heritage, which is the ethyl silicate or TEOS. It is an organic compound with chemical formula $\text{SiC}_8\text{H}_{20}\text{O}_4$ and tetrahedral structure [26]. These products were compared in relation to their effectiveness in the consolidation of other biocalcarenite specimens from Agrigento.

The products chosen are therefore: Nanorestore plus, Calosil, Nano-LAQ water, Nano-LAQ isopropanol and ethyl silicate, all at a concentration of 5 g/l, except for the ethyl silicate that is typically used at 70% in weight.

First of all, XRD measurements are carried out to evaluate the composition and the reactivity of the various nanolime suspensions. The suspensions are observed after drying in an inert atmosphere (N₂), while the reactivity is evaluated at RH of 45±5% and 75±5% up to 5 days. Three replicates are performed for each test and the average results are shown in Table 6.6.

Table 6.6. Average results obtained from XRD tests of 4 different nanolime suspensions exposed to different environments

Nanolime products 5 g/l	Inert atmosphere	RH 45±5%	RH 75±5%	RH 75±5% - 5 days
Calosil	100% calcium hydroxide	100% calcium hydroxide	100% calcium hydroxide	80±5% vaterite
				21±3% calcite
Nanorestore plus	100% calcium hydroxide	100% calcium hydroxide	100% calcium hydroxide	85±4% vaterite
				15±2% calcite
Nano-LAQ water	100% calcium hydroxide	100% calcite	100% calcite	100% calcite
Nano-LAQ isopropanol	100% calcium hydroxide	100% calcium hydroxide	100% calcium hydroxide	66±4% calcite
				34±3% calcium hydroxide

From the obtained diffraction data, it is evident that under normal environmental conditions (RH 45±5%) only the Nano-LAQ in aqueous solvent turns into calcite, highlighting the fundamental role of water in the carbonation process. Furthermore, this Nano-LAQ is more reactive than Calosil and Nanorestore plus (both dispersed in isopropanol) towards the formation of calcite even with the same alcoholic solvent, considering high RH conditions (75±5%) for 5 days. However, Calosil and Nanorestore plus after this period lose the presence of hydroxide, forming for about 80% a metastable calcium carbonate, called vaterite, which slowly turns into calcite (at least 28 days at RH 80% from literature). Instead the Nano-LAQ isopropanol within 10 days at RH 75±5% is completely converted into calcite, without going through the formation of metastable forms of calcium carbonate.

To evaluate the stability of the various nanolime suspensions at 5 g/l, tests are carried out with UV spectrophotometry, evaluating the change in absorbance over time (as described in paragraph 6.2), which can be correlated with the concentration of suspended nanoparticles. All the dispersions, before being analyzed, are placed in an ultrasonic bath for 15 minutes. For each sample, the absorbance is here

measured at 610 nm for 20 minutes, considered as the maximum application time, and the results are reported in the graph of Figure 6.11.

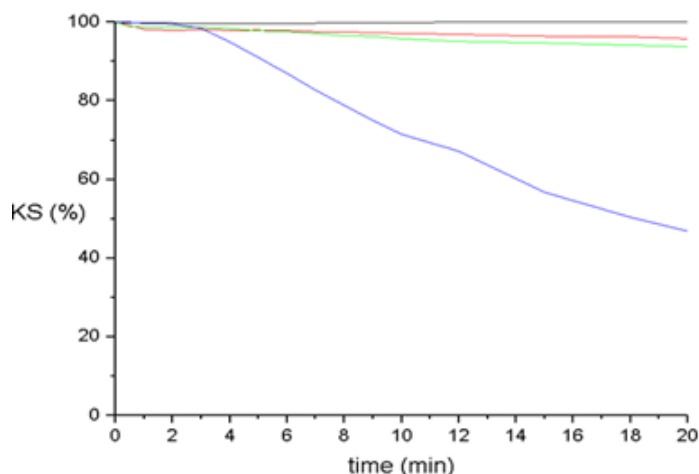


Figure 6.11. Stability curves for different nanolime suspensions, from top to bottom: Nano restore plus (gray), Calosil (red), Nano-LAQ isopropanol (green), Nano-LAQ water (blue)

From the stability curves, the Nano restore plus has the most stable suspension, while the Nano-LAQ water is the less stable, since in aqueous solution the nanoparticles tend to aggregate and precipitate. In fact, the Nano-LAQ isopropanol has a good stability, comparable to that of Calosil. However, the instability of the suspension over time is not a negative aspect, as it has been observed in the literature that alcoholic suspensions of nanoparticles may exhibit the already described back migration phenomena: the evaporation of the solvent drags to the surface the penetrated nanoparticles (paragraph 6.2).

From TEM micrographs, shown in Figure 6.12, the presence of hexagonal lamellae with side dimensions <100 nm is observed in all the suspensions considered. In particular, in Calosil generally regular and small hexagonal lamellae are noted, with side dimensions in the range 30-50 nm (Figure 6.12a). Both regular and non-regular hexagonal lamellae can be seen in the Nano restore plus suspension, with a wide dimensional range, 30-100 nm in side (Figure 6.12b). In the suspension of Nano-LAQ water there are more regular hexagonal lamellae with lateral dimensions of about 40-70 nm, but with thicknesses that seem reduced compared to the other samples (≤ 5 nm), so that some appear almost transparent to the electron beam (Figure 6.12c). Finally, in the suspension of Nano-LAQ isopropanol more elongated

hexagonal lamellae are noted, again with side dimensions of about 40-70 nm and very reduced thicknesses, which appear to be ≤ 10 nm (Figure 6.12d).

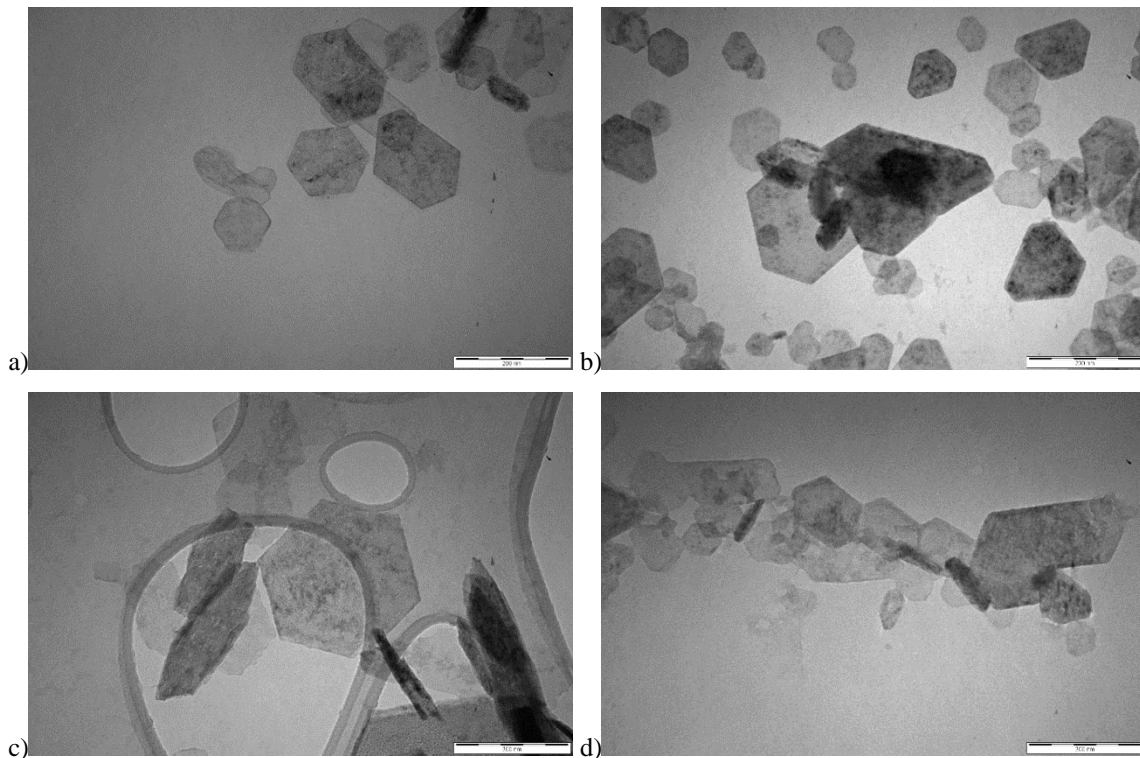


Figure 6.12. TEM micrographs with 200 nm marker nanolime particles from different suspensions:
a) Calosil, b) Nanorestore plus, c) Nano-LAQ water, d) Nano-LAQ isopropanol

At this point, the real applicative comparison between the 5 selected products is carried out, always using carbonatic substrates of historical and architectural value (the biocalcarenes of Agrigento). A total of 15 cubic specimens with a 3 cm side are realized from the same original stone, to have similar basic characteristics on each specimen (identified as D stone and characterized in paragraph 6.1). Each treatment is then applied to three specimens at a commercial concentration (5 g/l), using a treatment method suitable for all suspensions (spray), because the airbrush would nebulize and evaporate the alcohol too rapidly. The treatment is repeated 5 times on each specimen until saturation (intended as complete wetting, corresponding to about 10 ml of suspension for each application). As for the ethyl silicate, it is applied by brush for problems related to spray method with this compound, until the stone saturation (corresponding to 10 applications for each stone). [58] Between the treatment repetitions, the specimens are kept 24 hours at RH $75\pm 5\%$, in order to promote carbonation as much as possible even in alcoholic suspensions. The effective amount of consolidant product absorbed by the various

specimens is reported in Table 6.7, revealing that the nanolime quantities are very low compared to the weight of the specimens (about 40 g), while the ethyl silicate is brought in quantities 10 times higher respect to nanolime, because of its high suspension concentration.

Table 6.7. Chromatic alteration and effective quantity of consolidant absorbed by stone specimens

Treatment	Calosil	Nanorestore plus	Nano-LAQ water	Nano-LAQ isopropanol	Ethyl silicate
Average g absorbed	0.23±0.02	0.23±0.01	0.20±0.01	0.19±0.01	2.40±0.05
Chromatic alteration	Slight whitening	Slight whitening	Not detectable	Not detectable	Slight browning

Also visual observations are carried out on these specimens in a preliminary way, to evaluate their effect in the chromatic alteration, and reported in Table 6.7 as well. All the chromatic alterations can be acceptable on this kind of samples, but only the Nano-LAQ suspensions leave the treated specimens almost identical to the untreated ones. Following the treatments, the comparative tests carried out on the biocalcarenite specimens to evaluate their effectiveness are: capillary rise, scotch tape test and drilling resistance measure.

The capillary rise allows to obtain water absorption curves over time following the UNI EN 15801 standard (as described in paragraph 6.2), evaluating how the ability of the material to absorb water changes before and after treatments. Before the tests, the specimens are immersed in deionized water for 30 minutes to eliminate impurities and placed in an oven at 50°C to reach a constant mass. The results obtained for the same specimens, before and after the respective treatment, are shown in Table 6.8, in terms of Q_s (quantity of water at saturation), ΔCA (variation of the capillary rising speed) and E_p (protective efficacy, that is the variation of the amount of water to saturation).

Table 6.8. Capillary rise parameters for different treated specimens

Treatment	E_p (%)	ΔCA (%)	Q_s (mg/cm ²)
Calosil	3±1	30±10	430±20
Nanorestore plus	9±4	35±3	390±20
Nano-LAQ Water	7±4	33±4	400±20
Nano-LAQ Isopropanol	3±2	25±5	420±20
Ethyl silicate	89±1	98±1	60±2

From the capillary rise data, it appears that in all cases the treatments with nanolime do not greatly alter the amount of water absorbed by the stone specimens ($E_p < 10\%$). However, they act on the capillary rising kinetics, reducing the water rising rate by about 30%, probably due to a restriction of the stone pores. On the contrary, the specimens treated with ethyl silicate reveal a high alteration in the amount of absorbed water ($E_p = 89\pm 1\%$), corresponding to considerable reduction of the porosity of the specimens. This effect is not considered an advantage, because the almost total clogging of the pores prevents the stone from regular transpiration, leading to faster degradation due to the accumulation of water and salts internally. The scotch test tape or STT, according to ASTM D3359, is mainly used to evaluate the cohesion of the surface layer of the specimens before and after treatment. Table 6.9 shows the reduction % of material removed related to the tear surface (mg/cm²). The specimens result consolidated for all nanolime treatments, with a reduction % generally > 90%. However, the consolidant effect is lower in the specimens treated with Nano-LAQ isopropanol respect to other nanolime treatments, probably due to a greater presence of hydroxide after 5 days at RH 75±5%. Moreover, ethyl silicate does not consolidate the surface of the specimens as much as the nanolime, although it is brought in about 10 times greater amount on the substrates.

Table 6.9. Reduction % in the scotch tape test calculated for all treated specimens

Treatment	Calosil	Nanorestore plus	Nano-LAQ water	Nano-LAQ isopropanol	Ethyl silicate
Reduction %	93±1	89±2	95±2	74±3	75±3

The measurement of drilling resistance is essential to measure the consolidating effect based on the penetration depth of each treatment. The DRMS (Drilling

Resistance Measurement System) is a device designed to perform such measurements, as described in paragraph 6.2. Both the rotation speed (600 rpm) and the advancement speed (10 mm/min) of the drill bit (diameter 5 mm) are maintained constant during all the tests, making 5 holes on each specimen. The average graphs related to the tests on each specimen are shown in Figure 6.13, in which the y axis is the force (N) that the specimen impresses on the detector as resistance to penetration, while the x axis is the depth of penetration (mm).

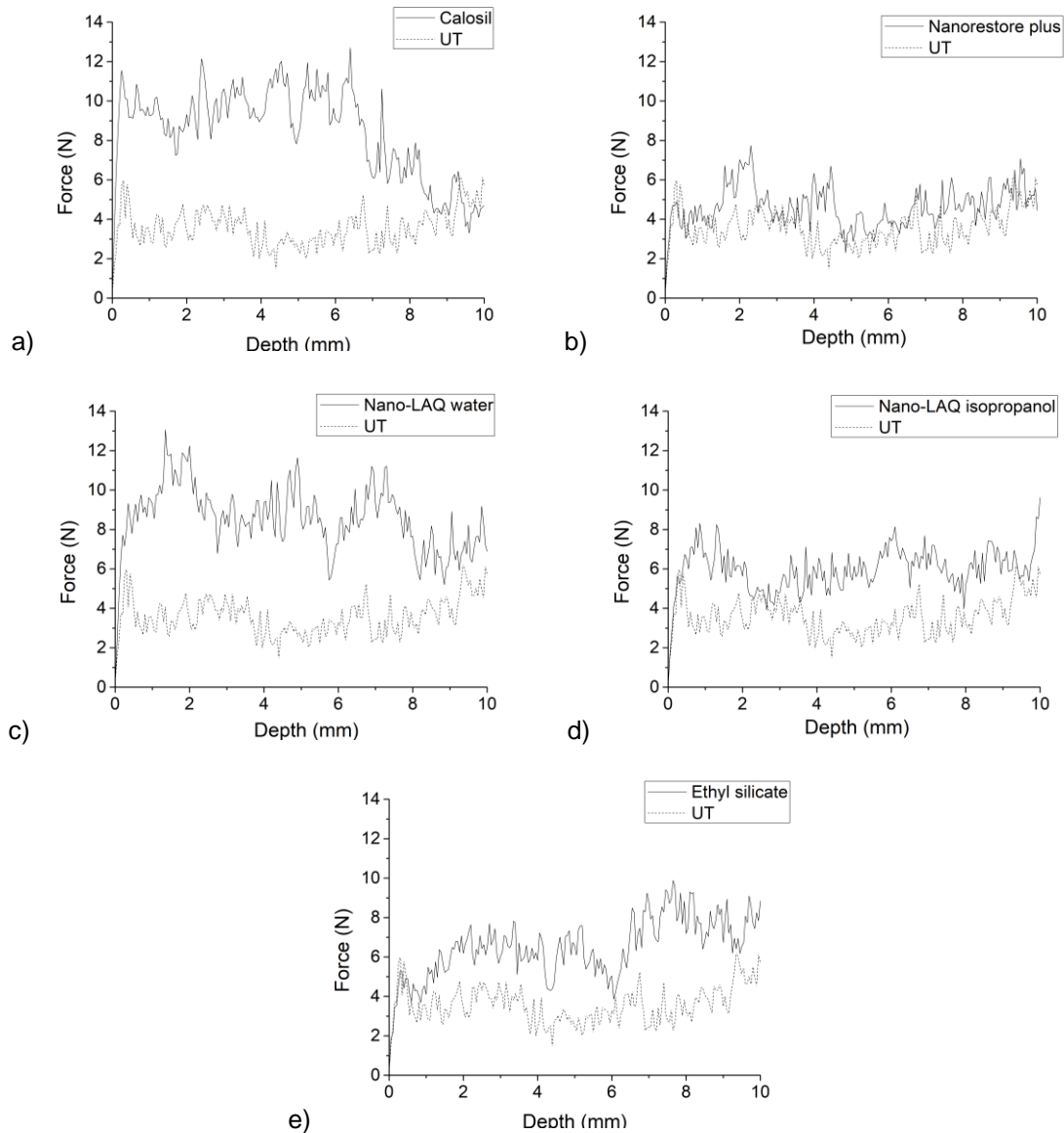


Figure 6.13. Drilling resistance profiles of untreated (UT, dot line) and treated specimens with different suspensions (continuous lines): a) Calosil, b) Nanorestore plus, c) Nano-LAQ water, d) Nano-LAQ isopropanol, e) Ethyl silicate

Table 6.10. Average force values obtained from drilling resistance measurements repeated 15 times on untreated and treated specimens with different suspensions

Treatment	Untreated (UT)	Calosil	Nanorestore plus	Nano-LAQ water	Nano-LAQ isopropanol	Ethyl silicate
Force (N)	4±1	9±2	6±3	9±1	6±2	6±2

The resistance to opposite perforation by a stone material is a function of its compositional, mechanical and microstructural characteristics and has been statistically correlated with the uniaxial compressive strength. By analyzing the average strength values obtained for all the stones treated with the various consolidant products (Table 6.10), it can be observed that Calosil and Nano-LAQ water significantly consolidated the specimens, doubling the average resistance to perforation. Among the nanolime suspensions, the worst consolidation is found in stones treated with Nanorestore Plus, with the specimens remaining almost unchanged as average force, while a modest consolidation is obtained in stones treated with Nano-LAQ isopropanol (about 50% increase on average strength). Ethyl silicate also gives a modest consolidation with an increase of about 50% in the average force of the specimens, in line with the values obtained in the STT, but it must be considered that the amount of ethyl silicate on the stones is about 10 times greater than that of the nanolime.

Therefore, from all the comparative tests, it appears that the most promising nanolime-based treatment is obtained using the nanolime produced by ion exchange method (Nano_LAQ) in water, as it gives the best consolidation results on STT and DRMS tests (similar to Calosil), without chromatically altering the stone and without occluding porosity. Furthermore, this suspension is also a consolidant product with a very low environmental impact and reduced risk for the human health of the operators, being completely in water, as well as perfectly eco-compatible with all carbonate matrix substrates (unlike ethyl silicate).

6.4 Synchrotron investigations of nanolime carbonation process

As part of a proposal at the MCX beamline of the Elettra-Synchrotron (Trieste, Italy), the reactivity of the nanolime synthesized with ion exchange method is better investigated. As already described, the carbonation process of the $\text{Ca}(\text{OH})_2$ nanoparticles can be affected by several parameters, such as the suspension concentration, the environmental conditions as well as the employed solvent. Both the time needed to complete the carbonation process and the stability of the CaCO_3 polymorphs that form strongly depend on the solvent and on the relative humidity (RH). For alcoholic nanolimes, the carbonation process can require long time to complete even for diluted samples (up to 28 days), also with the formation of CaCO_3 polymorphs, such as vaterite and aragonite [27-31].

It is well known that the carbonation process of lime takes place in the presence of carbon dioxide (CO_2) in aqueous conditions [32]. Specifically, in order to have carbonation, CO_2 must first diffuse in water. The CO_2 diffusion is a phenomenon that can be divided into three parts: diffusion in the gas phase ($\text{CO}_2(\text{g})$), adsorption in the gas-liquid interface and diffusion in the liquid phase ($\text{CO}_2(\text{aq})$), as schematized in Figure 6.14a. The concentration of $\text{CO}_2(\text{aq})$ depends, according to the Henry's law, on the partial pressure of CO_2 . Since CO_2 makes up 0.0355% of the atmosphere and $K_{\text{CO}_2} = 2 \cdot 10^{-3}$, at equilibrium $\text{CO}_2(\text{aq})$ is about $1.2 \cdot 10^{-5}$ mol/l. In water, an equilibrium between $\text{CO}_2(\text{aq})$ and carbonic acid (H_2CO_3) is established, and the concentration of $\text{CO}_2(\text{aq})$ is about 10^3 times greater than that of dissolved H_2CO_3 . Carbonic acid loses protons to form bicarbonate ions (HCO_3^-) and carbonate ions (CO_3^{2-}), decreasing the pH of water [33].

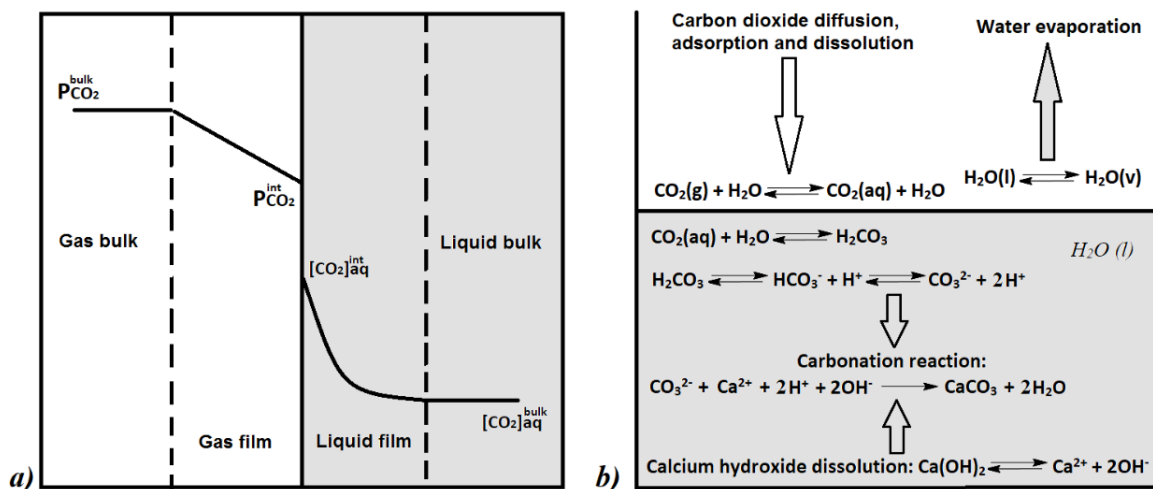


Figure 6.14. a) Diffusion of CO₂ from a bulk gas to a bulk liquid, the concentration of CO₂(g) is expressed as partial pressure of CO₂ (P_{CO2}) [34]; b) the main mechanisms at the basis of the carbonation process

In parallel, calcium hydroxide partially dissolves in water in Ca²⁺ and OH⁻ ions, (about 1,7 g/l at T = 25°C [35]), reacting with carbonate ions (CO₃²⁻) to form CaCO₃ that precipitates. Therefore, during the carbonation process, H₂CO₃ is continuously consumed and, for this reason, it is more important to consider the diffusion rate of CO₂(aq), which depends on the liquid surface exposed to air as well as on the liquid volume. The carbonation process proceeds until the solvent is completely evaporated, underlining the crucial role of water. The evaporation rate of water is affected by the external conditions, such as temperature, pressure, relative humidity and air-water surface, which in turn depends on the instantaneous shape of the drop, defined by drop volume and contact angle [36]. In Figure 6.14b, the main mechanisms that regulate the whole process involving carbonation of nanolime into calcium carbonate in water are shown.

Therefore, the parameters affecting the carbonation process can strongly influence the efficacy of consolidating nanolime treatments. The kinetic of the carbonation reaction and the phase evolution of the synthesized nanolime suspensions are investigated by means of time-resolved synchrotron radiation X-Ray diffraction (SR-XRD). Measures are performed in capillary sample holders, on laboratory glass slides and on artistic relevant stones (the biocalcarenite of Agrigento), considering different solvents. In this way, a carbonation rate (C_R) for the nanolime was estimated, depending on the solvent, the CO₂ conditions, the RH conditions and the substrate. Two kinds of experiments were performed, as described in the following paragraphs.

In the first experiment, nanolime suspensions, from 10 to 100 g/l, both in completely aqueous and completely alcoholic medium, were placed in boron capillaries (0.5 mm in diameter) and measured without air or under a CO₂ controlled flux at 1 bar, using a monochromatic X-ray beam with a wavelength of 1.033 Å.

From SR-XRD investigations, the nanolime, observed in suspension inside capillaries, did not show much difference when varying both the solvent and the concentration. On the contrary, in case of a constant CO₂ flux inside the capillaries, a clear difference in the reactivity of the aqueous or the alcoholic suspension was observed. Actually, we observed that, also at very high concentration (100 g/l), in

presence of a flux of CO₂ at 1 bar, the aqueous suspension (0.2 ml of volume) showed a complete transformation from pure calcium hydroxide to calcium carbonate in form of pure calcite (no other polymorphs were observed) in less than 15 seconds (the minimum time between two subsequent acquisitions). On the contrary, the alcoholic suspension, also at the lowest concentration (10 g/l), did not show the calcium carbonate transformation, also considering a constant flux of CO₂ at 1 bar for 10 minutes. As an example of these results, in Figure 6.x the SR-XRD patterns both of the aqueous nanolime suspension at 100 g/l (Figure 6.15a) and of the alcoholic one at 10 g/l (Figure 6.15b), before and after the application of the CO₂ flux, are reported. The large background is due to the solvents and the capillary.

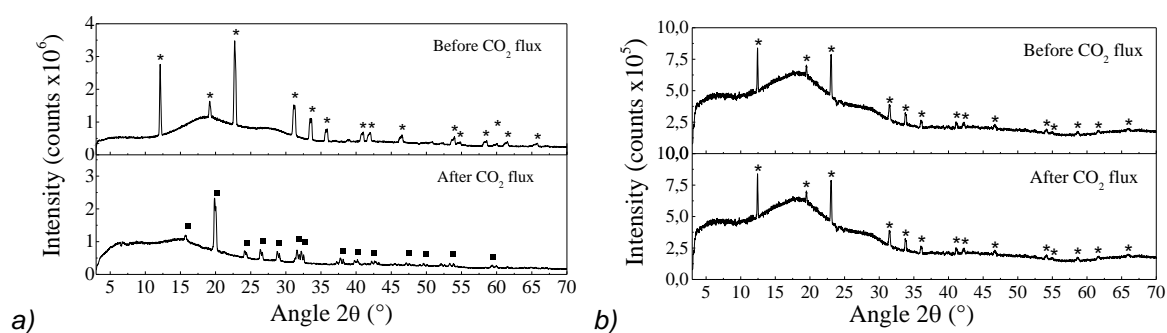


Figure 6.15. SR-XRD patterns measured inside a capillary sample holder on: a) aqueous nanolime suspension at 100g/l, b) alcoholic nanolime suspension at 10 g/l, before and after exposition to CO₂ flux. Legend: * = portlandite (Ca(OH)₂), ■ = calcite (CaCO₃)

These measurements show that only flux water is useful to convey the carbonation reaction and that this reaction in water, in presence of a CO₂ flux, is very fast (0.2 ml at 100 g/l of nanolime converted in < 15 seconds). For this reason, the diffusion of CO₂ inside water can be assumed as the rate-limiting step of the carbonation in air itself.

6.5 Synchrotron investigations of nanolime reactivity on biocalcarenites

In the second experiment, 0.5 ml of nanolime suspensions, from 10 to 100 g/L, were placed both on laboratory glass slides and on biocalcarenite stones (composed of about 98% calcite with traces of quartz and andradite, having a porosity of about 35%). The SR-XRD data were collected in grazing angle geometry (GIXRD) with the MARCCD detector using a monochromatic beam of $\lambda = 0.827 \text{ \AA}$, at laboratory

conditions ($p_{\text{CO}_2} \approx 10^{-3.5}$ atm, $T = 20 \pm 2$ °C and $\text{RH} = 20 \pm 5\%$). The incident-grazing angle was fixed at 5.0° to investigate changes at the air-substrate interface, the patterns were integrated using Fit2D program [37, 38]. On the patterns obtained from glass laboratory slides, a quantitative phase analysis (QPA) of the observed crystalline phases was carried out using the Rietveld method using the GSAS software [46]. The surface of the biocalcarenite samples showed a great heterogeneity in the particle size. Therefore, the integrated patterns were not of enough quality to allow a detailed QPA. However, semi quantitative information can be retrieved observing the changes in intensity of the most intense peaks of the $\text{Ca}(\text{OH})_2$.

Laboratory glass slides (non-porous substrate) and biocalcarenite stones (porous substrate) were chosen to evaluate the influence of the substrate porosity on the carbonation. In fact, the distribution of the applied suspension can affect the CO_2 diffusion rate as well as the water evaporation rate, so Figure 6.16 represents the distribution of the nanolime suspensions on this type of substrates.

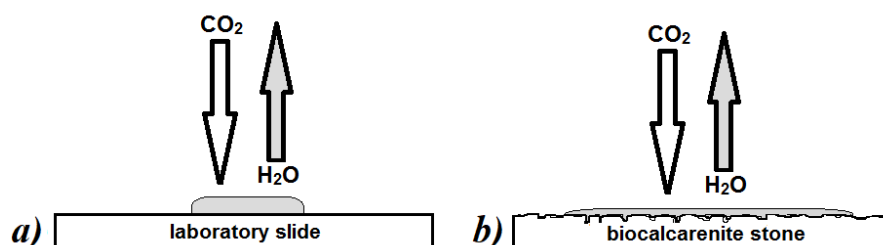


Figure 6.16. Distribution of the same volume of the nanolime suspension on the two different substrates: a) the non-porous glass slide, b) the porous biocalcarenite stone

The carbonation reaction has been investigated in air for this experiment, but considering the negligible reactivity of the completely alcoholic samples from the first experiment, only the aqueous suspensions of nanolime were considered. The SR-XRD patterns obtained on glass laboratory slides are reported in Figure 6.17, varying suspension concentration and time intervals during solvent evaporation. The pattern of the laboratory slide alone is reported as well, showing the typical pattern of amorphous silica. On the substrate where the nanolime suspension has been applied at 20 g/l, 0.5 ml of water was added after the initial suspension had dried, in order to check whether the carbonation proceeds and to evaluate the reaction rate.

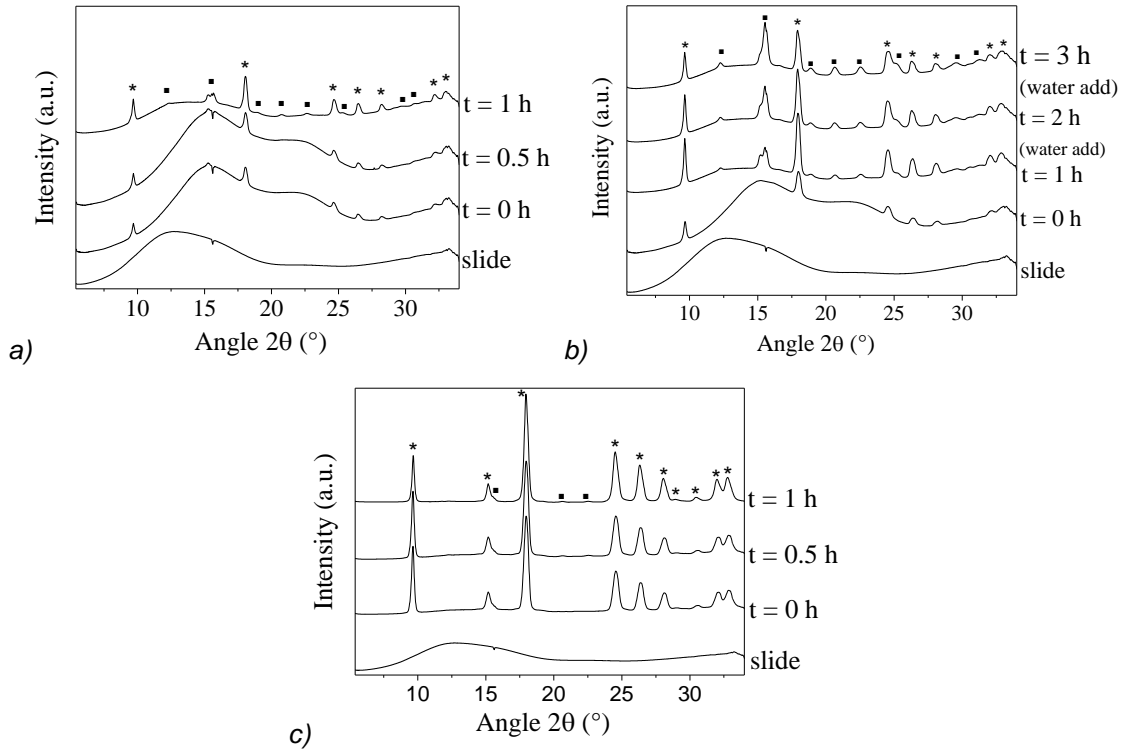


Figure 6.17. SR-XRD patterns of the laboratory slide without and with the aqueous nanolime suspension exposed to air, at suspension concentrations of: a) 10 g/l; b) 20 g/l; c) 100 g/l. The addition of water carried out on the sample at 20 g/l, together with the profile of the slide alone were represented too. Legend: * = portlandite ($\text{Ca}(\text{OH})_2$), ■ = calcite (CaCO_3)

The quantitative phase analyses (QPA), which provides the time evolution of each crystalline phase, are reported in Table 6.11. Firstly, we observed that the solvent (0.5 ml of water) was completely evaporated after 1 hour of air exposition in the experimental conditions and, over this period, $\text{Ca}(\text{OH})_2$ represented the main crystalline phase, with a percentage of 76%, 88% and 98% for suspension concentration of 10, 20 and 100 g/l respectively. In addition, the formed CaCO_3 was always characterized by the typical structure of calcite. However, working in laboratory conditions ($\text{RH} = 20 \pm 5\%$), once the solvent was completely evaporated, the carbonation did not continue at least up to 2 hours or more. Adding water after the solvent evaporation caused the carbonation process gradually to improve. In particular, from QPA, the nanolime suspension at 20 g/l showed that, after two successive additions of water, 33 % of CaCO_3 was formed. The nanolime carbonation rate (C_R) is here defined as the amounts of calcium carbonate that forms versus time (t):

$$C_R = \frac{M(\text{CaCO}_3)}{t} \quad (6.2)$$

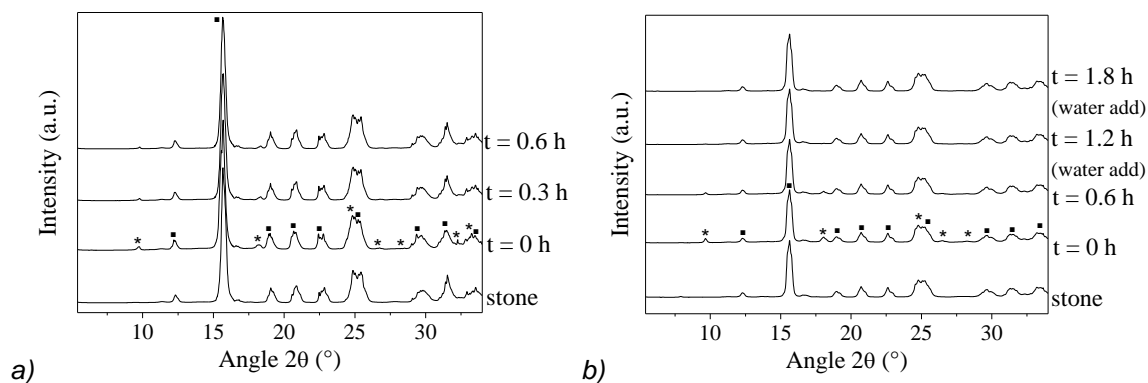
In these conditions with this substrate, the C_R values resulted practically constant and equal to about 1 mg/h, both considering different nanolime concentrations and adding water when the surface was dried; these results revealed a very slight influence of these two parameters on the carbonation rate.

Table 6.11. QPA analysis and carbonation rate (C_R) of the aqueous nanolime suspension (0.5 ml in volume) on laboratory slides, at different concentrations and at different times. The results obtained when the suspension was completely evaporated are shown in bold.

Nanolime on glass slides									
t (h)	Nanolime 10 g/l			Nanolime 20 g/l			Nanolime 100 g/l		
	Crystalline phases		C_R (mg/h)	Crystalline phases		C_R (mg/h)	Crystalline phases		C_R (mg/h)
	Ca(OH) ₂	CaCO ₃		Ca(OH) ₂	CaCO ₃		Ca(OH) ₂	CaCO ₃	
0	100 %	-	-	100 %	-	-	100 %	-	-
0.5	89 %	11 %	1.1	94 %	6 %	1.2	99 %	1 %	1.1
1	76 %	24 %	1.2	88 %	12 %	1.2	98 %	2 %	1.1
2 *				79 %	21 %	1.1			
3 *				67 %	33 %	1.1			

* 0.5 ml addition of water, after the complete evaporation of the solvent

The SR-XRD patterns obtained on biocalcarenite stones are reported in Figure 6.18, varying the nanolime suspension concentrations and time intervals during solvent evaporation. The pattern of the biocalcarenite alone is reported too, showing the typical pattern of calcium carbonate in the form of calcite. Again on the substrate where the nanolime suspension has been applied at 20 g/l, 0.5 ml of water was added after the initial suspension had dried.



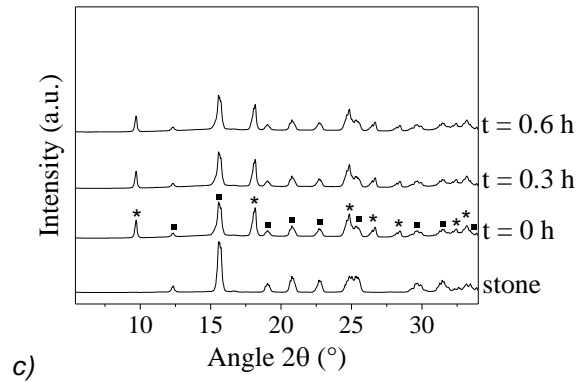


Figure 6.18. SR-XRD patterns of the biocalcarenite stone without and with the aqueous nanolime suspension exposed to air, varying the suspension concentration: a) at 10 g/l; b) at 20 g/l; c) at 100 g/l. Addition of water was performed two times on the sample b) to continue the carbonation.

Legend: * = portlandite ($\text{Ca}(\text{OH})_2$), ■ = calcite (CaCO_3)

The estimation of the quantity of $\text{Ca}(\text{OH})_2$ and CaCO_3 phases at different times, is shown in Table 6.12. Differently from what observed on the laboratory slides, when applied to the stone surface, the solvent tended to evaporate after only 0.6 hours of air exposition. Over this period, for a suspension concentration of 10 g/l, the amount of $\text{Ca}(\text{OH})_2$ converted into CaCO_3 reached a value of 62%. Increasing the suspension concentration up to 20 g/l, as also observed for the laboratory slides, the quantity of carbonate almost halved in value. At higher suspension concentration (100 g/l), only 8% of CaCO_3 was observed after the complete solvent evaporation. However, as seen before, working in the laboratory conditions, once the solvent was completely evaporated, the carbonation did not continue. Adding water helped the carbonation to improve. Differently from what observed on the laboratory slides, the nanolime carbonation process was fully completed on the biocalcarenite after two successive additions of water, using a nanolime suspension at 20 g/l.

Table 6.12. Semi quantitative analysis and carbonation rate C_R of the aqueous nanolime suspension (0.5 ml in volume) on biocalcarenite stones, at different concentrations and at different times. The results obtained when the suspension was completely evaporated were shown in bold.

Nanolime on biocalcarenite stones									
t (h)	Nanolime at 10 g/l			Nanolime at 20 g/l			Nanolime at 100 g/l		
	Crystalline phases		C_R (mg/h)	Crystalline phases		C_R (mg/h)	Crystalline phases		C_R (mg/h)
	$\text{Ca}(\text{OH})_2$	CaCO_3		$\text{Ca}(\text{OH})_2$	CaCO_3		$\text{Ca}(\text{OH})_2$	CaCO_3	
0	100 %	-	-	100 %	-	-	100 %	-	-
0.3	66 %	34 %	5.7	83 %	17 %	5.7	97 %	3 %	5.4

0.6	33 %	67 %	5.6	65 %	35 %	5.8	93 %	7 %	5.8
1.2 *				23 %	67 %	5.6			
1.8 *				-	100 %	5.6			

* 0.5 ml addition of water, after the complete evaporation of the solvent

These results clearly highlight a substrate-effect, related to the water evaporation rate. Actually, in the same experimental conditions, despite the same amount of applied suspension (0.5 ml), the water evaporation rate (W_{ER}) on the laboratory slides was almost half respect to the stone surface, with W_{ER} values of 0.50 ml/h and 0.83 ml/h, respectively. Moreover, the calculated C_R value was about 6 mg/h for the porous stones, which was about six times greater than the value for the laboratory slides. Finally, an interesting result is related to the fact that the C_R value seemed to remain constant for both the substrates, regardless of the nanolime suspension concentrations and of the water additions, underlining that, in presence of water, the C_R was not affected from the initial conditions of nanolime. Actually, the C_R parameter seemed to be influenced only by the porosity and by the water absorption ability of the considered substrate. Therefore, it is evident that the air-water interface constitutes a fundamental parameter both for water evaporation and for CO_2 diffusion. Increasing the surface exposed to air (the air-water interface), the CO_2 diffusion increased more significantly than the water evaporation, leading to a higher carbonation rate.

A last test was performed, directly on a wet stone (about 7 ml of water content) to simulate a possible application condition of wet substrate, as occurred in the consolidation of the mortar in paragraph 6.4, using the 100 g/l nanolime aqueous suspension. The results are reported in Figure 6.19, while the percentage of the formed phases at different times is shown in Table 6.13.

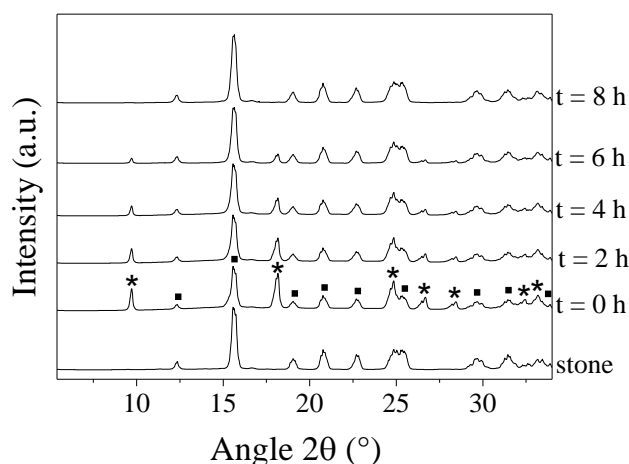


Figure 6.19. SR-XRD patterns of the aqueous nanolime suspension at 100 g/l exposed to air on the biocalcarene wet sample at different times. Legend: * = portlandite ($\text{Ca}(\text{OH})_2$), ■ = calcite (CaCO_3)

In this experiment, we observed that the solvent was completely evaporated after about 9 hours of air exposition and, over this period, all the $\text{Ca}(\text{OH})_2$ reacted leading to a complete carbonation process, without adding water. Moreover, a C_R value of about 6 mg/h was obtained, congruently with what observed for all the experiments on stone surface.

Table 6.13. Semi quantitative analysis and carbonation rate C_R of the aqueous nanolime suspension (0.5 ml in volume) at 100 g/l applied on a wet biocalcarene stone (about 7 ml water content). The results obtained when the suspension was completely evaporated were in bold

t (h)	Crystalline phases		C_R (mg/h)
	$\text{Ca}(\text{OH})_2$	CaCO_3	
0	100 %	-	-
2	75 %	25 %	6.2
4	51 %	49 %	6.1
6	26 %	74 %	6.1
8	-	100 %	6.2

Comparing the results obtained from the previous tests on biocalcarene stones with those referred to wet biocalcarene stone, it is possible to observe that the carbonation rate, C_R , is slightly higher in the latter case because of the more presence of water, so the carbonation reaction is facilitated in wet conditions.

However, on the biocalcarenes the C_R value remained around 6 mg/h, independently from nanolime concentration and time, while on the laboratory slides the C_R value remained around 1 mg/h. So, these experimental results suggest that

the influence on the carbonation process had to be ascribed to the presence of water and to the air-water interface, where the $\text{CO}_2(\text{aq})$ concentration is higher and the surface for the CO_2 diffusion is larger too. Actually, under the same external conditions, the presence of a porous substrate clearly favored the carbonation rate. Now the concentration of the nanolime suspension (N_C) assuring a complete carbonation on a particular kind of substrate, at normal CO_2 conditions, depends only from the water evaporation rate W_{ER} (expressed in ml/h) and from the carbonation rate C_R (expressed in mg/h). Therefore, it is possible to define a formula to evaluate N_C (g/l):

$$N_C = \frac{C_R}{W_{ER}} \quad (6.3)$$

Substituting in this formula the lowest value of C_R obtained from the synchrotron experiments (1 mg/h), it is possible to define the lowest nanolime concentration, N_C^* , able to guarantee a complete carbonation on every substrate simply measuring the water evaporation rate W_{ER} of the suspension in ml/h:

$$N_C^* = \frac{1 \text{ mg/h}}{W_{ER}} \quad (6.4)$$

where N_C^* values are obtained in mg/ml or g/l.

In the considered experimental conditions ($T = 20 \pm 2^\circ\text{C}$; $\text{RH} = 20 \pm 5\%$), still considering the relation (6.3), the nanolime concentrations to have a complete carbonation are about 2 g/l and 7 g/l, for the laboratory slides and for the biocalcarenite stones respectively. From these results, we can expect that at lower temperatures or at higher RH values, the water evaporation rate decreases, increasing the N_C value. Moreover, in case of replacement of water with alcohol, the N_C should decrease linearly with the replacement percentage, as confirmed from the carbonation results of the previous chapter. For example, considering normal conditions ($T = 20 \pm 2^\circ\text{C}$; $\text{RH} = 45 \pm 5\%$), where the water evaporation rate W_{ER} is about 0.12 ml/h, the nanolime concentrations to have a complete carbonation in water become about 8 g/l and about 30 g/l, for a planar substrate and a very porous substrate (biocalcarenite) respectively, consistently with the observations of the carbonation tests in chapter 5.

The possibility to evaluate the lowest nanolime concentration to ensure a complete carbonation can be extremely important for consolidation applications. Although the adding of water can assure the advancement of carbonation, it would be better if nanolime reacts before the complete evaporation of water. Actually, as it was

reported in literature, the drying process of $\text{Ca}(\text{OH})_2$ dispersions will cause an irreversible oriented attachment of the $\text{Ca}(\text{OH})_2$ nanoparticles: the strong coherent bonding among the oriented nanoparticles will prevent disaggregation upon re-dispersion in water [39]. For these reasons, the relation between carbonation rate and water evaporation time, at normal CO_2 conditions, results very useful to predict the carbonation process in any real situation.

6.6 Nanolime treatments of the original mortar of a medieval building in L'Aquila

Thanks to the scalability of the process and to the obtained results using nanolime in water, the first extensive application using these synthesized nanoparticles is realized, in relation to the consolidation of the façade of a historic building of L'Aquila (Palazzo Pica Alfieri, 14th-16th century), with a green and compatible treatment.

Lime-based mortars have been extensively used as constructive elements, from plasters to bedding for brick masonry or civil components [40]. Despite of their low strength respect to modern cement-based mortars [41], historic lime mortars have demonstrated a good durability [42], revealing that the recovery of the original components can constitute a crucial factor for the Historical Heritage. For this reason, the conservation and the repair interventions on historic mortars are becoming important issues, not only for their widespread use and the unavoidable decay phenomena (related to climatic agents, biological attack, and air pollution), but also due to numerous prior improper interventions, including the use of inappropriate repair materials (Portland cement, alcoxysilanes and synthetic polymers). In fact, the apparent advantages of Portland cement and alcoxysilanes consolidants, in terms of strength and quick hardening, can reveal detrimental effects over time, because of the great differences with the pre-existing mortars, in the mechanical and thermal performances, but also in the impermeable behaviour towards water [43, 44]. To achieve a proper treatment, several requirements have to be considered, such as: a low mechanical improvement, no chromatic alterations and no alterations of the water vapour permeability of the original mortar [45-47].

The façade of the considered palace of L'Aquila (about 200 m² of mortar surface), reported in Figure 6.20, characterized by an original pointing lime plastering (or

Pietra rasa lime mortar), presented an evident decay due to several factors, from atmospheric pollution and climatic effects to biological attacks, but also to prior inadequate restoration interventions. These factors can have contributed to a decay of the binder fraction in the course of time, leading to severe detachments and pulverization phenomena of the mortar itself (Figure 6.20b).



Figure 6.20. a) Façade of a historic building of L'Aquila (Palazzo Pica Alfieri, 14th-16th century), b) detail of the deterioration of the original pointing lime plastering

For the compatibility and sustainability reasons discussed before, an aqueous dispersion of pure calcium hydroxide nanoparticles is applied to consolidate this mortar. The use of alcoholic dispersions was not considered also because of the large surface to be treated (huge release of volatile organic compounds) [48, 49]. The optimal conditions for the treatment were preliminarily tested in laboratory on original mortar samples, taken from the most degraded areas (previously detached from the façade). Both the application procedure and the suspension concentration were varied, giving a special attention to limit chromatic alteration effects on the treated surfaces. Chemico-physical, mineralogical and mechanical characterizations were performed on untreated and treated specimens, in order to evaluate the efficacy of the treatments. Only the best treatment, in terms of application procedure and suspension concentration, was considered for the final application on the façade, in order to consolidate the weathered original mortar. Once in laboratory, the untreated mortar samples were characterized on the binder and the aggregate fractions separately, in order to obtain information on single components, aggregate size distribution and binder/aggregate ratio [50–53]. The aggregate size distribution was calculated after sieving the sample by means of a standard series and reported in Figure 6.21, considering as fine fraction that passing 150 μm and the remaining one as the aggregate fraction. It was obtained a

binder/aggregate ratio equal to about 1:6, denoting the lack of the binding component probably related to the degradation state of the considered historic building. Moreover, as defined from the standard procedure [50], the aggregate fraction was composed of about 19% of coarse sub-angular conglomerate (>4 mm), mildly selected, 33% of fine-grained conglomerate (ranging from 2 to 4 mm), and 48% of arenaceous sandstone (<2 mm).

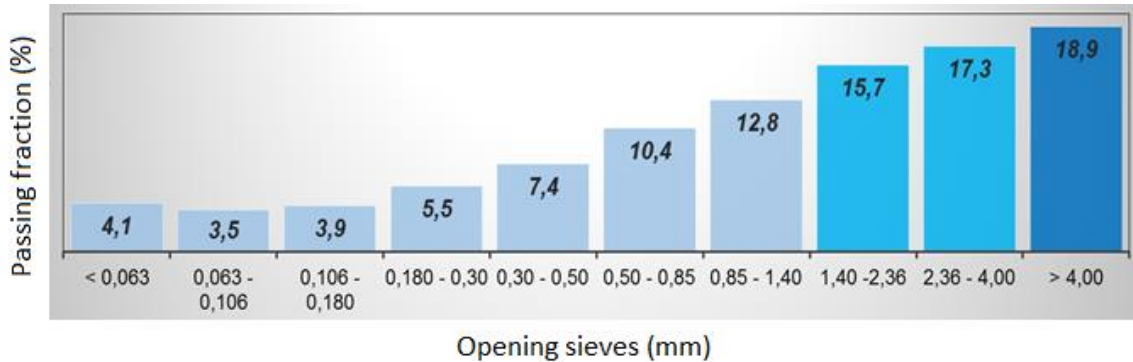


Figure 6.21. Aggregate size distribution of the historical mortar

The mineralogical analysis, performed by means of XRD, revealed that the binder was mainly composed of calcite (CaCO_3 , ICSD pattern #98-016-6365). As concerns the aggregate fraction, it was mainly constituted of about 91.3% calcite (CaCO_3 , ICSD pattern #98-016-6365) and 8.7% quartz (SiO_2 , ICSD pattern #98-002-7834). To consolidate this kind of substrate, four different suspensions of nanolime in water, characterized by different $\text{Ca}(\text{OH})_2$ concentrations, were prepared: 5 g/l (nCH5), 20 g/l (nCH20), 40 g/l (nCH40) and 60 g/l (nCH60). The reactivity of all the nanolime suspensions was analyzed by means of XRD in relative humidity conditions of $75 \pm 5\%$, to simulate the real in-situ conditions. From the analyses of the carbonation process, reported in Table 6.14, it can be observed that nCH5, nCH20 and nCH40 samples are characterized by a complete transformation into pure calcite during the solvent evaporation time (about 3h) at $T = 20 \pm 2^\circ\text{C}$ and $\text{RH} = 75 \pm 5\%$. As concerns the nCH60 sample, it revealed the presence of $42 \pm 3\%$ after 3h, reaching the completeness of the carbonation process only after 7 days.

Table 6.14. XRD results of the carbonation process in the suspensions of nanolime in water, in relation to concentration and RH conditions, as an average of 3 measures (calcite ICSD #98-002-0179, CCH ICDD #00-023-0107, Portlandite ICSD #98-020-2221)

RH conditions	nCH5	nCH20	nCH40	nCH60

75 ± 5% 3 hours	100% Calcite	100% Calcite	100% Calcite	42±3% Calcite 51±5% CCH 7±2% Portlandite
75 ± 5% 7 days	100% Calcite	100% Calcite	100% Calcite	100% Calcite

Concentrations up to 60 g/l were tested because of high moisture content inside the walls, which limits the possibility to perform repeated treatments, and a restricted time needed to complete the restoration interventions as well. For this aim, a whitening threshold was first evaluated, defining the highest suspension concentration that caused a visible chromatic surface alteration to the treated surface with different application procedures: by brush, spray and airbrush. The nanolime was applied until mortar saturation, by wiping, if necessary, the sample surface with a wet cloth in order to remove the excess of product, so reducing the surface whitening. The samples, having similar surfaces ($23 \pm 3 \text{ cm}^2$), absorbed before dripping about 10 ml for each treatment, corresponding to about 20-240 g/m² depending on the concentration of the applied suspension.

Actually, both the brush and the spray procedures revealed a moderate whitening at 20 g/l, so only the airbrush technique can guarantee no chromatic alterations up to 40 g/l. For this reason, in Figure 6.22 the photos and the images from stereomicroscope of the mortar samples treated by airbrush are reported, revealing that only the suspension at 60 g/l showed a whitening effect with airbrush treatment, due to an accumulation of the nanolime particles on the surface.

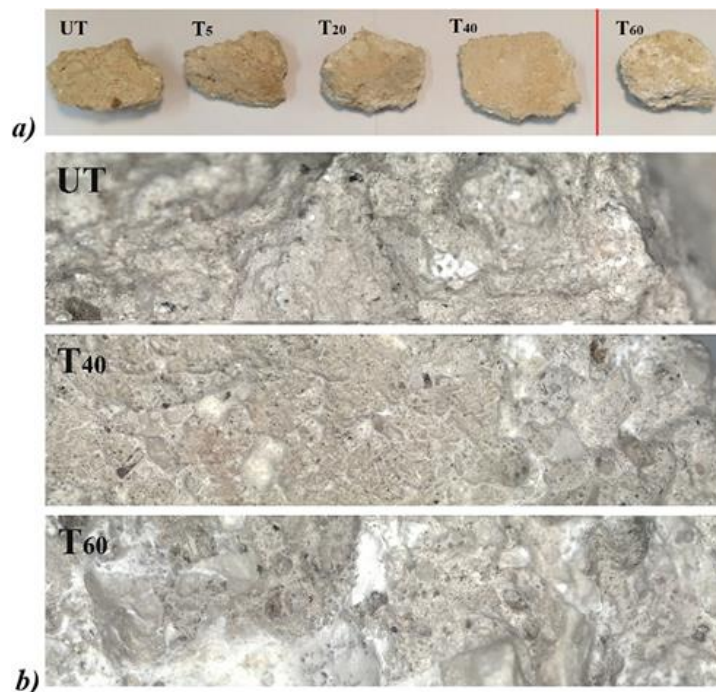


Figure 6.22. a) Photos of the historical mortar samples before (UT) and after (T) the nanolime treatments with airbrush at concentrations: 5, 20, 40 and 60 g/l (the red line indicated the *whitening threshold*); b) stereomicroscope images referred to UT, 40 and 60 g/l samples treated by airbrush

In addition, SEM micrographs of the UT mortar compared to 40 and 60 g/l samples treated by airbrush were shown in Figure 6.10, underlining that the treatment at 40 g/l did not cause great alteration of the mortar surface, while the treatment at 60 g/l created a more compact superficial layer (Figure 6.23a). At higher magnifications (2 μm marker), it is evident that the nanolime treatments tend to cover the surface of the pores of the mortar, but without filling them, maintaining unchanged the superficial structure of the mortar (Figure 6.23b). At 1 μm marker, in the treated samples the presence of nanocrystals of calcite is observed, agglomerated into compact and poly-disperse clusters: the dimension of these agglomerates increased by increasing the nanolime suspension concentration (Figure 6.23c).

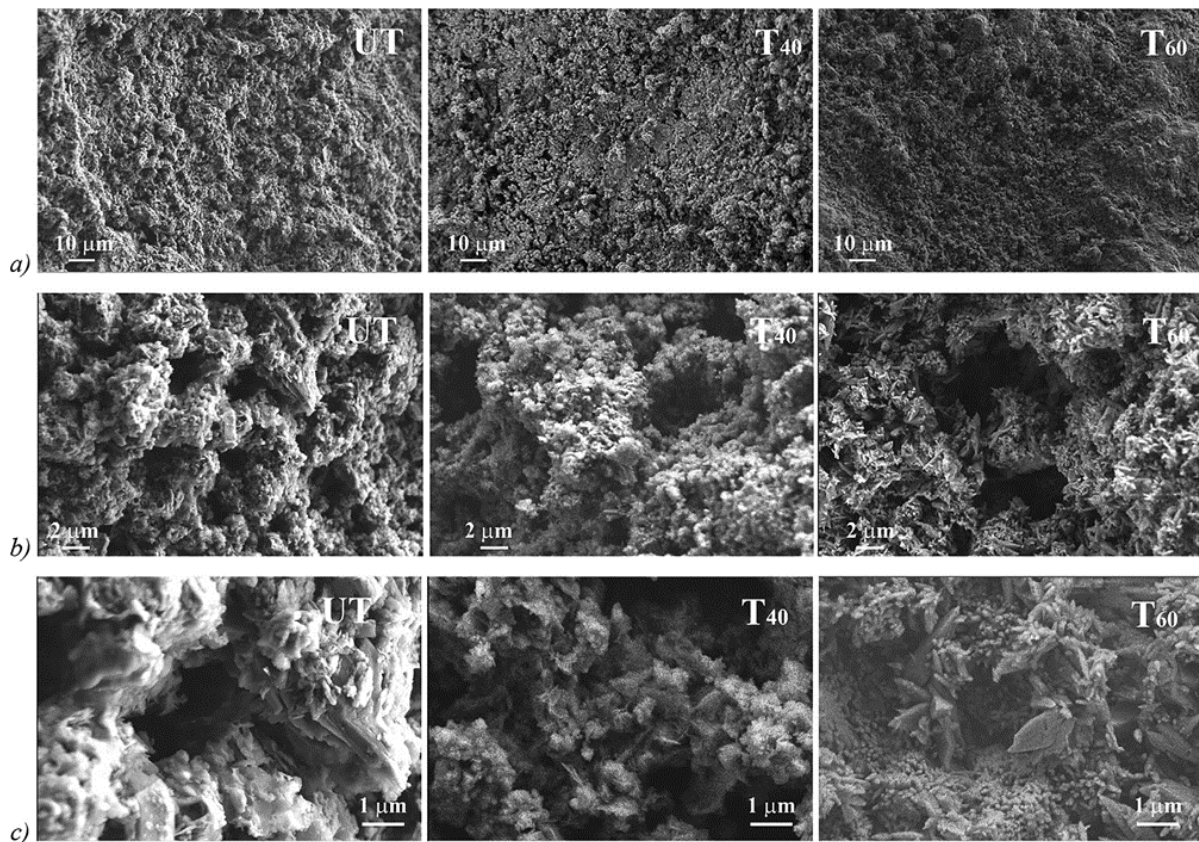


Figure 6.23. SEM micrographs, at different magnifications (scale bars: a) 10 μm , b) 2 μm , c) 1 μm), of the mortar samples before (UT) and after nanolime treatments at concentrations of 40 g/l (T_{40}) and 60 g/l (T_{60})

The results coming from visual inspections, stereomicroscope and SEM images allow to fix the whitening threshold of the airbrush technique at a concentration of 40 g/l. For this reason, the other mortar samples were treated by airbrush at 5, 20 and 40 g/l, then the treatment effectiveness was evaluated as well.

Firstly, phenolphthalein tests (a hydroxyl ion complexing substance for $\text{pH} > 8.2$) are performed by sectioning the samples soon after the nanolime treatments, in order to find the depth of penetration of the $\text{Ca}(\text{OH})_2$ particles (the color variation in the section of the sample is observed, measuring its depth).

Phenolphthalein tests are reported in Figure 6.24 and the sample treated at 40 g/l revealed the highest penetration depth (more than 10 mm from the treated surface), underlining that the penetration of the nanolime particles was related not to the suspension concentration so much as to the amount of materials applied to the surface. The obtained results were very promising if compared to those referred to the penetration depth of most of alcoholic nanolime treatments (about 3 mm) [54, 55].

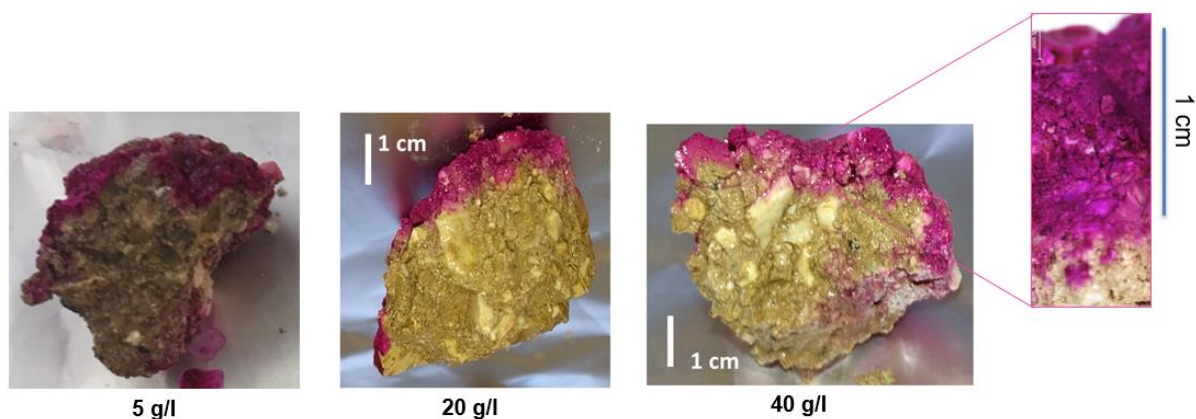


Figure 6.24. Phenolphthalein tests on the section of mortar samples soon after the nanolime treatments at 5, 20 and 40 g/l. The fuchsia color reveals the presence of nanolime at least up to 10 mm from the treated surfaces

Surface cohesion of the treated mortar samples is estimated and summarized in Table 6.15, by the “Scotch Tape Test” (STT), according to ASTM D3359, from the mean of three tests for each sample. [20] The STT results revealed as the nanolime treatment increased the superficial cohesion of the treated mortars, particularly when higher suspension concentrations were applied (20 and 40 g/l). In fact, the reduction of the removed material (ΔM), measured after treatment, varied from about 18% to 63% by increasing the suspension concentration from 5 to 20 g/l, reaching the 80% with the 40 g/l suspension. As concerns the porosity measurements performed by means of AccuPyc/GeoPyc instruments on smaller stone samples (about 0.5 mm in diameter), also reported in Table 6.15, both the untreated and the treated samples showed an average porosity value of about 38%. The porosity remained practically unchanged probably because the nanolime does not completely fill the pores of the stone. However, the unchanged porosity can be considered a positive result in terms of compatibility of the treatment, corresponding to an unchanged behaviour in the water absorption and water vapour permeability characteristics of the original mortar.

Table 6.15. Porosity, STT and drilling resistance values (10 mm depth) of the historical mortar, before and after the nanolime treatments by airbrush at 5, 20 and 40 g/l

Sample	Porosity (%)		Material removed from the surface (mg/cm ²)		ΔM	Average force (N)	
	Untreated	Treated	Untreated	Treated		Untreated	Treated
T ₅	38 ± 7	38 ± 8	116 ± 52	95 ± 4	- 18%	0.1 ± 0.3	0.1 ± 0.2
T ₂₀		38 ± 3	128 ± 47	48 ± 25	- 63%		1.0 ± 0.4
T ₄₀		38 ± 4	200 ± 72	39 ± 8	- 80%		3.4 ± 1.1

The STT results are confirmed by the Drilling Resistance Measurement System (DRMS) values, reported in Table 6.15 as well, where a significant rise in the average drilling resistance value is measured with the 40 g/l suspension (from 0.1±0.3 N to 3.4±1.1 N). In Figure 6.25 the drilling resistance profiles of the untreated and treated samples are shown. The increase of the average drilling resistance with 20 and 40 g/l treatments is directly observed, comparing the resistance profiles before and after nanolime treatments along 10 mm depth. These results confirm that the nanolime treatments were able to penetrate inside the mortar at least until 10 mm, performing their consolidating action also on the surface but without altering its esthetical features and its porosity.

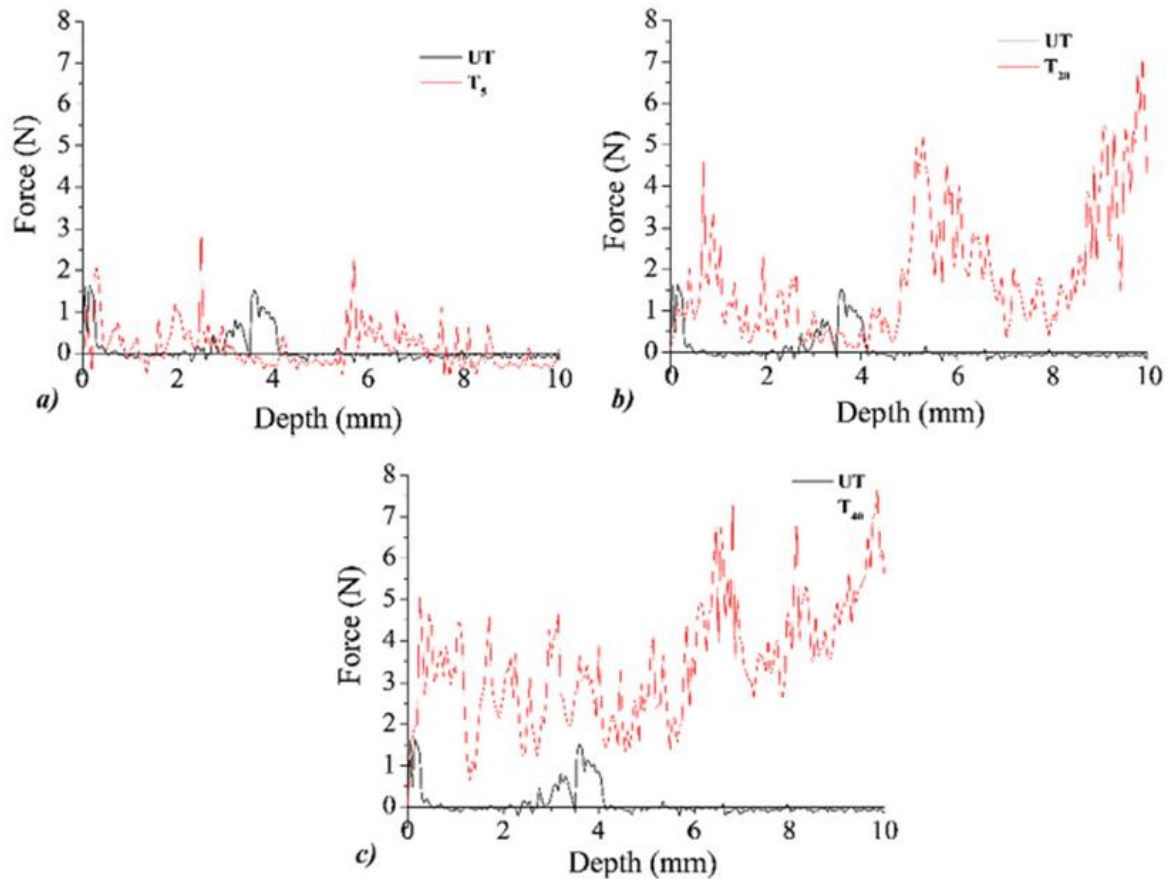


Figure 6.25. Drilling resistance profiles of untreated UT (dark line) and treated T (red line) mortar samples at: a) 5 g/l, b) 20 g/l and c) 40 g/l. The average value was calculated from 5 measurements for each treatment

Once established that the best efficacy in terms of mortar consolidation, without chromatic alterations, is achieved with the aqueous suspension at 40 g/l applied by airbrush, the 40 g/l treatment is finally applied on the whole façade of the building (200 m²). During the in-situ application, the high level of moisture inside the wall allowed to apply only 20 g/m² of nanolime until mortar saturation. After the treatment, the efficacy was evaluated by DRMS performed in situ, before and after three days from the application of the suspension. From the Figure 6.26, it can be observed that, before the treatment, the original mortar presented practically null values, not measurable by the sensitivity of the instrument (average force of -0.2 ± 0.4 N). After the nanolime treatment, despite of the low amounts of product applied to the surface, a significant increment of the drilling resistance was measured, with an average value of 2 ± 1 N up to 10 mm from the treaded surface.

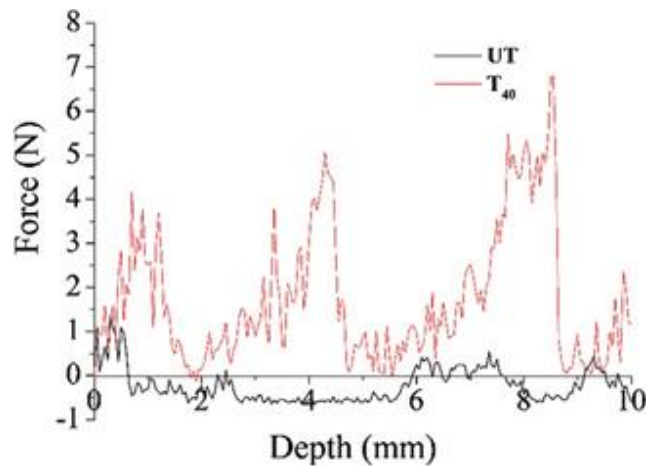


Figure 6.26. Drilling resistance profiles registered on the mortar directly in situ, before (black line) and after (red line) three days from the nanolime treatment at 40 g/l

The application of nanolime directly in situ confirmed the consolidating effect of nanolime applied by airbrush observed in laboratory, allowing to restore the physico-chemical characteristics of the precious plaster of the medieval building, without modifying its porosity. Therefore, the aqueous nanolime based treatments guarantee compatibility and mechanical resistance increase on the treated surfaces, without altering esthetical features and porosity, potentially ensuring over time a more effective and durable consolidating action respect to other materials (Portland cement, alcoxysilanes and synthetic polymers).

CHAPTER 7: SYNTHESIS AND APPLICATION OF TETRACALCIUM FERRITE HYDRATE NANOPARTICLES

This chapter presents a process for the synthesis of an innovative compound in the form of nanoparticles, namely tetracalcium ferrite hydrate, $\text{Ca}_4\text{Fe}_2(\text{OH})_{14}\cdot 6\text{H}_2\text{O}$, using ion exchange resins. This compound is characterized by very small lamellae (20-50 nm), which have the ability to carbonate forming particular calcites with iron. Therefore, the use of these nanoparticles can be related again to the consolidation of carbonate matrix substrates, allowing to restore the surface cohesion of deteriorated substrates, thanks to their ability to recreate a thin network of calcite with iron that adheres perfectly to the grains of the original substrate. However, one of the peculiarities of this tetracalcium ferrite hydrate, which appears as white aqueous suspension or white powder, is that following carbonation its color changes to almost brown. For this reason, this compound could be used exclusively as a non-toxic carbonation indicator in various situation sas well. A further application could be related to the removal of heavy elements and contaminants in water, such as arsenic, lead and fluorine, thanks to the presence of iron and calcium that can adsorb and separate these ions. Finally, the calcium nano-carbonates that can be obtained from this compound could be used as a filler for increasing the mechanical properties of thermoplastic polymers.

7.1 Synthesis of tetracalcium ferrite hydrate in nanometric form

Using the innovative ion exchange route described in this thesis, it is possible to synthesize nanoparticles of tetracalcium ferrite hydrate in pure form, having chemical formula $\text{Ca}_4\text{Fe}_2(\text{OH})_{14}\cdot 6\text{H}_2\text{O}$. Actually, these nanoparticles are not obtained by other methods in literature and could be used in various sectors, from Cultural Heritage to polymeric fillers. In fact, one of the characteristics of these nanoparticles is the ability, in the presence of CO_2 , to transform into calcite as only crystalline phase. The synthesis process involves the reaction between an aqueous solution containing a calcium salt (CaCl_2) and an iron salt ($\text{FeCl}_3\cdot 6\text{H}_2\text{O}$) in a molar ratio 2:1 with a strong anionic resin in OH^- form (Dowex Monosphere 550A), maintained under stirring for at least 5 minutes. Once the established time has

elapsed, a suspension of nanoparticles is obtained that can be separated from the resin mechanically, for example using a 180 μm sieve. It is observed that the resin leaves no residues and can later be quickly regenerated and reused. An illustrative scheme of the synthesis process is shown in Figure 7.1.

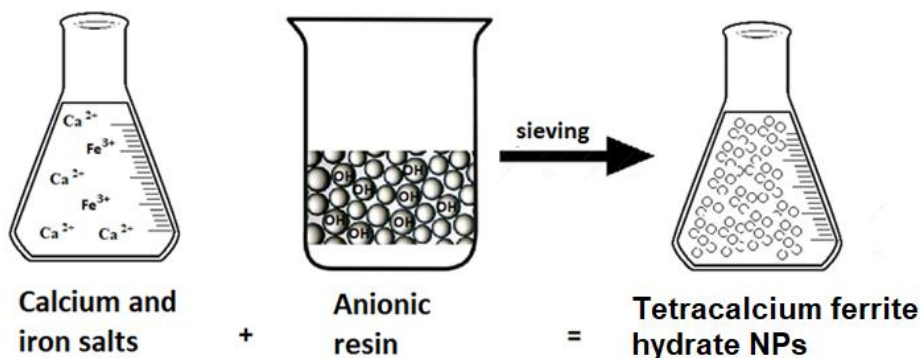


Figure 7.1. Illustrative scheme of the synthesis process of tetracalcium ferrite hydrate NPs

In particular, to obtain 100 ml of suspension at a concentration of about 10 g/l of pure tetracalcium ferrite hydrate, 30 g of Dowex 550A wet anion resin in the OH⁻ form are added to 100 ml of aqueous solution containing 1.10 g of CaCl₂ and 1.35 g of FeCl₃·6H₂O, at room temperature under moderate stirring. The quantity of resin used in the synthesis is calculated on the basis of its exchange capacity (1.1 eq/l of Cl) and of its density (0.67 kg/l), considering a small excess of resin (about 15%) to minimize the residual chlorides in the final suspension. When the resin is added to the aqueous solution of calcium and iron chlorides, a color change from yellow to white is instantly observed, attributable to the formation of tetracalcium ferrite hydrate phase. The quantity of chlorides still present in solution, corresponding in fact to the quantity of untransformed reagents, is negligible (< 100 mg/l) within the first 10 minutes of reaction, but to be sure to always have the minimum quantity of residual chlorides in solution, a reaction time of 60 minutes is considered. The overall synthesis process is characterized by a high yield (> 95%) and very short production times in one step, therefore it is potentially scalable.

The obtained nanoparticles are characterized by XRD, TEM and SEM, also analyzing their reactivity in relation to the carbonation process in air. From the XRD analyses, shown in Figure 7.2, it can be observed that these nanoparticles have phase variations depending on the drying conditions of the sample. In particular, in the pattern of Figure 7.2 c, which is the compound completely reacted with CO₂ by drying the suspension in air at RH 45±5%, CaCO₃ (ICDD #00-047-1743) is obtained

as the only identifiable crystalline phase, without the presence of contributions of any amorphous phase. In the pattern of Figure 7.2b, which is the compound partially reacted with CO₂ by drying the suspension with a direct nitrogen flow, there is an intermediate phase between the final carbonate and the starting hydrated oxide, identifiable as Ca₄Fe₂O₆CO₃·12H₂O (ICDD #00-043-0480), with a preferential orientation on the plane positioned at about 11°2θ. As regards the pattern of Figure 7.2a, which is the compound dried in a pure nitrogen atmosphere (absence of CO₂), a low-crystalline phase is observed, characterized by two broad diffraction peaks located at 11.2 °2θ and 22.5 °2θ respectively. The comparison with the reference databases revealed that these peaks did not match with any known iron oxide or iron calcium oxide pattern, except than with calcium iron oxide carbonate hydrate (Ca₄Fe₂O₆CO₃·12H₂O, ICDD pattern #00-043-0480). However, the attribution of a carbonated phase led to a discrepancy since the suspension was obtained under nitrogen. For these reasons, it is hypothesized that a little carbonation can be occurred during the drying steps or during the measurement itself. These result allow to assume that the exchange process led to the formation of a mixed Fe/Ca hydroxide, having the same Fe/Ca ratio of the Ca₄Fe₂O₆CO₃·12H₂O phase observed in Figure 2b. Between the known Fe/Ca hydroxides, only tetracalcium ferrite hydrate, Ca₄Fe₂(OH)₁₄·6H₂O, matched this Fe/Ca ratio, characterized by a hexagonal/trigonal crystal system, having cell parameters: a = 5.890 Å, c = 7.902 Å [1], and crystallizing in hexagonal plates. This phase has a preferential orientation on the plane positioned at about 11°2θ as well, with an average size of the crystallites, obtained following the evaluation of the peaks with Debye-Scherrer, of 21±1 nm.

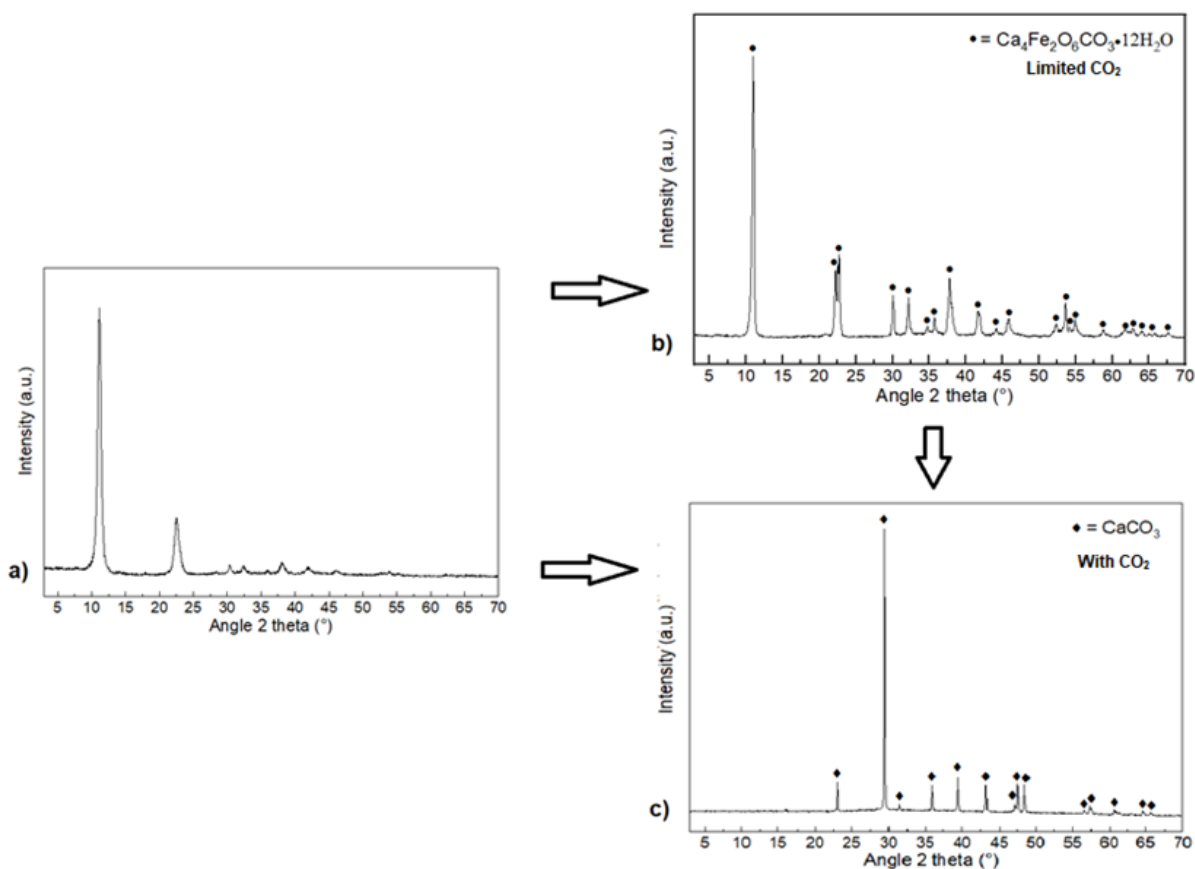


Figure 7.2. XRD patterns of the suspension of tetracalcium ferrite hydrate with drying under different conditions: a) absence of CO_2 with obtained phase $\text{Ca}_4\text{Fe}_2(\text{OH})_{14} \cdot 6\text{H}_2\text{O}$ or poorly crystalline $\text{Ca}_4\text{Fe}_2\text{O}_6\text{CO}_3 \cdot 12\text{H}_2\text{O}$ (ICDD #00-043-0480); b) limited presence of CO_2 with obtained phase pure $\text{Ca}_4\text{Fe}_2\text{O}_6\text{CO}_3 \cdot 12\text{H}_2\text{O}$; c) presence of CO_2 with obtained phase pure CaCO_3 (ICDD #00-047-1743)

A particular aspect related to this compound is that the calcite that forms as a result of the reaction with atmospheric CO_2 is almost brown in colour, while the tetracalcium ferrite hydrate dried under nitrogen is white (Figure 7.3). This indicates that, even if not revealed by the XRD spectrum of figure 7.2c, iron is certainly present in a different form than the initial compound, probably in a completely amorphous form.



Figure 7.3. Suspension of $\text{Ca}_4\text{Fe}_2(\text{OH})_{14}\cdot 6\text{H}_2\text{O}$ nanoparticles dried in absence or presence of CO_2

From the TEM micrographs in absence of CO_2 , shown in Figure 7.4, the synthesized tetracalcium ferrite hydrate phase appears in the form of lamellae with hexagonal morphology, having side dimensions in the range 10-30 nm and thicknesses in the range 5-10 nm, which are sometimes superimposed and semi-transparent to the incident electron beam.

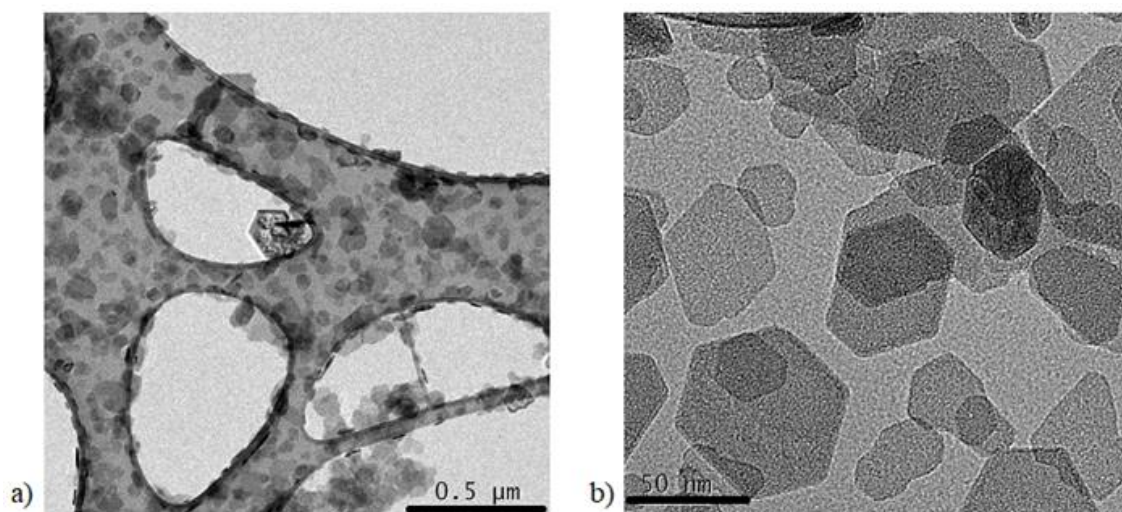


Figure 7.4. TEM micrographs of tetracalcium ferrite hydrate nanoparticles in absence of CO_2 : a) marker 0.5 μm , b) marker 50 nm

The SEM image of Figure 7.5a confirms what observed at TEM in absence of CO_2 , which is the presence of lamellae having hexagonal morphology with side dimensions generally < 30 nm and thicknesses < 10 nm. Observing in this case the samples dried in presence of CO_2 (Figure 7.5b), it transforms into cubes with side dimensions of about 50 nm, associated with the typical morphology of calcite, coated with thin filaments (diameter < 5 nm), almost forming a network, associated with the presence of iron in an amorphous form.

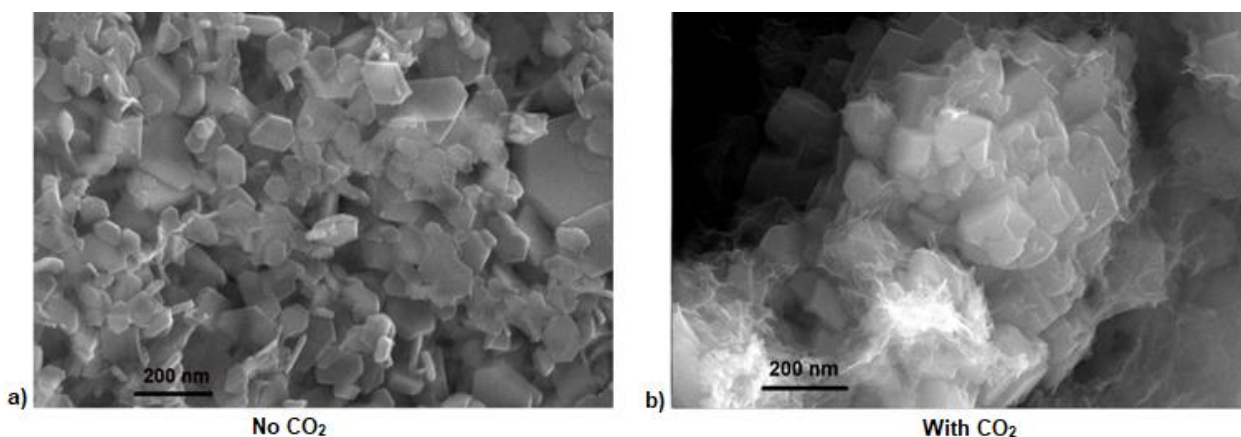


Figure 7.5. SEM images with 200 nm marker of tetracalcium ferrite nanoparticles: a) dried in absence of CO₂, b) dried in presence of atmospheric CO₂

To evaluate the reactivity of the produced NPs towards the conversion to calcite, which could significantly influence the applications of the compound itself, further measurements are carried out using XRD on the suspension of tetracalcium ferrite hydrate, dried in air, varying the suspension concentration and the relative humidity conditions. The samples were prepared by depositing 0.12 ml of aqueous suspensions at three different concentrations (5, 10, 20 g/l) on zero-background sample holders at $T = 20 \pm 2^\circ\text{C}$ and RH equal to $30 \pm 5\%$, $45 \pm 5\%$ or $75 \pm 5\%$, corresponding to average solvent evaporation times of approximately 30, 60 and 180 minutes respectively. On each XRD pattern, the ratio between the area of calcite peaks and the total area of all the peaks of the pattern is defined as carbonation efficiency (Y) and is shown in Table 7.1. It is found that at RH $75 \pm 5\%$ (long evaporation times) the maximum conversion into calcite (100% Y) is always obtained, while for shorter evaporation times the conversion into calcite increases as the concentration of the suspension decreases. From these values the complete reaction times with atmospheric CO₂ based on the concentration is defined, which allow to indirectly calculate a carbonation rate for this compound: about 10 g/l for hour, slightly higher than the carbonation rate of the pure nanolime (about 7 g/l for hour).

Table 7.1. Reactivity of the aqueous suspension of tetracalcium ferrite hydrate NPs in terms of conversion to calcite (Y)

Concentrazione	30 min (30±5% RH)	60 min (45±5% RH)	180 min (75±5% RH)
5 g/l	100% Y	100% Y	100% Y
10 g/l	53% Y	100% Y	100% Y
20 g/l	26% Y	51% Y	100% Y

7.2 Design of a nanolime with iron tailored for Cultural Heritage

The innovative compound, with chemical formula $\text{Ca}_4\text{Fe}_2(\text{OH})_{14}\cdot 6\text{H}_2\text{O}$, synthesized in form of NPs is characterized by the possibility of reacting quickly with CO_2 (in presence of water), forming a calcite covered with iron filaments at a nanometric level, which generates a colour change on the macroscopic scale.

As previously described, the use of compatible products is recommended in the consolidation and conservation of carbonate substrates of historical and architectural interest. The use of nano-sized particles of calcium hydroxide, as seen in the previous chapter, allows the consolidation of different stone substrates, reaching penetration depths with consolidant treatments of at least 1 cm from the surface. However, despite the described advantages of these treatments, some limitations remain to date, such as: the lower penetration capacity on low porous substrates (for example mortars or frescoes), together with the possible chromatic alteration of the treated surfaces, linked to the formation of white glazes (dependent on solvent, suspension concentration and method of application). In many natural carbonate substrates, as well as in historical mortars obtained from lime and pozzolan based formulations, the colour may depend on the presence of variable % of other chemical elements, such as iron, as for example found in the biocalcarenes treated in the previous chapter. In fact, calcarenites and other natural stone materials with a carbonate matrix, widely used in the Mediterranean area, often have a colour ranging from creamy yellow to brown.

Therefore, having synthesized $\text{Ca}(\text{OH})_2$ NPs (nanolime) and $\text{Ca}_4\text{Fe}_2(\text{OH})_{14}\cdot 6\text{H}_2\text{O}$ NPs by ion exchange route, both able to carbonate and therefore to bring new calcite to a substrate, it is possible to design a tailored nanolime containing both these phases, which can be applied on natural stones having iron content. This innovative nanolime would make it possible to bring the same mineralogical composition to the

substrate, in order to have both a perfect chemico-physical compatibility and a total absence of chromatic alteration, since iron is one of the elements mainly responsible for the appearance of the minerals containing it. Furthermore, this tailored nanolime, thanks to the slightly smaller dimensions compared to the nanolime, having iron as a nucleating agent both in the synthesis phase and in the carbonation phase, can guarantee a better penetration even in less porous substrates compared to the pure nanolime. Another advantage of having a nanolime with iron in the structure is to obtain more stable aqueous suspensions (always characterized by a white color), and when the carbonation process takes place, the colour changes according to the % of iron added in the synthesis phase with considerable versatility. Therefore, the function of this tailored nanolime is to restore the surface cohesion of deteriorated substrates, thanks to its ability, once carbonated, to recreate a thin network of calcium carbonate with amorphous iron that adheres perfectly to the grains of the original substrate.

Some syntheses are carried out following the procedure described in paragraph 7.1, but decreasing the quantity of iron chloride, in order to obtain variable Ca-Fe %, adjustable according to the composition of the substrates to be treated. To investigate the composition and morphology of the obtained phases, XRD and TEM analysis are performed, in order to evaluate more accurately the effect of adding iron to the nanolime. Figure 7.6 shows the XRD patterns of tailored nanolime as the % of iron added in synthesis varies (13%, 23%, 33%, these percentages refer to the mass composition of inorganic elements: Ca-Fe), and the identifiable phases are Ca(OH)_2 and $\text{Ca}_4\text{Fe}_2(\text{OH})_{14}\cdot 6\text{H}_2\text{O}$ or poorly crystalline $\text{Ca}_4\text{Fe}_2\text{O}_6\text{CO}_3\cdot 12\text{H}_2\text{O}$ (particularly oriented on the first two diffraction planes). The relative quantities of these 2 crystalline phases are reported in Table 7.2 and are certainly dependent on the % of iron added in the synthesis phase, furthermore the average size of the crystallites is reported, which is always lower in the compound having iron.

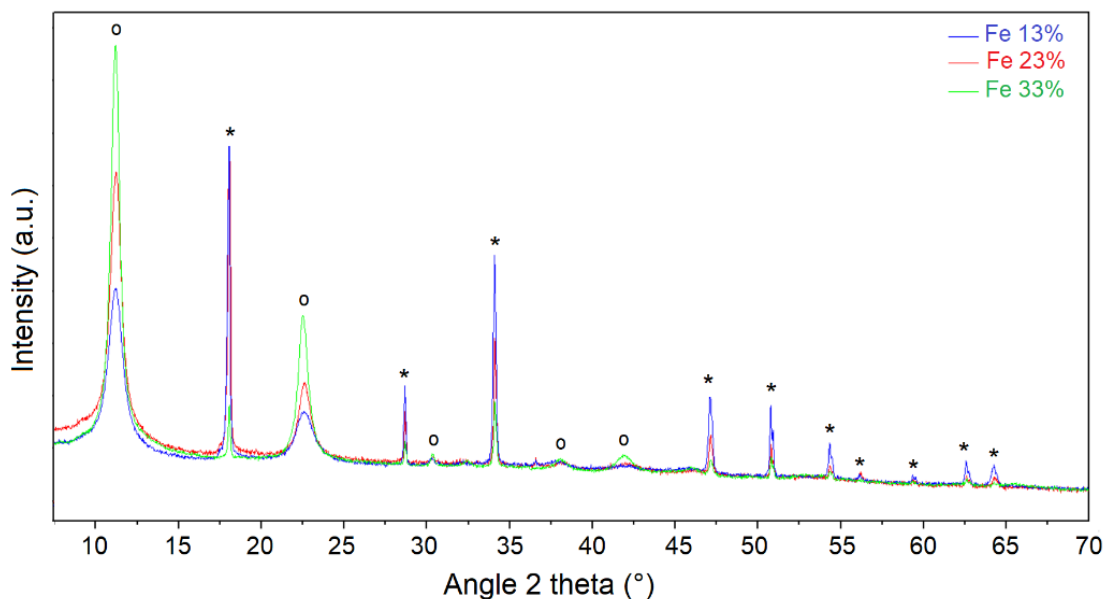


Figure 7.6. XRD patterns of tailored nanolimes as the % of iron added in synthesis varies, * = Ca(OH)_2 ICSD #98-020-2221, o = $\text{Ca}_4\text{Fe}_2(\text{OH})_{14}\cdot 6\text{H}_2\text{O}$ [1] or poorly crystalline $\text{Ca}_4\text{Fe}_2\text{O}_6\text{CO}_3\cdot 12\text{H}_2\text{O}$ ICDD #00-043-0480

Table 7.2. Crystalline phases observed in the tailored nanolime as the % of iron varies, with mass composition of the samples, relative % of crystalline phases and crystallite size

Tailored nanolime Composition of inorganic elements	Crystalline phases (%)		Crystallite size (nm)	
	Ca(OH)_2	$\text{Ca}_4\text{Fe}_2(\text{OH})_{14}\cdot 6\text{H}_2\text{O}$	Ca(OH)_2	$\text{Ca}_4\text{Fe}_2(\text{OH})_{14}\cdot 6\text{H}_2\text{O}$
Ca 87%, Fe 13%	61±4%	39±3%	114±2	7.2±0.1
Ca 77%, Fe 23%	38±3%	62±4%	100±4	10.0±0.3
Ca 67%, Fe 33%	16±2%	84±4%	100±10	13±1

For these 3 different selected compositions of calcium and iron, the transformation into calcite by exposure to atmospheric CO_2 is also investigated by XRD, at a concentration of 10 g/l at different RH conditions: 30±5% (Figure 7.7a) and 45±5% (Figure 7.7b). The relative quantities of the crystalline phases that are formed are reported in Table 7.3 and are certainly dependent on the % of iron added in the synthesis phase, moreover the average size of the crystallites is reported, which is always smaller in the compound with iron.

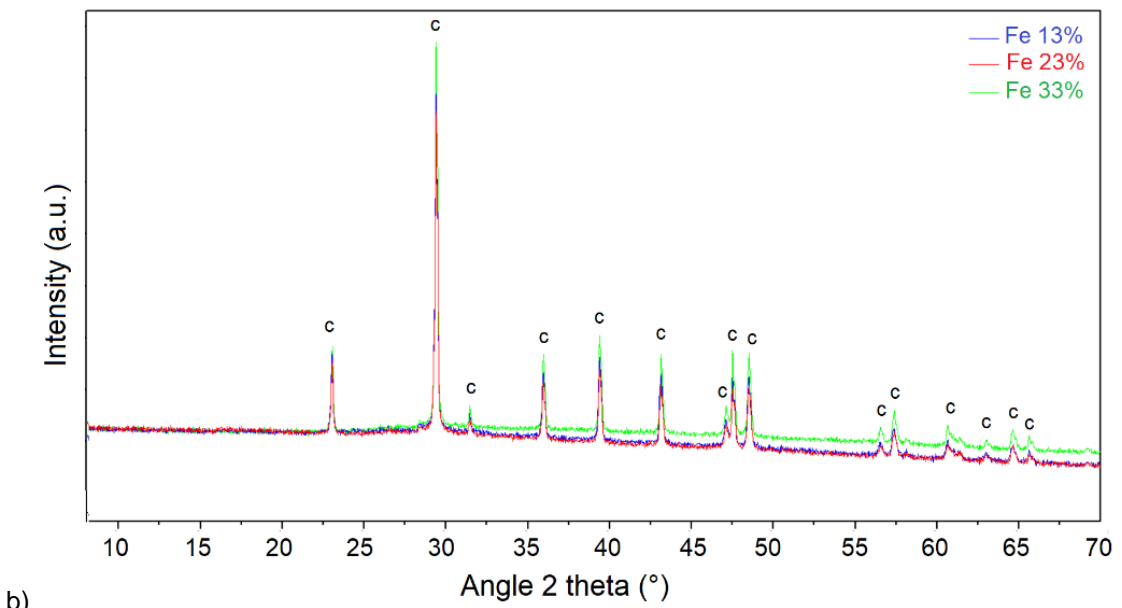
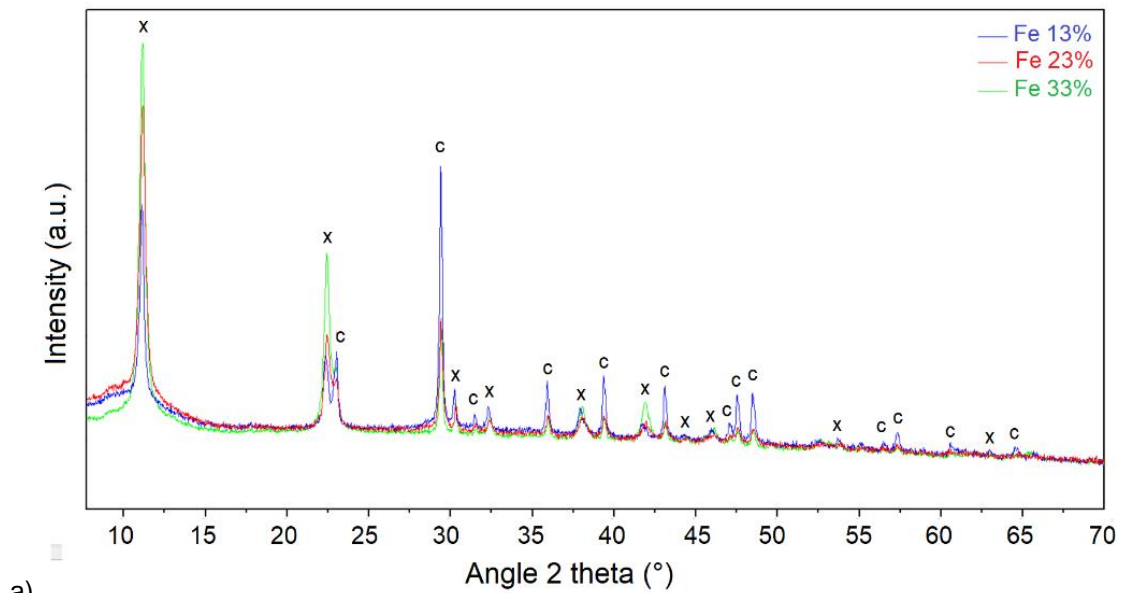


Figure 7.7. XRD patterns of tailored nanolimes as the % of iron added in synthesis varies, following exposure to different RH conditions: a) $30 \pm 5\%$, b) $45 \pm 5\%$. c = CaCO_3 (ICDD #00-043-0480), x = $\text{Ca}_4\text{Fe}_2\text{O}_6\text{CO}_3 \cdot 12\text{H}_2\text{O}$ (ICDD #00-043-0480)

Table 7.3. Crystalline phases observed in the tailored nanolime with the % variation of iron, exposed in different RH conditions, with mass composition of the samples, relative % of crystalline phases and crystallite size

Tailored nanolime	30±5% RH				45±5% RH	
	Crystalline phases (%)		Crystallite size (nm)		Crystalline phases(%)	Crystallite size (nm)
Composition of inorganic elements	CaCO ₃	Ca ₄ Fe ₂ O ₆ CO ₃ ·12H ₂ O	CaCO ₃	Ca ₄ Fe ₂ O ₆ CO ₃ ·12H ₂ O	CaCO ₃	CaCO ₃
Ca 87%, Fe 13%	49±3%	51±3%	80±10	24±2	100%	83±2
Ca 77%, Fe 23%	14±2%	86±2%	38±4	22.1±0.1	100%	79±1
Ca 67%, Fe 33%	10±2%	90±2%	71±3	24±1	100%	96±2

By comparing the XRD patterns of the 3 samples exposed to the carbonation process, it can be seen that calcite progressively forms until 100% transformation is always obtained. It is interesting that in all the samples pure calcium hydroxide reacts first to form CaCO₃, selectively with respect to Ca₄Fe₂(OH)₁₄·6H₂O, evidenced by the fact that the peak at 18°2θ disappears always as first in the patterns at 30±5% RH. This phenomenon may be due to a different solubility of the 2 compounds, so only after the removal of calcium hydroxide the compound containing iron reacts (with a slightly higher kinetic). Furthermore, the reaction of Ca₄Fe₂(OH)₁₄·6H₂O is observed to occur through the intermediate form Ca₄Fe₂O₆CO₃·12H₂O capturing CO₂. The presence of iron in the samples completely converted into calcite is perhaps found only in a homogeneous elevation of the background of the sample with 33% Fe, but without contributions that could allow the identification of some phases.

Figure 7.8 shows TEM images of tailored nanolime samples at different iron concentrations dried in absence of CO₂. The NPs appear always in the form of lamellae with hexagonal morphology, having thicknesses in the range 5-10 nm and side dimensions slightly variable based on the % of iron: with 13% Fe the dimensions are in the range 30-50 nm (Figure 7.8a), with 23% Fe the dimensions are in the range 20-40 nm (Figure 7.8b) and finally with 33% Fe the dimensions are in the range 10-30 nm (Figure 7.8c).

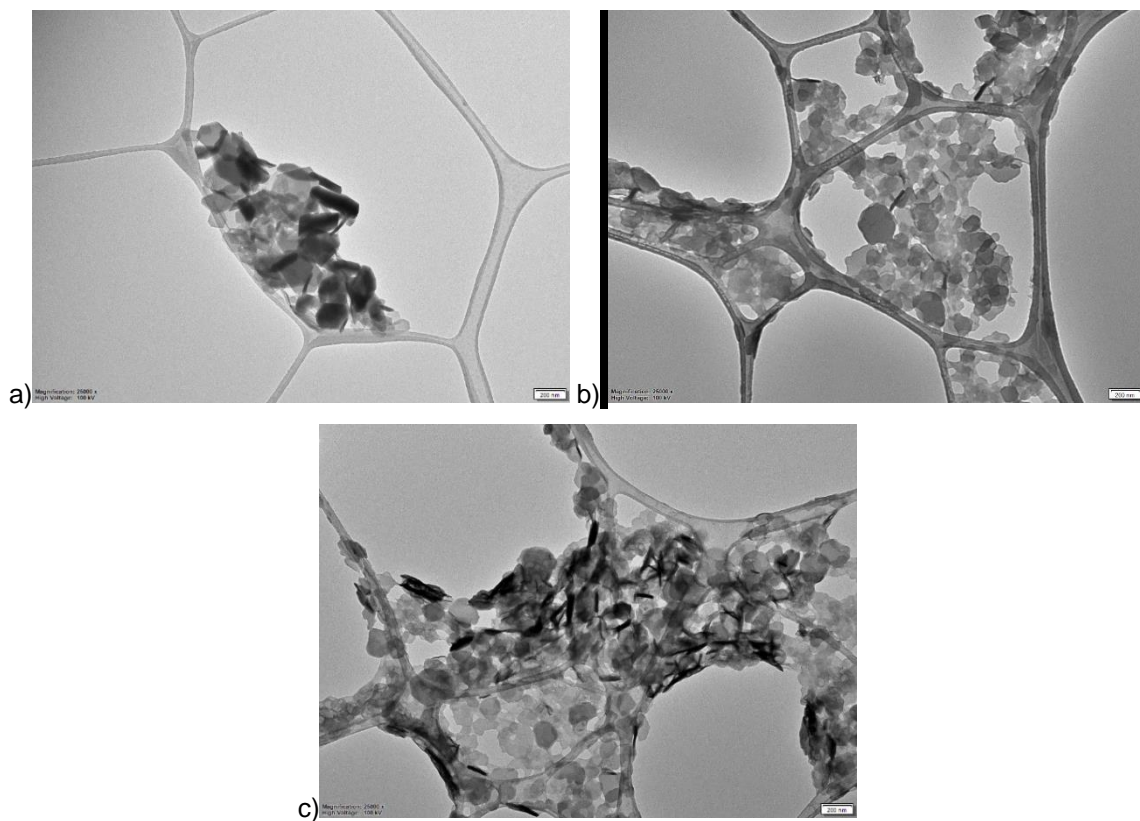


Figure 7.8. TEM micrographs with 200 nm marker of nanoparticles of tailored nanolime with different % of iron: a) 13% Fe, b) 23% Fe, c) 33% Fe

The possibility through this synthesis route to rapidly produce large quantities of these NPs could allow to easily reach the market of consolidating products and to broaden their application fields towards extensive uses, such as the treatment of large carbonatic surfaces of historical-architectural relevance, with or without the presence of iron inside. In particular, in this sector there are no perfectly compatible products having combined calcium and iron, able to carbonate recreating the same composition of the iron-containing carbonatic substrates, thus guaranteeing complete compatibility both aesthetic (no chromatic alteration) and chemico-physical. These NPs, thanks to their small size (10-50 nm side, 5-10 nm in thickness), guarantee a high penetration into the substrates and a high reactivity with CO₂. Therefore, they allow to restore the surface cohesion of deteriorated substrates, thanks to their ability, once carbonated, to recreate a thin network of calcium carbonate with iron that adheres perfectly to the grains of the original substrate.

7.3 EXAFS measurements on tetracalcium ferrite hydrate NPs and tailored nanolime

During the carbonation process of the $\text{Ca}_4\text{Fe}_2(\text{OH})_{14}\cdot 6\text{H}_2\text{O}$ NPs, it was observed that from the XRD analysis only calcite is present with a variable background associable with the presence of iron, but not identifiable as an amorphous or crystalline phase. Therefore, to identify the iron structure after the carbonation process, but also to confirm the structure of the $\text{Ca}_4\text{Fe}_2(\text{OH})_{14}\cdot 6\text{H}_2\text{O}$ phase itself, EXAFS tests with synchrotron light (European Synchrotron Radiation Facility of Grenoble) are performed, studying the absorption thresholds for both calcium and iron, before and after carbonation. To perform these measurements, samples of tailored nanolime with different % of iron analyzed in the previous paragraph (Fe 13%, Fe 23% and Fe 33%) are selected, together with the sample having $\text{Ca}_4\text{Fe}_2(\text{OH})_{14}\cdot 6\text{H}_2\text{O}$ as a pure compound (corresponding to Fe 41%). In addition, a tailored nanolime with low iron addition (Fe 5%) and a sample with excess iron (Fe 50%) with respect to the compound $\text{Ca}_4\text{Fe}_2(\text{OH})_{14}\cdot 6\text{H}_2\text{O}$ are included in the study, in order to better evaluate the influence of iron in the structure. All 6 samples considered are shown in Table 7.4 according to the increasing iron concentration.

Table 7.4. List of samples analyzed in EXAFS measurements with relative compositions and edge steps

Tailored nanolime Composition of inorganic elements	Crystalline phases (%)		Calcium		Iron	
	$\text{Ca}(\text{OH})_2$	$\text{Ca}_4\text{Fe}_2(\text{OH})_{14}\cdot 6\text{H}_2\text{O}$	Amount (mg)	Edge Ca	Amount (mg)	Edge Fe
Ca 95%, Fe 5%	88±4%	12±2%	1.7	0.85	7	0.10
Ca 87%, Fe 13%	61±4%	39±3%	1.8	0.82	6.6	0.23
Ca 77%, Fe 23%	38±3%	62±4%	2.1	0.78	6	0.36
Ca 67%, Fe 33%	16±2%	84±4%	2.3	0.74	5.6	0.47
Ca 59%, Fe 41%	-	100%	2.5	0.69	5.3	0.54
Ca 50%, Fe 50%	-	100%	2.8	0.65	5	0.61

The samples are selected in form of suspension (10 g/l) and prepared under 4 different conditions to better evaluate the effects of the carbonation process on phase transformations:

- 1) as they are under an inert atmosphere of N_2 ,
- 2) forced carbonation following the flow of CO_2 into the water,

- 3) partial carbonation in air for exposure at $30 \pm 5\%$ RH,
- 4) total carbonation in air for exposure at $45 \pm 5\%$ RH.

For each condition, the samples are prepared with respect to both the iron and calcium thresholds, by placing different quantities of sample depending on the considered element, as reported in Table 7.4. In order to have a homogeneous distribution of the samples, the starting suspensions are quickly filtered on polycarbonate filters with a small Venturi system and then sealed with capton as regards conditions 1) and 2). While as regards the exposures in air 3) and 4), the suspensions are deposited on capton and allowed to evaporate at the chosen RH conditions.

To better analyze the data, the central sample with 33% Fe is first reported as a representative sample for the results on the iron edge. Figure 7.9 shows this sample in the 4 different preparation conditions, first in E in the XANES region (Figure 7.9a), then in R (Figure 7.9b) and finally in k (Figure 7.9c) in the EXAFS region.

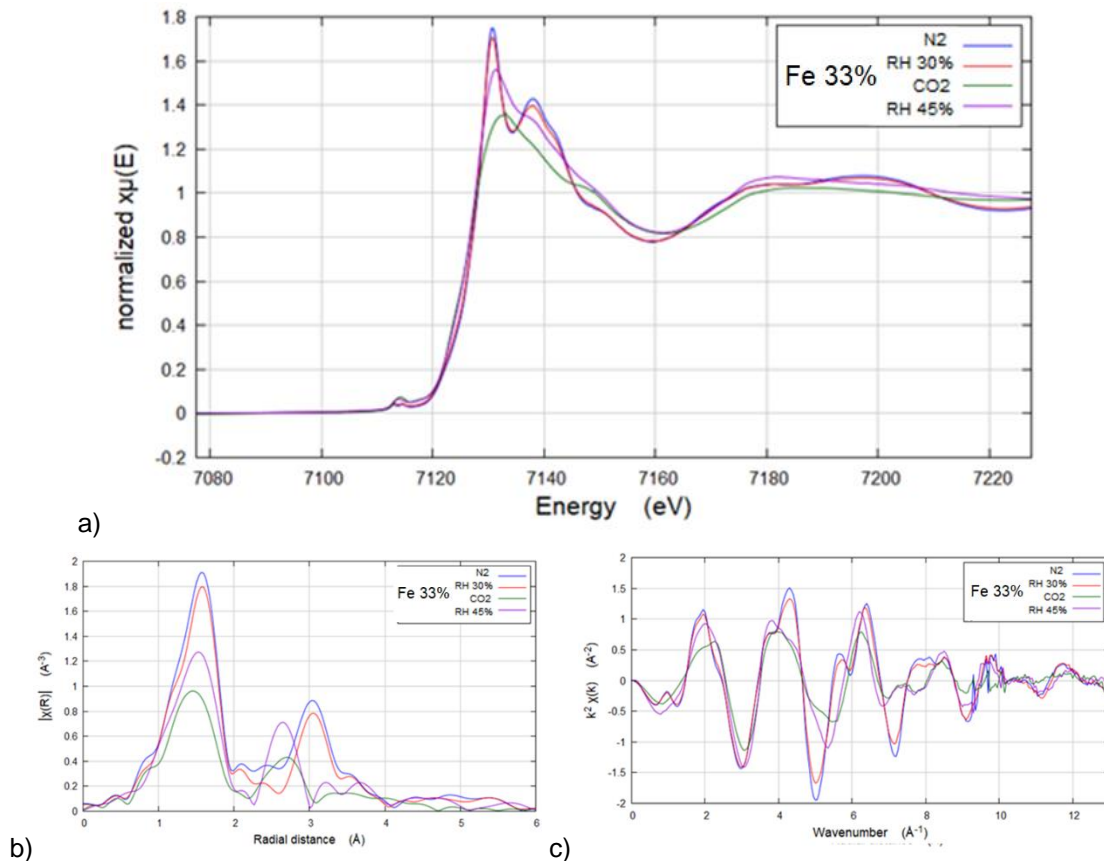


Figure 7.9. Sample with 33% Fe on the iron edge in the 4 different preparation conditions, plotted in: a) E in the XANES region, b) R and c) k in the EXAFS region

From the sample with 33% Fe in the XANES region (Figure 7.9a), it can be seen that for iron there are 2 different trends: the N₂ sample (0% carbonatate) shows a double signal with peaks at about 7130 and 7145 eV, while the CO₂ sample (100% carbonated) shows a single peak at about 7135 eV.

The 30% RH sample is similar to the N₂ sample because only the small fraction of calcium hydroxide has reacted (Table 7.3). Actually, Ca(OH)₂ reacts earlier compared to the calcium and iron compound which, in turn, transforms into an intermediate carbonated phase. On the contrary, the 45% RH sample is similar to the CO₂ sample, both being 100% carbonated. However, it is noted that the 45% RH sample, despite it shows a single signal, has a similar trend to the N₂ sample in XANES, so it could have slightly different characteristics from the CO₂ sample, due to the influence of the carbonation rate on the final equilibrium. That is, the reaction takes place in a slower way, so that it would allow the iron to reorient itself better when the calcite is formed, considering that calcite is formed starting from a mixed structure in calcium and iron passing through an intermediate carbonated.

The graphs in k and R in the EXAFS region for the sample with 33% Fe (Figures 7.9b-c), which are the most significant in this type of measurement, confirm the presence of the two different trends between the sample N₂ (0% carbonated) and the sample CO₂ (100% carbonated). The 30% RH sample is always similar to the N₂ sample, while the 45% RH sample is similar to the CO₂ sample, in this case without particular differences between these two completely carbonated samples.

At this point all the other 5 samples are compared with respect to the sample with 33% Fe, taken as a reference to investigate if there are further trends, under the same conditions: at first, when they are under N₂ (Figures 7.10a-b-c) and then, carbonated with CO₂ (Figures 7.10d-e-f).

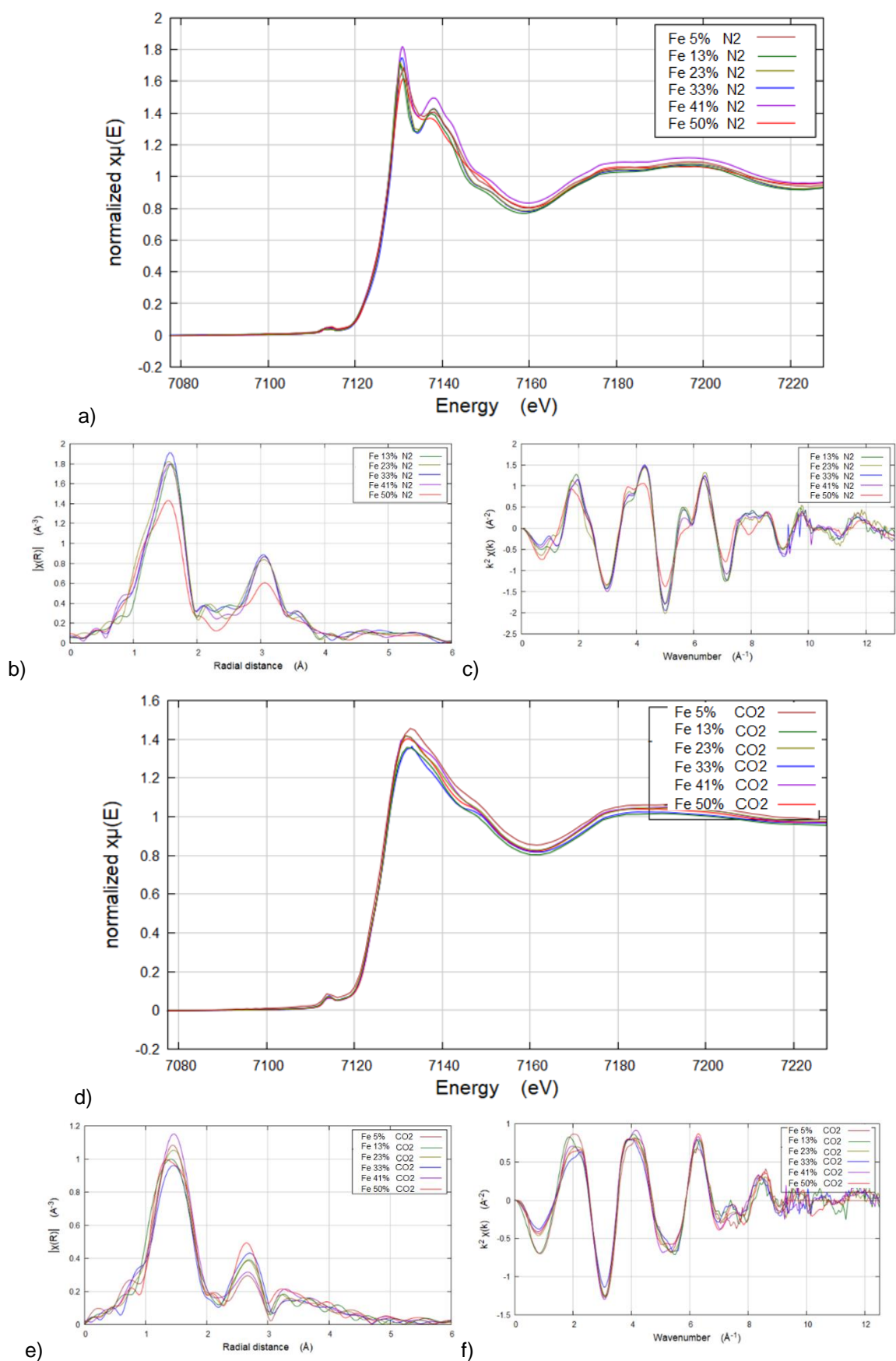
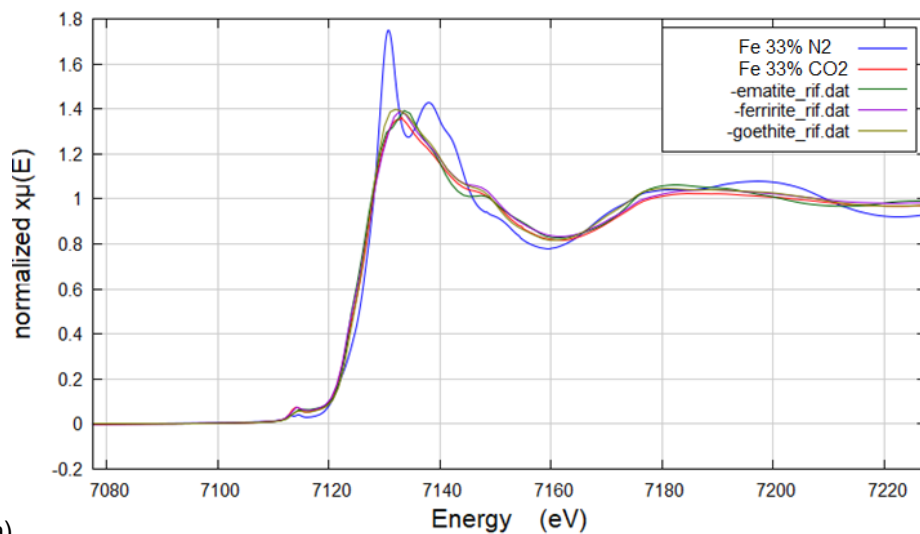


Figure 7.10. Samples with various % of Fe on the iron edge prepared under N₂ atmosphere, plotted in: a) E in the XANES region, b) R and c) k in the EXAFS region. Same samples prepared with CO₂ flow, plotted in: d) E in the XANES region, e) R and f) k in the EXAFS region

For all the samples with iron and calcium, the signals in E in the XANES region shows that they all behave like the reference sample (33% Fe) under the same conditions (N₂ or CO₂), so there are always the same 2 different trends for iron: the N₂ samples (0% carbonated) have a double signal with peaks at about 7130 and 7145 eV, while the CO₂ samples (100% carbonated) have a single peak at about 7135 eV. Only the sample with 50% Fe shows a difference in the peak at about 7145 eV under N₂, which is less evident, since in this sample there is iron in excess respect to calcium, considering that the compound Ca₄Fe₂(OH)₁₄·6H₂O (observed from XRD) has a calcium-iron ratio 2:1 in moles, corresponding to 41% Fe in weight. This excess iron should have a different structure, maybe similar with that of the iron released following carbonation. In fact, this sample presents small differences compared to the other 5 samples in terms of R and k. The same trends are also found in the other 5 samples exposed to RH 30% and RH 45% conditions.

At this point, the Fe 33% N₂ and Fe 33% CO₂ samples (corresponding to the two different trends identified) are considered as a reference, to make a first comparison with some noted iron phases acquired previously and with the published literature. From a first comparison in XANES respect to references phases (like hematite, goethite and ferrihydrite), shown in Figure 7.11a, it is observed that the Fe 33% N₂ sample presents a very different trend from all the reference phases, therefore it is not attributable to any of them. While, as regards the sample 33% Fe CO₂, it shows a trend that can be associated to both ferrihydrite and goethite.



a)

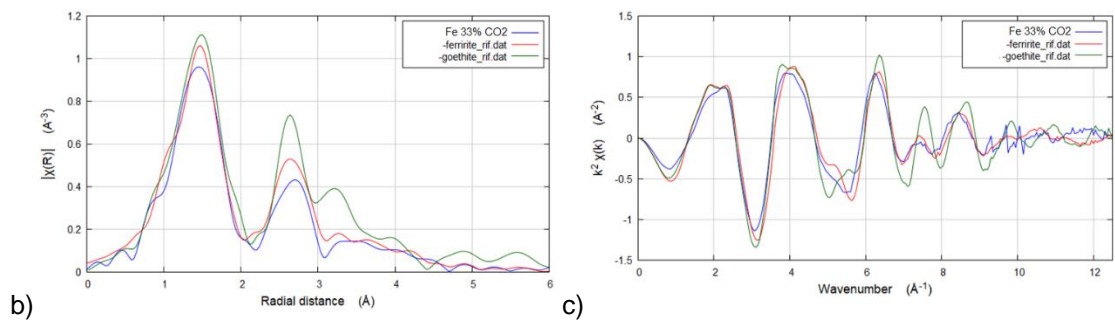


Figure 7.11. Sample with 33% Fe on the iron edge prepared under N₂ or with CO₂ flow, compared with probable phases (hematite, goethite and ferrihydrite), plotted in: a) E in the XANES region, b) R and c) k in the EXAFS region

Finally, by comparing the Fe 33% CO₂ sample with goethite and ferrihydrite in terms of R and k (Figure 7.11b-c), the carbonated phase appears to be very similar to ferrihydrite, precisely in the 2-line form (Figure 7.12) [2]. From the literature, ferrihydrite is an amorphous iron oxy-hydroxide, which can however have different short-range orders based on the size of the grains, the most ordered form in diffraction is called 6-line as it has 6 diffraction signals, while the most amorphous is the 2-line ferrihydrite, which has 2 wide diffraction signals (as it will be better described in the chapter on iron oxides). From Figure 7.12b it was observed that the EXAFS technique allows to distinguish the form of ferrihydrite based on the height of some signals in k, from which it is possible to note that the form of ferrihydrite obtained from the 33% Fe CO₂ sample corresponds to the less ordered form (2-line ferrihydrite), and really it seems even less ordered due to the absence of the satellite peak.

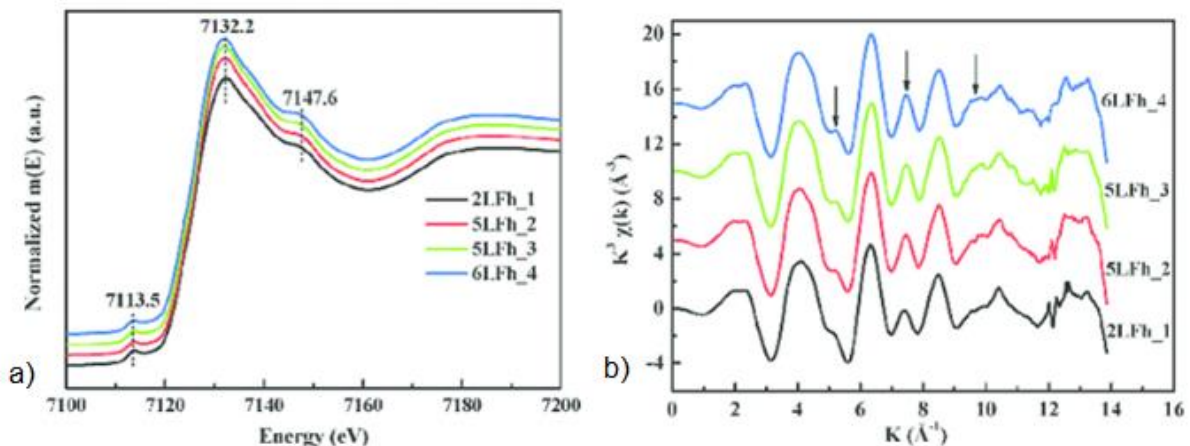


Figure 7.12. Different forms of ferrihydrite, from the most ordered (6-line) to the least ordered (2-line), with signals plotted in: a) E in the XANES region, b) k in the EXAFS region [2]

From the literature no EXAFS measurements have been found on mixed phases containing both calcium and iron. Therefore, on the samples considered significant for the iron edge, 33% Fe, and in addition the 50% Fe sample, which is slightly different, a fit is performed with ARTEMIS to calculate the distances in R. Since it was not possible to have the CIF files of the phase related to 2-line ferrhydrite (completely amorphous) in the carbonated phase, nor to the phase that should be $\text{Ca}_4\text{Fe}_2(\text{OH})_{14}\cdot 6\text{H}_2\text{O}$ in the initial samples, those of hematite and of a calcium and iron oxide 1:1 (CaFeO_2) are used as CIF, in order to generate valid paths between Fe-O, Fe-Fe and Fe- Ca. First of all, from the fit of the metal iron (CIF of CCC structure) used as a reference (fit up to $R = 5$), it is found the value of $S_0^2 = 0.8$ to be set in the fitting parameters.

The sample with 33% Fe N_2 (0% carbonated) is well fit respect to Fe with CIF of CaFeO_2 (Figure 7.13a), finding as 1st shell Fe-O with $R \approx 2.02 \text{ \AA}$, while the 2nd shell seems Fe-Ca with $R \approx 3.45 \text{ \AA}$ (Table 7.5).

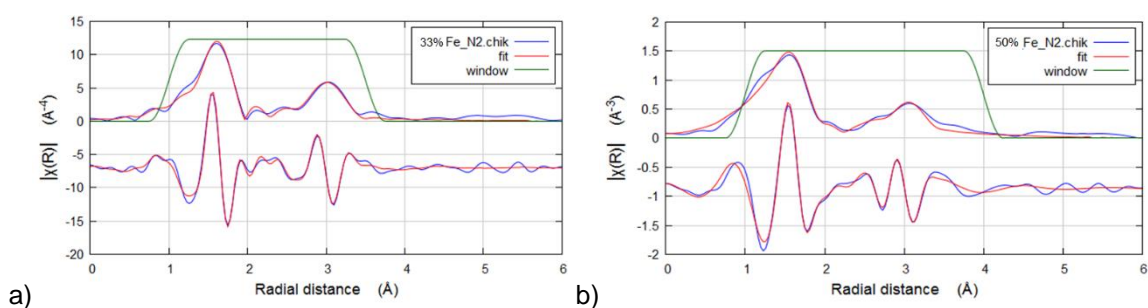


Figure 7.13. Fit respect to Fe with ARTEMIS of the samples analyzed by EXAFS: a) Fe 33% N_2 , b) Fe 50% N_2

Table 7.5. Fit parameters respect to Fe with ARTEMIS of the samples analyzed by EXAFS (k 3-13)

Sample	CIF	Element	N	s_0^2	ss	e_0	ΔR	R_{eff}	R
33%Fe_N2	CaFeO_2	O	6.26	0.8	0.004	-0.66	0.041	1.978	2.019
	CaFeO_2	Ca	9.72	0.8	0.011	-0.66	0.114	3.338	3.453
50%Fe_N2	CaFeO	O	6.78	0.8	0.008	-3	0.038	1.978	2.016
	CaFeO	Ca	9.68	0.8	0.012	-3	0.108	3.338	3.446

The sample with 50% Fe N_2 (0% carbonated) has always a good fit with the CIF of CaFeO_2 (Figure 7.13b), finding the 1st shell Fe-O with $R \approx 2.02 \text{ \AA}$, while the 2nd shell seems due to the Fe-Ca, with $R \approx 3.45 \text{ \AA}$ (Table 7.5).

Regarding the sample with 33% Fe at 45% RH (100% carbonated), it is well fitted respect to Fe with CIF of α -Fe₂O₃ (Figure 7.14a), finding the 1st shell Fe-O with $R \approx 2.01 \text{ \AA}$, while the 2nd shell appears to be due to Fe-Fe with $R \approx 3.06 \text{ \AA}$ (Table 7.6).

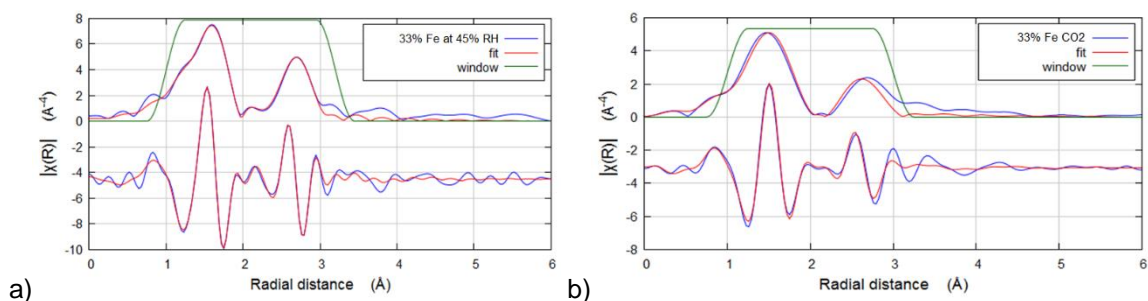


Figure 7.14. Fit respect to Fe with ARTEMIS of the samples analyzed by EXAFS: a) Fe 33% at RH 45%, b) Fe 33% with CO₂ flow

Table 7.6. Fit parameters respect to Fe with ARTEMIS of samples analyzed by EXAFS (k 3-13)

Sample	CIF	Element	N	s_0^2	SS	e_0	ΔR	R_{eff}	R
33%Fe_RH45%	a-Fe ₂ O ₃	O	8.15	0.8	0.013	-2.84	0.059	1.946	2.005
	a-Fe ₂ O ₃	Fe	3.1	0.8	0.007	-2.84	0.086	2.971	3.057
33%Fe_CO2	a-Fe ₂ O ₃	O	5.35	0.8	0.01	-2.91	0.042	1.946	1.988
	a-Fe ₂ O ₃	Fe	4.02	0.8	0.016	-2.91	0.064	2.971	3.035

Even the sample with 33% Fe CO₂ (100% carbonated), is well fitted respect to Fe with CIF of α -Fe₂O₃ (Figure 7.14b), having a 1st shell Fe-O with $R \approx 2.00 \text{ \AA}$, while the 2nd shell correspond to Fe-Fe with $R \approx 3.04 \text{ \AA}$ (Table 7.6). These R values are slightly lower than those obtained for the same sample carbonated in air, but it could still be the same phase.

Once the iron edge has been analyzed, the calcium edge is measured on the various samples, always first reporting the sample with 33% Fe as a representative central sample. Figure 7.15 shows this sample in the 4 different preparation conditions, first in E in the XANES region (Figure 7.15a), then in R (Figure 7.15b) and finally in k (Figure 7.15c) in the EXAFS region.

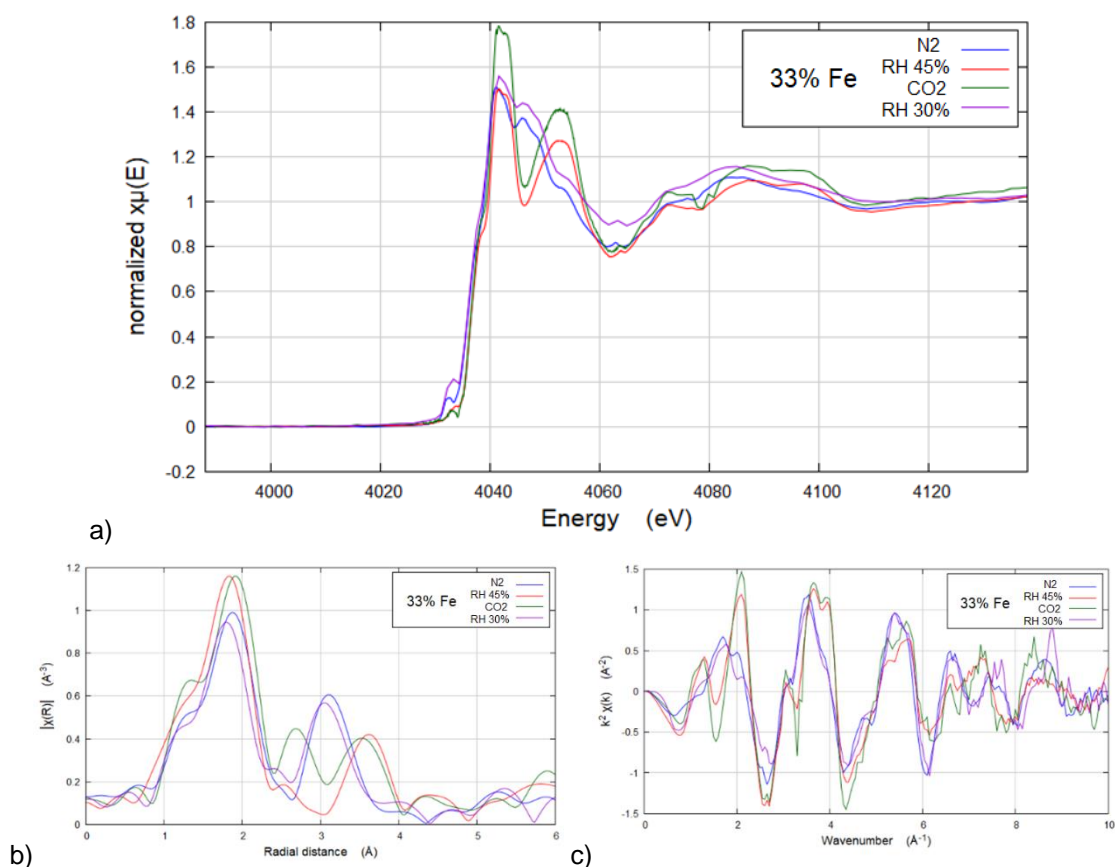


Figure 7.15. Sample with 33% Fe on the calcium edge in the 4 different preparation conditions, plotted in: a) E in the XANES region, b) R and c) k in the EXAFS region

From the sample with 33% Fe in E in the XANES region (Figure 7.15a), it can be seen that also for calcium there are 2 different trends: the sample under N₂ (0% carbonated) shows a very close double signal (about 4043 and 4048 eV), while the sample exposed to 45% RH (100% carbonated) has a more spaced double signal (about 4043 and 4053 eV). The sample exposed to RH 30% is again very similar to the sample below N₂, as only the small fraction of calcium hydroxide has reacted, while the sample with CO₂ is always similar to the sample exposed to 45% RH, both being 100% carbonated. The graphs in k and R in the EXAFS region for the sample with 33% Fe on the calcium edge (Figure 7.15b-c) confirm the presence of the 2 different trends between the sample N₂ (0% carbonated) and the sample CO₂ (100% carbonated). The CO₂ sample however presents a less defined signal, probably because, in this case, the CO₂ exposure method seems to lead to a separation of the calcium from the iron which then does not remain on the polycarbonate (noisy signal in R with an intermediate shell that could be partly fictitious).

At this point, to investigate if there are further trends under the same conditions, all the other 5 samples are compared to the sample with 33% Fe, taken as a reference:

first, as they are under N₂ (Figures 7.16a-b-c) and then, carbonated at 45% RH (Figures 7.16d-e-f).

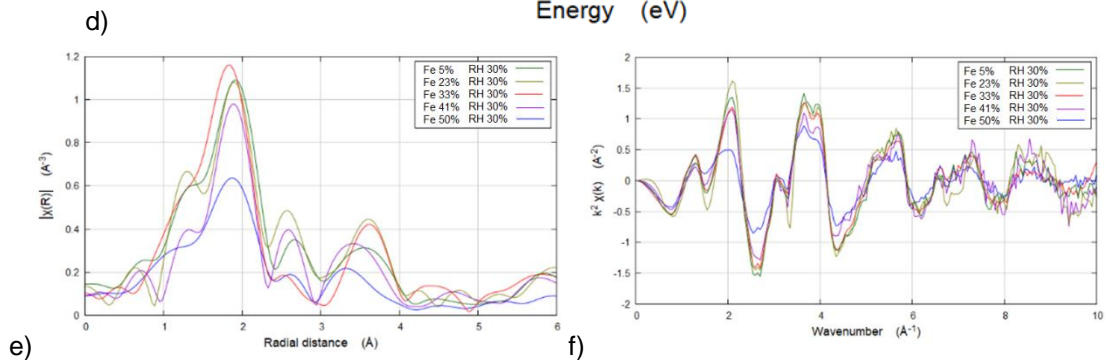
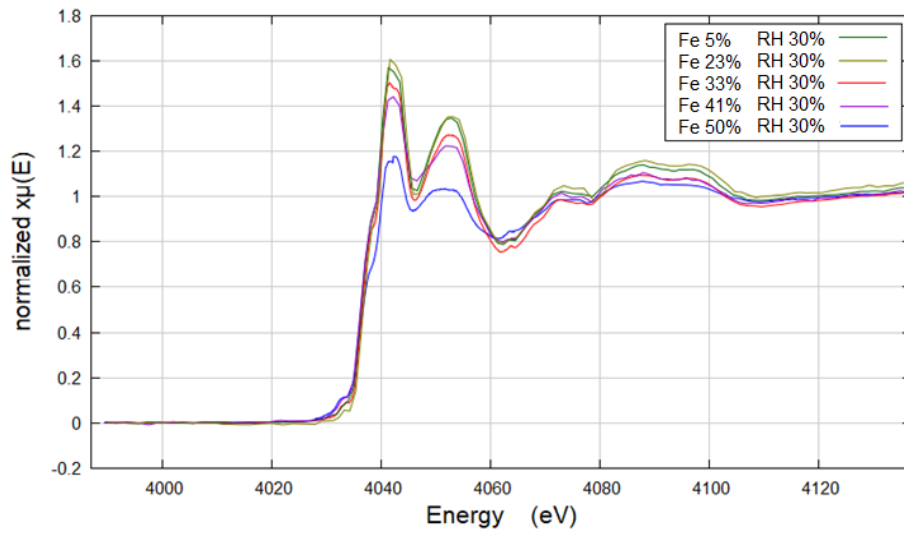
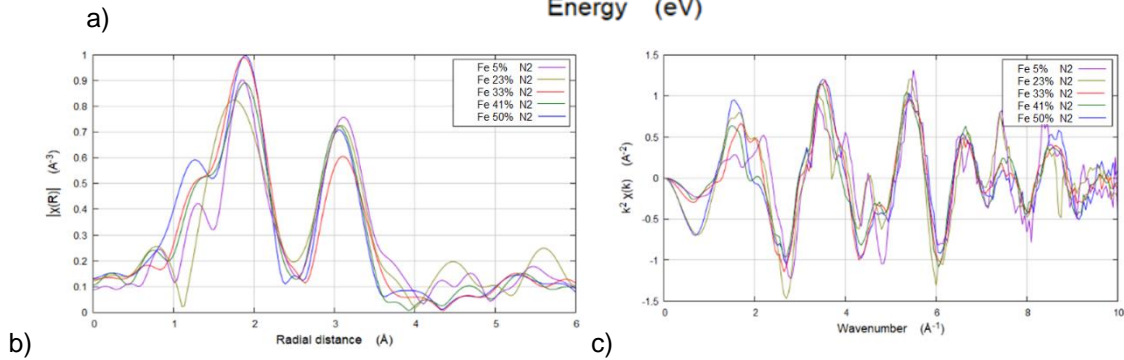
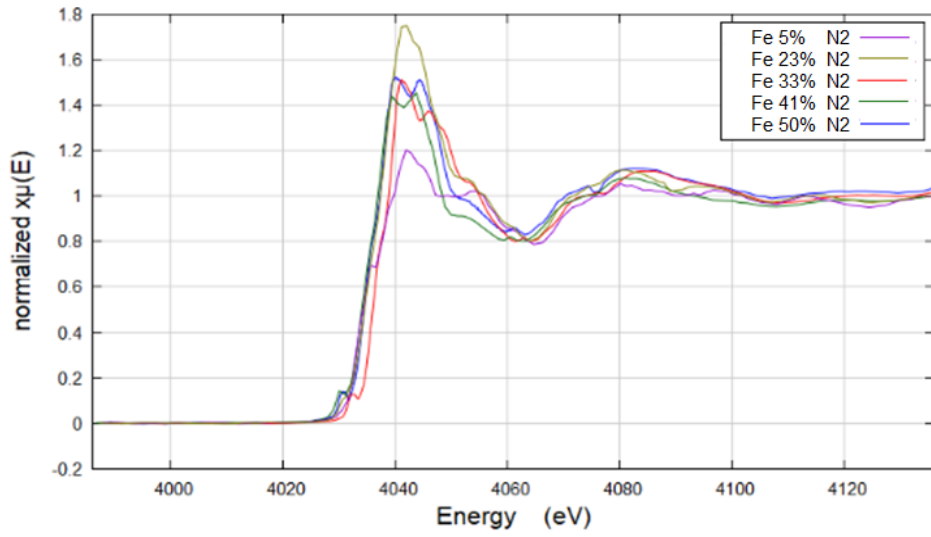
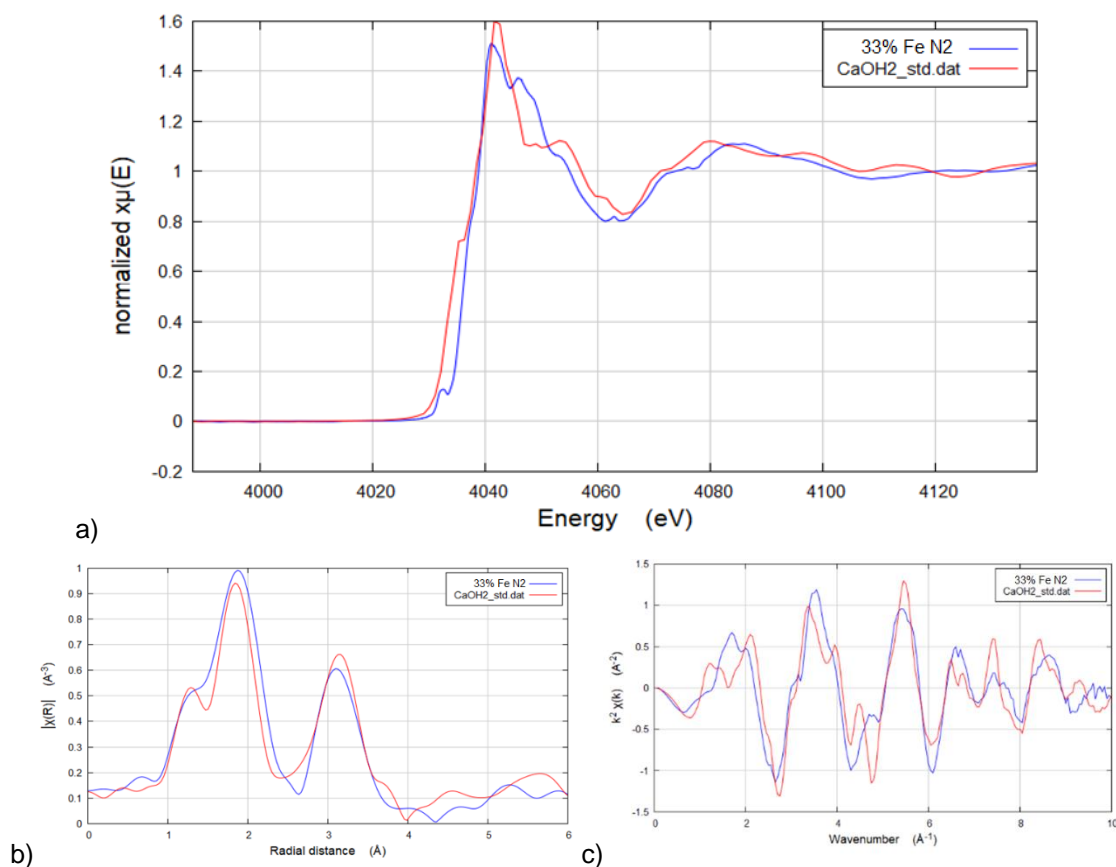


Figure 7.16. Samples with various % of Fe on the calcium edge prepared under an N₂ atmosphere, plotted in: a) E in the XANES region, b) R and c) k in the EXAFS region. Same samples prepared with 45% RH exposure, plotted in: d) E in the XANES region, e) R and f) k in the EXAFS region

The signals in XANES for the other samples under N₂ show that those with the highest concentration of iron (41% Fe and 50% Fe) are similar to the sample with 33% Fe, while those with a lower concentration of iron (5% Fe, 13% Fe and 23% Fe) are slightly different, as they should have a contribution of Ca(OH)₂ in the signal (phase more present in diffraction). In the carbonated samples at 45% RH, on the other hand, no particular differences are observed, and the signals are the same both in XANES and in EXAFS. Only the signal in R between the two main shells has changed little, but without a correlation between the % of iron. Probably, it could be a question of quality of data (less resolution on the calcium edge compared to the iron edge).

As before, a comparison of the samples with 33% Fe N₂ and with Fe 33% CO₂ is made with reference standards for Ca(OH)₂ and CaCO₃ (Figure 7.17).



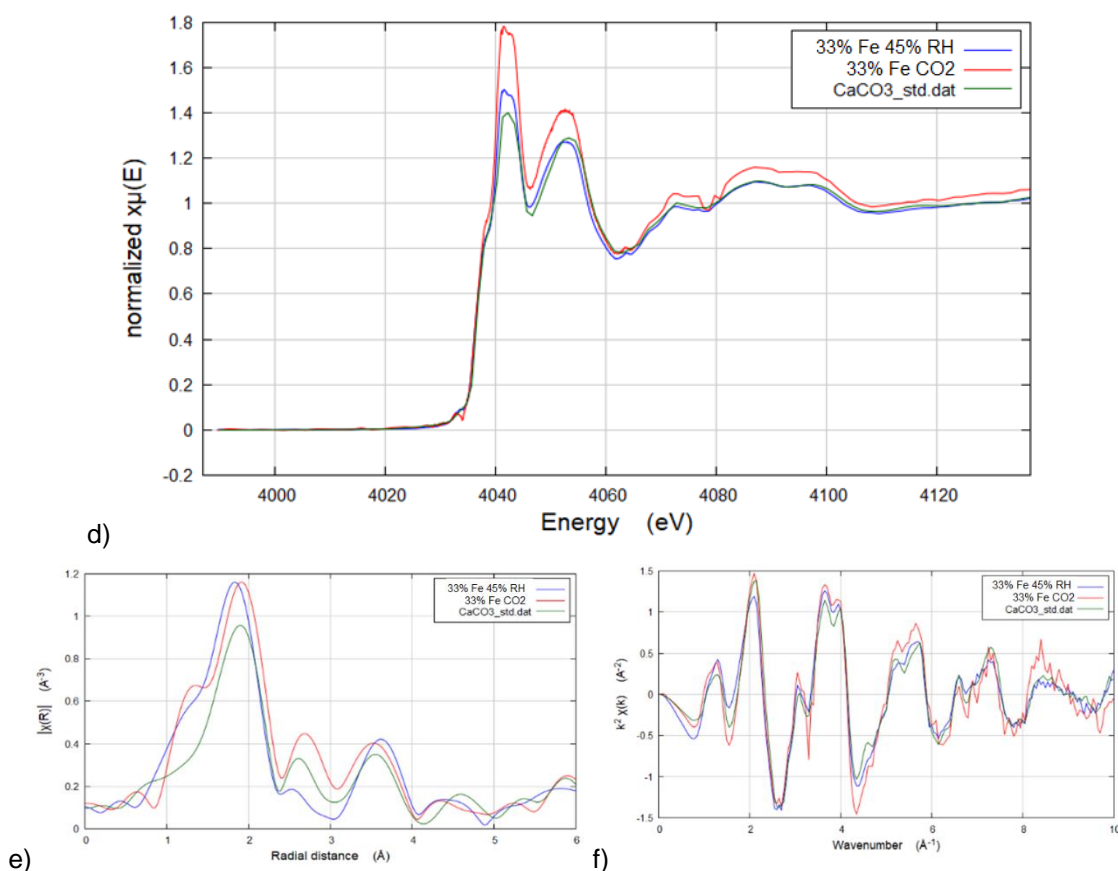


Figure 7.17. Sample with 33% Fe on the calcium edge prepared under N₂ compared with Ca(OH)₂, plotted in: a) E in the XANES region, b) R and c) k in the EXAFS region. Same sample with 33% Fe on the calcium edge prepared at 45% RH or with CO₂ flux compared to CaCO₃, plotted in: a) E in the XANES region, b) R and c) k in the EXAFS region

From the comparison between the sample with 33% Fe under N₂ and Ca(OH)₂ (Figures 7.17a-b-c), it is observed that the sample (0% carbonated) is different from Ca(OH)₂ in EXAFS and in k, but the position of the first two shells in R is very similar. While from the comparison between the sample with 33% Fe at 45% RH and CaCO₃ (Figures 7.17d-e-f), it appears that the sample (100% carbonated) is almost equal to CaCO₃ in k and in XANES, but it has a lower signal on the intermediate shell in R. In comparison to CaCO₃ the sample with 33% Fe fluxed with CO₂ is also reported, and it is similar to CaCO₃ in all signals.

Therefore, on the samples considered significant for the calcium edge (which are the ones having 33% Fe), and in addition the 41% Fe sample, which does not present Ca(OH)₂ in the XRD pattern, a fit with ARTEMIS is performed to calculate the distances in R. To generate valid paths, since the CIF of the phase that could be Ca₄Fe₂(OH)₁₄·6H₂O is not available, a calcium and iron oxide 1:1 (CaFeO₂) is used as CIF, together with the CIF of CaCO₃ and Ca(OH)₂.

First of all, pure $\text{Ca}(\text{OH})_2$ (Figure 7.18a) and pure CaCO_3 (Figure 7.19b) are fitted, used as reference standards for the calcium phases to optimize some parameters. From to the fit, the 1st shell results in both cases Ca-O with $R \approx 2.04 \text{ \AA}$, while the 2nd shell results in both cases Ca-Ca, but with different R : for the carbonate $R \approx 4.10 \text{ \AA}$, for the hydroxide $R \approx 3.61 \text{ \AA}$ (Table 7.7).

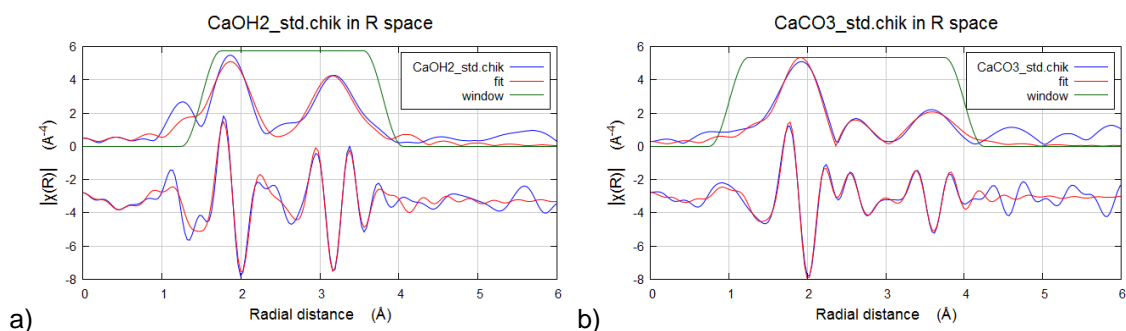


Figure 7.18. Fit respect to Ca with ARTEMIS of the standards analyzed by EXAFS: a) $\text{Ca}(\text{OH})_2$, b) CaCO_3

Table 7.7. Fit parameters respect to Ca with ARTEMIS of samples analyzed by EXAFS (k 3-10)

Sample	CIF	Element	N	s_0^2	ss	e_0	ΔR	R_{eff}	R
CaCO ₃ std	CaCO ₃	O	6	0.8	0.007	5.06	0.017	2.353	2.37
	CaCO ₃	Ca	6	0.8	0.016	5.06	0.065	4.032	4.097
Ca(OH) ₂ std	Ca(OH) ₂	O	6	0.8	0.007	-0.23	-0.013	2.363	2.35
	Ca(OH) ₂	Ca	6	0.8	0.007	-0.23	0.025	3.585	3.611

The sample with 33% Fe N₂ (0% carbonated) is well fitted respect to Ca with CIF of CaFeO_2 (Figure 7.19a), finding as 1st shell Ca-O with $R \approx 2.39 \text{ \AA}$, while the 2nd shell appears to be Ca-Fe with $R \approx 3.50 \text{ \AA}$ (Table 7.8).

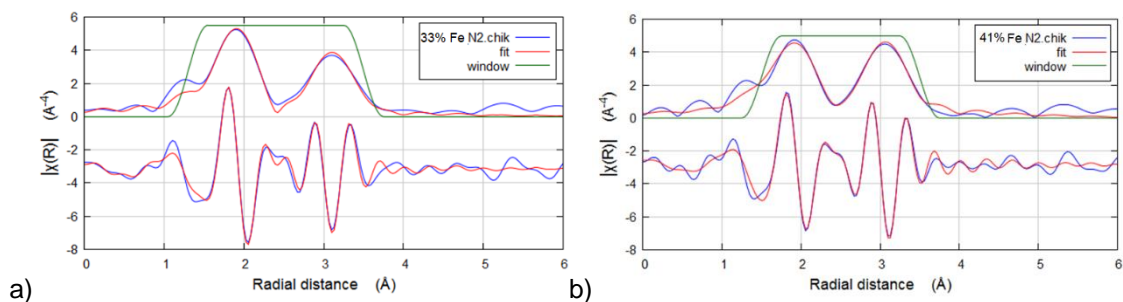


Figure 7.19. Fit respect to Ca with ARTEMIS of the samples analyzed by EXAFS: a) Fe 33% N₂, b) Fe 41% N₂

Table 7.8. Fit parameters respect to Ca with ARTEMIS of samples analyzed by EXAFS (k 3-10)

Sample	CIF	Element	N	s_0^2	ss	e_0	ΔR	R_{eff}	R
33%Fe_N2	CaFeO2	O	6	0.8	0.007	-1.21	-0.003	2.390	2.387
	CaFeO2	Fe	6	0.8	0.01	-1.21	0.157	3.338	3.495
41%Fe_N2	CaFeO2	O	6	0.8	0.011	-9.3	-0.044	2.390	2.346
	CaFeO2	Fe	6	0.8	0.006	-9.3	0.101	3.338	3.439

The sample with 41% Fe N₂ (0% carbonated) is well fit respect to Ca (always considering the CIF of CaFeO₂) (Figure 7.19b), finding as 1st shell Ca-O with R ≈ 2.35 Å, while the 2nd shell seems Ca-Fe with R ≈ 3.44 Å (Table 7.8).

Like the sample with 33% Fe, at 45% RH (100% carbonated), the sample is well fitted respect to Ca with CIF of CaCO₃ (Figure 7.20a), finding as 1st shell Ca-O with R ≈ 2.38 Å, while the 2nd shell is Ca-Ca with R ≈ 4.07 Å (Table 7.9).

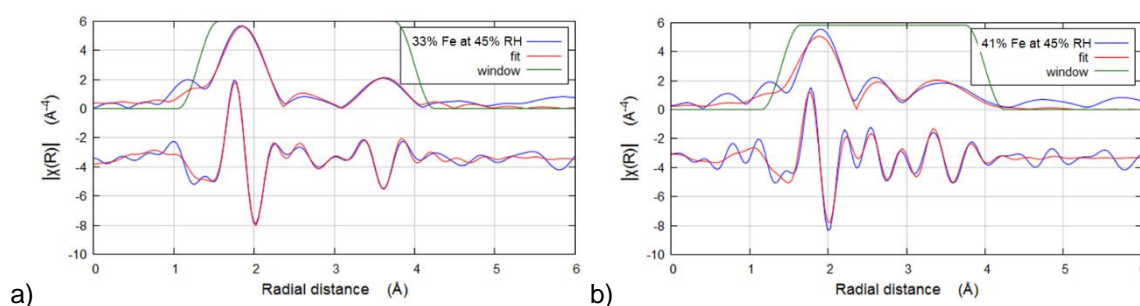


Figure 7.20. Fit respect to Ca with ARTEMIS of the samples analyzed by EXAFS: a) Fe 33% at RH 45%, b) Fe 41% at RH 45%

Table 7.9. Fit parameters respect to Ca with ARTEMIS of samples analyzed by EXAFS (k 3-10)

Sample	CIF	Element	N	s_0^2	ss	e_0	ΔR	R_{eff}	R
33%Fe_RH45%	CaCO3	O	6	0.8	0.006	6.29	0.024	2.353	2.377
	CaCO3	Ca	6	0.8	0.01	6.29	0.038	4.032	4.070
41%Fe_RH45%	CaCO3	O	6	0.8	0.007	3.99	0.011	2.353	2.365
	CaCO3	Ca	6	0.8	0.014	3.99	0.018	4.032	4.050

Also the sample with 41% Fe at 45% RH (100% carbonated), is well fitted respect to Ca with CIF of CaCO₃ (Figure 7.20b), finding as 1st shell Ca-O with R ≈ 2.37 Å, while the 2nd shell results Ca-Ca with R ≈ 4.05 Å (Table 7.9).

On all the samples, the edge steps were finally measured (after having optimized the background and the pre-edge and post-edge lines) in order to determine the average concentrations of the samples respect to the surface. In general, the samples present comparable values with the expected values of Table 7.4 (therefore

precise elemental concentrations), while the carbonated samples with CO₂ always present higher values of Fe (as already noted in the EXAFS spectra, it is as if the calcium carbonated in solution is separated from iron).

From this EXAFS study results that Fe is in coordination with calcium in the synthesized phase (Ca₄Fe₂(OH)₁₄·6H₂O), having a 1st shell Fe-O with R ≈ 2.02 Å and a 2nd shell probably Fe-Ca with R ≈ 3.45 Å. In the carbonated phase, this structure transforms in a very amorphous form of 2-line ferrhydrite, having a 1st shell Fe-O with R ≈ 2.00 Å and a 2nd shell Fe-Fe with R ≈ 3.06 Å. Similarly, in the synthesized phase (Ca₄Fe₂(OH)₁₄·6H₂O), Ca results in coordination with iron, having a 1st shell Ca-O with R ≈ 2.40 Å and a 2nd shell probably Ca-Fe with R ≈ 3.45 Å (practically the same as observed from the iron edge). In the carbonated phase, on the other hand, no significant differences are observed respect to a pure calcite phase, therefore, reacting with CO₂, the calcium-associated phase becomes pure CaCO₃ having the 1st shell Ca-O with R ≈ 2.38 Å and the 2nd shell Ca-Ca with R ≈ 4.07 Å.

Considering all the XRD, EXAFS, TEM and SEM measures, it can be deduced that calcium separates from the Ca₄Fe₂(OH)₁₄·6H₂O phase to react with CO₂, while iron remains as oxyhydroxide hydrate in amorphous form, which homogeneously covers the calcite crystals at a nanometric level. In fact, by following the carbonation process, occurring through the Ca₄Fe₂O₆CO₃·12H₂O intermediate phase, from which the main diffraction peak of calcite grows, the iron converts in a very amorphous 2-line ferrihydrite phase, having an atomic order so short to not be identified by XRD (but identifiable in EXAFS with Synchrotron light).

7.4 Possible applications of tetracalcium ferrite hydrate NPs

The innovative compound, with chemical formula Ca₄Fe₂(OH)₁₄·6H₂O, synthesized in form of NPs, is characterized by the possibility of reacting quickly with CO₂ (in the presence of water), forming a calcite covered with 2-line ferrhydrite at the nanometric level, accompanied by a colour change of the calcite itself. Therefore, in addition to applications in the field of Cultural Heritage by formulating a tailored nanolime, this compound could also be used exclusively as an indicator of carbonation in various situations, such as in mortars or reinforced concrete

structures, where the depth of carbonation is generally determined by the phenolphthalein test (carcinogenic substance) carried out on cylindrical samples extracted from the substrate (UNI 9944:1992).

In fact, from the carbonation tests carried out in paragraph 7.2, it was observed that this compound, together with $\text{Ca}(\text{OH})_2$, is selectively last transformed, as CO_2 reacts first with calcium hydroxide. This phenomenon can be linked to a different solubility of the two compounds, or even to the fact that the compound with calcium and iron passes through a more stable carbonated intermediate, but what can be observed on a practical level is that the colour change occurs only as a result of carbonation of $\text{Ca}_4\text{Fe}_2(\text{OH})_{14}\cdot 6\text{H}_2\text{O}$. Therefore, from an application point of view, this compound could be mixed in low quantities with $\text{Ca}(\text{OH})_2$, to observe a colour change only when the entire mixture is completely carbonated. In this way it could be monitored the carbonation inside the reinforced concrete, where it is important to maintain a basic pH (presence of lime) on the reinforcements to avoid corrosion, by observing the browning of the mixture over time.

A further application could be related to a use in the water purification sector, or to the removal of polluting ions from water, such as arsenic, lead and fluorine, thanks to the iron that is released in the form of ferrhydrite, which has the ability to adsorb and separate these ions [3-7]. In fact, the presence of calcite together with ferrhydrite (which is formed directly in the water following the carbonation of the compound), improves the adsorbing capacity of the ferrhydrite itself, as well as the possibility of separating this phase by sedimentation. Fluorine pollution in water occurs from both natural sources and anthropogenic structures. Adsorption is one of the main methods for the defluorination of water, which is why several adsorbents have already been used, including iron oxides. This adsorption is favored at $\text{pH} > 10$ and the ability of iron oxides to adsorb fluoride ions also depends on the presence of other metals: from literature the adsorption capacity is maximum together with lanthanum, followed by calcium hydroxide and aluminum [3]. Therefore by inserting calcium ions together with the iron oxides, the fluoride ions are incorporated on the surface as calcium binds with them, so the novelty of the tetracalcium ferrite hydrate nanoparticles produced lies in being able to form cationic complexes FeOOCa^+ , which constitute the active sites for the interaction with fluoride ions. [7]

Arsenic is a toxic element and its presence in drinking water should be minimized. The co-precipitation of arsenic with aluminum and ferric hydroxide is a practical and

economical method for purifying drinking water. In this context, the presence of calcium ions increases the zeta potential of ferric oxyhydroxides, a phenomenon that is more significant as the pH increases. The presence of calcium also facilitates the flocculation and therefore the precipitation of ferric oxyhydroxides, thus providing more solid precipitates available for arsenic removal. This effect is the main reason why this element improves the removal of arsenic through coprecipitation of ferric oxyhydroxides in different conditions (in particular in the presence of silicates). [4] Finally, this particular tetracalcium ferrite hydrate can be used directly for the production of calcium nano-carbonate coated with ferrihydrite, which can be used as a filler for increasing the mechanical properties of thermoplastic polymers. The addition of calcium nano-carbonate in fact improves the mechanical properties, crystallinity and thermal stability of the microcellular polypropylene. The maximum mechanical properties are obtained when the content of nano-CaCO₃ is 6% by weight. [8] The addition of calcium nano-carbonate as a filler also improves the characteristics of the polyurethane methacrylate, in particular it increases the resistance to traction, bending, abrasion, hardness and thermal stability of this polymer, with an excellent result that is obtained with 0.75% by weight of nano-CaCO₃. [9] Among the most commercial thermoplastic polymers is polyvinyl chloride (PVC), but despite its wide use, the workability and thermal stability are inferior to other commercial polymers, such as polyethylene and polystyrene. Therefore, the addition of inorganic fillers is often used to improve these properties. The use of calcium nano-carbonate in PVC increases the glass transition and thermal decomposition temperatures, as the nanoparticles limit long-range mobility [10]. Given that the mechanical properties of composite polymers are strongly related to the proportions of the filler, there is a growing interest in nanoscale fillers. In this context, calcium nano-carbonate coated with 2-line ferrihydrite (deriving from tetracalcium ferrite hydrate) could be used, both for its very small size (cubes of 50-100 nm per side) and for the presence of a layer of iron of the order of a few nm above the calcite cubes, which could improve the dispersion of the nanoparticles in the polymer with a consequent increase in the mechanical properties of the polymer itself.

7.5 Application of tailored nanolime in Cultural Heritage

The tailored nanolime (13% Fe) dispersed in an aqueous solvent is applied, for the first time, as innovative solutions at the base of a compatible and eco-friendly conservative treatment of relevant stones characterized by a carbonatic matrix containing iron, like the biocalcarene stones of Agrigento. The treatment effectiveness of the treatments carried out by means of the tailored nanolime is evaluated in terms of aesthetical features, superficial cohesion, and mechanical resistance (drilling test), and the results are compared with those obtained by using pure nanolime suspension. Moreover, both untreated and treated biocalcarenes are subjected to accelerated aging tests (salt crystallization) in order to verify the treatment durability.

The iron % in the tailored nanolime is chosen in relation to the chemical composition of the stone, as measured by XRF, resulting in a Fe/Ca ratio equal to about 1/6 in weight. The tailored nanolime is called nCH_Fe, to distinguish it from the pure nanolime, called nCH. For both the suspensions, the following concentrations are considered: 5, 10 and 20 g/l. The considered suspensions were applied on the Agrigento's biocalcarenes in form of cubic specimens (3 cm side), by airbrush, until stone saturation. In fact, this application procedure resulted the most suitable for aqueous nanolime treatments, thanks to its ability to combine feasibility in the on-situ application, no chromatic alteration, and a good penetration depth. During the treatments, all the samples absorbed about 10 ml of product and the total amount of nanoparticles applied to each stone, before dripping, is found of about 240 mg (corresponding to about 27 mg/cm²). The treatments are carried out in laboratory (RH of about 40 %); for this reason, at the end of the treatments, the samples were stored for 3 days at a RH of 75±5%, in order to promote carbonation. The kinetic stability measurements of the nanolime suspensions are reported in Figure 7.21. We can observe that the nCH suspensions, independently from concentration, show a general and almost constant reduction in stability up to 1 hour (Figure 7.21a), revealing a reduction of about 50% after 20 minutes. Differently, the graph referred to the kinetic stability of nCH_Fe suspensions (Figure 7.21b) shows a very stable behaviour for all the concentrations, revealing only a slight reduction in the kinetic stability (about 5%) after 60 minutes, probably due to a slight higher viscosity of the suspension.

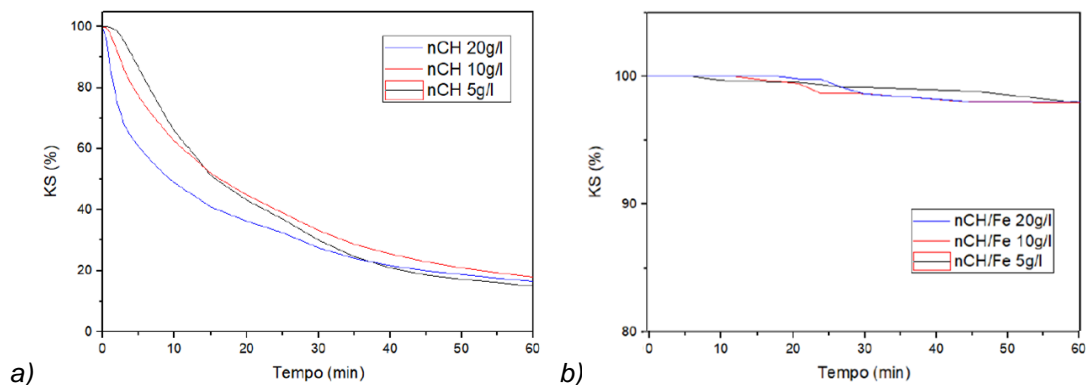


Figure 7.21. Kinetic stability measurements performed with 610 nm wavelength until 60 minutes for all the nanolime suspensions: a) nCH 5, 10, 20 g/L, b) nCH_Fe 5, 10, 20 g/l

Regarding the analysis of the carbonatation process, performed at different relative humidity conditions ($RH = 45 \pm 5\%$ and $75 \pm 5\%$), by depositing 0.2 ml of each suspension on a suitable sample holder, the XRD results referred to nCH suspensions are shown in Table 7.10.

Table 7.10. Analysis of the carbonatation process of nCH samples, in relation to different suspension concentrations and relative humidity (RH) conditions

Sample	Suspension concentration (g/l)	RH = 45 ± 5%			RH = 75 ± 5%		
		Ca(OH) ₂ crystalline phases	CaCO ₃ crystalline phases	χ (%)	Ca(OH) ₂ crystalline phases	CaCO ₃ crystalline phases	χ (%)
nCH	5	--	100% C	100	--	100% C	100
	10	--	73% C 27% CCH	100	--	100% C	100
	20	24%	46% C 30% CCH	76	--	100% C	100

Exposure times: 1 hour for RH = 50% and 3 hours for RH = 75%; T=20°C

C = Calcite (CaCO₃) (ICSD #98-002-0179)

CCH = calcium carbonate hydroxide hydrate (Ca₃(CO₃)₂(OH)₂·1.5H₂O) (ICDD #00-023-0107)

From these results, the carbonation process results always completed at RH = 75±5%, independently from the suspension concentration; at RH = 45±5%, it results completed at 5 g/l, almost completed for the 10 g/l suspension (73% calcite with 27% CCH) and, at 20 g/l a 24% of Ca(OH)₂ remains unreacted. On the contrary, regarding the carbonatation process of nCH_Fe suspensions, reported in Table 7.11, all the samples showed a complete carbonation process with the only

exception of the sample at 20 g/l at low RH. Actually, the suspension of tailored nanolime at 20 g/l transforms into 51% of calcite and 49% of calcium iron oxide carbonate hydrate, $\text{Ca}_4\text{Fe}_2\text{O}_6\text{CO}_3 \cdot 12\text{H}_2\text{O}$ (from here called CIOCH), an intermediate phase like that observed for CCH. Anyway, also in this case, the sample does not show an unreacted phase.

Table 7.11. Analysis of the carbonatation process of nCH_Fe samples, in relation to different suspension concentrations and relative humidity (RH) conditions

Sample	Suspension concentration (g/l)	RH = 50 ± 5%			RH = 75 ± 5%		
		Ca(OH) ₂ crystalline phases	CaCO ₃ crystalline phases	χ (%)	Ca(OH) ₂ crystalline phases	CaCO ₃ crystalline phases	χ (%)
nCH_Fe	5	--	100% C	100	--	100% C	100
	10	--	100% C	100	--	100% C	100
	20	--	51% C 49% CIOCH	100	--	100% C	100

Exposure times: 1 hour for RH = 50% and 3 hours for RH = 75%; T=20°C

C = Calcite (CaCO₃) (ICSD #98-002-0179)

CIOCH = calcium iron oxide carbonate hydrate ($\text{Ca}_4\text{Fe}_2\text{O}_6\text{CO}_3 \cdot 12\text{H}_2\text{O}$) (ICDD #00-043-0480)

These results show a slightly higher reactivity of the CH_Fe suspension respect to the pure nanolime (as observed in the paragraph 7.2).

The visual inspections of the nanolime based treatments, performed by varying the suspension concentration (5, 10 and 20 g/l), are reported in Figure 7.22, compared to untreated samples (MNT). These images show that up to 10 g/l, no particular chromatic alteration is observed for both the employed nanolime.

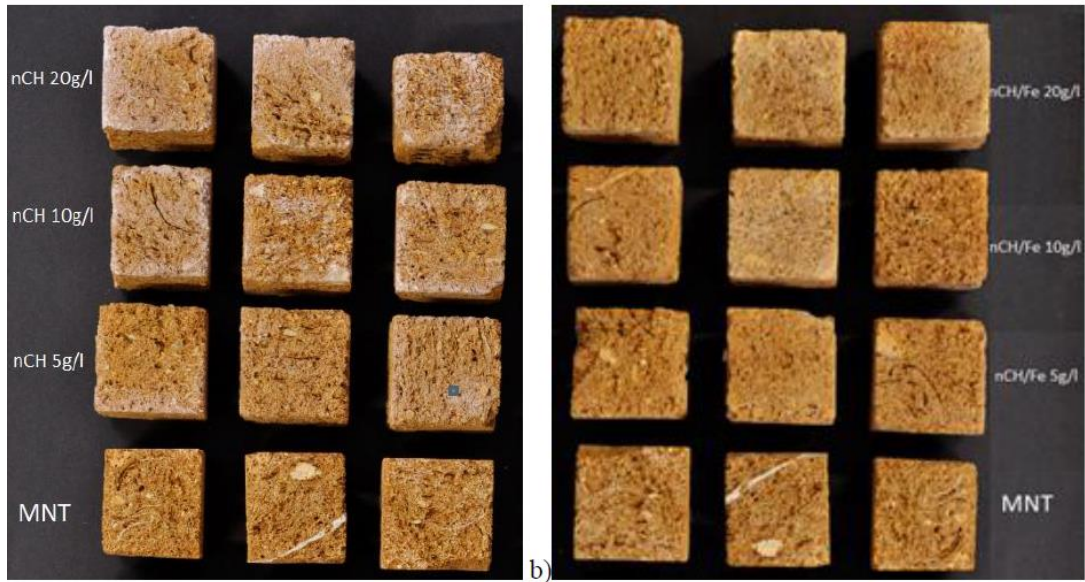
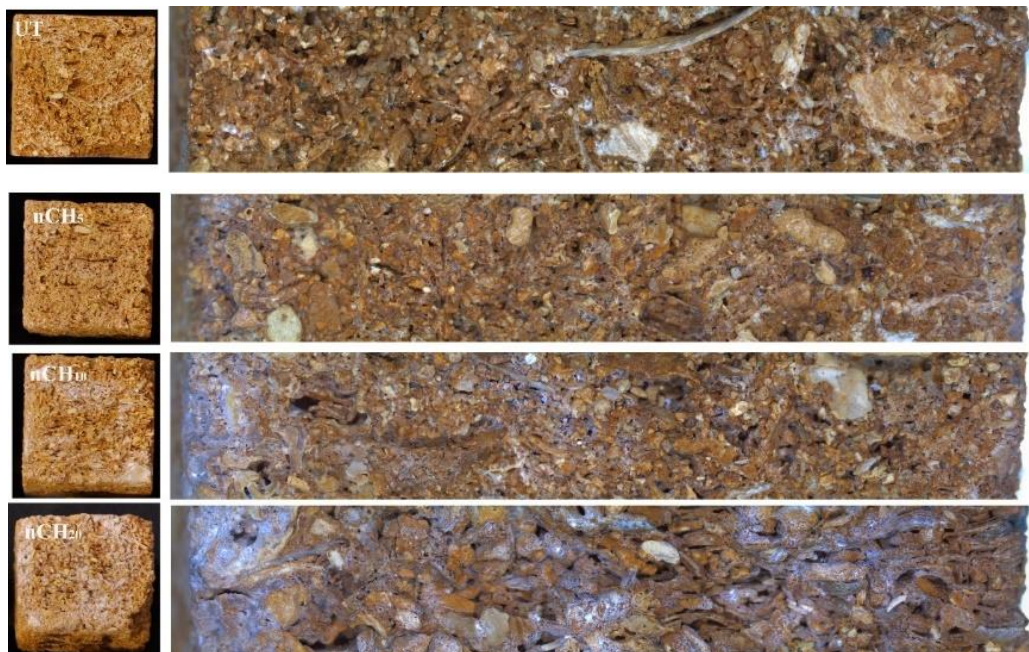


Figure 7.22. Visual inspections of the nanolime based treatments, performed by varying the suspension concentration (5, 10 and 20 g/l), compared to untreated samples (MNT)

The images collected from the stereomicroscope confirm these observations, reported in Figure 7.23. In particular, the samples treated by means of nCH suspensions, showed a slight whitening effect, particularly evident by increasing the suspension concentration. On the contrary, all the samples treated with nCH_Fe did not show significant alterations of the original colour of the stones.



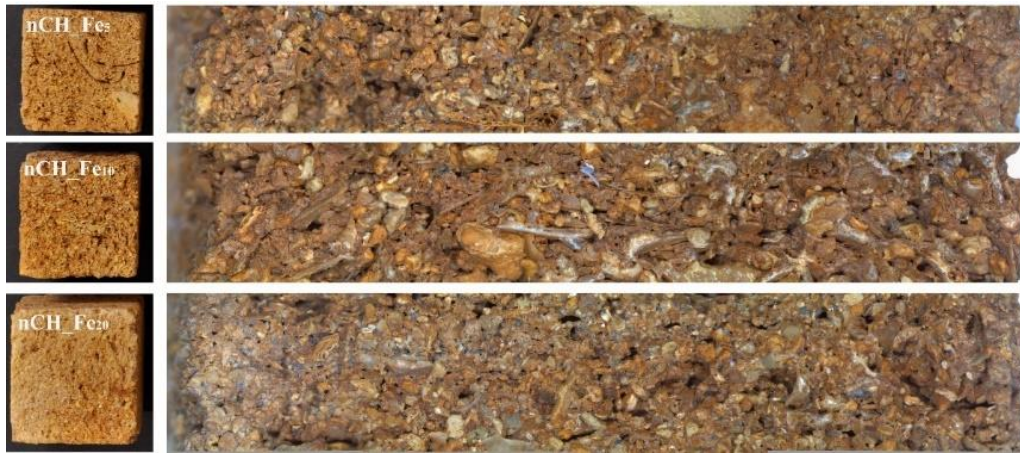


Figure 7.23. Stereomicroscope observations of the nanolime based treatments, performed by varying the suspension concentration (5, 10 and 20 g/l), compared to untreated sample (UT)

Therefore, the suspension concentration which allow to limit or even avoid visible chromatic alterations of the surfaces, with the considered amount of nanolime of about 240 mg), can be fixed at 10 g/l.

As concerns the surface adhesion, the results coming from the STT are reported in Table 7.12. The samples treated by using the suspension concentration at 10 g/l, yielded the highest cohesion increase of the treated surface with a reduction of the removed material (ΔM) ranging from 73% to 83%, for nCH and nCH_Fe 10 g/l suspensions respectively.

Table 7.12. Scotch Tape Test (STT) results on the biocalcarenite samples, before (UT) and after the treatments by using nCH and nCH_Fe suspensions

Scotch Tape Test (STT)					
Samples	M (mg cm ⁻²)	ΔM	Samples	M (mg cm ⁻²)	ΔM
UT	1.1 ± 0.6	27%	UT	2 ± 1	45%
nCH 5	0.8 ± 0.3		nCH_Fe 5	1 ± 0.6	
UT	2 ± 1	73%	UT	1.2 ± 0.5	83%
nCH 10	0.4 ± 0.2		nCH_Fe 10	0.2 ± 0.1	
UT	2 ± 1	64%	UT	2.5 ± 0.4	56%
nCH 20	0.5 ± 0.2		nCH_Fe 20	1.1 ± 0.4	

* The results are taken as the average of three measurements for each application procedure

The results obtained by the DRMS measurements are finally reported in Figure 7.24. They underline that the best values, in terms of drilling resistance improvement, are obtained by using 10 g/l suspensions. Specifically, all the samples treated with nCH,

if compared to the untreated stone (UT), reveal a general increase in strength up to almost 20 mm in depth (Figure 7.24a). In fact, while the UT stone presents an average resistance value of 2 ± 1 N, the nCH treated samples show average resistance values of 3 ± 1 N, 5 ± 1 N and 6 ± 1 N with increasing suspension concentration. As concerns the DRMS measurements referred to the samples treated with nCH_Fe, the best values are obtained with the suspensions 5 g/l and 10 g/l, showing average resistance values of 4 ± 1 N and 9 ± 2 N respectively (Figure 7.24b). On the contrary, the nCH_Fe 20 g/l gives an average resistance value comparable to the UT one, probably attributed to the higher viscosity characterizing this suspension respect to the others, so compromising the penetration of the treatment.

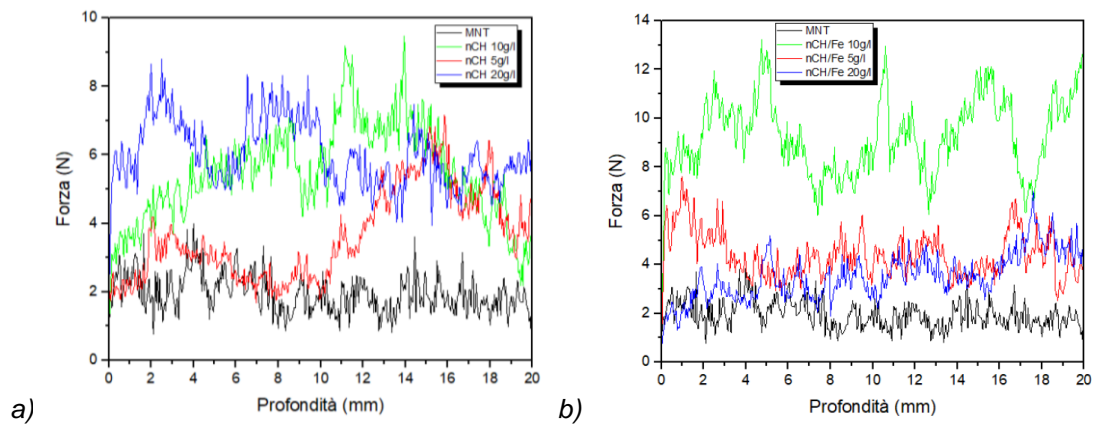


Figure 7.24. DRMS results on the biocalcarenite samples, before (UT) and after the treatments by using nCH and nCH_Fe suspensions

Considering that the best values, in terms of STT and DRMS, are reached by using both the treatments at 10 g/l, the porosity measurements as well as the SEM analyses are performed only on the samples treated by using this concentration.

As concerns the porosimetric investigations, while the UT samples were characterized by average values of porosity of $36\pm 4\%$, after the treatments a slight decrease in the porosity was observed, reaching values of $32\pm 3\%$ and $34\pm 3\%$ for nCH and nCH_Fe respectively. The slight changes in the porosity underline that the nanolime does not cause variations in the original pore system of the stone, allowing the natural breathability of the stone.

The microscopic modification of the surface after the nanolime-based treatments is analysed by SEM, reported in Figure 7.25. In particular, if compared to the UT stone (Figures 7.25a-b), the surfaces of nCH and nCH_Fe treated samples appear

homogeneously covered by a fine layer, mainly composed of an aggregation of small nanoparticles attributable to the nanolime treatments (Figures 25c-e, respectively). It is evident that this layer tends to cover the superficial pores of the stone without occluding them, so guaranteeing the breathability of the treated materials. The presence of the new formed calcite grains seems to be at the vibase of the improvement in the particle cohesion as well as in the mechanical strength of the treated surface [11].

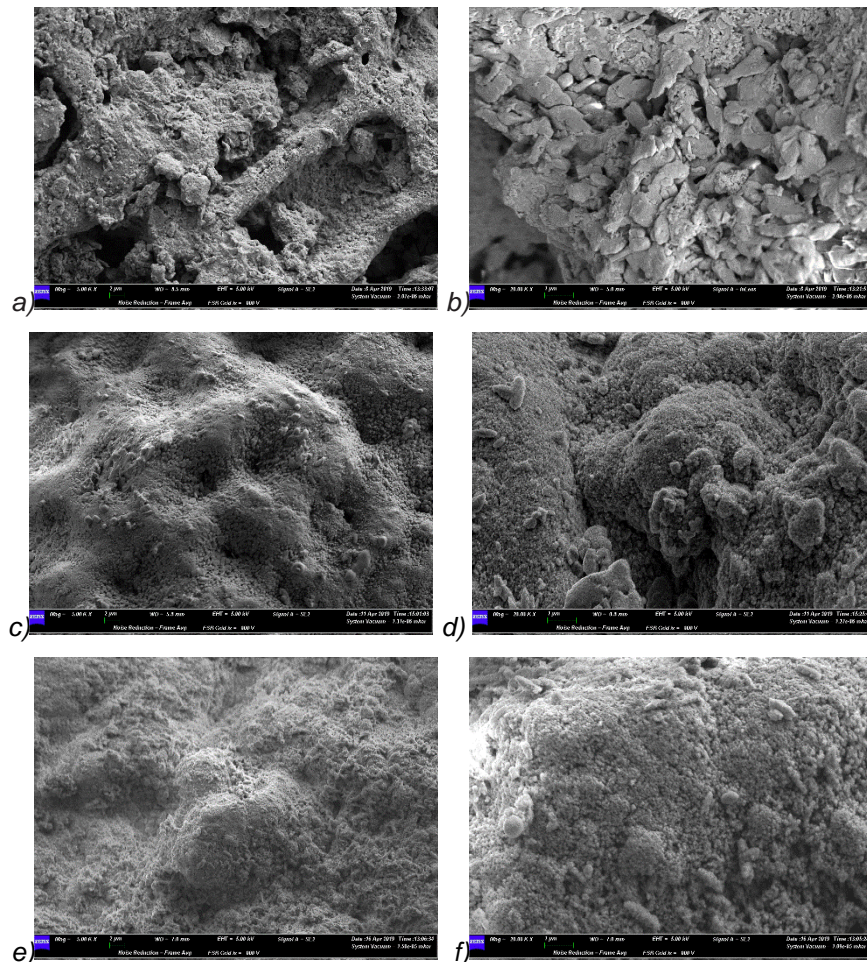


Figure 7.25. SEM images on the biocalcarenite samples: a-b) before treatment with 2 µm and 1 µm markers, c-d) nanolime 10 g/l treated with 2 µm and 1 µm markers, e-f) tailored nanolime 10 g/l treated with 2 µm and 1 µm markers

EDX-SEM microanalysis are finally performed on the section of both untreated and treated samples. In particular, the images referred to the untreated stone highlight their calcareous composition together with the presence of Al, Si, Fe and traces of homogeneously diffused Mg (Figure 7.26a). Considering the nanolime 10 g/l treated sample, the presence of a thin layer less than 50 µm is observed both on the external

surface and inside the internal pores (arrows in Figure 7.26b). Specifically, this layer can be related to the nanolime treatment which covers the internal pores without occluding them. Similar results are obtained on nanolime tailored 10 g/l treated sample, revealing the formation of a fine layer consisting of Ca, Fe and O, up to 1 cm from the treated surface, attributable to the nanolime treated treatment (Figure 7.26c). Also in this case, the treatment appeared to be not occlusive, but able to re-establish, in the same time, the cohesion between the grains of the original stone.

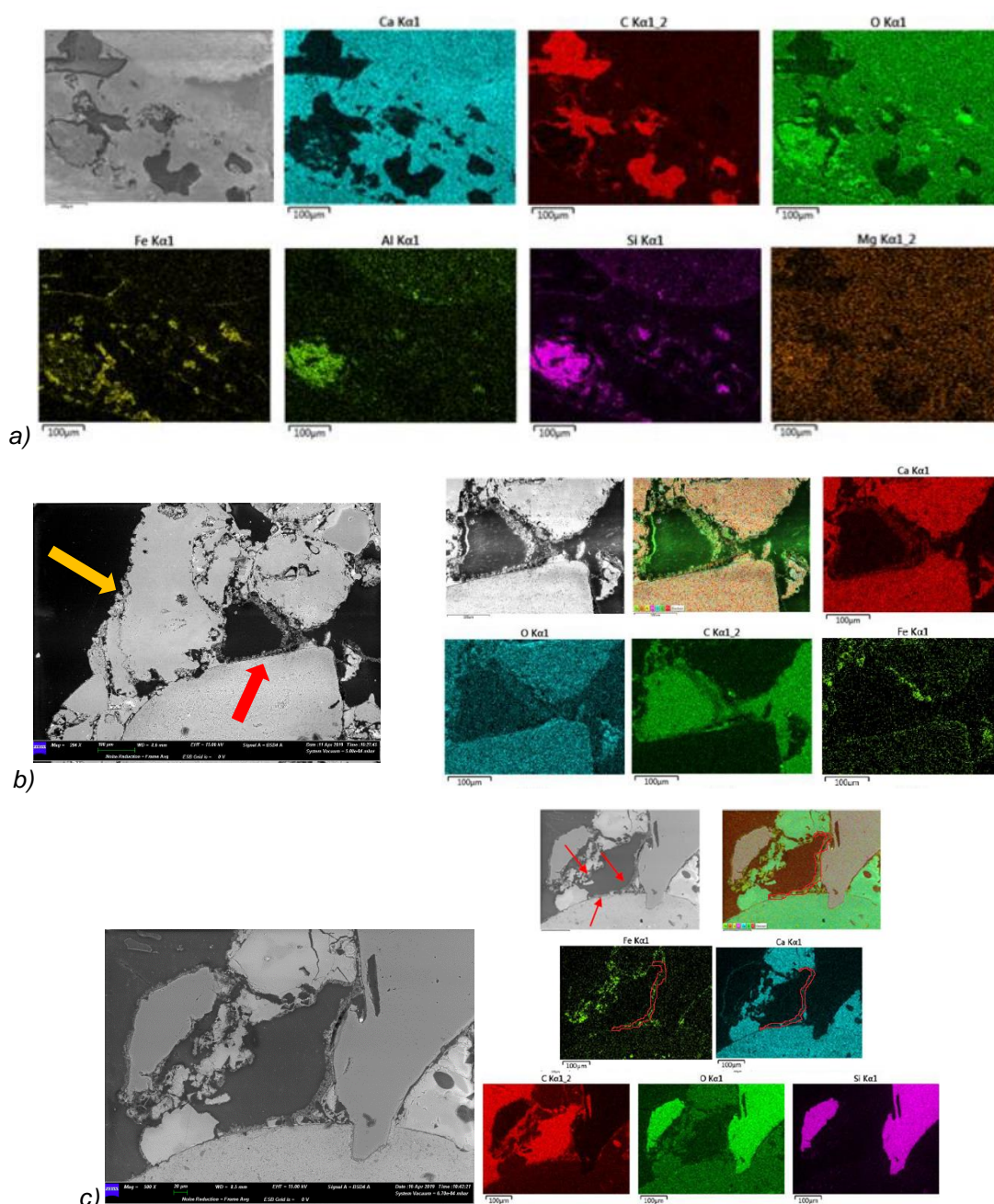


Figure 7.26. EDX-SEM microanalysis on the section of the biocalcarenite samples: a) before treatment, b) nanolime 10 g/l treated, c) tailored nanolime 10 g/l treated

As concerns the accelerated aging tests, the salt crystallization test is carried out on 7 untreated samples, 7 samples treated with nanolime 10 g/l and 7 samples treated with tailored nanolime 10 g/l. The test is performed in accordance to the standard procedure [12], by using a 14 wt% solution of sodium sulphate [13, 14]. Moreover, the test was performed by capillary rising considering that, in the on-situ conditions, the salt rich rising damp tends to penetrate inside the stones from behind the consolidated faces and leaving them through the consolidated surface [13, 15]. Ten cycles are performed, comprising 24 hours of immersion into the salt solution and 22 hours of drying in oven ($T = 50^{\circ}\text{C}$). After each cycle, the samples are properly weighed. At the end of all the cycles, the samples were gently washed with deionized water, and then left to dry at ambient temperature up to constant mass was reached. As observed from the visual inspections, reported in Figure 7.27, the salt crystallization tests cause an evident formation of saline efflorescence, already after 5 cycles of immersion, both in the untreated and treated stones. In particular, the treatments performed by using nCH_Fe suspension compared to the nCH one, seem to improve the stone resistance towards the salt crystallization phenomena, delaying the formation of saline efflorescence after 5 cycles from the beginning of the test (Figure 7.27c).

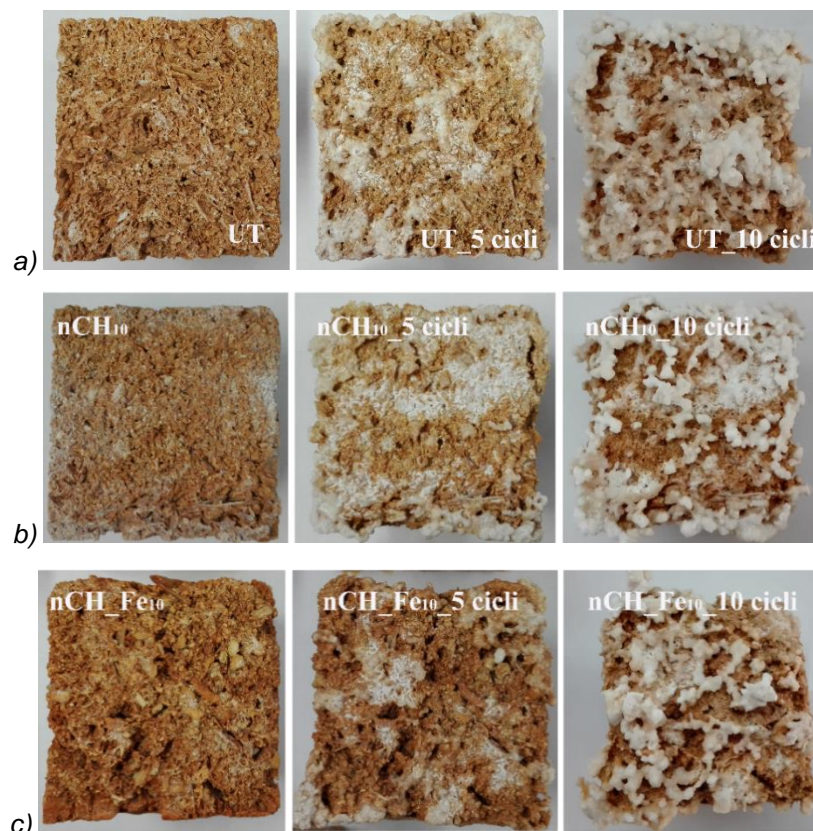


Figure 7.27. Visual inspections of the salt crystallization tests ad different cycles for different samples: a) untreated, b) nanolime 10 g/l treated, c) tailored nanolime 10 g/l treated

From a quantitative point of view, the resistance to salts crystallization can be expressed by evaluating the weight of the samples before and after each cycle: the mass variation (ΔM) as a function of the number of crystallization cycles is reported in Figure 7.28. Regarding the untreated samples, ΔM values tend to increase for all the samples up to the 4th cycle. Then, each sample present a different behaviour one each other, showing both increases and deceaces of weight, due to the formation of salts or to the loss of the original material respectively (Figure 7.28a). On the contrary, the treated samples with both the nanolimes display a more homogeneous behaviour showing a similar wight increase of the curves up to almost the 9th or 10th cycle (Figures 7.28b-c). In addition, after the desalination process, while the untreated samples show a ΔM decrease up to 13%, the treated stones reveal ΔM losses of about 5–7%. The obtained results underline the protective effectiveness of both the nanolime-based treatments, revealing their ability to limit the loss of material following the salt crystallization.

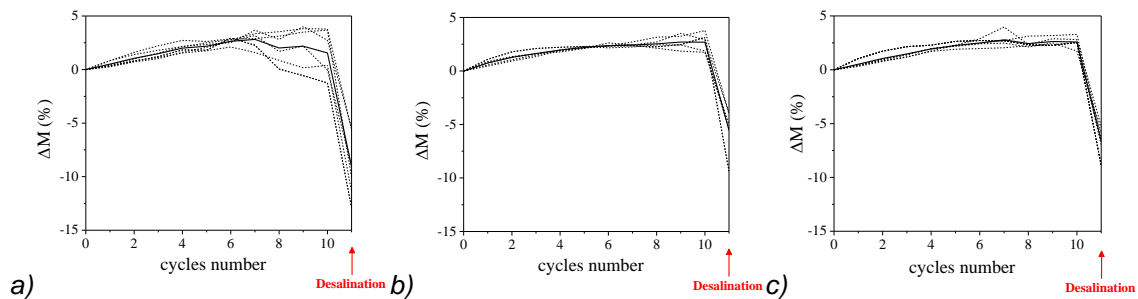


Figure 7.28. Salt crystallization tests mass variation for different samples: a) untreated, b) nanolime 10 g/l treated, c) tailored nanolime 10 g/l treated. The measurements are performed on several samples (*dot lines*) and the medium value is reported as *continuous line*

Considering all the results obtained with regard to the increase in the average surface resistance, the increase in resistance to drilling, the chromatic alteration and the durability of the various nanolimes suspension employed, it is possible to establish that the tailored nanolime on substrates containing iron (such as biocalcarenites) certainly guarantees better results than the traditional nanolime, under the same conditions.

CHAPTER 8: SYNTHESIS AND APPLICATIONS OF OTHER EARTH-ALKALINE NANOPARTICLES

In this chapter the development of innovative scalable methods for the synthesis of other alkaline earth metal nanoparticles, based on the ion exchange process, is investigated, in order to extend their use in the field of Cultural Heritage or in other fields. In particular, the synthesis of other alkaline-earth metal hydroxides, such as nano-sized $\text{Sr}(\text{OH})_2$ and $\text{Ba}(\text{OH})_2$, can be strongly disadvantaged due to their moderately high solubility in water. Following the ion exchange innovative method, according to a sustainable and scalable procedure, all alkaline-earth metal hydroxides nanoparticles, from calcium and magnesium to strontium and barium, are synthesized, overcoming the problems arising from their solubility.

After the synthesis, the application of magnesium hydroxide nanoparticles in restorative treatments on ancient wood samples of an historical vessel (Gallo-Roman wreck, 2nd century b.C.) is performed, obtaining always neutral pH values with treatments durable over time by penetrating inside the wood fibers.

Moreover, preliminary cytotoxicological tests on cancer cells using magnesium oxide nanoparticles, in collaboration with the research group of Pharmacology (MESVA Department of University of L'Aquila), are performed as well, resulting in a toxicity towards cancer cells attributed to the generation of reactive oxygen species (ROS).

8.1 Synthesis of nanoparticles based on magnesium, strontium, and barium

In accordance with the ion exchange synthesis procedure, magnesium, strontium, and barium hydroxide nanoparticles are synthesized by an innovative and one step procedure. Moreover, the synthesis of calcium hydroxide nanoparticles is here compared with the other alkaline-earth metals synthesis, to evaluate the influence of the considered metal on the features of the obtained particles. This innovative procedure is based on an ion exchange process that works in water, at room temperature and ambient pressure, operating with cheap or renewable reagents, without requiring further purification steps.

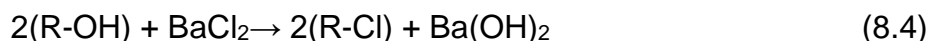
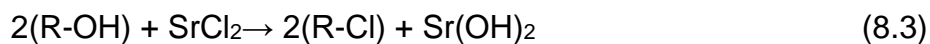
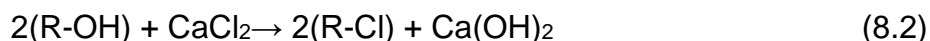
Calcium hydroxide (CH) NPs are here produced by mixing 1M calcium chloride (CaCl₂) aqueous solution with a proper resin amount at room temperature and maintaining them under moderate stirring. When mixed together, the substitution of -OH groups on the resin substrate with chlorides ions (Cl⁻) in solution led, in conditions of supersaturation, to the formation of pure CH NPs without any secondary phase. The synthesis is carried out up to 60 minutes and then the white precipitate phase is separated from the resin particles by a simple sieving procedure. A Ca(OH)₂ aqueous suspension is obtained, named CH sample.

By following the same procedure, it is possible to synthesize the other alkaline-earth metal hydroxides by employing, as initial reagents, magnesium chloride, strontium chloride and barium chloride. Considering that the precipitation of each metal hydroxide is strongly affected by the supersaturation conditions, in relation to the solubility in water (Table 8.1), it is chosen a temperature near 0°C to synthesize strontium and barium. Actually, at this temperature, Sr(OH)₂ and Ba(OH)₂ present the lowest solubility values, about the half respect to room temperature. The produced aqueous suspensions of magnesium, strontium and barium hydroxides are named MH, SH, BH samples, respectively.

Table 8.1. Solubility of alkaline earth hydroxide in water with temperature, at 1 atmosphere pressure. Units of solubility are given in grams per 100 milliliters of water (g/100 ml)

	T = 0°C	T = 10°C	T = 20°C
Mg(OH) ₂	-	-	0.0009
Ca(OH) ₂	0.185	0.176	0.165
Sr(OH) ₂	0.91	1.25	1.77
Ba(OH) ₂	1.67	2.48	3.89

For all the syntheses, the precipitation of the solid phase is regulated by the following reactions:



The kinetics of each synthesis is monitored in terms of the chloride concentration, by taking samples at different times t, from the beginning until the end of the process.

The results coming from the kinetics of the ion exchange process, in terms of chloride concentration measured at different times, (C_t), are reported in Table 8.2. The measures denoted a very fast rate of the ion exchange process for all the alkaline-earth metal compounds. In fact, after only 30 seconds, it is observed a reduction % in the chloride content ranging from 99.9% (MH sample) to 99.0% (BH sample), together with a saturation behavior in the remaining time of the synthesis. Moreover, considering that the reduction in the chlorides concentration is related to the magnesium, calcium, strontium and barium hydroxides production, according to the reactions (8.1-8.4), it is obtained a conversion higher than 99% respect to the maximum theoretical value in 30 seconds. However all the syntheses are continued until 60 minutes to reduce the residual chloride concentration. Finally, at the end of the synthesis, each suspension shows low residual chloride concentrations, particularly for the less water-soluble hydroxides.

Table 8.2. Chlorides concentration (C_t), measured after different times from the beginning of the synthesis ($t=0$). XRD qualitative investigation and quantitative analysis (Rietveld refinement) are reported as well

Sample	Chlorides concentration C_t [mg/l]				Composition Phase (XRD)	
	$t = 0$	$t = 30$ seconds	$t = 15$ minutes	$t = 60$ minutes	$t = 60$ minutes	
MH	70000	39	< 31*	< 31 *	Mg(OH) ₂	100%
CH		160	81	45	Ca(OH) ₂	100%
SH		281	116	106	Sr(OH) ₂	68.2%
					Sr(OH) ₂ ·H ₂ O	8.2%
BH				SrCO ₃	23.6%	
	700	570	483	Ba(OH) ₂ ·H ₂ O	39.0%	
				Ba(OH) ₂ ·8H ₂ O	11.5%	
			Ba(OH) ₂	3.2%		
				BaCO ₃	46.3%	

In Figure 8.1 the XRD patterns obtained from the suspensions dried under nitrogen atmosphere are reported.

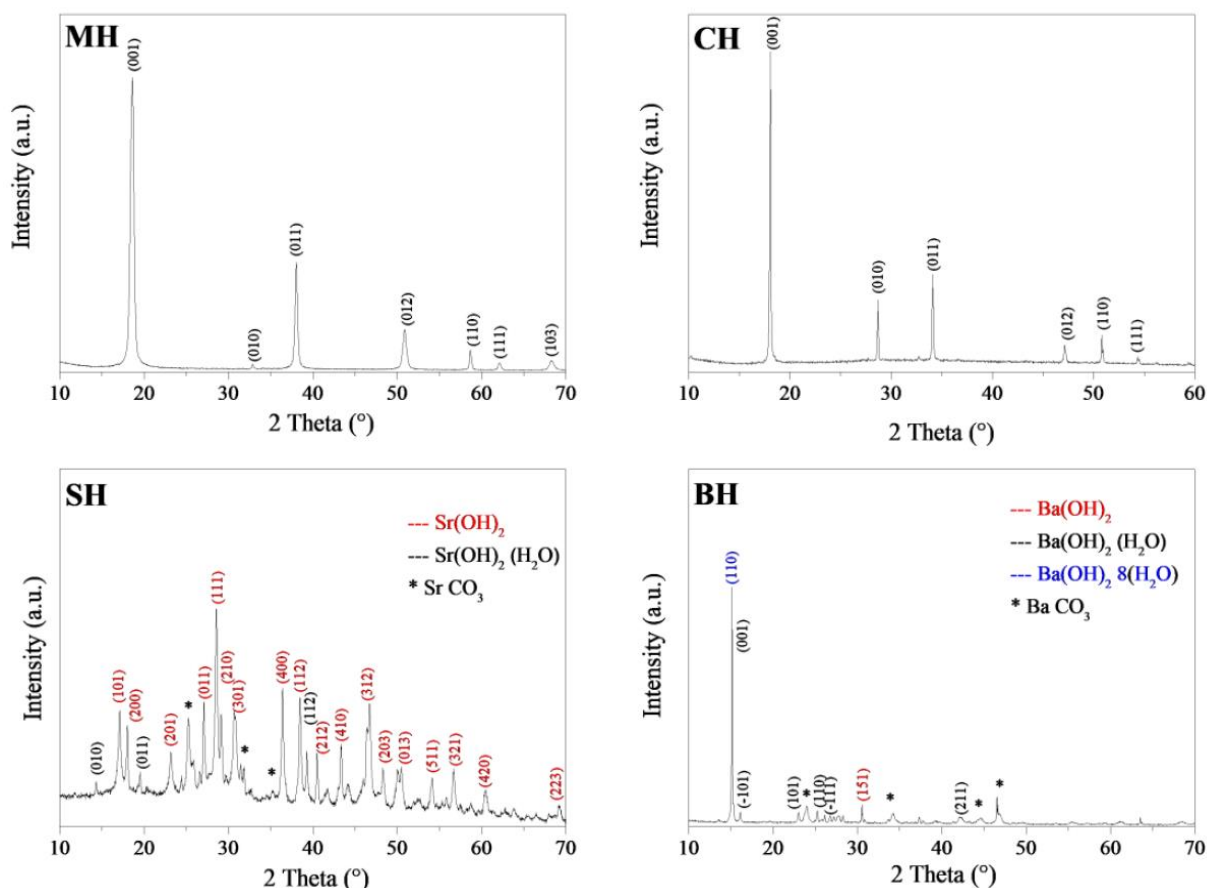


Figure 8.1. XRD patterns of the four suspensions dried under nitrogen. Main Bragg peaks are indexed by the Miller notation

For all the samples, the formation of hydroxide crystalline phases is observed (summarized in Table 8.1). In particular, all the Bragg peaks observed in MH and CH suspensions are well matched by the hexagonal structure of brucite ($\text{Mg}(\text{OH})_2$, ICSD pattern #98-008-9823) and by the hexagonal structure of portlandite ($\text{Ca}(\text{OH})_2$, ICSD pattern #98-020-2220), respectively. As concerned SH sample, from quantitative analyses is obtained a 68.2% of orthorhombic anhydrous strontium hydroxide ($\text{Sr}(\text{OH})_2$, ICSD pattern #98-001-5167), and 8.2% of orthorhombic monohydrate strontium hydroxide ($\text{Sr}(\text{OH})_2 \cdot \text{H}_2\text{O}$, ICSD pattern #98-006-0661). Finally, in BH sample three different forms of barium hydroxide are obtained: 39.0% monoclinic monohydrate barium hydroxide ($\text{Ba}(\text{OH})_2 \cdot \text{H}_2\text{O}$, ICDD pattern #01-077-2334), 11.5% monoclinic octahydrate barium hydroxide ($\text{Ba}(\text{OH})_2 \cdot 8\text{H}_2\text{O}$, ICSD pattern #98-003-3741), and 3.2% orthorhombic anhydrous barium hydroxide ($\text{Ba}(\text{OH})_2$, ICSD pattern #98-005-6828). In addition, the SH and BH suspensions show the presence of carbonates too, probably related to the soluble fraction that reacts with the carbon dioxide dissolved in water. In fact, more soluble is the

hydroxide, more amount of carbonate is observed in the dried powders: 46.3% of orthorhombic barium carbonate (BaCO_3 , ICSD pattern #98-020-2793) in BH, and 23.6% of orthorhombic strontium carbonate (SrCO_3 , ICSD pattern #98-020-2793) in SH, in agreement with the Ba(OH)_2 solubility in water, which is double of the Sr(OH)_2 one. So depending on the reaction conditions it is possible to have directly pure carbonates (rising the synthesis temperature) or pure hydroxides (inert atmosphere of reaction). The evaluations in terms of lattice parameters and crystallite size values, from each Bragg reflections (D_{hkl}), are reported in Tables 8.3-8.5, all data are elaborated by Rietveld method.

From such data, it is observed a good correspondence of the experimental lattice parameters with those of the standard reference patterns; besides MH and CH dried powders show a preferred orientation along the (001) basal plane. Moreover, all the crystallites exhibit a quite regular shape [1], and very small dimensions, with similar average D_{hkl} values of 22 ± 5 nm, 24 ± 2 nm and 25 ± 1 nm in relation to the anhydrous form of Mg(OH)_2 , Sr(OH)_2 , and Ba(OH)_2 , respectively. Really, as concerned Ca(OH)_2 , it is evaluated a larger average D_{hkl} value of 115 ± 5 nm, probably due to the typical oriented aggregation occurring during the drying process of the colloidal Ca(OH)_2 suspension [2]. Regarding the hydrated forms of Sr and Ba hydroxides, the crystallite sizes are larger as well, reaching the following values: 60 ± 20 nm for $\text{Sr(OH)}_2 \cdot \text{H}_2\text{O}$; 83 ± 2 nm and 300 ± 20 nm for monohydrate and octahydrate barium hydroxide, respectively.

Table 8.3. Lattice constants (a, c), relative intensities and crystalline size values (D_{hkl}) of the main Bragg peaks (MH and CH samples)

ICSD 98-008-9823			MH		ICSD #98-020-2220			CH	
$a = 3.14 \text{ \AA}$			$a = 3.14 \text{ \AA}$		$a = 3.59 \text{ \AA}$			$a = 3.59$	
$c = 4.77 \text{ \AA}$			$c = 4.77 \text{ \AA}$		$c = 4.91 \text{ \AA}$			$c = 4.91$	
<i>hkl</i>	<i>I</i> [%]	<i>2Theta</i> [°]	<i>I</i> [%]	D_{hkl} [nm]	<i>hkl</i>	<i>I</i> [%]	<i>2Theta</i> [°]	<i>I</i> [%]	D_{hkl} [nm]
001	96.3	18.598	100.0	16.8	001	63.6	18.067	100	109.9
010	2.6	32.879	1.16	18.0	010	9.3	28.674	6.28	109.6
011	100.0	38.038	27.47	18.7	011	100	34.100	34.78	110.4
012	37.8	50.881	11.75	21.2	012	24	47.145	6.7	115.8
110	27.8	58.703	4.06	23.8	110	29.7	50.795	3.47	118.3
111	15.7	62.144	2.30	25.4	111	16.2	54.353	1.76	121.2

Table 8.4. Lattice constants (a, c), relative intensities and D_{hkl} of main Bragg peaks (SH sample)

ICSD 98-001-5167			SH		ICSD 98-006-0661			SH-H ₂ O	
a = 9.89			a = 9.89		a = 3.65			a = 3.65	
b = 3.92			b = 3.92		b = 6.20			b = 6.20	
c = 6.12			c = 6.12		c = 6.71			c = 6.72	
hkl	I [%]	2Theta [°]	I [%]	D _{hkl} [nm]	hkl	I [%]	2Theta [°]	I [%]	D _{hkl} [nm]
101	55	17.024	46.94	21.5	010	94.3	14.279	55.36	42.3
200	19.3	17.925	23.29	21.5	011	92.5	19.477	54.18	46.5
201	37.4	23.107	35.11	21.7	100	42.6	24.380	30.63	51.3
011	37.1	27.000	36.53	22.0	002	60.7	26.55	42.57	50.0
111	100	28.493	100	22.1	110	41	28.366	31.92	47.7
210	20.4	29.055	20.42	22.1	111	46.4	31.395	33.51	46.3
301	45.5	30.784	45.37	22.2	021	60.5	31.778	53.59	46.7
400	21.6	36.309	20.64	22.8	102	49	36.342	49.92	52.6
112	47.2	38.388	42.45	23.0	112	78.2	39.231	72.28	56.9
212	11.1	41.633	10.09	23.4	121	100	40.454	100	58.9
410	22	43.237	24.73	23.6	133	26.9	42.937	22.01	63.3
312	55.7	46.627	54.80	24.1	031	19	45.922	23.61	69.3
203	18.1	48.218	15.56	24.4	200	19.4	49.961	25.10	79.0
013	13.9	50.392	12.69	24.8	113	18.9	49.989	22.33	79.0
511	19.5	54.011	19.52	25.6	123	23.3	56.616	38.84	100.3
321	14.6	56.642	15.50	26.2	221	15.6	60.436	30	117.9
420	7.6	60.224	7.49	27.2					

Table 8.5. Lattice constants (a, c), relative intensities and D_{hkl} of main Bragg peaks (BH sample)

ICSD 98-005-6828			BH		ICDD 01-077-2334			BH-H ₂ O		ICSD 98-003-3741			BH-8H ₂ O	
a = 11.03			a = 10.83		a = 7.05			a = 6.34		a = 9.27			a = 9.16	
b = 16.56			b = 17.02		b = 4.18			b = 4.18		b = 9.26			b = 9.19	
c = 7.11			c = 7.09		c = 6.33			c = 7.05		c = 13.84			c = 13.90	
hkl	I (%)	2Theta (°)	I (%)	D _{hkl} (nm)	hkl	I (%)	2Theta (°)	I (%)	D _{hkl} (nm)	hkl	I (%)	2Theta (°)	I (%)	D _{hkl} (nm)
210	33	16.931	32.41	24.3	001	100	15.018	100	81.1	110	100	14.813	100	333.2
002	29.9	25.028	42.86	24.6	-101	63.7	16.113	63.97	81	11-2	87.9	16.289	0.19	329.1
141	100	26.164	39.27	24.6	101	33.2	23.676	27.36	81	20-2	49.1	19.363	0.14	318.9
102	28.5	26.318	70.85	24.6	110	91.2	25.225	87.35	81.1	02-1	42.0	20.621	0.13	314.6
240	68	26.907	37.83	24.6	-111	59.3	26.757	57.77	81.3	11-3	34.3	21.522	0.16	312.3
301	96.2	27.285	100	24.7	-102	35.2	28.274	36.58	81.4	112	53.8	25.312	0.40	300.4
151	26.9	30.842	14.4	24.8	-211	26.7	33.627	24.06	82.4	20-4	31.8	26.518	0.10	297.3
142	28.4	34.197	14.56	25.1	012	51.4	37.290	45.11	83.3	023	22.4	29.973	0.19	287.6
242	36.7	37.075	43.78	25.2	-212	38.9	39.188	32.58	83.9	31-1	43.8	32.352	0.22	281.7
381	25.5	52.282	13.41	26.7	211	27.4	42.022	17.76	84.9	42-3	34.6	43.65	0.15	256.1

The molecular structure of the products, obtained from the four suspensions dried in oven, are analyzed by using FTIR spectroscopy. Figure 8.2 shows the FTIR spectra, which are attained in the range of 400-4000 cm^{-1} . In the MH and CH samples the characteristic sharp and strong peak at 3640 cm^{-1} is revealed, due to the O–H antisymmetric stretching vibrations [3]. Besides, in the CH sample the broad/sharp bands at 1500, 1080, 850 and 713 cm^{-1} are characteristic of the presence of CaCO_3 , occurred during the drying procedure in the oven [9, 11, 36]. In SH and BH samples, the observation of very narrow peak/doublet at about 3600 cm^{-1} are due to the anhydrous Sr/Ba hydroxides, while the peak at 3500 cm^{-1} (related to $\text{Sr}(\text{OH})_2$) or 3570 cm^{-1} (related to $\text{Ba}(\text{OH})_2$) is referred to the higher hydration level of the hydroxide forms [37]. As observed in CH sample, the presence of carbonates, from the bands around 1500, 1034, 860, 700 cm^{-1} , is revealed as well [18]. In particular, it is observed that, in BH sample, such bands showed a slight shift towards low wavenumbers respect to SH sample, confirming that the greater the masses of attached atoms, the lower the IR frequency at which the bond will absorb. In all the spectra, the following absorption bands, due to the physically adsorbed water molecule, are observed: a broad band around 3400 cm^{-1} , due to the symmetric and asymmetric stretching modes, and the overlapped adsorption peaks between 1440 and 1650 cm^{-1} , attributed to the O–H bending modes.

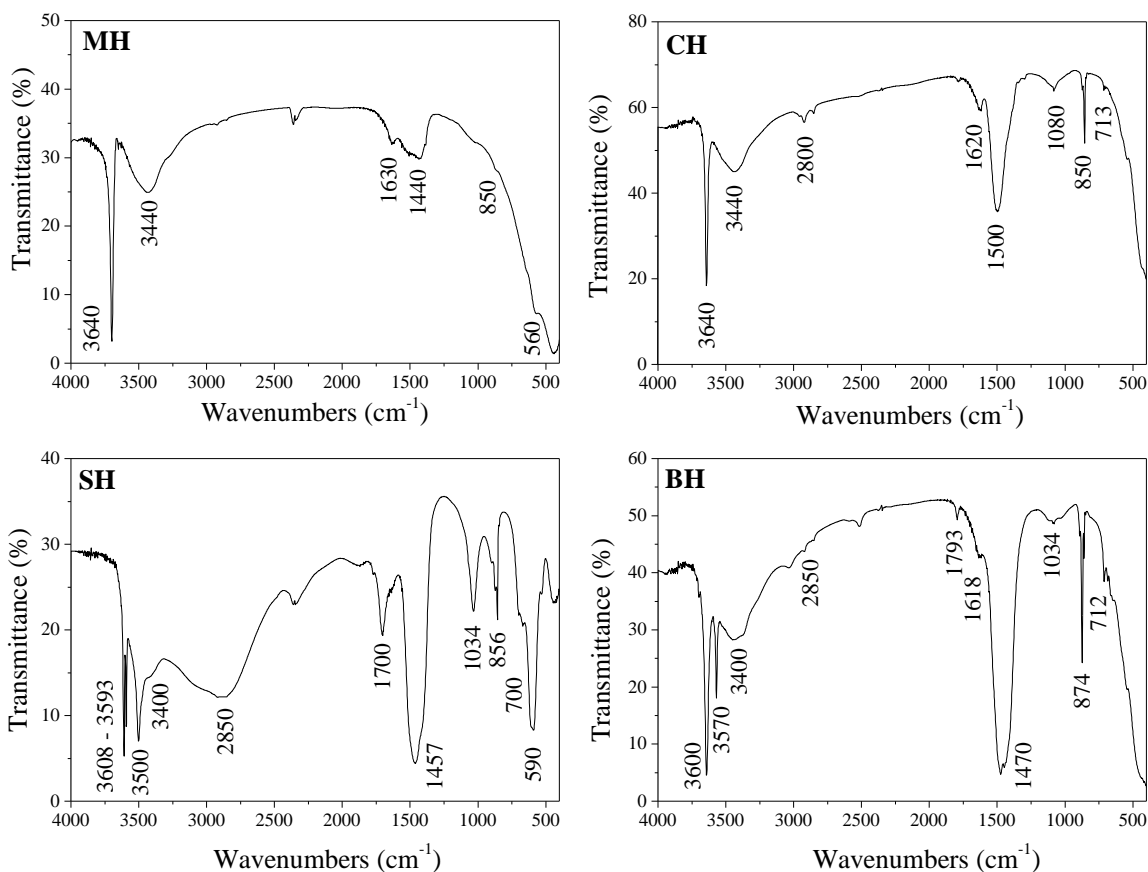
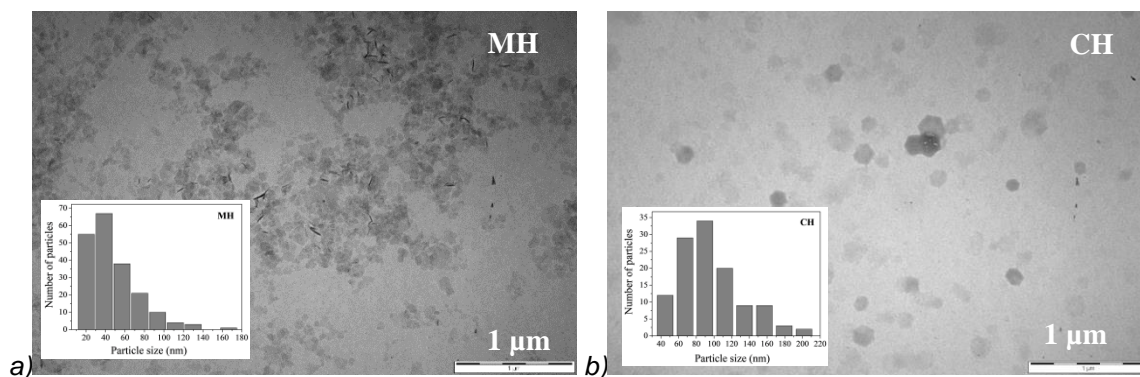


Figure 8.2. FTIR spectra of the dried powders obtained from the four suspensions

The morphological features and the dimensions of the synthesized nanoparticles are investigated by TEM, as shown in Figures 8.3-8.4. From Figures 8.3a-b it is possible to note that both MH and CH samples are composed by thin hexagonal lamellas, having a size distribution peaked at 40 nm and 90 nm respectively (insets). Moreover, the lamellas parallel to the electron beam show a thickness < 10 nm. Higher magnification images revealed that the lamellas are composed by a self-assembly of monodispersed primary nanoparticles, of about 2 nm for MH (Figure 8.3c) and of 5 nm for CH sample (Figure 8.3d).



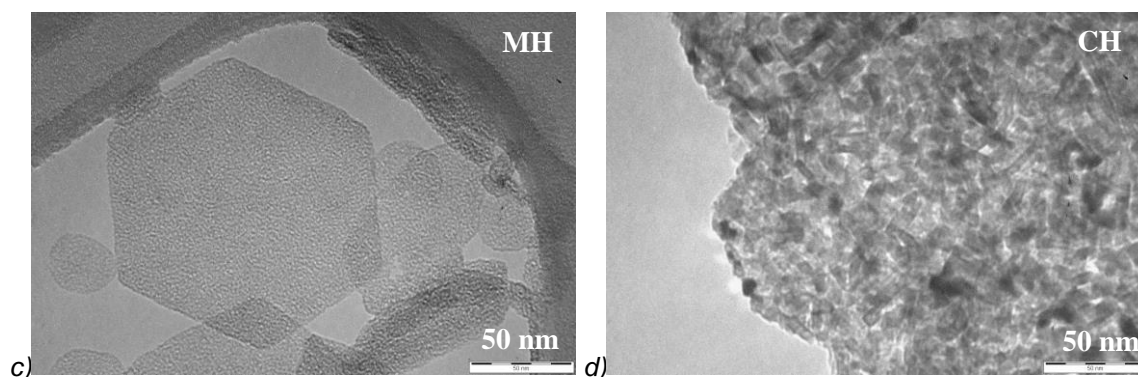
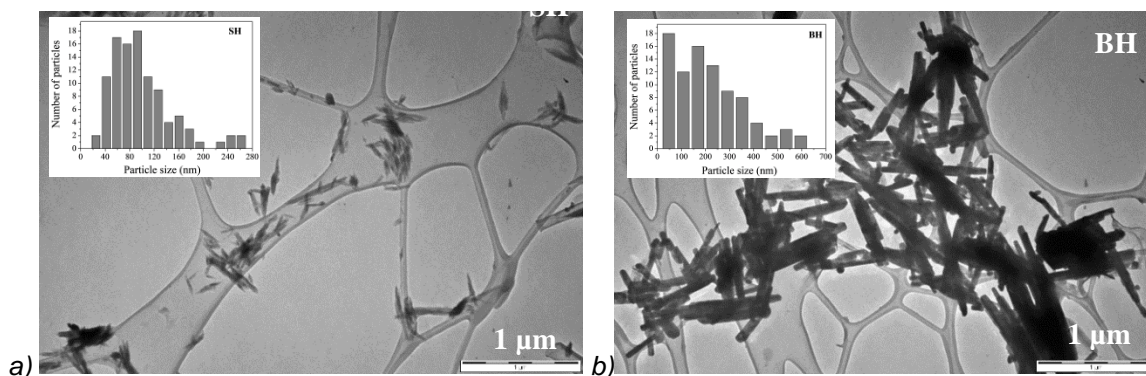


Figure 8.3. TEM images of the synthesized MH and CH nanoparticles: *a-b*) marker 1 μm ; *c-d*) marker 50 nm

TEM images of SH and BH samples show different morphologies (Figures 8.4 *a-b*): they are mainly constituted by a rod-like feature, with length of 30-250 nm (SH) and 50-600 nm (BH), as reported in the length distribution (insets). Rod thicknesses of about 30 nm (SH) and 60 nm (BH) are observed as well. Besides, in BH sample also hexagonal particles of dimensions of about 50 nm are observed (Figure 8.4*d*), probably related to different crystal forms of barium hydroxide, as revealed by XRD analysis. Despite of the different morphology, higher magnification images revealed that, as also observed in the hexagonal lamellas, the rods are composed by a self-assembly of primary nanoparticles: an average of 6 nm in SH (Figure 8.4*e*), and up to 15 nm in BH sample (Figure 8.4*f*).

The slight variation in the primary nanoparticles size can be attributed to the different supersaturation degree, reaching the highest value in the $\text{Mg}(\text{OH})_2$ suspension (or the lowest in $\text{Ba}(\text{OH})_2$), leading to a crystal nucleation that dominates crystal growth, ultimately resulting in smaller crystals (or larger crystals).



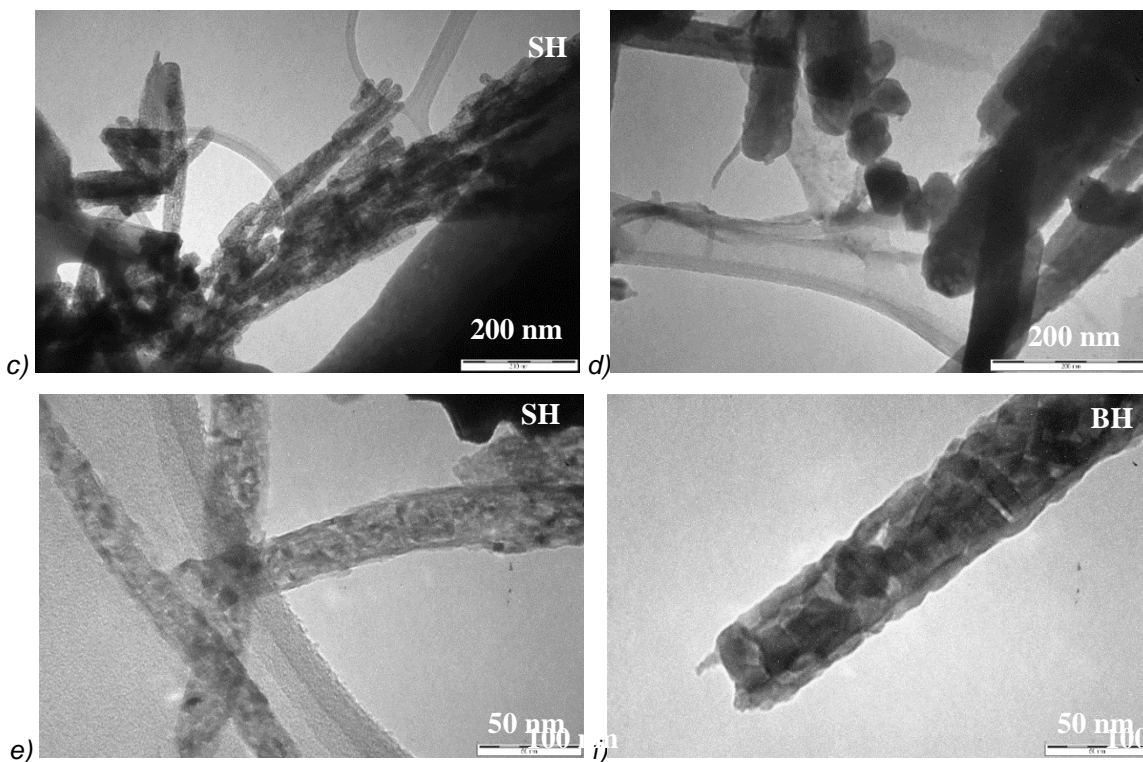
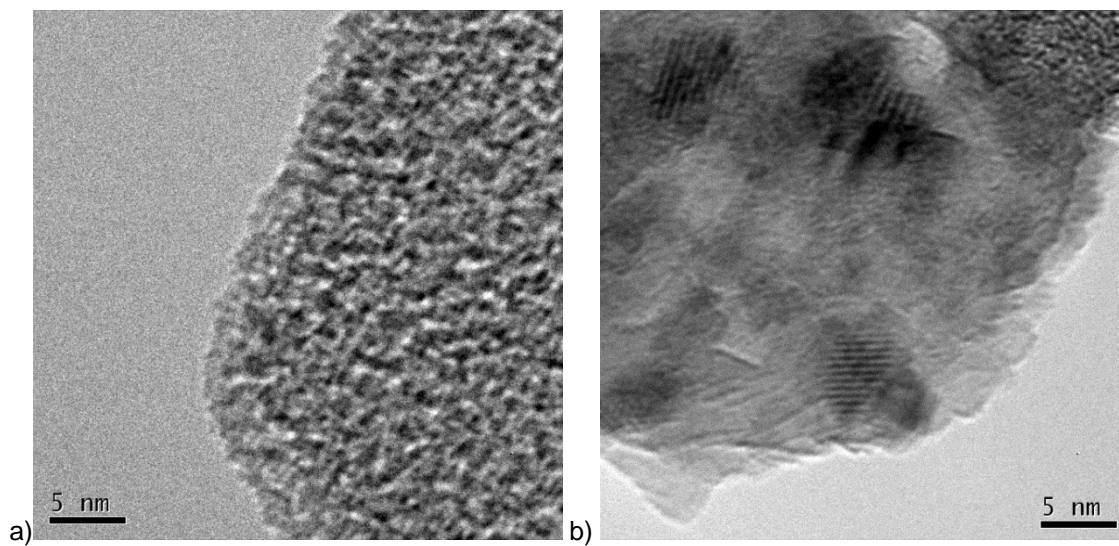


Figure 8.4. TEM images of the produced SH and BH nanoparticles: *a-b*) marker 1 μm ; *c-d*) marker 200 nm, *e-f*) marker 50 nm

To investigate the observed primary nanoparticles, HRTEM measurements are performed on the same samples as well and reported in Figure 8.5.



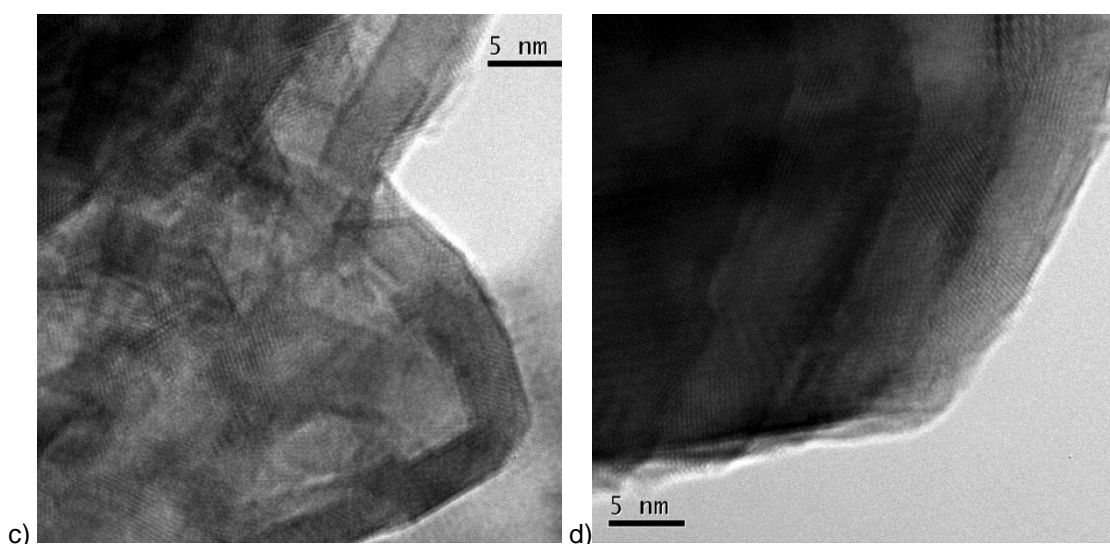


Figure 8.5. HRTEM images of the produced nanoparticles with marker 5 nm: a) MH, b) CH, c) SH, d) BH

The HRTEM images confirm the presence of different primary nanoparticles on each sample, related to the solubility (or to the supersaturation degree) for each obtained compound. In fact, for MH (Figure 8.5a) primary nanoparticles with dimensions of about 2 nm are clearly observed, while for CH (Figure 8.5b) the primary particles result of about 5 nm (as highlighted from the moiré fringes). For the SH sample (Figure 8.5c) the primary particles are more difficult to distinguish, but maybe they result of about 5 nm in dimensions as well. Finally in the BH sample (Figure 8.5d), it is evident a superimposition of hexagons, having lateral sizes of about 20 nm, which appear to be very thin lamellas superimposed by sliding: it is possible that these hexagons (about 50 nm in size) represent the primary particles for barium, because of the greater solubility of barium hydroxide.

So the proposed route results effective to synthesize various alkaline-earth metal hydroxide or carbonate nanoparticles, depending on the operative conditions (atmosphere and temperature). From XRD analysis and from TEM analysis the average particle size is in the nano range, but HRTEM images revealed that all the obtained samples are composed by superimpositions of primary monodispersed nanoparticles, having dimensions of about 2 nm for magnesium, 5 nm for calcium and strontium and about 50 nm for barium. The features of the synthetic procedure here proposed can be crucial for a large-scale production of the alkaline-earth metal hydroxides, so favoring their usage in more extensive applications in several fields: from the removal of water contaminants [4], additive in thermoplastics as well as for

lubricants and greases [5,6], antibacterial activities [7], optical or CO₂ sorption properties [8, 9], catalysis [10] and cultural heritage field [11-15].

8.2 Magnesium hydroxide nanoparticles for deacidification of waterlogged wood

In the field of preservation of the cultural heritage, the conservation of waterlogged wooden artifacts is extremely important since these artifacts represent an informative but extremely rare source of knowledge. Indeed, wooden relics contain important evidence about the main techniques and raw materials used for structures and artefacts, providing unique information about the economy, industry and buildings of ancient human societies. In addition, waterlogged environments usually provide the best possible conditions for limiting the decomposition of wood over time, as can be seen from the well-preserved archaeological objects and ships found after many centuries under the sea or at the bottom of lakes [16]. Nevertheless, the biological, chemical and mechanical changes caused by acid hydrolysis during long-term exposure to a marine or underground environment make the preservation of wooden artifacts difficult [17]. The iron present in the wooden structures corrodes and accelerates the degradation of the cell components. Anaerobic bacteria also contribute to the presence of iron sulfides within wooden structures (e.g. pyrite and pyrrhotite) by breaking down the abundant iron minerals present in the soil and by using sulfur from decaying vegetation [18]. If the reduced sulfur species cause little threat in anoxic conditions, once exposed to oxygen some of them can easily oxidize and form sulfuric acid.

Due to the fragile conditions of waterlogged woods, at first, research into treatments for waterlogged wood was mainly aimed at developing methods to prevent damage due to stress during the drying process. The most common treatment of waterlogged wood involved using an aqueous solution of polyethylene glycol (PEG) to replace the water and prevent cracking while the wood was drying [19]. Nevertheless, often these conventional procedures fail due to the formation, after many years from the treatment, of visible precipitates of acidic salts causing a pH \leq 3.5 on wood surface. With the introduction of nanotechnology in cultural heritage research, attention was focused on the use of alcoholic dispersions of calcium hydroxide (CH) or magnesium

hydroxide (MH) nanoparticles (NPs), but they cannot be used in large-scale treatments (conservation of boats, bridges and large artifacts), due to the alcoholic solvents. In fact, Health and Safety regulations have established that “VOC emissions produced by alcohol are harmful both to the environment and to human health as well as posing a fire hazard in the early stages” [20]. Therefore, to date, a satisfactory solution for the deacidification of ancient wood on a large scale has still not been found. In this paragraph eco-friendly, curative and preventive treatments using nanoparticles of calcium and magnesium hydroxides dispersed in water are tested for the first time to solve this problem. These tests are performed on archeological wood samples, containing the acidifying precursors (iron and sulfur), from a Gallo-Roman shipwreck (dated back to second century BC) loaned to the Atelier de Recherche et de Conservation ARC-Nucléart (Grenoble, France). For the preventive aim, some samples were treated with the NPs suspensions before an acidification process had begun, while, for the curative treatments, acidic or properly acidified samples were used. Preventive treatments include all direct measures and actions aimed at avoiding and minimizing future deteriorations or loss of materials or artefact, while curative treatments includes all actions directly applied to an object aimed at arresting damaging processes and, when possible, stabilizing their conditions against further deterioration.

The samples used in our work come from a wooden Gallo-Roman wreck, discovered in Lyon (France) in 2003 (Figure 8.6a), which was about 17 m long and was cut into 6 parts and stored in a lake near Lyon until 2014, when the French authorities decided to take it out of water and begin recovery and conservation treatments. The workshop ARC Nucléart was assigned the conservation and restoration work. The first step involved removing the metal parts (nails, etc.), salt efflorescence, mud and debris (quartz and calcite) covering the surface of the wreck. The next step was to immerse the wreck in pools containing an aqueous solution of 20 wt.% of PEG 200 (Merck KGaA, Darmstadt, Germany), followed by a treatment with 35 wt.% of PEG 2000 (Merck KGaA, Darmstadt, Germany), for a minimum of 4 months respectively (Figure 8.6b), to prevent the structure of the wood from collapsing during the subsequent drying process (Figure 8.6c).



Figure 8.6. a) Excavation site in Lyon; b) the large pools containing the polyethylene glycol (PEG) where the wreck is immersed to prevent the structure from collapsing and cracking during wood drying; c) drying process carried out inside the apparatus for large-scale lyophilization procedure.

For what concerns the available samples for the proposed experimentation, they were all contaminated by acid precursors and ranged approximately from $(2 \times 1 \times 1) \text{ cm}^3$ up to $(5 \times 3 \times 2) \text{ cm}^3$. Obviously the choices for the experimental plan in the present study were driven by the availability of the samples for the different treatments. The selected wood samples for NPs treatment were prepared by washing them in deionized water in order to remove the PEG, which could prevent the penetration of the NPs in the wood channels (vessels, water-conducting cells). To completely remove PEG from the treated wood, the samples were immersed in deionized water for several days and washed regularly. After the washing process, the samples were dried by means of a lyophilization procedure, which reduces the risk of damage or cracks. Once washed and dried, the samples were ready for the NPs treatments, whose main steps are schematized in Figure 8.7.

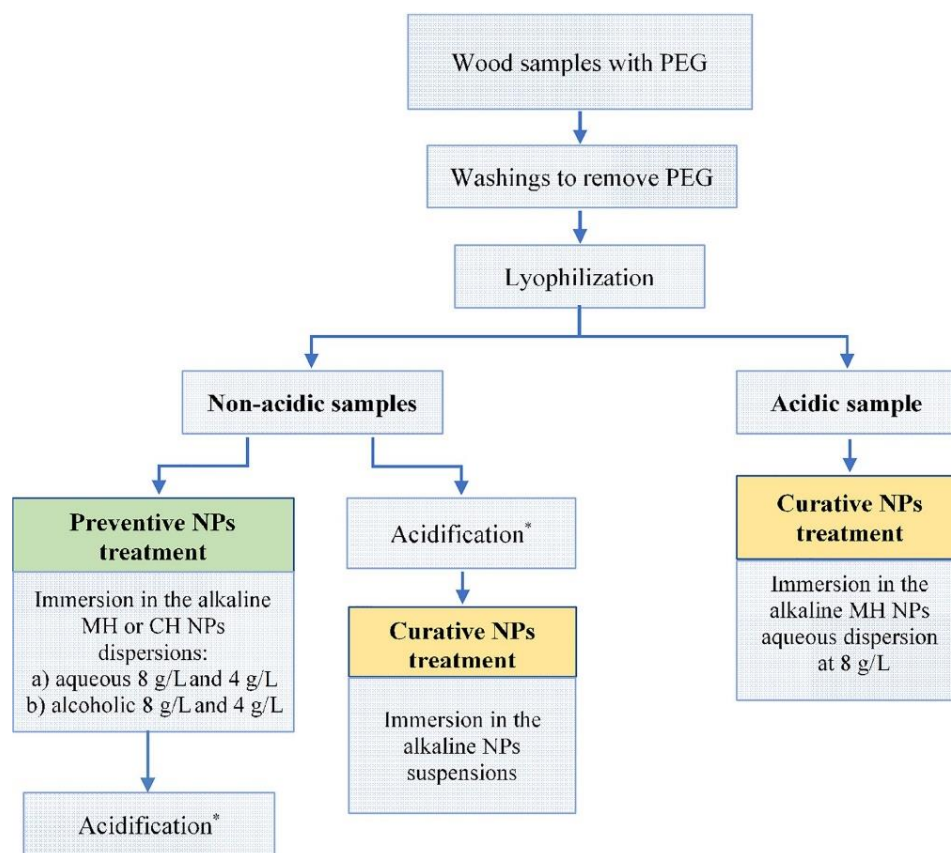


Figure 8.7. Scheme of the procedures followed for preventive and curative treatments of the Gallo-Roman wreck samples containing the acid precursors (iron and sulfur)

Specifically, some acidic samples were considered only for the curative treatment, while other non-acidic samples (but containing the acid precursor as well) were divided in two groups: the first group was selected for analyzing curative NPs treatments, and the second group for preventive NPs treatments. In all cases, the treatment was carried out by immersion of the wood samples in the NP suspensions for 30 days, considering an amount of nanoparticles dispersion over grams of wood of about 30 mL/g. In the case of the non-acidic samples, an acidification process was considered and it consisted in a hydrothermal ageing, carried out as follows: the samples were maintained at relatively high temperature ($T = 80 \pm 2^\circ\text{C}$) and high relative humidity ($\text{RH} = 80\% \pm 5\%$) for 48 h [21, 22]. In particular, to evaluate the curative efficacy of the NPs treatment, the acidification was performed before the treatment; while, to evaluate the preventive efficacy the acidification was performed after the NPs treatment.

Concerning the MH-based treatments, both alcoholic (2-propanol) and aqueous suspensions were considered, at a concentration of 8 g/L. This concentration was chosen because it is perfectly stable, thus guaranteeing a more homogeneous

dispersion over long periods, which is necessary for the immersion of large objects. In order to compare these results with previous literature, the alcoholic MH suspensions were prepared also at 4 g/L. For the CH-based treatments, we used only alcoholic suspensions and we did not investigate the aqueous dispersion because of its low stability and reactivity over time. In summary, for the treatments of the non-acidic samples, six suspensions were considered, four based on the MH NPs dispersed either in alcohol (a), or in water (w), and two based on the CH NPs dispersed in alcohol. They are named: MH_{a4}, MH_{a8}, MH_{w4}, MH_{w8}, CH_{a4} and CH_{a8}, where the subscripts “8” and “4” refer to the concentration of 8 g/L and 4 g/L, respectively.

A crucial step when studying the deacidification treatments on the wood samples is the characterization of the wood region around the position of the nail, that is at the origin of the presence of acidification precursors. Figure 8.8 reports the SEM image of a representative polished section of a core around a nail together with the EDX mapping of the acid precursors iron and sulphur, with the diffusion of iron and sulfur along the radial section. As a result, iron can be found from the surface up to 4 mm thick (green zone) with higher concentration mainly localized along the inner surface, while sulfur compound is essentially localized in the external part up to about 1 mm from the inner surface.

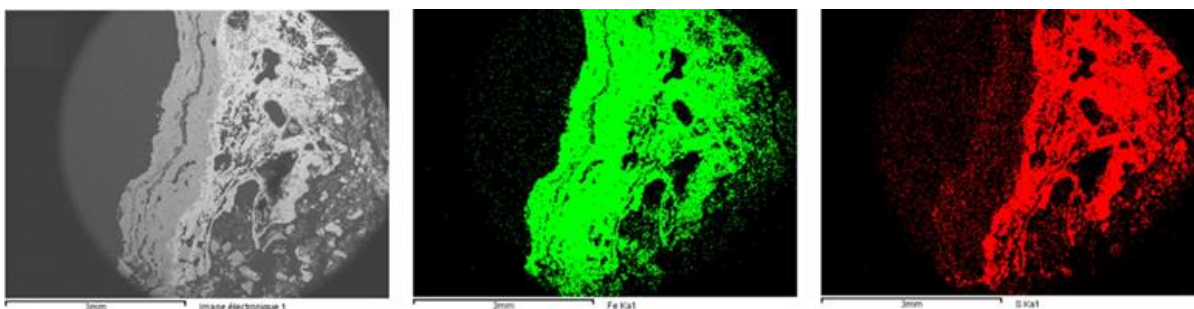


Figure 8.8. SEM image of a representative polished section of a core around a nail together with the EDX mapping of the acid precursors iron (green) and sulfur (red)

The untreated dry fragments were analyzed by optical stereomicroscope in order to determine the nature of the wood samples (Figure 8.9). They present a cellular structure, typical of hard woods (oak). In fact, 35-70% of the wood volume is made up of fiber cells and 5-60% of the wood volume is made up of vessels [23], as shown in Figure 8.9a. Furthermore, the vessels are characterized by diameters ranging from 50 to 500 μm and they are organized in a semi-ring porous arrangement, as

reported in the literature for hard woods [24]. The vessels were originally saturated with a whitish phase, due to PEG (Figures 8.9a-b) used in earlier treatments. This phase disappeared after the washing process (Figures 8.9c-d).

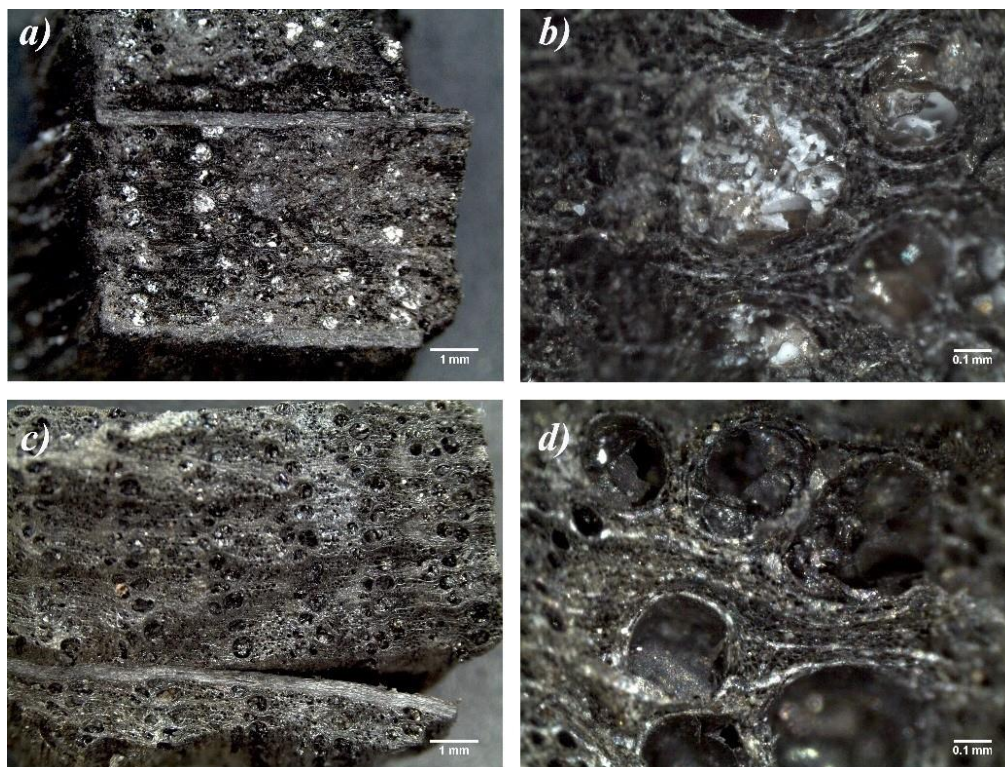


Figure 8.9. Optical stereomicroscopy images referred to the untreated dry wooden fragments before PEG washings (a,b) and after PEG washings (c,d).

The XRF analyses on the untreated dry samples revealed the presence of Fe and S, confirming and quantifying the occurrence of acid precursors in the selected samples. Small amounts of Ca and Si were also measured, probably related to the impregnation of the wood for over 2000 years while the wreck remained underground and also in the lake. The corresponding XRD characterization showed mainly the presence of pyrite (FeS_2 , ICSD #98-005-3529); low percentages of quartz (SiO_2 , ICSD #98-0041672) and calcite (CaCO_3 , ICSD #98-001-8164) were also observed, in agreement with the XRF analysis. The quantitative results from the XRF and XRD measurements are summarized in Table 8.6.

Table 8.6. XRF and XRD quantitative analyses of the untreated dry wood samples

XRF				XRD		
Fe	S	Ca	Si	FeS ₂	SiO ₂	CaCO ₃
15%	5%	0.8%	0.2%	95.5%	4.0%	0.5%

The deacidification efficiency of CH and MH NPs suspensions is evaluated by measuring the pH variations, as reported in Table 8.7. Regarding the pH measurements, which are a crucial step in assessing the efficiency of the NPs treatments, we followed the procedure reported in the literature [22]: 1 g of wood powder was suspended in 5 g of deionized water for 24 h, in a closed container. Then, we measured the pH value of the supernatant water by means of a digital pH-meter, equipped with a combined electrode (Mettler-Toledo, model S220, Mettler Toledo, Columbus, OH, USA). As described above, the treatments carried out on the “non-acidic” fragments were performed with both preventive and curative aims. For untreated samples, the hydrothermal ageing caused a dramatic decrease in the pH value of about 70%, reducing from 5.3 ± 0.1 (slightly acidic) up to 3.7 ± 0.1 (definitely acidic). Indeed, the presence of the acid precursors during the hydrothermal ageing clearly accelerated the acidification process of the wooden samples, as expected due to the fact that high relative humidity is linked to the development of acidity and due to the increased reactivity of the chemical processes with temperature [25]. It is a reliable estimate that the pH value reached after the hydrothermal ageing would be the final pH after a natural ageing, highlighting the necessity for preventive treatments, here proposed for the first time.

Table 8.7. Results of pH values refer to the “non-acidic” untreated wood samples, before and after the acidification treatment, and treated wood samples, in relation to the preventive and the curative treatments; results of pH values of the highly acidic wood sample, untreated and curative treatment

	“Non-Acidic” Wood Samples		Acidic Wood Sample	
Untreated	pH before acidification	pH after acidification	pH Untreated	pH Treated with MH _{8w}
	5.3 ± 0.1	3.7 ± 0.1		
Treated	pH preventive treatment #	pH curative treatment §		
CH _{4a}	7.5 ± 0.1	6.6 ± 0.1		
CH _{8a}	7.5 ± 0.1	6.7 ± 0.1	1.6 ± 0.1	6.7 ± 0.1
MH _{4a}	7.8 ± 0.1	7.7 ± 0.1		
MH _{8a}	7.9 ± 0.1	7.7 ± 0.1		
MH _{8w}	7.8 ± 0.1	7.7 ± 0.1		

pH values of the samples treated and then acidified by hydrothermal ageing; § pH values of the samples acidified and then treated by hydrothermal ageing

As can be seen in Table 8.7, all the preventive treatments proved to be highly effective, irrespective of the solvent concentration and the alkaline earth hydroxide used in the treatments themselves. This makes it possible to tailor the treatment to the specific requirements of the protective procedures being performed, something that is crucial if we consider the variety of needs that exist in conservation science. The results of curative treatments on the artificially acidified samples were also highly satisfactory. In fact, all of them resulted in a neutral pH value in the treated samples. These results confirm the efficiency of alcohol-based treatments as already observed in the literature for similar suspensions [26-28]. However, also the way for water-based $\text{Mg}(\text{OH})_2$ curative treatments is effective, representing an eco-friendly solution for large-scale applications, such as for wrecks and wooden artifacts. In fact, the MH aqueous suspension for the curative treatment of the very acidic sample ($\text{pH} = 1.6 \pm 0.1$) gives a satisfactorily deacidified, as shown in Table 8.7. Another important aspect to be considered was the preservation of the aesthetic features of the treated samples, which must remain unchanged as far as possible. The observations indicated that the treatments, irrespective of the dispersing medium, did not alter the samples, and any white hazes or residual substance would be not visible, by naked eyes, on the treated surfaces after the immersions in the NPs suspensions. An interesting parameter for conservation is the penetration of the treatments into the volume of the samples. This analysis is carried out only on the MH-in water treatment, as the best candidate for eco-friendly large-scale applications. To perform this analysis, the treated sample is cutted longitudinally to the fibers in order to obtain a radial section (where the fiber walls of the wood can be distinguished). The X-ray microanalysis, carried out by SEM-EDX, revealed the presence of Fe and S, and traces of Ca and Mg. The mapping of Mg confirmed a homogeneous distribution of MH NPs throughout the whole depth of the sample, as shown in Figure 8.10 (green colour).

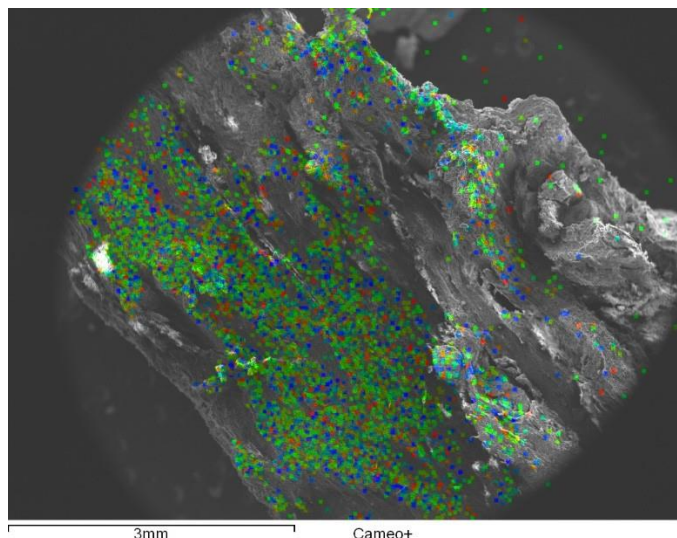


Figure 8.10. SEM-EDX image showed the penetrations of MH NPs inside the sample, following the Mg mapping (green)

The treatments based on MH NPs dispersed in water, therefore, proved to be a greatly efficient method of deacidification in both preventive and curative actions, serving to prevent the many phenomena that dramatically affect the life of ancient artifacts over the course of time. The large volumes of NPs dispersions and the use of water as solvent are vital for large-scale applications, since it allows operating with large wooden objects without the use of volatile organic compounds that are flammable and harmful for the environment and for human health. In today's society, where sustainability and environmental protection are crucial issues, the use of eco-friendly, non-destructive treatments is of fundamental importance for conservation science.

8.3 Synthesis of magnesium oxide nanoparticles

In order to obtain MgO NPs, the reagents are always magnesium chloride and an anionic resin in OH⁻ form (Dowex 550A). As in paragraph 8.1, first Mg(OH)₂ in form of NPs is synthesized using the innovative ion exchange process, then it is used as precursor to produce MgO NPs. In this case the synthesis is carried out through a prototype system on a total volume of 1.5 liters, obtaining about 25 g of Mg(OH)₂

with a single synthesis of 10 minutes. From the produced suspension, the hydroxide NPs are obtained in powder form using two different methods:

a) lyophilization (MH_{LYO}): 150 ml of suspension are frozen for 24h and subsequently subjected to lyophilization for about a day;

b) drying (MH_{OVEN}): 150 ml of suspension are put in an oven to dry at 80°C for about two days.

The obtained magnesium hydroxide suspension and powders are characterized by XRD, BET, TEM and TGA. Figure 8.11 shows the XRD patterns of the three samples.

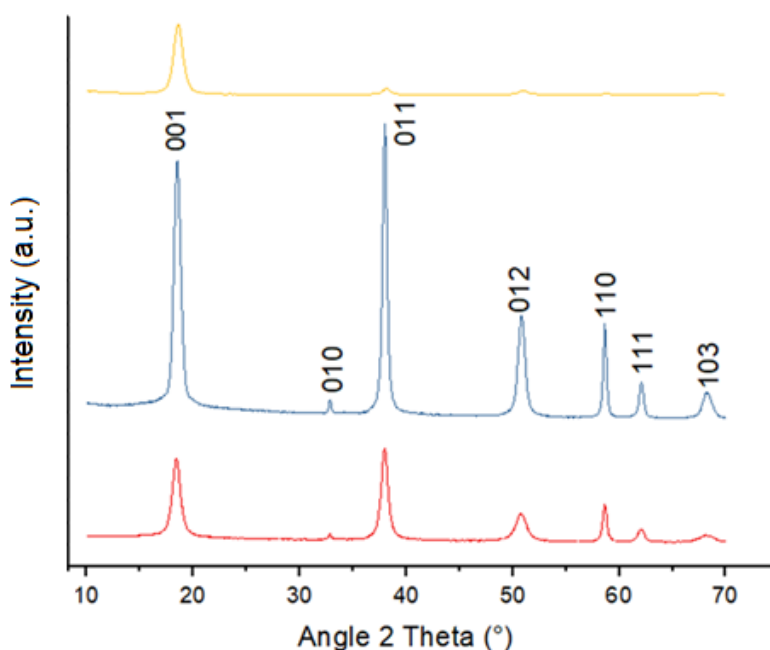


Figure 8.11: XRD pattern of the samples MH_{SUSP} (yellow), MH_{OVEN} (blue) and MH_{LYO} (red) with Bragg peaks indexed according to ICSD #98-016-9979 of the compound Mg(OH)₂

The powder samples show very similar XRD patterns, characterized by pure Mg(OH)₂ with hexagonal structure (ICSD #98-016-9979). On the other hand, in the pattern of the suspension dried directly on a single crystal, a preferential orientation on the basal atomic plane (001) of the crystalline cell of brucite can be observed. In fact, during evaporation an arrangement of the lamellae presumably occurs along the plane of the sample holder, so that the most "frequent" plane becomes the basal plane. Table 8.8 shows the cell parameters obtained for the three samples together with the grain sizes, calculated by the Rietveld method.

Table 8.8. Crystallographic data from the XRD patterns of samples M MH_{SUSP}, MH_{OVEN} and MH_{LYO}, reporting the cell parameters together with the relative intensity and Dhkl calculated for the main peaks (ICSD #98-008-9823)

ICSD #98-008-9823			MH _{SUSP}		MH _{OVEN}		MH _{LYO}	
a = 3.14 Å c = 4.77 Å			a = 3.14 Å c = 4.79 Å		a = 3.15 Å c = 4.78 Å		a = 3.14 Å c = 4.79 Å	
Hkl	I [%]	2Theta [°]	I [%]	D _{hkl} [nm]	I [%]	D _{hkl} [nm]	I [%]	D _{hkl} [nm]
001	96.3	18.598	100	7.5	96.2	12.61	97.29	8.34
010	2.6	32.879	0.22	7.77	5.15	12.95	5.15	8.57
011	100.0	38.038	9.43	7.88	100	13.13	100	8.69
012	37.8	50.881	5.29	8.25	37.86	13.76	37.92	9.1
110	27.8	58.703	2.55	8.56	27.75	14.28	27.59	9.47
111	15.7	62.144	0.79	8.72	15.72	14.55	15.65	9.62
103	15.3	68.295	2.49	9.03	15.39	15.1	15.43	9.96
			Σ=	8,2	Σ=	13,8	Σ=	9,1
			σ=	0,6	σ=	0,9	σ=	0,6

It is observed that the average value of the crystallite size varies between 8.2 ± 0.5 and 14 ± 1 nm, from which a slight growth of the crystallites is deduced by drying the hydroxide in an oven at 80°C for a extended period of time (about 2 days).

Figure 8.12 shows the TEM images of the three samples with 200 nm markers, preparing for the powder samples some suspensions in ethanol at suitable concentrations.

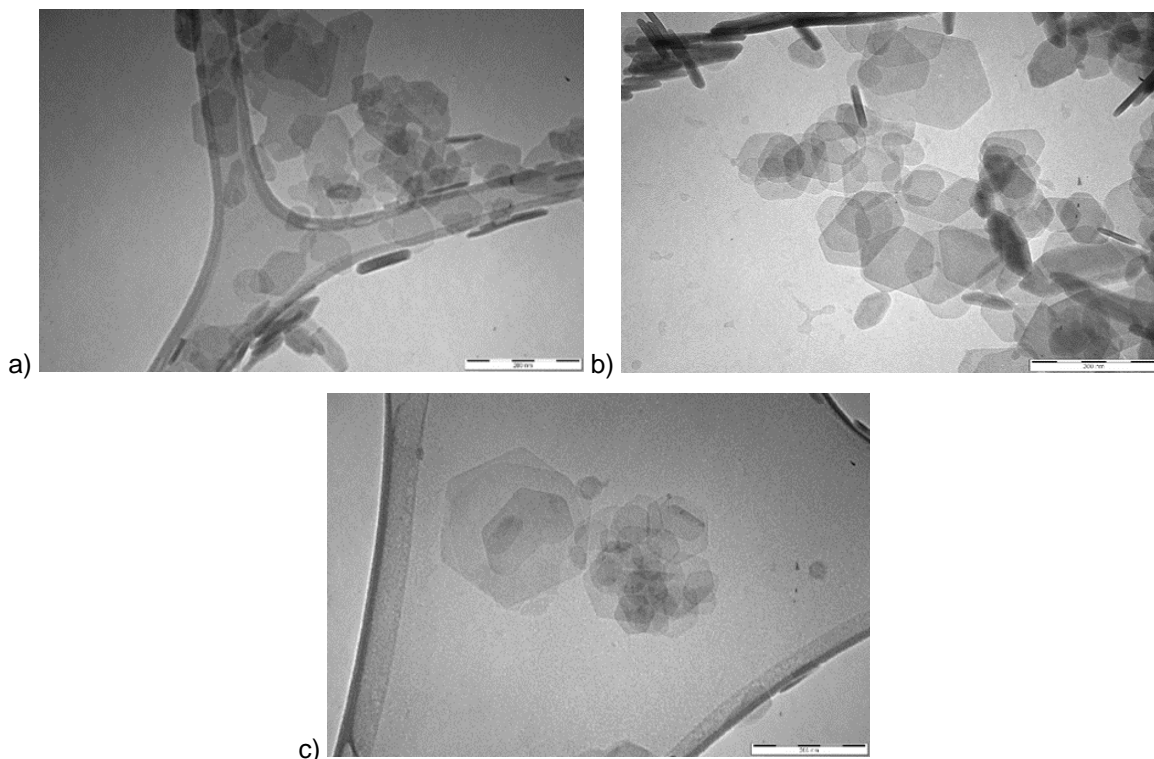


Figure 8.12 TEM images of samples a) MH_SUSP, b) MH_OVEN and c) MH_FREEZE with 200 nm marker

The morphology with hexagonal lamellae of the hydroxide is confirmed by all the images: the NPs are in hexagonal shape, with dimensions generally less than 100nm, with a thickness of 5-10 nm, such as to make them almost transparent to the TEM electron beam. However, it can be seen from the comparison of the various samples that the lyophilized hydroxide nanoparticles are those with the greatest degree of agglomeration.

Figure 8.13a shows the adsorption isotherm only of MH_{OVEN} sample, because the isotherm of MH_{LYO} sample results similar both in form and in values. A weak presence of hysteresis can be noted, but the isotherm can be classified as Type IV anyway, typical of mesoporous materials. From these measurements specific

surface values equal to 85.5 m²/g and 83.2 m²/g are obtained for MH_{OVEN} and MH_{LYO} samples respectively.

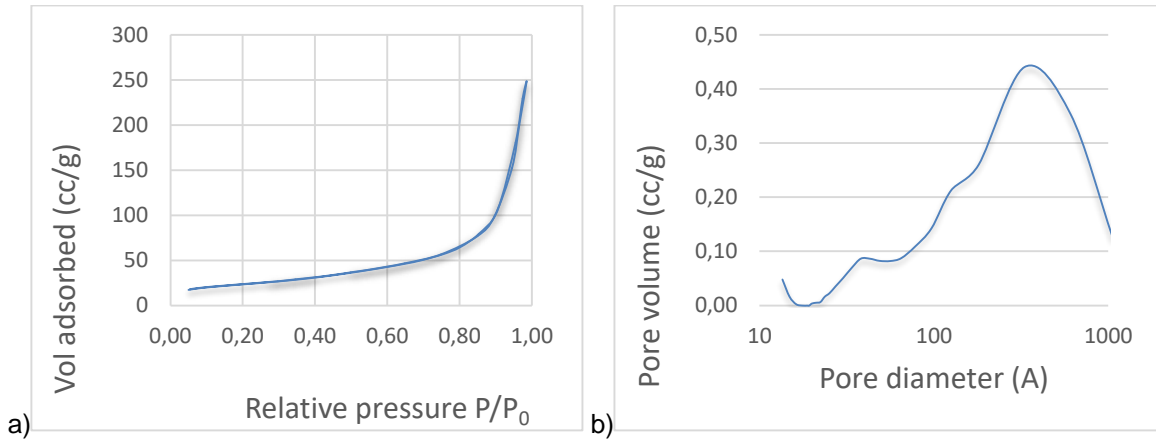
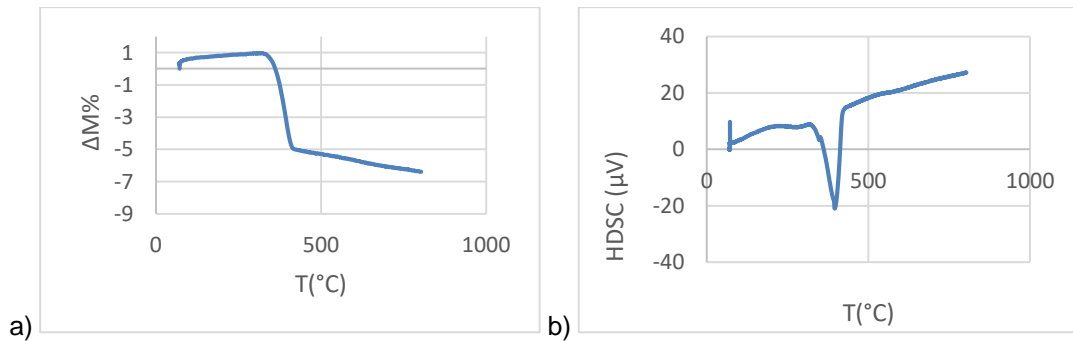


Figure 8.13. a) nitrogen adsorption isotherm of MH_{OVEN} sample, b) pore size distribution obtained from the desorption branch of the isotherm

The pore distribution was determined from the desorption branch of the isotherm using the BJH method and is reported in Figure 8.13b for MH_{OVEN} sample. The prevalence of mesopores (20-500 Å) can be seen from the pore distribution. The average size distribution of the pores estimated by BJH method reveals an average porosity of about 18 nm for both samples.

Finally, in Figure 8.14 the thermogravimetric analysis for the two powder samples are shown.



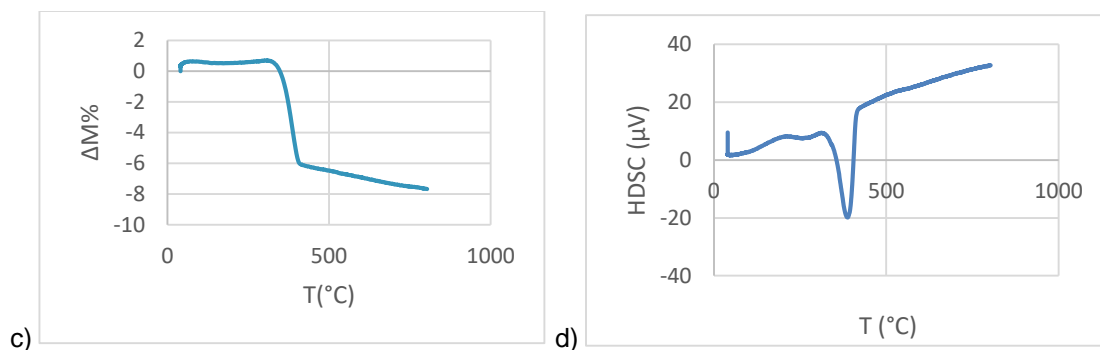


Figure 8.14. TGA profiles related to samples a) MH_{OVEN} and c) MH_{LYO}, with the relative DSC values: b) MH_{OVEN} and d) MH_{LYO}

The TGA profile of the MH_{OVEN} sample shows a phase of pronounced weight loss in the range 340-420°C, with the endothermic peak at 400°C, as can be seen from the DSC profile, attributable to the transformation into magnesium oxide. Weight loss during this decomposition is approximately 26.9%, perhaps due to an incompleteness of the decomposition reaction under the measurement conditions. The TGA profile of the MH_{LYO} sample shows a weight loss phase in an almost similar range, 330-400°C, with the endothermic peak at 395°C, as can be seen from the DSC profile, associated with the transformation into magnesium oxide as well. Weight loss during this decomposition is approximately 28.2%, which is more similar to the theoretical value of 30.8%.

Considering the various characterizations, there are no substantial differences between the two different methods for obtaining the powder precursor (lyophilization and oven). Therefore, the hydroxide powder from the oven is used to obtain nanoparticles of MgO through a dehydration reaction by raising the temperature, because it appears less agglomerated from TEM images. During this reaction Mg(OH)₂ and MgO maintain the same crystallographic orientation, as shown in Figure 8.15. The closely spaced hexagonal structure of O²⁻ ions rearranges into a closed cubic structure; then the remains of the hexagonal brucite lamella are retained.

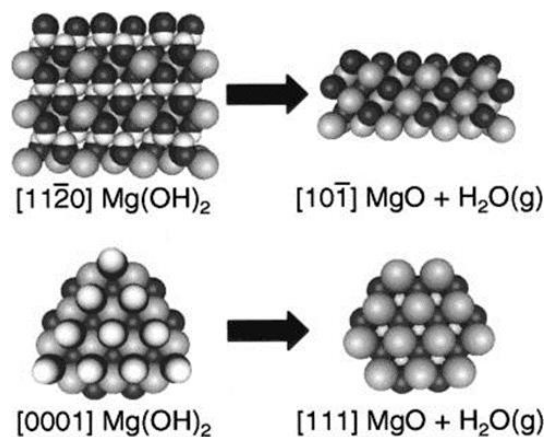


Figure 8.15. Crystallographic orientation of magnesium hydroxide and oxide during transformation

A temperature of 500°C is chosen to allow this reaction to occur, considering different stasis times (2h, 4h, 6h), in order to investigate if this time affects the dimensions and the morphology of the final oxide particles. These calcination tests are reported in table 8.9 together with the weight loss.

Table 8.9. Weight loss % of calcined MHOVEN at 500°C for 2h, 4h, 6h

Sample	Inizial weight (g)	Final weight (g)	Weight loss %
MO_2h; 500°C	3.00	2.15	28.3
MO_4h; 500°C	3.00	2.19	27.0
MO_6h; 500°C	3.00	2.13	29.0

The weight loss corresponding to the theoretical value of the decomposition reaction is equal to 30.8%, so the samples calcined for 2h and 6h show weight losses which are closer to the theoretical value. In the sample calcined for 4h it is possible that a slight rehydration of the powder occurred (but it is not revealed from the XRD pattern).

Once the calcination is carried out at different times, the samples obtained are again characterized from a structural and morphological point of view, by means of XRD and TEM. Figure 8.16 shows the XRD patterns of the three calcined samples.

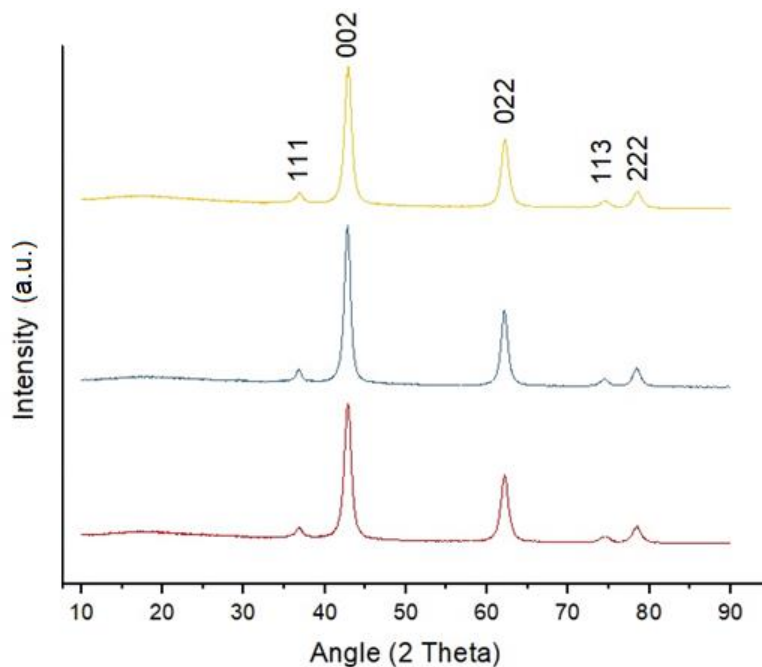


Figure 8.16. XRD pattern of samples calcined at 500°C: MO_2h (red), MO_4h (blue) and MO_6h (yellow) with Bragg peaks indexed according to ICSD #98-017-0905 of the compound MgO

The powder samples are characterized by very similar XRD patterns, characterized by pure MgO (ICSD #98-017-0905). Table 8.10 shows the cell parameters obtained for the three samples together with the grain sizes, calculated by the Rietveld method.

Table 8.10. Crystallographic data from the XRD patterns of the calcined samples at 500°C for 2h, 4h and 6h, reporting the cell parameters together with the relative intensity and the Dhkl calculated for the main peaks (ICSD #98-017-0905)

ICSD 98-017-0905 a = 4.23 Å c = 4.23 Å			MO_2h a = 4.23 Å c = 4.23 Å	MO_4h a = 4.22 Å c = 4.22 Å	MO_6h a = 4.21 Å c = 4.21 Å			
HKL	I [%]	2Theta [°]	I [%]	D _{hkl} [nm]	I [%]	D _{hkl} [nm]	I [%]	D _{hkl} [nm]
111	11.4	36.8	11.45	6.62	11.47	7.53	11.49	6.78
002	100	42.75	100	6.75	100	7.67	100	6.91
022	45	62.05	45.05	7.34	44.95	8.35	44.91	7.52
113	4.9	74.37	4.95	7.92	4.94	9.01	4.94	8.12
222	10.8	78.29	10.87	8.15	10.83	9.27	10.82	8.35
			Σ=	7.4	Σ=	8.4	Σ=	7.5
			σ=	0.7	σ=	0.7	σ=	0.7

The dimensions of the crystallites are similar for the three samples, with dimensions equal to 7.4 ± 0.7 nm, 8.4 ± 0.7 nm and 7.5 ± 0.7 nm for the samples MO_2h, MO_4h and MO_6h respectively. Therefore, the sample of MgO calcined for 2h and 6h have smaller crystal dimensions, while the sample calcined for 4h has slightly larger dimensions, in agreement with the weight losses.

Figure 8.17 shows the TEM images of samples calcined for different times. In all the images with 200 nm markers it is noted that the obtained MgO nanoparticles maintain a pseudo-hexagonal morphology, similar to that of the $\text{Mg}(\text{OH})_2$ precursor.

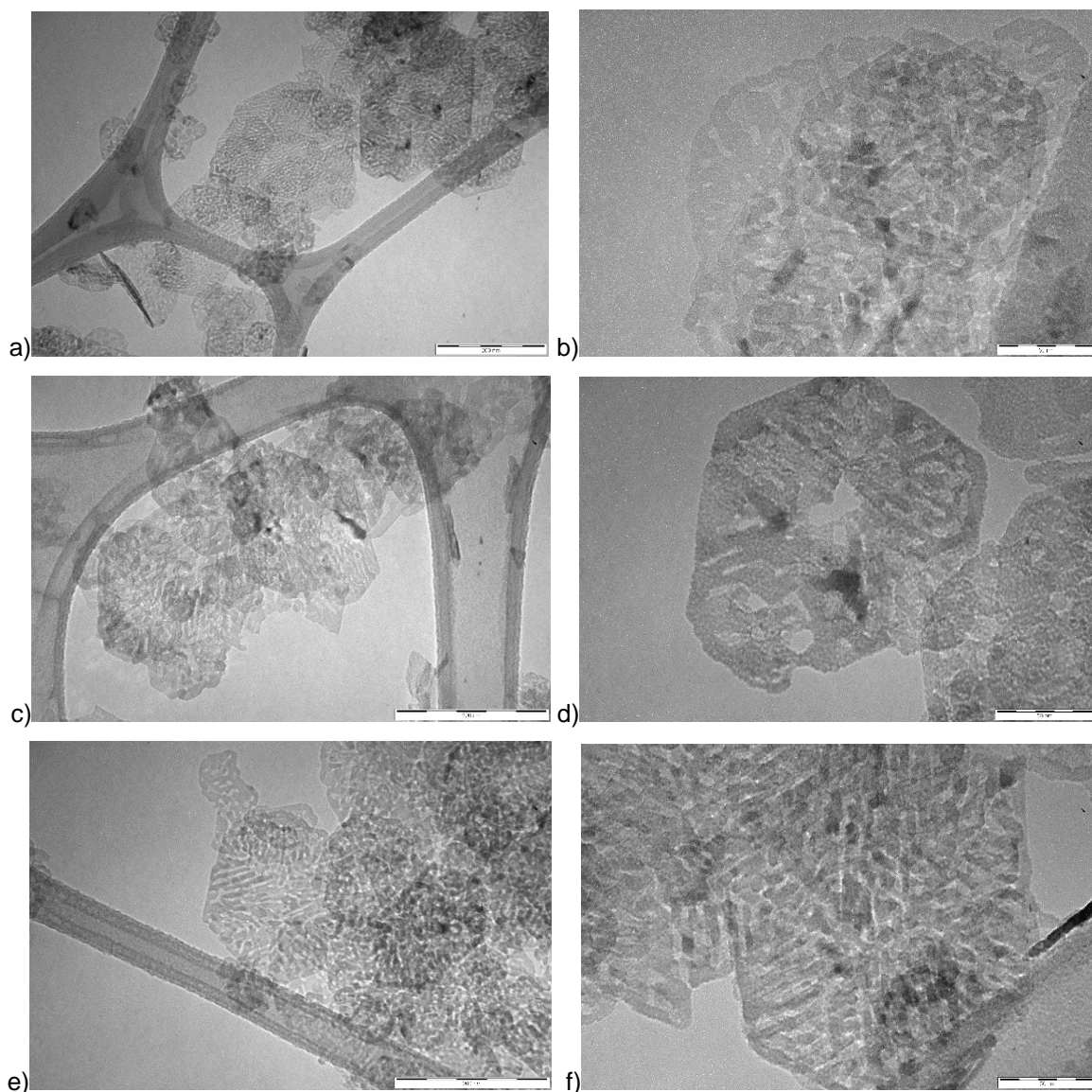


Figure 8.17. TEM images of nanoparticles of samples calcined at 500°C: a-b) MO_2h with 200 nm and 50 nm markers, c-d) MO_4h with 200 nm and 50 nm markers, e-f) MO_6h with 200 nm and 50 nm markers

In the TEM images with 50 nm markers, the empty channels formed inside the hexagonal structure are evident, arranged in a radial direction with respect to the center of the original lamella. The decomposition of hydroxide into oxide therefore seems to involve the entire volume of the original lamella and not only the external surface, demonstrating that the individual lamellae of the starting hydroxide are actually formed by an aggregation of primary particles, the singlets [29]. It can be hypothesized that the dehydration process leads to the formation of primary particles homogeneously dispersed within the entire volume of the original lamella, of which traces remain at the morphological level in the resulting aggregate. In particular, the channels inside the structure can be attributed to the loss of water associated with the decomposition process that took place. Furthermore, it can be noted that, on the surface, the particles tend to unite as if to form a continuous outer edge, probably due to cohesion forces between the particles, favored by diffusion mechanisms. The MO_6h shows the greatest weight loss, the smallest crystallite dimensions and the highest quantity of empty channels in the hexagonal lamellae observed by TEM, so it is chosen to perform BET analysis. Figure 8.18a shows the adsorption isotherm of MO_6h sample, the presence of hysteresis can be noted, so the isotherm can be classified as Type IV, typical of mesoporous materials. From this measure a specific surface value equal to 139.3 m²/g is obtained, which is about double the value of the precursor Mg(OH)₂.

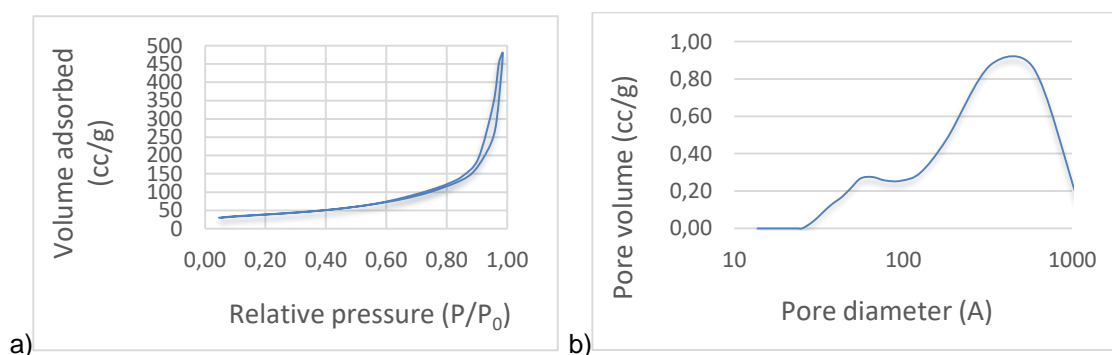


Figure 8.18. a) nitrogen adsorption isotherm of the MO_6h sample, b) pore size distribution obtained from the desorption branch of the isotherm

The pore distribution was determined from the desorption branch of the isotherms using the BJH method and is reported in Figure 8.18b for the sample MO_6h. The

prevalence of mesopores (20-500 Å) can be seen from the pore distribution, in fact the BJH method reveals an average porosity of about 21 nm.

8.4 Magnesium oxide nanoparticles for anticancer applications

Cancer is one of the principal causes of death in economically developed countries. Neoplasms in early stages can be effectively treated through surgical removal. In other cases, surgery is accompanied or replaced by radiotherapy, chemotherapy or a combination of them. Both therapies are characterized by high toxicity. In fact, chemotherapeutic agents preferentially act on tumor cells, but also damage healthy cells, causing limitations of the maximum tolerated dose.

There is a growing field of research on the use of nanoparticles against the formation, development and progression of tumors, due to their intrinsic anticancer effects, such as their antioxidant action. Several studies have shown that various metal oxide nanoparticles induce cytotoxicity in cancer cells, but not in healthy cells [30].

In particular regarding MgO nanoparticles, there are some studies available in the literature:

- Sun et al. examined the cytotoxicity of several metal oxide nanoparticles including MgO NP on human cardiac microvascular endothelial cells. [31]
- Chalkidou et al. demonstrated the application of Fe/MgO nanoparticles as a magnetically mediated hyperthermia agent in cancer therapy. [32]
- More recently, Di et al. reported the promising application of NP of MgO in nanocryosurgery for the treatment of cancer. [33]
- In the study by Krishnamoorthy et al. the cytotoxic effects of magnesium oxide nanoparticles against normal lung fibroblast cells and different types of cancer cells were examined. MgO NPs exhibited a preferential ability to kill cancer cells such as HeLa, AGS, and SNU-16. [34]

In general, the toxicity of MgO nanoparticles is attributed to the generation of reactive oxygen species (ROS), the most widespread free radicals, on the surface of the oxide. Figure 8.19 shows the main ROS species.

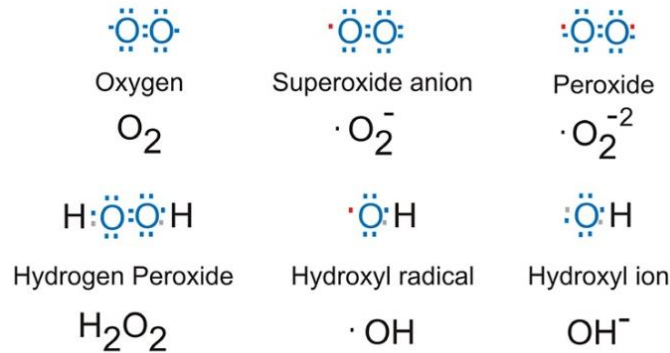


Figure 8.19. Main reactive oxygen species: oxygen, superoxide anion, peroxide anion, hydrogen peroxide, hydroxyl radical and hydroxide ion

The main factors of oxidative stress induced by nanoparticles concern:

- the oxidative properties of the nanoparticles themselves; characteristics such as size distribution, state of aggregation, surface charge, composition and presence of metals influence the cellular uptake of metal oxide nanomaterials, as shown in Figure 8.20;
- the generation of oxidants following the interaction of the nanoparticles with the cellular material; in addition to cell damage, ROS can also derive from interactions of the nanoparticles with different biological targets, such as the effect of cellular respiration, metabolism, etc.

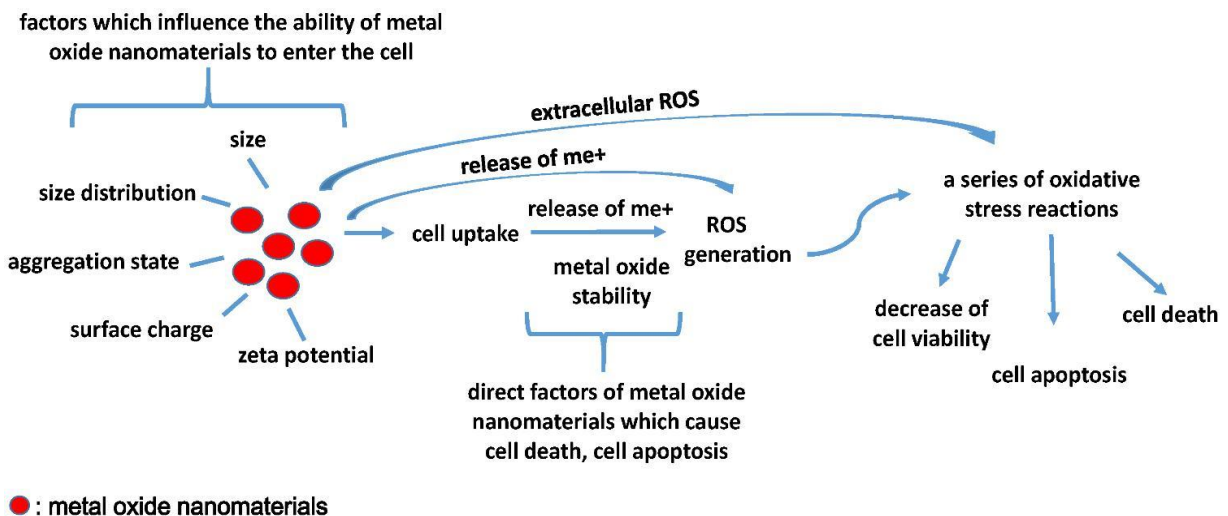


Figure 8.20. Characteristics of the NPs that cause the generation of ROS and the consequent oxidative stress [35]

In the cell, the stability of the metal oxide is an important factor that causes toxic effects: the ions that detach from the surface of the oxide, induce the production of ROS and therefore cause a series of oxidative stress reactions related to cell viability, cell apoptosis and cell death. Most metal-based nanoparticles stimulate free radical-mediated toxicity through Fenton-like reactions [36]. Oxidative stress results from an imbalance between ROS production and a biological system's ability to readily detoxify reactive intermediates or repair the resulting damage. To respond to the excessive presence of ROS, cells can activate enzymatic and non-enzymatic antioxidant systems. According to this model, cells and tissues respond to increasing levels of oxidative stress through antioxidant enzyme systems upon exposure to nanoparticles. [37]

The mechanism of cell death through apoptosis, outlined in Figure 8.21, involves the following phases:

1. The cell is damaged, stressed and apoptosis begins;
2. The cell begins to shrink and form blisters;
3. Enzymes break down the nucleus and the cell emits signals to attract macrophages;
4. The cell breaks down into many tiny pieces containing the components of the destroyed cell and nucleus;
5. Macrophages recognize parts of the cell and remove them from the body.

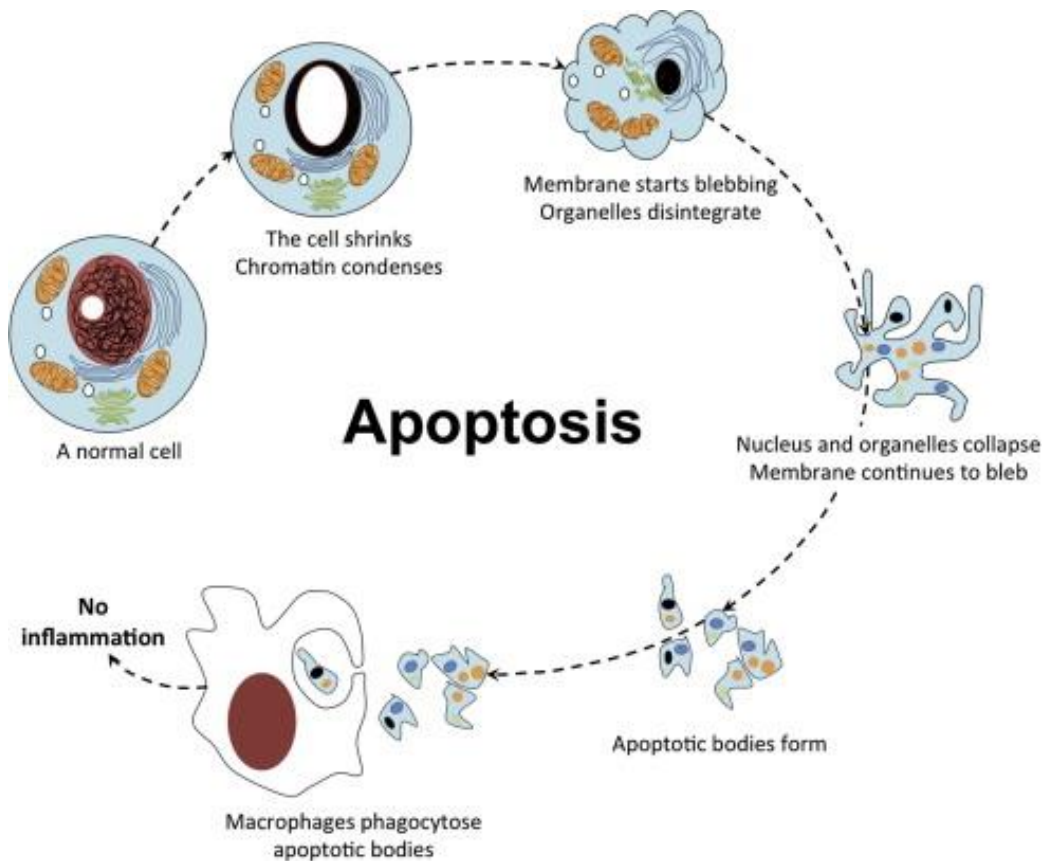


Figure 8.21. Mechanism of cellular apoptosis [35]

In collaboration with the Pharmacology research group (MESVA Department of the University of L'Aquila), preliminary *in vitro* tests are carried out on the use of the synthesized nanostructured MgO as an anticancer agent. These tests are performed in order to generate growth curves after the treatment of cultures of melanoma cells (Figure 8.22), with increasing concentrations of nanostructured MgO, as a function of different times of growth. The cell mortality rate is evaluated at different concentrations of the MgO agent and at different times, as well, with cell activity assays.

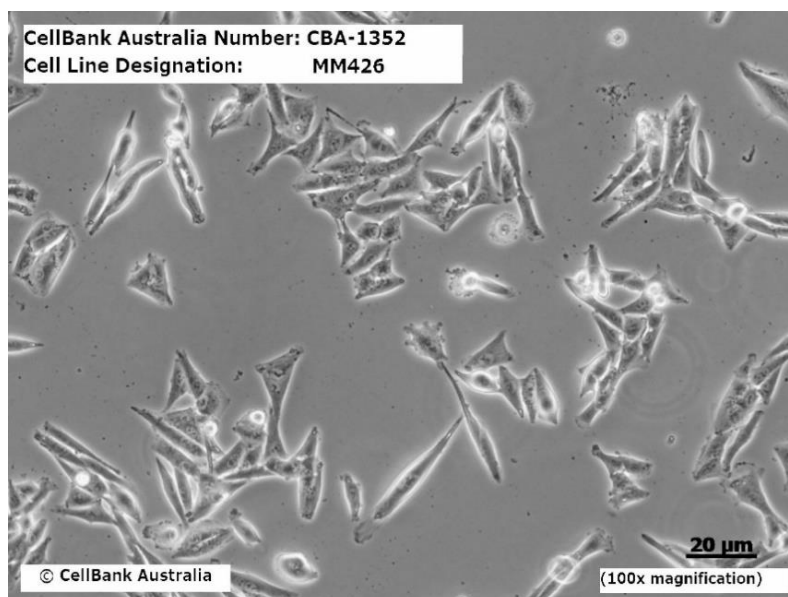


Figure 8.22. Melanoma cells (Cell Bank Australia)

Cytotoxicity is defined as the effect of a chemical (a molecule), physical (temperature, radiation or electromagnetic wave) or biological (a cell of the immune system) type agent capable of inducing damage to a cell. [38] The agent that induces this damage is often referred to as cytotoxin. Cytotoxicity tests therefore represent an "evaluation method" of the biological damage caused by substances. The cell culture assay represents one of the main methods that is used to evaluate, at a preliminary level, the cytotoxicity of a material. This refers to the in vitro evaluation of the material to determine if it releases toxic chemicals in sufficient quantities to kill cells directly or indirectly through inhibition of cellular metabolic pathways.

As explained in paragraph 8.3, the potential cytotoxicity of metal oxide nanoparticles arises from oxidative stress induced by reactive oxygen species (ROS), which induce significant damage to the cellular structure of membrane lipids, membrane proteins and nuclear membrane, until leading to cellular apoptosis.

Following the indications from the literature, it is here decided to use MgO calcined for 6h at 500°C (the one with the greater weight loss) for the preparation of an oxide suspension in a phosphate buffer saline (PBS). The buffer helps to keep the pH constant, while the concentration of salts and osmolarity are generally correlated with those of the human body (isotonic solution). [39, 40]

In particular, a stock solution, at a known concentration of 80 g/l, of MgO in PBS was prepared, from which other solutions are subsequently prepared by dilution.

The suspension thus prepared was placed in an ultrasonic bath for 30 minutes and subsequently subjected to vigorous manual stirring for 1 minute. This suspension was also analyzed by TEM, first analyzing the pure PBS (Figure 8.23a) and then the suspension of MgO in PBS (Figure 8.23b).

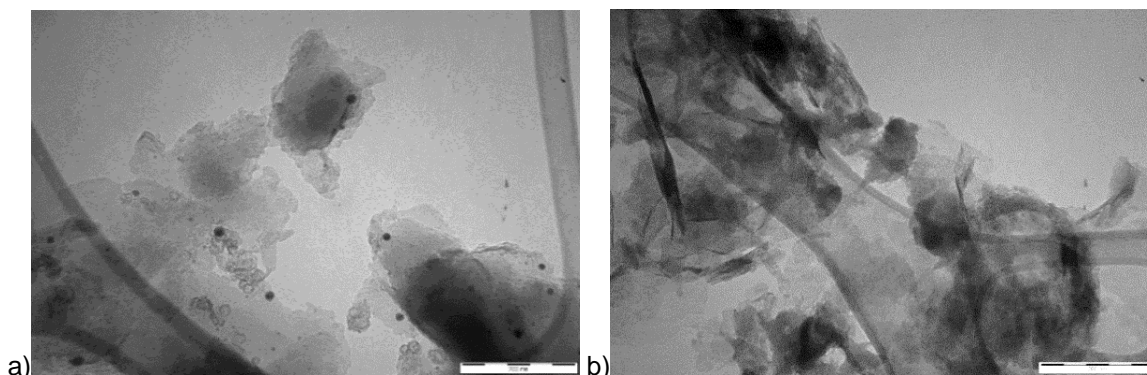


Figure 8.23 TEM images with 200 nm markers of a) phosphate buffered saline (PBS) and b) suspension of MgO in PBS

In Figure 8.23b, darker transversely arranged lamellae can be seen, representing the lamellar hexagons of magnesium oxide, dispersed in saline structures contained in the PBS similar to those of Figure 8.23a.

At this point, human melanoma cells (Bmel) were used; cells were maintained in modified Dulbecco's culture medium (DMEM), supported with 10% fetal bovine serum (FBS), glutamine (2 mM), penicillin (100 IU/ml) and streptomycin (100 µg/ml), to 37 ° C, 5% CO₂ in a humidified environment. 10 cm² cell culture capsules were used. It was decided to run the tests with three different concentrations of MgO in PBS, comparing the results with a reference sample consisting of melanoma cells only in the culture medium. The tests were repeated twice, the time established for each test is 72h, with an analysis time of 24h. A total of 24 plates were therefore prepared as shown in Figure 8.24: three different concentrations of MgO with one reference sample, replicated twice for 24h, 48h and 72h.



Figure 8.24. Culture plates used for seeding Bmel melanoma cells. There are 24 plates, including 3 groups of 4 plates replicated twice, each of these relating to a different growth time (24h, 48h, 72h)

15000 cells per cm^2 were used, corresponding to 150000 cells for capsule and approximately 3.8 million cells were used in a total of 25 plates.

The suspensions of MgO in PBS were prepared, at three concentrations: 0.1 g/l, 0.2 g/l and 0.4 g/l, corresponding to 100 $\mu\text{g/ml}$, 200 $\mu\text{g/ml}$ and 400 $\mu\text{g/ml}$. The suspensions are vigorously shaken before being added to the culture plates, in order to have a homogeneous distribution of nanoparticles in the culture medium. Figure 8.25 shows an image related to the work environment, all the procedures were carried out under a laminar flow hood (Aura 2000 MAC).

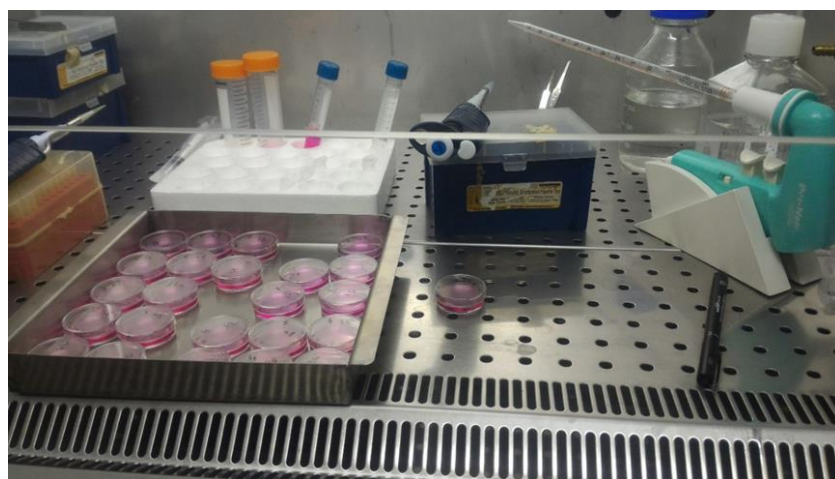


Figure 8.25. Work environment under laminar flow hood

A cell count is performed 24h, 48h, 72h after the treatment; the cells were detached by trypsin/EDTA and counted by Neubauer counting chamber using the Trypan blue dye, which penetrates only cells with damaged membrane, to discriminate between living and dead cells. Table 8.11 shows the results of the cell count at different times. The lines named (*) and (**) refer to the 2 replicates of the tests.

Table 8.11. Count of the number of live melanoma cells after 24h, 48h and 72h for the 2 replicates as the concentration of MgO introduced into the plates varies. The mean values and standard deviation of the samples are reported as well

		<i>n° of live cells</i>			
		<i>Control</i>	<i>100 µg/ml</i>	<i>200 µg/ml</i>	<i>400 µg/ml</i>
24h	*	383600	350000	264000	246000
	**	363000	286000	276000	238000
	Σ	373300	318000	270000	242000
	Σ	14566	45254	8485	5656

		<i>n° of live cells</i>			
		<i>Control</i>	<i>100 µg/ml</i>	<i>200 µg/ml</i>	<i>400 µg/ml</i>
48h	*	566000	450000	414000	350000
	**	530000	519000	356000	332000
	Σ	548000	484500	385000	341000
	Σ	25456	48790	41012	12728

		<i>n° of live cells</i>			
		<i>Control</i>	<i>100 µg/ml</i>	<i>200 µg/ml</i>	<i>400 µg/ml</i>
72h	*	930000	785000	546000	476000
	**	872500	700000	641000	502500
	Σ	901250	742500	593500	489250
	Σ	40659	60104	67175	18738

Starting from the average values of the number of live cells in Table 8.11, histograms of growth of the melanoma cells are constructed, according to the variation of the growth time and of the oxide concentration, shown in Figure 8.26.

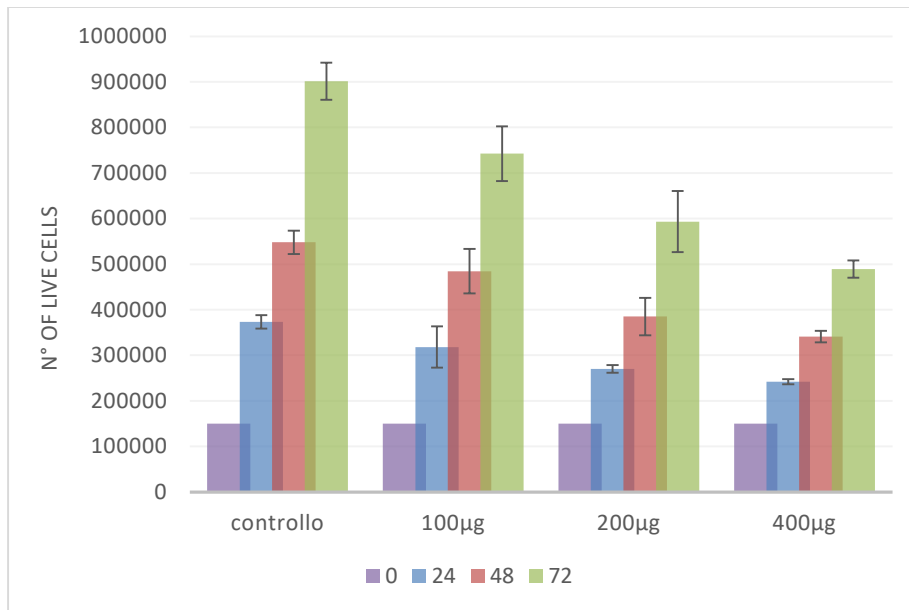


Figure 8.26. Growth histograms of melanoma cells as the concentration of MgO increases (control, 100 µg/ml, 200 µg/ml, 400 µg/ml); the growth time (0, 24h, 48h, 72h) is used as a parameter

The growth histograms show a significant decrease in the growth of melanoma cells. In particular, the inhibition of cell growth increases linearly as the oxide concentration increases. In Figure 8.27 it can be seen from the growth curves that the growth inhibition increases linearly with increasing time as well. At 72h using 400 µg/ml the growth of melanoma cell is reduced of about 45% respect to the control sample.

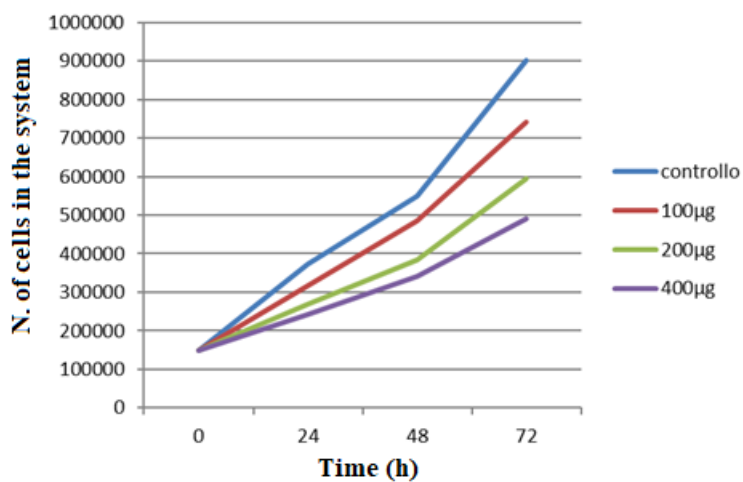


Figure 8.27. Growth curves of melanoma cells as a function of growth time, as the concentration of MgO varies

In addition, an estimate of dead cells is also made, highlighted under a microscope using Trypan Blue dye, where a slight increase in the mortality rate at high oxide concentrations is noted after 48 hours of treatment. Table 8.12 shows an estimate of the mortality % at 48h.

Table 8.12. Cell mortality % at different concentrations after 48h of treatment

	Control	100µg/ml	200µg/ml	400µg/ml
% dead cells	1.6	3.7	3.6	16

It can be observed that after 48h of treatment an increase in mortality is registered, going from 1.6% of the control to 16% at a concentration of 400 µg/ml. The effects related to 72h of treatment are not relevant and are not reported, because the dead cells break down after a certain time and do not always give a measure of mortality. A calculator is used to obtain the IC₅₀ value, the inhibitory concentration, which is the concentration of an enzyme inhibitor (drug, toxin or poison, etc.) required to inhibit 50% of the target under examination (enzyme, cell, receptor or microorganism). [41] The IC₅₀ is therefore a parameter used to evaluate the efficacy of a substance in inhibiting the target and is one of the methods commonly used in drug research to measure the potency of an antagonist. In the case under examination, Table 8.13 shows the inhibitory concentration values obtained for the different treatment times.

Table 8.13. Values of the IC₅₀ inhibitory concentration of the nanoparticles for different treatment times

Treatment time	IC ₅₀ [µg/ml]
24h	126.3
48h	135.6
72h	143.0

8.5 Results of anticancer tests compared with the literature

At this point, a comparison is made between the results of the cytotoxicological tests carried out in this thesis work with the results achieved in some studies, regarding the anticancer effect of MgO nanoparticles.

In the article by Krishnamoorthy et al. [40] the cytotoxicological effect of magnesium oxide nanoparticles on fibroblasts and different types of cancer cells was investigated. The results showed a preferential ability in killing different tumor cell lines such as HeLa, human cervical adenocarcinoma cells, AGS, human gastric adenocarcinoma cells, SNU-16, human gastric cancer cells and CCD-25Lu lung cells. human (healthy cells). In this study, the effect of MgO nanoparticles on cell viability was determined using the MTT assay, a standard colorimetric assay for measuring the activity of enzymes that reduce MTT to formazan, giving the substance a blue / purple color. After incubation, the cells were treated with various concentrations of MgO nanoparticles for 24, 48 and 72 hours. In addition to the viability assay, flow cytometry measurements for ROS production, lipid peroxidation measurements, western blot analysis and staining experiments were performed to evaluate morphological changes in the shape of the nanoparticles and study the apoptotic behavior. The cytotoxicity results of the MgO nanoparticles against cancer cells obtained from the Krishnamoorthy study are shown in Figure 8.28, where 4 graphs are reported, each of them relating to a different cell line treated.

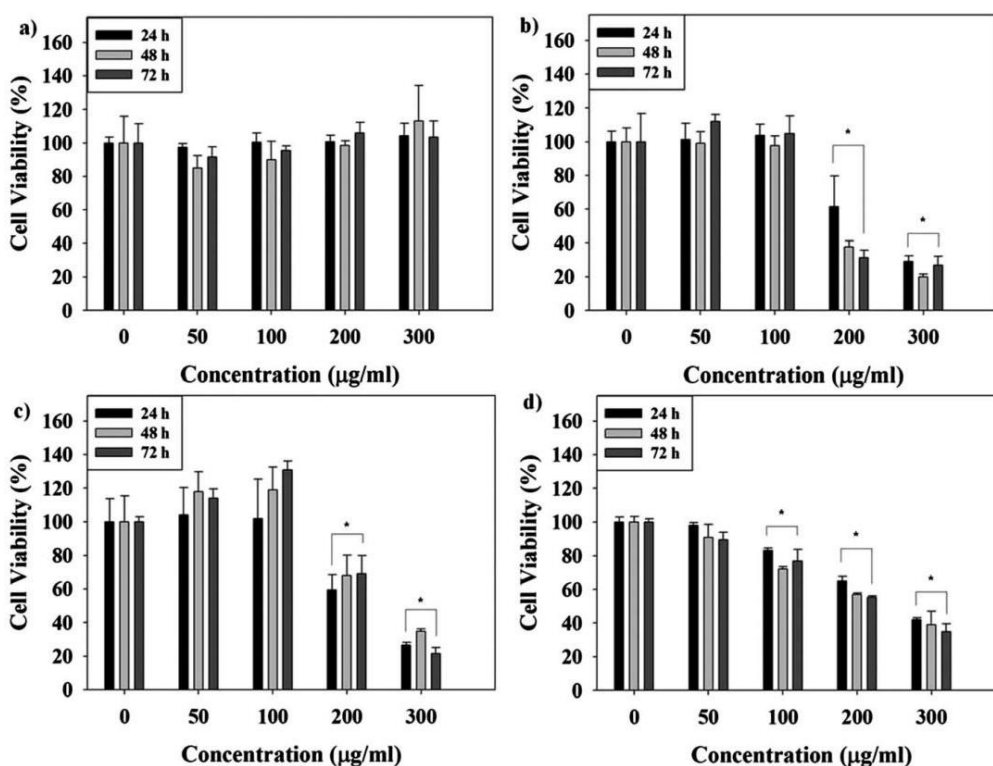


Figure 8.28. Cytotoxicity of MgO nanoparticles compared to (a) healthy human CCD-25Lu lung cells, (b) HeLa cells, (c) SNU-16 cells and (d) AGS cell lines treated for 24, 48 and 72 hours, respectively. Untreated cells were used as controls. Cell viability without treatment was considered to be 100% [40]

No toxicity of MgO NPs compared to fibroblasts is observed, even for higher concentrations of MgO (300 $\mu\text{g/ml}$) as shown in Figure 4a). Figures 4b-d) show the sensitivity of cancer cells to MgO nanoparticles. Also in this study the results show a dose and time dependent toxicity of the MgO nanoparticles towards cancer cells. In particular, MgO can effectively kill tumor cells in a dose-dependent manner in 24 hours and only a small difference in toxicity was observed for 72 hours. Furthermore, significant toxicity was observed in cancer cells at higher MgO concentrations (200 and 300 $\mu\text{g/ml}$). The IC_{50} values of MgO nanoparticles compared to HeLa cells, SNU-16 and AGS cell types were 174.0, 240.0 and 223.3 $\mu\text{g/ml}$ after 72 hours of exposure.

In the study by Moustafa et al. [42] the inhibitory activity against the MCF-7 cell line of breast cancer of some selected nanometric magnesium oxides (M2, M3, M7 prepared respectively from tartaric acid, citric acid and glycine, respectively) was

studied. compared to the standard anticancer drug Vinblastine. Results are graphed in Figure 8.29 and lethal concentration values (IC_{50}) are listed in Table 8.14.

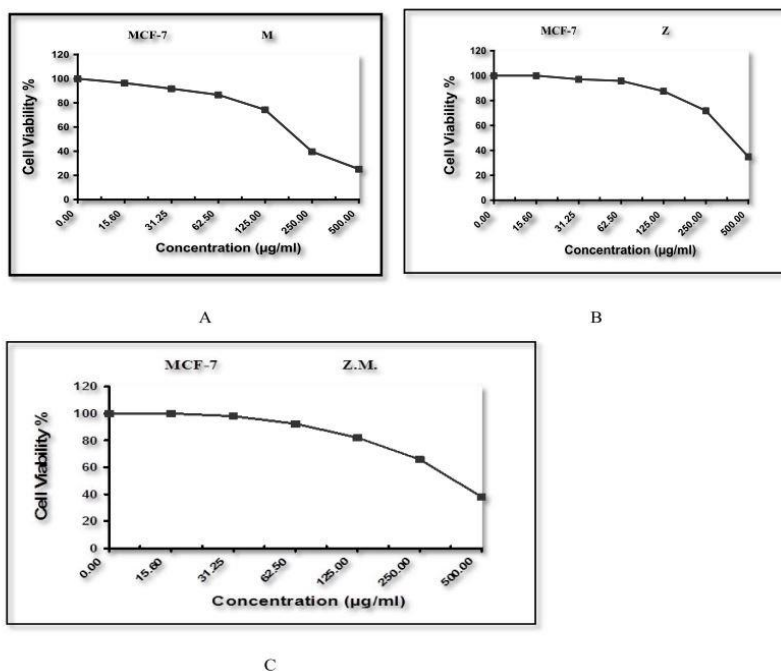


Figure 8.29. Inhibitory activity of nanooxide A) M2 ($IC_{50} = 213 \mu\text{g/mL}$), B) M3 ($IC_{50} = 398 \mu\text{g/mL}$) and C) M7 ($IC_{50} = 391 \mu\text{g/mL}$) against MCF-7 breast cancer cells [42]

Table 8.14. Lethal concentration (IC_{50}) of M2, M3 and M7 nanostructured oxides [42]

Oxide	IC_{50} ($\mu\text{g/ml}$)
Vinblastine	4.6
M2	213
M3	398
M7	391

From the inspection of cytotoxic data, it is found that magnesium oxide M2 (prepared from tartaric acid) is, in general, more effective than those of M3 (prepared with citric acid) and M7 (prepared with glycine).

Finally, from the comparison between the results in the literature and those achieved in this thesis, a general congruence is observed, in all three cases the magnesium oxide appears to be active against various tumor cells, with comparable IC_{50} values, varying around 100 and 200 $\mu\text{g/ml}$. The trends of the growth curves are similar in all three cases, and the effects are dose and time dependent.

CHAPTER 9: SYNTHESIS OF NANO-SIZED IRON OXIDES

Among the transition metal oxides, iron oxides nanoparticles are of technological and scientific importance because their relevant properties are size-dependent. In addition, their variety gives rise to a plethora of possible applications in different fields: from sensors and devices to medical diagnostic and treatments strategies, batteries, and catalysis as well as in environmental remediation. Specifically, iron compounds with oxygen are polymorphic in nature, having sixteen phases considering hydroxides, oxides and oxyhydroxides (chapter 3). The most relevant iron-based nanoparticles, from a technological point of view, are magnetite (Fe_3O_4), maghemite ($\gamma\text{-Fe}_2\text{O}_3$), hematite ($\alpha\text{-Fe}_2\text{O}_3$) and ferrihydrite ($\text{Fe}_5\text{HO}_8 \cdot 4\text{H}_2\text{O}$), thanks to their unique properties, such as superparamagnetism, surface/volume ratio, great surface area, and easy separation methodology. [1-9]

This chapter introduces an innovative, sustainable, and scalable synthesis to obtain the principal iron oxides nanoparticles. The method is always based on an ion exchange process, which is a one-step and energy saving procedure, operating in water and at room temperature, using cheap or renewable reagents. In particular, 3 iron nanostructured compounds are directly obtained: 2-lines ferrihydrite, delta iron oxyhydroxide ($\delta\text{-FeOOH}$) and magnetite, which in turn are used as precursors to obtain also nanostructured hematite and maghemite. All the obtained kinds of NPs are characterized by a specific morphology, are monodisperse and with large values of specific surface area, underlining the possibility of the synthetic method to provide a new tunable and scalable iron NPs production.

9.1 Synthesis and characterization of various iron oxides NPs

The most used iron oxide NPs synthesis methods, as discussed in chapter 3, include chemical precipitation, hydrothermal, sol-gel, electro-deposition, emulsion precipitation, surfactant mediated precipitation, microemulsion precipitation and microwave assisted hydrothermal technique. Therefore, the main synthesis techniques are based on chemical routes, which often require the necessity of high

temperature/pressure and always need extra purification steps to remove organic substances and/or secondary products. Such features lead to an unavoidable decrease of production yields also increasing the times and costs to obtain the final pure product, so there is a lack of a method able to realize productions on large scale, which is of paramount importance for industrial applications.

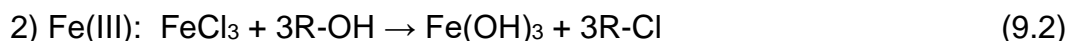
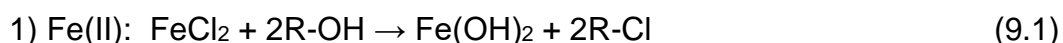
In this context, an innovative one-step synthesis is here developed, based on the exposed ion exchange method, which is able to produce different kinds of iron compounds NPs, with high yields, low costs and short times, paying also a special attention towards the environmental impact (limited production of wastes and limited energetic costs of the process itself). The synthesis procedure, occurring in water at room temperature and ambient pressure, involves an anionic resin (Dowex Monosphere 550A OH⁻ form) and two different iron chlorides (FeCl₃·6H₂O and FeCl₂·4H₂O). As explained, the anionic resin is able to rapidly absorb chloride ions to release hydroxyl groups, then the low solubility of iron compounds brings to high supersaturation conditions, favoring a burst nucleation of the solid phase. This phenomenon allows synthesizing pure iron-based NPs, properly tuned according to the reagents, without any purifications steps. After the exchange process, the resin, removed by a sieving procedure, can always be regenerated in order to be ready for a new production again, making the process practically at very low wastes. The synthesized NPs are studied in terms of structure, crystallinity, morphology, dimensions and specific surface area by several techniques, such as XRD, TEM, SEM, AFM, BET and magnetic measurements.

Specifically, three different solutions of initial reagents are reported in relation to the iron oxidation state:

- 1) Fe(II), corresponding to FeCl₂·4H₂O;
- 2) Fe(III), corresponding to FeCl₃·6H₂O;
- 3) Fe(III) and Fe(II) in a weight ratio of 2:1, corresponding to FeCl₃·6H₂O and FeCl₂·4H₂O.

For each initial reagent, considering operating with a total of 0.5 moles, a proper amount of the anionic resin is employed, and the mixing procedure is carried out under moderate stirring, at room temperature and ambient pressure, for 10 minutes. After this period, the obtained NPs are separated from the resin through a simple sieving procedure (mesh 180 μm). In order to determine if the environment of

reaction affects the quality of the final product, each synthesis is performed both in air and in nitrogen as an inert atmosphere. Depending on the oxidation state of the initial reagent and on the reaction environment, it is possible to expect different hydroxides from each synthesis (then confirmed by XRD analysis), according to the following reactions [10]:



However, in the reaction (1), it is expected that the ferrous hydroxide, Fe(OH)_2 , develops only in an environment without oxygen, because in aerobic conditions the iron(II) will be rapidly oxidized by the protons of water to form iron(II, III) oxide and molecular hydrogen. This process is described by the Schikorr reaction [11]:



Also under inert atmosphere, Fe(OH)_2 could be not stable in presence of hydroxyl ions. Indeed, we can expect the following reaction [21]:



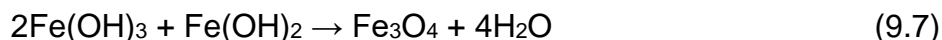
which leads to the formation of a polymorph of oxy-hydroxides compounds [12].

Concerning the reaction (2), the ferric hydroxide, Fe(OH)_3 , is unstable, because the molecules, formed during the hydrolysis of ferric solutions, interact to produce an amorphous ferric oxide hydrate precipitate, named ferrihydrite [13], according to the following reaction:



This iron oxy-hydroxide ferrihydrite is considered the first stable product of the hydrolysis of iron(III) ions in water. Ferrihydrite has different formulas depending on its crystallinity, from an amorphous state called two-line to a more crystalline called six-line [1].

Finally, when both oxidation states of iron are present, the two iron hydroxides tend to combine to directly form magnetite:



In summary, by varying the oxidation state of the initial reagent and the atmosphere (air or N_2), the syntheses lead to six different samples, from here named S1_{N_2} , S1_{air} , S2_{N_2} , S2_{air} , and S3_{N_2} , S3_{air} . Specifically, the numbers 1, 2 and 3 are related to Fe(II),

Fe(III) and mixed Fe(II)+Fe(III) initial reagents respectively. The expected iron compounds are summarized in Table 9.1.

Table 9.1. Obtained iron oxides samples from the innovative ion exchange syntheses, with initial reagents, reaction atmosphere, expected iron compounds and expected reactions

Samples	Initial reagents with	Oxidation state of initial reagents	Reaction atmosphere	Expected compounds	Expected reactions
S1 _{N₂}	FeCl ₂ ·4H ₂ O	Fe (II)	N ₂	FeOOH	5
S1 _{air}			air	Fe ₃ O ₄	4
S2 _{N₂}	FeCl ₃ ·6H ₂ O	Fe(III)	N ₂	Fe ₅ HO ₈ ·4H ₂	6
S2 _{air}			air	O	6
S3 _{N₂}	FeCl ₃ ·6H ₂ O and FeCl ₂ ·4H ₂ O 2:1 ratio	Fe(II) + Fe(III)	N ₂	Fe ₃ O ₄	7
S3 _{air}			air		7

The results of these six syntheses are reported in Table 9.2, in which the kinetic results are reported in relation to residual chloride content (RCC) as well as to the ΔCC reduction between the initial chloride concentration and the chloride concentration after 1 and 10 minutes of the ion exchange process. By measuring from each suspension the real dry product obtained after the resin separation, named DRY_{meas} (which are the grams of NPs produced), it is possible to estimate the yield of production for each synthesis, Y, as follows:

$$Y = \frac{DRY_{meas}}{DRY_{stoich}} \times 100$$

Where DRY_{stoich} is the stoichiometric value of the grams that are produced for each compound, estimated from the expected chemical reactions reported in table 9.1.

Table 9.2. Obtained iron oxides samples from the innovative ion exchange syntheses with reduction of the chloride concentration (Δ CC), residual chloride concentration (RCC), grams of NPs produced in 10 minutes and yield of production (Y)

Suspension sample	Δ CC (%) 1 min	Δ CC (%) 10 min	RCC (mg/l)	NPs produced in 10 min (g)	Y (%)
S1 _{N₂}	96.8	99.1	29.7	44	92
S1 _{air}	96.9	99.3	27.3	45	94
S2 _{N₂}	99.2	99.9	21.4	41	94
S2 _{air}	99.1	99.9	21.6	42	95
S3 _{N₂}	98.2	99.5	24.5	36	94
S3 _{air}	98.3	99.7	23.4	37	96

The obtained values denote a reagents consumption > 96% in the first minute of the exchange process, which saturates at values higher than 99% after only 10 minutes, denoting a very fast reaction and residual chloride contents (RCC) values of about 20-30 mg/l. Very high yields of production are measured as well, related to the productions of about 40 g for each compound, with values from 92% up to 96%. XRD analyses allowed investigating the solid phase that formed after the exchange process. Figure 9.1 shows the XRD patterns of the obtained compounds, revealing 3 different pure phases depending on the initial reagent or atmosphere, confirming the expected compounds reported in Table 9.1. Moreover, since from samples S2 and S3 we obtain the same results both in air and in N₂, only the samples obtained in air are reported.

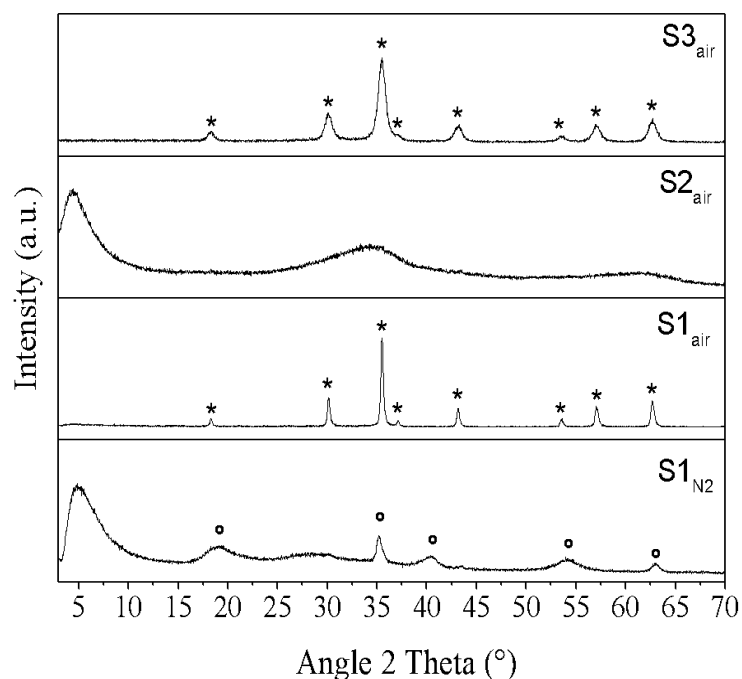


Figure 9.1. XRD patterns of the iron oxides samples from the innovative ion exchange syntheses.

Legend: ° = δ -FeOOH (delta iron oxyhydroxide), * = Fe₃O₄ (magnetite)

The synthesis carried out starting from iron(II) in inert atmosphere (S1_{N₂} sample) leads to the formation of δ -FeOOH (delta iron oxyhydroxide, ICSD pattern # 98-003-8299), characterized by a hexagonal crystal structure and showing a differential line broadening in the (001) Bragg peak, indicative of a platelet shape of diffraction domains [28-29]. By means of profile analysis, an average crystal grain size of about 6 nm is evaluated, as reported in Table 9.3. Moreover, a strong broad reflection at around 5 °2 θ is observed, corresponding to a d-spacing of about 2 nm. This reflection is not observed for the empty sample holder or for other samples, such as pure hematite, so it can be connected to an ordered mesoporous structure of this phase or to the presence of a uniform size of very small NPs, as previously discussed in literature [18, 30, 31]. In fact, small particles could act as scattering centers, giving rise to scattering signal at low angles (SAXS peak) due to the particle size (10–100 Å). Contrarily, the synthesis performed starting from iron(II) ions but carried out in air, (S1_{air} sample), reveals the formation of a crystalline phase attributed to well-defined Bragg peaks of cubic magnetite (Fe₃O₄, ICSD # 98-015-9967). Regarding the samples with only iron(III) ions, carried out both in inert atmosphere and in air (S2_{N₂} and S2_{air} samples), they present the same diffraction

pattern, characterized by the presence of two broad halos, peaked around $34^\circ 2\theta$ and $61^\circ 2\theta$ respectively, attributable to the formation of the 2-line ferrihydrite [13]. As in the S1_{N2} sample, it is possible to observe the strong reflection at around $5^\circ 2\theta$, but it results slightly shifted at lower 2θ angles, denoting a slightly larger distance between the particles into the mesoporous structure. Finally, from both the two syntheses starting from iron(II) and iron(III) ions (S3_{N2} and S3_{air} samples), a crystalline phase attributable to very small cubic magnetite, (Fe₃O₄, ICSD # 98-015-9967), is shown. In fact, the magnetite phase of S3_{air} sample is clearly characterized by broader Bragg peaks than the magnetite of S1_{air} sample, corresponding to an average crystallite size $\langle D \rangle$ of about 8 nm, as reported in Table 9.3. This result could be ascribed to a more sudden and denser nucleation step in the samples characterized by the mixed Fe(II)/Fe(III) stoichiometry, leading to smaller crystal dimensions. These results confirm the formation of the compounds reported in Table 9.1, but underlining different crystal dimensions depending on the synthesis conditions and individuating the nanometric features and the crystal structure of the specific iron compounds.

Table 9.3. Crystallographic parameters and average crystallite size $\langle D \rangle$ related to the crystalline iron phases of the ion exchange syntheses, as evaluated by Rietveld refinements.

sample	phase	crystal system	a (Å)	b (Å)	c (Å)	cell volume (Å ³)	$\langle D \rangle$ (nm)
S1 _{N2}	δ-FeOOH	hexagonal	2.96	2.96	4.55	34.54	6
S1 _{air}	Fe ₃ O ₄	cubic	8.38	8.38	8.38	588.53	29
S3 _{air}	Fe ₃ O ₄	cubic	8.38	8.38	8.38	588.81	8

To confirm that the completely amorphous phase is pure 2-line ferrihydrite, ATR-FTIR and XPS measurements are performed on the S2_{air} sample and reported in Figure 9.2. In the ATR-FTIR spectrum of Figure 9.2a, the large bands at around 3250 cm^{-1} are attributed to the broad O-H stretching vibration, related to the structural hydroxide of the 2-line ferrihydrite at 3315 cm^{-1} , as well as from adsorbed H₂O at 3200 cm^{-1} . The small reflection band at 1630 cm^{-1} is related to the O-H bending vibration from H₂O, while the strong and broad bands at 565 and 420 cm^{-1} are typical of the low crystalline ferrihydrite and are attributed to the Fe-O-Fe

stretching vibrations. Moreover, the asymmetric and symmetric C-O stretching modes at 1470 cm^{-1} and 1350 cm^{-1} , respectively, are observed. These bands are typically found in 2-line ferrihydrite samples, due to the carbonate and/or bicarbonate absorbed from water and to the CO_2 from the air as well [14-16].

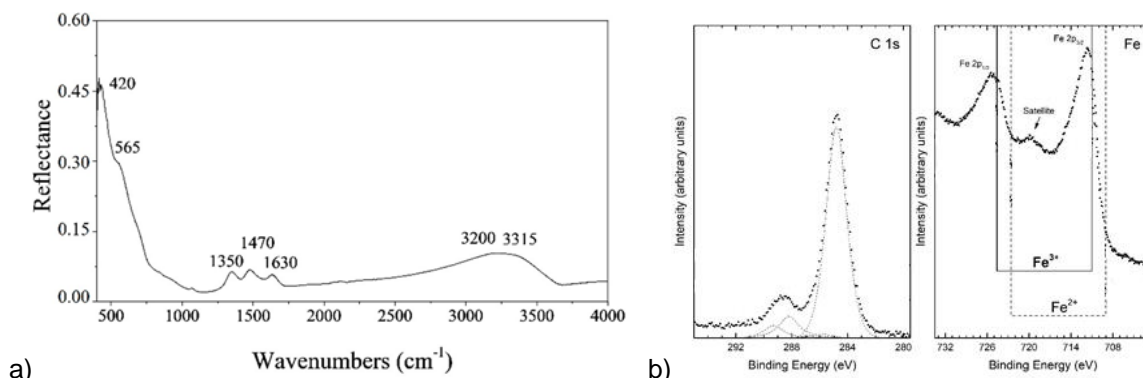


Figure 9.2. a) ATR-FTIR spectrum of 2-line ferrihydrite S2_{air} sample; b) core level C 1s and Fe 2p XPS spectra of 2-line ferrihydrite S2_{air} sample

XPS survey spectra for 2-line ferrihydrite (Figure 9.2b) reveal the presence of Fe, O and C as the only elements, confirming that the initial reagent has been completely used up, and no contamination species, such as Cl and N, are observed within the sensitivity of the technique. The binding energy (BE) calibration of the spectra has been referred to as carbon 1s peak located at $\text{BE} = 284.8\text{ eV}$. The C 1s spectrum is typical of the adventitious carbon layer, due to atmosphere exposition (CO_2), characterized by the main peak around 285 eV. In particular, the peaks are all nicely fitted by the sum of five components assigned to C atoms belonging to: C–C (284.8 eV), C–OH (285.9 eV), C–O–C (286.9 eV), C=O (288.2 eV), C=O(OH) (289.3 eV) [17-19]. The Fe 2p spectrum shows a characteristic satellite peak at approximately 8 eV higher than the main Fe $2p_{3/2}$ peak [20, 21]. The binding energies of Fe $2p_{3/2}$ and Fe $2p_{1/2}$ obtained from the present study are 711.4 and 725.0 eV, respectively. The satellite peak obtained at 719.6 eV is clearly distinguishable and does not overlap with the Fe $2p_{3/2}$ or Fe $2p_{1/2}$ peaks. From these results, it is possible to conclude that the oxidation state is Fe^{+3} , as also shown in Figure 9.2b with the dotted and continuous lines indicating the position in the binding energy of the $2p_{3/2}$ and $2p_{1/2}$ of iron peaks for the oxidation state Fe^{2+} and Fe^{3+} , respectively.

In order to investigate size and morphology of the produced particles, the samples are analyzed by TEM (Figure 9.3). Confirming XRD results, the atmosphere of reaction (N_2 or air) strongly affects Fe(II) samples but it does not affect the phases in Fe(III) and Fe(II)+Fe(III) ones. For this reason, only the best representative images for $S2_{air}$ and $S3_{air}$ samples are reported, showing that the particles of all the synthesized phases are in the nano-range. Specifically, $S1_{N_2}$ sample, shown in Figure 9.3a, reveals a superimposition of extremely thin hexagonal lamellas, attributing to the δ -FeOOH phase, similarly to literature results but presenting a definite mesoporous structure as well [22]. In addition, these lamellas show a thickness of about 10 nm, as marked by the arrows. As concerns $S1_{air}$ sample, it presents the typical cubic morphology of magnetite, with size dimensions of about 20 nm, as observed in Figure 9.3b. $S2_{air}$ sample of Figure 9.3c appears constituted by a mesoporous aggregation of very small spherical particles of size dimension of about 2-3 nm, as typical of the 2-line ferrihydrite structure [23]. Finally, nanoparticles of about 6 nm constitute the $S3_{air}$ sample (Figure 9.3d), still representing the cubic morphology of magnetite but definitely smaller than what observed in $S1_{air}$ sample, confirming the XRD results. In addition, comparing the particles observed by TEM with the crystallite size evaluated by XRD measurements, it is possible to say that each nanoparticle in $S1_{air}$ as well as in $S3_{air}$ samples corresponds to a single crystal. From Figure 9.3 it is also possible to notice that, except for $S1_{N_2}$ sample where the hexagonal lamellas could derive from a self-assembling of primary nanoparticles, the other samples exhibit that the nanoparticles are monodisperse, as shown in the insets. This result can be strongly related to the fact that, during the synthesis, for all the samples a fast and diffuse nucleation occurs, and all the crystallites form at the same time and under the same environment, in the whole volume of reaction. Moreover, due to a very quick kinetic of the ion exchange process and due to a small solubility of the formed phases, the growth rate of such crystallites is limited as well.

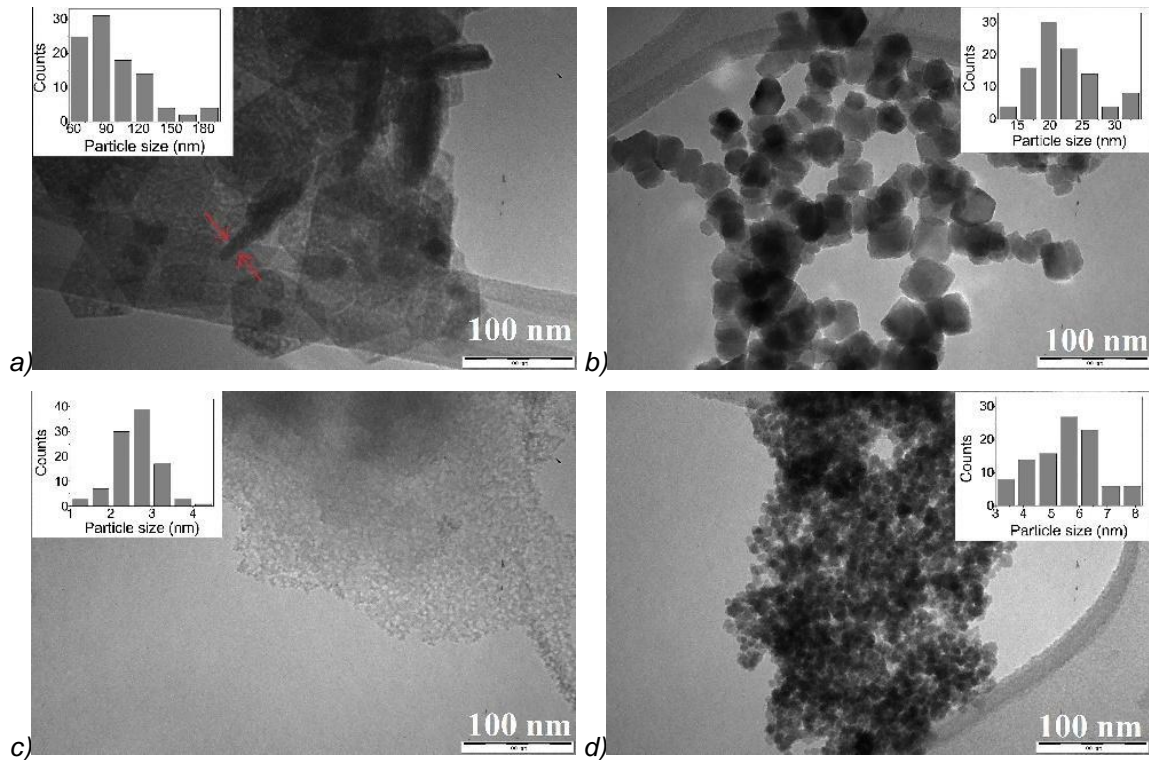
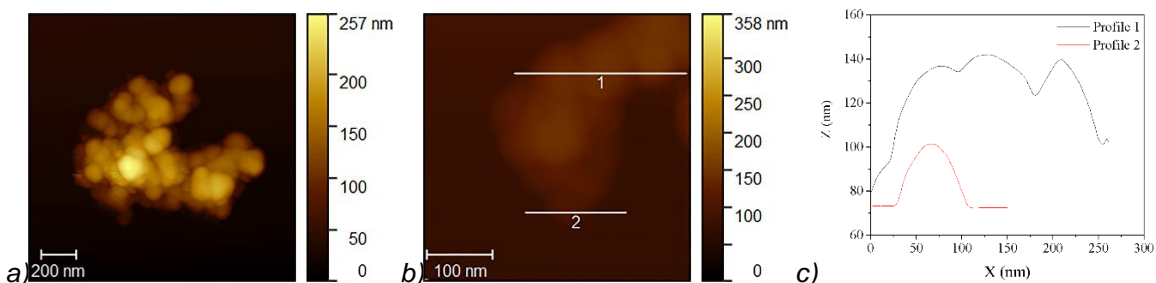


Figure 9.4. TEM images of the NPs obtained from the different ion exchange syntheses: a) iron oxyhydroxide δ -FeOOH nanoparticles in S1_{N2} sample, with arrows underlining the thickness of lamellae; b) magnetite nanoparticles in S1_{air} sample; c) ferrihydrite nanoparticles of S2_{air} sample; d) magnetite nanoparticles in S3_{air} sample

AFM observations of S1_{air}, S2_{air} and S3_{air} samples are reported in Figure 9.4. For each sample, both representative images, at lower and higher magnification, and the corresponding profile analysis along the Z axis of single nanoparticles, are shown. The analyses allow confirming the differences between the two magnetite samples, with height of about 20 nm in S1_{air} sample and 3 nm in S3_{air} sample (Figures 9.4b-c and 9.4h-i respectively). As concerns the ferrihydrite S2_{air} sample, very close aggregates are observed (Figure 9.4d), probably due to the extremely fine monodisperse nanoparticles, with dimensions of about 2 nm (Figures 9.4e-f).



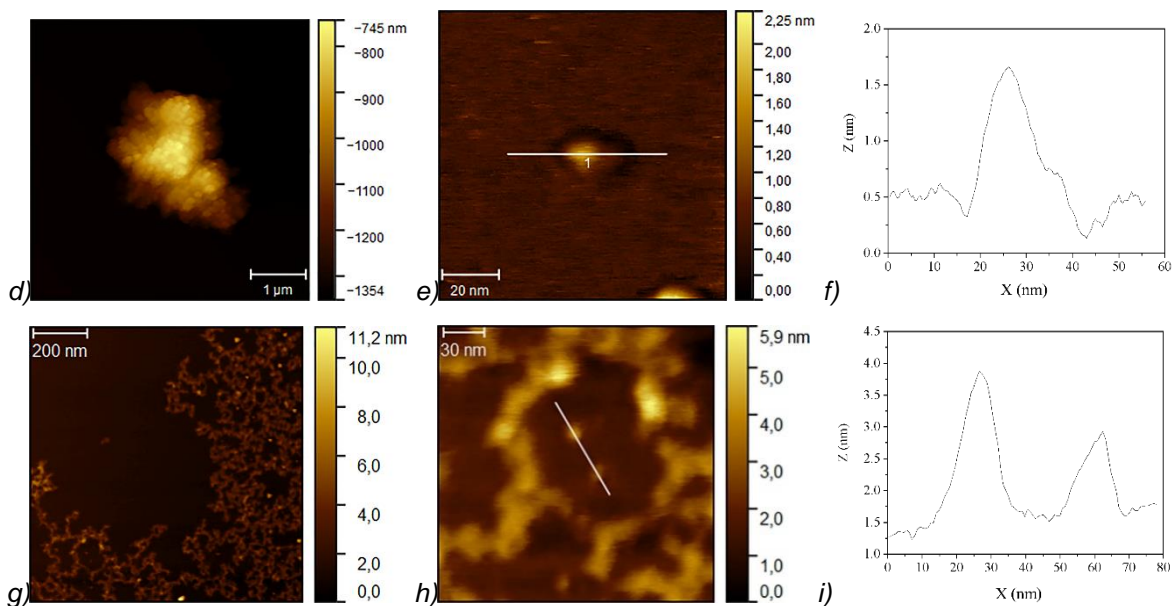


Figure 9.4. AFM observations of the nanoparticles obtained from the different ion exchange syntheses and corresponding profile analyses along Z-axis of single particles: a-c) magnetite nanoparticles in S1_{air} sample; d-f) ferrihydrite nanoparticles of S2_{air} sample; g-i) magnetite nanoparticles in S3_{air} sample

SEM images, shown in figure 9.5, underline the aggregation behavior, in relation to the different morphologies characterizing each sample. The δ -FeOOH sample S1_{N2} denotes spherical aggregations organized in an ordered network of nano-platelets, all having thicknesses < 20 nm, forming flower-like particles [24], as shown in Figure 9.5a. In addition, this network presents both macropores and mesopores, resulting characterized by a high whole porosity. The magnetite phases composing S1_{air} and S3_{air} samples are shown in Figures 9.5b and 9.5d respectively, they seem very similar with SEM observations, composed by a dense aggregation of small particles. However, the S3_{air} sample exhibits a denser nanoparticles aggregation probably due to the smaller dimensions observed by XRD and TEM. Finally, a spongy, mesoporous, and spherically shaped assembly of very small nanoparticles is observed for the ferrihydrite phase of S2_{air} sample, shown in Figure 9.5c, confirming the observations of TEM.

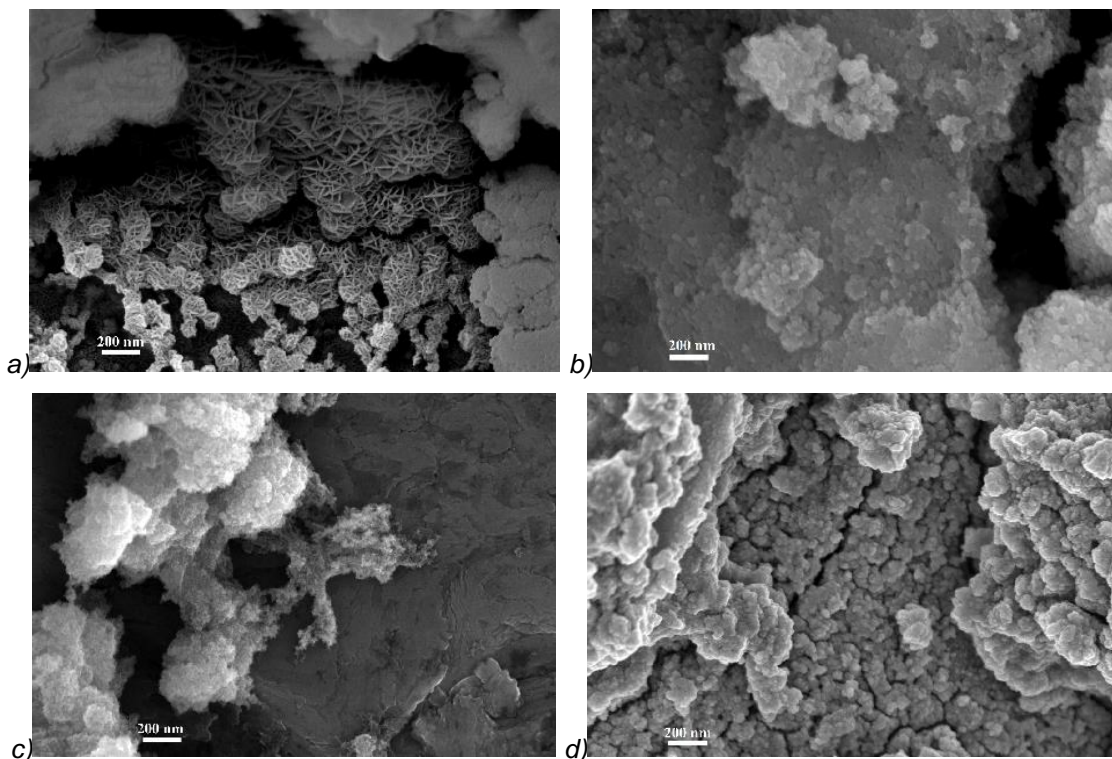


Figure 9.5. SEM images of the NPs obtained from the different ion exchange syntheses: a) delta iron oxyhydroxide particles of S1_{N2} sample; b) magnetite particles of S1_{air} sample; c) ferrihydrite particles of S2_{air} sample; d) magnetite particles of S3_{air} sample

The surface area and the porosity of the samples are then evaluated and classified by the nitrogen adsorption measurements, reported in Figure 9.6. Concerning the isotherm of the iron oxyhydroxide S1_{N2} sample, it can be related to type IV, typical of mesoporous materials, characterized by a large hysteresis loop associated with capillary condensation in mesopores. The hysteresis is attributable to H4 type, characteristic of agglomerates of plate-like particles forming slit-like pores, but also internal voids of irregular shape [25]. The deviation between the adsorption and desorption curves in the initial section can be due to the resolution limit of the instrument ($> 10 \text{ \AA}$) or to limitations related to monolayers [26]. The isotherm of the S1_{air} sample can be ascribed to type IV as well, but with a very little hysteresis due to mesopores, confirmed by a pore distribution centered in the macropore range. Ferrihydrite S2 samples exhibit a type I(b) isotherm, typical of materials having pores with dimensions in the upper range of the micropore domain, containing both micropores and narrow mesopores ($< 25 \text{ \AA}$) [27]. The little adsorption-desorption hysteresis in the range $0.30 < P/P_0 < 0.60$ underlines a very small contribution of

mesopores. Finally, the isotherm of the magnetite S3 samples can be related to type IV, with a well-defined hysteresis loop, attributable to the H1 classification, where agglomerates or spherical particles are arranged in a fairly uniform way, indicating a relatively high pore size uniformity.

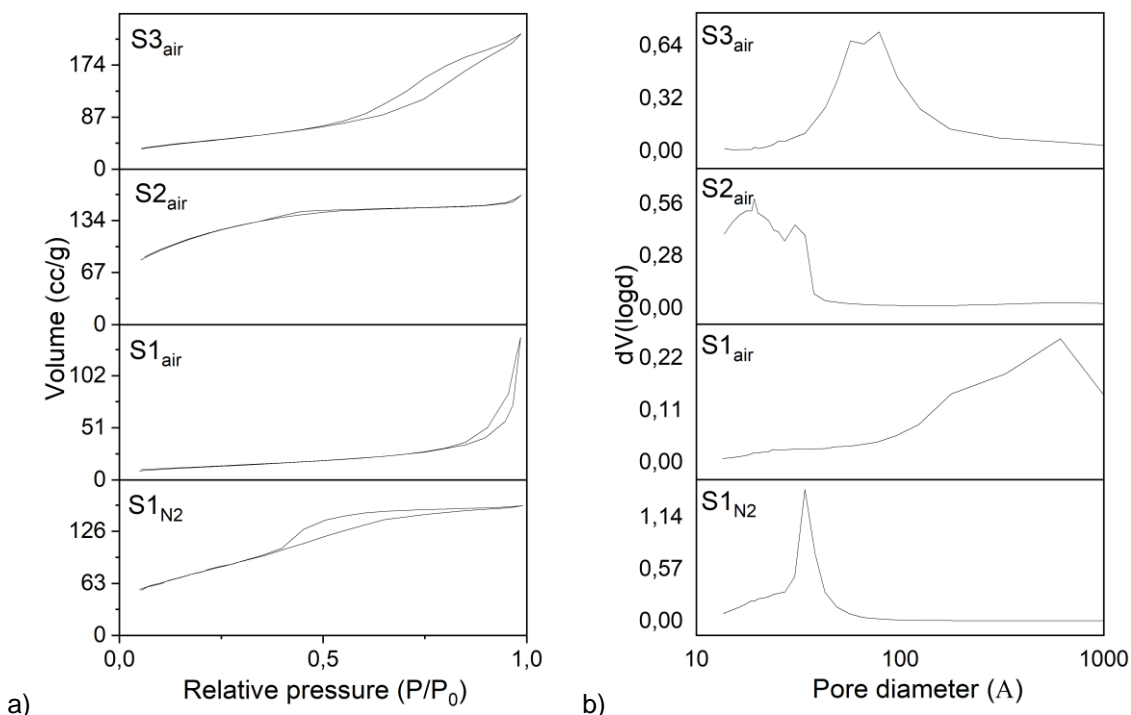


Figure 9.6. a) N₂ adsorption/desorption isotherms and b) distributions BJH for desorption branch of the isotherms of the different synthesized iron oxides samples

The corresponding BJH pore size distributions and calculations are reported in figure 9.6b and in Table 9.4 respectively. The delta iron oxyhydroxide of S1_{N₂} sample has a pore size distribution mainly peaked around 4 nm, with pore volume values of 0.25 cc/g. Magnetite of S1_{air} sample is instead characterized by a broad pore size distribution, shifted towards the macropores region, with a low presence of mesopores (< 50 nm) and revealing the lowest value of pore volume (0.22 cc/g). Confirming the adsorption isotherm, ferrihydrite of S2 sample has a bimodal pore size distribution, peaked around 3-4 nm and 1-2 nm, corresponding to micropores and narrow mesopores, with a pore volume of about 0.25 cc/g. Finally, the magnetite S3 sample show a well-defined and bimodal pore distribution around the value of 10 nm, with the highest value of pore volume (0.36 cc/g) measured between the various samples.

Table 9.4. BET specific surface areas of the synthesized iron oxides samples, with pore volume and pore diameters from BJH calculations

	Iron oxyhydroxide S1 _{N2}	Magnetite S1 _{air}	Ferrihydrite S2 _{air}	Magnetite S3 _{air}
BET surface area (m ² /g)	271	46	420	169
BJH pore diameter D _v (d) (nm)	3.41	2.38	1.50	5.69
BJH pore volume (cc/g)	0.25	0.22	0.24	0.36

Concerning the BET specific surface areas of Table 9.4, all the samples exhibit considerably high values respect to the results reported in literature [27-31]. In particular, the BET surface area of the ferrihydrite of S2_{air} sample is about 420 m²/g, while the BET surface area of the magnetite of S3_{air} sample is about 169 m²/g, values higher than those measured in literature for ferrihydrite and magnetite.

From the characterization analyses, it appears evident that the iron exchange process is suitable to obtain different iron oxides in form of nanoparticles in great quantity (about 40 grams in a single step), controlling the results of the process by adjusting the initial parameters (reagents state and reaction environment). Moreover, also the concentration of the reagent can affect the dimensions of the obtained particles (not reported here but tested for other syntheses and for ferrihydrite). Therefore, this method of synthesis results very effective and tunable for engineering scopes, modulating the characteristics and the produced amounts of the iron oxide NPs, in order to tailor them with the envisaged applications.

9.2 Calcination of iron oxides NPs as precursors to obtain hematite and maghemite NPs

As already known in literature [32, 33], most iron hydroxides and oxides can be oxidized to form other iron oxides as well. There are different ways to oxidize iron compounds; the most typical approaches consist in the reaction with oxidizing agents or in increasing the temperature, maintaining the compounds in air. For these reasons, the iron compounds obtained from the ion exchange process can be

considered as precursors to obtain other iron oxides nanoparticles. The calcination treatments are carried out at different temperatures, up to 700°C, in order to find the minimum temperature necessary to observe phase transformations, limiting the diffusive growth phenomena of the new formed NPs.

From the six initial precursors reported in Table 9.1 it is possible to obtain different calcined samples, depending on the oxidation or on the dehydration phenomena occurring during the calcination treatment [34]. The calcined samples showing a complete phase transformation are reported, named as the precursor samples adding a subscript relating to the minimum temperature T to which they are obtained.

XRD results of the samples obtained after the calcination treatments of the phases synthesized by the ion exchange process are reported in Figure 9.7, while the crystallographic parameters of the obtained phases as well as their average D values, evaluated by the Rietveld refinements, are reported in Table 9.5. In sample S1_{N2_200} the initial delta iron oxyhydroxide presents a conversion into hematite (α -Fe₂O₃, hexagonal crystal structure, ICSD# 98-002-2505) at extraordinarily low temperature conditions (1 hour at 200°C), characterized by a $\langle D \rangle$ value of about 3 nm. However, probably due to the unavoidable presence of oxygen during the calcination treatment, a maghemite phase is observed too, (γ -Fe₂O₃, cubic crystal structure, ICSD# 98-008-7119), in a relative amount of 13,9%, as evaluated by Rietveld analysis. Differently, the magnetite S1_{air} sample shows, at 200°C, a complete transformation into pure maghemite, (γ -Fe₂O₃), (sample S1_{air_200}), which in turn transforms into pure hematite increasing temperature up to 600°C (sample S1_{air_600}). Regarding the ferrihydrite S2 samples, it is observed a phase transformation only at a temperature of 500°C into pure hematite, with an average $\langle D \rangle$ value of 20 nm, as shown in the representative XRD pattern of S2_{air_500} sample. For magnetite S3 samples the transformation into maghemite at a temperature of 200°C (sample S3_{air_200}) and into hematite at 600°C (sample S3_{air_600}) is observed. In terms of phase transformations, these results are the same of the S1_{air} sample, since both S3 and S1_{air} precursors are pure magnetite, but the broadening analyses reveal small crystal sizes for the maghemite and the hematite coming from S3 samples, as shown in Figure 9.7 and in Table 9.5. Specifically, the maghemite and hematite phases are characterized by an average crystallite size $\langle D \rangle$ of about 22

nm and 64 nm if obtained by S1_{air} precursor sample, respect to values of 6 nm and 42 nm, when the S3 precursor samples are used.

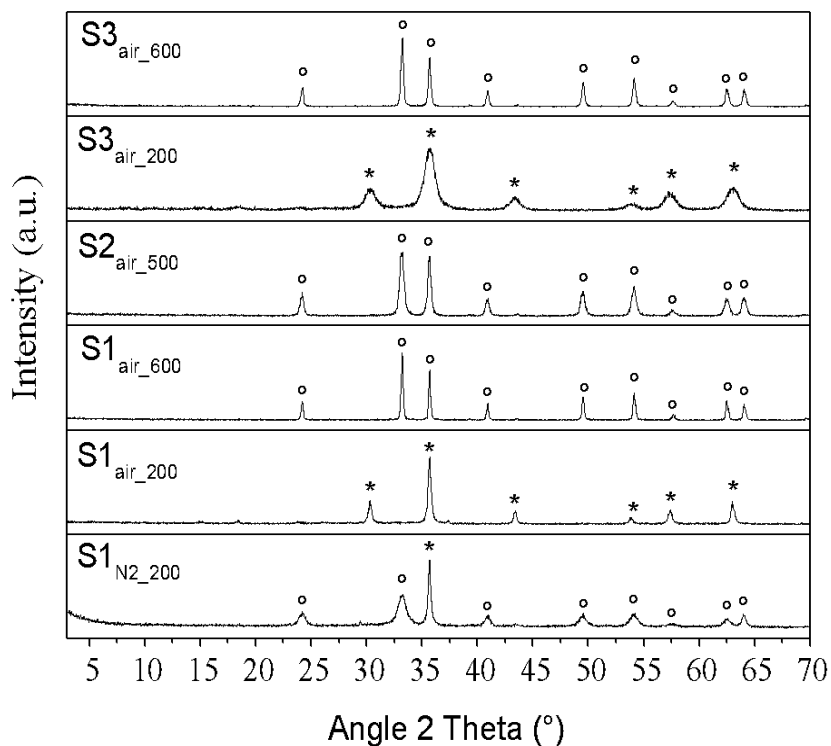


Figure 9.7. XRD patterns of calcined samples, obtained at different temperatures from different precursors. Legend: * = γ -Fe₂O₃ (maghemite), ° = α -Fe₂O₃ (hematite).

Finally, the analyses of the crystallographic parameters, reported in Table 9.5, show slight larger cell volumes in the phases characterized by lower D values, denoting greater amounts of lattice defects. In any case, for all the obtained maghemite and hematite phases, the D_{hkl} values are similar for all peaks, denoting a uniform growth of crystal size in all directions [35].

Table 9.5. Crystallographic parameters and average crystallite size $\langle D \rangle$ related to the calcined iron phases, resulting by Rietveld refinement.

sample	phase	crystal system	a (Å)	b (Å)	c (Å)	cell volume (Å ³)	$\langle D \rangle$ (nm)
S1 _{N2_200°C}	α -Fe ₂ O ₃	hexagonal	5.05	5.05	13.88	306.48	3
	γ -Fe ₂ O ₃	cubic	8.35	8.35	8.35	581.35	16
S1 _{air_200°C}	γ -Fe ₂ O ₃	cubic	8.34	8.34	8.34	580.04	22
S1 _{air_600°C}	α -Fe ₂ O ₃	hexagonal	5.03	5.03	13.75	301.74	64
S2 _{air_500°C}	α -Fe ₂ O ₃	hexagonal	5.03	5.03	13.75	301.86	20
S3 _{air_200°C}	γ -Fe ₂ O ₃	cubic	8.34	8.34	8.34	581.06	6
S3 _{air_600°C}	α -Fe ₂ O ₃	hexagonal	5.04	5.04	13.75	302.03	42

TEM images reported in Figure 9.8 show dimensions and morphologies of the calcined particles. S1_{N2_200} sample appears constituted by very small hexagonal nanoparticles, which could be attributed to hematite, having dimensions of less than 5 nm (as marked by in the rectangular insert in Figure 9.8a, in agreement with the low crystallinity of the hematite phase observed by XRD. Traces of the precursor as well as pseudo-circular particles, with dimensions from 20 to 50 nm, are clearly observed too, attributable to the formation of maghemite phase. These particles are indeed similar to those observed in S1_{air_200} sample (Figure 9.8b), characterized by a pure maghemite phase. Concerning the S1_{air_600} sample, TEM images show the presence of nanoparticles characterized by a rhombohedral morphology (Figure 9.8c), the other typical feature of hematite nanoparticles [36]. The particles in S2_{air_500} sample, reported in Figure 9.8d, show a tiny and quasi-spherical shape, related to the hexagonal morphology, frequently observed after the dehydration of ferrihydrite particles and the subsequent gradual structural ordering to hematite structure [37-39]. Concerning the S3_{air_200} sample, (Figure 9.8e), it appears constituted by thin lamellae composed of very small nanoparticles (≈ 7 nm) through a mesoporous assembly characterized by pores less than 10 nm in size. S3_{air_600} sample of Figure 9.8f presents hematite with rhombohedral morphology, similarly to what observed for hematite S1_{air_600} nanoparticles, but with smaller dimensions. All these results strongly underline the influence that the initial precursor provides on the formation of the subsequent iron oxides NPs, in relation to dimensions as well as to morphology that is very important for the applications.

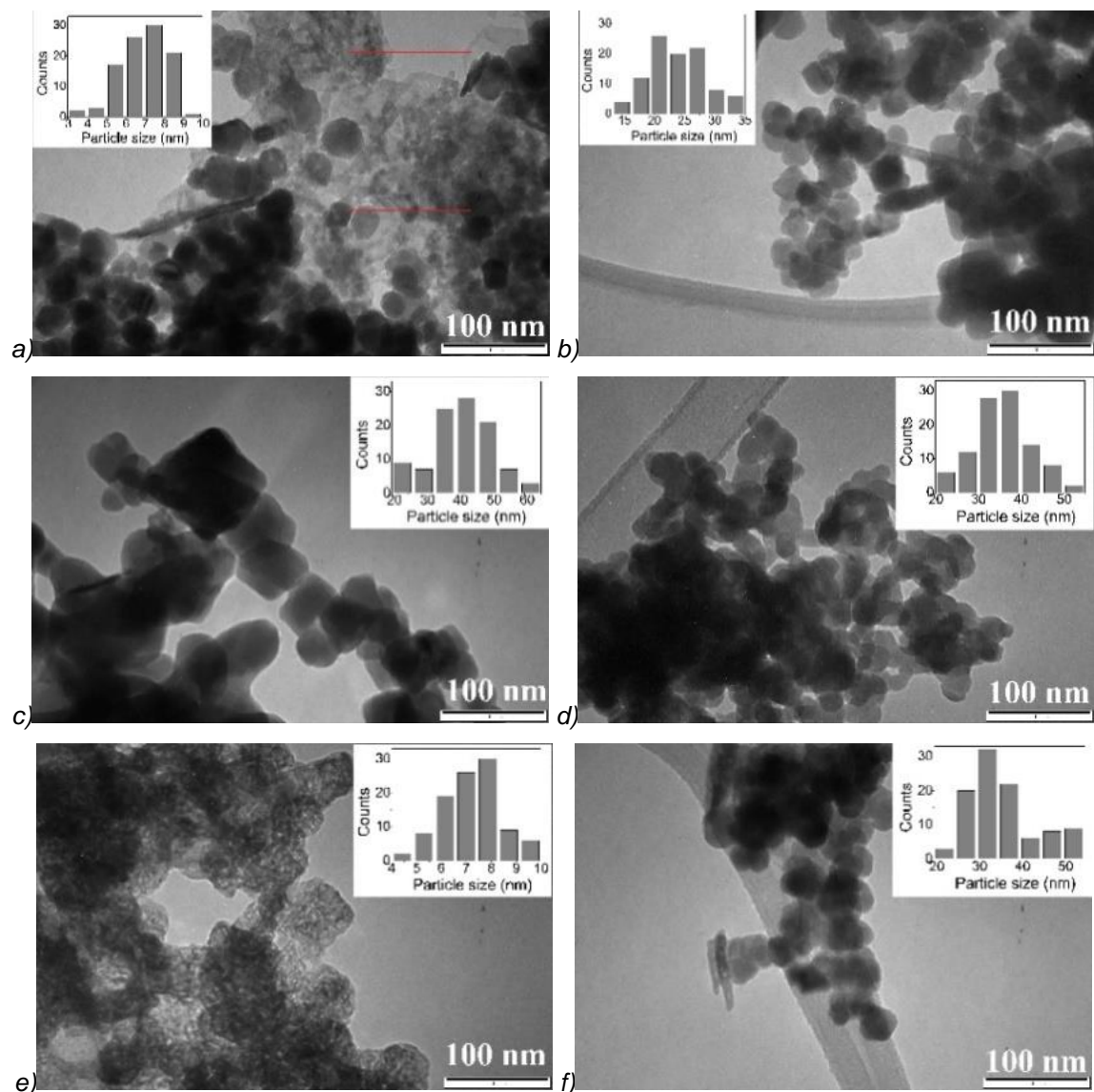


Figure 9.8. TEM images of calcined samples, obtained at different temperatures: *a)* hematite/maghemite S1_{N2_200} sample; *b)* maghemite S1_{air_200} sample; *c)* hematite S1_{air_600} sample; *d)* hematite S2_{air_500} sample; *e)* maghemite S3_{air_200} sample; *f)* hematite S3_{air_600} sample.

AFM investigations allow confirming what is observed by TEM, providing further important information as well. In particular, in S1_{N2_200} sample very fine and monodisperse particles of about 10 nm length and 0,6 nm height are observed (Figure 9.9a-b), which can be attributable to the small hexagonal hematite nanoparticles, clearly characterized by monodisperse and spherical shaped particles. A plate-like shape for hematite nanoparticles is also confirmed for the S2_{air_500} sample, but with larger dimensions of about 20 nm length and 4 nm height (Figure 9.9g-h). Concerning the particles observed in maghemite S1_{air_200} (Figures 9.9c-d) and hematite S1_{air_600} samples (Figures 9.9e-f), they present a circular and

an elongated shape respectively, confirming TEM observations, both revealing very reduced thickness (about 1-2 nm). In the S3_{air_200} sample, AFM allows confirming and evaluating the dimensions of the small particles which composed the maghemite phase, resulting in about 5 nm length and 0,5 nm height (Figure 9.9*i-l*). Finally, tiny single particles of about 20 nm are observed for hematite S3_{air_600} sample (Figures 9.9*m-n*).

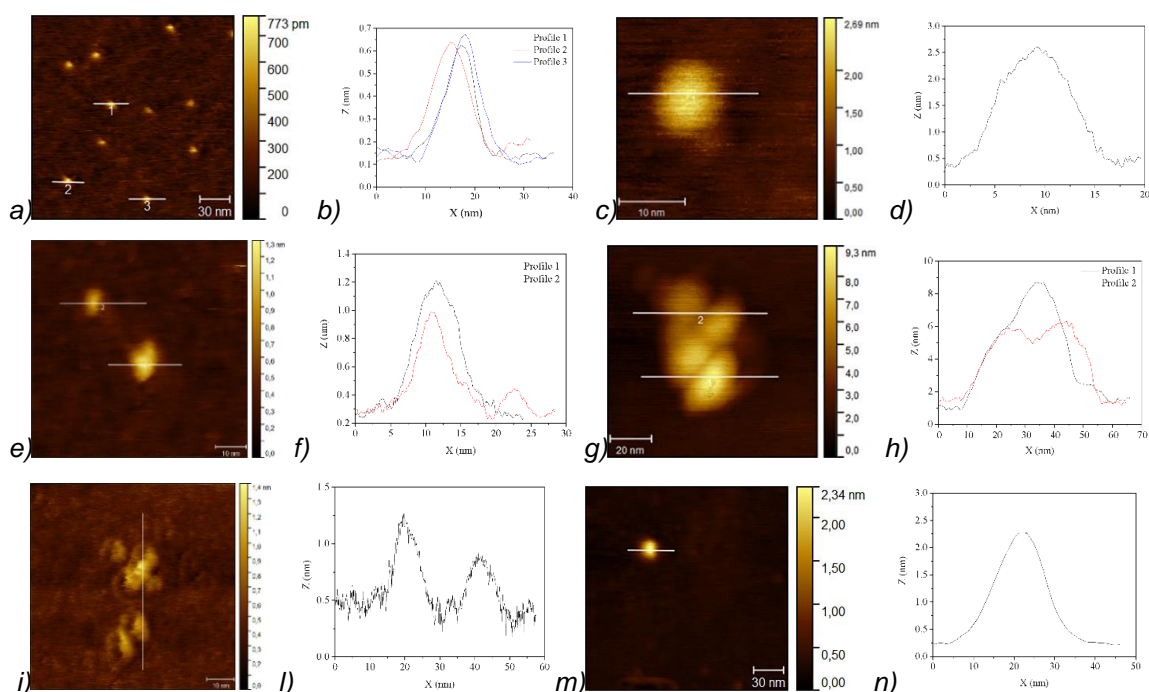


Figure 9.9. AFM images of calcined samples, obtained at different temperatures: *a-b*) hematite S1_{N2_200} sample; *c-d*) maghemite S1_{air_200} sample; *e-f*) hematite S1_{air_600} sample; *g-h*) hematite S2_{air_500} sample; *i-l*) maghemite S3_{air_200} sample; *m-n*) hematite S3_{air_600} sample

SEM images, reported in Figure 9.10, show that the NPs obtained after the calcination process form spherical aggregates independently from the precursors and the formed phase. However, hematite S2_{air_500} sample shows smaller aggregates respect to the other samples, probably due to its smaller dimensions and to the plate-like morphology as well.

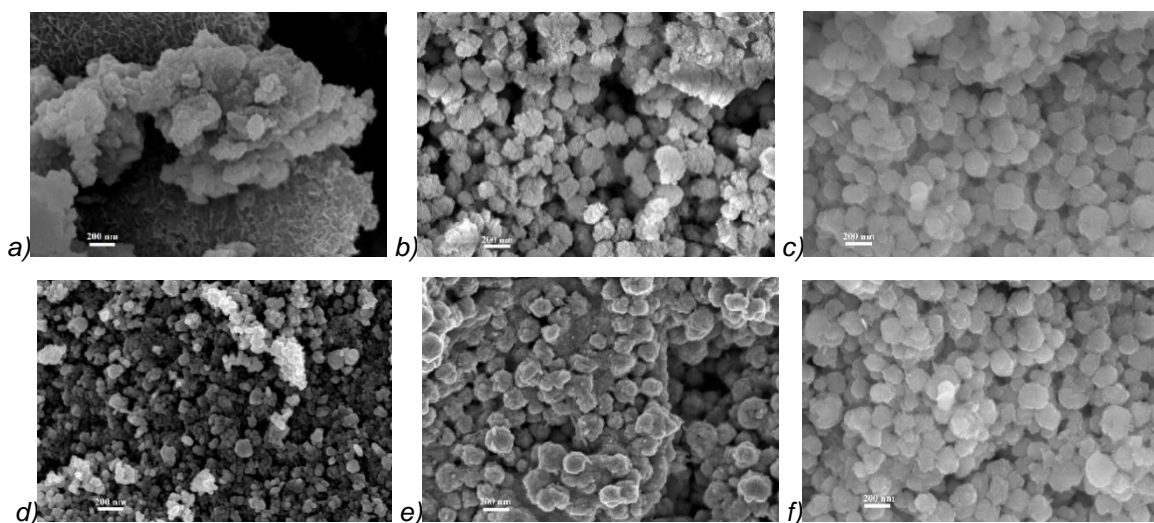


Figure 9.10. SEM images of the nanoparticles aggregation from different samples: a) hematite/maghemite S1_{N2_200} sample; b) maghemite S1_{air_200} sample; c) hematite S1_{air_600} sample; d) hematite S2_{air_500} sample; e) maghemite S3_{air_200} sample; f) hematite S3_{air_600} sample.

Finally, in Figure 9.11a the nitrogen adsorption isotherms of the calcined samples are shown. The isotherms are all attributable to type IV isotherm, typical of mesoporous materials, as also evidenced by the hysteresis loop between the adsorption and desorption branches. Nevertheless, if the type of isotherms is the same, the hysteresis loops allow distinguishing the samples: hematite/maghemite S1_{N2_200} sample exhibits a type H2 hysteresis loop, occurring in highly heterogeneous pore networks [40] and a large pore distribution around 8 nm. In the S1_{air_200} sample, the maghemite NPs are characterized by a type H1 hysteresis loop, corresponding to the presence of both cylindrical and plate-like pores, with the cylindrical pores having a pore size distribution between 50 and 200 nm (macropores range) and the plate-like pores generally varying in the range 5–50 nm [41]. This result is confirmed by the pore size distribution in Figure 9.11b, confirming the prevalence of macropores, but having a small peak at around 3 nm as well. Similar results are observed for hematite S1_{air_600} and S3_{air_600} samples but limiting the hysteresis to the presence of cylindrical and relatively larger pores, as verified in the corresponding pore size distribution. A H1 type hysteresis loop can be also remarked for hematite S2_{air_500} sample, in this case associated with a bimodal pore distribution in the mesopores region, around 8 nm and around 20 nm, which defines only the presence of plate-like mesopores. Differently from the other samples, the hysteresis loop of maghemite obtained in the S3_{air_200} sample is a H3 type, with the

characteristic step down at relative pressures ≈ 0.4 . This kind of hysteresis is usually related to non-rigid aggregates of plate-like particles or assembly of slit-shaped pores determining two classes of pores size: in the range 2-50 nm and 50-100 nm, due to slit-/plate-like particles respectively [40,42].

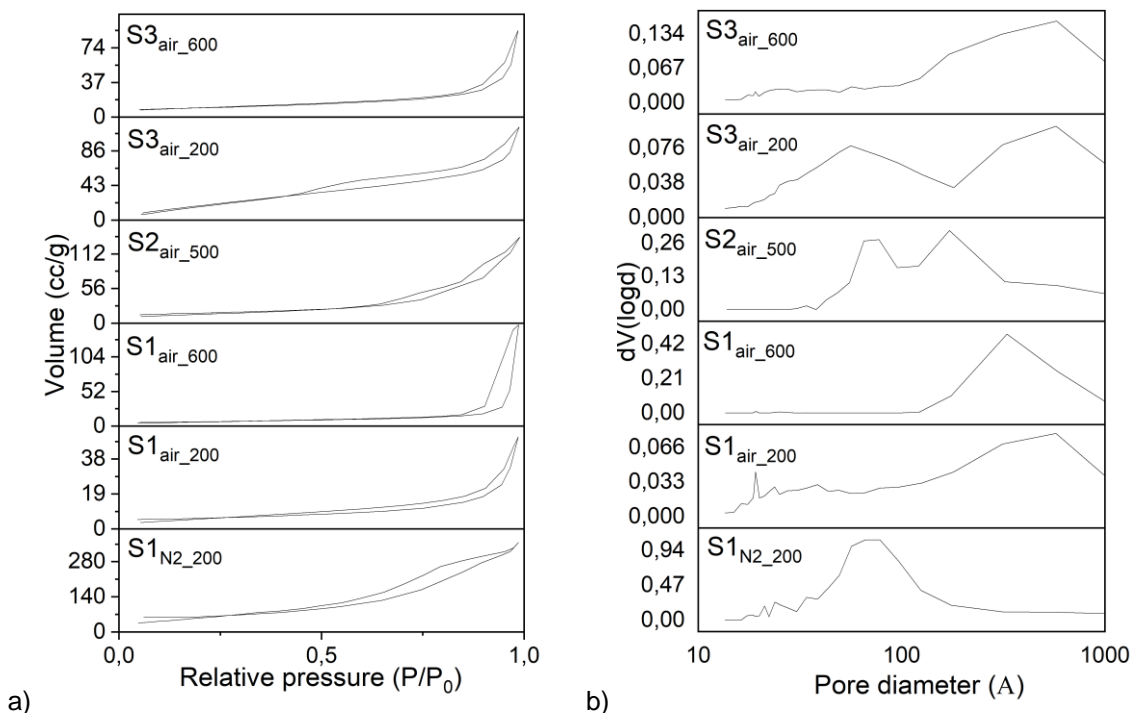


Figure 9.11. a) N_2 adsorption/desorption isotherms and b) distributions BJH for desorption branches of the isotherms of different calcined samples.

Table 9.6. Specific surface areas calculated by BET method for N_2 adsorption isotherms of the calcined samples, with pore volume and pore diameters from BJH calculations

Starting Sample	S1 _{N2}	S1 _{air}		S2 _{air}	S3 _{air}	
Calcination temperature	200 °C	200 °C	600 °C	500 °C	200 °C	600 °C
Obtained Compound	Hematite	Maghemite	Hematite	Hematite	Maghemite	Hematite
BET surface area (m ² /g)	205	20	22	58	37	34
BJH pore diameter Dv(d) (nm)	5.67	1.91	32.99	6.53	3.43	3.91
BJH pore volume (cc/g)	0.60	0.08	0.24	0.22	0.21	0.14

As expected from the XRD and TEM analyses, the S2_{N2_200} and the S2_{air_500} hematite samples exhibit the highest values of specific surface area. Moreover, it is

to be remarked these BET surface areas are higher than most of the experimental results actually reported in literature for hematite [43].

Figure 9.12 shows a final scheme to summarize all the possible NPs obtainable starting from ion exchange syntheses and calcination techniques, together with their main features.

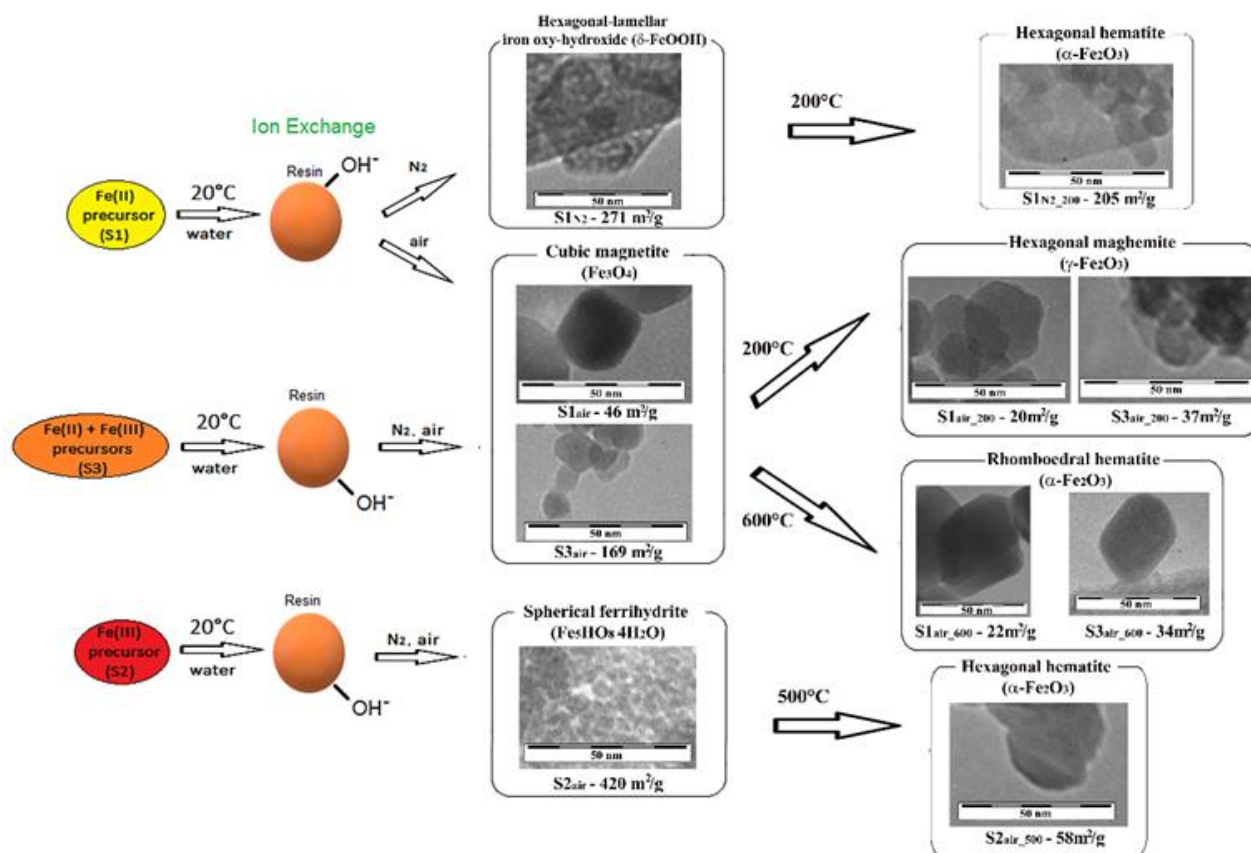


Figure 9.12. Final scheme to summarize all the possible NPs obtainable starting from ion exchange syntheses and calcination techniques

9.3 Tunable transformation of ferrihydrite NPs into of Hematite NPs

As already observed in the literature [44-48], ferrihydrite is a metastable iron compound, and it can be transformed into hematite, goethite or akageneite, depending on temperature, pH and composition. The transformation of ferrihydrite into hematite can occur in water, at neutral pH, at room temperature. However, in these conditions it requires very long times to complete (up to 12 years), revealing after one year a transformation not more than 40%. The transformation in water can

be accelerated by increasing the temperature, but in order to have a complete and fast transformation, dry heating at high temperature is needed (calcination process). Therefore, because hematite nanoparticles can be useful to various applications, in this paragraph, the transformation from the obtained ferrihydrite to hematite is investigated considering 2 procedures, in order to control and regulate the characteristics of the final nanoparticles. In the first procedure, 2-line ferrihydrite (called here Fh) is maintained in aqueous suspension at room temperature (RT) up to seven months of aging. In the second procedure, Fh is calcined in form of dry powder, performing heat treatments at different temperatures (from 100°C to 700°C, for 2h at each considered T). The phase transformations are analyzed by XRD, ATR-FTIR, XPS, TEM, SEM, BET and AGM measurements.

Firstly, thermogravimetric and differential thermal analyses (TG-DTA) are carried out on Fh dry powder, reported in Figure 9.13. From TGA a whole weight variation of about 15% is measured, consistent with the dehydration of ferrihydrite towards hematite. However, the highest weight loss (12%) is observed up to 250°C, corresponding to about 80% of the whole weight loss during the analysis. Moreover, in accordance with literature references on 2-line ferrihydrite, the DTA curve shows an endothermic peak, at about 100 °C, and two exothermic peaks, at about 230°C and 280°C, due to the dehydration of ferrihydrite. [49]

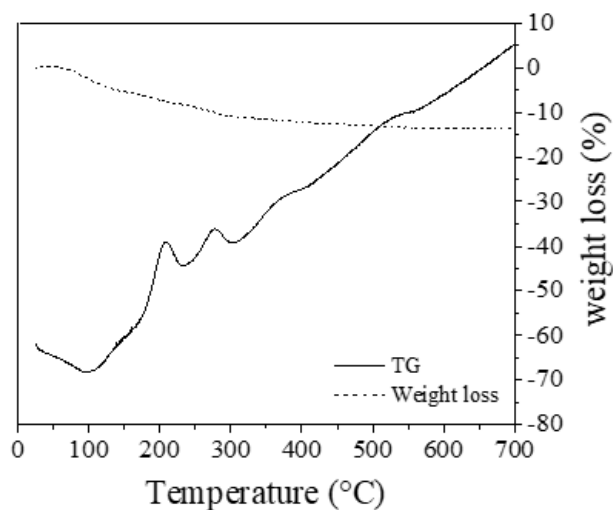


Figure 9.13. TG-DTA analysis at a heating rate of 10°C/min of dry powder from ferrihydrite sample

XRD results of 2-line ferrihydrite samples aged in water at RT up to 7 months (first procedure) and calcined at different temperatures (second procedure) are reported in Figure 9.14. With the aging in water (Figure 9.14a), a gradual conversion of the 2-line ferrihydrite into hematite is observed. In particular, after 1 month the formation of the main Bragg peaks attributable to the hexagonal crystalline structure of α -hematite (α -Fe₂O₃, ICSD #98-016-1292) is observed, that proceeds up to 7 months where α -hematite represents the main observable phase, characterized by an average crystallite size of about 40 nm. In parallel to the formation of hematite, the progressive transformation of ferrihydrite is shown, having its main broad halo at 34° 2 θ , which tends to show a more defined profile with time (inset). In addition, increasing the aging time, a progressive decrease of the peak at 5° 2 θ is clearly observed as well, resulting not completely absent after 7 months, probably corresponding to a residual content of ferrihydrite.

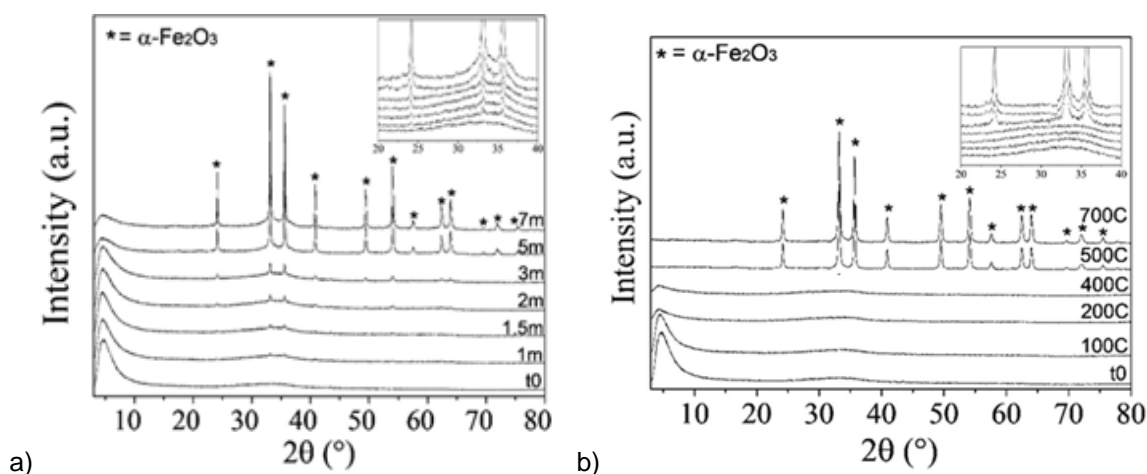


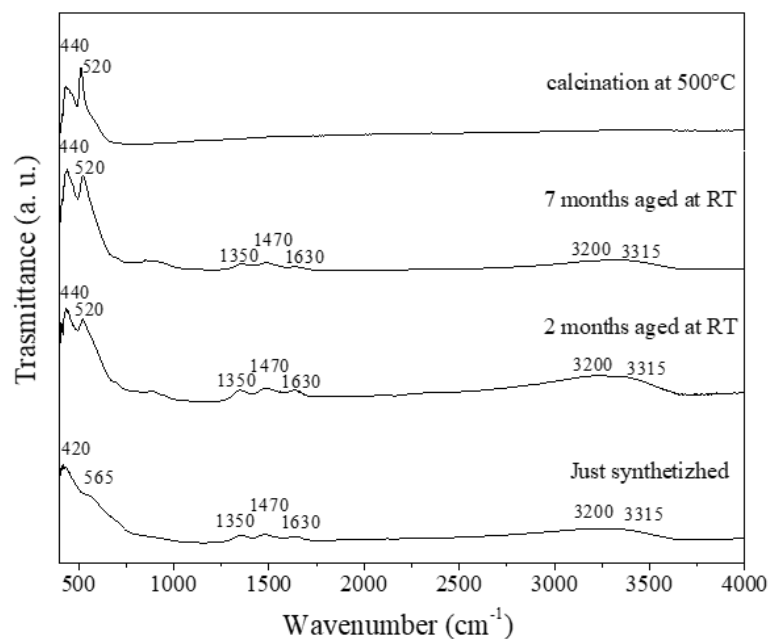
Figure 9.14. XRD patterns of ferrihydrite samples: a) at different aging times at RT (t_0 = just synthesized, m = months); b) at different calcination temperatures until 700°C. In the insets: enlargement of the 20–40° range

Concerning the XRD patterns at different calcination temperatures (Figure 9.14b), the formation of the hexagonal crystalline structure of α -Fe₂O₃ is observed only after 2h at 500°C or more, but not at lower temperatures. In particular, at 500°C the broad halos completely disappear, indicating that the conversion of ferrihydrite into hematite can be considered complete. Regarding X-rays broadening analysis, the hematite phase is here characterized by an average crystallite size of about 20 nm.

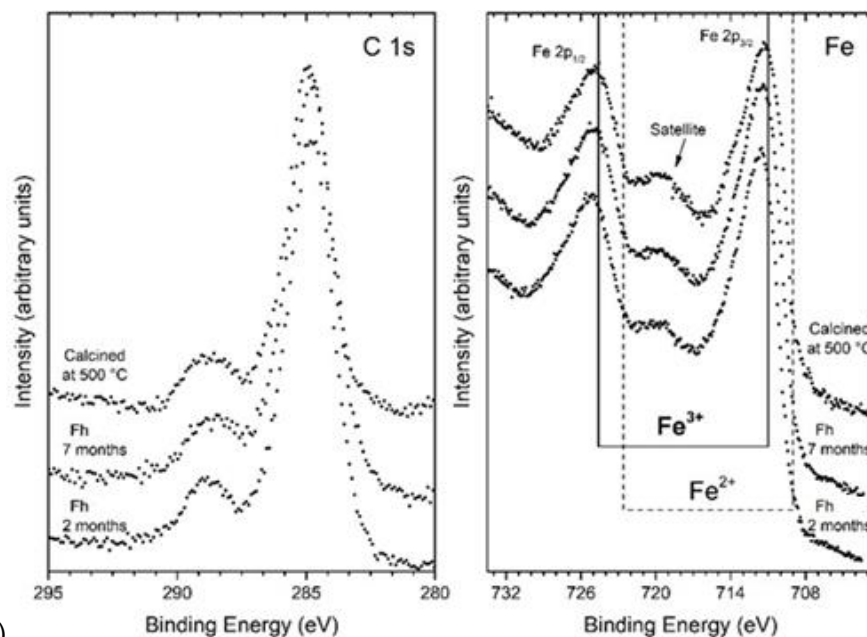
In addition, the peak at $5^\circ 2\theta$ drastically reduces at 200°C , where we measured the most dehydration of ferrihydrite in DTA analysis. Considering that this peak can be associated with an ordered mesoporous structure or with a uniform size of very small NPs of 2-line ferrihydrite, this significant reduction of the $5^\circ 2\theta$ peak can be related to a strong aggregation of the ferrihydrite NPs, caused from dehydration phenomena.

The differences observed from the two procedures, both in the formation of hematite and in the reduction of the peak at $5^\circ 2\theta$, underline different mechanisms of phase transformation from ferrihydrite into hematite. Actually, during the aging in water, the transformation occurs by a gradual oriented attachment of the ferrihydrite NPs that helps or is even necessary to have crystallization. During such gradual oriented attachment, the $\alpha\text{-Fe}_2\text{O}_3$ crystallization can occur by a topotactic transformation at solid phase, through dehydration of ferrihydrite and reorientation of iron ions favored, under water, also at room temperature [44, 46, 50]. On the contrary, in dry heating conditions, with increasing temperature, ferrihydrite NPs tend to dehydrate and aggregate, but the reorientation of iron ions, and consequently the formation of $\alpha\text{-Fe}_2\text{O}_3$, is limited, due to the restricted mobility of ions and it can occur only at high temperatures (500°C or above).

The ATR-FTIR and XPS spectra performed on the ferrihydrite samples aged in water for 2 and 7 months and calcined at 500°C are reported in Figure 9.15. The ATR-FTIR results of Figure 9.15a confirm that in water, by increasing the aging time, ferrihydrite gradually and partially converts into hematite, while following the calcination process, ferrihydrite transforms into pure hematite at temperatures $\geq 500^\circ\text{C}$. The bands attributed to hematite are the typical Fe-O stretching vibrations at about 520 and 440 cm^{-1} , in particular these Fe-O bands become more defined with increasing the aging time. Conversely, in H_{500} sample these bands result well defined and the only ones present.



a)



b)

Figure 9.15. a) ATR-FTIR spectra and b) core level C 1s and Fe 2p XPS spectra, of the samples of ferrihydrite aged in water for 2 and 7 at RT and calcined at 500°C

XPS results of Figure 9.15b show the presence of only Fe³⁺ oxidation state, underlining the existence of hematite or ferrihydrite. Moreover, for the samples aged 7 months and calcined at 500°C, a slight shifting of the Fe 2p_{2/3} peak towards lower binding energy is observed, in accordance with the typical signal related to the prevalence of hematite with respect to other oxy-hydroxy Fe(III) compounds [51]. As

concerns the C 1s signals, similarly to what observed for the ferrihydrite samples, the results are attributable to the presence of the adventitious carbon contamination (CO_2).

TEM and SEM images of the ferrihydrite samples aged in water for 1 week, 2 weeks, 2 months and 7 months and calcined at 500°C are reported in Figure 9.16. TEM images referred to the sample aged for 1 week (Figure 9.16a) reveal the presence of dark particles, with dimensions of about 10 nm, homogeneously dispersed in the amorphous ferrihydrite matrix. The further evolution is shown in the sample aged for 2 weeks (Figure 9.16b), where darker and denser aggregates are visible in the ferrihydrite matrix, reaching diameters of about 50–100 nm. With increasing time, such aggregates become larger and well defined (Figure 9.16c), and after 7 months, they appear organized into dense and pseudo-spherical clusters (Figures 9.16d-e). From the corresponding SEM image these pseudo-spherical clusters are clearly visible (Figure 9.16f), characterized by two distinct morphologies of the assembled particles: a spherical morphology, attributed to the residual ferrihydrite, and a rhombohedral one, that can be related to the hematite particles emerging on the surface of the aggregate as well. These observations confirm the hypothesis that the phase transformation from ferrihydrite to hematite is due to an oriented attachment growth, where the ferrihydrite NPs form aggregates, already visible after two weeks of aging, and becoming larger with time until they define a typical crystalline morphology of hematite [52].

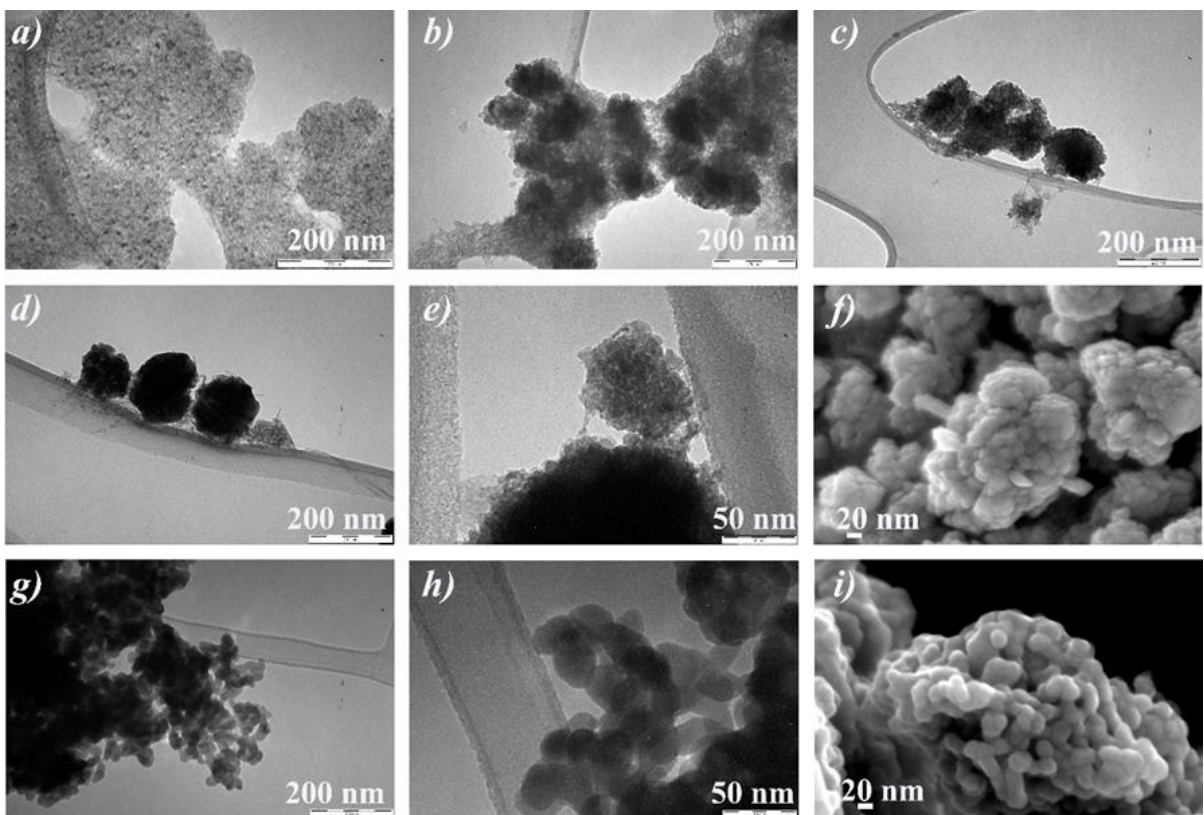


Figure 9.16. TEM images of ferrihydrite samples observed after aging in water for the following times: a) 1 week, b) 2 weeks, c) 2 months, d, e) 7 months. g, h) TEM images of the ferrihydrite sample calcined at 500°C. SEM images of the ferrihydrite samples: f) after aging in water for 7 months, i) calcined at 500°C

TEM images of the sample calcined at 500°C (Figures 9.16g-h), show that the hematite NPs formed by calcination in dry conditions seem to have plate-like morphologies, almost hexagonal, with dimensions between 25 and 35 nm. These samples differ from the aged ones because they do not show an aggregation nature, and besides the ferrihydrite matrix is never observed. The corresponding SEM image (Figure 9.16i) confirms that the NPs have all similar dimensions, of about 30 nm. The described mechanisms, at the base of the transformation from ferrihydrite to hematite according to the two procedures, can explain why the NPs produced by calcination is smaller and monodispersed in dimensions with respect to those obtained after aging in water. In fact, in dry conditions, the reorientation of the iron ions is very fast, and the mobility of the ions is definitely reduced, generating a fast transformation and successively inhibiting the growth of the particles themselves.

The nitrogen adsorption measurements (BET) performed on the ferrihydrite samples aged in water for 2 and 7 months and calcined at 500°C are reported in Figure 9.17a). According to the IUPAC classification [53], the isotherm of the sample aged 2 months can be related to isotherms of type IV, with the typical hysteresis loop of mesoporous materials, associated with capillary condensation in mesopores. The isotherm of the sample aged 7 months results comparable with type IV as well, having a very small type H4 hysteresis loop, which can be associated with spheres composed of ordered mesopores. Finally, the isotherm of the sample calcined at 500°C results again comparable with type IV, but having a type H3 hysteresis loop, which is associated with non-rigid aggregates of plate-like particles.

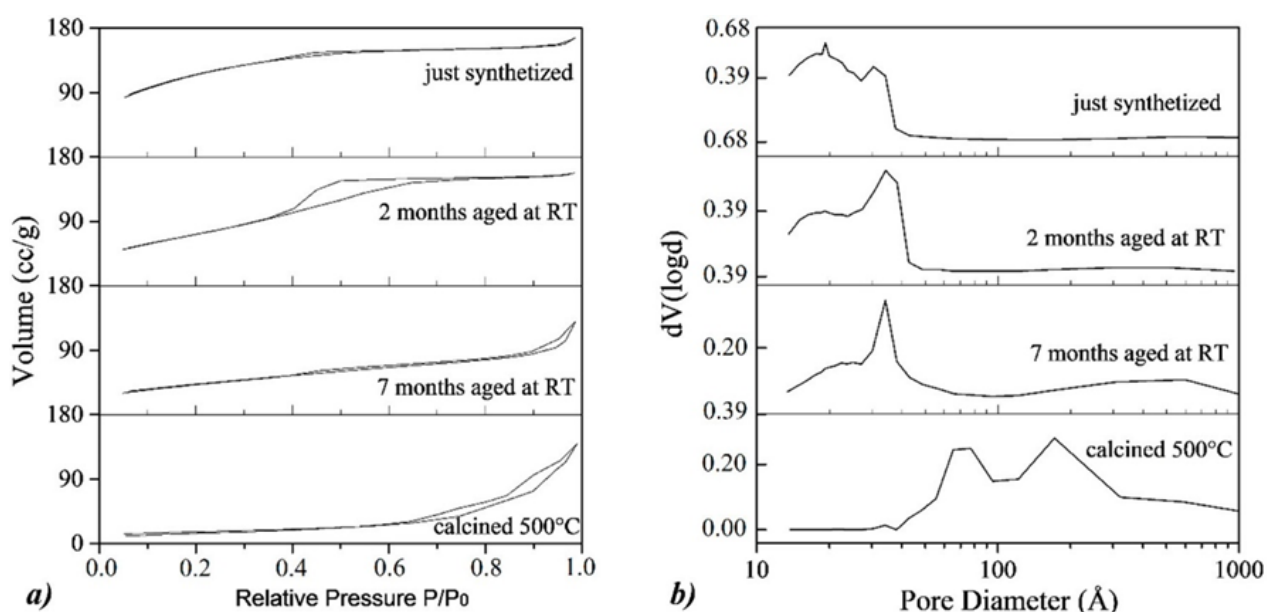


Figure 9.17. a) N₂ adsorption/desorption isotherms and b) BJH distributions for the desorption branch of the isotherms for the samples of ferrihydrite aged in water for 2 and 7 at RT and calcined

Regarding the BJH distributions of Figure 9.17b, the samples aged at RT show the presence of narrow mesopores (< 4 nm), that can be related to the residual ferrihydrite, and macropores (20–100 nm), particularly evident in the 7 months aged sample, and for this reasons, related to the formation of hematite. On the contrary, in the sample calcined at 500°C, the typical mesopores observed in the ferrihydrite samples are absent, while mesopores peaked at around 8 nm and 30 nm are observed, associated with the hematite phase. In Table 9.7, the summaries of the BET and BJH desorption analysis, in terms of surface area values and pore diameters for aged and calcined samples, are reported. It is possible to note that,

increasing the aging time, BET values gradually reduce from 2 to 7 months, ranging from 263 m²/g to 154 m²/g, respectively. This trend reflects the results discussed for the BJH desorption curves, so that the BET surface area of 154 m²/g measured for H_{RT7} sample can be attributable not only to hematite, but also to a residual content of ferrihydrite. On the contrary, for the calcined sample, a BET surface area of 57 m²/g is observed, and it is attributable only to the hematite phase.

Table 9.7. Specific surface areas obtained by the BET equation fit for N₂ gas adsorption isotherms of the samples of hematite obtained from two and seven months of aging at RT and from calcination at 500 °C. Pore diameters and pore volume from BJH analysis are also reported.

Sample	BJH Pore Diameter (nm)	BJH Pore Volume (cc/g)	BET Surface Area (m ² /g)
HRT2	2.9	0.261	263
HRT7	3.5	0.200	154
H500	6.5	0.221	57

Finally, the magnetization response at room temperature is investigated using an alternating gradient magnetometer (AGM) and reported in Figure 9.18, for the ferrihydrite samples just synthesized, with different aging times at RT (2 and 7 months) or with heat treatment (500°C). The 2-line ferrihydrite NPs just synthesized give a linear magnetic field dependence, which is consistent with the paramagnetic behavior found by most of the authors at ambient temperature, where also a contribution from antiferromagnetic susceptibility must be taken into account [54-56]. The magnetic susceptibility is 7.54×10^{-5} emu/(g·Oe), assuming Curie-like temperature dependence, this value corresponds to about 3.0 μ_B, which is lower than the theoretical value for isolated Fe³⁺ ions (5.9 μ_B).

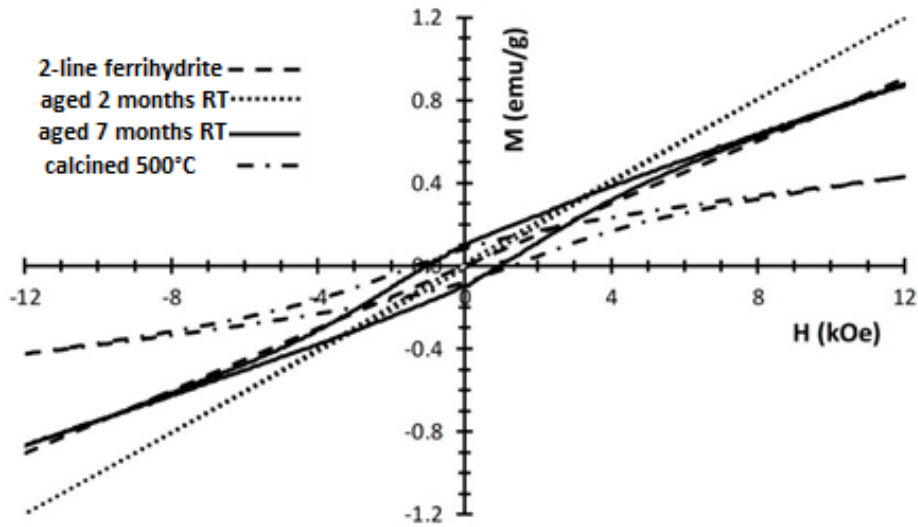


Figure 9.18. Room temperature magnetization data, with maximum applied field of 12kOe, for different iron oxide NPs samples: 2-line ferrihydrite; ferrihydrite aged 2 months, ferrihydrite aged 7 months and ferrihydrite calcined at 500°C (corresponding to pure hematite)

In the same figure an initial increase of magnetic susceptibility is observed for ferrihydrite after 2 months aging, indicating that the average particle magnetic moment is increasing as a consequence of aggregation. In ref. [56] a similar and even more dramatic result, although under substantial different aging conditions, is observed and attributed to dipolar interaction between magnetic particles. A slight appearance of hysteresis is consistent with the formation of the hematite phase [55], as detected by the XRD patterns. At higher aging times (7 months), the magnetization decreases as the presence of hematite prevails, so magnetic hysteresis is more pronounced. This trend is confirmed for the sample calcined at 500°C, where the ferrihydrite disappears and only hematite is present. Also the shape magnetic anisotropy, as well as other morphology details, contributes to the higher observed coercivity of this pure α -Fe₂O₃ sample [57].

The results coming from all the characterization techniques underline the influence of temperature, time and water and the transformation from ferrihydrite to hematite. Two extreme conditions are evaluated (water at RT and dry powder at high temperatures), but the obtained results were useful to fully understand the mechanism of transformation into hematite. Therefore, it is possible to obtain a wide range of surface area values and different hematite morphologies starting from the

ferrhydrite produced by ion exchange method, by adjusting the investigated parameters (or combining them).

CHAPTER 10: COATED MAGNETITE NANOPARTICLES FOR MRI

The synthesis of nanoparticles for magnetic resonance imaging (MRI) presented in Chapter 3 can present various disadvantages, such as high temperatures, numerous washing steps necessary to remove secondary phases and/or additives, long synthesis times, small amounts of obtained products, limiting therefore their potential on a greater scale. Using the innovative ion exchange synthesis route it is possible to obtain various iron oxides NPs, including magnetite and maghemite, which are suitable for biomedical applications. In particular, these NPs can be coated with different agents to obtain SPIONs (superparamagnetic iron oxide nanoparticles) to be used as contrast agents in MRI. For this reason, several coating procedures are performed and the obtained particles are tested using an Aspect Imaging Scanner (present in the high field MRI laboratory of the MESVA Department of the University of L'Aquila) having a magnetic field of 1 T.

10.1 Coating of the synthesized magnetite nanoparticles

For applications in the biomedical field, the considered nanoparticles should have superparamagnetic properties, as described in chapter 3. Therefore, among the various synthesized iron phases, magnetite of sample S3_{air} of the previous chapter is selected, because of its dimensions that result below the critical diameter for this phase (about 14 nm). In fact, from specific characterization techniques, they appear to have dimensions around 6-8 nm, as observed from XRD crystallite size (Table 9.3) and TEM analysis (Figure 9.2d). Moreover, a BET value of 169 m²/g with a BJH pore diameter of 5.7 nm is measured as well for

these NPs (Table 9.4), showing an absorption isotherm of type IV typical of mesoporous materials.

The alternating gradient magnetometry (AGM), performed on these particles and reported in Figure 10.1, reveals that magnetite NPs produced by ion exchange synthesis (S3_{air}) exhibit a superparamagnetic behavior. In fact, they have relatively high magnetization values as the magnetic field increases (up to 55 emu/g), without residual magnetization by removing the magnetic field, such as paramagnetic materials.

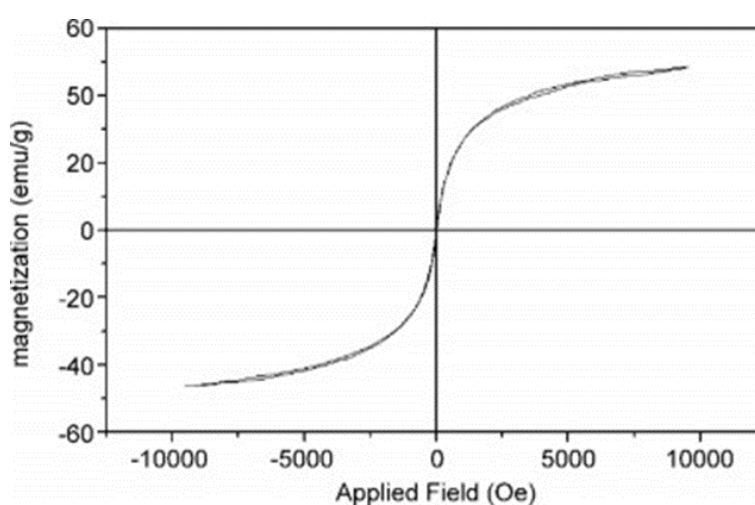


Figure 10.1. Magnetic measurement with alternating gradient magnetometry of magnetite NPs

For these superparamagnetic magnetite NPs, before being applied in the field of MRI, the addition of a surface coating is required to improve their magnetic stability and their biocompatibility, in order to keep them circulating in organisms for a longer time. A procedure for the addition of a surface coating to NPs consist in the use of coating agents following the NPs synthesis, through different temperatures and dispersion modes based on the type of coating used. For this task, ultrasonic bath, ultrasonic cavitation and stirring up to several hours at different temperatures are here considered as dispersion mode. Various dispersing agents among the most common reported in the literature are used, in

particular polyethylene glycol (PEG) with different molecular weight (400, 600, 1000, 1500, 4000), polyvinyl alcohol (PVA), polyvinylpyrrolidone (PVP) and dextran. For each obtained suspension of coated magnetite NPs, the magnetic stability is evaluated up to 60 minutes on a strong niobium magnet ($\geq 10,9$ kOe), to investigate the effectiveness of the coating, reporting the time for which the first particles deposits are observed near the magnet (Table 10.1). Some examples of coated NPs suspensions are shown in Figure 10.2.

Table 10.1. Obtained suspensions of coated magnetite NPs performed by adding dispersing agents following the NPs synthesis, with the relative magnetic stability

Dispersing agent	Magnetite concentration (g/l)	Dispersion mode	Higher magnetic stability (min)
Dextran 3%	1 – 5	Stirring 6h at 80°C	< 1
Dextran 40%	3 – 10	Stirring 6h at 80°C and ultrasonic bath 30 min	< 1
PEG-400 50%	1 – 5	Ultrasonic bath or ultrasonic cavitation 30 min	< 5
PEG-400 95%	1 – 5	Ultrasonic bath 30 min	< 10
PEG-600 95%	1 – 5	Ultrasonic bath 30 min	< 15
PEG-6000 25%	1 – 10	Ultrasonic bath or ultrasonic cavitation 30 min	< 1
PVP 15%	1 – 5	Ultrasonic bath 30 min	< 30
PVA 3%	1 – 5	Ultrasonic bath or ultrasonic cavitation 30 min	< 1
PVA 15%	1 – 5	Ultrasonic bath or ultrasonic cavitation 30 min	< 5

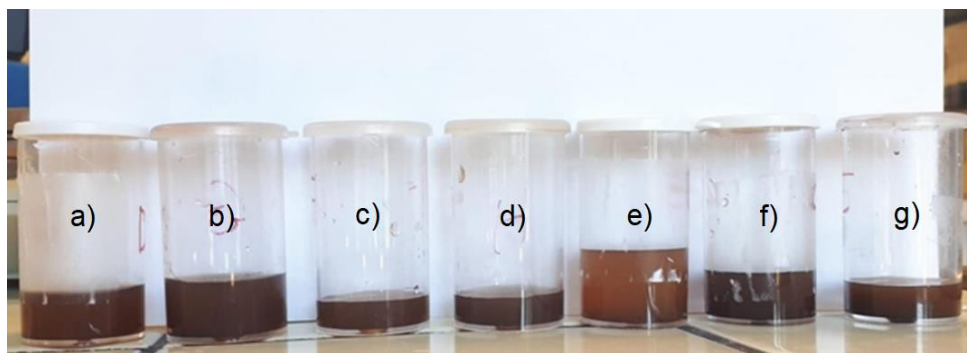


Figure 10.2. Some coated magnetite NPs suspensions with: a) PEG-400 95%, b) PEG-600 95%, c) PEG-6000 25%, d) PVP 15%, e) PVA 3%, f) dextran 40%, g) dextran 3%

Considering the magnetic stability, for all the obtained suspensions of coated magnetite NPs there are no relevant differences between ultrasonic bath and ultrasonic cavitation. The suspensions having the best result in terms of magnetic stability result PEG-400 95%, PEG-600 95% and PVP 15%, so only these 3 samples, among the coatings after synthesis, will be tested in the MRI.

10.2 Direct synthesis of coated superparamagnetic NPs (SPIONs)

To improve the effectiveness of the coatings of magnetite NPs, using the innovative ion exchange route it is possible to perform the addition of some coating agents directly in the synthesis step. In particular, syntheses are carried out using iron(III) chloride hexahydrate ($\text{FeCl}_3 \cdot 6\text{H}_2\text{O}$) and iron(II) chloride tetrahydrate ($\text{FeCl}_2 \cdot 4\text{H}_2\text{O}$), in molar ratio 2:1, with an ion exchange resin in OH^- form (Dowex Monosphere 550A), by dissolving the precursors together with the previously used coating agents. The synthesis route remains conceptually similar to one without dispersing agents, but some interactions can occur between these agents and the obtained products, so also the influence of some parameters, such as time, temperature and reaction environment (air or inert) must be considered. The basic steps of the syntheses with coating agents are:

- 1) preparation of an aqueous solution of the coating agent at a given concentration, under stirring and at different T according to the compound;
- 2) dissolution of iron chlorides in the solution prepared in the step 1) or in another solution, under magnetic stirring and typically at RT;
- 3) preparation of the resin mixed with the solution prepared in the step 1) or with another solution;
- 4) carrying out the synthesis by putting the solution containing chlorides in contact with the wet resin, keeping the system under agitation in an atmosphere of air or nitrogen, at a temperature up to 60°C for a certain period of time;
- 5) separation of the solution with coated NPs from the resin through a sieve and eventually remove the uncoated ones using magnetic separation.

Some of the main syntheses with coating agents performed are reported in Table 10.2.

Table 10.2. Main syntheses of coated superparamagnetic NPs, performed with different dispersing agents in different operating conditions, with the relative magnetic stability

Dispersing agents	FeCl ₃ ·6H ₂ O concentration (M)	Synthesis conditions	Higher magnetic stability (min)
PEG-600 20%	0.2	Air 20°C	< 1
PEG-600 50%	0.1	Air 20°C	< 30
PEG-6000 10%	0.05	Air 20°C	< 1
PEG-6000 25%	0.025	Nitrogen 50°C	< 1
Dextran 40%	0.1	Air 20°C	< 1
PVA 0.3%	0.1	Nitrogen 50°C	> 60
PVP 2%	0.1	Air 20°C	< 20

From the various syntheses the influence of different parameters on the obtained NPs has been evaluated, in particular the concentration of the dispersing agents depends on their ability to influence the viscosity of the liquid, therefore the PEG-600 coats the particles at 50%, while the PVA gives great magnetic stability already at 0.3%. The optimal temperature and precursor concentration depends on the type of coating used (some polymers dissolution is favoured at higher T and too high reagent concentrations lead to uncoated fractions). The nitrogen atmosphere is preferable with temperatures above 40°C to prevent some reactants from oxidizing uncontrollably before ion exchange, so also in this case the choice depends from the type of coating.

According to the magnetic stability tests, showing in a preliminary way the effectiveness and the homogeneity of the coatings, the syntheses with PVA, PVP and PEG-600 give the best results. Therefore, to verify the presence of magnetite NPs having characteristics comparable to those obtained without dispersing agents, XRD measurements are performed and reported in Figure 10.3.

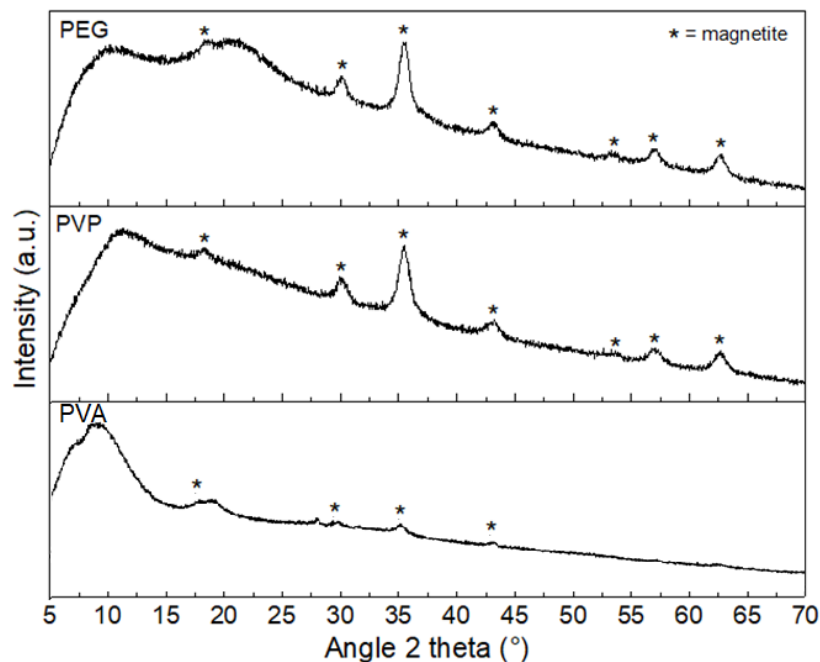


Figure 10.3. XRD patterns of more stable suspensions with synthesized coated magnetite NPs

From the diffraction patterns, the influence of the dispersing agents is found in the background, but the only crystalline phase is always magnetite, having a crystallite size of about 8 nm with PEG and PVP coatings, and of about 9 nm for PVA coating. These values are similar respect to the one observed in the synthesis of magnetite NPs without dispersing agents (about 8 nm).

Transmission electron microscopy investigations, shown in Figure 10.4, are carried out only on the sample containing PVA, because of its higher magnetic stability. Actually, due to an instrument failure, it was possible to analyze only one TEM grid, which was too concentrated, so it was not possible to observe isolated particles. However, it is noted how the PVA is able to separate each nanoparticle, thus avoiding strong magnetic interactions between them. These particles seem to have sizes of about 4-5 nm dispersed fairly homogeneously within the polymer matrix, with some dimensional exception for some agglomerates (10-15 nm). The morphology seems spherical or cubic, because it is not very appreciable with the considered resolution.

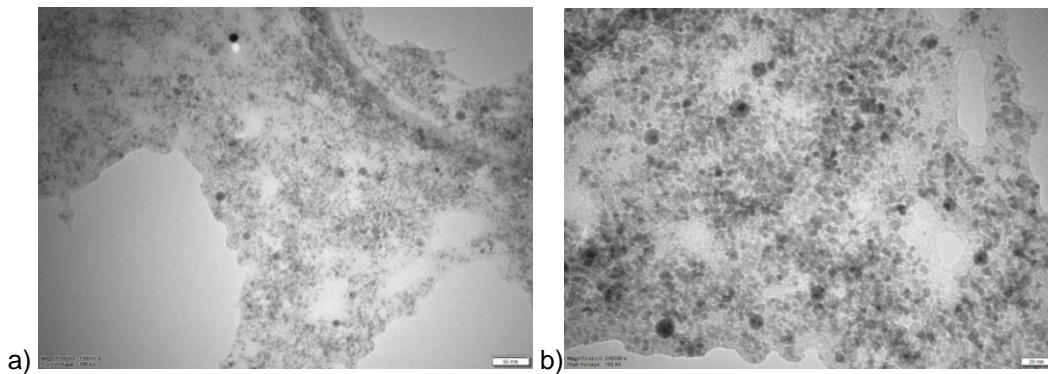


Figure 10.4. TEM micrographs of PVA-coated synthesized magnetite NPs at different magnifications: a) marker 50 nm, b) marker 20 nm

10.3 MRI measurements using optimal samples of SPIONs

Considering magnetic stability, the more stable suspensions, obtained from the different coating procedures of the two previous paragraphs, are used to perform magnetic resonance imaging tests with an Aspect Imaging Scanner (high field MRI laboratory of the MESVA Department) having a magnetic field of 1 T (Figure 10.5).



Figure 10.5. Aspect Imaging scanner 1 T used for MRI acquisitions

Therefore, the obtained samples of SPIONs tested as contrast agents in MRI are:

- 1) PEG-400 95% added after the synthesis,
- 2) PEG-600 95% added after the synthesis,
- 3) 15% PVP added after the synthesis
- 4) PEG-600 50% in direct synthesis,
- 5) 2% PVP in direct synthesis,
- 6) 0.3% PVA in direct synthesis.

For each of these suspensions, 5 dilutions are prepared at established concentrations (0.01 g/l, 0.02 g/l, 0.05 g/l, 0.10 g/l and 0.20 g/l) in water, to perform the MRI tests, as shown in Figure 10.6.



Figure 10.6. Example of sample dilutions for MRI tests, with decreasing concentrations of magnetite NPs from left to right: 0.20 g/l, 0.10 g/l, 0.05 g/l, 0.02 g/l and 0.01 g/l

It is possible to study the relaxation times of a sample through a series of MRI images, calculating T_1 and T_2 by fitting the intensity of the image signal at various TR or TE. For this purpose, multiple images are acquired, each at a different TE or TR. So, one of the typical approaches to obtain relaxation maps is to use Spin-Echo sequences. In a Spin-Echo, the intensity trend (modulus) of the SI signal emitted by each voxel follows an exponential law [1] of the type:

$$SI(TR, TE) = \rho_0 \left(1 - e^{-\frac{TR}{T_1}}\right) e^{-\frac{TE}{T_2}} \quad (10.1)$$

where ρ_0 is the proton density. In these conditions the noise of the system can give a non-zero contribution, therefore a term c is added.

To measure ρ_0 and T_1 is necessary to have a signal with a negligible contribution of $e^{-\frac{TE}{T_2}}$, that is for $TE \ll T_2$ of the sample. On the contrary, for $TR \gg T_1$ of the sample, $e^{-\frac{TR}{T_1}}$ becomes negligible and in this way it is possible to obtain from each voxel the value of ρ_0 . Having several images acquired with various values of TR (therefore weighted in T_1) and $TE \ll T_2$, it is possible to calculate the value of T_1 in each voxel. On the contrary, to calculate the value of T_2 in each voxel, the images are acquired at different TE values using $TR \gg T_1$.

To obtain comparable images, each used Spin-Echo sequence is acquired with the same parameters:

- Field of view (FOV): 32x32 mm,
- Phase encoding: 32,
- Samples: 32,
- Receiver gain: 18,
- Slice thickness: 5 mm,
- Slice: only 1, in an axial position and centered in the isocenter.

The Spin-Echo sequence, for T_1 -weighted images, is used with the minimum TE possible, equal to 4.144 ms, and various TR values in a range between approximately 0 and $3T_1$ (the hypothetical T_1 is estimated through a fast sequence IR-SNAPSHOT after a pulse with a flip angle of 180°). The Spin-Echo sequence, for T_2 -weighted images, is used by choosing $TR = 4T_1$ and various TE values in a range between 0 and $3T_2$.

The images thus acquired are analyzed through a specially written program using the MatLab Software, shown in Appendix A. Thanks to this program, it is possible to fit the data and then obtain T_1 and T_2 values for each sample voxel. By averaging the voxel values of each sample (assuming it is homogeneous) the mean value of the sample is determined. From these values, a graph is constructed, in the inverse of the relaxation time as a function of the concentration in millimoles of Fe, to calculate the trend line. The slope of this line represents the relaxivity, that is the quantification of the variation induced in T_1 or T_2 by the contrast agent (or the coated magnetite NPs in this case) respect to the initial values.

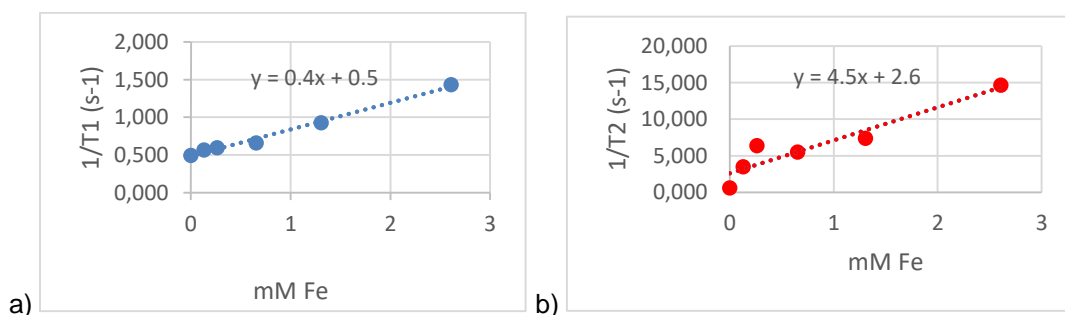
The values obtained for T_1 and T_2 are shown below, as well as the graphs with the calculation of the relaxivity, for each group of analyzed samples. The starting dispersions have different concentrations which depend on the quantity of dispersing agent needed, however the tests are carried out at the same 5

concentrations by diluting them with deionized water. The blank tests made with PEG, PVP and PVA at the concentrations used showed that these polymers alone do not affect the magnetic properties of deionized water. The analyzed samples are therefore:

1) Magnetite suspension 1 g/l with 95% PEG-400 added after the synthesis, suitably diluted for MRI tests. T_1 and T_2 values are reported in Table 10.3 and the graphs on their inverse are reported in Figure 10.7.

Table 10.3. Values of T_1 and T_2 measured from the suspension of magnetite with PEG-400 added

Concentration (g/l)	T_1 (ms)	Error	T_2 (ms)	Error	mM Fe (mmol/l)	$1/T_1$ (s^{-1})	$1/T_2$ (s^{-1})
0	2030	10	1670	10	0	0.49	0.60
0.01	1775	5	286	1	0.13	0.56	3.50
0.02	1685	6	157	1	0.26	0.59	6.37
0.05	1526	6	182	1	0.65	0.66	5.50
0.10	1082	3	135	1	1.30	0.93	7.39
0.20	698	3	68	1	2.61	1.43	14.66



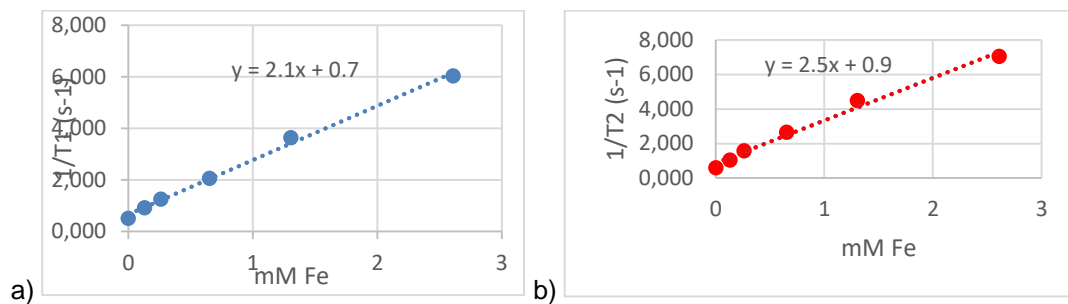
Dal grafico	r_1 ($mM^{-1}s^{-1}$)	0.4
	r_2 ($mM^{-1}s^{-1}$)	4.5

Figure 10.7. Graphs for a) T_1 and b) T_2 with relative relaxivity values, measured from the suspension of magnetite with PEG-400 added

2) Magnetite suspension 1 g/l with 95% PEG-600 added after synthesis, suitably diluted for MRI tests. T_1 and T_2 values are reported in Table 10.4 and the graphs on their inverse are reported in Figure 10.8.

Table 10.4. Values of T_1 and T_2 measured from the suspension of magnetite with PEG-600 added

Concentration (g/l)	T_1 (ms)	Error	T_2 (ms)	Error	mM Fe (mmol/l)	$1/T_1$ (s ⁻¹)	$1/T_2$ (s ⁻¹)
0	1960	10	1670	10	0	0.51	0.60
0.01	1077	4	958	1	0.13	0.93	1.04
0.02	791	4	628	1	0.26	1.26	1.59
0.05	484	1	375	1	0.65	2.07	2.66
0.10	275	1	222	1	1.30	3.64	4.50
0.20	166	1	142	1	2.61	6.04	7.04



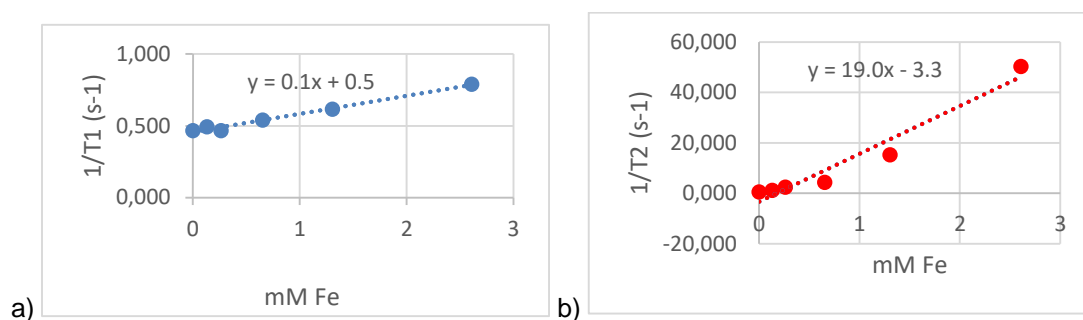
Dal grafico	r_1 (mM ⁻¹ s ⁻¹)	2.1
	r_2 (mM ⁻¹ s ⁻¹)	2.5

Figure 10.8. Graphs for a) T_1 and b) T_2 with relative relaxivity values, measured from the suspension of magnetite with added PEG-600

3) Magnetite suspension 1g/l with 15% PVP added after synthesis, suitably diluted for MRI tests. T_1 and T_2 values are reported in Table 10.5 and the graphs on their inverse are reported in Figure 10.9.

Table 10.5. Values of T_1 and T_2 measured from the suspension of magnetite with added PVP

Concentration (g/l)	T_1 (ms)	Error	T_2 (ms)	Error	mM Fe (mmol/l)	$1/T_1$ (s ⁻¹)	$1/T_2$ (s ⁻¹)
0	2150	10	1670	10	0	0.47	0.60
0.01	2030	10	884	2	0.13	0.49	1.13
0.02	2140	10	400	1	0.26	0.47	2.50
0.05	1860	10	232	1	0.65	0.54	4.31
0.10	1620	10	66	1	1.30	0.62	15.24
0.20	1270	10	20	1	2.61	0.79	50.28



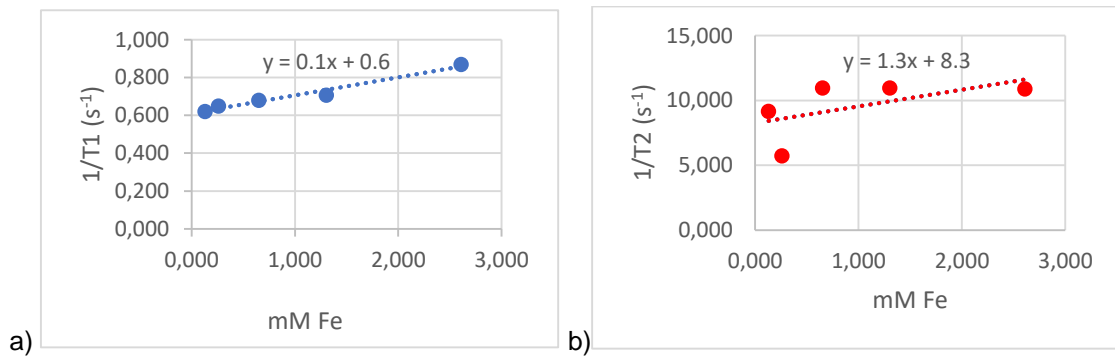
Dal grafico	r_1 (mM ⁻¹ s ⁻¹)	0.1
	r_2 (mM ⁻¹ s ⁻¹)	19.0

Figure 10.9. Graphs for a) T_1 and b) T_2 with relative relaxivity values, measured from the magnetite suspension with added PVP

4) Magnetite suspension 10 g/l with 50% PEG-600 in synthesis, suitably diluted for MRI tests. T_1 and T_2 values are reported in Table 10.6 and the graphs on their inverse are reported in Figure 10.10.

Table 10.6. Values of T_1 and T_2 measured from the suspension of magnetite with PEG-600 insynthesis

Concentration (g/l)	T_1 (ms)	Error	T_2 (ms)	Error	mM Fe (mmol/l)	$1/T_1$ (s^{-1})	$1/T_2$ (s^{-1})
0.01	1610	30	109	1	0.13	0.62	9.16
0.02	1540	30	175	1	0.26	0.65	5.72
0.05	1500	50	91	1	0.65	0.68	10.96
0.10	1420	20	91	1	1.30	0.71	10.97
0.20	1150	20	92	1	2.61	0.87	10.89



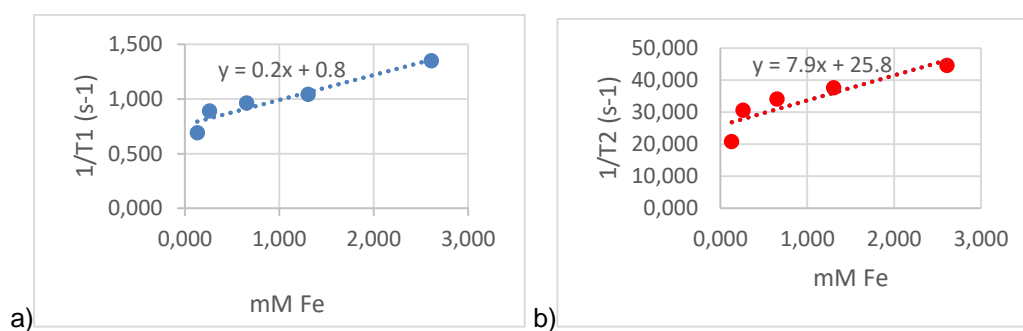
Dai grafici	r_1 ($mM^{-1}s^{-1}$)	0.1
	r_2 ($mM^{-1}s^{-1}$)	1.3

Figure 10.10. Graphs for a) T_1 and b) T_2 with relative relaxivity values, measured from the suspension of magnetite with PEG-600 in synthesis

5) Magnetite suspension 1 g/l with 2% PVP in synthesis, suitably diluted for MRI tests. T_1 and T_2 values are reported in Table 10.7 and the graphs on their inverse are reported in Figure 10.11.

Table 10.7. Values of T_1 and T_2 measured from the suspension of magnetite with PVP in synthesis

Concentration (g/l)	T_1 (ms)	Error	T_2 (ms)	Error	mM Fe (mmol/l)	$1/T_1$ (s ⁻¹)	$1/T_2$ (s ⁻¹)
0.01	1450	20	48	1	0.13	0.69	20.84
0.02	1120	10	33	1	0.26	0.89	30.59
0.05	1040	10	29	1	0.65	0.96	34.10
0.10	960	10	26	1	1.30	1.04	37.64
0.20	741	4	22	1	2.61	1.35	44.68



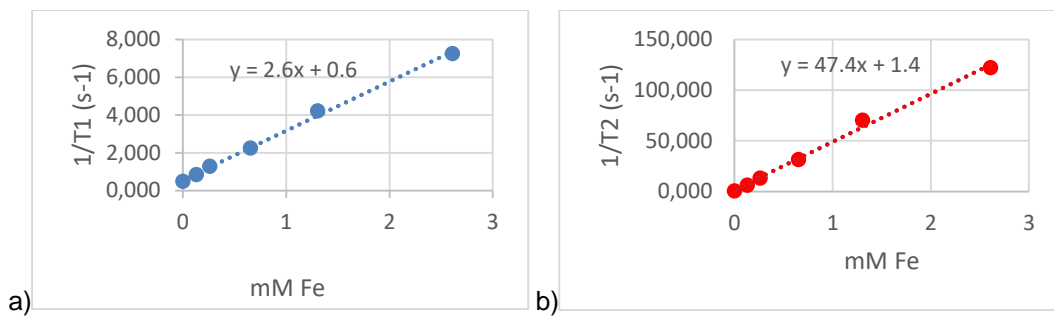
Dal grafico	r_1 (mM ⁻¹ s ⁻¹)	0.2
	r_2 (mM ⁻¹ s ⁻¹)	7.9

Figure 10.11. Graphs for a) T_1 and b) T_2 with relative relaxivity values, measured from the suspension of magnetite with PVP in synthesis

6) Magnetite suspension 1 g/l with 0.3% PVA in synthesis, suitably diluted for MRI tests. T_1 and T_2 values are reported in Table 10.8 and the graphs on their inverse are reported in Figure 10.12.

Table 10.8. Values of T_1 and T_2 measured from the suspension of magnetite with PVA in synthesis

Concentration (g/l)	T_1 (ms)	Error	T_2 (ms)	Error	mM Fe (mmol/l)	$1/T_1$ (s ⁻¹)	$1/T_2$ (s ⁻¹)
0	2060	10	1670	10	0	0.49	0.60
0.01	1187	3	166	1	0.13	0.84	6.02
0.02	785	1	75	1	0.26	1.27	13.25
0.05	444	1	32	1	0.65	2.26	31.44
0.10	238	3	14	1	1.30	4.21	70.37
0.20	138	1	8	1	2.61	7.25	121.95



Dal grafico	r_1 (mM ⁻¹ s ⁻¹)	2.6
	r_2 (mM ⁻¹ s ⁻¹)	47.4

Figure 10.12. Graphs for a) T_1 and b) T_2 with relative relaxivity values, measured by the suspension of magnetite with PVA in synthesis

Table 10.9. Summary of results obtained from MRI tests using magnetite NPs coated with different dispersing agents

Dispersing agent	Core	Core size (nm)	Applied field (T)	r_1 (mM ⁻¹ s ⁻¹)	r_2 (mM ⁻¹ s ⁻¹)
PEG-400 95% added	Fe ₃ O ₄	8	1	0.4	4.5
PEG-600 95% aggiunto	Fe ₃ O ₄	8	1	2.1	2.5
PVP 15% aggiunto	Fe ₃ O ₄	8	1	0.1	19.0
PEG-600 50% sintesi	Fe ₃ O ₄	8	1	0.1	7.9
PVP 2% sintesi	Fe ₃ O ₄	3	1	0.2	1.5
PVA 0,3% sintesi	Fe ₃ O ₄	8	1	2.6	47.4

Comparing all the results obtained for the relaxivity (Table 10.9) with the principal results found in the literature, summarized in Table 10.10, it is possible to note that the magnetite NPs coated with PVP added and coated with PVA in synthesis have good r_2 values, equal to 19 and 47 $\text{mM}^{-1}\text{s}^{-1}$ respectively. Even the samples coated with PEG-600 give positive results but much lower than PVA.

Table 5.1 Commercial MRI contrast agents [2]

Contast agent	Dispersing agent	MRI dose	Size (nm)	Applied field (T)	T (°C)	r_1 ($\text{mM}^{-1}\text{s}^{-1}$)	r_2 ($\text{mM}^{-1}\text{s}^{-1}$)
Endorem (Feridex) SPIO	Dextran	11.2 mg Fe/ml	5-6	0.47	37	30	100
Resovist (Clivist) SPIO	Carboxy-dextran	0.5 mmol/l	4	0.47	37	25.4	151
Sinerem (Combidex) USPIO	Dextran	20 mg Fe/ml	4-6	0.47	37	31	78
Supravist USPIO	Carboxy-dextran	0.5 mmol/l	3-4	0.47	37	9	20
Clariscan USPIO	Starch/PEG	29.8 mg Fe/ml	4-7	0.47	37	10	17
MION-46L	Dextran		4-6	0.47	37	16.5	34.8
Gastromark (Lumirem) SPIO	Silicon	52.5 mg Fe/300 ml	10	0.97	37	3.4	3.8

Probably a possible further refinement of the procedures used to obtain coated magnetite NPs can be realized, in order to obtain higher values of relaxivity. It is also possible to continue towards a possible functionalization of these NPs for

uses as contrast agents MRI of specific organs or cancer cells. Furthermore, thanks to the advantages of the innovative synthesis route (low production costs, reduced synthesis times, high yields, and single step reaction), the production of SPIONs could be easily scaled towards industrial developments.

CONCLUSIONS

Nanoscience is one of the most important research and development frontiers in modern science. The possibility to produce nanostructured particles with high purity and controlled features in a sustainable and scalable way, characterized, in turn, by low toxicity and low costs, can represent a global challenge for the development of responsible innovation.

In order to design and engineer the nanoparticles and to tailor their characteristics to the final application, this thesis work is focused on innovative synthetic processes aimed at producing several metal oxides/hydroxides nanoparticles (NPs) according to high yield, scalable and sustainable synthesis procedures. The different synthesized NPs are successfully employed in different fields, in particular in Cultural Heritage for the consolidation of carbonatic substrates and for the deacidification of waterlogged woods, and in biomedical sector, as anticancer agents and as contrast agents for magnetic resonance imaging (RMI). The innovative synthetic route is based on ion exchange single-step processes, allowing obtaining pure and monodisperse NPs working in water, at room temperature and ambient pressure, without chemical solvents and any purifying or washing procedures to remove impurities or secondary products. The described processes overcome the main drawbacks associated with current procedures to produce NPs, low cost and low environmental impact for a great variety of metal hydroxide/oxide NPs: from earth alkaline metal hydroxides/oxides to iron hydroxides/oxides, with the possibility to increase the production from lab to pilot scale. In addition, most applications require the NPs to be chemically stable, tailored, uniform in size, and easily dispersed in liquid media. In particular, for magnetite NPs surface coatings are realized to enhance their biocompatibility and magnetic stability, in order to use them as contrast agents for RMI. A complete investigation of the produced NPs is carried out by a wide array of techniques, starting from consolidated laboratory techniques (XRD, XRF, XPS,

FTIR, TG-DTA, BET, TEM, SEM-EDX, AFM, AGM, MRI) to cutting edge techniques in large scale facilities (XAS and XRD by synchrotron radiation).

The innovative synthesis techniques reported in this thesis, and developed at the Laboratory of Technology of Materials and Applied Chemistry of the DIIE Department of University of L'Aquila, are also object of a previous European patent (EP2880101, 2016) and of two recently deposited Italian patents. Moreover, this PhD work involved several relationships with different national and international research groups, including the Departments of Physics and Industrial Engineering of the University of L'Aquila, the Department of Life Health and Environmental Sciences (MESVA) of the University of L'Aquila and the CNR-IOM-OGG group in the European Photon and Neutron Science Campus (EPN) of Grenoble.

Pure or coated nanostructured compounds are obtained, such as calcium hydroxide, calcium/iron oxide hydrate, magnesium hydroxide/oxides, strontium hydroxide/carbonate, barium/hydroxide carbonate as well ferrihydrite, hematite, maghemite and magnetite with polymeric coatings.

Specifically, this study started from the optimization of a production process on scales of calcium hydroxide NPs (commonly called nanolime) which is currently mainly used in the Cultural Heritage sector. In fact, nanolime dispersions are the basis of compatible consolidation treatments for all the widespread carbonate-based substrates (mural paintings, stuccoes, natural stones and all historic mortars), since they offer an innovative alternative to organic consolidants or ineffective traditional treatments. Nevertheless, nanolime syntheses generally require organic compounds, and multi-step, time and energy-consuming procedures, and commercial nanolimes are dispersed in alcoholic media, disadvantageous for treatment efficacy (reduced reactivity and back migration effects) and environmental impact (inflammability and VOC release). The calcium hydroxide NPs here obtained from a prototype system of 10 liters in volume, appeared as hexagonal lamellae, with side dimensions < 70 nm and thicknesses

< 10 nm, composed of primary nanoparticles of about 5 nm in length. These NPs resulted very reactive in the carbonation process, so they were employed in conservative treatments on biocalcarene stones of Agrigento (Italy), composed of calcite, quartz, feldspar and shells, restoring the cohesion of the surface grains: increased tear resistance of 60-95% and increased average drilling resistance of 2-6 N until 10 mm depending on the considered stone. These effects were obtained without altering the aesthetical features and the natural water permeability of the treated stones. Considering these encouraging results, the first extensive application of nanolime was realized in relation to the consolidation of the original mortar of a historic building of L'Aquila (Palazzo Pica Alfieri, 14th-16th century), obtaining a depth of penetration of at least 10 mm, with an increased tear resistance of 80% and increased average drilling resistance of 3 N directly in situ.

In this field, also a tailored nanolime containing iron was developed using an innovative synthesis procedure, in order to enhance the application toward particular kind of stones, having iron in the mineralogical composition. In particular, this nanolime has variable % of a new nanometric compound, $\text{Ca}_4\text{Fe}_2(\text{OH})_{14}\cdot 6\text{H}_2\text{O}$, constituted of hexagonal lamellae having side dimensions in the range 10-30 nm and thicknesses in the range 5-10 nm, able to react with atmospheric CO_2 to form cubic calcite (50-100 nm side dimensions) covered with a very amorphous phase constituted by 2-line ferrihydrite at a nanometric level. This phase was investigated also by XAS measurements with synchrotron light (European Synchrotron Radiation Facility of Grenoble), obtaining a binding shell Fe-Ca with $R \approx 3,45 \text{ \AA}$, which disappears after the carbonation process, where it is possible to find 2-line ferrihydrite having a binding shell Fe-Fe with $R \approx 3,06 \text{ \AA}$. Following the synthesis, the tailored nanolime was applied on other biocalcarene samples of Agrigento, reaching enhanced results in terms of consolidation and durability: increased tear resistance of about 85% and increased average drilling resistance of about 8 N, without any chromatic

alteration of the treated surface and a reduced weight loss of 60% in 10 salt crystallization cycles.

Other alkaline earth metal NPs were synthesized with the innovative route, in particular magnesium, strontium and barium, which were produced in form of hydroxides in short times and without intermediate steps. $\text{Mg}(\text{OH})_2$ NPs appeared as hexagonal lamellae having side dimensions < 20 nm and thicknesses of about 5 nm, which resulted formed by an oriented aggregation of primary particles (singlets), with dimensions of 2-3 nm. On the contrary $\text{Sr}(\text{OH})_2$ NPs and $\text{Ba}(\text{OH})_2$ NPs appeared as bars of about 200 and 500 nm in length respectively, composed of primary particles of about 5 and 40 nm respectively. All these particles can be employed in the field of Cultural Heritage, and among them $\text{Mg}(\text{OH})_2$ NPs demonstrated an extraordinary ability to solve the long-standing problems of deacidification of waterlogged woods. The executed tests concerned both curative and preventive treatments on small fragments of an historical vessel (Gallo-Roman wreck, 2nd century b.C.), obtaining always neutral pH values with treatments durable over time by penetrating inside the wood fibers.

Starting from the synthesized $\text{Mg}(\text{OH})_2$ as precursor, it is possible to obtain MgO NPs, which were employed in preliminary cytotoxicological tests on melanoma cells, in collaboration with the research group of Pharmacology (MESVA Department of University of L'Aquila), resulting in a good toxicity towards cancer cells attributed to the generation of reactive oxygen species (ROS). In particular, the growth of melanoma cells resulted reduced of about 45% after 72h using a MgO concentration of 400 $\mu\text{g}/\text{ml}$, accompanied by an increase of cell mortality of about 16%. Moreover, an IC_{50} value of 143 $\mu\text{g}/\text{ml}$ was estimated, in agreement with the literature of cytotoxicological tests using MgO NPs.

Finally, also iron hydroxides/oxides NPs are synthesized using innovative processes, obtaining several kinds of compounds covering a lot of applicative fields, such as ferrihydrite (spherical particles of 2-3 nm having a BET value of about 420 m^2/g), hematite (hexagonal particles of 30-40 nm having a BET value

of about 60 m²/g), magnetite (cubic particles of 5-6 nm having a BET value of about 170 m²/g) and maghemite (rhombohedral particles of 40- 50 nm having a BET value of about 40 m²/g). For their peculiar magnetic properties, non-toxicity and biodegradability, the interest for iron oxide NPs is continuously increasing in biomedicine (for magnetic resonance imaging, drug delivery and magnetic hyperthermia), as well as in environmental remediation. In particular, MRI tests were here performed using coated superparamagnetic NPs as contrast agents, in collaboration with the high-field MRI Laboratory (MESVA Department of University of L'Aquila). The best relaxivity values ($r_2 = 47 \text{ mM}^{-1}\text{s}^{-1}$) were obtained using magnetite NPs coated with PVA, in order to improve both their magnetic stability and biocompatibility.

Given the obtained results concerning the development of the prototype system for large-scale sustainable productions of NPs, as well as the successful outcomes in the Cultural Heritage and in the biomedical sectors, this thesis allows defining a first crucial step to extend the ionic exchange route towards versatile NPs productions for several applications areas. In addition, this work takes up the challenge of producing technologies and products that allow healthcare safety and low environmental impact, according to the latest indications from the European Community.

APPENDIX A –MATLAB PROGRAM

FIT DATI T_1

Section to open images and create their pixel matrix as data:

1. clearvars;
2. Dirname='1.2.826.0.1.3680043.8.1276.2021295357.153.1000.';
3. Nstart=number ID of the first image for T_1 ;
4. Nend= number ID of the last image for T_1 ;
5. Nimmagini=length(Nstart:Nend);
6. File='UnscaledComplexImage_slice0001_complex.img';
7. Npe=number of phase encodings of the images;
8. Nread=number of the samples of the images;
9. TR=flip([range of TR of images acquisition]);
10. daticompleti=zeros(Npe,Nread,Nimmagini);
11. for k=Nstart:Nend
12. name=strcat(Dirname,num2str(k),'Data/');
13. filename=strcat(name,File);
14. hfile=fopen(filename);
15. data=fread(hfile,'double');
16. fclose(hfile);
17. dato=complex(data(1:2:end-1),data(2:2:end));
18. Img = reshape(dato,Npe,Nread);
19. #figure; imshow(abs(Img),[]); **to view all images**
20. daticompleti(:, :, k-Nstart+1)=Img;
21. end

22. `Aspace=abs(daticompleti);` **matrix of the data in absolute values (intensities)**
23. `Max=max(max(max(Aspace)));` **most intense pixel of all images**
24. `#for i=1:Nimmagini` **to view all images in relation to the most intense**
25. `#figure; imshow(Aspace(:,i),[0 Max])`
26. `#end`

Section to create the mask to be applied on the points of the image, in order to calculate the fit of the data only on the points of the sample

27. `name=strcat(Dirname,num2str(ID immagine),'Data/');` **first image of T₁ ID**
28. `filename=strcat(name,File);`
29. `hfile=fopen(filename);`
30. `data=fread(hfile,'double');`
31. `fclose(hfile);`
32. `dato=complex(data(1:2:end-1),data(2:2:end));`
33. `Imgmax= reshape(dato,Npe,Nread);`
34. `massimo=abs(Imgmax);`
35. `mask=imbinarize(massimo,0.2*(max(max(massimo))));` **mask**
36. `#figure; imshow(mask);` **to view the image with mask**
37. `erode=1;`
38. `if erode==1` **Edge erosion for better fit**
39. `mask=imerode(mask, strel('square',2)) ;`
40. `end`

Data fit section to calculate T₁:

41. `tmap = zeros(Npe*Nread,1);` **map of T₁ values for each image**
42. `amap = zeros(Npe*Nread,1);` **map of proton density values ρ_0**

```

43. Nv=length(TR);
44. F=reshape(Aspace,Npe*Nread,Nv); Data vector to perform the analysis
45. NN=Npe*Nread;
46. for i=1:NN
47. if mask(i)==1 to perform the fit only on the points of the image where the
    sample is present
48. x=TR;
49. y=flip(squeeze(F(i,:)));
50. [xData, yData] = prepareCurveData( x, y );
51. f_o2=fitoptions('Method','Nonlinear','StartPoint',[Max,x(floor(Nimmagini/2))]);
52. f2=fittype('a*(1-exp(-x/b))','coefficients',{'a','b'},'dependent',{'y'},'options',f_o2);
53. [curve,f2_out] = fit(xData,yData,f2);
54. variables = coeffvalues(curve);
55. T = variables(2);
56. A = variables(1);
57. tmap(i) = T;
58. amap(i) = A;
59. end
60. end
61. tmap = reshape(tmap,Npe,Nread);
62. amap = reshape(amap,Npe,Nread);
63. figure; surf(tmap); shows the data surface obtained from the fit, i.e. the T1
    value for each pixel
64. icount=0; Calculation of T1 of the sample with associated error
65. T1 = [ ];
66. for i=1:Nread

```

67. for j=1:Npe
68. if mask(i,j)==1
69. icount=icount+1;
70. T1 = [T1 tmap(i,j)];
71. end
72. end
73. end
74. mean(T1) **gives the T₁ value**
75. std(T1)/sqrt(icount) **gives the error on T₁ value**

DATA FIT T₂

Section to open images and create their pixel matrix as data:

1. clearvars;
2. Dirname='1.2.826.0.1.3680043.8.1276.2021295357.153.1000.';
3. Nstart=number ID of the first image for T₂;
4. Nend=number ID of the last image for T₂;
5. Nimmagini=length(Nstart:Nend);
6. File='UnscaledComplexImage_slice0001_complex.img';
7. Npe=number of phase encodings of the images;
8. Nread=numer of the samples of the images;
9. TE=[TE range of images acquisition];
10. daticompleti=zeros(Npe,Nread,Nimmagini);
11. for k=Nstart:Nend
12. name=strcat(Dirname,num2str(k),'Data/');
13. filename=strcat(name,File);
14. hfile=fopen(filename);

```

15. data=fread(hfile,'double');
16. fclose(hfile);
17. dato=complex(data(1:2:end-1),data(2:2:end));
18. Img = reshape(dato,Npe,Nread);
19. #figure; imshow(abs(Img),[ ]); to view all images
20. daticompleti(:,k-Nstart+1)=Img;
21. end
22. Aspace=abs(daticompleti); matrix of the data in absolute vaues (intenisties)
23. Max=max(max(max(Aspace))); most intense pixel of all images
24. #for i=1:Nimmagini to view all images in relation to the most intense
25. #figure; imshow(Aspace(:,i),[0 Max])
26. #end

```

Section to create the mask to be applied on the points of the image, in order to calculate the fit of the data only on the points of the sample:

```

27. name=strcat(Dirname,num2str(ID immagine),'Data/'); For the T2 image ID is the first image
28. filename=strcat(name,File);
29. hfile=fopen(filename);
30. data=fread(hfile,'double');
31. fclose(hfile);
32. dato=complex(data(1:2:end-1),data(2:2:end));
33. Imgmax= reshape(dato,Npe,Nread);
34. massimo=abs(Imgmax);
35. mask=imbinarize(massimo,0.2*(max(max(massimo)))); mask
36. #figure; imshow(mask); to view image with mask

```

```

37. erode=1;
38. if erode==1 edge erosion
39. mask=imerode(mask, strel('square',2)) ;
40. end

```

Data fit to calculate T_2 :

```

41. tmap = zeros(Npe*Nread,1); map of  $T_2$  values for each image
42. amap = zeros(Npe*Nread,1); map of proton density values  $\rho_0$ 
43. Nv=length(TR);
44. F=reshape(Aspace,Npe*Nread,Nv); data vector
45. NN=Npe*Nread;
46. for i=1:NN
47. if mask(i)==1 to perform the fit only on the points of the image where the
    sample is present
48. x=TE;
49. y=squeeze(F(i,:));
50. [xData, yData] = prepareCurveData( x, y );
51. f_o2=fitoptions('Method','Nonlinear','StartPoint',[Max,x(floor(Nimmagini/2))]);
52. f2=fittype('a*exp(-x/b)','coefficients',{'a','b'},'dependent',{'y'},'options',f_o2);
53. [curve,f2_out] = fit(xData,yData,f2);
54. variables = coeffvalues(curve);
55. T=variables(2);
56. A=variables(1);
57. tmap(i) = T;
58. amap(i) = A;
59. end
60. end

```

```
61. tmap = reshape(tmap,Npe,Nread);
62. amap = reshape(amap,Npe,Nread);
63. figure; surf(tmap); Shows the data surface obtained from the fit, i.e. the T2
    value for each pixel
64. icount=0; Calculation of the T2 of the sample with associated error
65. T2 = [];
66. for i=1:Nread
67. for j=1:Npe
68. if mask(i,j)==1
69. icount=icount+1;
70. T2 = [T2 tmap(i,j)];
71. end
72. end
73. end
74. mean(T2) gives the T2 value
```

BIBLIOGRAPHY

BIBLIOGRAPHY CHAPTER 1

- [1] Nanotechnologies for the Life Sciences Vol. 10, Nanomaterials for Medical Diagnosis and Therapy. Edited by Challa S. S. R. Kumar 2007, WILEY-VCH Copyright
- [2] L.G. Gutwein, T.J. Webster; American Ceramic Society 26th Annual Meeting Conference Proceedings, 2003
- [3] Andrew W. Salamon, Patrick Courtney and Ian Shuttler. Nanotechnology and Engineered Nanomaterials, 2010
- [4] The Royal Society, Nanoscience and nanotechnologies: opportunities and uncertainties, 2004, pp. 1-49
- [5] Al-Jumaili, A.; Alancherry, S.; Bazaka, K.; Jacob, M. Review on the Antimicrobial Properties of Carbon Nanostructures. *Materials (Basel)*. 2017, 10:1066
- [6] C.A. Charitidis, P. Georgiou, M.A. Koklioti, A.F. Trompeta, V. Markakis. Manufacturing nanomaterials: from research to industry. *Manufacturing Rev.* 2014, 1:11
- [7] Tiwari, J.N.; Tiwari, R.N.; Kim, K.S. Zero-dimensional, one-dimensional, two-dimensional and three-dimensional nanostructured materials for advanced electrochemical energy devices. *Prog. Mater. Sci.* 2012, 57:724–803
- [8] Wagner, R.S.; Ellis, W.C. Vapor-Liquid-Solid Mechanism of single crystal growth. *Appl. Phys. Lett.* 1964, 4:89–90
- [9] Sen, S.; Kanitkar, P.; Sharma, A.; Muthe, K.P.; Rath, A.; Deshpande, S.K.; Kaur, M.; Aiyer, R.C.; Gupta, S.K.; Yakhmi, J. V Growth of {SnO}₂/W₁₈O₄₉ nanowire hierarchical heterostructure and their application as chemical sensor. *Sensors Actuators B Chem.* 2010, 147:453–460
- [10] E. Mansfield, D. L. Kaiser, D. Fujita, *Metrology and Standardization for Nanotechnology: Protocols and Industrial Innovations*, Wiley-Ych, 2017
- [11] A. R. Muxworthy, W. Williams. Critical superparamagnetic/single-domain grain sizes in interacting magnetite particles: implications for magnetosome crystals. *J. R. Soc. Interface* 2009, 6:1207-1212
- [12] Y. C. Yeh, B. Creran, V. M. Rotello. Gold nanoparticles: preparation, properties, and applications in bionanotechnology. *Nanoscale* 2012; 4(6):1871-1880
- [13] S. Behzadinasab, A. Chin, M. Hosseini, L. M. Poon, W. A. Ducker. A Surface Coating that Rapidly Inactivates SARS-CoV-2. *ACS Applied Materials & Interfaces* 2020
- [14] G.F. Goya, V. Grazù, M.R. Ibarra, "Magnetic nanoparticles for cancer therapy", *Current Nanoscience* 2008, 1-16

- [15] A. Jordan, "Presentation of a new magnetic field therapy system for the treatment of human solid tumors with magnetic fluid hyperthermia," *J. Magn. Mater* 2001, 118
- [16] A. Candeo and F. Dughiero, "A first 3D numerical model for the treatment planning of hepatocellular carcinoma by magnetic fluid hyperthermia," *Proc. ICHO 2008*, 112
- [17] Zhou, W.; Zou, X.; Najmaei, S.; Liu, Z.; Shi, Y.; Kong, J.; Lou, J.; Ajayan, P.M.; Yakobson, B.I.; Idrobo, J.-C.C. Intrinsic Structural Defects in Monolayer Molybdenum Disulfide. *Nano Lett.* 2013, 13:2615–2622
- [18] Rabouw, F.T.; de Mello Donega, C. Excited-State Dynamics in Colloidal Semiconductor Nanocrystals. *Top. Curr. Chem.* 2016, 374
- [19] Sun, Y.-F.; Liu, S.-B.; Meng, F.-L.; Liu, J.-Y.J.-H.; Jin, Z.; Kong, L.-T.; Liu, J.- Y.J.-H. Metal Oxide Nanostructures and Their Gas Sensing Properties: A Review. *Sensors* 2012, 12, 2610–2631
- [20] Komsa, H.-P.; Krasheninnikov, A. V Native defects in bulk and {monolayerMoS₂} from first principles. *Phys. Rev. B* 2015, 91
- [21] R. Weissleder, G. Elizondo, J. Wittenburg, C.A. Rabito CA; *Radiology* 1993, 175:489-493
- [22] S. Tong, S. Hou, Z. Zheng, J. Zhou, G. Bao; Coating optimization of superparamagnetic iron oxide nanoparticles for high T2 relaxivity. *Nano Lett.* 2010, 10(11):4607-4613
- [23] S. Tong, S. Hou, B. Ren, Z. Zheng, G. Bao; Self-Assembly of Phospholipid–PEG Coating on Nanoparticles through Dual Solvent Exchange. *Nano Lett.* 2011, 11(9):3720-3726
- [24] J.R. Garrett, X. Wu, J. Sha, K. Ye. pH-insensitive glucose indicators. *Biotechnol. Prog.* 2008, 24(5):1085-1089
- [25] C. Mah, I. Zolotukhin, T.J. Fraitas, J. Dobson, C. Batich, B.J. Byrne. Microsphere-mediated delivery of recombinant AAV vectors in vitro and in vivo. *Mol Therapy.* 2000; 1:S239
- [26] M. Bruchez, M. Moronne, P. Gin, S. Weiss; Semiconductor nanocrystals as fluorescent biological labels *Science* 1998, 281(5385):2013-2016
- [27] H. Mainul, W. Chaoming, S. Ming; Multiplexed biomarker detection using x-ray fluorescence of composition-encoded nanoparticles. *Appl. Phys. Lett.* 97, 263704 (2010)
- [28] D. Panatarotto, C.D. Prtidos, J. Hoebeke, F. Brown, E. Kramer, J.P. Briand; Immunization with peptide-functionalized carbon nanotubes enhances virus-specific neutralizing antibody responses. *Chemistry & Biology* 2003, 10(10):961-966
- [29] R.L. Edelstein, C.R. Tamanaha, P.E. Sheehan; The BARC biosensor applied to the detection of biological warfare agents. *Biosensors Bioelectron* 2000, 14(10-11):805-813
- [30] R. Mahtab, J.P. Rogers, C.J. Murphy; Protein-Sized Quantum Dot Luminescence Can Distinguish between "Straight", "Bent", and "Kinked" Oligonucleotides. *J Am Chem Soc* 1995, 117(35):9099-9100

- [31] J. Ma, H. Wong, L.B. Kong, K.W. Peng; Biomimetic processing of nanocrystallite bioactive apatite coating on titanium. *Nanotechnology* 2003, 14(6):619-623
- [32] R.S. Molday, D. MacKenzie; Immunospecific ferromagnetic iron-dextran reagents for the labeling and magnetic separation of cells. *J Immunol Methods* 1982, 52(3):353-367
- [33] O.V. Salata. Applications of nanoparticles in biology and medicine. *Journal of Nanobiotechnology* 2004, 2:3
- [34] J.M. Wilkinson. Nanotechnology applications in medicine. *Med. Device Technol.* 2003, 14(5):29-31
- [35] M. Sprintz, C. Benedetti, M. Ferrari. Applied nanotechnology for the management of breakthrough cancer pain. *Minerva Anesthesiol.* 2005, 71(7-8):419-423
- [36] T. Kubik, K. Bogunia-Kubik, M. Sugisaka. Nanotechnology on duty in medical applications. *Curr. Pharm. Biotechnol.* 2005, 6(1):17-33
- [37] D. F. Emerich, C. G. Thanos. Nanotechnology and medicine. *Expert Opin. Biol. Ther.* 2003, 3(4):655-663
- [38] D. F. Emerich. Nanomedicine--prospective therapeutic and diagnostic applications. *Expert Opin. Biol. Ther.* 2005, 5(1):1-5
- [39] K.K. Jain. Challenges of drug discovery for personalized medicine. *Curr. Opin. Mol. Ther.* 2006, 8(6):487-492
- [40] D. Proske; *Appl. Microbiol. Biotechnol.* 2006, 69(5):485-492
- [41] A.K. Deisingh, M. Thompson. Biosensors for the detection of bacteria. *Can. J. Microbiol.* 2004, 50(2):69-77
- [42] P. Prasad. Emerging Opportunities at the Interface of Photonics, Nanotechnology and Biotechnology. *Molecular Crystals and Liquid Crystals* 2004, 415(1):1-7
- [43] J.A. Coplan. *Mol. Imaging Biol.* 2004, 6:341-349
- [44] R.A. Farrer, F.L. Butterfield, V.W. Chen, J.T. Fourkas. Highly Efficient Multiphoton-Absorption-Induced Luminescence from Gold Nanoparticles. *Nano Lett.* 2005, 5(6):1139-1142
- [45] P. Gould. *Material Today* 2004, 7:36
- [46] W.E. Doering, S. Nie. Spectroscopic Tags Using Dye-Embedded Nanoparticles and Surface-Enhanced Raman Scattering. 2003, 75(22):6171–6176

BIBLIOGRAPHY CHAPTER 2

- [1] A. Chroneos, K. Desai, S.E. Redfern, M.O. Zacate, R.W. Grimes. New atomic scale simulation models for hydroxides and oxyhydroxides. *Journal of Materials Science* 2006, 41:675–687

- [2] Ashurst J., Dimes F.G. Conservation of Building and Decorative Stone. Butterworth-Heinemann: London; 1990
- [3] Elert K., Rodriguez-Navarro C., Pardo S.E., et al. Lime Mortars for the Conservation of Historic Buildings. *Studies in Conservation* 2002, 47:62-75
- [4] M. Ambrosi, L. Dei, R. Giorgi, C. Neto, P. Baglioni. Colloidal Particles of Ca(OH)₂: Properties and Applications to Restoration of Frescoes. *Langmuir* 2001, 14(17):4251-4255
- [5] B. Salvadori, L. Dei. Synthesis of Ca(OH)₂ Nanoparticles from Diols. *Langmuir* 2001, 17(8):2371–2374
- [6] V. Daniele, G. Taglieri. Synthesis of Ca(OH)₂ nanoparticles with the addition of Triton X-100. Protective treatments on natural stones: Preliminary results. *Journal of Cultural Heritage* 2012, 13(1):40-46
- [7] G. Poggi, N. Toccafondi, D. Chelazzi, P. Canton, R. Giorgi, P. Baglioni. Calcium hydroxide nanoparticles from solvothermal reaction for the deacidification of degraded waterlogged wood. *J Colloid Interface Sci* 2016, 1(473):1-8
- [8] K. Kukli, M. Ritala, T. Sajavaara, T. Hanninen, M. Leskela. Atomic layer deposition of calcium oxide and calcium hafnium oxide films using calcium cyclopentadienyl precursor. *Thin Solid Films* 2006, 500:322–329
- [9] O. Nilsen, H. Fjellvag, A. Kjekshus. Growth of calcium carbonate by the atomic layer chemical vapour deposition technique. *Thin Solid Films*. 2004, 450:240–247
- [10] M.A. Alavi, A. Morsali. Ultrasonic-assisted synthesis of Ca(OH)₂ and CaO nanostructures. *Journal of Experimental Nanoscience* 2010, 5:93-105
- [11] Giorgio Nasillo, Maria Luisa Saladino, Delia Chillura Martino, Irene Natali, Luigi Dei, Eugenio Caponetti. A new preparation method of nanolime dispersion for the conservation of art works. YOCOCU: Contribute and role of youth in conservation of cultural heritage
- [12] C. Rodriguez-Navarro, A. Suzuki, E. Ruiz-Agudo. Alcohol Dispersions of Calcium Hydroxide Nanoparticles for Stone Conservation. *Langmuir* 2013, 29:11457–11470
- [13] Bermejo Sotillo M. A. et al. CO₂-capturing binder, production method thereof based on the selection, purification and optimization of carbide lime, and agglomerates having and environmental activity. Eur. Pat. EP2500328; published September 19th 2012
- [14] P. Baglioni, D. Chelazzi, R. Giorgi, G. Poggi. Colloid and Materials Science for the Conservation of Cultural Heritage: Cleaning, Consolidation, and Deacidification. *Langmuir* 2013, 29(17):5110-5122
- [15] Salvadori B., Dei L. Synthesis of Ca(OH)₂ Nanoparticles from Diols. *Langmuir* 2001, 17:2371-2374

- [16] Daniele V., Taglieri G. Synthesis of Ca(OH)₂ nanoparticles with the addition of Triton X-100. Protective treatments on natural stones: Preliminary results. *Journal of Cultural Heritage* 2012, 13:40–46
- [17] Ziegenbalg G., Verfahren zur verfestigenden Behandlung von mineralischen anorganischen Baustoffen. Patent DE 10327514B3 (2005)
- [18] Poggi G. Calcium hydroxide nanoparticles from solvothermal reaction for the deacidification of degraded waterlogged wood. *Journal of Colloid and Interface Science* 2016, 473:1–8
- [19] Asikin-Mijan N. Synthesis of clamshell derived Ca(OH)₂ nano-particles via simple surfactant-hydration treatment. *Chemical Engineering Journal* 2015, 262:1043–1051
- [20] S. Bastone, D.F. Chillura Martino, V. Renda, M.L. Saladino, G. Poggi, E. Caponetti. Alcoholic nanolime dispersion obtained by the insolubilisation-precipitation method and its application for the deacidification of ancient paper. *Colloids and Surfaces A: Physicochem. Eng. Aspects* 2017, 513:241–249
- [21] Boynton R.S. Chemistry and technology of lime and limestone. Wiley edition: New York; 1980.
- [22] Hansen, E., Doehne, E., Fidler, J., et al. A review of selected inorganic consolidants and protective treatments for porous calcareous materials. *Reviews in Conservation* 2003, 4:13-25
- [23] Doehne, E., Price, C.A. Stone Conservation: An Overview of Current Research. The Getty Conservation Institute: Los Angeles; 2010
- [24] Baglioni, P., Dei, L., Pique, F., et al. New autogenous lime-based grouts used in the conservation of lime-based wall paintings. *Studies in Conservation* 1997; 42:43-54
- [25] A. Zornoza-Indarta, P. Lopez-Arce, N. Leal, J. Simão, K. Zoghlami. Consolidation of a Tunisian bioclastic calcarenite: From conventional ethyl silicate products to nanostructured and nanoparticle based. *Construction and Building Materials* 2016, 116:188-202
- [26] R. Giorgi, D. Chelazzi, P. Baglioni. Nanoparticles of Calcium Hydroxide for Wood Conservation. The Deacidification of the Vasa Warship. *Langmuir* 2005, 21(23):10743–10748
- [27] O. Dianat, S. Saedi, M. Kazem, M. Alam. Anti-microbial activity of nanoparticle calcium hydroxide against *Enterococcus Faecalis*. *Iran Endod J. Winter* 2015, 10(1):39-43
- [28] Aniruddha Samanta, Soumik Podder, Chandan Kumar Ghosh, Manjima Bhattacharyac, Jiten Ghosh, Awadesh Kumar Mallik, Arjun Dey, Anoop Kumar Mukhopadhyay. ROS mediated high anti-bacterial efficacy of strain tolerant layered phase pure nano-calcium hydroxide. *J Mech Behav Biomed Mater.* 2017, 72:110-128
- [29] R. Badri Narayan, R. Goutham, B. Srikanth, K. P. Gopinath. A novel nano-sized calcium hydroxide catalyst prepared from clam shells for the photodegradation of methyl red dye. *Journal of Environmental Chemical Engineering* 2018, 6(3):3640-3647

- [30] P.L. Boey, G.P. Maniam, S.A. Hamid. Performance of calcium oxide as a heterogeneous catalyst in biodiesel production: a review. *Chem. Eng. J.* 2011, 168:15–22
- [31] Y.H. Taufiq-Yap, H.V. Lee, R. Yunus, J.C. Juan. Transesterification of non-edible *Jatropha curcas* oil to biodiesel using binary Ca–Mg mixed oxide catalyst: effect of stoichiometric composition. *Chem. Eng. J.* 2011, 178:342–347
- [32] J. Guan, Q. Wang, X. Li, Z. Luo, K. Cen. Thermodynamic analysis of a biomass anaerobic gasification process for hydrogen production with sufficient CaO. *Renewable Energy* 2007, 32:2502–2515
- [33] Q. Zhang, J. Chang, T. Wang, Y. Xu. Upgrading bio-oil over different solid catalysts. *Energy Fuels* 2006, 20:2717–2720
- [34] L.G. Hwa, C.-C. Chen, S.L. Hwang. Optical properties of calcium-aluminate oxide glasses. *Chin. J. Phys.* 1997, 35:78–89
- [35] L. Promsong, M. Sriyudthsak. Thin tin-oxide film alcohol-gas sensor. *Sensors Actuators B Chem.* 1995, 25:504–506
- [36] Kambiz Tahvildari, Yasaman Naghavi Anaraki, Reza Fazaeli, Sogol Mirpanji, and Elham Delrish. The study of CaO and MgO heterogenic nano-catalyst coupling on transesterification reaction efficacy in the production of biodiesel from recycled cooking oil. *J Environ Health Sci Engineer* 2015, 13:73
- [37] www.ibz-freiberg.de/downloads/pdf/produkte/tm/ital/Calosil_allgemein.pdf
- [38] http://www.csgi.unifi.it/products/plus_ita.html
- [39] P.R. Hornsby, J. Wang, R. Rotheron, G. Jackson, G. Wilkinson. Thermal decomposition behaviour of polyamide fire-retardant compositions containing magnesium hydroxide filler. *Polym. Degrad. Stab.* 1996, 51:235
- [40] C.M. Tai, R. K. Y. Li. Studies on the impact fracture behaviour of flame retardant polymeric material 2001, 22(1):15–19
- [41] S. Zhang, A.R. Horrocks. A review of flame retardant polypropylene fibres. *Prog. Polym. Sci.* 2003, 28:1517
- [42] M. Sain, S.H. Park, F. Suhara, S. Law. Flame retardant and mechanical properties of natural fibre–PP composites containing magnesium hydroxide. *Polymer Degradation and Stability* 2004, 83:363–367
- [43] Z. Shen, X. Chen, M. Tong, S. Guo, M. Ni, J. Lu. Studies on magnesium-based wet flue gas desulfurization process. *Fuel* 2013, 105:578–584
- [44] ZHU Hong-tao. Study on decolour of reactive brilliant red using magnesium hydroxide, *Chemical Engineer* 2007, 3:55–57

- [45] J. Kang, P. Schwendeman. Comparison of the effects of Mg(OH)₂ and sucrose on the stability of bovine serum albumin encapsulated in injectable poly(d,l-lactide-co-glycolide) implants. *Biomaterials* 2002, 23:239
- [46] H. S. Shin, S. M. Lee. Removal of Nutrients in Wastewater by using Magnesium Salts, *Environmental Technology* 1998, 19(3):283-290
- [47] M. M. Rahmana, M. A. M. Salleha, U. Rashida, A. Ahsana, M. M. Hossain, C. S. Rae. Production of slow release crystal fertilizer from wastewaters through struvite crystallization – A review. *Arabian Journal of Chemistry* 2014, 7(1):139–155
- [48] R. Giorgi, C. Bozzi, L. Dei, C. Gabbiani, B.W. Ninham, P. Baglioni. Nanoparticles of Mg(OH)₂: synthesis and application to paper conservation. *Langmuir* 2005, 21:8495–8501
- [49] C. Dong, J. Cairney, Q. Sun, O. Lee Maddan, G. He, Y. Deng. Investigation of Mg(OH)₂ nanoparticles as an antibacterial agent. *J Nanopart Res* 2010, 12:2101-2109
- [50] R.C. Xie and B. J. Qu, 2001. Preparation of needle-shaped Mg(OH)₂ nanoparticles. Patent Application Number 00135436 of P. R. China
- [51] M. Alexandre, G. Beye, C. Henrist, R. Cloots, A. Rulmont, R. Jerome, Ph. Dubois. Preparation and Properties of Layered Silicate Nanocomposites Based on Ethylene Vinyl Acetate Copolymers. *Macromol. Rapid Commun.* 2001, 22:643
- [52] C. M. Jiao, Z. Z. Wang, Z. Ye, Y. Hu, W.C. Fan. Flame retardation of ethylene–vinyl acetate copolymer using nano magnesium hydroxide and nano hydrotalcite. *J Fire Sci* 2006, 24:47–64
- [53] J.P. Lv, L.Z. Qiu, B.J. Qu. Controlled synthesis of magnesium hydroxide nanoparticles with different morphological structures and related properties in flame retardant ethylene–vinyl acetate blends. *Nanotechnology* 2004, 15:1576–1581
- [54] L.Z. Qiu, R.C. Xie, P. Ding, B.J. Qu. Preparation and characterization of Mg(OH)₂ nanoparticles and flame-retardant property of its nanocomposites with EVA. *Composite Structures* 2003, 62:391-195
- [55] Y. Li, M. Sui, Y. Ding, G. Zhang, J. Zhuang, C. Wang. Preparation of Mg(OH)₂ Nanorods. *Adv. Mater.* 2000, 12:818
- [56] L. Yan, J. Zhuang, X.M. Sun, Z.X. Deng, Y.D. Li. Formation of rod-like Mg(OH)₂ nanocrystallites under hydrothermal conditions and the conversion to MgO nanorods by thermal dehydration. *Mater. Chem. Phys.* 2001, 76(2):119
- [57] C. L. Yan, D. F. Xue, L. J. Zou, X. X. Yan and W. Wang. Preparation of magnesium hydroxide nanoflowers. *J. Cryst. Growth* 2005, 282:448
- [58] C. Henrist, J.P. Mathieu, C. Vogels, A. Rulmont, R.J. Cloots. Morphological study of magnesium hydroxide nanoparticles precipitated in dilute aqueous solution. *J. Cryst. Growth* 2003, 249:321

- [59] C. Liang, T. Sasaki, Y. Shimizu, N. Koshizaki. Pulsed-laser ablation of Mg in liquids: surfactant-directing nanoparticle assembly for magnesium hydroxide nanostructures. *Chemical Physics Letters* 2004, 389:58–63
- [60] M.A. Alavi, A. Morsali. Syntheses and characterization of Mg(OH)₂ and MgO nanostructures by ultrasonic method. *Ultrasonics Sonochemistry* 2010, 17:441–446
- [61] H.Q. Wu, M.W. Shao, J.S. Gu, X.W. Wei. Microwave-assisted synthesis of fibre-like Mg(OH)₂ nanoparticles in aqueous solution at room temperature. *Mater. Lett.* 2004, 58:2166
- [62] C.Y. Tai, C.T. Tai, M.H. Chang, H.S. Liu. Synthesis of Magnesium Hydroxide and Oxide Nanoparticles Using a Spinning Disk Reactor. *Ind. Eng. Chem. Res.* 2007, 46:5536-5541
- [63] J. Lv, L. Qiu, B. Qu. Controlled growth of three morphological structures of magnesium hydroxide nanoparticles by wet precipitation method. *Journal of Crystal Growth* 2004, 267:676-684
- [64] J.C. Yu, A.W. Xu, L.Z. Zhang, R.Q. Song, L. Wu. Synthesis and Characterization of Porous Magnesium Hydroxide and Oxide Nanoplates. *J. Phys. Chem. B.* 2004, 108:64
- [65] W. Jiang, X. Hua, Q. Han, X. Yang, L. Lu, X. Wang. Preparation of lamellar magnesium hydroxide nanoparticles via precipitation method. *Powder Technology* 2009, 191:227–230
- [66] J.P. Hsu, A. Nacu. Preparation of submicron-sized Mg(OH)₂ particles through precipitation. *Colloids Surf. A* 2005, 262:220-231
- [67] Z.G. Zhao, F.X. Geng, H.T. Cong, J.B. Bai, H.M. Cheng. Low temperature synthesis of Mg(OH)₂ nanotubes in aqueous solutions of block copolymer P12., *Nano* 2006, 1(2):185–189
- [68] B. Li, Y. Zhang, Y. Zhao, Z. Wu, Z. Zhang. A novel method for preparing surface-modified Mg(OH)₂ nanocrystallines. *Mater. Sci. Eng. A* 2007, 452/453:302–305
- [69] H. Yan, J.M. Wu, X.H. Zhang, Y. Zhang, L.Q. Wei, X.G. Liu, B.S. Xu. Synthesis of magnesium hydroxide nanoneedles and short nanorods on polymer dispersant template. *J. Mater. Res.* 2007, 22(9):2544-2549
- [70] M. S. Mastuli, N. S. Ansari, M. A. Nawawi, A. M. Mahat. Effects of Cationic Surfactant in Sol-gel Synthesis of Nano Sized Magnesium Oxide. *APCBEE Procedia* 2012, 3:93–98
- [71] Y. Zhang, M. Ma, X. Zhang, B. Wang, R. Liu. Synthesis, characterization, and catalytic property of nanosized MgO flakes with different shapes. *Journal of Alloys and Compounds* 2014, 590:373–379
- [72] S. Li, B. Zhou, B. Ren, L. Xing, L. Tan, L. Dong, J. Li. Preparation of MgO nanomaterials by microemulsion-based oil/water interface precipitation. *Materials Letters* 2016, 171:204–207
- [73] M. A. Alavi, A. Morsali. Syntheses and characterization of Mg(OH)₂ and MgO nanostructures by ultrasonic method. *Ultrasonics Sonochemistry* 2010, 17:441–446

- [74] S. Demirci, B. Öztürk, S. Yildirim, F. Bakal, M. Erol, O. Sancakoğlu, R. Yigit, E. Celik, T. Batar. Synthesis and comparison of the photocatalytic activities of flame spray pyrolysis and sol-gel derived magnesium oxide nano-scale particles, *Materials Science in Semiconductor Processing* 2015, 34:154–161
- [75] J. S. Matthews, O. Just, B. Obi-Johnson, W. Rees, Jr. CVD of MgO from a Mg(β -ketoiminate)₂: Preparation, Characterization, and Utilization of an Intramolecularly Stabilized, Highly Volatile, Thermally Robust Precursor. *Chem. Vap. Deposition* 2000, 6:3
- [76] G. Carta, N. El Habra, L. Crociani, G. Rossetto, P. Zanella, A. Zanella, G. Paolucci, D. Barreca, E. Tondello. CVD of MgO Thin Films from Bis(methylcyclopentadienyl)Magnesium. *Chem. Vap. Deposition* 2007, 13:185–189
- [77] L. Sun, H. He, C. Liu, Z. Ye. Local super-saturation dependent synthesis of MgO nanosheets, *Applied Surface Science* 2011, 257:3607–3611
- [78] S. Chae, H. Lee, P. V. Pikhitsa, C. Kim, S. Shin, D. Kim, M. Choi. Synthesis of terraced and spherical MgO nanoparticles using flame metal combustion, *Powder Technology* 2017, 305:132–140
- [79] Magnesium Oxide (MgO) Nanoparticles - Properties, Applications. Azonano 2013
- [80] Tucker, M.E.; Wright, V.P. Carbonate. *Carbonate Sedimentology*, Editorial Wiley-Blackwell 1991
- [81] P. López-Arce, L.S. Gomez-Villalba, L. Pinho, M.E. Fernández-Valle, M. Álvarez de Buergo, R. Forta. Influence of porosity and relative humidity on consolidation of dolostone with calcium hydroxide nanoparticles: Effectiveness assessment with non-destructive techniques. *Materials Characterization* 2010, 61(2):168-184
- [82] D. Min, T. Mingshu. Measures to inhibit alkali-dolomite reaction. *Cement and Concrete Research* 1993, 23(5):1115-1120
- [83] C. Ayora, C. Taberner, M.W. Saaltinka, J. Carrera. The genesis of dedolomites: a discussion based on reactive transport modeling. *Journal of Hydrology* 1998, 209(1–4):346-365
- [84] Marc-André Bérubé, Marc Choquette, Jacques Locat. Effects of lime on common soil and rock forming minerals. *Applied Clay Science* 1990, 5(2):145-163
- [85] L.S. Gomez-Villalba, P. López-Arce, A. Zornoza, M. Álvarez de Buergo, R. Fort. Evaluación del tratamiento de consolidación de dolomías mediante nanopartículas de hidróxido de calcio en condiciones de alta humedad relativa. *Bol. Soc. Esp. Ceram. Vidr.* 2011, 50(2):85-92
- [86] D. Chelazzi, G. Poggi, Y. Jaidar, N. Toccafondi, R. Giorgi, P. Baglioni. Hydroxide nanoparticles for cultural heritage: Consolidation and protection of wall paintings and carbonate materials. *Journal of Colloid and Interface Science* 2013, 392:42-49

- [87] E. Ciliberto, G.G. Condorelli, S. La Delfa, E. Viscuso. Nanoparticles of Sr(OH)₂: synthesis in homogeneous phase at low temperature and application for cultural heritage artefacts. *Applied Physics A* 2008, 92:137–141
- [88] S. Vijayalakshmi, P. Anupriya, P. Surya, Vijayalakshmi C. Synthesis and characterization of strontia nanoparticles. *International Journal of Pure and Applied Mathematics* 2018, 119(15):1299-1305
- [89] Amy L. Linsebigler, Guangquan Lu, and John T. Yates Jr. Photocatalysis on TiO₂ Surfaces: Principles, Mechanisms, and Selected Results. *Chem. Rev.* 1995, 95(3):735–758
- [90] Placido Munafò, Giovanni Battista Goffredo, Enrico Quagliarini. TiO₂-based nanocoatings for preserving architectural stone surfaces: An overview. *Construction and Building Materials* 2015, 84:201-218
- [91] E. Ciliberto, G.G. Condorelli, S. La Delfa, E. Viscuso. Nanoparticles of Sr(OH)₂: synthesis in homogeneous phase at low temperature and application for cultural heritage artefacts. *Applied Physics A* 2008, 92:137–14
- [92] Sa Lv, Ji Sheng, shuang Zhang, Wendong Sun. “Effects of reaction time and citric acid contents on the morphologies of BaCO₃ via PVP-assisted method”. *Material Research Bulletin* 2008, 43:1099-1105
- [93] Fangzhi Huang, Yuhua Shena, Anjian Xie, Li Zhang, Wanghua Xuc, Shikuo Lia and Wensheng Lua. “Polymorph control of a complex BaCO₃ superstructure through the cooperation of an insoluble polylactide self-assembled film and soluble poly allylamine modifie”. *Reactive & Functional polymers* 2009, 69:843-850
- [94] Khaled M. Saoud, Imen Ibala, Dana El Ladki, Omar Ezzeldeen, Shaukat Saeed. Microwave Assisted Preparation of Calcium Hydroxide and Barium Hydroxide Nanoparticles and Their Application for Conservation of Cultural Heritage. *EuroMed 2014: Digital Heritage. Progress in Cultural Heritage: Documentation, Preservation, and Protection* pp 342-352
- [95] Amir Zelati, Ahmad Amirabadizadeh, Ahmad Kompany. Preparation and Characterization of Barium Carbonate Nanoparticles. *International Journal of Chemical Engineering and Applications* 2011, 2(4):299-303
- [96] José Delgado Rodrigues, Ana Paula Ferreira Pinto. Laboratory and onsite study of barium hydroxide as a consolidant for high porosity limestones *Journal of Cultural Heritage* 2016, 19:467-476
- [97] Ioannasis Karatasios, Vassilis Kilikoglou, Belinda Colston, Panagiotis Theoulakis, David Watt. Setting process of lime-based conservation mortars with barium hydroxide. *Cement and Concrete Research* 2007, 37(6):886-893

- [98] A.P. Ferreira Pinto, J. Delgado Rodrigues. Stone consolidation: The role of treatment procedures. *Journal of Cultural Heritage* 2008, 9(1):38-53
- [99] Rodorico Giorgi, Moira Ambrosi, Nicola Toccafondi, Piero Baglioni. Nanoparticles for Cultural Heritage Conservation: Calcium and Barium Hydroxide Nanoparticles for Wall Painting Consolidation. *Chemistry European Journal* 2010, 16(31):9374-9382
- [100] Piero Baglioni, Rodorico Giorgi. Soft and hard nanomaterials for restoration and conservation of cultural heritage. *Soft Matter* 2006, 4
- [101] Keun-Hyeok Yang, Jae-II Sim, Sang-Ho Nam. Enhancement of reactivity of calcium hydroxide-activated slag mortars by the addition of barium hydroxide. *Construction and Building Materials* 2010, 24(3):241-251

BIBLIOGRAPHY CHAPTER 3

- [1] D. Ramimoghadam, S. Bagheri, S.B. Abd Hamid. Progress in electrochemical synthesis of magnetic iron oxide nanoparticles. *Journal of Magnetism and Magnetic Materials* 2014, 368:207-229
- [2] M. Benz. Superparamagnetism: Theory and Applications. *Materials Science* 2012
- [3] Leslie-Pelecky D. L., Rieke R. D. Magnetic properties of nanostructured materials. *Chemistry of Materials* 1996, 8(8):1770– 83
- [4] V.J. Mohanraj, Y. Chen. Nanoparticles - A review. *Tropical Journal of Pharmaceutical Research* 2006, 5(1):561-573
- [5] {<http://webmineral.com/data/Maghemite.shtml>}
- [6] {<http://webmineral.com/data/Magnetite.shtml>}
- [7] K. Raj, B. Moskowitz, R. Casciari. Advances in ferrofluid technology. *Journal of Magnetism and Magnetic Materials* 1995, 149(1-2):174-180
- [8] Marta Sartor. Dynamic Light Scattering. University of California, San Diego
- [9] Sun S. N., Wei C., Zhu Z. Z., Hou Y. L., Venkatraman S. S., Xu Z. C. Magnetic iron oxide nanoparticles: synthesis and surface coating techniques for biomedical applications. *Chin. Phys. B* 2014, 23(3)
- [10] A. K. Gupta, S. Wells. Surface-modified superparamagnetic nanoparticles for drug delivery: preparation, characterization, and cytotoxicity studies. *IEEE Transactions on nanobioscience* 2004, 3(1):66-73
- [11] http://www.ultrasonic-systems.com/ultrasonics/precipitation_01.html

- [12] J. Vidal-Vidal, J. Rivasb, M.A. Lopez-Quintela. Synthesis of Monodisperse Maghemite Nanoparticles by the Microemulsion Method. *Colloids and Surfaces A: Physicochemical and Engineering Aspects* 2006, 288:44-51
- [13] X. Zeng, Z. Wang, Y. Liu, M. Ji. γ -Fe₂O₃ nanoparticles prepared by laser ablation of a tiny wire. *Appl. Phys. A* 2005, 80:581-584
- [14] M.D. Barankin, Y. Creighton, A. Schmidt-Ott. Synthesis of nanoparticles in an atmospheric pressure glow discharge. *Journal of Nanoparticle Research* 2006, 8:511-517
- [15] A.K. Gupta, M. Gupta. Synthesis and surface engineering of iron oxide nanoparticles for biomedical applications. *Biomaterials* 2005, 26:3995-4021
- [16] A. Petri-Fink, M. Chastellain, L. Juillerat-Jeanneret. Development of functionalized superparamagnetic iron oxide nanoparticles for interaction with human cancer cells. *Biomaterials* 2005, 26:2685-2694
- [17] O. Strbak, I. Antal, D. Gongola, M. Kubovcikova, M. Koneracka, V. Zavisova, A. Krafcik, M. Masarova-Kozelova, P. Kopcansky, I. Frollo. Measurement of the magnetic nanoparticles' relaxivity during encapsulation into polyactide carriers. *Measurement* 2017, 104:89-92
- [18] Cheng Tao, Yanan Chen, Danli Wang, Yu Cai, Qiang Zheng, Lu An, Jiaomin Lin, Qiwei Tian, Shiping Yang. Macromolecules with Different Charges, Lengths, and Coordination Groups for the Coprecipitation Synthesis of Magnetic Iron Oxide Nanoparticles as T1 MRI Contrast Agents. *Nanomaterials* 2019, 9(5):699
- [19] Ariya Saraswathy, Shaiju S Nazeer, Madhumol Jeevan, Nirmala Nimi, Sabareeswaran Arumugam, Vijayakumar S Harikrishnan, P R Harikrishna Varma, Ramapurath S Jayasree. Citrate coated iron oxide nanoparticles with enhanced relaxivity for in vivo magnetic resonance imaging of liver fibrosis. *Colloids and Surfaces B: Biointerfaces* 2014, 117:216–224
- [20] Ariya Saraswathy, Shaiju S Nazeer, Nirmala Nimi, Sabareeswaran Arumugam, Sachin J Shenoy, Ramapurath S Jayasree. Synthesis and characterization of dextran stabilized superparamagnetic iron oxide nanoparticles for in vivo MR imaging of liver fibrosis. *Carbohydrate Polymers* 2014, 101:760–768
- [21] Ning Xiao, Wei Gu, Hao Wang, Yunlong Deng, Xin Shi, Ling Ye. T1–T2 dual-modal MRI of brain gliomas using PEGylated Gd-doped iron oxide nanoparticles. *Journal of Colloid and Interface Science* 2014, 417:159–165
- [22] Paramagnetic colloidal ferrihydrite nanoparticles for MRI contrasting. COLSUA 22109
- [23] Maria F. Casula, Patrizia Floris, Claudia Innocenti, Alessandro Lascialfari, Massimo Marinone, Maurizio Corti, Ralph A. Sperling, Wolfgang J. Parak, Claudio Sangregorio. Magnetic Resonance Imaging Contrast Agents Based on Iron Oxide Superparamagnetic Ferrofluids. *Chem. Mater.* 2010, 22(5):1739-1748

- [24] A. Masotti, A. Pitta, G. Ortaggi, M. Corti, C. Innocenti, A. Lascialfari, M. Marinone, P. Marzola, A. Daducci, A. Sbarbati, E. Micotti, F. Orsini, G. Poletti, C. Sangregorio. Synthesis and characterization of polyethylenimine-based iron oxide composites as novel contrast agents for MRI", *Magnetic Resonance Materials in Physics, Biology and Medicine* 2009, 22:77–87
- [25] A. Ali, H. Zafar, M. Zia, I. ul Haq, A. R. Phull, J. S. Ali, A. Hussain. Synthesis, characterization, applications, and challenges of iron oxide nanoparticles. *Nanotechnology, Science and Applications* 2016, 19(9):49-67
- [26] Iron powder product with high specific surface area. United States Patent Application 20160096739
- [27] J. Antelo, F. Arce, S. Fiol. Arsenate and phosphate adsorption on ferrihydrite nanoparticles: Synergetic interaction with calcium ions. *Chemical Geology* 2015, 410:53-62
- [28] S. Das, M. J. Hendry, J. Essilfie-Dughan. Transformation of Two-Line Ferrihydrite to Goethite and Hematite as a Function of pH and Temperature. *Environmental Science Technology* 2011, 45:268-275
- [29] P. G. Weidler. BET Sample Pretreatment of Synthetic Ferrihydrite and its Influence on the Determination of Surface Area and Porosity. *Journal of Porous Materials* 1997, 4:165-169
- [30] K. Rout, M. Mohapatra, S. Anand. 2-line ferrihydrite: synthesis, characterization and its adsorption behaviour for removal of Pb(II), Cd(II), Cu(II) and Zn(II) from aqueous solutions. *Dalton Transactions* 2012, 41:3302-3312
- [31] Z. Li, T. Zhang, K. Li. One-step synthesis of mesoporous two-line ferrihydrite for effective elimination of arsenic contaminants from natural water. *Dalton Transactions* 2011, 40:2062-2067
- [32] Z. Khayat Sarkar, F. Khayat Sarkar. Synthesis and Magnetic Properties Investigations of Fe₃O₄ Nanoparticles. *International Journal of Nanoscience and Nanotechnology* 2011, 7(4):197-200
- [33] S. L. Iconaru, R. Guégan, C. Popa, M. Motelica-Heino, C. S. Ciobanu, et al. Magnetite (Fe₃O₄) nanoparticles as adsorbents for As and Cu removal. *Applied Clay Science* 2016, 134:128-135
- [34] P.K. Singh, C.H. Weng, Y.C. Sharma. Economically viable synthesis of Fe₃O₄ nanoparticles and their characterization. V. Srivastava, *Polish Journal of Chemical Technology* 2011, 13(2):1-5
- [35] M. Bobik, I. Korus, L. Dudek. The effect of magnetite nanoparticles synthesis conditions on their ability to separate heavy metal ions. *Archives of Environmental Protection* 2017, 43(2):3-9
- [36] E. Di Iorio, C. Colombo, Z. Cheng, G. Capitani, D. Mele, G. Ventruti, R. Angelico. Characterization of magnetite nanoparticles synthesized from Fe(II)/nitrate solutions for arsenic removal from water. *Journal of Environmental Chemical Engineering* 2019, 7(2):102986

- [37] OV Salata. Applications of nanoparticles in biology and medicine. *Journal of Nanobiotechnology* 2004, 2:3
- [38] D. Peer, J. M. Karp, S. Hong, O.C. Farokhzad, R. Margalit, R. Longer. Nanocarriers as an emerging platform for cancer therapy. *Nature Nanotechnology* 2007, 2(12):751-760
- [39] F. Dughiero, A. Candeo, E. Sieni. Modelli numerici per il trattamento di tumori mediante ipertermia con nanoparticelle magnetiche. Dipartimento di Ingegneria Elettrica, Università di Padova; www-1.unipv.it/et2008/memorie/Dughiero.pdf
- [40] Giustini A. J., Petryk A. A., Cassim S. M., Tate A. J., Baker I., Hoopes J. P. Magnetic nanoparticle hyperthermia in cancer treatment. *Nano Life* 2010, 1:2
- [41] Rosensweig R. E. Heating magnetic fluid with alternating magnetic field. *Journal of Magnetism and Magnetic Materials* 2002, 252:370–374
- [42] R. Weissleder, G. Elizondo, J. Wittenberg, C.A. Rabito, H.H. Bengele, L. Josephson. Ultrasmall superparamagnetic iron oxide: characterization of a new class of contrast agents for MR imaging. *Radiology* 1990, 175(2):489-493
- [43] M.F. Bellin, C. Beigelman, S. Precetti-Morel. Iron oxide-enhanced MR lymphography: initial experience. *Eur. J. Radiol.* 2000, 34(3):257-264
- [44] H.H. Bengele, S. Palmacci, J. Rogers, C.W. Jung, J. Crenshaw, L. Josephson. Biodistribution of an ultrasmall superparamagnetic iron oxide colloid, BMS 180549, by different routes of administration. *Magn. Reson. Imaging* 1994, 12(3):433-442
- [45] M. Song, W. Kyung Moon, Y. Kim, D. Lim, I. Song, B. Yoon. Labeling Efficacy of Superparamagnetic Iron Oxide Nanoparticles to Human Neural Stem Cells: Comparison of Ferumoxides, Monocrystalline Iron Oxide, Cross-linked Iron Oxide (CLIO)-NH₂ and tat-CLIO. *Korean J. Radiol.* 2007, 8(5):365-371
- [46] A. Petri-Fink, M. Chastellain, L Juillerat-Jeanneret, A. Ferrari, H. Hofmann. Development of functionalized superparamagnetic iron oxide nanoparticles for interaction with human cancer cells. *Biomaterials* 2005, 26(15):2685-2694
- [47] S. Metz, G. Bonaterra, M. Rudelius, M. Settles, E.J. Rummeny, H Daldruplink. Capacity of human monocytes to phagocytose approved iron oxide MR contrast agents in vitro. *Eur. Radiol.* 2004, 14(10):1851-1858
- [48] E Schulze, J.T. Ferrucci, K. Poss, L. Lapointe, A. Bogdanova, R. Weissleder. Cellular uptake and trafficking of a prototypical magnetic iron oxide label in vitro. *Invest. Radiol.* 1995, 30(10):604-610
- [49] W. Leenders. Ferumoxtran-10 Advanced Magnetics. *IDrugs* 2003, 6(10):987-993

[50] J. Schnorr, M. Taupitz, S. Wagner, H. Pilgrimm, J. Hansel, B. Hamm. Age-related blood half-life of particulate contrast material: experimental results with a USPIO in rats. *J. Magn. Reson. Imaging* 2000, 12(5):740-744

BIBLIOGRAPHY CHAPTER 4

- [1] Bruce P. G. *Powder Diffraction: Theory and Practice*. Royal Society of Chemistry, 2008
- [2] Watts J.F., Wolstenholme J. *An Introduction to Surface Analysis by XPS and AES*. Wiley, 2003
- [3] PENNER-HAHN, J. E. *X-ray Absorption Spectroscopy*. University of Michigan, Ann Arbor, MI, USA
- [4] Cramer, S. P.; Tench, O.; Yocum, M.; George, G. N. *Nucl. Instrum. Methods Phys. Res. Sect. A-Accel. Spectrom. Dect. Assoc. Equip.* 1988, 266:586–591
- [5] Que, L. Jr. (ED.). *Physical Methods in Bioinorganic Chemistry: spectroscopy and magnetism*. Sausalito, Calif., University Science Books, 2000
- [6] Lytle, F. W. (1999), *J. Synchrotron Rad.* 6, 123–134 and Stumm von Bordwehr, R. (1989), *Ann. Phys. (Paris)* 14, 377–465
- [7] Sayers, Stern and Lytle. EXAFS scattering theory. *Phys. Rev. Lett.* 1971, 27:1204–1207
- [8] Rehr and Albers, *Rev. Mod. Phys.* 2000, 72:621–654
- [9] A. Lee, P.H. Citrin, P. Eisenberger, B.M. Kincaid. Etended x-ray absorption fine structure – its strengths and limitations as a structural tool. *Reviews of Modern Physics* 1981, 53(4) Part I
- [10] B.D. Shrivastava. X-ray absorption fine structure (XAFS) spectroscopy using synchrotron radiation. *J. Phys.: Conf.* 2012; Ser. 365 012002
- [11] Stuart B. *Infrared Spectroscopy: Fundamentals and Applications*. Wiley, 2004
- [12] Gabbot P. *Principles and Applications of Thermal Analysis*. Wiley-Blackwell, 2007
- [13] Williams D. B.; Carter C. B. *Transmission Electron Microscopy*, Springer 2009, Volumes 1-4
- [14] Fadley C.S., *J. Electron. Spectrosc. Relat. Phenom.* 2010, 178-179, 2-32
- [15] Sing et.al, *Pure & Appl. Chem.* 1985, 57:603-619
- [16] McElfresh M. *Fundamentals of Magnetism and magnetite Measurements*. Purdue University, 1994
- [17] Cullity B. D.; Graham C.D. *Introduction to Magnetic Materials*, Wiley-IEEE Press, 2008
- [18] *Elementi di risonanza magnetica*, Coriasco, Rampado, Boris Badrac, 2014
- [19] *MRI in practice*. Westbrook, Kauth Roth, Talbot, 2011
- [20] *Fundamentals of MRI*, Berry, Bulpitt, 2008

BIBLIOGRAPHY CHAPTER 5

- [1] Giuliana Taglieri, Benito Felice, Valeria Daniele, Roberto Volpe and Claudia Mondelli. Analysis of the carbonatation process of nanosized $\text{Ca}(\text{OH})_2$ particles synthesized by exchange ion process. Proceedings of the Institution of Mechanical Engineers Part N Journal of Nanoengineering and Nanosystems 2014, 230(1)
- [2] Montes-Hernandez, G., Pommerol, A., Renard, F., et al. In situ kinetic measurements of gas–solid carbonation of $\text{Ca}(\text{OH})_2$ by using an infrared microscope coupled to a reaction cell. Chem. Eng. J. 2010, 161:250–256
- [3] Cizer, O., Rodriguez-Navarro, C., Ruiz-Agudo, E., et al. Phase and morphology evolution of calcium carbonate precipitated by carbonation of hydrated lime. J. Mater. Sci. 2012, 47:6151–6165
- [4] Ryski, Y.I. The infrared spectra of minerals. In: FARMER V.C. eds. Mineralogical society monograph 4: Mineralogical Society, London, 1974, 137–182
- [5] Montes-Hernandez, G., Pommerol, A., Renarda, F., et al. In situ kinetic measurements of gas–solid carbonation of $\text{Ca}(\text{OH})_2$ by using an infrared microscope coupled to a reaction cell. Chem. Eng. J. 2010, 161:250–256
- [6] Rodriguez-Blanco, J.D., Shaw, S., Benning, L.G. The kinetics and mechanisms of amorphous calcium carbonate (ACC) crystallization to calcite, via vaterite. Nanoscale 2011, 3:265
- [7] Rodriguez-Navarro, C., Suzuki, A., Ruiz-Agudo, E. Alcohol Dispersions of Calcium Hydroxide Nanoparticles for Stone Conservation. Langmuir 2013, 29:11457–11470
- [8] Vladimir Privman, Dan V. Goia, Jongsoon Park, Egon Matijevic. Mechanism of Formation of Monodispersed Colloids by Aggregation of Nanosize Precursors. J. Colloid and Interface Sci. 1999, 213:36-45
- [9] Jillian F. BanPeld, Susan A. Welch, Hengzhong Zhang, Tamara Thomsen Ebert, R. Lee Penn. Aggregation-Based Crystal Growth and Microstructure Development in Natural Iron Oxyhydroxide Biomineralization Products. Science 2000, 289(5480):751-754
- [10] Clarkson, R., Price, T.J., Adams, C.J. Role of metastable phases in the spontaneous precipitation of calcium carbonate. J. Chem. Soc., Faraday Trans 1992, 88:243–249
- [11] Tlili, M. M., Ben Amor, M., Gabrielli, C., et al. Characterization of CaCO_3 hydrates by micro-Raman spectroscopy. J. Raman Spectrosc. 2002, 33:10–16
- [12] Stepkowska, E.T., Aviles, M.A., Blanes, J.M., et al. Gradual Transformation of $\text{Ca}(\text{OH})_2$ into CaCO_3 on Cement Hydration. XRD study. Journal of Thermal Analysis and Calorimetry 2007, 87(1):189–198

- [13] Cizer, O., Van Balen, K., Elsen, J., et al. Crystal morphology of precipitated calcite crystals from accelerated carbonation of lime binders. Proceedings of ACEME08, 2nd International Conference on Accelerated Carbonation for Environmental and Materials Engineering, Rome, Italy, 2008:149-158
- [14] Chen, S.F., Yu, S.H., Jiang, J., et al. Polymorph Discrimination of CaCO₃ Mineral in an Ethanol/Water Solution: Formation of Complex Vaterite Superstructures and Aragonite Rods. Chem. Mater. 2006, 18:115– 122
- [15] Sand, K.K., Rodriguez-Blanco, J.D., Makovicky, E., et al. Crystallization of CaCO₃ in Water–Alcohol Mixtures: Spherulitic Growth, Polymorph Stabilization, and Morphology Change. Cryst. Growth Des. 2012, 12:842–853
- [16] Alvarez de Buergo, M., Fort, R. Structural stability of a colloidal solution of Ca(OH)₂ nanocrystals exposed to high relative humidity conditions. Appl. Phys. A 2011, 104:1249–1254

BIBLIOGRAPHY CHAPTER 6

- [1] R.P. Castellanza, R. Nova. Oedometric tests on artificially weathered carbonatic soft rocks. Journal of Geotechnical and Geoenvironmental Engineering 2004, 130(7):728-739
- [2] S. Ghabezloo, A. Pouya. Numerical modelling of the effect of weathering on the progressive failure of underground limestone mines. Multiphysics Coupling and Long Term Behaviour in Rock Mechanics: Proceedings of the International Symposium of the International Society for Rock Mechanics, Eurock 2006, Liège, Belgium
- [3] M.O. Ciantia et al. Effects of mineral suspension and dissolution on strength and compressibility of soft carbonate rocks, Engineering Geology 2015, 184:1-18
- [4] G.F. Andriani, N. Walsh. Rocky coast geomorphology and erosional processes: a case study along the Murgia coastline South of Bari, Apulia – SE Italy. Geomorphology 2007, 87:224–238
- [5] G.F. Andriani, N. Walsh. The effects of wetting and drying, and marine salt crystallization on calcarenite rocks used as building material in historic monuments. Geochem. Soc. Lond. Spec. Publ. 2007, 271:179–188
- [6] P. Tiano et al. Biomediated reinforcement of weathered calcareous stones. Journal of Cultural Heritage 2006, 7(1):49-55
- [7] G.G. Amoroso, V. Fassina. Stone decay and conservation. Material Science Monographs 11, Elsevier, Amsterdam (1983)

- [8] M. Ioele, U. Santamaria, P. Tiano. Comparative study of commercial ethyl silicates and testing in comparison with acrylic microemulsions for the consolidation of matrices carbonates strongly decayed. *International Congress Silicates in the Conservation 2002*, 121-128
- [9] M. Licchelli et al. Nanoparticles for conservation of bio-calcarene stone *Appl. Phys. A* 2014, 114(3):673-683
- [10] Young M.E., Murray M., Cordiner P. *Stone consolidants and chemical treatments in Scotland*. Edinburgh: Historic Scotland, 1999
- [11] Steinemann A. Volatile emissions from common consumer products. *Air Qual Atmos Health* 2015, 8(3):273-281
- [12] Bennardo C. et al. Comparative study of different methods for gap filling applications and use of adhesive on the biocalcarene surfaces of the "Tempio della Concordia" in Agrigento. 9th Intern. Congress on deterioration and conservation of stone, Elsevier, 2000
- [13] Cotecchia V., D'Ecclesiis G., Polemio M. La dinamica dei versanti della Valle dei Templi di Agrigento. *Geol. Appl. Idrogeol.* 1995, XXX (I), 369-383
- [14] Andriani G.F., Walsh N. Physical properties and textural parameters of calcarenitic rocks: qualitative and quantitative evaluations. *Eng. Geol.* 2002, 67:5-15
- [15] Lindqvist J.E., Åkesson U., Malaga K. Microstructure and functional properties of rock materials. *Mater. Charact.* 2007, 58:1183-1188
- [16] Taglieri G., Daniele V., Macera L., Mondelli C. Nano Ca(OH)₂ synthesis using a cost-effective and innovative method: reactivity study. *J. Am. Ceram. Soc.* 2017, 100:5766-5778
- [17] Borsoi G, et al. Effect of solvent on nanolime transport within limestone: how to improve in-depth deposition. *Colloids Surf A* 2016, 497:171-181
- [18] Dei L., Salvadori B. Nanotechnology in cultural heritage conservation: nanometric slaked lime saves architectonic and artistic surface from decay. *J. Cult. Herit.* 2006, 7:110-115
- [19] Determinazione dell'assorbimento d'acqua per capillarità. UNI EN 15801 (2010).
- [20] ASTM D3359-02: "Standard test methods for measuring adhesion by tape test". ASTM International, 2002
- [21] Fratini F., et al. A new portable system for determining the state of conservation of monumental stones. *Mater. Struc.* 2006, 39(286):125-132
- [22] Henriques F.M.A., Charola A.E. Comparative study of standard test procedures for mortars. 8th International Congress on Deterioration and Conservation of Stone, Berlin, 1996
- [23] Montes-Hernandez G. et al. In-situ kinetic measurements of gas-solid carbonation of Ca(OH)₂ by using an infrared microscope coupled to a reaction cell. *Chemical Engineering Journal* 2010, 161:250-256

- [24] Rodriguez-Navarro C., Elert K., Ševčík R. Amorphous and crystalline calcium carbonate phases during carbonation of nanolimes: implications in heritage conservation. *Cryst Eng Comm.* 2016, 18:6594-6607
- [25] Sand K.K. et al. Crystallization of CaCO₃ in Water-Alcohol Mixtures: Spherulitic Growth, Polymorph Stabilization, and Morphology. *Cryst. Growth Des.* 2012, 12:842–853
- [26] Elisa Franzoni, Gabriela Graziani, Enrico Sassoni, Ginevra Bacilieri, Michele Griffa, Pietro Lura. Solvent-based ethyl silicate for stone consolidation: influence of the application technique on penetration depth, efficacy and pore occlusion. *Materials and Structures* 2015, 48:3503–3515
- [27] P. López-Arce, L.S. Gómez-Villalba, S. Martínez-Ramírez, M. Álvarez de Buergo, R. Fort. Influence of relative humidity on the carbonation of calcium hydroxide nanoparticles and the formation of calcium carbonate polymorphs. *Powder Technology* 2011, 205:263–269
- [28] L.S. Gomez-Villalba, P. López-Arce, R. Fort. Nucleation of CaCO₃ polymorphs from a colloidal alcoholic solution of Ca(OH)₂ nanocrystals exposed to low humidity conditions. *Appl Phys A* 2012, 106:213–217
- [29] L.S. Gomez-Villalba, P. López-Arce, M. Alvarez de Buergo, R. Fort. Structural stability of a colloidal solution of Ca(OH)₂ nanocrystals exposed to high relative humidity conditions. *Applied Physics A* 2011, 81049:1249
- [30] C. Rodriguez-Navarro, A. Suzuki and E. Ruiz-Agudo. Alcohol Dispersions of Calcium Hydroxide Nanoparticles for Stone Conservation. *Langmuir* 2013, 29:11457–11470
- [31] P. Lopez-Arce, A. Zornoza-Indart. Carbonation acceleration of calcium hydroxide nanoparticles induced by yeast fermentation. *Appl. Phys. A* 2015, 120(4):1475–1495
- [32] O. Cizer, C. Rodriguez-Navarro, E. Ruiz-Agudo, J. Elsen, D. Van Gemert, K. Van Balen. Phase and morphology evolution of calcium carbonate precipitated by carbonation of hydrated lime. *J Mater Sci* 2012, 47:6151–6165
- [33] W.G. Mook. Environmental isotopes in the hydrological cycle: Principles and applications. International Atomic Energy Agency and United Nations Educational, Scientific and Cultural Organization Vienna 2000, volume 1, chapter 9.
- [34] C. Zhu, H. Wang, G. Li, S. An, X. Ding, H.H. Teng, L. Zhao. CO₂ Absorption and Magnesium Carbonate Precipitation in MgCl₂–NH₃–NH₄Cl Solutions: Implications for Carbon Capture and Storage. *Minerals* 2017, 7:172
- [35] Boynton RS. Chemistry and Technology of Lime and Limestone. NY: Wiley edition, 1980
- [36] O. Carrier, N. Shahidzadeh-Bonn, et al. Evaporation of water: evaporation rate and collective effects. Cambridge University Press 2016, 798:774-786

- [37] A.P. Hammersley, S.O. Svensson, M. Hanfland, A. N. Fitch, D. Häusermann. Two-Dimensional Detector Software: From Real Detector to Idealised Image or Two-Theta Scan. *High Pressure Research* 1996, 14:235-248
- [38] W.M. Haynes, D.R. Lide, T.J. Bruno. *CRC Handbook of Chemistry and Physics*. CRC Press, 97st Edition, 2016-2017, Section 6
- [39] C. Rodriguez-Navarro, E. Ruiz-Agudo, M. Ortega-Huertas, et al. Nanostructure and Colloidal Behavior of Ca(OH)₂: implications for the Conservation of Cultural Heritage. *Langmuir* 2005, 21:10948-10957
- [40] Ö. Kirca. Ancient binding materials, mortars and concrete technology: history and durability aspects. Modena, Lourenço, Roca (Eds.), *Structural Analysis of Historical Constructions*, Taylor & Francis Group, London, 2005
- [41] N. Bianco et al. Hydraulic mortar and problems related to the suitability for restoration. *Period. Mineral.* 2013, 82(3):29–542
- [42] I. Papayianni. The longevity of old mortars. *Appl. Phys. A* 2006, 83:685–688
- [43] R.P.J. Van Hees, L. Binda, I. Papayianni, E. Tombbakari. Damage analysis as a step towards compatible repairs mortars. RILEM Report 28, in: C. Groot, G. Ashall, J. Hughes (Eds.), *RILEM TC COM 167: Characterization of Old Mortars respect to their Repair*, RILEM Publications S.A.R.L, France, 2005
- [44] L. Toniolo, A. Paradisi, S. Goidanich, G. Pannati. Mechanical behaviour of lime based mortars after surface consolidation. *Constr. Build. Mater.* 2011, 25:1553–1559
- [45] E. Hansen et al. A review of selected inorganic consolidants and protective treatment for calcareous materials. *Rev. Conserv.* 2003, 4:13–25
- [46] A.H.P. Maurenbrecher. Mortars for repair of traditional masonry. *Prac. Period. Struct. Des. Constr.* 2004, 9(2):62–65
- [47] P.J. van Hees. Damage diagnosis and compatible repair mortars Paisley, Scotland. *Proceeding of the International Rilem Workshop, Historic Mortars: Characterisation and Tests*, 2000, pp. 27–36
- [48] A. Steinemann. Volatile emissions from common consumer products. *Air Qual. Atmos. Health* 2015, 8(3):273–281
- [49] J.L. Hull. *Can Nanolime Stone Consolidations Offer a Feasible Conservation Method for Limestone Ecclesiastical Buildings*. Dissertation A-UBILF3-20-3. University of the West of England, Bristol, 2012
- [50] Cultural heritage. Petrographic description of a mortar. UNI 11176, 2006

- [51] F. Casadio, G. Chiari, S. Simon. Evaluation of binder/aggregate ratios in archaeological lime mortars with carbonate aggregate: a comparative assessment of chemical, mechanical and microscopic approaches. *Archaeometry* 2005, 47(4):671–689
- [52] Malte storiche. Linee guida per la caratterizzazione mineralogico-petrografica, fisica e chimica delle malte. UNI 11305, 2009
- [53] G. Borsoi et al. Application protocol for the consolidation of calcareous substrates by the use of nanolimes: from laboratory research to practice. *Restor. Build. Monuments* 2016, 22(4–6):99–109
- [54] G. Borsoi, B.A. Lubelli, R.P.J. van Hees, R. Veiga, A.S. Silva, L. Colla, L. Fedele. Effect of solvent on nanolime transport within limestone: how to improve in- depth deposition. *Colloids Surface A* 2016, 497:171–181
- [55] G. Borsoi, R. van Hees, B. Lubelli, R. Veiga, A. Santos Silva. Nanolime deposition in Maastricht limestone: back-migration or accumulation at the absorption surface. 15th Euroseminar on Microscopy Applied to Building Materials, 2015 Delft, The Netherlands

BIBLIOGRAPHY CHAPTER 7

- [1] H.E. Schwiete, T. Iwai. The behavior of the ferritic phase in cement during hydration, *Zement-Kalk-Gips* 1964, 17:379-386
- [2] Xiaoming Wang, Mengqiang Zhu, Luuk K. Koopal, Wei Li, Wenqian Xu, Fan Liu, Jing Zhang, Qingsong Liu, Xionghan Feng, Donald L. Sparks. Effects of crystallite size on the structure and magnetism of ferrihydrite. *Environmental Science: Nano* 2016, 1
- [3] J.J. García-Sánchez, M. Solache-Ríos, V. Martínez-Miranda, I. Rodríguez-Torres. Removal of fluoride ions by calcium hydroxide-modified iron oxides. *Desalination and Water Treatment* 2017, 94:31–39
- [4] L. Ruiping, L. Xing, X. Shengji, Y. Yanling, W. Rongcheng, L. Guibai. Calcium-Enhanced Ferric Hydroxide Co-Precipitation of Arsenic in the Presence of Silicate. *Water Environment Research* 2007, 79(11):2260 – 2264
- [5] Z. Li, T. Zhang, K. Li. One-step synthesis of mesoporous two-line ferrihydrite for effective elimination of arsenic contaminants from natural water. *Dalton Trans.* 2011, 40:2062–206620
- [6] K. Rout, M. Mohapatra, S. Anand. 2-line ferrihydrite: Synthesis, characterization and its adsorption behaviour for removal of Pb(II), Cd(II), Cu(II) and Zn(II) from aqueous solutions. *Dalton Trans.* 2012, 41:3302–3312

- [7] K.J. Farley, D.A. Dzombak, F.M.M. Morel. A surface precipitation model for the sorption of cations on metal oxides. *Journal of Colloid and Interface Science* 1985, 106:226-242
- [8] H. Mao, B. He, W. Guo, L. Hua, Q. Yang. Effects of Nano-CaCO₃ Content on the Crystallization, Mechanical Properties, and Cell Structure of PP Nanocomposites in Microcellular Injection Molding. *Polymers* 2018, 10:1160
- [9] S. Dev Maurya, M. Purushothaman, P. Santhana, G. Krishnan, S.K. Nayak. Effect of nano-calcium carbonate content on the properties of poly(urethane methacrylate) nanocomposites. *Journal of Thermoplastic Composite Materials* 2014, 27(12):1711-1727
- [10] P. Liu, M. Zhao, G. Guo. Thermal Stabilities of Poly(Vinyl Chloride)/Calcium Carbonate (PVC/CaCO₃) Composites. *Journal of Macromolecular Science Part B* 2006, 45(6)
- [11] G. Borsoi, M. Tavares, M.D.R. Veiga, A. Santos Silva. Microstructural Characterization of Consolidant Products for Historical Renders: An Innovative Nanostructured Lime Dispersion and a More Traditional Ethyl Silicate Limewater Solution. *Microsc. Microanal.* 2012, 18:1181–1189
- [12] Natural stone test methods—determination of resistance to salt crystallization. UNI EN 12370, 2001
- [13] E. Sassoni, G. Graziani, E. Franzoni. An innovative phosphate-based consolidant for limestone. Part 2: Durability in comparison with ethyl silicate. *Construction and Building Materials* 2016, 102:931–942
- [14] P. López-Arce, L.S. Gomez-Villalba, L. Pinho, M.E. Fernández-Valle, M. Álvarez de Buergo, R. Fort. Influence of porosity and relative humidity on consolidation of dolostone with calcium hydroxide nanoparticles: effectiveness assessment with non-destructive techniques. *Mater Charact* 2010, 61:168-184
- [15] B. Lubelli, R.P.J. van Hees, T.G. Nijland. Salt weathering damage: how realistic are existing ageing tests. H. De Clercq (Ed.), *Proceedings of SWBSS2014, 3rd International Conference on Salt Weathering of Buildings and Stone sculptures*, 2014, 259-273

BIBLIOGRAPHY CHAPTER 8

- [1] S. Junaid S. Qazi, Adrian R. Rennie, et al. Use of wide-angle X-ray diffraction to measure shape and size of dispersed colloidal particles. *Journal of Colloid and Interface Science* 2209, 338:105–110
- [2] C. Rodriguez-Navarro, E. Ruiz-Agudo, M. Ortega-Huertas, et al. Nanostructure and Colloidal Behavior of Ca(OH)₂: implications for the Conservation of Cultural Heritage. *Langmuir* 2005, 21:10948-10957

- [3] G. Taglieri, B. Felice, V. Daniele, F. Ferrante. Mg(OH)₂ nanoparticles produced at room temperature by an innovative, facile, and scalable synthesis route. *J Nanopart Res* 2015, 17:411-424
- [4] M.M. Rahmana, M.A.M. Salleha, U. Rashida, A. Ahsana, M.M. Hossain, C.S. Rae. Production of slow release crystal fertilizer from wastewaters through struvite crystallization-a review. *Arab J Chem* 2014, 7(1):139–155
- [5] M. Sain, S.H. Park, F. Suhara, S. Law. Flame retardant and mechanical properties of natural fibre–PP composites containing magnesium hydroxide. *Polym Degrad Stab* 2004, 83:363–367
- [6] S. Gryglewicz. Alkaline and alkaline-earth compounds as alcoholysis catalysts for ester oils synthesis. *Applied Catalysis A: General* 2000, 192:23-28
- [7] C. Dong, J. Cairney, Q. Sun, O. Lee Maddan, G. He, Y. Deng. Investigation of Mg(OH)₂ nanoparticles as an antibacterial agent. *J Nanopart Res* 2010, 12:2101–2109
- [8] L. Kumari, W.Z. Li, et al. Synthesis, characterization and optical properties of Mg(OH)₂ micro-/nanostructure and its conversion to MgO. *Ceramics International* 2009, 35:3355–3364
- [9] Y. Duan, D.C. Sorescu. CO₂ capture properties of alkaline earth metal oxides and hydroxides: A combined density functional theory and lattice phonon dynamics study. *The Journal of Chemical Physics* 2010, 133:074508
- [10] G. Arzamendi, E. Arguiñarena, et al. Alkaline and alkaline-earth compounds as catalysts for the methanolysis of sunflower oil. *Catalysis Today* 2008, 133-135:305-313
- [11] E.J. Schofield, R. Sarangi, et al. Strontium carbonate nanoparticles for the surface treatment of problematic sulfur and iron in waterlogged archaeological wood. *J. of Cultural Heritage* 2016, 18:306–312
- [12] R. Giorgi, M., et al. Nanoparticles of Mg(OH)₂: synthesis and application to paper conservation. *Langmuir* 2005, 21:8495–8501
- [13] A. Sierra-Fernandez, L.S. Gomez-Villalba, et al. New nanomaterials for applications in conservation and restoration of stony materials: a review. *Materiales de Construcción* 2017, 67(325):107
- [14] G. Taglieri, V. Daniele, G. Rosatelli, S. Sfarra, M.C. Mascolo, C. Mondelli. Eco-compatible protective treatments on an Italian historic mortar (XIV century). *J. of Cultural Heritage* 2017, 25:135-141
- [15] K.M. Saoud, I. Ibala, D. El Ladki, O. Ezzeldeen, S. Saeed. Microwave Assisted Preparation of Calcium Hydroxide and Barium Hydroxide Nanoparticles and Their Application for Conservation of Cultural Heritage, in: Ioannides M., Magnenat-Thalmann N., Fink E., Žarnić R., Yen AY., Quak E. (eds) *Digital Heritage. Progress in Cultural Heritage: Documentation,*

Preservation, and Protection. EuroMed 2014. Lecture Notes in Computer Science, vol 8740. Springer, Cham. (2014)

[16] Fojutowski, A.; Wróblewska, H.; Komorowicz, M.; Kropacz, A.; Noskowiak, A.; Pomian, I. Changes in the properties of English oak wood (*Quercus robur* L.) as a result of remaining submerged in Baltic Sea waters for two years. *Int. Biodeterior. Biodegrad.* 2014, 86B:122–128

[17] Gjelstrup Björdal, C. Microbial degradation of waterlogged archaeological wood. *J. Cult. Herit.* 2012, 13:118–122

[18] Almkvist, G.; Hocker, E.; Sahlstedt, M. *Iron Removal from Waterlogged Wood*; Swedish University of Agricultural Sciences: Uppsala, Sweden, 2013

[19] Stramm, J.A. Dimensional stabilization of Wood with Carbowaxes. In *Forest Products Research Society*; Box, P.O., Ed.; University Station: Madison, WI, USA, 1956; 5:201–204

[20] Steinemann, A. Volatile emissions from common consumer products. *Air Qual. Atmos. Health* 2015, 8:273–281

[21] Giorgi, R.; Chelazzi, D.; Baglioni, P. Nanoparticles of calcium hydroxide for wood conservation. The deacidification of the Vasa warship. *Langmuir* 2005, 21:10743–10748

[22] Giorgi, R.; Chelazzi, D.; Baglioni, P. Conservation of acid waterlogged shipwrecks: Nanotechnologies for de-acidification. *Appl. Phys. A* 2006, 83:567–571

[23] Gibson, L.J. The hierarchical structure and mechanics of plant materials. *J. R. Soc. Interface* 2012, 9:2749–2766

[24] Falk, R.H. *Wood Handbook, Wood as an Engineering Material*. U.S. Department of Agriculture, Forest Products Laboratory: Hanover, NH, USA, 2010

[25] Kránitz, K.; Sonderegger, W.; Bues, C.T.; Niemz, P. Effects of aging on wood: A literature review. *Wood Sci. Technol.* 2016, 50:7–22

[26] Poggi, G.; Toccafondi, N.; Chelazzi, D.; Canton, P.; Giorgi, R.; Baglioni, P. Calcium hydroxide nanoparticles from solvothermal reaction for the deacidification of degraded waterlogged wood. *J. Colloid Interface Sci.* 2016, 473:1–8

[27] Giorgi, R.; Chelazzi, D.; Baglioni, P. Conservation of acid waterlogged shipwrecks: Nanotechnologies for de-acidification. *Appl. Phys. A* 2006, 83:567–571

[28] Andriulo, F.; Braovac, S.; Kutzke, H.; Giorgi, R.; Baglioni, P. Nanotechnologies for the restoration of alum- treated archaeological wood. *Appl. Phys. A* 2016, 122

[29] Mark A. Shand. *The Chemistry and Technology of Magnesia*, Wiley online library, 2006

[30] R. Kumaran et al. In Vitro Cytotoxic Evaluation of MgO Nanoparticles and Their Effect on the Expression of ROS Genes. *Int. J. Mol. Sci.* 2015, 16:7551-7564

[31] Sun et al. Cytotoxicity, permeability, and inflammation of metal oxide nanoparticles in human cardiac microvascular endothelial cells. *Cell Biol Toxicol* 2011, 27:333–342

- [32] A. Chalkidou, K. Simeonidis, M. Angelakeris, T. Samaras, C. Martinez-Boubeta, L.I. Balcells, K. Papazisis, C. Dendrinou-Samara, O. Kalogirou. In vitro application of Fe/MgO nanoparticles as magnetically mediated hyperthermia agents for cancer treatment. *Journal of Magnetism and Magnetic Materials* 2011, 323:775–780
- [33] D. Di, Z. He, Z. Sun, J. Liu. A new nano-cryosurgical modality for tumor treatment using biodegradable MgO nanoparticles. *Nanomedicine: Nanotechnology, Biology, and Medicine* 2012, 8:1233–1241
- [34] K. Krishnamoorthy, J. Y. Moon, H. B. Hyun, S. K. Cho, S. J. Kim. Mechanistic investigation on the toxicity of MgO nanoparticles toward cancer cells. *J. Mater. Chem.* 2012, 22:24610
- [35] J. Ying, T. Zhang, M. Tang. Metal Oxide Nanomaterial QNAR Models: Available Structural Descriptors and Understanding of Toxicity Mechanisms. *Nanomaterials* 2015, 5:1620-1637
- [36] A. Manke, L. Wang, Y. Rojanasakul. Mechanisms of Nanoparticle-Induced Oxidative Stress and Toxicity. *BioMed Research International* 2013, Article ID 942916
- [37] Y. Huang, C. Wu and R. S. Aronstam. Toxicity of Transition Metal Oxide Nanoparticles: Recent Insights from in vitro Studies. *Materials* 2010, 3:4842-4859
- [38] www.cancer.gov/publications/dictionaries/cancer-terms/def/cytotoxic-agent
- [39] R. S. Kumaran, Y. Choi, V. Singh, H. Song, K. Song, K. J. Kim, H.J. Kim. In Vitro Cytotoxic Evaluation of MgO Nanoparticles and Their Effect on the Expression of ROS Genes. *Int. J. Mol. Sci.* 2015, 16:7551-7564
- [40] K. Krishnamoorthy, J. Y. Moon, H. B. Hyun, S. K. Cho, S. J. Kim. Mechanistic investigation on the toxicity of MgO nanoparticles toward cancer cells. *J. Mater. Chem.* 2012, 22:24610
- [41] <https://www.aatbio.com/tools/ic50-calculator/>
- [42] Moustafa et al. Synthesis of MgO Nanoparticles from Different Organic Precursors; Catalytic Decontamination of Organic Pollutants and Antitumor Activity. *J Material Sci Eng* 2017, 6:4

BIBLIOGRAPHY CHAPTER 9

- [1] M. Cornell, U. Schwertmann, *The Iron Oxides: Structure, Properties, Reactions, Occurrences and Uses*, Second Edition, Weinheim, Wiley-VCH, 2003
- [2] C. Fu, N.M. Ravindra. Magnetic iron oxide nanoparticles: synthesis and applications, *Bioinspir. Biomim. Nan.* 2012, 1(4):229-244
- [3] L. Daishun, N. Lee, T. Hyeon. Chemical Synthesis and Assembly of Uniformly Sized Iron Oxide Nanoparticles for Medical Applications, *Acc. Chem. Res.* 2015, 48(5):1276-1285

- [4] M.M. Lin, H. Kim, M. Mohammad. Iron oxide nanomagnets in nanomedicine: fabrication and applications. *Nano Rev.* 2010, 1:1-17
- [5] G. Xinglong, W. Guoxiu, P. Jinsoo, L. Hao, Y. Juan. Monodisperse hematite porous nanospheres: synthesis, characterization, and applications for gas sensors. *Nanotechnology* 2008, 19(12):125606
- [6] S. Chaudharia, M. Srinivasan. 1D hollow α -Fe₂O₃ electrospun nanofibers as high performance anode material for lithium ion batteries. *J. Mater. Chem.* 2012, 22(43):23049-23056
- [7] H. Hashimoto, M. Ukita, R. Sakuma, M. Nakanishi, T. Fujii, N. Imanishi, J. Takada. Bio-inspired 2-line ferrihydrite as a high-capacity and high-rate-capability anode material for lithium-ion batteries. *J. Power Sources* 2016, 328(1):503-509
- [8] N. Pariona, A. Martinez, H. Hdz-Garci, L. Cruz, A. Hernandez-Valdes. Effects of hematite and ferrihydrite nanoparticles on germination and growth of maize seedlings. *Saudi J. Biol. Sci.* 2017, 24(7):1547-1554
- [9] M. Mohapatra, S. Anand, Synthesis and applications of nano-structured iron oxides/hydroxides – a review, *Int. J. Eng. Sci. Technol.* 2010, 2(8):127-146
- [10] T. Sulistyaningsih, S.J. Santosa, D. Siswanta, B. Rusdiarso, Synthesis and Characterization of Magnetites Obtained from Mechanically and Sonochemically Assisted Co-precipitation and Reverse Co-precipitation Methods, *Int. J. Mater. Mech. Manuf.* 2017, 5(1):16-19
- [11] G. Schikorr, Über die Reaktionen zwischen Eisen, seinen Hydroxyden und Wasser, *Z Elektrochem.* 1929, 35:65–70
- [12] P. Chagas, A.C. da Silva, E.C. Passamani, J.D. Ardisson, L.C. Alves de Oliveira, et al., δ -FeOOH: a superparamagnetic material for controlled heat release under AC magnetic field, *J. Nanoparticle Res.* 2013, 15:1544
- [13] Z. Li, T. Zhang, H. Li, One-step synthesis of mesoporous two-line ferrihydrite for effective elimination of arsenic contaminants from natural water, *Dalton Trans.*, 40(9) (2011) 2062-2066
- [14] Hausner, D.; Bhandari, N.; Pierre-Louis, A.; Kubicki, J.; Strongin, D. Ferrihydrite reactivity toward carbon dioxide. *J. Colloid Interface Sci.* 2009, 337:492–500
- [15] Rahman, M.; Khan, S.; Jamal, A.; Faisal, A.; Aisiri, A. Iron Oxide Nanoparticles. *Nanomaterials* 2011
- [16] Zhu, B.S.; Jia, Y.; Jin, Z.; Sun, B.; Luo, T.; Kong, L.; Liu, J.H. A facile precipitation synthesis of mesoporous 2-line ferrihydrite with good removal properties. *RSC Adv.* 2015, 103:84389
- [17] Greczynski, G.; Hultman, L. X-ray photoelectron spectroscopy: Towards reliable binding energy referencing. *Prog. Mater. Sci.* 2020, 107:100591

- [18] Miller, D.; Biesinger, M.; Mc Intyre, N. Interactions of CO₂ and CO at fractional atmosphere pressures with iron and iron oxide surfaces: One possible mechanism for surface contamination. *Surf. Interface Anal.* 2002, 33:299–305
- [19] D'Archivio, A.; Maggi, M.; Odoardi, A.; Santucci, S.; Passacantando, M. Adsorption of triazine herbicides from aqueous solution by functionalized multiwall carbon nanotubes grown on silicon substrate. *Nanotechnology* 2018, 29:065701
- [20] Scarselli, M.; Limosani, F.; Passacantando, M.; D'Orazio, F.; Nardone, M.; Cacciotti, I.; Arduini, F.; Gautron, E.; De Crescenzi, M. Influence of Iron Catalyst in the Carbon Spheres Synthesis for Energy and Electrochemical Applications. *Adv. Mater. Interfaces* 2018, 5:1800070
- [21] Preisinger, M.; Krispin, M.; Rudolf, T.; Horn, S.; Strongin, D. Electronic structure of nanoscale iron oxide particles measured by scanning tunneling and photoelectron spectroscopies. *Phys. Rev. B* 2005, 71:165409
- [22] A. Yu Polyakov, A.E. Goldt, T.A. Sorkina, I.V. Perminova, D.A. Pankrato, E.A. Goodilin, Y.D. Tretyakov. Constrained growth of anisotropic magnetic δ -FeOOH nanoparticles in the presence of humic substances. *Crys. Eng. Comm.* 2012, 14:8097-8102
- [23] X. Zhang, Y. Chen, N. Zhao, H. Liuac, Y. Wei. Citrate modified ferrihydrite microstructures: facile synthesis, strong adsorption and excellent Fenton like catalytic properties, *RSC Adv.* 2014, 41:21575-21583
- [24] A.K. Patra, D. Ki., Smart Design of Self-Assembled Mesoporous α -FeOOH Nanoparticles: High-Surface-Area Sorbent for Hg₂⁺ from Wastewater. *ACS Sustain. Chem. Eng.* 2017, 5(2):1272-1279
- [25] M. Thommes, K. Kaneko, A.V. Neimark, J.P. Olivier, F. Rodriguez-Reinoso, J. Rouquerol, K.S.W. Sing. Physisorption of gases, with special reference to the evaluation of surface area and pore size distribution (IUPAC Technical Report). *Pure Appl. Chem.* 2015, 87(9-10)
- [26] F. Ambroz, T. Macdonald, V. Martis, I. Parkin. Evaluation of the BET Theory for the Characterization of Meso and Microporous MOFs. *Small methods* 2018, 2(11):1800173
- [27] M. Křížek, J. Pechoušek, J. Tuček, K. Šafařová, I. Medřík, L. Machala. Iron oxide nanoparticle powders with high surface area. *AIP Conf. Proc.* 2012, 1489(1):88
- [28] E. Di Iorio, C. Colombo, Z. Cheng, G. Capitani, D. Mele, G. Ventruti, R. Angelico. Characterization of magnetite nanoparticles synthesized from Fe(II)/nitrate solutions for arsenic removal from water. *J. Environ. Chem. Eng.* 2019, 7(2)102986
- [29] S.L. Iconaru, R. Guégan, C. Popa, M. Motelica-Heino, C.S. Ciobanu, D. Predoi. Magnetite (Fe₃O₄) nanoparticles as adsorbents for As and Cu removal. *Appl. Clay Sci.* 2016, 134:128-135
- [30] A. Mishra, R. Sundara. Nano magnetite decorated multiwalled carbon nanotubes: a robust nanomaterial for enhanced carbon dioxide adsorption. *Energy Environ. Sci.* 2011, 4(3):889-895

- [31] V. Srivastava, P.K. Singh, C.H. Weng, Y.C. Sharma. Economically viable synthesis of Fe₃O₄ nanoparticles and their characterization. *Pol. J. Chem. Technol.* 2011, 13(2):1-5
- [32] J. Soltis, J. Feinberg, B. Gilbert, R. Lee Penn. Phase transformation and particle-mediated growth in the formation of hematite from 2-line ferrihydrite. *Cryst. Growth Des.* 2016, 16(2):922-932
- [33] U.S. Khan, Amanullah, A. Manan, N. Khan, A. Mahmood, A. Rahim. Transformation mechanism of magnetite nanoparticles. *Materials Science-Poland* 2015, 33(2):278-285
- [34] I. Kazeminezhad, S. Mosivand. Phase Transition of Electrooxidized Fe₃O₄ to γ and α -Fe₂O₃ Nanoparticles Using Sintering Treatment. *Acta physica polonica A* 2014, 125(5):1210-1214
- [35] S.J.S. Qazi, A.R. Rennie, J.K. Cockcroft, M. Vickers. Use of wide-angle X-ray diffraction to measure shape and size of dispersed colloidal particles. *J. Colloid Interface Sci.* 2009, 338:105-110
- [36] M. Tadic, L. Kopanja, M. Panjan, J. Lazovic, B.V. Tadic, B. Stanojevic, L. Motte. Rhombohedron and plate-like hematite (α -Fe₂O₃) nanoparticles: synthesis, structure, morphology, magnetic properties and potential biomedical applications for MRI. *Mater. Res. Bull.* 2021, 133:111055
- [37] Y. Cudennec, A. Lecerf. The Transformation of Ferrihydrite into Goethite or Hematite, Revisited. *J. Solid State Chem.* 2006, 179:716-722
- [38] U. Schwertmann, J. Friedl, H. Stanjek. From Fe(III) Ions to Ferrihydrite and then to Hematite. *J. Colloid Interface Sci.* 1999, 209:215-223
- [39] N. Pariona, K.I. Camacho-Aguilar, R. Ramos-Gonzales, A.I. Martinez, M. Herrera-Trejo, E. Baggio-Saitkovitch. Magnetic and structural properties of ferrihydrite/hematite nanocomposite. *J. Magn. Magn. Mater.* 2016, 406:221-227
- [40] M. Thommes. Physical Adsorption Characterization of Nanoporous Materials. *Chem. Ing. Tech.* 2010, 82(7):1059-1073
- [41] S. Yu, J. Bo, L. FengLi, L. Jiegang. Structure and fractal characteristic of micro- and mesopores in low, middle-rank tectonic deformed coals by CO₂ and N₂ adsorption. *Microporous Mesoporous Mater.* 2017, 253:191–202
- [42] C. Shan, T. Zhang, X. Liang, Z. Zhang, M. Wang, K. Zhang, H. Zhu. On the fundamental difference of adsorption-pores systems between vitrinite- and inertinite-rich anthracite derived from the southern Sichuan basin, China. *J. Nat. Gas Sci. Eng.* 2018, 53:32–44
- [43] A. Dehbi, Y. Dehmani, H. Omari, A. Lammini, K. Elazhari, A. Abdallaoui. Hematite iron oxide nanoparticles (α -Fe₂O₃): Synthesis and modelling adsorption of malachite green. *J. Environ. Chem. Eng.* 2020, 8:10339

- [44] Soltis, J.A.; Feinberg, J.M.; Gilbert, B.; Lee Penn, R. Phase transformation and particle-mediated growth in the formation of hematite from 2-line ferrihydrite. *Cryst. Growth Des.* 2016, 16:922–932
- [45] Das, S.; Jim Hendry, M.; Essilfie-Dughan, J. Transformation of two-line ferrihydrite to goethite and hematite as a function of pH and temperature. *Environ. Sci. Technol.* 2011, 45, 268–275
- [46] Burrows, N.D.; Hale, C.R.; Lee Penn, R. Effect of pH on the kinetics of crystal growth by oriented aggregation. *Cryst. Growth Des.* 2013, 13:3396–3403
- [47] Jiang, Z.; Liu, Q.; Dekkers, M.; Barrón, V.; Torrent, J.; Roberts, A. Control of Earth-like magnetic fields on the transformation of ferrihydrite to hematite and goethite. *Sci. Rep.* 2016, 6:30395
- [48] Schwertmann, U.; Friedl, J.; Stanjek, H. From Fe(III) ions to Ferrihydrite and then to Hematite. *J. Colloid Interface Sci.* 1999, 209:215–2237
- [49] Földvári, M. Handbook of Thermogravimetric System of Minerals and Its Use in Geological Practice, 1st ed.; Geological Institute of Hungary: Budapest, Hungary, 2011
- [50] Schwaminger, S.; Surya, R.; Filser, S.; Wimmer, A.; Weigl, F.; Fraga-García, P.; Berensmeiern, S. Formation of iron oxide nanoparticles for the photooxidation of water: Alteration of finite size effects from ferrihydrite to hematite. *Sci. Rep.* 2017, 7:126097
- [51] Grosvenor, A.P.; Kobe, B.A.; Biesinger, M.C.; Mc Intyre, N.S. Investigation of multiplet splitting of Fe 2p XPS spectra and bonding in iron compounds. *Surf. Interface Anal.* 2004, 36:1564–1574
- [52] Pariona, N.; Camacho, K.; Ramos-González, R.; Martínez, A.; Herrera-Trejo, M.; Baggio-Saitovitch, E. Magnetic and structural properties of ferrihydrite/hematite nanocomposites. *J. Magn. Magn. Mater.* 2016, 406:221–227
- [53] Thommes, M.; Kaneko, K.; Neimark, A.; Olivier, J.P.; Rodríguez-Reinoso, F.; Rouquerol, J.; Stafford, K.; Sing, W. Physisorption of gases, with special reference to the evaluation of surface area and pore size distribution (IUPAC Technical Report). *Pure Appl. Chem.* 2015, 8:1429–1715
- [54] Stolyar, S.; Yaroslavtsev, R.; Bayukov, O.; Balaev, D.; Krasikov, A.; Iskhakov, R.; Vorotynov, A.; Ladygina, V.; Purtov, K.; Volochaev, M. Preparation, structure and magnetic properties of synthetic ferrihydrite nanoparticles. *J. Phys. Conf. Ser.* 2018, 994:012003
- [55] Villalobos, M.; Antelo, J. A unified surface structural model for ferrihydrite: Proton charge, electrolyte binding, and arsenate adsorption. *Rev. Int. Contam. Ambient.* 2011, 27:139–151
- [56] Pariona, N.; Camacho, K.; Ramos-González, R.; Martínez, A.; Herrera-Trejo, M.; Baggio-Saitovitch, E. Magnetic and structural properties of ferrihydrite/hematite nanocomposites. *J. Magn. Magn. Mater.* 2016, 406:221–227

[57] Gutiérrez, L.; Barrón, V.; Andrés-Vergés, M.; Serna, C.J.; Veintemillas-Verdaguer, S.; Morales, M.P.; Lázaro, F.J. Detailed magnetic monitoring of the enhanced magnetism of ferrihydrite along its progressive transformation into hematite. *J. Geophys. Res. Solid Earth* 2016, 121:4118–4129

[58] Chakrabarty, S.; Jana, T.; De, K.; Das, S.; Dey, K.; Chatterjee, K. Morphology dependent magnetic properties of α -Fe₂O₃ nanostructures. *Mater. Res. Express* 2014, 1:046104

BIBLIOGRAPHY CHAPTER 10

[1] *Magnetic Resonance Imaging: Physical Principles and Sequence Design*, 2nd edition. E.M. Haacke, M.R. Thompson, R. Venkatesan, R.W. Brown e Y.N. Cheng, Chichester, UK: John Wiley & Sons Ltd 2014, p. 976

[2] Ittrich et al. Superparamagnetic Iron Oxide Nanoparticles in Biomedicine: Applications and Developments in Diagnostics and Therapy. *Rofo* 2013, 185(12):1149-66